NBSIR 87-3067

TECHNICAL REPORTS

MATERIALS STUDIES FOR MAGNETIC FUSION ENERGY APPLICATIONS AT LOW TEMPERATURES -X

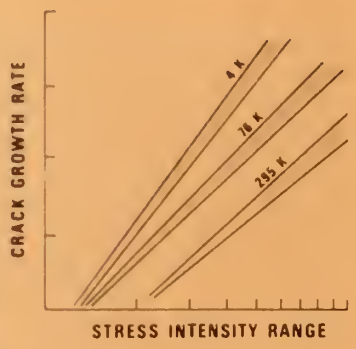

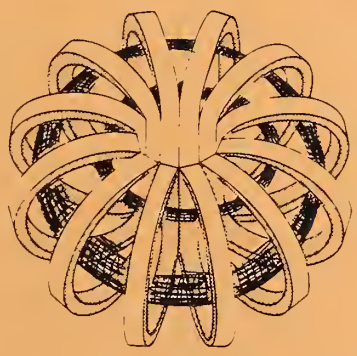

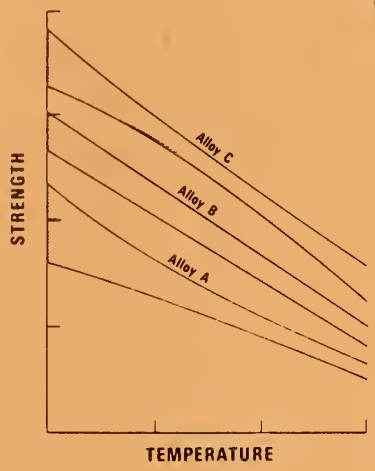

To
Department of Energy
Office of Fusion Energy
Washington, D.C. 20545

Prepared by
Fracture and Deformation Division
National Bureau of Standards
Boulder, Colorado 80303

NBSIR 87-3067

TECHNICAL REPORTS

MATERIALS STUDIES FOR MAGNETIC FUSION ENERGY APPLICATIONS AT LOW TEMPERATURES -X

Edited by

R.P. Reed
Fracture and Deformation Division
National Bureau of Standards
Boulder, Colorado 80303

May 1987

Sponsored by

Department of Energy
Office of Fusion Energy
Washington, D.C. 20545

U.S. DEPARTMENT OF COMMERCE, Malcolm Baldrige, Secretary

NATIONAL BUREAU OF STANDARDS, Ernest Ambler, Director

CONTENTS

SUMMARY

This report contains the results of a research program to determine the properties of materials that may be used in cryogenic structures for the superconducting magnets of magnetic fusion energy power plants and prototypes. Its purpose is to facilitate their design and development. The program was developed jointly by the staffs of the National Bureau of Standards and the Office of Fusion Energy of the Department of Energy; it is managed by NBS and sponsored by DOE. Research is conducted at NBS and at other laboratories through subcontracts with NBS.

Research results for 1986 are presented in technical papers under five headings that reflect the main program areas: Structural Alloys, Welding, Nonmetallics, Technology Transfer, and United States-Japan Cooperative Program. Objectives and research highlights are summarized in the introduction to each program area.

Note: Certain commercial equipment, instruments, or materials are identified in this report to specify the experimental procedure adequately. In a few instances, company names are used to identify the source of specific research. In no case does such identification imply recommendation or endorsement by the National Bureau of Standards, nor does it imply that the material or equipment identified is necessarily the best available for the purpose.

ORGANIZATIONAL CONTACTS

Specific technical questions may be directed to the following people, who contributed to major aspects of the program during the fiscal year 1987.

Department of Energy, Office of Fusion Energy, Washington, D.C. 20545

Program Monitor	V. K. Der	(301) 353-5736

National Bureau of Standards, Boulder, Colorado 80303

Program Manager	R. P. Reed	(303) 497-3870 (FTS) 320-3870
Structural Alloys	M. W. Austin	(303) 497-3504
	H. M. Ledbetter	(303) 497-3443
	P. T. Purtscher	(303) 497-5789
	R. P. Reed	(303) 497-3870
	N. J. Simon	(303) 497-3687
	R. L. Tobler	(303) 497-3421
Welding	C. N. McCowan	(303) 497-3480
	T. A. Siewert	(303) 497-3523
Nonmetallics	M. B. Kasen	(303) 497-3558
	R. D. Kriz	(303) 497-3547
Technology Transfer	R. P. Reed	(303) 497-3870
	N. J. Simon	(303) 497-3687

PROGRAM DESCRIPTION

The overall objective of the program is to assist in the design, construction, and safe operation of low-temperature magnetic fusion energy (MFE) systems, especially superconducting magnets, through effective materials research and materials technology transfer. The specific steps taken to achieve this objective are: (1) evaluation of the materials research needs specific to MFE devices; (2) development and monitoring of a research program to acquire the necessary data; and (3) rapid dissemination of the data to potential users through personal contacts, publications, and workshops.

Efforts directed at the first specific objective began with the publication of the "Survey of Low Temperature Materials for Magnetic Fusion Energy" in March 1977. A recent publication updating part of this survey, "Structural Alloys for Superconducting Magnets in Fusion Energy Systems," was included in volume IV (1981) of this series. In volume VI (1983), reviews of the properties of austenitic stainless steels and of austenitic-steel elastic constants also contributed to this objective. Through interactions with low-temperature design, construction, and measurement programs, such as the Large Coil Project and MFTF-B, we are aware of new problems as they arise. This year we have included for the first time results of research on copper and copper alloys, in support of Compact Ignition Tokamak designs by Princeton and Massachusetts Institute of Technology. Research projects contributing to the second objective are described in the technical papers. Again, research toward the establishment of test standards was emphasized. The third objective is satisfied, in part, by these annual reports and by the series of workshops on Materials at Low Temperatures. Since 1982, handbook pages presenting the available data for specific materials have been distributed to members of the magnetic fusion energy community who are involved with low-temperature materials.

STRUCTURAL ALLOYS

STRUCTURAL ALLOYS PROGRAM

LEADER: R. P. Reed
CONTRIBUTORS: M. W. Austin, S. A. Kim, H. M. Ledbetter, P. T. Purtscher, N. J. Simon, R. L. Tobler, R. P. Walsh

OBJECTIVES

- Development of strong, tough structural alloys for use in superconducting magnets
- Development of strong, fatigue-resistant structural alloys for use in pulsed superconducting magnets
- Development of effective codes and standards for low-temperature property measurements and structural design

RESEARCH HIGHLIGHTS

- The effects of strain rate on the tensile properties of three austenitic stainless steels at 4 K were examined. In the range 4.4×10^{-6} s^{-1} to 8.8×10^{-3} s^{-1}, strain rates less than 2.2×10^{-3} s^{-1} had no effect on tensile properties, and strain rates of 4.4×10^{-3} s^{-1} or larger reduced the ultimate tensile strength. Estimates of the work put into the specimen during deformation, the stored energy in terms of dislocations and dislocation interactions, and the dissipated heat were calculated. The reduction of tensile strength was associated with specimen warming (to 100 K), which was caused by the transition from nucleate to film-boiling heat transfer on the specimen surface.

- Mechanical properties and electrical resistivity of three copper alloys were measured at 4, 76, and 295 K. Effects of specimen orientation, load- and displacement-control tensile testing, degree of hardness, and grain structure and size were studied. Yield strengths were increased by cold-rolling, but at the expense of electrical conductivity, ductility, and toughness. Of the three alloys, CDA 104, 155, and 175, alloy 104 in the hard condition had the best combination of yield strength and electrical conductivity.

- The elastic constants of the CDA 104 and 155 copper alloys were studied semicontinuously between 295 and 4 K by ultrasonic methods. At 295 K, cold-rolling reduced the elastic stiffness of the alloys, reflecting changes in texture, nonpinned dislocation density, and anisotropic dislocation array; after this plastic deformation, the elastic constants showed time-dependent recovery. The dislocation-array anisotropy destroyed the usual $C_{ijkl} = C_{ijlk}$ macroscopic symmetry for the elastic shear stiffness, suggesting large, fictitious internal strains. Between

295 and 4 K, the elastic-constant temperature dependence of the deformed coppers approximated that of annealed texture-free copper.

- The effects of molybdenum and manganese on the elastic constants and volume of Fe–Cr–Ni alloys were studied. Molybdenum alloying caused unusual increases in volume that were attributed to changes in interatomic bonding. Molybdenum decreased the shear and Young's moduli and increased the bulk modulus and Poisson's ratio. Manganese produced predictable effects: it increased volume and decreased all the elastic-stiffness constants. For manganese, the 4-K alloying effect resembled the 295-K effect.

SUMMARY OF MECHANICAL PROPERTY MEASUREMENTS OF STRUCTURAL ALLOYS

Alloy [Designation]	Country of Supplier	Tensile 295-4 K	Elastic 295-4 K	Fracture Toughness 295, 76, 4 K	Fatigue Crack Growth Rate 295, 76, 4 K	Fatigue S-N 4 K	Report Volume* (page)
AUSTENITIC STEELS							
Fe-5Cr-25Mn-0.2C	Japan	VII					VII (65)
Fe-5Cr-26Mn	Japan		VI				VI (181)
Fe-13Cr-19Mn	USSR		III		VI		III (79) VI (41)
Fe-13Cr-22Mn-0.2N	Japan	VI					VII (65)
Fe-16Cr-8Ni-8Mn	U.S.	VIII		VIII			VIII (151,181)
Fe-17Cr-18Mn-0.5N	U.S.	VII, VIII		VIII			VII (65) VIII (181)
Fe-17Cr-9Ni-8Mn	U.S.		III				III (91)
Fe-17Cr-13Ni-2Mo [316]	U.S.	I,II, III,IV, VI,VIII, IX	VI	I,II, VIII, IX	II,VIII, IX	I	I (15,71) II (79) III (49,105,117) IV (147) V (185) VI (157) VIII (181,209,251) IX (15,27,43)
Fe-17Cr-13Ni-2Mo [316LN]	U.S.	II,IX		II,IX	II		II (79) IX (15,27,53)
Fe-18Cr-3Ni-13Mn	U.S.	I,VI, VIII	III	I,VIII	I,VI,VII		I (93) III (91) VI (53) VII (85) VIII (167,219)
Fe-19Cr-(6-15)Ni-4Mn-(0.1-0.3)N	USSR	VIII		VIII,IX			VIII (123) IX (53)
Fe-19Cr-9Ni [304]	U.S.	I,II, III,IV, VI,VII, IX	I,II, III,IV, VI,VII	I,II, III,IV, IX	II,III,IV		I (15,71,213) II (79,149,175) III (15,91,105,117 IV (37,101,203, 215,227) V (71) VI (73) VII (13,47,75,157) IX (27)
Fe-19Cr-9Ni [304L]	U.S.	II,III, IV,VIII, IX	I,II,IV	II,IV VIII,IX	III,IV, VIII		I (213) II (79,123,175) IV (37,101,131, 215,302) VIII (181,229,251) IX (27,141)

*MATERIALS STUDIES FOR MAGNETIC FUSION ENERGY APPLICATIONS AT LOW TEMPERATURES: NBSIR 78-884 (I); NBSIR 79-1609 (II); NBSIR 80-1627 (III); NBSIR 81-1645 (IV); NBSIR 82-1667 (V); NBSIR 83-1690 (VI); NBSIR 84-3000 (VII); NBSIR 85-3025 (VIII); NBSIR 86-3050 (IX).

SUMMARY OF MECHANICAL PROPERTY MEASUREMENTS OF STRUCTURAL ALLOYS, continued

Alloy [Designation]	Country of Supplier	Tensile 295-4 K	Elastic 295-4 K	Fracture Toughness 295, 76, 4 K	Fatigue Crack Growth Rate 295, 76, 4 K	Fatigue S-N 4 K	Report Volume* (page)
Fe-19Cr-9Ni-(1-10)Mn	U.S.	IV,V, VIII	V	IV,V,VIII, IX			IV (77) V (15,59,189) VIII (181) IX (53)
Fe-19Cr-9Ni-N [304N]	U.S.	I,III, IV,IX	IV	I,III,IV, IX	I,III,IV		I (93) III (15) IV (37,101,203, 215) IX (27)
Fe-19Cr-9Ni-N [304LN]	U.S.	II,III, IV,V,VI VIII,IX	IV,VIII	II,III,IV, VIII,IX	II,III,IV, VIII		II (35,79) III (15) IV (37,101,203) V (29) VI (113) VIII (181,207,229) IX (159)
Fe-19Cr-10Ni-(0.03-0.29)N-(0.03-0.09)C	U.S.	III,VIII	VIII,IX	III,VIII	III		III (15) VIII (145,181) IX (159)
Fe-20Cr-7Ni-8Mn [216]	U.S.	VIII		VIII			VIII (151,181)
Fe-20Cr-8Ni-2Mn [304HN]	U.S.	VIII		VIII			VIII (151,181)
Fe-20Cr-16Ni-6Mn	USSR	V,VI	V				V (29,213) VI (113)
Fe-21Cr-6Ni-9Mn	U.S.	I,VIII	III,VI	I,VIII		I	I (15,71) III (91) VI (157) VIII (151,181)
Fe-21Cr-12Ni-5Mn	U.S.	I,II	III	I,II	I,II		I (93) II (79) III (91)
Fe-25Cr-21Ni [310]	U.S.	V,VI, VII, VIII, IX	III,VI	V,VIII			III (105,117) V (71,145) VI (73) VII (65) VIII (181) IX (95)
Fe-19Ni-9Co [200-300 grades]	U.S.		IV				IV (237)
Reviews of Alloys		IV,V,VI	IV,V,VI	IV,V,VI	IV,V,VI,VII	IV, VI	IV (17,257), V (171) VI (11,127,157) VII (103)

*MATERIALS STUDIES FOR MAGNETIC FUSION ENERGY APPLICATIONS AT LOW TEMPERATURES: NBSIR 78-884 (I); NBSIR 79-1609 (II); NBSIR 80-1627 (III); NBSIR 81-1645 (IV); NBSIR 82-1667 (V); NBSIR 83-1690 (VI); NBSIR 84-3000 (VII); NBSIR 85-3025 (VIII); NBSIR 86-3050 (IX).

SUMMARY OF MECHANICAL PROPERTY MEASUREMENTS OF STRUCTURAL ALLOYS, continued

Alloy [Designation]	Country of Supplier	Tensile 295-4 K	Elastic 295-4 K	Fracture Toughness 295, 76, 4 K	Fatigue Crack Growth Rate 295, 76, 4 K	Fatigue S-N 4 K	Report Volume* (page)
ALUMINUM ALLOYS							
Al-6Cu-0.2Mn-0.1Fe [5083-O]	U.S.		II	II	II	II	II (19)
Al-0.6Fe-0.2Cu-0.1Si [1100]	U.S.	IX					IX (107)
Al-4Mg [5083-O]	U.S.	IV				II	II (35) IV (185)
COPPER ALLOYS							
99.99Cu-Ag [CDA 101,102]	U.S.	IX					IX (95,107)
SUPERCONDUCTORS							
Nb-45Ti	U.S.		III				III (133)

*MATERIALS STUDIES FOR MAGNETIC FUSION ENERGY APPLICATIONS AT LOW TEMPERATURES: NBSIR 78-884 (I); NBSIR 79-1609 (II); NBSIR 80-1627 (III); NBSIR 81-1645 (IV); NBSIR 82-1667 (V); NBSIR 83-1690 (VI); NBSIR 84-3000 (VII); NBSIR 85-3025 (VIII); NBSIR 86-3050 (IX).

TENSILE STRAIN-RATE EFFECTS IN LIQUID HELIUM*

R. P. Reed and R. P. Walsh
Fracture and Deformation Division
National Bureau of Standards
Boulder, Colorado

The effects of strain rate on tensile properties of three austenitic stainless steels at 4 K were examined. Strain rates ranged from 4.4×10^{-6} s^{-1} to 8.8×10^{-3} s^{-1}. Strain rates less than 2.2×10^{-3} s^{-1} had no effect on tensile properties. Strain rates of 4.4×10^{-3} s^{-1} or larger reduced the ultimate tensile strength, and stress-strain curves and temperature measurements indicated specimen warming to 100 K. Calculations are presented to estimate the work put into the specimen during deformation, stored energy in terms of dislocations and dislocation interactions, and dissipated heat. The reduction of tensile strength was associated with specimen warming, which was caused by the transition from nucleate to film-boiling heat transfer on the specimen surface.

INTRODUCTION -

Internal specimen heating effects during tensile tests at 4 K have been questioned for a long time. The very low specific heat and thermal conductivity of metals at low temperatures lead one to anticipate near-adiabatic conditions. Discontinuous yielding, a phenomenon in which very high strain rates are experienced in local regions (similar to Lüders band regions in steel at ambient temperatures), complicates the question, and the answer is prerequisite to the establishment of test standards.

Read and Reed[1] studied discontinuous yielding during tensile tests of alloy 304L at 4 K. Using embedded thermocouples and superconducting filaments in contact with the (flat) specimen surfaces, they showed that specimens heated locally to about 50 K during discontinuous yields. The yields occurred in bands, about 10^{-2} m wide, across the specimen. The specimen extension corresponding to a typical load drop was about 1.3×10^{-4} m. The temperature rise, confined to the strained regions, was adequately described by assuming adiabatic conditions, that is, all mechanical work was converted to heat. The temperature returned to 4 K following each discontinuous yield.

*Submitted to Advances in Cryogenic Engineering Materials—vol. 34.

Ogata and Ishikawa[2] studied the effects of strain rate on the tensile properties of austenitic stainless steels at 4 K. Strain rates were varied from 8.3×10^{-5} to 8.3×10^{-3} s^{-1} on 6.25-mm-diameter round specimens. They reported that the yield strength of alloy 304L was insensitive to strain rate; at strain rates less than 3×10^{-3} s^{-1}, its ultimate strength was also insensitive to strain rate; at strain rates above 3×10^{-2} s^{-1}, the ultimate strength decreased. They also measured the internal specimen temperature during deformation by inserting a thermocouple into a small hole drilled longitudinally into the specimen. Thermal spikes, associated with discontinuous yielding, occurred at the lower strain rates, and the magnitude of the thermal spikes increased with increasing strain rate. At the highest strain rate (3×10^{-2} s^{-1}), the temperature rose continuously from 4 to almost 150 K at failure. Temperature profiles for alloys 304L and 310 were similar, but larger thermal spikes were observed in alloy 304L. Temperature rises of about 50 K occurred during discontinuous yielding.

The same temperature rise during discontinuous yielding was observed by Dobson and Johnson.[3] For alloy 304L, they reported a steady decline of ultimate strength over their strain rate range, 3×10^{-5} to 3×10^{-3} s^{-1}, and a linear decrease of yield strength when it was plotted versus the log of strain rate.

Yamagami et al.[4] recently reported the tensile strain-rate sensitivity at 4 K of three Fe–21Mn–14Cr–7.5Ni (wt.%) austenitic alloys with varying N content (0.02 to 0.20 N) and grain size (42 to 284 μm). They measured temperature rises with embedded thermocouples at strain rates from 1.2×10^{-4} s^{-1} to 1.2×10^{-2} s^{-1}. Sudden spikelike temperature increases (up to about 40 K) were found at lower strain rates ($\leq 1.2 \times 10^{-4}$ s^{-1}). At higher strain rates, the temperature at the thermocouple rose and fell much more gradually, but in larger increments. At the larger strains and the highest strain rates, temperatures over 60 K were recorded, and the minimum temperature remained above 20 K. Associated with internal specimen heating, the ultimate strengths decreased at the higher strain rates (8×10^{-3}, 11.2×10^{-2} s^{-1}). They found that tensile yield strength was insensitive to low strain rates, but tended to decrease at strain rates greater than 5×10^{-3} s^{-1} if the yield strength exceeded about 1000 MPa. Two steels with yield strengths of less than 900 MPa showed no change in yield strength at higher strain rates. Thus, except for that of Dobson and Johnson, these studies support the premise that the strain rate sensitivity of yield strength depends on the magnitude of the yield strength: for stronger alloys, yield strengths decrease at higher strain rates.

This paper presents the results and analysis of the dependence of the tensile properties of three austenitic stainless steel alloys on strain rate at 4 K. Alloys 310, 316LN, and 304L were selected because of their varying yield strengths and austenite stabilities. Alloy 310, containing 25% Cr and 21% Ni, does not transform partially to body-centered-cubic martensite during plastic deformation at 4 K.[5] Alloy 304, containing only 18% Cr and 10% Ni with low N and C, has the least stable austenite and transforms almost completely to body-centered-cubic martensite during deformation at 76 K; at 4 K the transformation is not as complete.[5]

EXPERIMENTAL PROCEDURE

Specimens of alloys 310 and 304L were machined from 1.9-cm-diameter bar stock; specimens of alloy 316LN, from 5.0-cm-thick plate. Alloy 304L was tested in two conditions: annealed at 1066°C for 25 min (labeled 304L-A), and annealed at 1050°C for 45 min (labeled 304L-B). Microstructures of alloy 304L are shown in Fig. 1. Two groups of alloy 316LN were annealed at 1150°C for 1 h; 316LN-A had a larger grain size and inclusion density than 316LN-B (see Fig. 2). The 316LN-A specimens, taken from near the plate surface of the 5.0-cm-thick plate, had a N content of 0.167 wt.%; 316LN-B, from the interior, had a N content of 0.149 wt.%. Alloy 310 was tested in the partially sensitized condition; its microstructure is shown in Fig. 3. The chemical composition, hardness, and grain size of the alloys are listed in Table 1.

Round, tensile specimens (see Fig. 4) were machined to a 6.35-mm diameter along a gage length of 41.9 mm, increasing with a radius of 9.52 mm to 12.7-mm-diameter threaded ends. The entire specimen length was 71.4 mm.

The cryostat equipment has been described in reference 6. Tests at 4 K were conducted in boiling liquid He. New, high-elongation strain-gage extensometers that have been developed for use at low temperatures were used for these measurements. These extensometers, which are capable of sensitivities of 10^{-5}, have three flexing Al beams whose geometry enables sensing of specimen strain to elongations of over 30% at low temperatures. Four 350-Ω strain gages were mounted to each beam and wired in a Wheatstone bridge configuration. A 5-V dc power supply was used to supply the excitation. For maximum sensitivity (10^{-6}) at low strain, a set of three-beam strain-gage extensometers was also used for yield-strength determination. Elongation was measured over a specimen gage length of 3.8 cm.

Crosshead rates were varied from 0.001 $cm \cdot min^{-1}$ to 2 $cm \cdot min^{-1}$. Since measurements at the lowest strain rate took over four hours to reach the yield strength, these tests were not continued to specimen failure. Reported strain rates refer to the rate of plastic deformation within the reduced section of the specimens.

Type E (NiCr–Constantan) thermocouples were attached to some specimens for temperature measurements during straining. These fine (0.25-mm) wire thermocouples were first varnished, then taped, and finally clamped to the midsection of the specimen. They recorded specimen temperature throughout the tensile test in liquid He. By a similar technique, the same thermocouples were occasionally used to measure the temperature of the specimen grips. Magnetic readings of deformed specimens were obtained from a bar-magnet, torsion-balance, commercial magnetometer.

EXPERIMENTAL RESULTS

The dependences of ultimate and tensile yield strength on strain rate at 4 K are shown in Figs. 5 and 6. Notice the abrupt decrease of ultimate strength at strain rates greater than 2.2×10^{-3} s^{-1}. Yield strength remained almost independent of strain rate; with increasing strain rate, it increased slightly for alloys 310 and 316LN and decreased slightly for alloy 304L.

Reduction of area and tensile elongation are shown as a function of strain rate in Fig. 7. These ductility parameters were nearly independent of strain rate. Increased necking (higher reduction of area) appeared only at the higher strain rates. Tensile elongation gradually decreased with increasing strain rate. However, the considerable data scatter in both parameters weakens the evidence for clear trends.

For all alloys, the yield strength, elongation, and reduction of area were insensitive to strain rate. The ultimate strength of all alloys decreased at the same high strain rate and showed similar trends at lower rates.

The stress–strain curves at differing strain rates are shown in Figs. 8 through 10. At the lower two strain rates, discontinuous yielding is prominent. At the highest strain rate, discontinuous yielding is less evident, the curves have an erratic appearance, and reduction of ultimate strength is apparent. Clearly, the nature of the deformation process has changed. The onset of discontinuous yielding is dependent on both alloy and strain rate.

The dependences of ultimate strength on strain rate are similar despite differing modes of austenite fracture. In alloys 304L and 316LN, microvoids initiate at inclusion sites in the specimen interior and coalesce to form cracks (Figs. 11 and 12); usually a shear lip connects this interior region to the specimen surface to form some sort of "cup-cone" fracture morphology. Alloy 310 was partially sensitized (Fig. 13d), and as Fig. 13 (a and b) illustrates, its primary fracture path was intergranular. In Fig. 13c, notice the very fine microvoid sites within the grain boundary; presumably these initiate at the carbides.

The temperature measurements of one thermocouple attached to the central portion of the specimen surface of alloys 316L and 304LN are shown in Figs. 9 and 10. Notice the change from thermal spikes at lower strain rates to thermal waves at the highest strain rate. The thermal spikes are associated with individual discontinuous yielding events. The maximum temperature rise ranges from 50 to 85 K and varies with strain and strain rate, in agreement with earlier work.[1,4] The thermal waves, which gradually build up to temperatures as high as 96 K, are associated with the lack of discrete discontinuous yields and with the wavy nature of the stress–strain curves. The temperature rise of the surface, as measured here, is less than the internal temperature measured by Ogata and Ishikawa:[2] at high strain rates the internal temperature rises steadily to about 150 K; the surface temperature variation is wavelike, and maximum temperatures approach about 100 K.

The transformed body-centered-cubic (α') martensite in austenitic stainless steels is ferromagnetic; the parent austenite phase is paramagnetic. Magnetic readings were taken on deformed specimens to obtain relative amounts of α' martensite as a function of strain rate. The amount of α' formation is depends on elongation. The normalized results (magnetic readings per unit percent elongation) are reported as a function of strain rate in Fig. 14. The results are surprising: in alloy 304L the relative amount of α' martensite transformation increases with increasing strain rate, but in alloy 316LN, α' decreases with increasing strain rate.

DISCUSSION

The work of deformation (E_{def}) either remains stored in the specimen (E_{SE}) or is dissipated as heat (Q). Energy is stored primarily in dislocations created during plastic deformation and, in the process of work hardening, as interactive, dislocation stress fields. Heat is conducted from the deformed volume, through the specimen (Q_S), and to the liquid He via the specimen surface (Q_L).

The purpose of these calculations is to describe specimen heating at the higher strain rates, where ultimate strength suddenly decreases. In another paper we will describe localized, discontinuous yielding. We want to calculate or estimate the parameters E_{def}, E_{SE}, Q_S, and Q_L for tensile tests at two strain rates ($\dot{\epsilon}$) from the data of alloy 316LN (Figs. 5 and 9). From the experimental results at the strain rate of 2.2×10^{-3} s^{-1}, we assume that the average specimen temperature is 4 K. Thermal spikes are associated with discontinuous yielding. But, because of the local nature of the temperature spike, the specimen temperature relatively quickly returns to 4 K; the ultimate tensile strength is unaffected by these events. At the strain rate of 4.4×10^{-3} s^{-1}, however, the stress–strain curves and internal[2] and surface measurements indicate an overall increase of specimen temperature, affecting the stress–strain relationship and ultimate tensile strength.

For these calculations it is useful to consider energy per unit time, or the derivative of E_{def}, E_{SE}, and Q as a function of time. From Rönnpagel and Schwink,[7] $E_{def} = \dot{E}_{def}/\dot{\epsilon}$, $E_{SE} = \dot{E}_{SE}/\dot{\epsilon}$, and $Q = \dot{Q}/\dot{\epsilon}$. Then

$$\dot{E}_{def} = \dot{E}_{SE} + \dot{Q}, \qquad (1)$$

and energy is conserved at any instant of time.

Deformation Work

The work of deformation is the product of flow stress (σ_f), strain (ϵ), and volume of the deformed region (V): The rate of work of deformation, therefore, is

$$\dot{E}_{def} = \dot{\epsilon}\sigma_f V. \qquad (2)$$

The rate of work of deformation scales directly with flow strength, as seen in Eq. 2. Higher strength alloys require more work. Using the strain rate

immediately preceding the detection of thermal waves in the deforming 316LN specimen, 2.2×10^{-3} s^{-1}, and the ultimate tensile strength of 1650 MPa, we find that $\dot{E}_{def} = 2.9$ W. For the next highest strain rate tested, 4.4×10^{-3} s^{-1} (which produced thermal waves during deformation and a reduced ultimate strength, 1520 MPa), $\dot{E}_{def} = 5.5$ W. For these calculations, V is considered to be the entire specimen volume within the gage length (2.54 cm).

Stored Energy

The stored energy may be estimated as the sum of the elastic strain energy of the dislocations created during the deformation process and the long-range elastic internal stresses.[7]

$$\dot{E}_{SE} = \dot{N}E_d V + \dot{\varepsilon}\sigma_f^2 V/(2Y). \qquad (3)$$

Here, $\dot{N}$ is the rate of dislocation production, E_d is the dislocation strain energy, and Y is Young's modulus.

The strain energy of a dislocation is typically represented as:

$$E_d = (\mu b^2/4\pi k) \ln R/r_o \simeq \mu b^2, \qquad (4)$$

where μ is the shear modulus, b is the Burgers vector, k = 1 for screw dislocations, and $k = 1-\nu$ for edge dislocations (ν = Poisson's ratio). The term R/r_o is the ratio of the outer radius to the inner radius of the cylinder (about the dislocation core) through which strain energy is calculated.

The rate of energy to create dislocations, $\dot{N}E_d V$, is quite small. The plastic deformation of the test to failure of 316LN specimens at a strain rate of 2.2×10^{-3} s^{-1} lasts about 200 s, and an estimate of the maximum number of dislocations created during this test is 10^{16} dislocations per m^2. From the values $V = 1.2 \times 10^{-6}$ m^3 for our tensile specimens, $\mu = 81$ GPa for alloy 316LN at 4 K, and $b = 2 \times 10^{-10}$ m, $\dot{N}E_d V$ is about 0.2 W. The internal stress term is smaller, insignificant in these calculations.

From calorimetric measurements of deformed Cu at room temperature, the stored energy represents from 5 to 10% of the deformation energy at large strains.[8] Taking the higher percentage, because one would expect much less recovery at lower temperatures, we estimate that the stored energy is roughly 0.4 W for the high strain rate and 0.3 W for the lower strain rate. Therefore, the maximum possible calculated stored energy (from Eq. 3) is less than the probable experimental value of deformation work. Thus, either significant work is expended in creation of other defects, such as dislocation loops,[7] vacancies, or interstitials, or other forms of the long-range stress fields must be considered. Also, since the total stored energy is relatively small compared with the work of deformation, considerable heat must be removed from the specimen during a tensile test.

Heat Conduction Through a Solid

The conductance of heat along the specimen, assuming a uniform temperature gradient across the specimen, is represented as:

$$\dot{Q}_s = 2KA\Delta T/\Delta x, \qquad (5)$$

with K, the thermal conductivity; A, the cross-sectional area; ΔT, the temperature change over Δx, the distance of conduction. A factor of two is included since heat is conducted to both ends of the specimen. At the strain rate 2.2×10^{-3} s^{-1}, the bulk temperature is assumed to be 4 K, discounting localized thermal spikes that do not affect the ultimate tensile strength. Thus, $\dot{Q}_s$ for the lower strain rate is zero. At the strain rate of 4.4×10^{-3} s^{-1}, the bulk temperature at fracture is assumed to be 150 K, from the internal temperature measurements of Ogata and Ishikawa.[2] The temperature gradient is estimated to occur from the fracture surface to the specimen grips. During strain-rate change experiments,[6] small temperature increases of less than 1 K were occasionally detected by thermocouples attached to the grip. Considering that the maximum internal temperature, measured at 150 K, is associated with specimen necking, Δx is approximately 2.5×10^{-2} m and the specimen cross-sectional area is 0.32×10^{-4} m^2. For a temperature gradient of 150 K, we assume an average thermal conductivity for alloy 316LN of 5.5 $W \cdot m^{-1} \cdot K^{-1}$.[9] From Eq. 5, one obtains $\dot{Q}_s = 2.1$ W for $\dot{\epsilon} = 4.4 \times 10^{-3}$ s^{-1}.

Thus, at the high strain rate (4.4×10^{-3} s^{-1}), $\dot{E}_{def} - \dot{E}_{SE} - \dot{Q}_s = (5.5 - 0.4 - 2.1)$ W = 3.0 W, and at the lower strain rate (2.2×10^{-3} s^{-1}), $\dot{E}_{def} - \dot{E}_{SE} - \dot{Q}_s = (2.9 - 0.3)$ W = 2.6 W. These excess heat quantities must be conducted through the specimen surface to liquid He.

Solid-to-Liquid Heat Conduction

From the above calculation, most of the deformation work is apparently converted into heat and most of the heat conduction is to the liquid He rather than through the specimen. Heat conduction to the fluid, $\dot{Q}_L$, is

$$\dot{Q}_L = H_K A_s \Delta T, \qquad (6)$$

where H_K is the heat transfer coefficient at the solid-liquid surface and A_s is the surface area. In boiling liquid He at 4 K, H_K represents a bulk coefficient associated either with steady-state nucleate or film boiling from the solid surface. The conditions for nucleate or film boiling depend on the temperature difference and on the heat flux per unit area, $\dot{Q}/A_s$; these are portrayed in Fig. 15.[10] Thus, when $\dot{Q}/A_s > 1 \times 10^4$ $W \cdot m^{-2}$ or $\Delta T > 10$ K, film boiling is present at the specimen surface. The factor $\dot{Q}_L/A_s$ for high strain rate is $(\dot{E}_{def} - \dot{E}_{SE} - \dot{Q}_s)/A_s$ or 3.0 W/3×10^{-4} m^2 = 1.0×10^4 $W \cdot m^{-2}$. Since $\dot{Q}_L/A_s$ is about 1 and ΔT is approximately 100 K, Fig. 15 indicates that film boiling is predominant. For the lower strain rate $(\dot{E}_{def} - \dot{E}_{SE} - \dot{Q}_s)/A_s = 2.6$ W/3.0×10^{-4} m^{-2} = 0.87×10^4 $W \cdot m^{-2}$ and $\Delta T < 1$ K; in this regime nucleate boiling is prevalent. Thus, changing from the strain rate 2.2×10^{-3} s^{-1} to 4.4×10^{-3} s^{-1} results in a change

in the heat transfer mechanism to liquid He; nucleate boiling changes to film boiling. At the higher strain rate, heat transfer cannot keep up with heat input, and the tensile specimen warms considerably.

Since these calculations depend on the geometry and thermal conductivity of the specimen, they may not be applicable to other specimen shapes and materials. Alloys with higher thermal conductivities are expected to remain at 4 K at higher strain rates.

Martensitic Transformation

The divergence of the trends of percent α' martensite as a function of strain rate (Fig. 14) are, at first, perplexing. The probable explanation for the increased transformation of alloy 304L and decreased transformation of alloy 316LN at high strain rates must involve the temperature dependence of the strain-induced transformation. We have shown earlier[5] for highly metastable austenitic steels, such as 304L, that there is increased strain-induced transformation at 76 K and that the transformation is suppressed at lower temperatures. Temperature measurements of alloy 304L reveal that the discontinuous yielding events result in instantaneous warm-up to 50 to 100 K, the temperature range of maximum α' formation in alloy 304L. In contrast, no suppression of alloy 316LN α' per unit strain is apparent at very low temperatures.[11] Tobler et al. reported continuously increasing amounts of α' per unit strain from 175 K to 4 K. Therefore, whereas temperature increases at higher strain rates stimulate α' formation in alloy 304L, temperature increases in alloy 316LN suppress α' formation.

SUMMARY

Tensile tests of alloys 304L, 310, and 316LN were conducted as a function of strain rate in boiling liquid He (4 K). At strain rates less than 2.2×10^{-3} s^{-1}, all tensile properties remain insensitive to strain rate. At strains rates of 4.4×10^{-3} s^{-1} or larger, ultimate tensile strengths were less, and stress–strain characteristics were altered. Measurements indicated specimen warming up to 100 K. From heat balance calculations, we conclude the following:

1. Relatively little of the work of deformation is retained as stored energy in the specimen; we estimate about 10%.

2. Heat transfer through the solid specimen is less than that to the liquid He.

3. Heat transfer to liquid He at strain rates $\leq 2.2 \times 10^{-3}$ s^{-1} is via nucleate boiling.

4. Heat transfer to liquid He at strain rates $\geq 4.4 \times 10^{-3}$ s^{-1} is via film boiling.

5. Thus, specimen warming during tensile tests in liquid He at high strain rates (resulting in reduced ultimate strengths) is associated with the transition from nucleate to film boiling on the specimen surface.

ACKNOWLEDGMENTS

The Office of Fusion Energy (DOE), Victor Der project monitor, sponsored this research.

The authors thank P. T. Purtscher (NBS) for the excellent fractographs and L. A. Delgado (NBS) for assisting in metallography. Lawrence Livermore National Laboratory provided the 316LN alloy plate.

REFERENCES

1. D. T. Read and R. P. Reed, Adv. Cryo. Eng.—Mater. 26:91–101 (1980).

2. T. Ogata and K. Ishikawa, Workshop on Standardization of Fracture Toughness Testing of Low Temperature Structural Materials, National Research Institute for Metals, Tsukuba Labs., Sengen, Sakura-mura, Niihari-gun, Ibaraki, Japan, (March 1986).

3. W. G. Dobson and D. L. Johnson, Adv. Cryo. Eng.—Mater. 30: 185–192 (1984).

4. N. Yamagami, Y. Kohsaka, and C. Ouchi, Report to Joint U.S./ Japan Working Group on Structural Materials at Low Temperatures, Technical Research Center, Nippon Kokan K.K., Kawasaki, Japan (October 1986).

5. R. P. Reed, "Materials at Low Temperatures," American Society for Metals, Metals Park, Ohio (1983), pp. 295–341.

6. R. P. Reed and R. P. Walsh, in: "Materials Studies for Magnetic Fusion Energy Applications at Low Temperatures—IX," NBSIR 86-3050, National Bureau of Standards, Boulder, Colorado (1986), pp. 107–140.

7. D. Rönnpagel and C. Schwink, Acta Metall. 26:319–331 (1978).

8. T. Ungar, H. Mughrabi, D. Rönnpagel, and M. Wilkins, Acta Metall. 32:333–342 (1984).

9. N. J. Simon and R. P. Reed, in: "Materials for Superconducting Magnet Systems," National Bureau of Standards, Boulder, Colorado (June 1982), pp. 316–363.

10. E. G. Brentari, P. J. Giarratano, and R. V. Smith, "Boiling Heat Transfer for Oxygen, Nitrogen, Hydrogen, and Helium," NBS Tech. Note 317, National Bureau of Standards, Boulder, Colorado (Sept. 20, 1965).

11. R. L. Tobler, D. H. Beekman, and R. P. Reed, in: "Materials Studies for Magnetic Fusion Energy Applications at Low Temperatures—VI," NBSIR 83-1690, National Bureau of Standards, Boulder, Colorado (1983) pp. 87–112.

Table 1. Material Characterization

Alloy	Chemical Composition (wt.%)	Hardness (R_B)	Grain Size (μm)
304L-A	18.4 Cr, 9.7 Ni, 1.4 Mn, 0.02 C, 0.03 N, 0.02 P, 0.01 S, 0.6 Si, balance Fe	72	70
304L-B	same as 304L-A	73	72
310	24.8 Cr, 20.8 Ni, 1.7 Mn, 0.093 C, 0.031 N, 0.02 P, 0.02 S, 0.7 Si, 0.1 Mo, 0.1 Cu, balance F	72	161
316LN-A	18.0 Cr, 10.5 Ni, 1.1 Mn, 0.016 C, 0.167 N, 0.02 P, 0.015 S, 0.5 Si, 2.12 Mo, 0.2 Cu, 0.25 Co, balance Fe	77	78
316LN-B	18.0 Cr, 10.5 Ni, 1.1 Mn, 0.016 C, 0.149 N, 0.02 P, 0.015 S, 0.5 Si, 2.12 Mo, 0.2 Cu, 0.25 Co, balance Fe	81	57

Fig. 1. Microstructures of alloy 304L-A (a) and 304L-B (b) with similar grain size and hardness, but slightly varying yield strength.

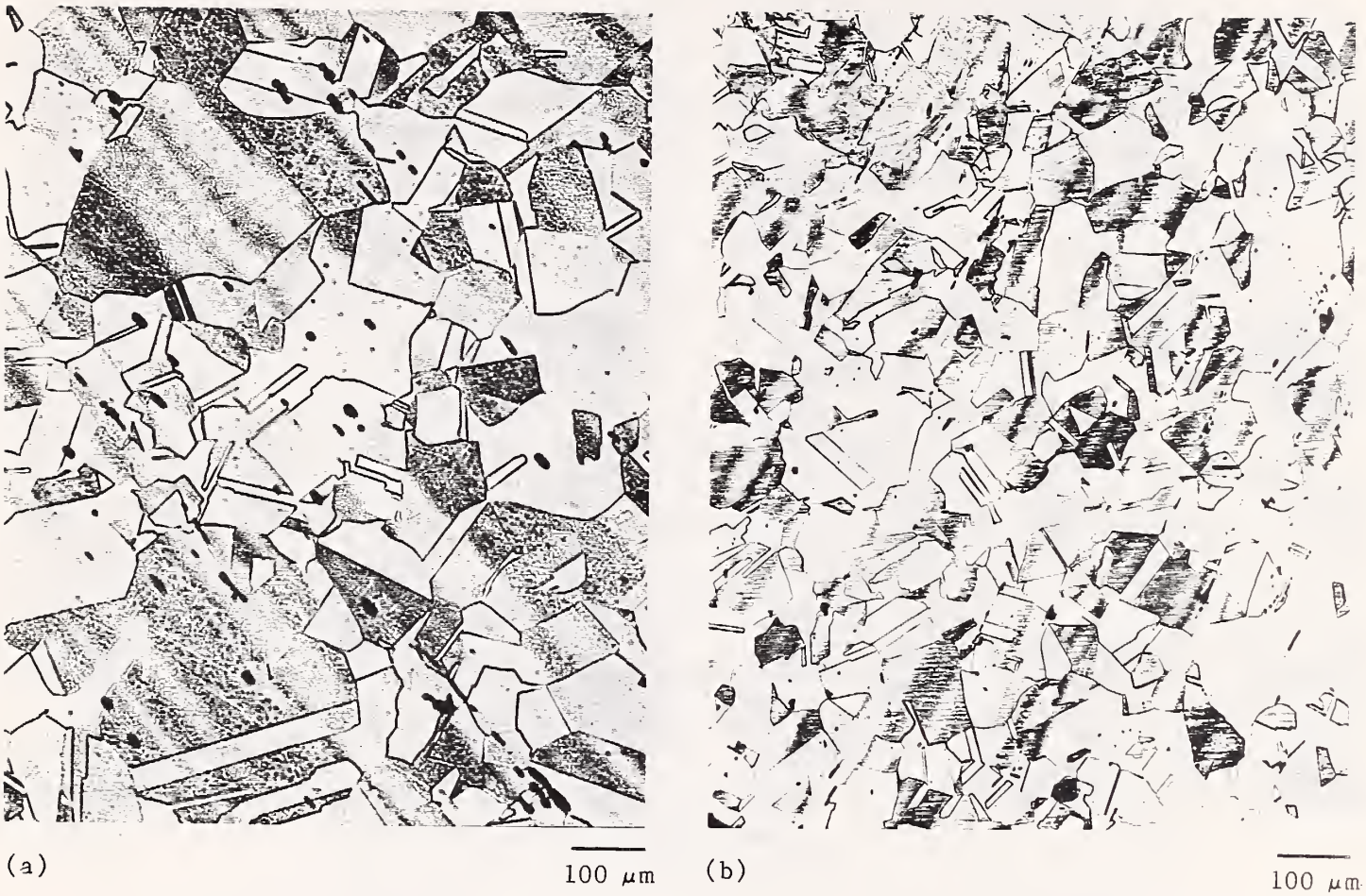

Fig. 2. Microstructure of alloy 316LN-A (a) and 316LN (b) taken from the same plate, but with varying grain size, hardness, inclusion density, and yield strength.

Fig. 3. Microstructure of alloy 310, partially sensitized with carbide formation at grain boundaries.

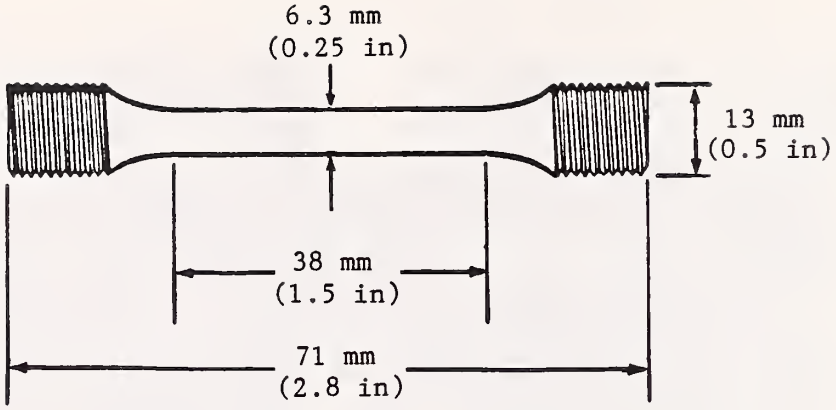

Fig. 4. Tensile specimen.

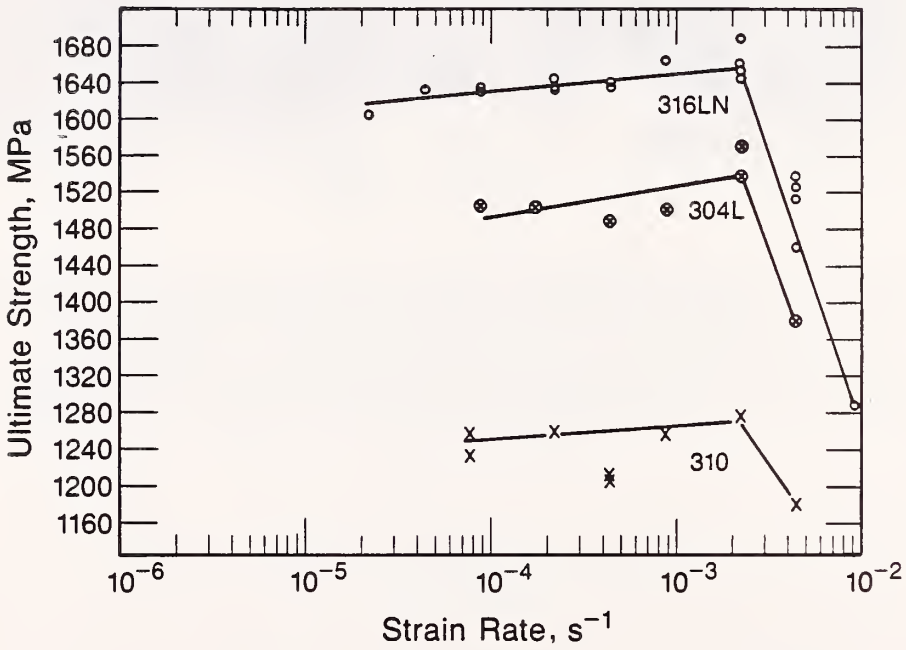

Fig. 5. Dependence of tensile ultimate strength on strain rate at 4 K.

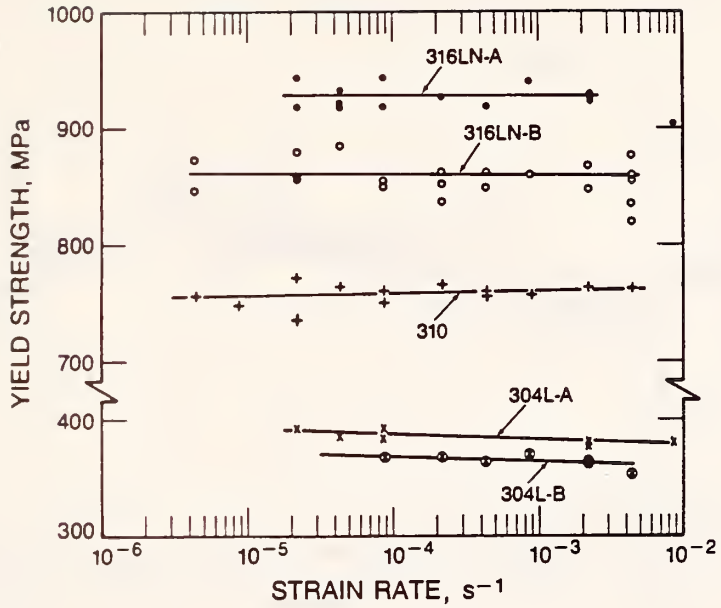

Fig. 6. Dependence of tensile yield strength on strain rate at 4 K.

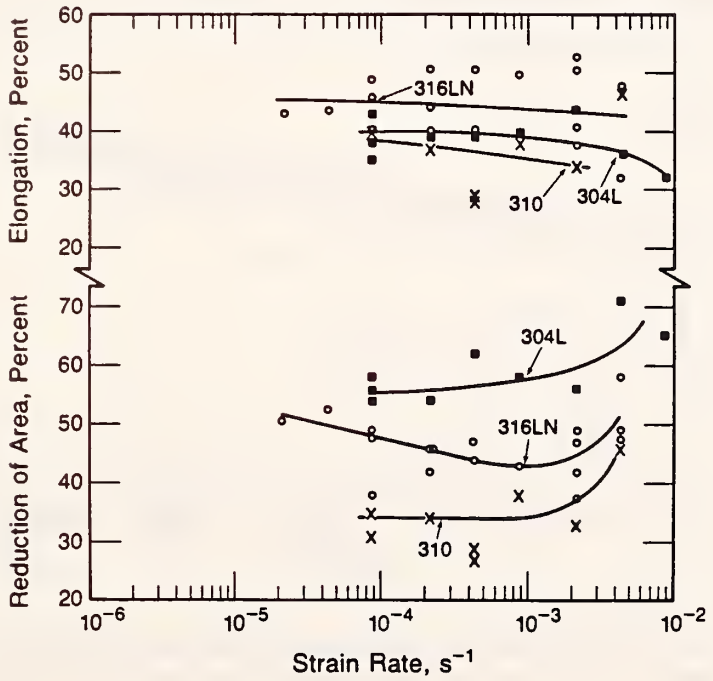

Fig. 7. Dependence of reduction of area and tensile elongation on strain rate at 4 K.

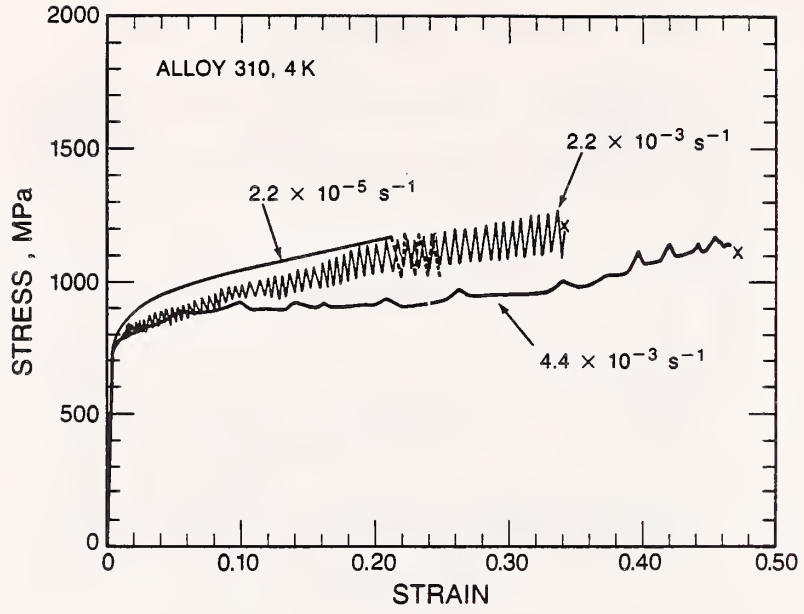

Fig. 8. Tensile stress-vs.-strain curves at various strain rates for alloy 310 at 4 K.

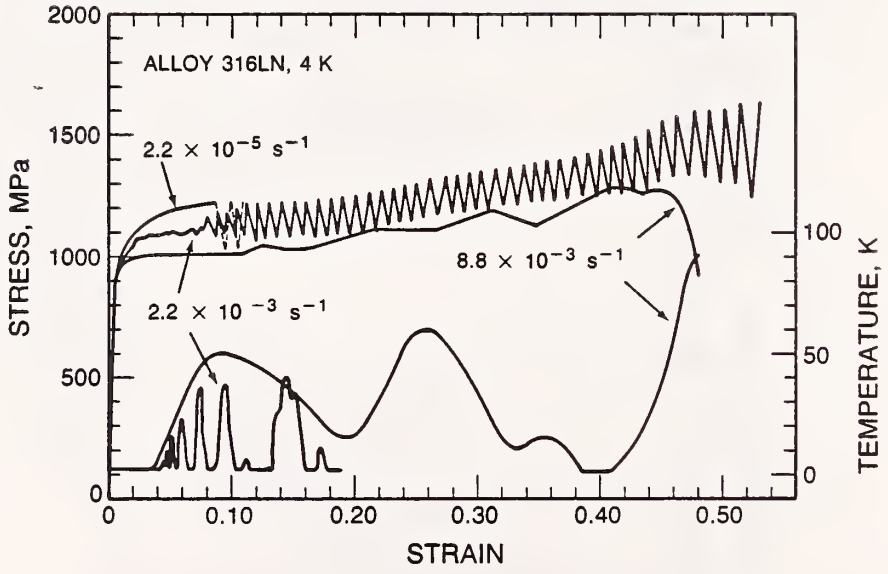

Fig. 9. Tensile stress-vs.-strain curves and specimen surface temperature at various strain rates for alloy 316LN.

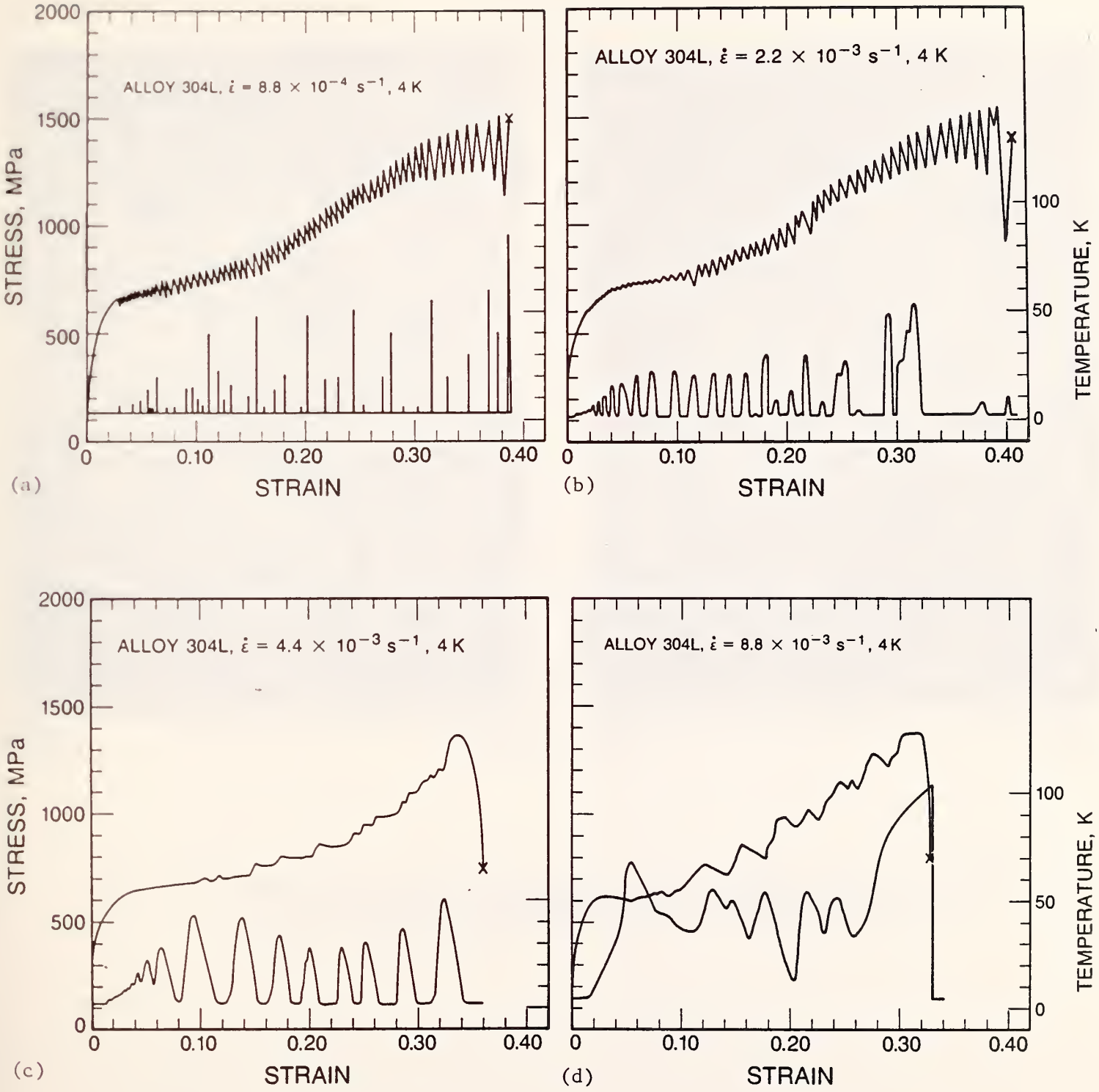

Fig. 10. Tensile stress-vs.-strain curves and specimen surface temperatures at various strain rates for alloy 304L.

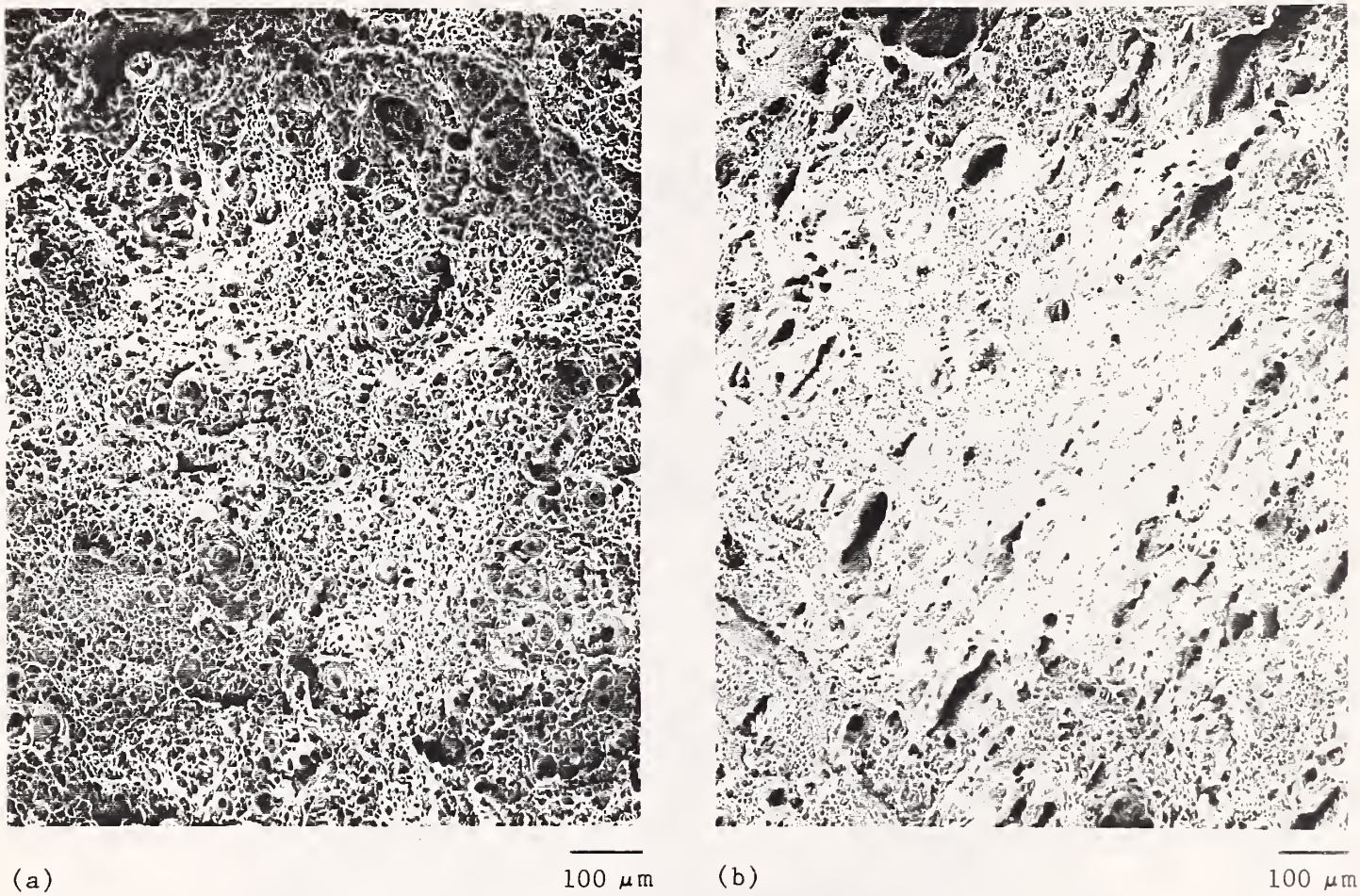

Fig. 11. Fractograph produced by scanning electron microsopy (SEM) of alloy 304L tensile specimens at strain rates of 4.4×10^{-4} s^{-1} (a) and 4.4×10^{-3} s^{-1} (b).

(a)

100 μm

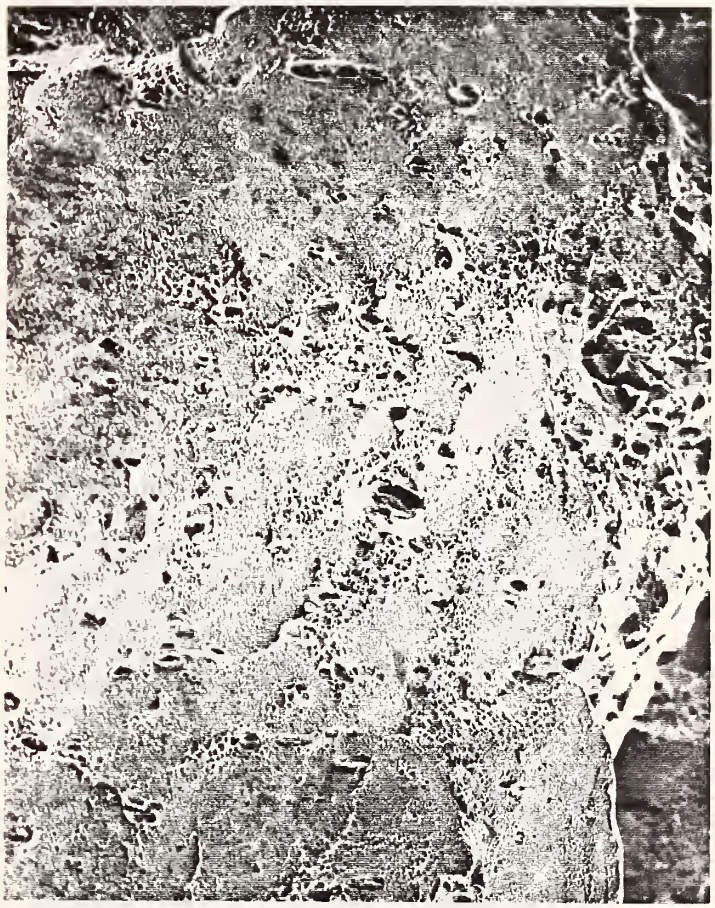

(b)

100 μm

Fig. 12. SEM fractograph of alloy 316LN tensile specimens at a strain rate of 4.4×10^{-4} s^{-1}. Regions of microvoid coalescence (a) and shear (b) are shown.

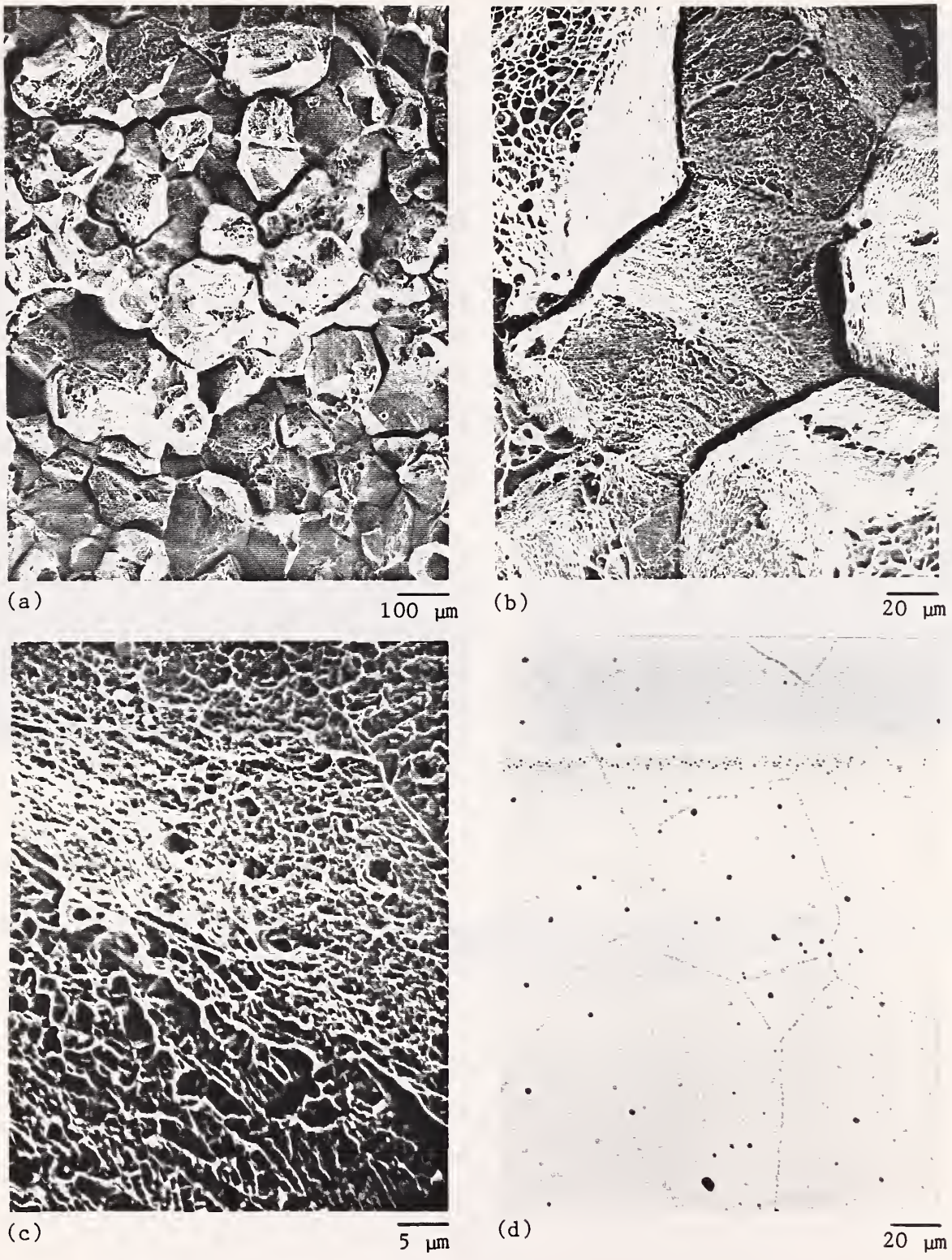

Fig. 13. SEM fractography of alloy 310 sensitized tensile specimens at a strain rate of 4.4×10^{-4} s^{-1}. Part (c) illustrates microvoid coalescence on the grain boundary. Part (d) is polished and etched (oxalic acid) surface.

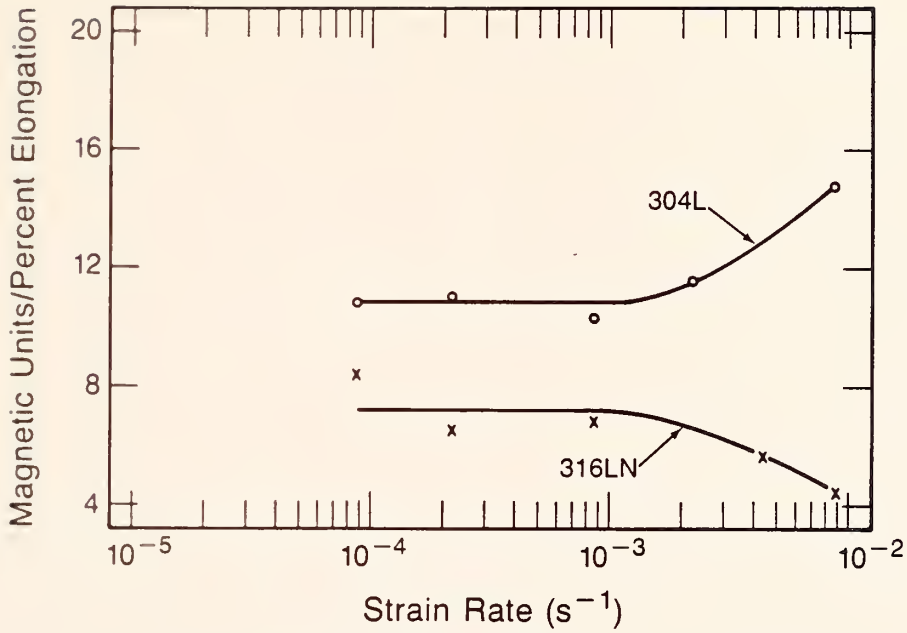

Fig. 14 Normalized amount of α' martensite formed in uniform elongation portion of 304L and 316LN tensile specimens at 4 K as a function of tensile strain rate.

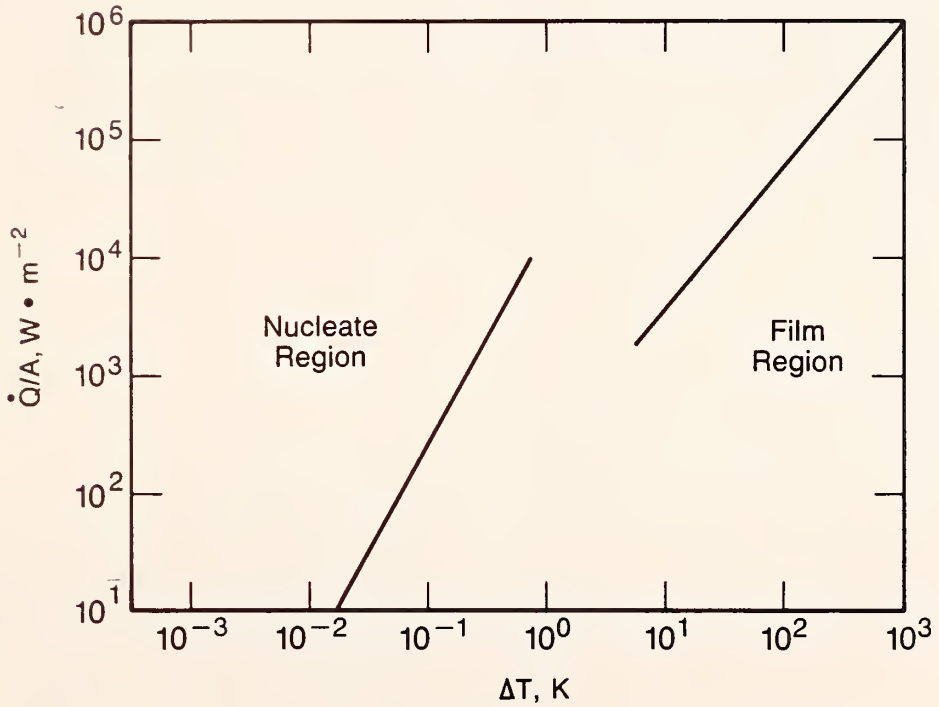

Fig. 15. Heat flow per surface area as a function of temperature difference of smooth, solid, metal surface in liquid helium.

MODIFICATION OF 316LN-TYPE ALLOYS

P. T. Purtscher, R. P. Walsh, and R. P. Reed
Fracture and Deformation Division
National Bureau of Standards
Boulder, Colorado

A series of eight austenitic stainless steels was tested in liquid helium to determine the effect of Mo and Ni variations on the strength and toughness. The Mo content ranged from 0 to 4 wt.%; the Ni content varied from 11 and 14 wt.%. The microstructure of the alloys depended upon the composition and annealing temperature. Higher alloy content and lower annealing temperatures, 1000 to 1050°C, resulted in a nonuniform structure. The higher temperature, 1150°C, produced a uniform austenitic structure. The mechanical test results showed that Mo additions increased the yield strength (to a maximum at 3 wt.%) and decreased the $K_{Ic}(J)$ values, so that there was no improvement in the strength–toughness relationship. Increasing the Ni content decreased the strengthening effect of Mo and increased $K_{Ic}(J)$. This supports earlier work that showed that Ni does improve the strength–toughness relationship. The strain-induced martensitic transformation was suppressed by increases in Ni, Mo, or N.

INTRODUCTION

The structures used to support superconducting magnets are fabricated from austenitic stainless steels. In the first generation of magnets, types 304LN and 316LN were used extensively because they were commercially available and their mechanical properties met the minimum requirements. The 316LN composition is similar to 304LN except that it contains 2 to 3 wt.% Mo and 10 to 14 wt.% Ni, rather than the 8 to 12 wt.% Ni specified for 304LN. Future designs for superconducting magnets will require structural alloys with improved mechanical properties, particularly the yield strength in relation to the fracture toughness.

The purpose of this work is to determine whether modification of the existing 316LN alloy composition would significantly improve the yield strength and fracture toughness at 4 K. Past experience with 304LN and 316LN[1] has shown that adding Mo and increasing Ni improves the yield strength at 4 K with little change in fracture toughness (thus, a better

strength–toughness combination). In this study, we evaluated the effect of Mo and Ni additions on the strength and fracture toughness as a function of annealing treatments.

MATERIALS

Eight 30-kg laboratory heats were vacuum-induction melted and cast under an Ar atmosphere into round ingots, 127 mm in diameter and 203 mm in length. The compositions are listed in Table I. Sulfur was removed from the heats by adding 50 g of calcium silicon to the melt before pouring.

The ingots were forged at 1200°C to billets 76 mm by 76 mm in cross section. Sections of the billets were hot-rolled to a final thickness of 25 mm. The hot-rolled sections were annealed in an Ar atmosphere at temperatures between 1000 and 1150°C followed by quenching in an agitated water tank. The time and temperature at which each specimen was treated is shown in Table II along with comments about the resulting microstructure. Figure 1 shows a representative microstructure of those specimens that contained an unknown second phase in the austenitic matrix. The unknown phase was nonmagnetic and typically had a lower Mo content than the matrix. Figure 2 shows an example of the microsegregation found in several specimens. The second phase was dissolved, but the etch revealed a "ghost" structure that is an indication of nonuniform composition.

PROCEDURES

The 4-K mechanical properties were determined according to the proposed standard procedures set forth by the United States-Japan Cooperative Program Committee on Test Methodology. These new test standards are based on the existing ASTM E 8 and E 813 standards.[2,3]

The mechanical properties are a function of grain size, N content, and the test variables, Mo and Ni concentration. Therefore, it is useful to adjust the mechanical properties to reduce the influence of variables other than those that we wish to analyze. The yield strengths measured in this study were adjusted to a nominal N content of 0.20 wt.% and grain size of 50 μm according to equation 1:[4]

$$\sigma_y = \text{constant} + 2778[N] + 811d^{-\frac{1}{2}}, \qquad (1)$$

where σ_y is the tensile yield strength in MPa, [N] is in wt.%, and d is the austenite grain size in μm. The constant was calculated for each σ_y measured, and then the nominal [N] and d were added to the constant to determine the adjusted σ_y.

The fracture toughness is a strong function of the tensile yield strength. To evaluate the effect of the composition variables on both the yield strength and fracture toughness, the quality index (QI), the product of the yield strength and fracture toughness, can be calculated. The QI

gives a direct means of relating metallurgical parameters to the strength–toughness relationship.[5] Our previous study showed that increasing the Ni content in a series of 304LN-type alloys did not affect the yield strength significantly, but increased the fracture toughness (the QI increased by approximately 20 GPa·MPa$\sqrt{m}$); increasing the N content increased the yield strength and decreased the fracture toughness (no clear effect on the QI). An adjusted QI (for constant Ni content) was calculated according to the trend previously established, so that any effect of Mo on the strength–toughness relationship would be shown.

RESULTS AND DISCUSSION

The measured mechanical properties are summarized in Table III. Fracture toughness as a function of yield strength is plotted in figure 3. The reference trend line refers to a series of annealed Fe-18Cr-10Ni steels with various C and N contents to increase the strengths.[6] Most data fall within the range of values reported previously for the reference trend.

From figure 3, we see that the temperature for the annealing treatment affected the strength–toughness relationship. Higher annealing temperatures raised the values (for alloys 0/11, 4/12, and 4/14) into the range previously measured for the reference trend. Metallography of the annealed specimens revealed the presence of an unknown second phase (see figure 1) in the microstructure of most of those specimens with a low strength–toughness relationship. Annealing at higher temperatures dissolved the second phase and resulted in better properties. For alloys with no apparent segregation problems, higher annealing temperatures resulted in larger austenite grain sizes, which produced lower yield strengths and correspondingly higher fracture toughness values.

To evaluate the effect of Mo on the yield strength, only specimens in which the second phase was dissolved were considered (elongation > 30% and reduction in area > 45%). The adjusted yield strength plotted as a function of Mo content are shown in figure 4. Between 0 and 3 wt.% Mo, the strength increases, but for the 4 wt.% Mo alloys, the strength levels off. Two lines are drawn on the figure to reflect a possible influence of Ni on the strengthening effect of Mo.

To determine whether Ni influences the Mo strengthening, we plotted the adjusted yield strength as a function of Ni content in figure 5. At a constant Ni content, 3 wt.% Mo apparently produces the highest strength, the same conclusion drawn from figure 4. Also, at the three different Mo contents, increasing the Ni content decreased the strength.

Next, we considered the effect of Mo on the strength–toughness relationship. The adjusted QI values for specimens with a uniform microstructure are plotted as a function of Mo in figure 6. The adjusted QI does not increase, as it does for increasing Ni content, but decreases slightly as Mo is added. Apparently the higher Ni content in 316LN results in properties superior to those of 304LN.

There is a considerable range of QI values for the alloys with about 2 wt.% Mo (316LN). An earlier report[4] summarizes the properties of 316LN alloys from different sources. If the QI is calculated and adjusted to 12 wt.% Ni, there is an even larger range of values--approximately 170 to 270 on the scale of figure 6. Clearly, the QI for 316LN alloys is not a constant, but varies considerably depending upon the heat treatment and inclusion content of the particular alloy.

The austenitic matrix partially transforms to the α' martensite phase in these alloys during plastic deformation. The extent of the transformation depends upon the alloy content, the amount of plastic deformation, and the temperature. The average martensite content after fracture of selected tensile specimens is divided by the percent elongation for that specimen and plotted in figure 7 as a function of the M_D, the strain-induced martensite start temperature, as calculated from equation 2:[7]

$$M_D = 686 - 6[Cr] - 25[Ni] - 16[Mn] + 21[Si] - 222[C+N] - 11[Mo], \quad (2)$$

where M_D is in degrees K and the alloy contents are in wt.%. As predicted by equation 2, the results show that Mo does reduce the M_D.

CONCLUSIONS

1. Molybdenum additions increase the yield strength at 4 K, up to a maximum at 3 wt.% Mo. The fracture toughness decreases and the adjusted QI decreases slightly over the range of 0 to 4 wt.% Mo.

2. Molybdenum additions are less effective in increasing the yield strength of alloys with high nickel content. Nickel and molybdenum apparently have interactive effects on the yield strength.

3. Higher annealing or processing temperatures are required to produce a completely austenitic microstructure as the molybdenum content in the alloy increases.

4. Molybdenum additions, as well as nickel and nitrogen additions, suppress the strain-induced martensitic transformation at 4 K.

5. The 316LN composition has a better combination of strength and toughness than 304LN at 4 K because of its higher nickel content.

REFERENCES

1. D. T. Read, and R. P. Reed, Cryogenics, vol. 21, 1981, p. 415.
2. ASTM E 8-85b, in: 1986 Annual Book of ASTM Standards, American Society for Testing and Materials, Philadelphia, 1986, p. 124.
3. ASTM E 813-81, in: 1986 Annual Book of ASTM Standards, American Society for Testing and Materials, Philadelphia, 1986, p. 768.

4. R. P. Reed, P. T. Purtscher, N. J. Simon, and R. L. Tobler, in: Materials Studies for Magnetic Fusion Energy Applications at Low Temperature—IX, R. P. Reed, ed., National Bureau of Standards, Boulder, Colorado, 1986, p. 15.
5. R. P. Reed, P. T. Purtscher, and K. A. Yushchenko, in: Advances in Cryogenic Engineering, vol. 30, R. P. Reed and A. F. Clark, eds., Plenum Press, New York, 1986, p. 43.
6. R. L. Tobler, D. T. Reed, and R. P. Reed, in: Fracture Mechanics, Thirteenth Conference, ASTM STP 743, R. Roberts, ed., American Society for Testing and Materials, Philadelphia, 1981, p. 350.
7. I. Williams, R. G. Williams, and R. C. Capellaro, in: Proceedings of Sixth International Cryogenic Engineering Conference, IPC Science and Technology Press, Guildford, Surrey, England, 1976, p. 337.

Table I. Chemical Composition (wt.%)

Alloy†	Cr	Ni	Mo	Mn	N	% α'/% elongation	M_D^*(K)
0/11	18.0	10.8	0	1.0	0.13	2.05	261
2/11	18.6	10.9	2.2	1.0	0.13	1.88	237
2/12	18	12	2	1.0	0.18	0.75	200
3/12	18	12	3	1.0	0.19	0.75	187
4/12	18.2	12	4	1.0	0.19	0.45	176
2/14	18.5	14	2	1.1	0.17	0.33	152
3/14	18.2	14	3	1.0	0.18	0.12	139
4/14	18	14	4	1.0	0.19	0.08	126

* $M_D = 686 - 6[Cr] - 25[Ni] - 16[Mn] - 11[Mo] - 222[N]$
† Alloy's designation refers to the Mo content/Ni content

Table II. Summary of Heat Treatment

Spec.#	Temperature (°C)	Time (min)	Grain size (μm)	Comments
0/11-1	1000	15	23	---
0/11-2	1050	60	75	---
0/11-3	1050	1440	80	---
0/11-4	1150	1440	161	---
2/11-1	1000	6	7	---
2/11-2	1000	15	11	---
2/11-3	1000	60	20	---
2/12-1	1000	30	34	---
2/12-2	1000	30	28	---
2/12-4	1150	120	100	---
3/12-1	1000	30	34	---
3/12-2	1000	30	35	---
3/12-4	1150	120	70	---
4/12-1	1000	30	25	2nd phase present
4/12-2	1000	30	31	2nd phase present
4/12-4	1150	120	75	---
2/14-1	1000	30	37	microsegregation
2/14-2	1000	30	36	microsegregation
2/14-3	1050	60	47	---
2/14-4	1050	240	57	---
2/14-5	1050	1440	127	---
2/14-6	1150	30	68	---
2/14-7	1150	90	94	---
2/14-8	1150	330	118	---
3/14-1	1000	30	29	microsegregation
3/14-2	1000	30	33	microsegregation
3/14-3	1150	120	100	---
4/14-1	1000	30	31	2nd phase present
4/14-2	1000	30	39	2nd phase present
4/14-3	1050	240	59	microsegregation
4/14-4	1050	1200	93	microsegregation
4/14-5	1050	5760	177	microsegregation
4/14-6	1150	45	78	---
4/14-7	1150	210	118	---
4/14-8	1150	600	187	---

Table III. Summary of Mechanical Properties

wt.% Mo / wt.% Ni	Yield Strength (MPa)	Adjusted Yield Strength (MPa)†	Ultimate Strength (MPa)	%Elong. / %R.A.	Fracture Toughness (Mpa√m)	Quality Index (GPa·MPa√m)	Adjusted Quality Index†
0/11-1	784	960	1654	42/55	193	151	176
0/11-2	715	924	1620	42/51	202	144	169
0/11-3	677	953	1588	41/50	212	144	169
0/11-4	720	994	1606	40/48	269	194	219
2/11-1	1056	1087	1733	36/49	146	154	177
2/11-2	935	1092	1686	41/54	177	165	188
2/11-3	885	1042	1618	41/58	187	165	188
2/12-1	1049	1078	1598	43/50	163	173	173
2/12-2	1014	1048	1602	44/55	172		
2/12-4	945	1035	1527	45/55	---	---	---
3/12-1	1109	1114	1620	41/50	157	169	173
3/12-2	1119	1124	1617	40/47	148		
3/12-4	1096	1142	1562	52/62	---		
4/12-1*	1222	1203	1580	22/23	98	120	118
4/12-2*	1181	1162	1569	21/28	103		
4/12-4	1067	1116	1549	44/54	---	---	---
2/14-1*	1063	1128	1532	37/49	188	207	170
2/14-2*	1060	1125	1546	39/49	202		
2/14-3	931	1012	1523	43/56	211	196	159
2/14-4	934	1026	1503	42/53	226	211	174
2/14-5	863	990	1477	43/54	241	208	171
2/14-6	894	995	1514	41/58	201	180	143
2/14-7	903	1018	1490	37/47	213	192	155
2/14-8	905	1029	1473	40/52	210	190	153
3/14-1*	1129	1150	1558	32/53	167	195	
3/14-2*	1109	1130	1565	34/48	181		
3/14-3	994	1084	1478	39/59	---	---	---
4/14-1*	1164	1161	1548	25/33	98	114	69
4/14-2*	1161	1158	1534	26/35	---	---	---
4/14-3*	942	979	1534	39/48	149	140	95
4/14-4*	968	1027	1523	37/45	165	160	115
4/14-5*	915	997	1493	32/44	145	133	88
4/14-6	1013	1064	1530	34/52	193	196	151
4/14-7	1007	1075	1508	41/55	170	171	126
4/14-8	981	1065	1502	40/49	195	191	146

* Not fully austenitic; nonuniform composition
† See Procedures section of text

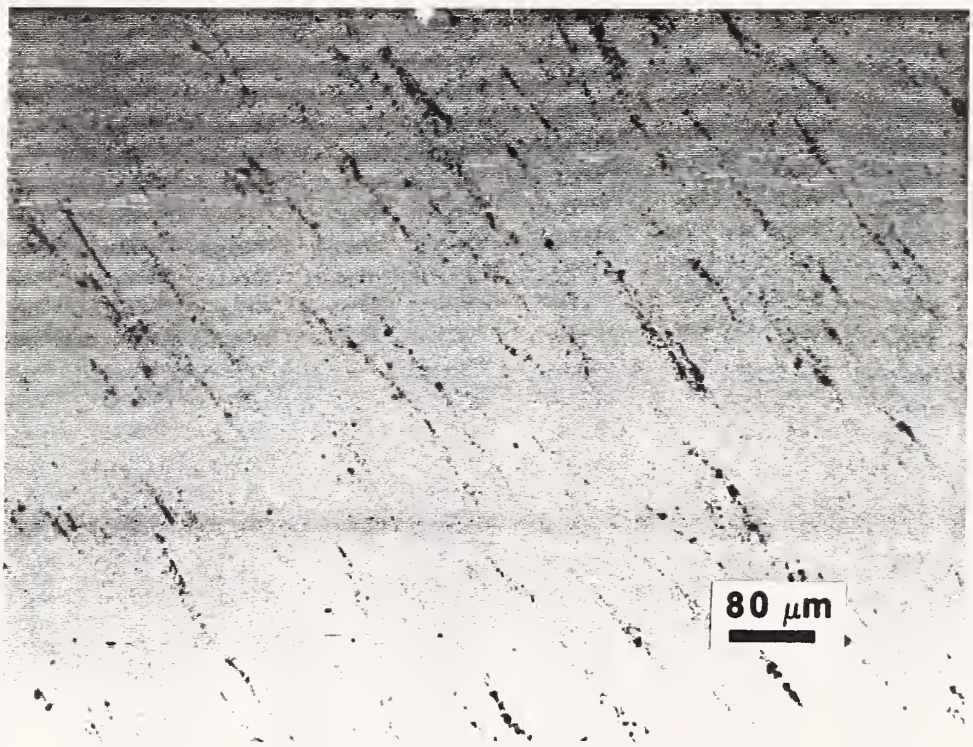

Figure 1. Microstructure of specimen 4/14-1, etched in potassium hydroxide electrolyte.

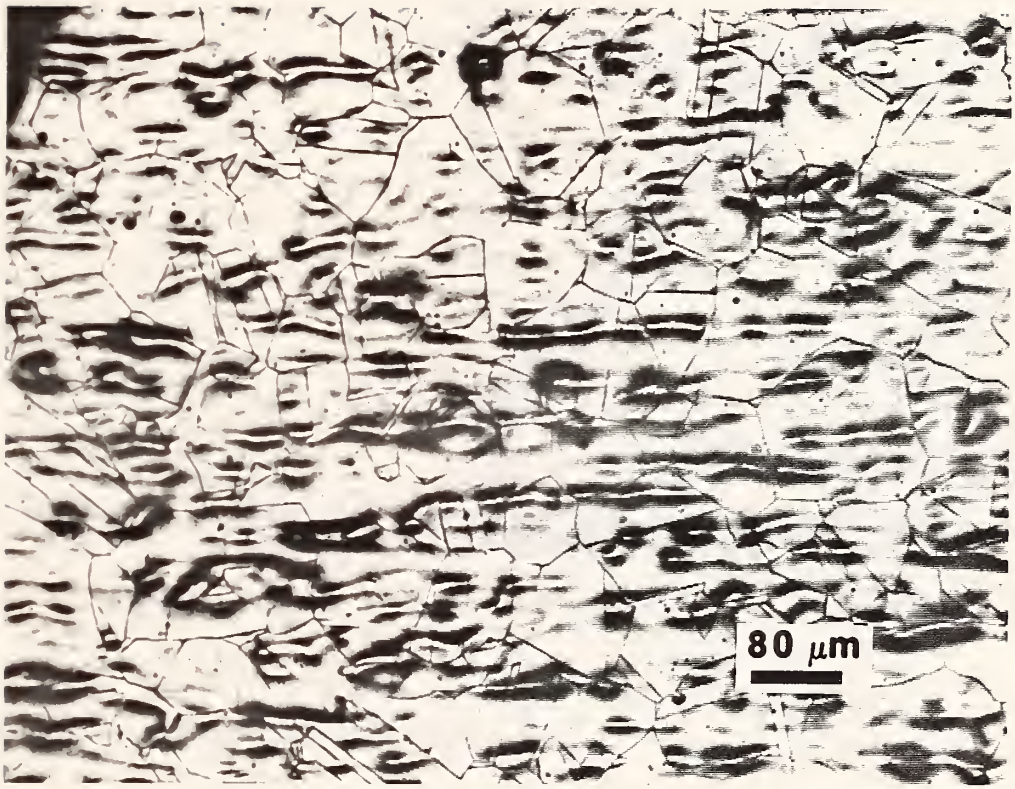

Figure 2. Microstructure of specimen 4/14-3, etched in oxalic acid electrolyte.

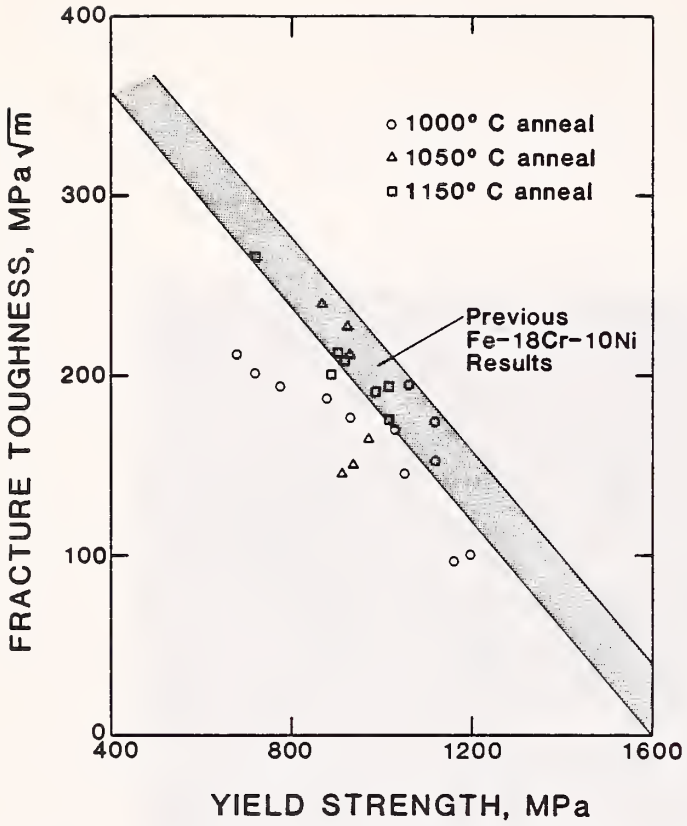

Figure 3. Fracture toughness versus tensile yield strength.

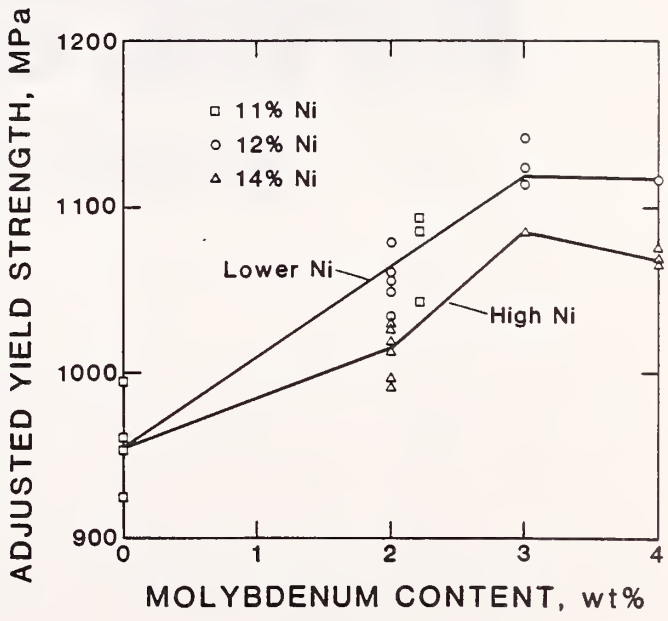

Figure 4. Adjusted yield strength versus Mo content for specimens with a uniform austenitic structure.

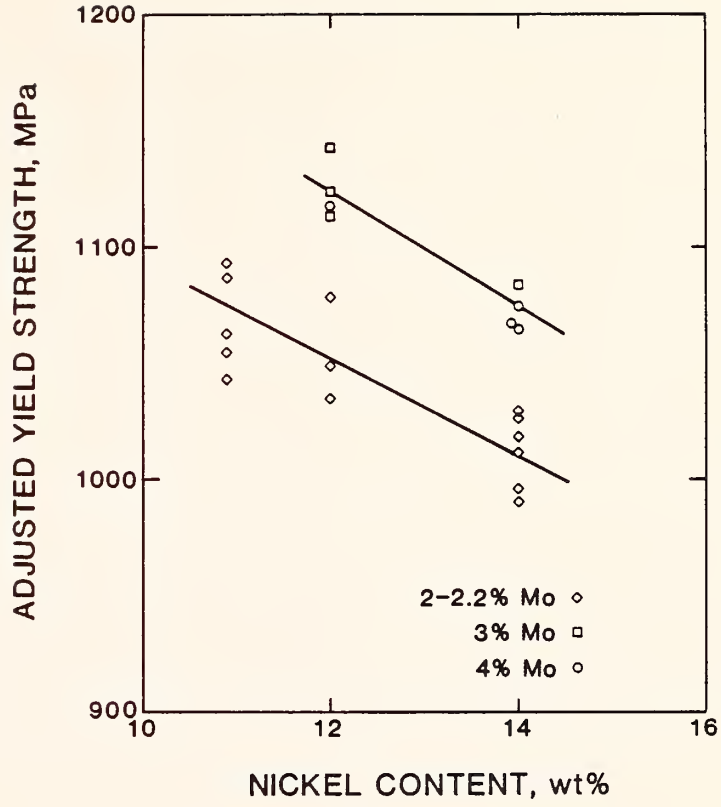

Figure 5. Adjusted yield strength versus Ni content for specimens with a uniform austenitic structure.

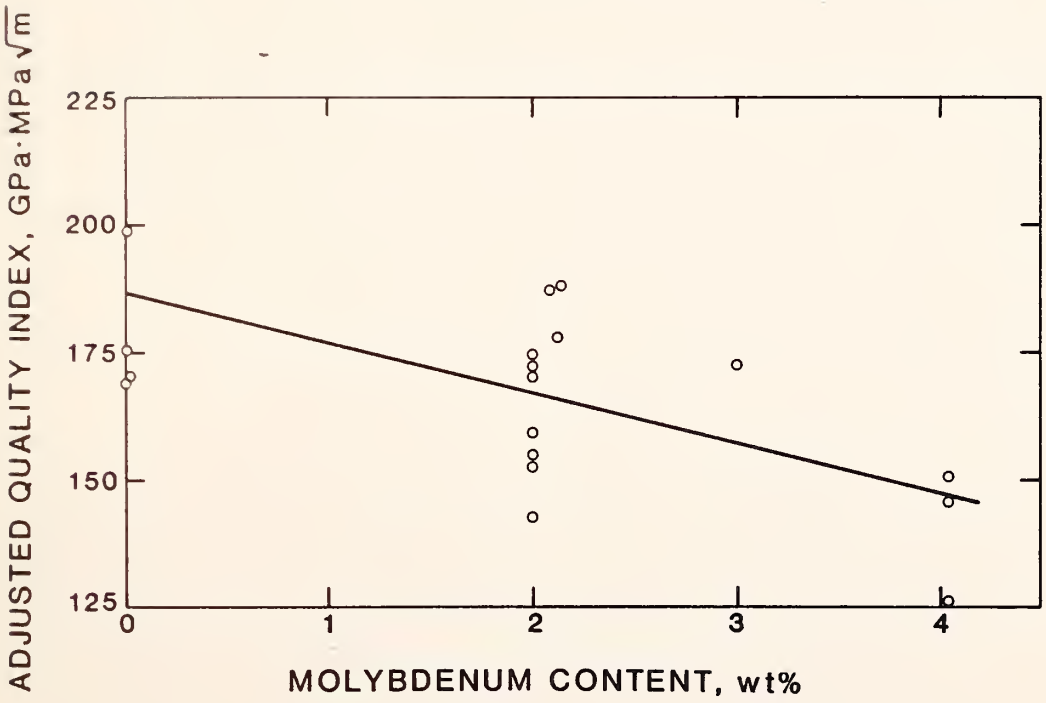

Figure 6. Adjusted Quality Index, QI, versus Mo content for specimens with a uniform austenitic structure.

MOLYBDENUM EFFECT ON Fe–Cr–Ni–ALLOY ELASTIC CONSTANTS*

H. M. Ledbetter and S. A. Kim
Fracture and Deformation Division
Institute for Materials Science and Engineering
National Bureau of Standards
Boulder, Colorado

By ultrasonic methods, using polycrystalline specimens, we determined the elastic constants of six face-centered-cubic Fe–Cr–Ni alloys, nominally Fe–19Cr–12Ni (at. pct.). In these alloys, Mo content ranged up to 2.4 at. pct. We found that Mo lowers the Young and shear moduli, and it raises the Poisson ratio. Contrary to expectation (because it increases volume), Mo raises the bulk modulus. Qualitatively, our results show that Ni raises the bulk modulus and Poisson ratio, but Ni lowers the Young and shear moduli. (Nickel decreases the alloy's atomic volume.) Our discussion includes existing models based on 3d-electron theory.

INTRODUCTION

Because 3d-transition-metal alloys provide the basis for commercial austenitic stainless steels, their physical properties provide much practical interest. Recent attempts to improve the traditional steels through chemical-composition changes create many new questions.

Compared to alloys of simple (s-p-electron) metals, or even noble metals, the theory of 3d-electron metals remains unsettled. Thus, for alloy improvement, theory provides mainly guidelines for interpretation; it fails to provide a scientific basis for physical-property prediction.

Because they relate to various solid-state phenomena—interatomic potentials, dislocation mechanisms, empirical models, macroscopic plastic deformation, elastic properties rank high among the physical properties. They contain enormous information. Gilman[1] remarked that "the most important mechanical characteristic of a crystal is its elastic modulus." Rather than Young modulus, a physical chemist might choose the bulk modulus, or reciprocal compressibility.[2] Many physicists,[3] including Einstein,[4] saw the bulk modulus as the principal elastic constant for considering solid-state properties. For studying interatomic-bonding changes, the Poisson ratio provides a valuable viewpoint.[5,6]

*Intended for publication in Journal of Materials Research

This study considers alloying effects in face-centered-cubic Fe–Cr–Ni–base alloys. Specifically, it considers the changes in the elastic constants caused by adding Mo, a 4d body-centered-cubic element. Indeed, as described below, Mo represents a b.c.c. paradigm. Because it represents a strong b.c.c. element and because it possesses a large atomic volume, one expects large elastic-constant changes.

By ultrasonic methods (near 10 MHz), we determined the complete elastic-constant set. We report results for four: E = Young modulus, G = shear modulus, B = bulk modulus, and ν = Poisson ratio.

Previously, for Fe–Cr–Ni alloys, we reported similar studies for alloying with substitutional Mn[7] and interstitial C-plus-N.[8] In both studies, these elements increased atomic volume and lowered all the elastic stiffnesses: B, E, and G. As described in detail by Gilman,[9] when atomic volume increases, we expect lower elastic stiffness. All simple interatomic potentials predict this inverse relationship.

MEASUREMENTS

Materials

We obtained polycrystalline alloys from the research laboratory of a major manufacturer. Table I shows their chemical compositions. The alloys were prepared in a vacuum induction furnace, cast into round ingots 13.3 cm in diameter and 21.8 cm in length, cropped and forged at 1100°C to billets 7.6 cm in cross section, rolled at 1100°C, to 2.5-cm plate, annealed for 30 min at 1000°C, and water quenched.

Method

We determined sound velocities by a method described elsewhere.[10] Briefly, 1.5-cm cubes were prepared by grinding so that opposite faces were flat and parallel within 5 μm. Quartz piezoelectric crystals with fundamental resonances between 4 and 7 MHz were cemented to the specimens with phenyl salicylate. An x-cut transducer was used for longitudinal waves and an ac-cut for transverse waves. Ultrasonic pulses 1 to 2 cycles long were launched into the specimen by electrically exciting the transducer. The pulses propagated through the specimen, reflected from the opposite face, and propagated back and forth. The pulse echoes were detected by the transducer and displayed on an oscilloscope equipped with a time delay and a microprocessor for time-interval measurements. The sound velocity was computed by

$$v = 2\ell/t. \qquad (1)$$

Here, ℓ denotes specimen length, and t denotes the round-trip transit time. On the oscilloscope, t was the time between adjacent echoes, usually the first and second echoes, and within these the time between leading cycles. Elastic-stiffness constants were computed from the general relationship

$$C = \rho v^2. \tag{2}$$

Here, ρ denotes mass density. The usual quasi-isotropic elastic constants are related to the longitudinal and transverse sound velocities, v_ℓ and v_t, by

$$\text{longitudinal modulus} = C_\ell = \rho v_\ell^2, \tag{3}$$

$$\text{shear modulus} = G = \rho v_t^2 \tag{4}$$

$$\text{bulk modulus} = B = C_\ell - (4/3)G, \tag{5}$$

$$\text{Young modulus} = E = 3GB/(C_\ell - G), \tag{6}$$

$$\text{Poisson ratio} = \nu = (E/2G) - 1 \tag{7}$$

$$= (1/2)(C_\ell - 2G)/(C_\ell - G).$$

RESULTS

Table II shows the numerical results for ρ, C_ℓ, G, B, E, and ν. Figure 1 shows these results graphically. Figure 2 shows the relative elastic-constant changes. Table III gives the least-squares results obtained for a linear fit: $y = a + bx$. This table also shows b/a, the percentage change in elastic constant per percentage change in alloying element. Here, x denotes the Mo atomic fraction. For comparison, Table III contains b/a results obtained previously for Mn[7] and for C-plus-N[8] alloying into Fe–Cr–Ni alloys.

DISCUSSION

Since Mo is a 4d rather than a 3d element, its atomic volume exceeds considerably that of Fe, Cr, Ni, and the Fe–Cr–Ni alloy. (In Å^3, the volumes are Fe = 11.78, Cr = 12.00, Ni = 10.94, Fe–Cr–Ni = 11.59,[11] and Mo = 15.58.) That Mo's atomic volume exceeds the alloy's effective atomic volume by 34 percent deserves attention. Small volume changes often correspond to large physical-property changes. For example, consider Fe's bulk modulus. From 0 to 300 K, it decreases 3.0 percent, while volume increases only 0.6 percent. Ignoring the thermal contribution to elastic softening, we obtain

$$\frac{\Delta B/B}{\Delta V/V} = -\frac{0.0295}{0.00594} = -4.96. \tag{8}$$

Similarly, for Fe, from pressure studies,[12] we find

$$\frac{\Delta B/B}{\Delta V/V} = -\frac{\Delta B}{\Delta P} = -5.29. \tag{9}$$

Thus, we expect the bulk modulus to decrease approximately 5 percent per percent volume increase.

Studies by Ledbetter and Austin[11] show that Mo's excess effective volume in these alloys equals 52 percent, far exceeding the expected 34 percent. Models based on volumes and atomic elastic constants fail to explain this large increase. An atomic-volume linear-rule-of-mixture model, which probably represents an upper bound, predicts, of course, 34 percent. A more realistic model, say that of Gschneidner and Vineyard,[13] which contains both second-order and third-order elastic constants appropriate to large local strains, predicts 28 percent, too low by approximately one-half.

Because the bulk modulus relates intimately to the atomic volume, we need to consider why Mo fits so poorly in the host f.c.c. Fe–Cr–Ni crystal structure. Mo prefers a b.c.c. crystal structure. Among the 4d elements, Mo shows the highest melting point. Outside the metallic orbital, Pauling[14] assigns Mo a valence of 5.0, exactly the number of bonding electrons for maximum cohesion. The potency of Mo as a b.c.c. stabilizer emerged in Pfeil's[15] studies on Zr alloys. Altmann et al.[16] point out that the b.c.c. stabilizing "should be more marked for Mo and W, where we have a peak of the d weight." Altmann et al. also point out that, despite favorable size factors, Mo shows practically no solid solubility in Ag. In their theory of ferromagnetism and band structure in transition metals, Bader et al.[17] focus on the 3d bonding orbitals. They show that the d^3, or T_{1g}, orbitals lie along the four [111] directions in a b.c.c. crystal structure; in an f.c.c. structure, they lie along the six [110] directions. From this b.c.c.–f.c.c. bonding-orbital symmetry mismatch, we expect strong physical-property changes, changes exceeding those expected for crystal-field-symmetry changes of s-electron or p-electron orbitals.

Results in Fig. 1 show the remarkable feature that, despite increased atomic volume, the bulk modulus increases with increasing Mo.

Explanation of this phenomenon lies embedded in quantum-mechanical d-electron theory, which presents one of solid-state-physics's most difficult problems. Despite enormous effort—for example Mott,[18] Pauling,[19] Zener,[20] Bader et al.,[17] Goodenough,[21] the problem remains unsolved. Herring[22] gave an elementary critique of the state of d-electrons in transition metals. He concluded that elements in the 3d row should resemble the free atoms and that most of these metals possess itinerant electrons. This reference contains Herring's much-cited remark on 3d-electron theories: "It is like mixing a few liquors in various proportions to get a variety of different cocktails." Mainly from the view of d-band theory, Brooks[23] reviewed the subject. In his review, Brooks disputes ideas based on crystal-field theory and separation of d-levels into E_g and T_{2g} subbands. (A recent successful tight-binding calculation of iron's elastic constants invokes the E_g orbitals.[24])

A theory by Ducastelle[25] leads to simple relationships for the volume and the bulk modulus. In the theory, the total energy arises from two sources: d-band energy calculated by a tight-binding approximation and Born–Mayer repulsive energy. Although this model is too simplified to explain present results, it displays the principal features necessary for an improved calculation. For the Wigner–Seitz radius, r_o, Ducastelle obtained

$$r_o = \frac{1}{p - q} \ln \frac{pC}{qAW_o} . \tag{10}$$

The bandwidth-energy approximation is

$$U_b = W_o e^{-qr}. \tag{11}$$

The repulsive energy is

$$U_r = Ce^{-pr}. \tag{12}$$

and

$$A = z(10 - z)/20. \tag{13}$$

Here, z denotes the average number of electrons per atom in the d-band, and $U = U_b + U_r$ denotes the total energy. For the bulk modulus, Ducastelle obtained

$$B = V_o \left(\frac{\partial^2 U}{\partial V^2}\right)_{V=V_o} = \frac{r_o^2}{9} \left(\frac{\partial^2 U}{\partial r_o^2}\right)_{r=r_o} = pqr_o^2 U_c/9. \tag{14}$$

Thus, Ducastelle's model predicts that increased atomic volume ($V_o = 4\pi r_o^3/3$) leads to decreased bulk modulus because U_c represents cohesive energy per unit volume.

Despite the deficiencies (for present purposes) of Ducastelle's model, we can use it to estimate pr_o and qr_o. For this estimate, we need one more relationship among p, q, and physical properties. We choose the bulk-modulus pressure derivative:

$$\frac{\partial B}{\partial P} = -\frac{1}{BV_o} \left(\frac{\partial^3 U}{\partial v^3}\right)_{v=1} . \tag{15}$$

Here, $v = V/V_o$, and we obtain

$$\frac{\partial B}{\partial P} = \frac{6 + (p + q)r_o}{3} . \tag{16}$$

Taking $U_c = 58.6$ GJ/m^3 (the value for iron), B = 160.4 GPa, and $\partial B/\partial P = 5.57$,[26] we obtain

$$pr_o = 7.37, \quad qr_o = 3.34. \tag{17}$$

These results compare favorably with Ducastelle's estimates for a typical transition metal: $pr_o = 9$ and $qr_o = 3$. Despite the different interatomic pair potential, Ducastelle's model corresponds closely to the results of a Mie–Grüneisen interatomic potential:[27]

$$U = \alpha r^{-n} + \beta r^{-m}, \tag{18}$$

$$B = mnU_c/9V_o, \tag{19}$$

and

$$\partial B/\partial P = (m + n + 9)/3. \tag{20}$$

In considering metallic elements, Fürth[28] concluded that $m = 4$ and $n = 7$ for Fe, Co, Ni, and Cu. Fürth's coefficients lead to $pr_o = 11.58$ and $qr_o = 2.42$.

For Ducastelle's model, we can get the relative contributions of U_b and U_r by imposing mechanical equilibrium:

$$\partial U/\partial r = 0. \tag{21}$$

This leads to

$$|U_b/U_r| = q/p, \tag{22}$$

$$|B_b/B_r| = (2 + pr_o)/(2 + qr_o), \tag{23}$$

and

$$|(\partial B/\partial P)_b/(\partial B/\partial P)_r| = (10 + 6pr_o + p^2r_o^2)/(10 + 6qr_o + q^2r_o^2). \tag{24}$$

The band-structure term contributes 31 percent to the energy, 64 percent to B, and 73 percent to $\partial B/\partial P$. Thus, the band-structure energy contributes more to the higher order elastic constants; contrary to expectation, for this particular interatomic potential, the repulsive energy contributes less.

Aside from the complications of 3d electrons, another factor arises in these alloys: magnetization. Even though the alloys show macroscopic paramagnetism, disordered local atomic moments may affect the physical properties. The usual view is that magnetization increases volume and decreases bulk modulus.[29] In extending Ducastelle's model to allow for electron correlation, Friedel and Sayers[29] concluded that both correlation and magnetization increase volume and decrease the bulk modulus.

Using a second-order perturbation treatment of electron correlation, Friedel and Sayers[30] reconsidered this question. They found that the bulk modulus may increase with magnetization and increasing volume. They expect such bulk-modulus increases to occur in elements with a high electron-density-of-states, transition elements to the right: Fe, Cu, and Ni. Such bulk-modulus increases are consistent with, or predicted by, other transition-metal electron-theory models.[31–33]

Finally, we note that Fig. 1 shows also the effects of alloying Ni into Fe–Cr–Ni. Nickel decreases effective atomic volume, raises the bulk modulus and Poisson ratio, and lowers the Young and shear moduli. Roughly, the Ni effect on the bulk modulus, $(\Delta B/B)/(\Delta V/V)$, equals −1.62. Because we failed to study systematically the Ni effects, we avoid comparisons with models,

but we remark that Ni parallels Mo in changing B, E, G, and ν. These conclusions apply only to the studied alloys, which contain 12 to 14 percent Ni. In another study, where the alloys contained as low as 5 percent Ni, we observed other effects, sometimes opposite.

CONCLUSIONS

From this study, there emerge three conclusions:

1. Added to f.c.c. Fe–Cr–Ni alloys, Mo increases the bulk modulus, B, and the Poisson ratio, ν. It decreases the Young and shear moduli, E and G. Because Mo increases the effective atomic volume, V, one expects a decreased bulk modulus.

2. Most existing 3d-electron-theory models predict that B decreases when V increases; but several models allow, or predict, the reverse effect, which we observe when we alloy Mo into Fe–Cr–Ni.

3. Nickel alloyed into f.c.c. Fe–Cr–Ni parallels Mo in changing the elastic constants: B and ν increase, E and G decrease. Unlike Mo, Ni decreases atomic volume, but the decrease is small.

ACKNOWLEDGMENT

Partial support for this study came from the DoE Office of Fusion Energy. M. W. Austin assisted with measurements.

REFERENCES

1. J. J. Gilman, Austr. J. Phys. 13, 327 (1960).
2. E. A. Moelwyn-Hughes, "Physical Chemistry" (Pergamon, Oxford, 1961), p. 210.
3. F. Seitz,"The Modern Theory of Solids" (McGraw-Hill, New York, 1940), p. 373.
4. A. Einstein, Ann. Phys. 34, 170 (1910–11).
5. W. Köster, Metall. Rev. 6, 1 (1961).
6. H. M. Ledbetter, S. Chevacharoenkul, and R. F. Davis, J. Appl. Phys. 60, 1614 (1986).
7. H. M. Ledbetter, J. Mater. Sci. 20, 2923 (1985).
8. H. M. Ledbetter and M. W. Austin, Mater. Sci. Eng. 70, 143 (1985).
9. J. J. Gilman, "Micromechanics of Flow in Solids" (McGraw-Hill, New York, 1969), p. 29.
10. H. M. Ledbetter, N. V. Frederick, and M. W. Austin, J. Appl. Phys. 51, 305 (1980).
11. H. M. Ledbetter and M. W. Austin, unpublished research, National Bureau of Standards, Boulder, Colorado (1986).
12. M. W. Guinan and D. N. Beshers, J. Phys. Chem. Solids 29, 541 (1968).
13. K. A. Gschneidner and G. H. Vineyard, J. Appl. Phys. 33, 3444 (1962).

14. L. Pauling, "The Nature of the Chemical Bond" (Cornell U.P., Ithaca, 1969), p. 403.
15. P. C. L. Pfeil, AERE Harwell Report M/TN11 (1952).
16. S. L. Altmann, C. A. Coulson, and W. Hume-Rothery, Proc. Roy. Soc. Lond. A240, 145 (1957).
17. F. Bader, K. Ganzhorn, and U. Dehlinger, Z. Phys. 137, 190 (1954).
18. N. F. Mott, Adv. Phys. 13, 325 (1964).
19. L. Pauling, Phys. Rev. 54, 899 (1938).
20. C. Zener, Phys. Rev. 81, 440 (1951); 82, 403 (1951); 83, 299 (1951); 85, 324 (1952).
21. J. B. Goodenough, Phys. Rev. 120, 67 (1960).
22. C. Herring, J. Appl. Phys. 31, 3S (1960).
23. H. Brooks, in "Electronic Structure and Alloy Chemistry of the Transition Elements" (Interscience, New York, 1963), p. 3.
24. J. Hasegawa, M. W. Finnis, and D. G. Pettifor, J. Phys. F: Met. Phys. 15, 19 (1985).
25. F. Ducastelle, J. Physique 31, 1055 (1970).
26. D. Gerlich and S. Hart, J. Appl. Phys. 55, 880 (1984).
27. E. Grüneisen, in "Handbuch der Physik," Volume 10 (Springer, Berlin, 1926), p. 1.
28. R. Fürth, Proc. Roy. Soc. A183, 87 (1944).
29. J. Friedel and C. M. Sayers, J. Phys. Lett. 38, L263 (1977).
30. J. Friedel and C. M. Sayers, J. Phys. Lett. 39, L59 (1977).
31. M. Shimizu, J. Phys. Soc. Japan 44, 792 (1978).
32. G. Hausch, J. Phys. F: Met. Phys. 7, L127 (1977).
33. J. Kollar and G. Solt, in "Phonons" (Flammarion Sciences, Paris, 1971), p. 331.

TABLE I. Chemical compositions (mass pct.).

Alloy	Mo	Cr	Ni	Mn	C	N	S	Si	P
1	2.05	18.5	13.8	1.05	0.021	0.180	0.004	0.30	0.002
2	2.06	18.0	12.0	1.00	0.024	0.188	0.004	0.30	0.003
3	2.98	18.2	14.0	1.02	0.022	0.188	0.005	0.30	0.002
4	3.00	18.0	11.8	1.01	0.023	0.200	0.005	0.29	0.002
5	4.02	17.9	14.2	1.00	0.022	0.196	0.004	0.30	0.002
6	4.08	18.2	12.1	1.03	0.020	0.204	0.005	0.28	0.002

TABLE II. Mass density and elastic constants.

Alloy	Density (g/cm^3)	C_ℓ (GPa)	G (GPa)	B (GPa)	E (GPa)	ν
1	7.972	262.6	77.28	159.6	199.6	0.292
2	7.961	262.9	77.52	159.6	200.2	0.291
3	7.989	262.8	76.72	160.5	198.5	0.294
4	7.980	263.0	77.18	160.1	199.5	0.292
5	8.004	263.1	76.27	161.4	197.7	0.296
6	7.995	263.0	76.44	161.0	198.0	0.295

TABLE III. Elastic-constant compositional variation based on y = a + bx relationship, where x denotes atomic fraction. Based on lower Ni alloys. Except ν, units are GPa.

	a	b	b/a
Molybdenum:			
G	78.7	−93	−1.18
B	158.1	−125	0.79
E	202.5	−185	−0.91
ν	0.287	0.349	1.22
Manganese:[a]			
G	78.3	−21	−0.27
B	158.2	−72	−0.45
E	201.7	−60	−0.30
ν	0.288	− 0.035	−0.12
Carbon-plus-Nitrogen:[b]			
G	78.4	−59	−0.76
B	159.6	−147	−0.93
E	202.0	−158	0.78
ν	0.288	− 0.034	−0.12

[a] Ref. 7.
[b] Ref. 8.

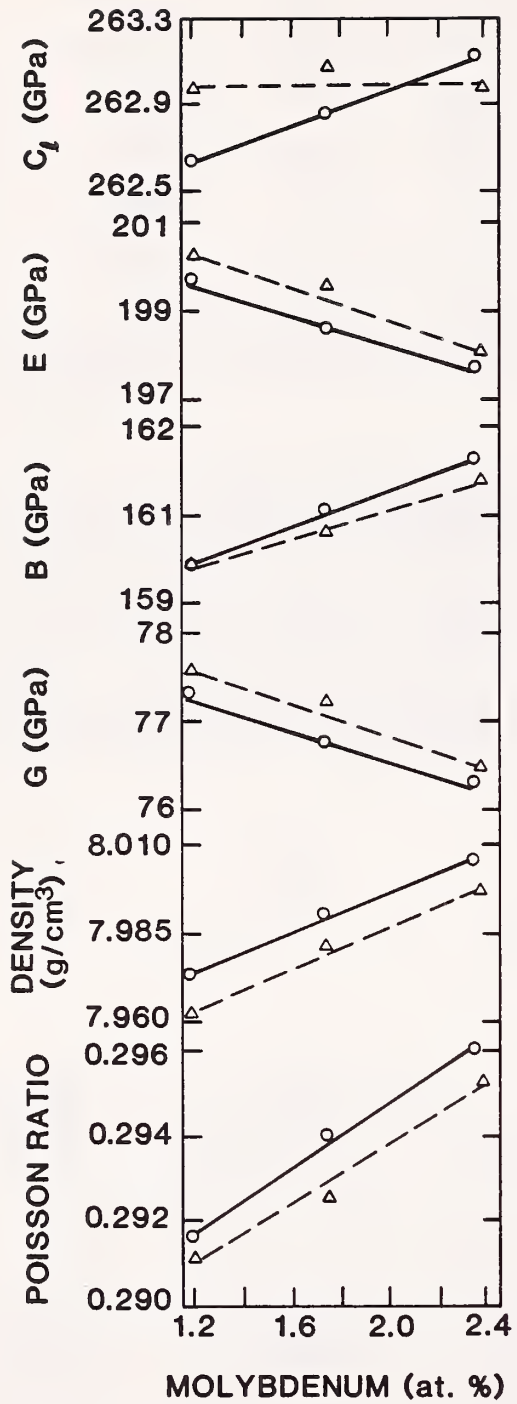

Fig. 1. Compositional variation of ρ = mass density, C_ℓ = longitudinal modulus, G = shear modulus, B = bulk modulus, E = Young modulus, and ν = Poisson ratio. Solid lines represent higher Ni content; dashed lines, lower Ni content.

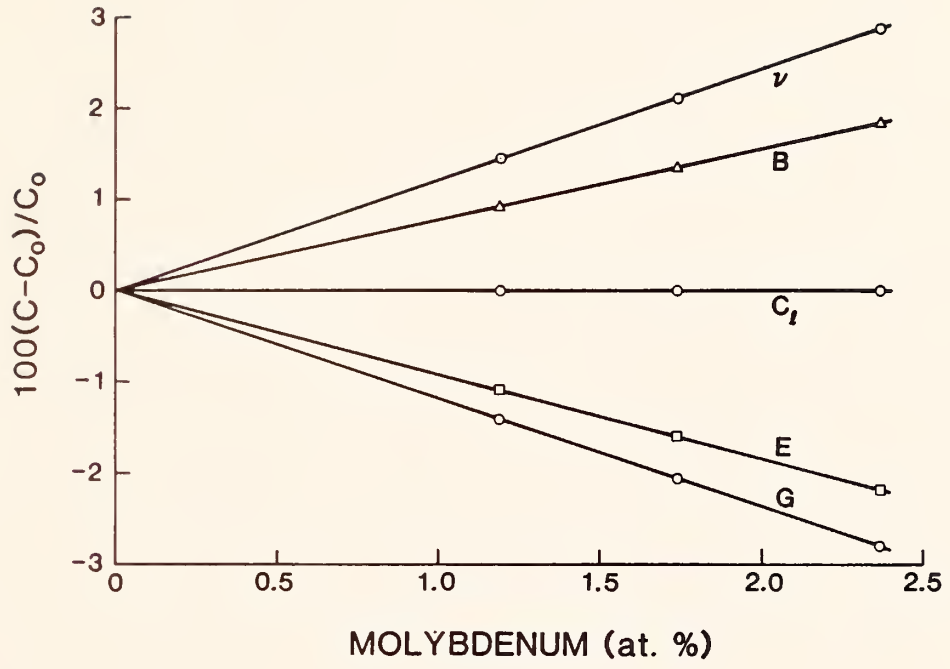

Fig. 2. Relative compositional variation of various elastic constants. The results represent the lower Ni alloys shown in Fig. 1.

MOLYBDENUM EFFECT ON VOLUME IN Fe–Cr–Ni ALLOYS*

H. M. Ledbetter and M. W. Austin
Fracture and Deformation Division
Institute for Materials Science and Engineering
National Bureau of Standards, Boulder, Colorado

By x-ray diffraction on powder specimens, we determined the unit-cell size for six face-centered-cubic Fe–Cr–Ni alloys, nominally Fe–19Cr–12Ni (at.%). In these alloys, the Mo content ranged up to 2.4 at.%. We found that Mo increases volume: 0.45% per at.% Usual models based on atomic volumes and elastic compressibilities fail to explain the large volume increase. We ascribe the discrepancy to changes in interatomic bonding, which we describe in terms of 3d-electron models.

INTRODUCTION

Among a solid's most important physical properties, atomic volume ranks foremost. Volume relates directly and inextricably to fundamental interatomic forces. Usual models of cohesion deal principally with three physical quantities: cohesive energy, bulk modulus, and atomic volume. Consider, for example, a Mie–Grüneisen interatomic potential:

$$U(r) = Ar^{-n} - Br^{-m}. \tag{1}$$

Here, r denotes interatomic spacing; A and n are coefficients of the repulsive energy; B and m are coefficients of the attractive energy. In this model, one obtains for the bulk modulus (reciprocal compressibility) [1]

$$B_o = V_o(\partial^2 U/\partial V^2)_{V=V_o} = mnU_o/9V_o. \tag{2}$$

Here U denotes internal energy; V, volume; U_o, cohesive energy; and V_o, equilibrium atomic volume. (Do not confuse B and B_o.)

More than fifty years ago, the strong effect of atomic size on solid-state alloy properties, especially solid solubility, was established by Hume–Rothery et al. [2,3]. Even earlier, Wasastjerna [4] and

*Intended for publication in Journal of Materials Science.

Goldschmidt [5] realized the importance of establishing elements' atomic radii. Pauling [6] found the concept of atomic radius essential for understanding molecular and crystal structures, which play vital roles in determining properties. Pauling [7] argued that a resonating-covalent-bond concept combined with atomic radii gives qualitative explanations of many properties: magnetic, heat capacity, hardness, compressibility, and thermal expansion. Waser and Pauling [8] related compressibilities and force constants to interatomic distance; they ascribed behavioral deviations to a change in bond type (electronic structure). Friedel [9] explained the nonlinear volume dependence of alloys as arising from the constituents' compressibility differences. Rudman [10] reviewed the atomic volumes of the metallic elements. He reported a range of atomic volumes from 8.1 $Å^3$ for Be to 116.0 $Å^3$ for Cs. The 3d transition metals from Cr through Ni show a narrow range between 10.9 and 12.2 $Å^3$.

The atomic-volume and elastic-constant interrelationship is well established. On this, the Waser and Pauling study was mentioned above. At least since Fuchs [11], we have known that the bulk modulus that arises from the free-electron gas varies as r^{-5}, where $V_o = (4/3)\pi r_o^3$. Gilman [12] showed that B varies as r^{-n}, where n equals 4 for alkali metals, 4 for covalent tetrahedrally bonded crystals, 8 for fcc carbides, 4 for fluorite-type crystals, 4 for ionic crystals, and 3 for solid rare gases. No simple B–r relationship arises for the transition metals. The explanation of why B decreases with increasing r clearly lies at some level more fundamental than the interatomic potential, which imposes no constraint on $[\partial^2 U(V)/(\partial V^2)]_{V=V_o}$ and V_o. If the interatomic-potential minimum shifts to another equilibrium volume, why should its curvature change?

In discussing cohesive forces in metals and alloys, Mott [13] cited experimental and theoretical reasons why the energy of an atom depends on the volume available to it rather than on the co-ordination number or its surroundings. Mott emphasized that atomic volume is more important than interatomic distance, which depends on co-ordination number.

The present study considers the volume change caused by alloying Mo, a body-centered-cubic element, into a face-centered-cubic Fe–Cr–Ni alloy. Fe, Cr, and Ni are 3d transition elements. Mo is a 4d transition element with much larger atomic volume: V(Mo)/V(Fe) = 15.50 $Å^3$/11.78 $Å^3$ = 1.32.

MEASUREMENTS

Materials

We obtained alloys from the research laboratory of a major manufacturer of Mo. Table I shows their chemical compositions. Alloys were prepared in a vacuum induction furnace, cast into round ingots 13.3 cm in diameter and 21.8 cm long, cropped and forged at 1100°C to billets 7.6 cm in cross section, rolled at 1100°C to 2.5-cm plate, annealed for 30 min at 1000°C, and water quenched. To prepare materials for x-ray diffraction, we filed the plates, sieved the powders to 0.053 to 0.150 mm, and annealed the powders in evacuated quartz ampules at 1050°C for 35 min.

X-ray diffraction

We prepared specimens by pressing the powders into viscous silicone grease in a flat sample holder. Specimens were placed in a commercial, horizontally polarized, Bragg–Brentano x-ray diffractometer. A 0.3-mm (0.18-degree) receiving slit at the goniometer radius of 22.5 cm was step-scanned in 0.02-degree 2θ increments at 60 s per step. The radiation consisted of Cu Kβ(1,3), wavelength 1.39225 Å, excited at 44 kV and 40 mA. Using a Ge solid-state detector, we measured each specimen twice. During measurements, temperature varied between 307 and 310 K.

We determined peak positions by fitting to a Lorentzian:

$$I = I_{max} \left[1 + \frac{(\theta - \theta_{max})^2}{2W^2} \right]^{-2} .$$

Here, I_{max} denotes maximum intensity; θ, diffraction angle; and W, full peak width at half-maximum intensity. We obtained nine f.c.c. diffraction lines: 111, 200, 220, 311, 222, 400, 331, 420, 422. To determine the unit-cell size, we used the 422 diffraction line calibrated against silicon (NBS Standard Reference Material SRM-740A). For Cu Kβ radiation, the 422 line appears at 143 degrees in 2θ.

RESULTS

Figure 1 shows the principal results: measured unit-cell size, a, together with a linear-least-squares best-fit line (in angstroms):

$$a = a_1 + bc = 3.5926 + 0.5385c. \qquad (3)$$

Here a_1 denotes the zero–Mo intercept; b, the slope da/dc; and c, the atomic fraction of Mo. For purposes below, we shall rewrite Eq. 3:

$$\frac{a - a_1}{ca_1} = \frac{\Delta a}{ca_1} = \frac{b}{a_1} = 0.1499 \qquad (4)$$

And, using simple models, we shall try to estimate this quantity. For cell-size measurements, we estimate the systematic uncertainty as 0.0006 Å and the random uncertainty as 0.0001 Å. For the slope da/dc, we estimate the uncertainty as 0.05 Å. From this result, it follows that the volume change equals

$$\frac{V - V_1}{cV_1} = 0.4504 \qquad (5)$$

Thus, volume increases approximately one-half percent per atomic percent Mo. If volume followed a linear rule-of-mixture, this result implies that Mo's effective atomic volume exceeds the average Fe–Cr–Ni–alloy atomic volume by 45%.

In Table I, one sees two sets of alloys differing in Ni content by approximately 2%. The measurement results in Fig. 1 are different for low-Ni and high-Ni alloys. Compared with Mo, the Ni effect on volume is negligible, and we ignore it. Thus, the line in Fig. 1 represents the average Ni content: 13.0 wt.%.

DISCUSSION

First, we shall consider whether existing simple models explain the volume change shown in Fig. 1. We consider six models, use them to calculate $(d - d_1)/cd_1$, and show the results in Table II. By d, we mean the nearest-neighbor spacing. Subscript 1 denotes the Mo-free Fe–Cr–Ni alloy, the reference state. Other measures of interatomic spacing include the unit-cell size, a, where

$$d = (\sqrt{2}/2)\, a, \tag{6}$$

and the effective atomic volume,

$$V = (4\pi/3)r^3 = a^3/4. \tag{7}$$

Among these, we find the relationships

$$\frac{\Delta d}{d} = \frac{\Delta a}{a} = \frac{\Delta r}{r}. \tag{8}$$

Some of the models calculate $\Delta V/V$ rather than $\Delta d/d$. To compare these, we used the relationship

$$\frac{\Delta V}{V_1} = \frac{d^3 - d_1^3}{d_1^3} = 3\left(\frac{d - d_1}{d_1}\right) + 3\left(\frac{d - d_1}{d_1}\right)^2 + \left(\frac{d - d_1}{d_1}\right)^3. \tag{9}$$

Vegard's model

In 1921, Vegard [14] proposed that the unit-cell size follows a linear rule-of-mixture:

$$d = (1 - c)d_1 + cd_2. \tag{10}$$

Here, subscript 1 denotes the solvent, subscript 2 denotes the solute, and c denotes the atomic fraction. Thus,

$$\frac{\Delta d}{cd_1} = \frac{d_2 - d_1}{d_1}. \tag{11}$$

Volume model

A simple alternative to Eq. (10) substitutes atomic volume for interatomic distance:

$$V = (1 - c)V_1 + cV_2. \tag{12}$$

Zen [15] adopted this model. And, in discussing cohesion in metals and alloys, Mott [13] argued that atomic volume rather than interatomic distance tends to remain constant. Thus,

$$\frac{\Delta d}{cd_1} \approx \frac{1}{3}\frac{\Delta V}{cV_1} = \frac{V_2 - V_1}{3cV_1}. \tag{13}$$

Sphere-in-hole model

The above two models focus on atomic size and neglect atomic compressibility, or the elastic-stiffness constants. An isotropic material possesses two independent elastic constants, often chosen as bulk modulus (reciprocal compressibility), B, and shear modulus, G. Related to these is the Poisson ratio

$$\nu = \frac{1}{2}\frac{3B - 2G}{3B + G}. \tag{14}$$

The sphere-in-hole model originated with Bitter [16] and received much elaboration by Eshelby [17]. For the key equations, we take those given by Teodosiu [18]:

$$\Delta V = \frac{1 + (4G_1/3B_1)}{1 + (4G_1/3B_2)}\Delta V'. \tag{15}$$

Here, $\Delta V'$ represents the solvent-atom—solute-atom volume difference:

$$\Delta V' = (4\pi/3)(r_2^3 - r_1^3). \tag{16}$$

4.4 Friedel model

Based on a modified Eshelby model, Friedel [9] gives the basic relationship:

$$\frac{d - d_1}{cd_1} = \frac{d_2 - d_1}{d_1} + \frac{x + 1}{x + B_1/B_2}. \tag{17}$$

If ν denotes the Poisson ratio defined in Eq. (14), then

$$x = (1 + \nu)/[2(1 - 2\nu)]. \tag{18}$$

4.5 Zener's model

Both the sphere-in-hole model and the Friedel model depend on atomic volumes and on elastic constants, the second-order elastic constants B and G. The large strains suggest that third-order elastic constants may enter the problem. In 1942, Zener [19] developed a model that contains one third-order elastic constant: dG/dP, the shear-modulus pressure derivative. Zener used an atomic-volume rule-of-mixture, Eq. (12), and found two volume-change components:

$$\Delta V = \Delta V^{(1)} + \Delta V^{(2)}. \tag{19}$$

The two components are given by

$$\Delta V^{(1)} = 12\pi r_1^2 \Delta r(1 - \nu_1)/(1 + \nu_1), \tag{20}$$

and

$$\Delta V^{(2)} = \frac{2\Delta r}{r_1}\left(\frac{dG_1}{dP} - \frac{G_1}{B_1}\right)\Delta V^{(1)}. \tag{21}$$

4.6 Gschneidner–Vineyard model

Another model containing a third-order elastic constant arose in a study by Gschneidner and Vineyard [20]. They found that

$$\Delta V = c(1 - c)\, 8\pi\bar{r}(\Delta r)^2. \tag{22}$$

Here,

$$\bar{r} = (1 - c)r_1 + cr_2. \tag{23}$$

Note that this relationship contains a c^3 term. For dilute concentrations, $c \ll 1$, Gschneidner and Vineyard found

$$\frac{d - d_1}{cd_1} = \frac{d_2 - d_1}{d_1} + 2\left(\frac{dG_1}{dP} - \frac{G_1}{B_1}\right)\left(\frac{\Delta d}{d_1}\right)^2. \tag{24}$$

Table II shows results from the above six models. As input for the calculations, we used $r_1 = 2.5389$ Å, $r_2 = 2.7252$ Å, $B_1 = 158$ GPa, $B_2 = 260$ GPa, $\nu_1 = 0.275$, $G_1 = 83.5$ GPa, $G_2 = 260$ GPa, and $dG/dP = 1.75$. The second-order elastic constants for the Mo-free state were reported by Ledbetter and Kim [21] and dG/dP by Gerlich and Hart [22]. We took the remaining input from standard sources.

The results in Table II, ranging from 0.073 to 0.099, fall far below the observed value: 0.15. For Mo, if we adopt the Pauling radius for coordination number twelve [23], 2.792 Å replacing 2.7252 Å, the model calculations improve, but they remain well below observation.

The measurement-model discrepancy suggests that alloying Mo into Fe–Cr–Ni involves electron-structure changes. This observation contains no

surprise for several reasons. First, we are placing an element that prefers the b.c.c. structure into an f.c.c. structure. From a chemical-bond viewpoint, an electron cloud with lobes in {111} directions must adjust to electron clouds with lobes in {110} directions [24]. Second, Mo represents no ordinary b.c.c. metal, but a paradigm. Among the 4d elements, Mo shows the highest melting point. Outside the metallic orbital, Pauling [23] assigns Mo a valence of 5.0, exactly the number of bonding electrons for maximum cohesion. The potency of Mo as a b.c.c. stabilizer emerged in Pfeil's [25] studies on Zr alloys. Altmann et al. [26] point out that the b.c.c. stabilizing effect "should be more marked for Mo and W, where we have a peak of the d weight." Altmann et al. also point out that, despite favorable size factors, Mo shows practically no solid solubility in Ag, and Cr, none in Cu. Thus, when alloyed into an f.c.c. Fe–Cr–Ni alloy, we expect Mo to cause strong physical-property changes.

In trying to understand the physical properties of these alloys, we confront one of solid state physics's most difficult problems: quantum-mechanical theory of d electrons. Despite enormous effort—for example Mott [27], Pauling [28], Zener [29], Bader et al. [24], Goodenough [30], Friedel et al. [31]—the problem remains unsolved. Herring [32] gave an elementary critique of the state of d electrons in transition metals. He concluded that elements in the 3d row should resemble the free atoms and that most of these metals possess itinerant electrons. This reference contains Herring's much-cited remark on the electronic theories: "It is like mixing a few liquors in various proportions to get a variety of different cocktails." Mainly from the viewpoint of d-band theory, Brooks [33] reviewed the subject. In his review, Brooks disputes ideas based on crystal-field theory and separation of d levels into E_g and T_{1g} subbands. (However, a recent, successful, tight-binding calculation of iron's elastic constants invokes the E_g orbitals [34].)

In general, we expect that whatever increases volume will decrease cohesion and decrease elastic stiffness. The present alloy system violates this precept. Ledbetter and Kim [21] showed that alloying Mo into Fe–Cr–Ni increases the bulk modulus. Thus, to understand these alloys, we must identify an electronic effect that simultaneously increases volume and increases bulk modulus, the V_o and B_o in Eq. (2).

A theory by Ducastelle [35] leads to simple relationships for the volume and the bulk modulus. He assumed that the total energy arises from two sources: d-band energy calculated by a tight-binding approximation and Born–Mayer repulsive energy. Although this model is too simplified to explain present results, it displays the principal features necessary for an improved calculation. For the Wigner–Seitz radius, r_o, Ducastelle obtained

$$r_o = \frac{1}{p - q} \ln\frac{pc}{qAW_o}. \tag{25}$$

The bandwidth approximation is

$$W = W_o e^{-qr}. \tag{26}$$

The repulsive energy is

$$E_r = Ce^{-pr} \tag{27}$$

and

$$A = z(10 - z)/20. \tag{28}$$

Here, p and q are constants and z denotes the average number of electrons per atom in the d-band. For the bulk modulus, Ducastelle obtained

$$B_o = V_o \left[\frac{\partial^2 E}{\partial V^2}\right]_{V=V_o} = \frac{r_o^2}{9} \left[\frac{\partial^2 E_c}{\partial r_o^2}\right]_{r=r_o} = pqr_o^2 E_c/9. \tag{29}$$

Thus, Ducastelle's model predicts that increased atomic volume ($V_o = 4\pi r_o^3/3$) leads to decreased bulk modulus because E_c represents cohesive energy per unit volume.

Aside from the complications of 3d electrons, another factor arises in these alloys: magnetization. Even though the alloys show macroscopic paramagnetism, disordered local atomic moments may affect the physical properties. The usual view is that magnetization increases volume and decreases bulk modulus [36,37]. However, several recent studies [38–41] show that the bulk modulus may increase with magnetization and increasing volume. On the basis of their model, Friedel and Sayers [40] expect such bulk-modulus increases to occur in elements with a high electron-density-of-states, transition elements to the right: Fe, Co, and Ni.

Finally, we note that the measurements shown in Fig. 1 suggest that Ni content affects the slope da/dc. Lower Ni content gives a lower slope. This effect presents little surprise. Nickel, with ten electrons outside the Ar shell, represents the transition metal that differs most from Mo (with six outside electrons). Along with Cu, Ni represents a prototype f.c.c. metal. Thus, we expect its reluctance to accept Mo as an alloying element.

SUMMARY

By x-ray diffraction, we measured the volume change accompanying Mo alloying into an Fe–Cr–Ni alloy. In volume, Mo atoms are approximately 30% larger than Fe atoms. We found that Mo increases volume by 45%. Existing models based on atomic volume and elastic compressibility fail to explain the large volume increase. We ascribe this large increase to electronic effects associated with substituting Mo, which prefers a b.c.c. crystal structure, into an f.c.c. crystal structure. Another study showed that the alloy's bulk modulus increases with increasing volume. This unexpected result—increased volume, increased bulk modulus—is consistent with some recent theoretical studies.

REFERENCES

1. E. Grüneisen, in "Handbuch der Physik, Volume 10" (Springer, Berlin, 1926) p.1.
2. W. Hume-Rothery, G. W. Mabbott, and K. M. Channel-Evans, Philos. Trans. Roy. Soc. A233 (1934) 1.
3. W. Hume-Rothery, R. E. Smallman, and C. W. Haworth, "The Structure of Metals and Alloys" (Inst. Metals, London, 1969) pp. 71-109.
4. J. A. Wasastjerna, Soc. Sci. Fenn. Comm. Phys. Math. 38 (1923) 1.
5. V. M. Goldschmidt, Ber. Deut. Chem. Ges. 60 (1927) 1263.
6. L. Pauling, "The Nature of the Chemical Bond" (Cornell U.P., Ithaca, 1960) esp. pp. 393-448.
7. L. Pauling, Proc. Roy. Soc. Lond. A196 (1949) 343.
8. J. Waser and L. Pauling, J. Chem. Phys. 18 (1950) 747.
9. J. Friedel, Philos. Mag. 46 (1955) 514.
10. P. S. Rudman, Trans. Metall. Soc. AIME 233 (1965) 864.
11. K. Fuchs, Proc. Roy. Soc. Lond. A158 (1935) 585.
12. J. J. Gilman, "Micromechanics of Flow in Solids: (McGraw-Hill, New York, 1969) pp. 29-41.
13. N. F. Mott, Rep. Prog. Phys. 25 (1962) 218.
14. L. Vegard, Z. Phys. 5 (1921) 17.
15. E. Zen, Amer. Mineralogist 41 (1956) 523.
16. F. Bitter, Phys. Rev. 37 (1931) 1527.
17. J. D. Eshelby, Solid State Phys. 3 (1956) 79.
18. C. Teodosiu, "Elastic Models of Crystal Defects" (Springer, Berlin, 1982) pp. 287-295.
19. C. Zener, Trans. AIME 147 (1942) 361.
20. K. A. Gschneidner and G. H. Vineyard, J. Appl. Phys. 33 (1962) 3444.
21. H. M. Ledbetter and S. A. Kim, unpublished research, National Bureau of Standards, Boulder, Colorado (1986).
22. D. Gerlich and S. Hart, J. Appl. Phys. 55 (1984) 880.
23. Ref. 6, p. 403.
24. F. Bader, K. Ganzhorn, and U. Dehlinger, Z. Phys. 137 (1954) 190.
25. P. C. L. Pfeil, AERE Harwell Report M/TN 11 (1952).
26. S. L. Altmann, C. A. Coulson, and W. Hume-Rothery, Proc. Roy. Soc. Lond. A240 (1957) 145.
27. N. F. Mott, Adv. Phys. 13 (1964) 325.
28. L. Pauling, Phys. Rev. 54 (1938) 899-904.
29. C. Zener, Phys. Rev. 81 (1951) 440; 82 (1951) 403; 83 (1951) 299; 85 (1952) 324.
30. J. B. Goodenough, Phys. Rev. 120 (1960) 67.
31. J. Friedel, G. Leman, and S. Olszewski, J. Appl. Phys. 32 (1961) 3255.
32. C. Herring, J. Appl. Phys. 31 (1960) 3S.
33. H. Brooks, in "Electronic Structure and Alloy Chemistry of the Transition Elements" (Interscience, New York, 1963) pp. 3-28.
34. H. Hasegawa, M. W. Finnis, and D. G. Pettifor, J. Phys. F: Met. Phys. 15 (1985) 19.
35. F. Ducastelle, J. Physique 31 (1970) 1055.
36. J. F. Janak and A. R. Williams, Phys. Rev. B 14 (1976) 4199.
37. J. Friedel and C. M. Sayers, J. Phys. Lett. 38 (1977) L263.
38. G. Hausch, J. Phys. F: Met. Phys. 7 (1977) L127.
39. M. Shimizu, J. Phys. Soc. Japan 44 (1978) 792.

40. J. Friedel and C. M. Sayers, J. Phys. Lett. 39 (1977) L59.
41. J. Kollar and G. Solt, in "Phonons" (Flammarion Sciences, Paris, 1971) pp. 331–335.

TABLE I Chemical compositions (wt. %)

Alloy	Mo	Cr	Ni	Mn	C	N	S	Si	P
1	2.05	18.5	13.8	1.05	0.021	0.180	0.004	0.30	0.002
2	2.06	18.0	12.0	1.00	0.024	0.188	0.004	0.30	0.003
3	2.98	18.2	14.0	1.02	0.022	0.188	0.005	0.30	0.002
4	3.00	18.0	11.8	1.01	0.023	0.200	0.005	0.29	0.002
5	4.02	17.9	14.2	1.00	0.022	0.196	0.004	0.30	0.002
6	4.08	18.2	12.1	1.03	0.020	0.204	0.005	0.28	0.002

TABLE II Model predictions of (1/a) (da/dc)

Model	Prediction
sphere-in-hole	0.069
Vegard	0.073
Gschneidner, Vineyard	0.086
Friedel	0.087
Zener	0.099
Volume	0.104
Observed	0.150

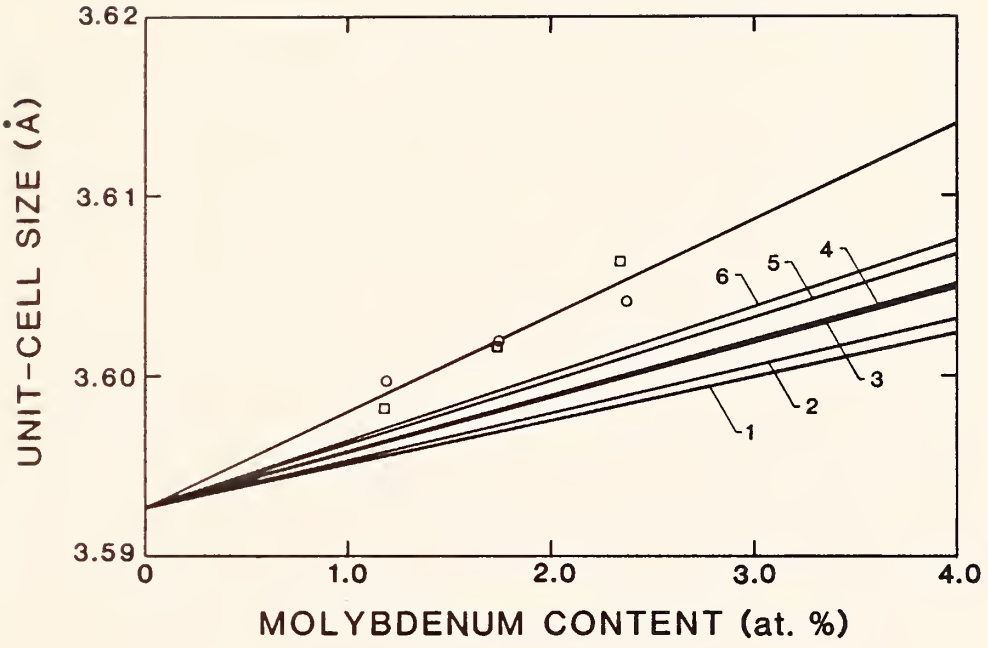

Fig. 1. Compositional variation of unit-cell dimension, a. Curve through measurement points represents a linear-least-squares fit to six values. Open circles represent lower Ni alloys; open squares represent higher Ni alloys. Lower curves represent six model predictions: (1) sphere-in-hole; (2) Vegard; (3) Gschneidner, Vineyard; (4) Friedel; (5) Zener; (6) volume.

LOW-TEMPERATURE MANGANESE CONTRIBUTIONS TO THE ELASTIC CONSTANTS OF FACE-CENTERED-CUBIC Fe–Cr–Ni STAINLESS STEEL*

H. M. Ledbetter and S. A. Kim
Fracture and Deformation Division
Institute for Materials Science and Engineering
National Bureau of Standards
Boulder, Colorado

By ultrasonic methods, we determined the elastic constants between 295 and 4 K of nominally Fe–18Cr–8Ni alloys containing up to six percent Mn. We report five elastic constants: C_ℓ = longitudinal modulus, B = bulk modulus, E = Young modulus, G = shear modulus, and ν = Poisson ratio. At all temperatures, Mn lowers all these elastic constants. Except for ν, larger reductions occur at 4 K than at 295 K. At 4 K, the bulk modulus decreases more than the shear modulus: approximately 0.54 and 0.30 percent per percent Mn, respectively. Manganese raises the magnetic-transition temperature, which occurs between 40 and 90 K, by approximately 9 K per percent Mn. A simple model predicts the volume increase accompanying Mn alloying. But, a simple model fails to predict the elastic-constant reductions; this suggests magnetic interatomic interactions.

INTRODUCTION

Previously [1], we reported the ambient-temperature contribution of Mn to the elastic constants of face-centered-cubic (f.c.c.) Fe–Cr–Ni alloys. Nominally, these alloys contained 18 percent Cr and 8 percent Ni (mass percentage). Our results showed that Mn lowers all the elastic-stiffness constants and the Poisson ratio. The largest effect occurred in the bulk modulus:

$$\frac{\Delta B}{cB} = -0.47. \qquad (1)$$

---

*Intended for Journal of Materials Science.

Here c denotes fractional Mn concentration. Thus, the bulk modulus decreases approximately 0.5 percent per percent solute. Because Mn's atomic mass (54.94) differs only slightly from the alloy's effective atomic mass (55.33), differences between atomic and mass percentages are small.

Here, for the same polycrystalline alloys, we report further studies: elastic-constant measurements between 295 and 4 K. These studies answer two questions. First, how does the low-temperature magnetic phase transition affect the elastic constants? Second, does the Mn-concentration dependence at 4 K resemble that at 295 K? In studying similar Fe–Cr–Ni alloys alloyed with interstitial carbon and nitrogen, Ledbetter et al. [2] found strongly different composition effects at 4 and 295 K.

Previously [1], we described Mn's peculiar atomic properties and their possible effect on alloy physical properties. These peculiarities include a 58-atom unit cell, a bulk modulus 0.35 that of Fe's (despite similar atomic volumes), antiferromagnetic electronic interactions, and negative low-temperature thermal expansivity.

We determined the elastic constants by measuring mass density and the near-10-MHz ultrasonic velocities.

MEASUREMENTS

Most of the measurement details we reported previously [1]. We achieved low-temperature measurements to 4 K by procedures described by Naimon et al. [3].

RESULTS

For ten alloys at both 295 and 4 K, Table I shows the following measured and computed quantities: ρ = mass density, v_ℓ = longitudinal sound velocity; v_t = transverse sound velocity; C_ℓ = longitudinal modulus = ρv_ℓ^2; G = shear modulus = ρv_t^2; B = bulk modulus = $C_\ell - 4G/3$; E = Young modulus = $9GB/(3B + G)$; and ν = Poisson ratio = $[E/(2G)] - 1$. For 295 and 4 K, Figs. 1 and 2 show graphs of the measured quantities plotted versus composition.

For one alloy, Fig. 3 shows the temperature variation of the elastic constants.

Figure 4 shows the effect of Mn on the magnetic-transition temperature. We estimated that the transition temperature for both v_ℓ and v_t corresponds to the temperature halfway between the maximum and minimum sound velocities. Also in Fig. 4, we include results from magnetic-susceptibility measurements [4].

DISCUSSION

First, we consider volume effects. Uncorrected for Cr and Ni fluctuations, our mass-density measurements give the volume change:

$$\frac{\Delta V}{cV} = -\frac{\Delta \rho}{c\rho} = 0.092. \tag{2}$$

Here, c denotes fractional Mn concentration. Thus, one percent of Mn raises the effective atomic volume approximately 0.1 percent. Many models exist for predicting the alloying volume change. The simplest is a linear rule-of-mixture:

$$V = (1 - c)V_1 + cV_2. \tag{3}$$

Here, subscript 1 denotes the reference material, the Fe–Cr–Ni alloy, and subscript 2 denotes the alloy element, Mn. From our mass-density measurements and corroborating x-ray-diffraction measurements [5], we find V_1 equals 11.60 Å^3. The volume V_2 corresponding to a Mn atom in an f.c.c. crystal structure remains uncertain. For the α-Mn crystal structure, V_2 equals 12.21 Å^3. For f.c.c. Mn, Pauling [6] estimated V_2 to be 11.58 Å^3. Studies on Mn–Cu alloys predict V_2 values of 12.59 [7], 12.67 [8], and 13.02 Å^3 [9]. We adopt a V_2 value of 12.59 Å^3. Then Eq. (3) predicts

$$\frac{\Delta V}{cV} = 0.085. \tag{4}$$

A more realistic model, which uses both second-order and third-order elastic constants, was given by Gschneidner and Vineyard [10]:

$$\frac{\Delta d}{cd} = \frac{d_2 - d_1}{d_1} + 2\left(\frac{dG}{dP} - \frac{G}{B}\right)\left(\frac{\Delta d}{d_1}\right)^2 \tag{5}$$

Here, d denotes interatomic spacing; G, shear modulus; B, bulk modulus; and P, pressure. From Gerlich and Hart [11], dG/dP = 1.75, and d relates to volume according to

$$d = (\sqrt{2}/2)a = (\sqrt{2}/2)\,(V/4)^{1/3}. \tag{6}$$

Here, a denotes cubic unit-cell dimension, and

$$\frac{\Delta V}{V_1} = \frac{d^3 - d_1^3}{d_1^3} = 3\,\frac{d - d_1}{d_1} + 3\left(\frac{d - d_1}{d_1}\right)^2 + \left(\frac{d - d_1}{d_1}\right)^3. \tag{7}$$

Substituting into Eq. (5) and using Eq. (7), we obtain

$$\frac{\Delta V}{cV} = 0.091. \tag{8}$$

Thus, a simple model predicts the observed volume change.

Second, we consider the observed elastic-constant reductions caused by Mn alloying. As described elsewhere [12], a model by Eshelby predicts the elastic-constant changes arising from volume change caused by dilatation centers:

$$\frac{\Delta B}{B} = - \frac{dB}{dP} \frac{\gamma - 1}{\gamma} \frac{dV}{V} \tag{9}$$

and

$$\frac{\Delta G}{G} = - \frac{dG}{dP} \frac{B}{G} \frac{1}{\gamma} \frac{dV}{V} . \tag{10}$$

Here,

$$\gamma = \frac{3B + 4G}{3B} = 3 \frac{1 - \nu}{1 + \nu} . \tag{11}$$

From Gerlich and Hart [11], dB/dP = 5.57 and dG/dP = 1.75. Thus, on the basis of the observed volume change, these relationships predict $\Delta B/cB = -0.20$ and $\Delta G/cG = -0.21$. These predictions fall well below observation: -0.54 and -0.30 for B and G, respectively. This discrepancy, especially for B, means that a simple model based on volume change and second-order and third-order elastic constants fails to explain observation. We conclude that other interatomic interactions occur: probably local magnetic interactions, which affect B more than G. As described below, two other observations support the hypothesis of local magnetic interactions. First, Mn raises the magnetic-transition temperature, stabilizing an ordered magnetic phase. Second, upon cooling, far above the magnetic transition, B softens before G. This suggests that as interatomic spacing decreases, magnetic repulsion interactions intensify and volume increases, lowering B.

Third, we compare the 295-K and 4-K composition effects. Figures 1 and 2 show their similarity, the 4-K changes being slightly larger. (The Poisson ratio provides an exception: at 4 K, it changes less with composition.) This similarity suggests that the Mn—Fe—Cr—Ni interactions do not differ much at temperatures above and below the magnetic-transition temperature.

Fourth, we consider the cooling curves, which reproduced reversibly during heating. At the magnetic transition temperature (confirmed separately by magnetic-susceptibility measurements [4]), all the elastic stiffnesses decrease and the Poisson ratio increases. Although we did not measure the volume change associated with the magnetic transition, we suspect that this expansion during cooling may explain most of the elastic-stiffness decrease. Above, we mentioned that the bulk modulus begins to soften at temperatures well above the magnetic-transition temperature. This softening we ascribe to increased (by lattice contraction) local magnetic interactions, interactions that soften B but not G. Below the magnetic-transition temperature, all the elastic stiffnesses resume usual temperature behavior, except the Poisson ratio. Instead of decreasing as expected, it tends to increase. Again, we ascribe this unexpected tendency to increase as showing changes in magnetic interactions, this time <u>below</u> the magnetic-transition temperature.

Fifth, we consider how Mn changes the magnetic-transition temperature. If Mn only increased volume, we would expect the transition temperature to decrease, because the interacting species are farther apart, but, we observe an increase: approximately 9 K per atomic percent Mn. Again, we suspect that increased local magnetic interactions enhance the existing tendency of the Fe–Cr–Ni alloy to order magnetically. Whether the dominant interaction is Fe–Mn, or otherwise, remains uncertain.

CONCLUSIONS

From this study of nominally Fe–18Cr–8Ni alloys, there emerge five conclusions:

1. Elastic-constant changes caused by Mn alloying at 4 K strongly resemble the changes at 295 K. Except for the Poisson ratio, the 4-K results show slightly larger reductions. Thus, cooling through the magnetic phase transition produces no large changes in the Mn elastic-constant contributions.

2. As expected from previous studies, cooling through the magnetic phase transition decreases all the elastic stiffnesses and increases the Poisson ratio. Above the magnetic phase transition, the bulk modulus begins to soften.

3. Manganese raises the magnetic-transition temperature by a large amount: 9 K per atomic percent Mn.

4. A simple model based on atomic volumes and second-order and third-order elastic constants explains the volume increase.

5. Simple models fall short by approximately one-half in explaining the elastic-constant decreases. Especially, the bulk modulus decreases more than expected. We attribute this softening to local magnetic interatomic interactions.

ACKNOWLEDGMENT

This study received support from the U.S. DoE Office of Fusion Energy. M. W. Austin consulted on the sound-velocity measurements.

REFERENCES

1. H. M. Ledbetter, J. Mater. Sci. 20 (1985) 2923.
2. H. M. Ledbetter, M. W. Austin, and S. A. Kim, Mater. Sci. Eng., forthcoming.
3. E. R. Naimon, W. F. Weston, and H. M. Ledbetter, Cryogenics 14 (1974) 246.
4. E. R. Jones, T. Datta, C. Almasan, D. Edwards, and H. M. Ledbetter, Mater. Sci. Eng., forthcoming.

5. H. M. Ledbetter and M. W. Austin, unpublished research, National Bureau of Standards, Boulder, Colorado (1986).
6. L. Pauling, "The Nature of the Chemical Bond" (Cornell U.P., Ithaca, 1960) p. 403.
7. F. T. Worrell, J. Appl. Phys. **19** (1948) 929.
8. ASTM card 17-910, American Society for Testing and Materials, Philadelphia.
9. P. Venkateswararao and D. K. Chatterjee, J. Mater. Sci. **15** (1980) 139.
10. K. A. Gschneidner and G. H. Vineyard, J. Appl. Phys. **33** (1962) 3444.
11. D. Gerlich and S. Hart, J. Appl. Phys. **55** (1984) 880.
12. H. M. Ledbetter and M. W. Austin, Mater. Sci. Eng. **70** (1985) 143.

TABLE I Measured and derived quantities

Mn (mass %)	ρ (g/cm^3)	v_ℓ (cm/μs)	v_t (cm/μs)	C_ℓ (GPa)	G (GPa)	B (GPa)	E (GPa)	ν
T = 295 K								
1.02	7.904	0.5752	0.3145	261.5	77.18	157.3	201.2	0.287
2.01	7.861	0.5761	0.3145	260.9	77.75	157.2	200.3	0.288
3.85	7.875	0.5738	0.3143	259.3	77.79	155.6	200.0	0.286
5.81	7.862	0.5717	1.3131	257.0	77.08	154.2	198.2	0.286
T = 4 K								
1.02	7.975	0.5783	0.3206	266.7	81.94	157.4	209.5	0.278
2.01	7.931	0.5794	0.3204	266.2	81.39	157.7	208.3	0.280
3.85	7.9448	0.5761	0.3193	263.7	80.98	155.7	207.0	0.278
5.81	7.9329	0.5742	0.3185	261.5	80.45	154.3	205.6	0.278

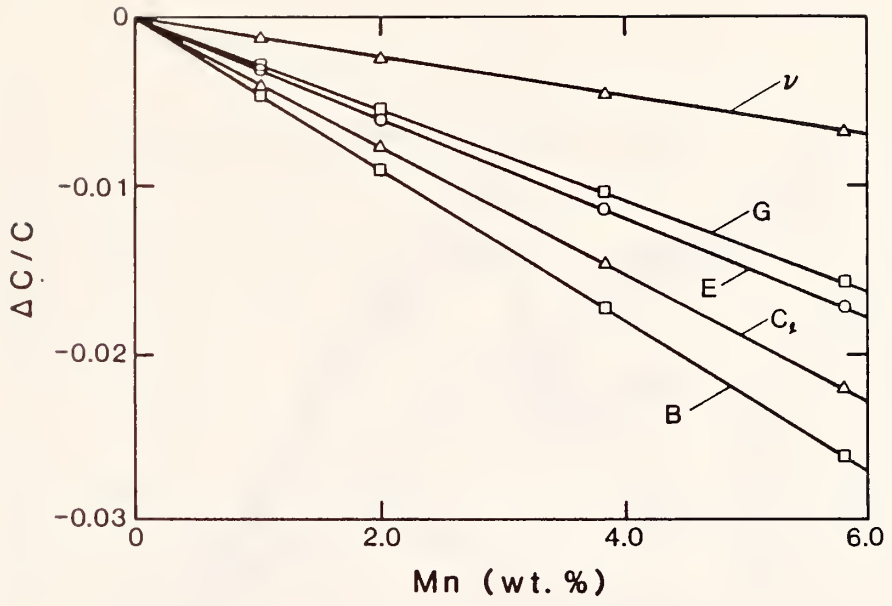

Fig. 1. Compositional variation of several measured quantities: C_ℓ = longitudinal modulus, B = bulk modulus, G = shear modulus, E = Young modulus, ν = Poisson ratio. Temperature equals 295 K.

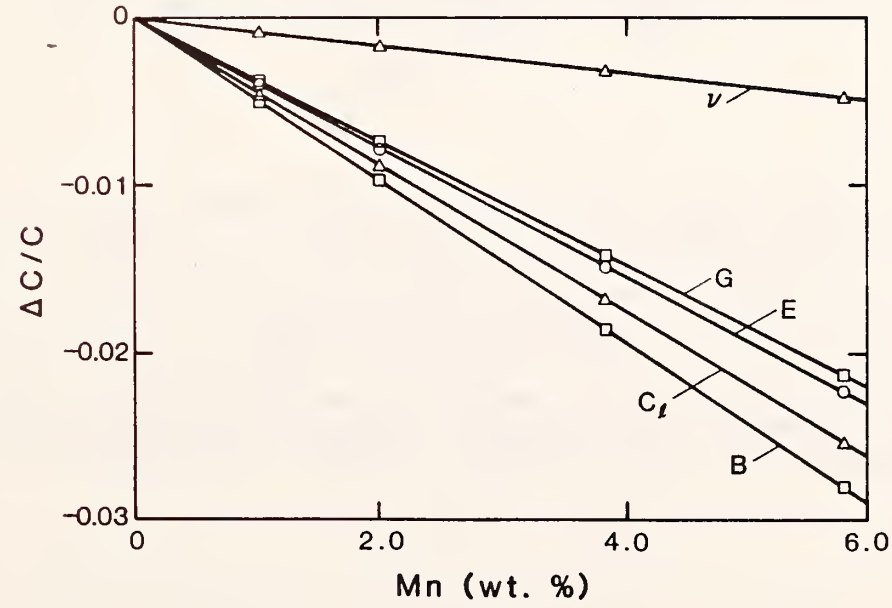

Fig. 2. Companion figure to Figure 1, except temperature equals 4 K.

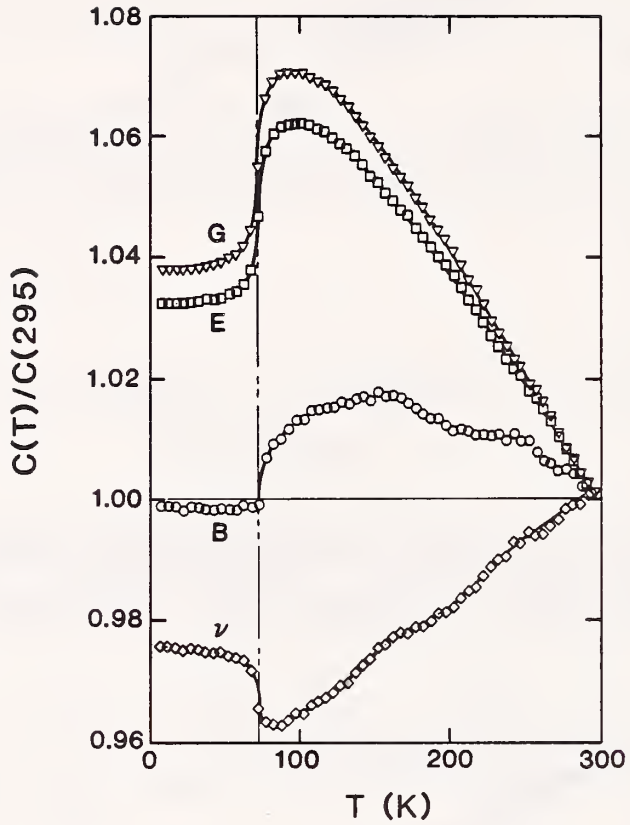

Fig. 3. For the 3.85-Mn alloy, variation with temperature of several measured quantities: B = bulk modulus, G = shear modulus, E = Young modulus, ν = Poisson ratio. Nonregular behavior arises from a reversible magnetic phase transition. The dashed line indicates temperature corresponding to cusp in magnetic-susceptibility versus temperature. The negative slope $d\nu/dT$ suggests further low-temperature magnetic changes. Softening of B during cooling suggests magnetic changes premonitory to paramagnetic–antiferromagnetic (Néel) transition.

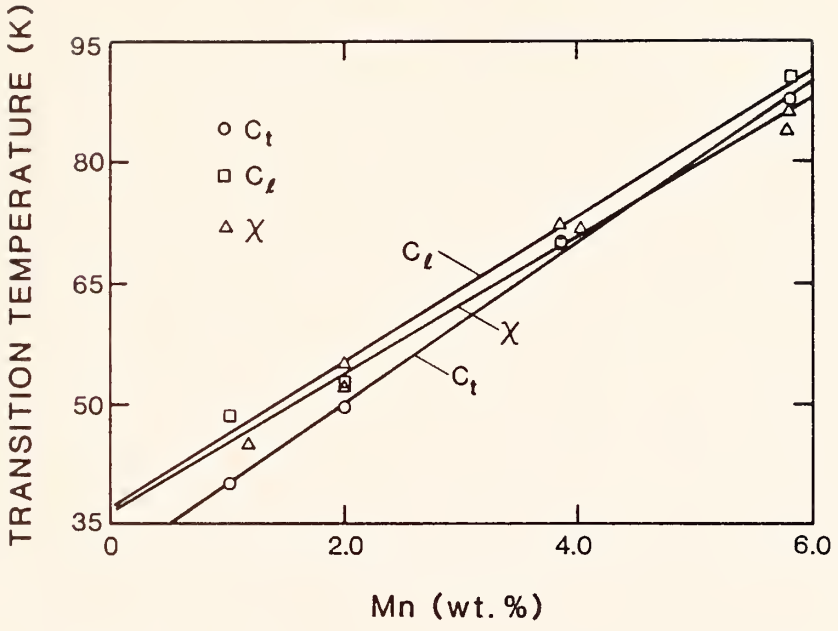

Fig. 4. Manganese alloying effect on magnetic (Néel) transition temperature. Chi denotes dc magnetic susceptibility.

Journal of Nuclear Materials 141–143 (1986) 44–48
North-Holland, Amsterdam

STRENGTH AND TOUGHNESS OF AISI 304 AND 316 AT 4 K *

N.J. SIMON and R.P. REED

Fracture and Deformation Division, National Bureau of Standards, 325 Broadway, Boulder, CO 80303, USA

Structural design of superconducting magnets in fusion energy devices requires reliable property data at 4 K. Nitrogen-strengthened AISI 304 and 316 stainless steels are considered to be the best currently available low temperature structural alloys on the basis of their fabricability and their potential to meet the US fusion research goals of combined 1000 MPa yield strength and 200 MPa $m^{1/2}$ fracture toughness at 4 K. This paper presents provisional equations for the yield strength of 304- and 316-type alloys at 4 K as a function of N content and grain size. Provisional equations for the 4 K fracture toughness, $K_{Ic}(J)$, of these alloys are presented, in which the effects of yield strength, Ni and Mn content, and inclusion spacing are expressed quantitatively. The equations result from regression analyses of a matrix of NBS measurements that includes more extensive numerical data on alloying, refining, and processing parameters than have previously been available.

1. Introduction

Superconducting magnets for future fusion energy reactors will require cryogenic structural alloys with improved combinations of yield strength and fracture toughness at 4 K. Recently we have made considerable progress in understanding how quantitative parameters of alloying, refining, and processing can be specified for AISI 300 series stainless steels to achieve the strength-toughness goals of the US fusion program [1].

The structural alloy is required to withstand large magnetic forces in a superconducting magnet system of restricted dimensions, and thus, high strength is needed. In addition, because most structures are complex and have regions of high stress concentration, good fracture toughness is required. Our research has focused on the various AISI types of austenitic steels, especially 304 and 316. Metallurgical parameters affecting low temperature mechanical properties have been studied using a series of laboratory heats.

We have found that the strength at 4 K of austenitic steels depends quite heavily on N content: each 0.1 wt.% N raises the tensile yield strength (σ_y) by approximately 300 MPa [2]. Additions of other elements, such as C, Ni, Mn, and Cr, contribute much less significantly to the low temperature strength. The yield strength is also dependent on grain size: an increase of grain size from 20 to 200 μm results in a decrease of σ_y of about 90 MPa [3]. Thus, one can affect the strength through alloying and thermomechanical processing.

Toughness is adversely affected by increased strength because less energy is dissipated by plastic deformation during the void growth typical of ductile fracture. We have shown that the elastic stress intensity factor $K_{Ic}(J)$ (obtained from measurement of the elastic/plastic critical J-integral (J_{Ic}) and calculated from $K_{Ic}(J) = (J_{Ic}E)^{1/2}$, where E is Young's modulus) is linearly inversely proportional to σ_y at 4 K [4]. Toughness also is adversely affected by the presence of inclusions [3,5], which act as initiation sites for microvoid formation. The addition of some alloying elements, such as Ni, has previously been shown to increase the low temperature toughness of austenitic steels when strength and inclusion content are held constant [6].

In comparing heat-to-heat strength and toughness at 4 K, we found a large amount of scatter in the data, about ±100%. Such large scatter in mechanical property data is typical at 4 K: a much smaller variation is usual at room temperature [7]. To analyze this variability, we assembled a more extensive set of 4-K strength and fracture toughness data than has previously been available, combining our recent test data for the two high strength cryogenic alloys, 304LN and 316LN, with earlier NBS measurements. We determined quantitatively the effects of grain size and N content on strength and the effects of strength, alloying, and inclusions on toughness. Our analyses resulted in predictive relations that considerably reduced the scatter of the data. Alloy design (in terms of strength and toughness) is now feasible, within statistical limits of uncertainty. Of course, at this time only research data are generally available. Before large-scale use of these alloys in a low temperature structural application, additional heat-by-heat qualification tesing is imperative.

2. Procedure

2.1. Data matrices

A series of specimens from both laboratory and commercial heats of AISI 304- and AISI 316-type alloys were tested. The alloys were prepared in the US, Japan, Europe, and the USSR [3,4,8]. Measurements were made of fracture toughness [$K_{Ic}(J)$], tensile yield strength, and other tensile properties at 4 K. Grain size, hardness, and chemical composition were also determined and inclusion counts were obtained, as described by R.P. Reed et al. [3]. Only measurements made at NBS were used to make up the data matrices, because previous experience has indicated that lab-to-lab variations in

* Work supported by the US Department of Energy; not subject to US copyright.

0022-3115/86/$03.50

30 measurements is:

$$\sigma_y(\text{MPa}) = 215 + 3190[\text{N}] + 1093d^{-1/2}. \quad (4)$$

The standard deviation (SD) of the fit to the data is 84 MPa; the SDs of the three coefficients are 62, 230 and 383, respectively. For AISI 316-type alloys, the comparable equation resulting from regression on a set of 26 measurements is:

$$\sigma_y(\text{MPa}) = 381 + 2776\,[\text{N}] + 811d^{-1/2}. \quad (5)$$

The SD of the fit to the data is 55 MPa; the SDs of the three coefficients are 34, 193, and 199. Figs. 1 and 2 show the measured σ_y versus the σ_y predicted by eqs. (4) and (5) for both alloys.

The dependence of σ_y on N in eqs. (4) and (5) is slightly less than that reported by Reed and Simon [2] from a different set of AISI 304-type alloy data (not restricted to NBS measurements). The higher value of σ_0 for AISI 316-type alloys reflects the strengthening contribution of Mo. It is not clear why we obtain a better data fit (lower SD) for the AISI 316-type alloys. Many of the AISI 316 alloys are from commercial heats (17 out of 26); more of the AISI 304-type alloys are from laboratory heats (27 of 30). Perhaps these data reflect better quality control of the producers in the larger commercial heats.

3.2. Fracture toughness

The fit of eq. (2) to the 304 data gives:

$$K_{Ic}(J)(\text{MPa m}^{1/2}) = 209 - 0.226\sigma_y + 14.4\,([\text{Ni}] + 0.5\,[\text{Mn}]) + 294n^{-1/2}, \quad (6)$$

where the SD of the fit to the data is 31 MPa $\text{m}^{1/2}$ and the SDs of the coefficients are 40, 0.026, 2.9 and 316. For the 316 data, the analogous result is:

$$K_{Ic}(J)(\text{MPa m}^{1/2}) = 130 - 0.338\sigma_y + 20.2\,[\text{Ni}] + 2252n^{-1/2}. \quad (7)$$

The SD of the fit to the data is 31 MPa $\text{m}^{1/2}$, and the SDs of the coefficients are 89, 0.59, 5.2 and 310. Figs. 3 and 4 show the measured $K_{Ic}(J)$ versus the $K_{Ic}(J)$ predicted from eqs. (6) and (7). Eqs. (6) and (7) imply that the fracture toughness of the AISI 316 alloys is more sensitive to all major variables than that of the AISI 304 alloys. The explanation of this awaits more detailed studies of the effects of metallurgical variables on the J-integral fracture toughness at low temperatures.

The SDs of the fits of both alloy types eqs. (2) were considered to be small enough (31 MPa) that the equations can give useful predictions for alloy design. How-

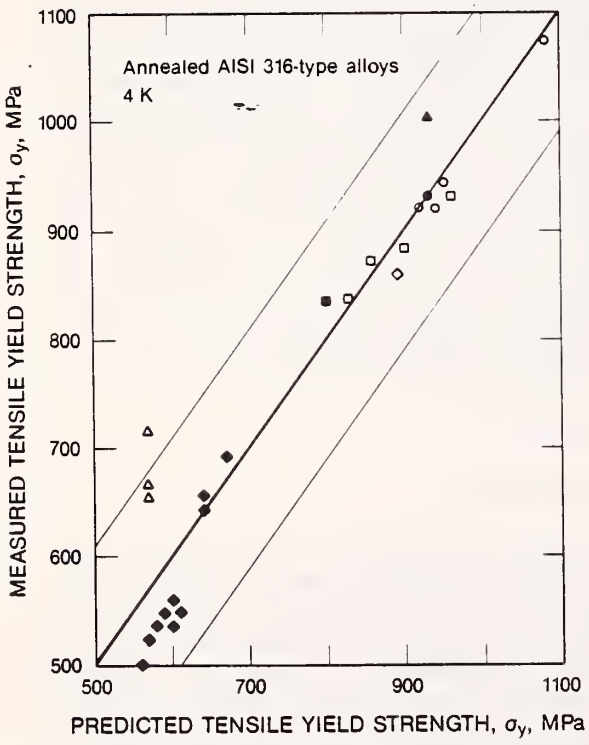

Fig. 2. Measured tensile yield strength at 4 K of AISI 316-type alloys versus tensile yield strength calculated from eq. (5). The scatterband indicates ±2 SDs. Keys to symbols representing test specimens are given in ref. [8].

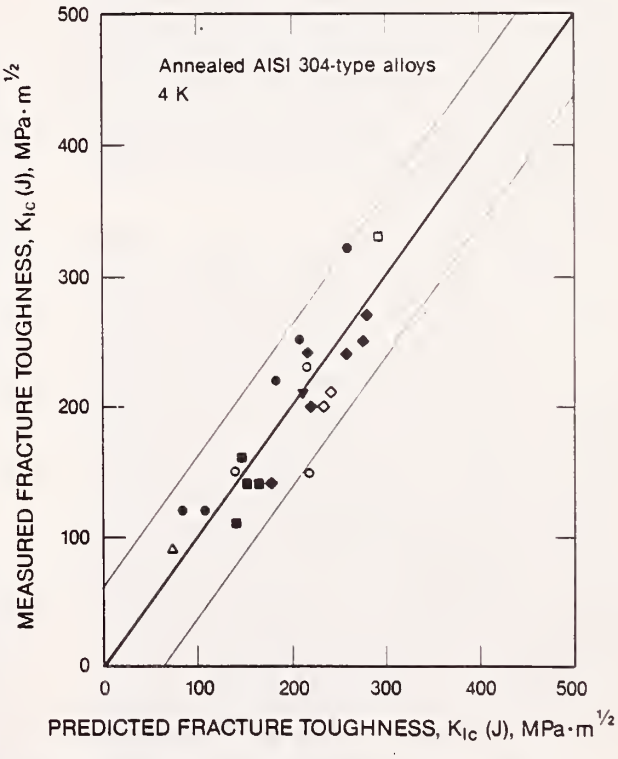

Fig. 3. Measured fracture toughness at 4 K of AISI 304-type alloys versus fracture toughness calculated from eq. (6). The scatterband indicates ±2 SDs. Keys to symbols representing test specimens are given in ref. [8].

test results are large enough to obscure dependence of cryogenic properties upon parameters.

There were 25 rows in the complete matrix for AISI 304-type alloys and 19 rows in the complete matrix for AISI 316-type alloys. Additional tensile data without corresponding $K_{Ic}(J)$ measurements were used in the regression analyses of the tensile yield strength. Nitrogen content ranged from 0.03 to 0.29 wt.% for AISI 304- and from 0.03 to 0.17 wt.% for AISI 316-type alloys. Nickel content varied from 7.2 to 14.9 wt.% for AISI 304-, and from 10.5 to 13.9 wt.% for AISI 316-type alloys. Manganese content ranged from 1.0 to 10.22 wt.% for the AISI 304-type alloys. Variation of Mn and Ni content outside the AISI 304 specifications permitted an evaluation of the effects of these elements; also, AISI 304-type alloys have recently been modified for cryogenic service by addition of Mn and Ni. Grain size varied from 19 to 385 μm in the AISI 304 matrix, and from 11 to 138 μm in the AISI 316 matrix. Inclusion spacing (defined as $n^{-1/2}$, where n = number of inclusions per mm^2) ranged from 0.041 to 0.12 mm for the AISI 304 matrix and from 0.044 to 0.11 mm for the AISI 316 matrix. Hardness (R_B) was not used in the analysis, but was found to vary from 72 to 90 for the AISI 304-type specimens and from 79 to 100 for the AISI 316-type specimens. The complete data matrices will be published elsewhere [3,8]. The $K_{Ic}(J)$ values obtained from the relationship $K_{Ic}(J) = [J_{Ic}E/(1-\nu^2)]^{1/2}$, where ν is Poisson's ratio, were adjusted in accord with the formulation $K_{Ic}(J) = (J_{Ic}E)^{1/2}$. All data points of the matrices were weighted equally in the regression analyses described below.

2.2. Analysis of tensile yield strength

Enough data were available to assess quantitatively the effects of grain size and nitrogen content upon 4-K yield strength of both AISI 304- and AISI 316-type alloys. Earlier studies cited above have shown that these are the most significant variables. In accord with the well-known Hall–Petch grain size effect on yield strength and the higher temperature results of Norström [9], the form of the equation fitted to the data was

$$\sigma_y = \sigma_0 + \sigma_N[\mathrm{N}] + \sigma_d d^{-1/2}, \quad (1)$$

where [N] is wt.% N, d is the grain size (μm), and σ_0 is the yield strength in the absence of N with infinite grain size. Quantification of the strengthening effects of solid-solution alloying elements such as Ni would require a more extensive data set, but are expected to be much less. The contribution from C is expected to be about one-half that of N [2], but it is best to hold C content low (-0.03 wt.%) to minimize sensitization during welding.

2.3. Analysis of fracture toughness

The dependence of $K_{Ic}(J)$ upon yield strength at 4 K has been observed previously in our laboratory [10,11], and a recent study of the effect of Ni on toughness of AISI 304-type alloys showed a strong dependence [6]. Manganese is expected to have a similar, but weaker, effect. To assess the relative importance of inclusion spacing with respect to the other two variables, the following equation was fitted to the AISI 304 data:

$$K_{Ic}(J) = k_0 + k_\sigma\sigma_y + k_N([\mathrm{Ni}] + 0.5[\mathrm{Mn}]) + k_n/\sqrt{n}, \quad (2)$$

where [Ni] represents wt.% Ni, [Mn] wt.% Mn, and k_0 is a constant. Another way of handling the effect of inclusion spacing is to to normalize $K_{Ic}(J)$ as follows:

$$K_{Ic}(J)/n^{-1/2} = k'_0 = k'_\sigma\sigma_y + k'_N([\mathrm{Ni}] + 0.5[\mathrm{Mn}]). \quad (3)$$

This equation also was fitted to the 304 data. Since Mn content of the AISI 316-type alloys varied only slightly, the [Mn] term was dropped from eqs. (2) and (3) for the analyses of these alloys.

3. Results and discussion

3.1. Tensile yield strength

The equation for 4-K tensile yield strength of AISI 304-type alloys resulting from a regression on a set of

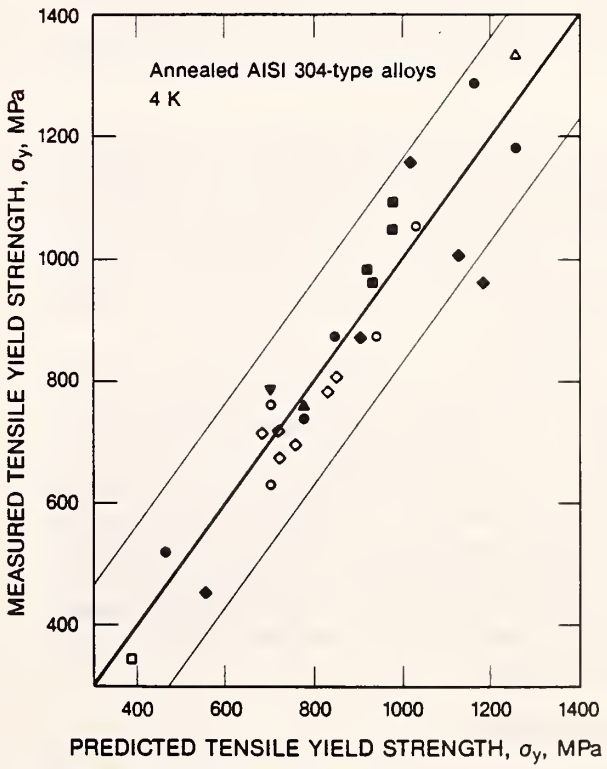

Fig. 1. Measured tensile yield strength at 4 K of AISI 304-type alloys versus tensile yield strength calculated from eq. (4). The scatterband indicates ± 2 SDs. Keys to symbols representing test specimens are given in ref. [8].

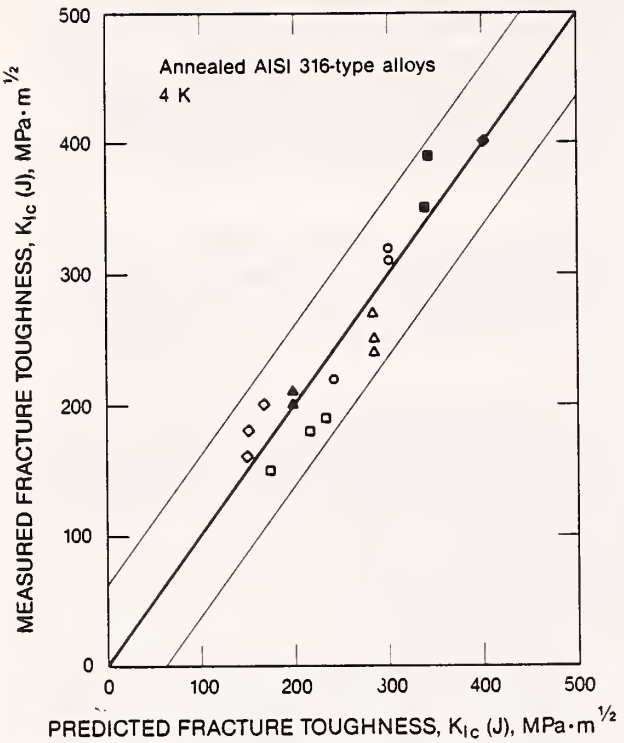

Fig. 4. Measured fracture toughness at 4 K of AISI 316-type alloys versus fracture toughness calculated from eq. (7). The scatterband indicates ±2 SDs. Keys to symbols representing test specimens are given in ref. [8].

ever, there are significant differences in the coefficients for AISI 304- and 316-type alloys. In contrast, the coefficients resulting from fits of eq. (3) to both alloy series were remarkably similar. The SDs of these fits to eq. (3) were higher than for the fits to eq. (2), so these equations are not set forth here but are discussed elsewhere [8].

Compared to a fit of $K_{Ic}(J)$ on σ_y alone, the additions of both the $n^{-1/2}$ term and the [Ni] or ([Ni] + 0.5 [Mn]) term were effective in reducing the SD of the fits, except for eq. (6), in which the addition of the $n^{-1/2}$ term does not affect the SD. This term is presented for comparison with eq. (7). It is difficult to measure inclusion spacing unambiguously [3], but inclusions do have a pronounced effect upon the 4-K fracture toughness of the AISI 316-type alloys. Further inclusion studies should be carried out on commercial heats of AISI 304-type alloys.

3.3. Alloy design

Eqs. (4) through (7) can be used to set provisional design values for yield strength and fracture toughness. For example, to achieve the US research goal of σ_y = 1000 MPa [1] for a 304LHN (316LHN) with [N] = 0.20 wt.%, a grain size of less than 55 (162) μm is required. (The uncertainty in grain size is ±25 (44) μm, assuming that the the fractional error in grain size is given by the square root of the sum of the squares of the fractional errors in the other terms of the equation. The fractional error of each term is obtained by dividing the SD of the coefficient by the value of the coefficient.) Since the control of grain size to 55 μm is difficult for most mills when rolling thick-section (50–120 mm) plate, this implies that AISI 316- type alloys would be a sounder choice to achieve such high strength.

Assuming further that [Ni] = 12 wt.% and [Mn] = 2 wt.%, achievement of the US research goal of K_{Ic} = 200 MPa m$^{1/2}$ would require minimum inclusion spacing of 0.10 (0.073) mm for AISI 304LHN (316LHN). However the uncertainty is too large: ±0.11 (0.056) mm. This indicates that additional studies are required to characterize the effect of inclusions on the fracture toughness of austenitic steels at 4 K. Further studies to relate composition and other variables to the weldability of these alloys are also necessary [12].

4. Summary

Matrices of NBS measurements of σ_y and $K_{Ic}(J)$ at 4 K that include numerical data on alloying, refnining, and processing variables were analyzed using linear regression methods. The AISI 304- and 316-type alloys tested were obtained from a variety of sources and included both commercial and laboratory heats.

Tensile yield strength: Provisional equations were developed for estimating σ_y at 4 K from [N] and $d^{-1/2}$.

Fracture toughness: Provisional equations for estimating $K_{Ic}(J)$ at 4 K from σ_y, [Ni], [Mn], and $n^{-1/2}$ were determined. In addition, the predictions of the quantity $K_{Ic}(J)/n^{-1/2}$ from σ_y and [Ni] were found to be similar, within the statistical uncertainty, for both AISI 304- and 316-type alloys.

The equations presented are expected be useful for alloy design, and in placing tentative estimates on attainable fracture toughness and tensile yield strength at 4 K for austenitic stainless steels.

The research was partially supported by the Office of Fusion Energy, US Department of Energy, V. Der, Project Monitor. We are indebted to R.P. Walsh, P.T. Purtscher, and L.L. Scull for many of the measurements. Provision of alloys from a number of sources is described and acknowledged elsewhere [8].

References

[1] H.I. McHenry, in: Materials Studies for Magnetic Fusion Energy Applications at Low Temperatures – VIII, Internal Rept. 85–3025, Ed. R.P. Reed (US National Bureau of Standards, Boulder, Colorado, 1985) p. 21.

[2] R.P. Reed and N.J. Simon, in: Advances in Cryogenics Engineering – Materials, Vol. 30, Eds. A.F. Clark and R.P. Reed (Plenum Press, New York, 1984) p. 127.

[3] R.P. Reed, P.T. Purtscher, N.J. Simon, and R.L. Tobler, submitted to Proc. 11th Intern. Cryo Engr. Conf. (Butterworth Scientific, London 1986).
[4] R.L. Tobler, D.T. Read, and R. P. Reed, in: ASTM STP 743 (American Society Testing Materials, Philadelphia, Pennsylvania, 1982) p. 250.
[5] T. Sakamoto, Y. Nakagama, I. Yamauchi, and T. Zaizen, Advances in Cryogenic Engineering – Materials, Vol. 30, Eds. A.F. Clark and R.P. Reed (Plenum Press, New York, 1984) p. 137.
[6] R.P. Reed and P.T. Purtscher, Advances in Cryogenics Engineering – Materials, Vol. 32, Eds. R.P. Reed and A.F. Clark (Plenum Press, New York, 1986) p. 43, in press.
[7] N.J. Simon and R.P. Reed, Preliminary Draft, Structural Materials for Superconducting Magnets – III, AISI 304 Stainless Steel (US National Bureau of Standards, Boulder, Colorado, 1985), unpublished.
[8] N.J. Simon and R.P. Reed, in: Materials Studies for Magnetic Fusion Energy Applications at Low Temperatures – IX, Internal Rept., Ed. R.P. Reed (US National Bureau of Standards, Boulder, Colorado, 1986), to be published.
[9] L.-Å. Norström, Met. Sci. 11 (1977) 208.
[10] R.L. Tobler and R.P. Reed, in: Materials Studies for Magnetic Fusion Energy Applications at Low Temperatures – III, Internal Rept. 80–1627, Ed. R.P. Reed, (US National Bureau of Standards, Boulder, Colorado, 1980) p. 15.
[11] R.L. Tobler, T.A. Siewert and H.I. McHenry, Cryogenics (1986), to be published.
[12] E.N.C. Dalder and M.C. Juhas, Nucl. Eng. Des. (1986), to be published.

PROPERTIES OF CDA 104, 155, AND 175 COPPER ALLOYS

R. P. Reed, R. P. Walsh, and F. R. Fickett

National Bureau of Standards
Boulder, Colorado

Three copper alloys, designated 104, 155, and 175 by the Copper Development Association (CDA), were evaluated for use as the structural conductor in the compact ignition tokamak project. Mechanical properties and electrical resistivity were measured for the annealed, half-hard, and hard conditions of alloys 104 and 155 and for the hard condition of alloy 175. Tensile, creep, fatigue, and combined creep and fatigue were measured at 4, 76, and 295 K. Extensive metallurgical characterization of grain structure, grain size, and hardness was obtained. Effects of specimen orientation relative to the rolling direction and of load- and displacement-control tensile tests were studied. Data are presented in both tables and graphs; metallurgical characteristics are shown in micrographs. Cold-rolling increased yield strengths, but at the expense of electrical conductivity, ductility, and toughness. On the basis of our tests, alloy 104 in the hard condition had the best combination of yield strength and electrical conductivity.

INTRODUCTION

The compact ignition tokamak requires a high-conductivity, high-strength conductor to produce pulsed, high magnetic fields at ambient temperatures. The task is to achieve high strength, good conductivity, and high material consistency by means of thorough, but inexpensive, alloy design and processing. Copper and copper alloys are candidate materials.

Three copper alloys were evaluated in this study. To assess the influence of cold-rolling, materials were tested in the half-hard and fully hard

conditions as well as the annealed condition. At 4, 76, and 295 K, tensile, electrical resistivity, fatigue, and creep properties were measured; to simulate pulsed-magnet operating conditions, a combination of fatigue and creep was also measured. For some alloys, measurements were taken in both the longitudinal and transverse orientations. The distinction between load- and displacement-control testing was also determined, because load control from magnetic forces is considered the most dominant condition in magnets. Grain size, hardness, and microstructure were characterized for each alloy and condition.

This report summarizes all data and experimental techniques; the results are discussed briefly. More extensive analysis and discussion of these results will be published later.

MATERIALS

Three copper alloys, designated 104, 155, and 17510 by the Copper Development Association (CDA), were included in this study. The CDA 104 was received as 32-mm-thick plate in the half-hard condition; the CDA 155, as 39-mm-thick plate in the half-hard condition; and the CDA 17510 (abbreviated CDA 175), as 25-mm-thick plate in the hard condition.

The hard conditions (H) for alloys 104 and 155 were obtained by cold-rolling the as-received half-hard (1/2 H) plate. The annealed conditions (A) for alloys 104 and 155 were obtained by heat treatments at the National Bureau of Standards. A summary of the alloys, conditions, and compositions appears in Table I.

Metallurgical specimens for each alloy and condition listed in Table I were cut from the same plates as the tensile specimens. The specimens were blocks, with their largest dimension in the longitudinal (rolling) direction; thus the orthogonal directions of the specimen were maintained throughout the process of specimen preparation.

After the specimens were mechanically polished with a 220-grit abrasive, hardness was measured on the surface perpendicular to the short transverse direction. Then three surfaces of the specimens were mechanically polished with a 0.05-μm alumina abrasive and chemically etched with an aqueous solution of potassium dichromate and sulfuric acid.[1] The grain structures of the specimens were observed with an optical microscope; photomicrographs of the three polished surfaces of the specimens were made (Figs. 1–7). In the annealed condition, the recrystallized grain structure was fairly equiaxed. In the half-hard condition, some texture was observed, a result of the cold-rolling. In the hard condition, the grain structure of each alloy was quite lamellar.

EXPERIMENTAL PROCEDURES

Mechanical Property Measurements

The tensile properties of three copper alloys were characterized by (a) standard displacement-control tensile tests, (b) modified load-control tensile tests, (c) fatigue tests, (d) creep tests, and (e) fatigue-plus-creep tests. The tests were performed at three temperatures: 295 K (ambient), 76 K (liquid nitrogen), and 4 K (liquid helium).

Tensile specimens taken from the plate material were rods, 6.3 mm in diameter and 38 mm in gage length, with threaded ends. For rolled plate materials, the specimens were oriented so that the tensile force was applied transverse to the rolling direction.

For all tests, specimen strain was monitored with three clip-on strain-gage extensometers, 25 mm in gage length. They were mounted on the specimen diametrically opposite and equally spaced over a 25-mm gage section of the 38-mm specimen gage length. They were excited with a 5 V dc power supply; their outputs were parallel electronically to give an average of the three strain measurements. From specimen to specimen, the outputs of these extensometers reproduced within 14 μm with a sensitivity of 0.03 strain per volt (corresponding to a readout of ± 0.04 μm).

a. Displacement-control tensile tests

The tensile testing machine had a cryostat fixture mounted to the bottom of its screw-driven crosshead (see Fig. 1). The crosshead displacement rate was 0.2 mm/min. An XY chart recorder recorded specimen load and the strain measured by the extensometers.

Ultimate tensile strength, 0.2% offset yield strength, elongation, and reduction in area were determined from displacement-control tests.

b. Modified load-control tensile tests

The programmable servohydraulic test machine was equipped with a cryostat test fixture to enable testing in liquid nitrogen and liquid helium. The machine was programmed for a ramp function in a load-control mode; that is, the machine uniformly increased the load on the specimen until failure. In the previous displacement-control tests, the loading rate in the linear-elastic region of the stress–strain curves was calculated to be 57 MPa/min. This loading rate was used in the load-control tests. Thus, the strain rate of the load-control tests was identical to the displacement-control tests until yielding occurred. As soon as the stress–strain curve deviated from linearity, the specimen strain rate ($\dot{\epsilon}$) began to increase (from 0.8×10^{-5} s^{-1}) as the machine tried to maintain a constant loading rate, and it continued to increase until failure. The maximum strain rate was actually dictated by the maximum actuator velocity of the test machine. The maximum strain rate measured during discontinuous yielding was 0.8 s^{-1}.

Ultimate tensile strength, 0.2% offset yield strength, elongation, and reduction in area were determined from the load-control tensile tests.

c. Fatigue tests

Fatigue tests were performed to measure the resistance of the copper alloys to high-stress-level fatigue cycles. The servohydraulic test machine was programmed for a fatigue cycle with a tension–tension triangular waveform at a frequency of 0.10 Hz. The peak stress levels of the waveform were 0.9 and 0.1 of the yield strength (σ_y). Thus, during the fatigue cycle, the test specimen was loaded to $0.9\sigma_y$ in 5 s and then unloaded to $0.1\sigma_y$ in 5 s; this stress spectrum is delineated in Fig. 2. These tests were run in load control to maintain peak stress levels after plastic strain had occurred in the specimen. All fatigue tests were run for a minimum of 5000 cycles. Specimen stress and strain were recorded on an XY chart recorder at chosen places in the fatigue cycle. Measurements were recorded more frequently early in the test when there is a large amount of plastic strain per cycle.

d. Creep tests

Because copper conductors could be subjected to high stress levels throughout the life of high-power magnets, creep tests were performed at 295, 76, and 4 K.

In these tests, the specimen stress was ramped up to $0.9\sigma_y$ in 5 s and held at this level for a minimum of 1000 min. This was done on a servohydraulic test machine in the load-control mode. The load–time history is shown in Fig. 2. The 25-mm gage-length extensometers monitored specimen strain within ± 5 $\mu\epsilon$ as a function of time. During the test, the stress level on the specimen was maintained within 0.1%.

e. Fatigue-plus-creep tests

In these tests, the specimens were subjected to a combination of fatigue and creep stresses. To accomplish this, a trapezoidal waveform (Fig. 2) was programmed on the servohydraulic test machine. During one test cycle, the specimen tensile stress was increased uniformly up to $0.9\sigma_y$ in 5 s, held for 10 s, and then decreased uniformly to $0.1\sigma_y$ in 5 s and held for 10 s. Since the machine was in the load-control mode, the peak stress levels were maintained after plastic strain had occurred in the specimen. During the 5000-cycle-minimum test, single-cycle stress–strain measurements were recorded with an XY chart recorder at chosen places in the fatigue cycle. Measurements were recorded more frequently early in the test when there is a large amount of plastic strain per cycle.

Electrical Resistivity Measurements

A conventional, four-probe resistivity technique[2] with a commercial nanovoltmeter was used; the distance between voltage taps was 14.0 cm. The sample current was in the range 1.9 to 2.0 A for all measurements, giving voltages in the microvolt range. Potential heating effects were evaluated

by measuring the resistance as a function of current at room temperature. The resistance was linear with current to well above the chosen current.

Resistance measurements were made at room temperature and with the sample immersed in liquid nitrogen (76 K) and in liquid helium (4 K). At each temperature, an automated data acquisition system made twelve sets of measurements. Each set consisted of readings with the current flow in the sequence forward–reverse–forward. The program monitored drift of the readings and remeasured the resistance if the variation between the two forward readings exceeded 0.1%. Precision measurement of the sample cross section enabled calculation of the resistivity to an accuracy better than 1%.

EXPERIMENTAL RESULTS AND DISCUSSION

Tensile Tests

Tensile properties, including yield strength (σ_y), ultimate strength (σ_u), elongation (EL), and reduction of area (R.A.) are given in Tables II through IV for each alloy and each condition. All data are included. The strain rate for displacement-control tests and the load rate for load-control tests are identified.

The results for each alloy and condition are plotted individually against temperature in Figs. 10 through 16. In Figs. 17 through 20, all data for each tensile property of transversely oriented specimens are combined and plotted versus temperature. The stress–strain curves of alloys 104, 155, and 175 under various processing and test conditions are shown in Figs. 21 through 23, 24 through 29, and 30, respectively.

The ultimate strength was strongly dependent on temperature and only mildly dependent on cold working and alloying. For the annealed alloys, the ultimate strength at 4 K was nearly twice that at 295 K (see Fig. 18). Even for the strengthened alloys, the ultimate strength was at least 20% higher at 4 K than at 295 K.

Elongation for all alloys and conditions increased at lower temperatures (Fig. 19). Compared with values at room temperature, elongation at 4 K was about 50% higher for annealed alloys and about 100% higher for the cold-rolled alloys. This disparity was due, in part, to the incursion of localized necking during room-temperature tests at very low strains (discussed below).

Reduction of area remained nearly constant as a function of temperature (Fig. 20), but there were distinctions between specimen necking at room temperature and at low temperatures, especially in the cold-rolled alloys. As illustrated in Figs. 22, 23, 25, and 26, the ultimate load was reached at relatively low strains (usually <0.02) at room temperature in both displacement- and load-control tests. Subsequently, during load or displacement extension, the specimen began to neck. As depicted by these engineering stress–strain curves, when the load began to drop in

displacement-control tests (and even in load-control tests), the pace of the extension could not keep up with specimen straining; probably adiabatic heating conditions existed in the necked region. At low temperatures, the specimens strained more uniformly; consequently, more elongation was achieved, and the reduction of area reflected both uniform elongation and specimen necking.

The reduction of area was inversely related to the amount of cold work. The reduction of area of ductile materials has been associated with fracture toughness, since the induced triaxial state after necking simulates blunt notch conditions. The reduction of area for alloys 104 and 155 was inversely related to yield strength (Fig. 31), like the relationship between fracture toughness [$K_{Ic}(J)$] and tensile yield strength (σ_y) in austenitic stainless steels at low temperatures, and the slopes of these curves are similar. All austenitic alloys that failed by ductile rupture in a fracture toughness test fell within a rather narrow band on a plot of $K_{Ic}(J)$ versus σ_y, but the absolute values of the inverse linear relationship for the copper alloys appear to be distinct. The lack of overlapping lines for alloys 104 and 155 (Fig. 31) implies that either the fracture mode was different (unlikely, since both alloys fail after much ductility) or that the reduction of area depended on alloying.

Alloy 175 was considerably stronger at all test temperatures than alloys 155 and 104 in the hard condition. However, the ductility of this stronger alloy was less, as expected, implying that the toughness of alloy 175 should also be lower than those of alloys 104 and 155.

The yield strength of these copper alloys was mildly dependent on temperature, but strongly dependent on cold work and alloying. Cold-rolling to the half-hard condition increased the yield strength by about a factor of 10 for alloy 104 and a factor of 4 for alloy 155. The addition of only 0.06 wt.% phosphorus and 0.11 wt.% magnesium increased the yield strength by a factor of 2.5. The temperature dependence of the yield strength was also affected by cold work: Between 76 and 4 K no change in yield strength was measured for the annealed 104 and 155 alloys, whereas the yield strength of the cold-rolled alloys continued to increase with decreasing temperature. The work-hardening rate of alloys 104 and 155 in the annealed condition increased with decreasing temperature (Figs. 21 and 24). Cold-rolling reduced the amount and rate of work hardening in both alloys (Figs. 22, 23, 25, and 26).

For alloys 155–H and 175–H, tensile measurements were made on specimens of both longitudinal and transverse orientation with respect to the rolling direction of the plate. Little effect of rolling direction on the tensile properties is seen in Tables II and IV. Occasional disparities among the data of the two orientations are believed to be due to variations in the material.

Both displacement- and load-control tests were conducted for alloys 104–1/2 H, 104–H, 155–1/2 H, and 155–H (Figs. 11, 12, 14, 15, and 16). There was some disagreement in the results for alloys 155–1/2 H and 155–H,

but the tensile properties of the other two alloy conditions were remarkably consistent; there were no differences due to test control method. Therefore, the disagreement in the data of alloys 155–1/2 H and 155–H is thought to be due to material variations rather than method of test control.

Electrical Resistivity

The electrical resistivities (ρ) of all conditions of the three copper alloys were measured at 295, 76, and 4 K and are given in Fig. 32 and Table V. Table V also includes the residual resistivity ratio (RRR), which is the ratio of resistivity at 295 K to that at 4 K. Many consider the RRR to be a more reliable, relative estimate of material imperfection because it is independent of specimen area and other absolute measurement inconsistencies. Cold-rolling increased the resistivity of alloys 104 and 155. As a result of annealing, phosphorus and magnesium in alloy 155 were no longer precipitates, but were solutes, thus increasing the resistivity of the alloy. Higher strength alloys generally have higher resistivities. The ratio σ_y/ρ for each alloy and condition is listed in Table V and plotted versus temperature in Fig. 33. For high-field magnets, designers tend to select conductors that have high ratios. Alloy 104–H had the best σ_y/ρ value at 4 and 76 K, only slightly less than that of alloys 104–1/2 H and 155–H at 295 K. No practical gains are achieved by selecting alloy 175, unless a very high yield strength is required for the alloy.

The changes in resistivity, $\Delta\rho$, due to changes in condition are shown in Fig. 34 for alloy 104. Cold-rolling obviously increased $\Delta\rho$. The temperature dependence of the H condition followed that found in a review of the literature by Simon and Reed;[3] that is, $\Delta\rho$ changes are larger at higher temperatures. However, the 76-K data did not follow this trend, and this disparity likely represents data scatter.

Elastic Properties

The elastic moduli of alloys 104 and 155 were measured at 295, 76, and 4 K for all conditions. These are discussed in other papers of this report.[4-6]

Fatigue and Creep

The creep data for all alloys and conditions are summarized in Fig. 35. The creep rates are mainly logarithmic, with specimen strain (ϵ) proportional to log t, where t is time. Except for alloy 104–H, the alloys and conditions have a nearly constant ϵ/log t value. For the annealed alloys (104 and 155), the slope of ϵ versus log t was lower. Therefore, except for that of 104–H, the creep rate of the alloys was logarithmic at the stress level of $0.9\sigma_y$.

The fatigue data are summarized in Fig. 36. All alloys have two distinct ranges of specimen strain versus the log of the number of cycles (log N). The early range, at about 10 cycles or less, contains a creep component and, therefore, exhibits a higher rate of strain. Subsequently,

the strain contains only the fatigue-induced component. In both stages, ϵ is proportional to log N.

A combination of fatigue and creep was also measured for these alloys. These data are summarized in Fig. 37. Two stages are apparent when strain is plotted versus log N. The early stage has a steeper slope (higher ϵ/N) and is dominated by primary creep strain. For the annealed alloys, the first stage has a larger slope and extends to larger values of N.

All data are summarized in Fig. 38; the strain components are separated into initial and total contributions. The contribution of elastic strain is shown by the solid lines in the figure. All strain contributions scale with the applied stress. The total strain increased as the applied stress increased. The relative contributions of elastic and plastic strain are shown more clearly in Fig. 39. The elastic strain (ϵ_e) naturally increased with applied stress (σ_a), following $\epsilon_e = \sigma_a/E$, where E is Young's modulus. The total plastic strain decreased with applied stress, following the inverse linear dependence depicted by the solid line in Fig. 39. These dependences of plastic strain on applied stress were roughly independent of the type of test: creep, fatigue, or fatigue plus creep. For most tests, alloys 104–1/2 H and 155–1/2 H had much lower plastic strains than the other alloys (see data at $\sigma_a \simeq 250$ MPa in Fig. 39). Perhaps these lower strain values are associated with room-temperature aging effects in cold-rolled copper, since these two alloys were the "as-received" material and had been rolled to the half-hard condition about seven years earlier. We are now exploring ambient temperature aging effects following cold-rolling.

SUMMARY

Tensile, creep, fatigue, combined creep and fatigue, and electrical resistivity properties at 4, 76, and 295 K were measured for three alloys in various conditions—annealed, half-hard, and hard. The data were summarized and compared to determine trends as a function of temperature, alloy condition, time (creep), number of cycles (fatigue), and applied stress (creep, fatigue, and combined creep and fatigue).

Yield strengths were increased by cold-rolling, but at the expense of electrical conductivity, ductility, and toughness. Cold-rolling considerably reduced the work-hardening capacity of copper alloys, and it increased the yield strength much more than the ultimate strength. Therefore, the increase in yield strength due to cold-rolling is partially negated in applications where ultimate strength is also important. Furthermore, the reduced toughness in cold-rolled alloys, combined with the expected higher operating stresses, places a premium on the alleviation of stress concentrations in structural design. Since heavily cold-rolled copper has less strain accommodation than other copper alloys, safety factors must be carefully evaluated before using these alloys in applications requiring high yield strength.

On the basis of our tests, alloy CDA 104 in the hard condition had the best combination of yield strength and electrical conductivity.

ACKNOWLEDGMENTS

This study was sponsored by the Office of Fusion Energy, U.S. Department of Energy.

The authors thank Lonnie Scull for cold-rolling the half-hard plate and Patrick Purtscher for assistance in annealing the half-hard plate. Edward Dalder of Lawrence Livermore National Laboratory (LLNL) and Charles Bushnell of Princeton Plasma Physics Laboratory (PPPL) helped us to obtain the copper alloys. Herbert Becker of the National Magnet Laboratory at MIT assisted in material selection. Colorado School of Mines kindly allowed us to use their cold-rolling facilities. The CDA 104 plate was provided by LLNL, who obtained the plate from PPPL. The CDA 155 plate, produced by the Copper Range Company for fabrication of the B-coil center post for Doublet III, was supplied by General Atomic. The CDA 17510 plate, developed jointly by LLNL, PPPL, and Cabot Berylco Corporation, was provided by LLNL.

REFERENCES

1. Metals Handbook, 9th edition, vol. 9. Metals Park, Ohio: American Society for Metals; 1985, p. 401.

2. F. R. Fickett, Electrical properties, chapter 5 in Materials at Low Temperatures, R. P. Reed and A. F. Clark, eds. Metals Park, Ohio: American Society for Metals; 1983, p. 166.

3. N. J. Simon and R. P. Reed, Cryogenic properties of copper and copper alloys, to be published.

4. H. M. Ledbetter and S. A. Kim, Low-temperature elastic constants of deformed polycrystalline copper, in Materials Studies for Magnetic Fusion Energy Applications at Low Temperatures—X, NBSIR 87-3067, National Bureau of Standards, Boulder, Colorado; 1987, p. 139.

5. H. M. Ledbetter, Acoustoelastic residual stress measurements: role of anisotropic dislocation arrays, in Materials Studies for Magnetic Fusion Energy Applications at Low Temperatures—X, NBSIR 87-3067, National Bureau of Standards, Boulder, Colorado; 1987, p. 151.

6. H. M. Ledbetter and M. W. Austin, Deformed-polycrystalline-copper elastic constants, in Materials for Magnetic Fusion Energy Applications at Low Temperatures—X, NBSIR 87-3067, National Bureau of Standards, Boulder, Colorado; 1987, p. 127.

Table I. Copper Alloys

CDA Type	Condition	Composition (wt.%)
104	Annealed 1/2 hard Hard	99.5 [Cu + Ag] 0.027 Ag
155	Annealed 1/2 hard	99.75 [Cu + Ag] 0.027 Ag, 0.06 P, 0.11 Mg
17510	Hard	97.6 [Cu + Ag] 1.8 Ni, 0.38 Be

Table II. Tensile Properties of CDA 175 Copper

TEST CONTROL	CONDITION	ORIENTATION	TEMPERATURE (K)	TENSILE PROPERTIES σ_y (MPa)	σ_u (MPa)	EL (%)	R.A. (%)
DISPLACEMENT ($\dot{\epsilon} = 1 \times 10^{-4}\ s^{-1}$)	H	long.	295	715	783	10	24
			76	783	888	15	49
			4	814	972	17	35
DISPLACEMENT ($\dot{\epsilon} = 1 \times 10^{-4}\ s^{-1}$)	H	transv.	295	718	777	9	34
			76	799	890	14	47
			4	793	937	18	46

Table III. Tensile Properties of CDA 104 Copper

TEST CONTROL	CONDITION	ORIENTATION	TEMPERATURE (K)	TENSILE PROPERTIES σ_y (MPa)	σ_u (MPa)	EL (%)	R.A. (%)
DISPLACEMENT ($\dot{\varepsilon} = 1 \times 10^{-4}$ s^{-1})	A	transv.	295	23.0	205	48	87
			76	30.5	336	57	87
			4	30.5	410	76	82
DISPLACEMENT ($\dot{\varepsilon} = 1 \times 10^{-4}$ s^{-1})	1/2 H	transv.	295	275	277	13	78
			76	315	375	37	82
			4	331	446	—	—
LOAD (P = 1 MPa s^{-1})	1/2 H	transv.	4	326	440	49	81
DISPLACEMENT ($\dot{\varepsilon} = 1 \times 10^{-4}$ s^{-1})	H	transv.	295	342	357	9	72
			76	401	442	19	78
			4	431	509	32	72
LOAD (P = 1 MPa s^{-1})	H	transv.	295	342	356	10	76
			76	408	452	20	76
			4	432	503	30	75

Table IV. Tensile Properties of CDA 155 Copper

TEST CONTROL	CONDITION	ORIENTATION	TEMPERATURE (K)	TENSILE PROPERTIES σ_y (MPa)	σ_u (MPa)	EL (%)	R.A. (%)
DISPLACEMENT ($\dot{\epsilon}$ = 1 x 10^{-4} s^{-1})	A	transv.	295	65	244	44	79
			76	81	378	55	72
			4	81	457	62	69
DISPLACEMENT ($\dot{\epsilon}$ = 1 x 10^{-4} s^{-1})	1/2 H	transv.	295	277	306	15	63
			76	307	411	27	53
			4	314	479	37	56
LOAD (P = 1 MPa s^{-1})	1/2 H	transv.	295	275	310	18	62
			76	300	415	32	63
			4	315	479	37	58
DISPLACEMENT ($\dot{\epsilon}$ = 1 x 10^{-4} s^{-1})	H	long.	295	383	394	8	58
			76	466	520	16	41
			4	470	579	32	57
DISPLACEMENT ($\dot{\epsilon}$ = 1 x 10^{-4} s^{-1})	H	transv.	295	397	412	8	51
			76	460	500	19	53
			4	494	560	28	57
LOAD (P = 1 MPa s^{-1})	H	long.	295	360	379	10	61
			76	460	524	22	52
			4	468	515	15	37
LOAD (P = 1 MPa s^{-1})	H	transv.	295	388	404	8	51
			76	460	498	20	52
			4	484	548	16	49
LOAD (P = 70 MPa s^{-1})	H	long.	295	380	403	10	60
Load (P = 80 MPa s^{-1})	H	transv.	76	451	496	15	52

Table V. Electrical Resistivity Data

Alloy	T (K)	σ_y (MPa)	ρ ($\mu\Omega\cdot$cm)	σ_y/ρ (MPa/$\mu\Omega\cdot$cm)	RRR
155-H	4	483	0.2005	2409	
	76	460	0.398	1156	
	295	382	1.92	199	9.6
155-1/2 H	4	315	0.177	1780	
	76	306	0.384	797	
	295	280	1.955	143	11.0
155-A	4	81	0.358	226	
	76	81	0.562	144	
	295	65	2.09	31	5.8
104-H	4	432	0.0392	11020	
	76	406	0.241	1685	
	295	343	1.785	192	45.5
104-1/2 H	4	328	0.0278	9892	
	76	315	0.2195	1435	
	295	275	1.735	191	61.7
104-A	4	30.5	0.010	3000	
	76	30.5	0.206	148	
	295	23	1.75	0.6	175.0
175-H	4	803	1.50	535	
	76	791	1.80	439	
	295	716	3.98	180	29.3

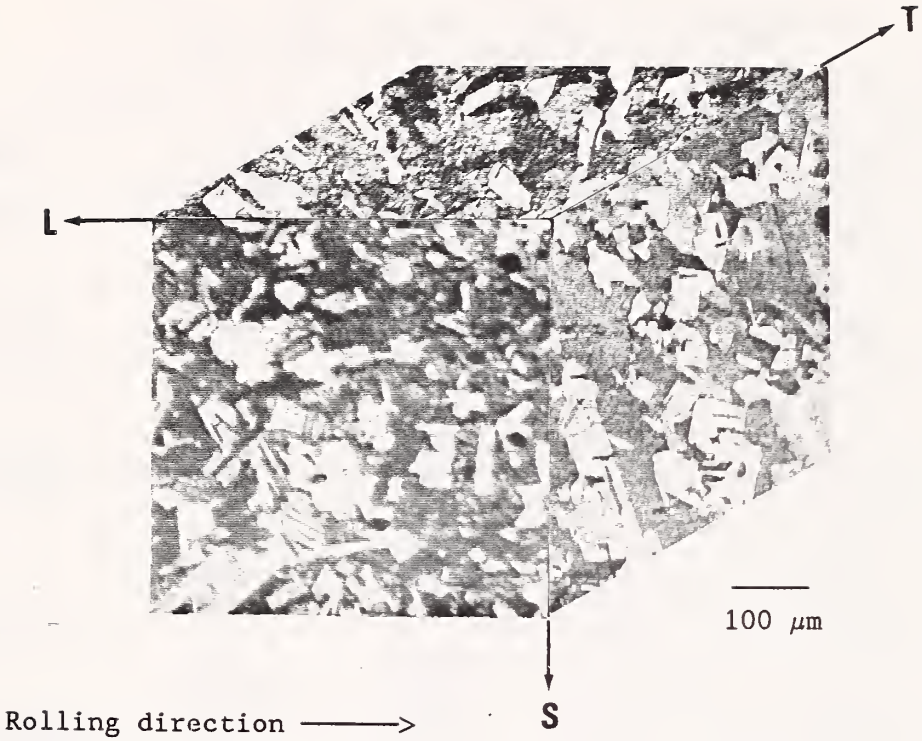

Fig. 1. Alloy CDA 104. Form: 32-mm-thick plate.
Condition: annealed at 510°C, 1 h, Ar atmosphere, air cooled.
On face normal to S direction, hardness = 53 R_F; grain size = 80 μm.

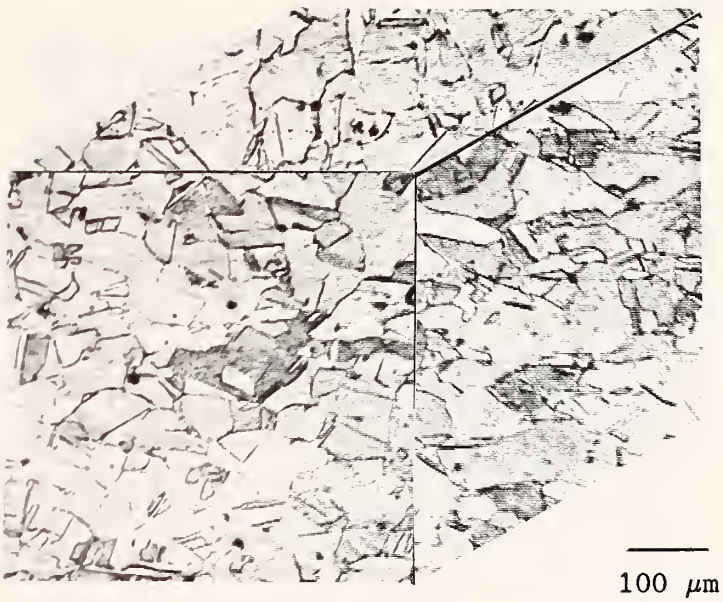

Rolling direction ——————>

Fig. 2. Alloy CDA 104. Form: 32-mm-thick plate.
Condition: half-hard.
On face normal to S direction, hardness = 80 R_F; grain size = 77 μm.

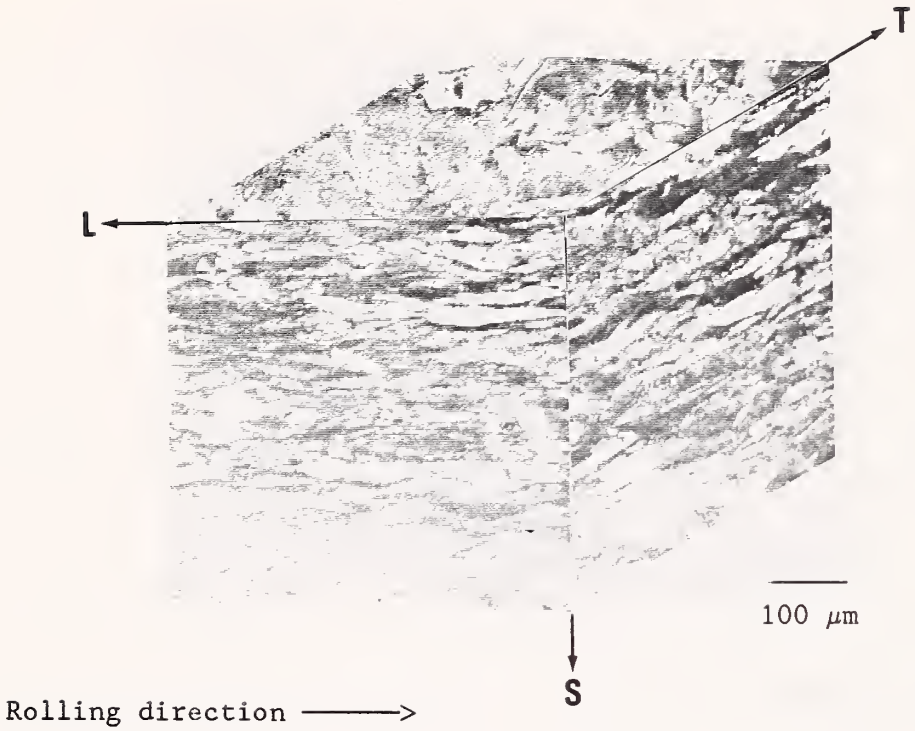

Fig. 3. Alloy CDA 104. Form: 15-mm-thick plate.
Condition: hard (cold-rolled 50% from half-hard condition).
On face normal to S direction, hardness = 88 R_F; grain size was not measured owing to extensive texture.

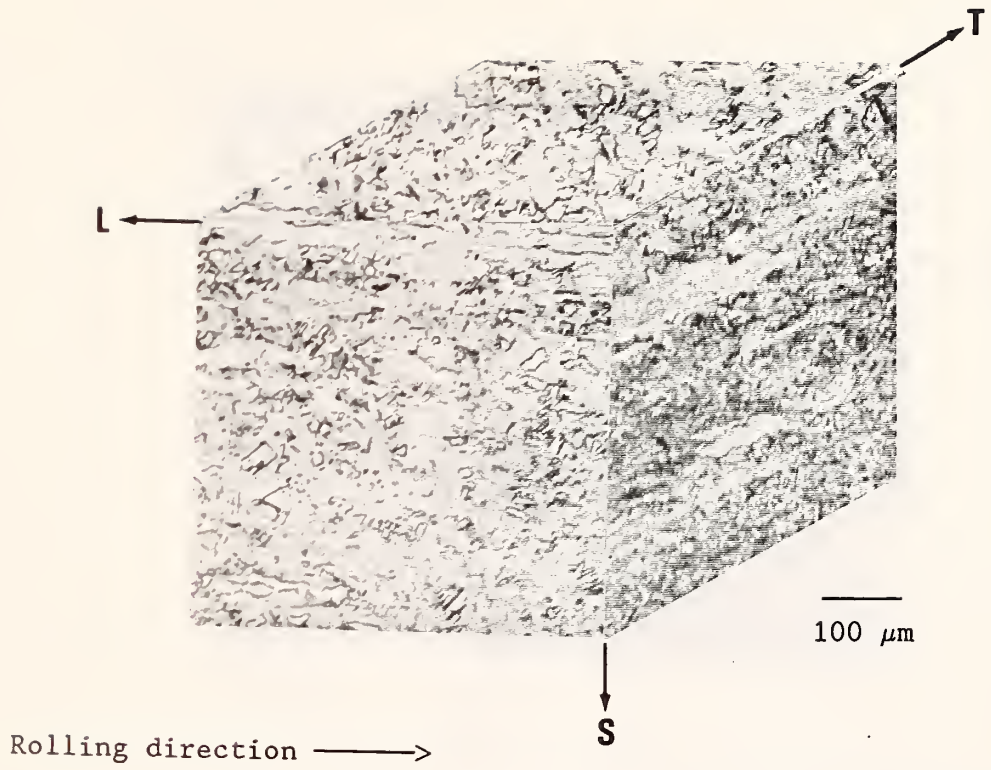

Fig. 4. Alloy CDA 155. Form: 39-mm-thick plate.
Condition: annealed at 550°C, 1.25 h, Ar atmosphere, air cooled.
On face normal to S direction, hardness = 63 R_F; grain size = 75 μm.

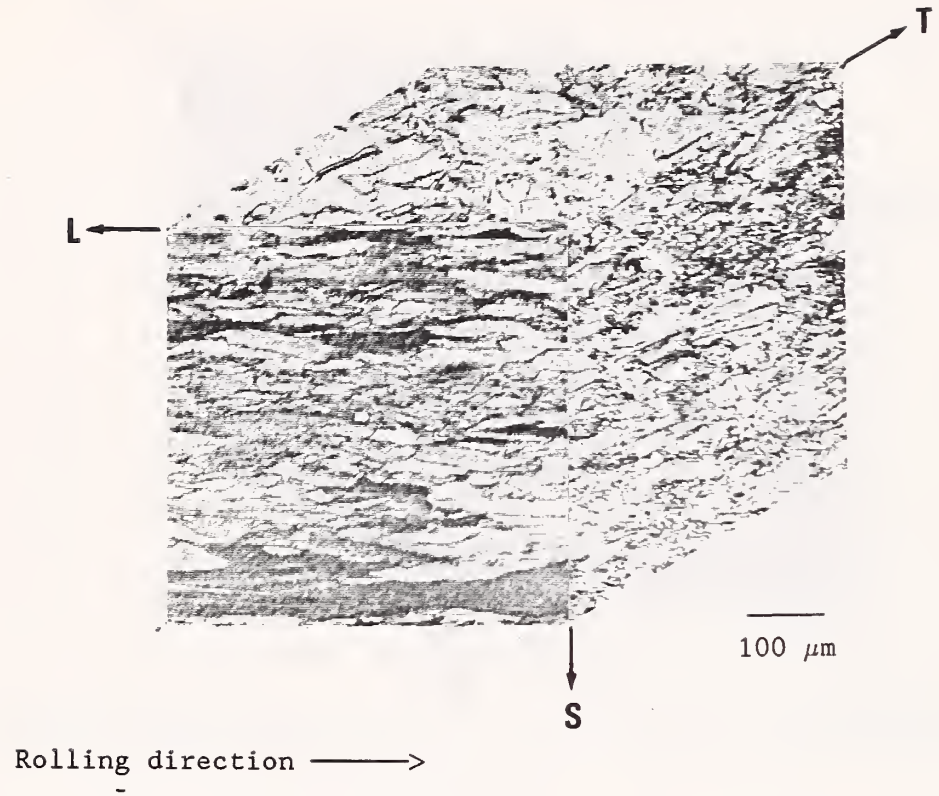

Fig. 5. Alloy CDA 155. Form: 39-mm-thick plate.
Condition: half-hard.
On face normal to S direction, hardness = 88 R_F; grain size = 72 μm.

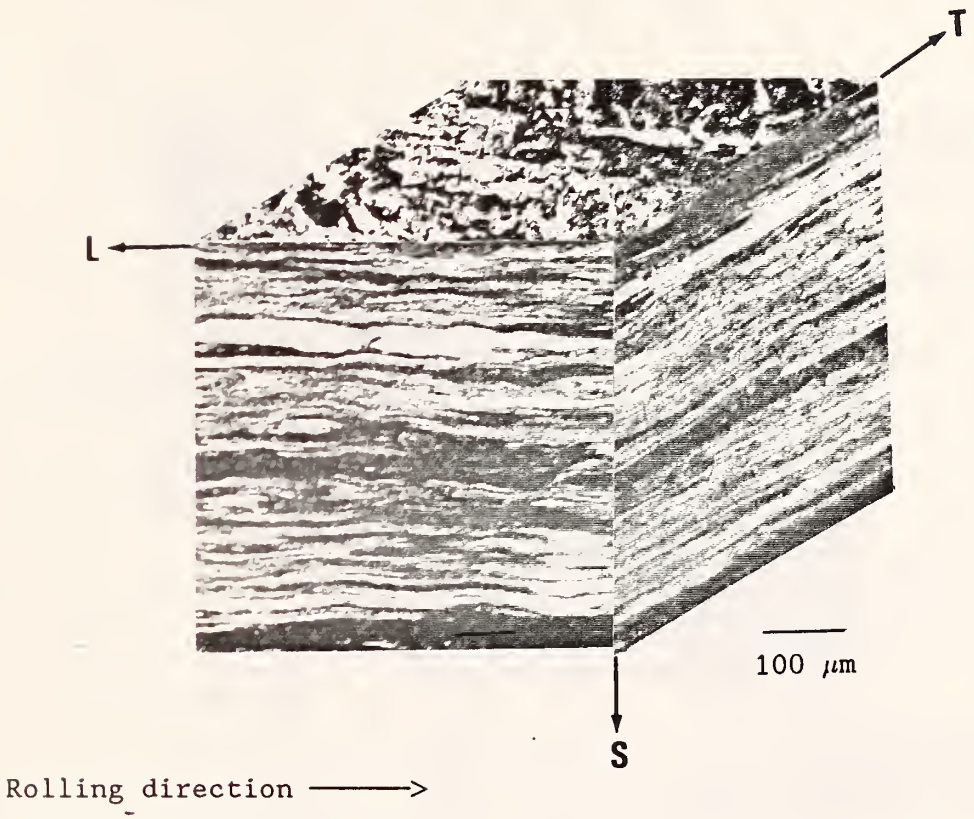

Fig. 6. Alloy CDA 155. Form: 15-mm-thick plate.
Condition: hard (cold-rolled 60% from half-hard condition).
On face normal to S direction, hardness = 96 R_F; grain size was not measured owing to extensive texture.

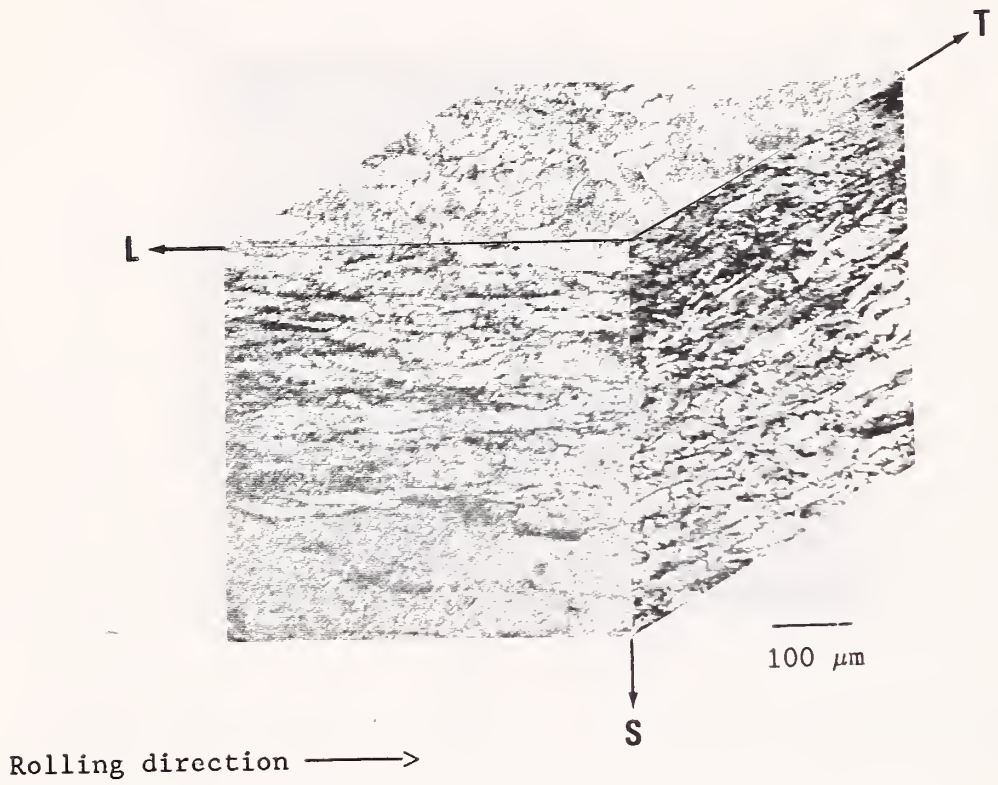

Fig. 7. Alloy CDA 175. Form: 25-mm-thick plate.
Condition: hard.
On face normal to S direction, hardness = 92 R_F; grain size was not measured owing to extensive texture.

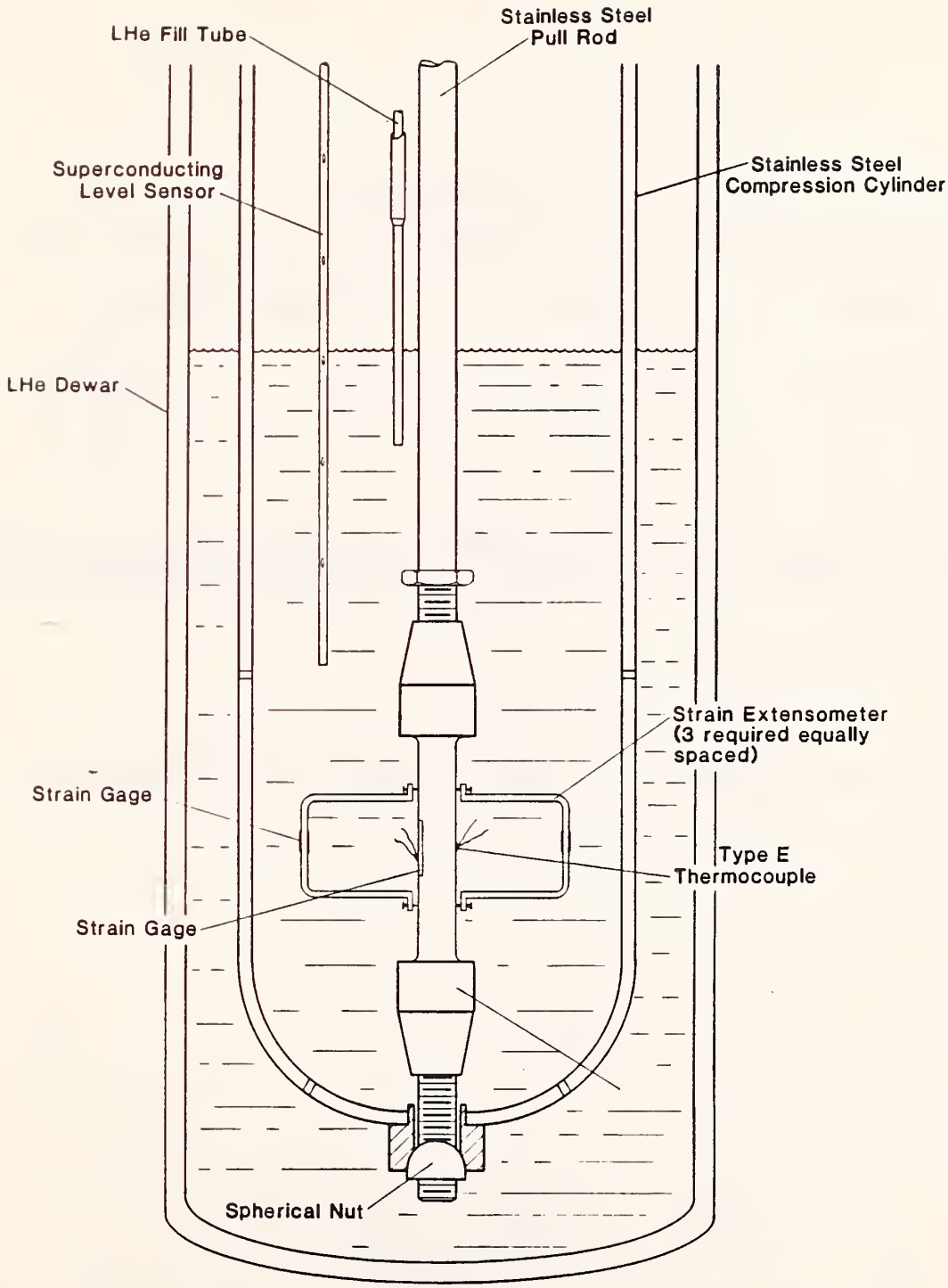

Fig. 8. Apparatus for displacement-control tests.

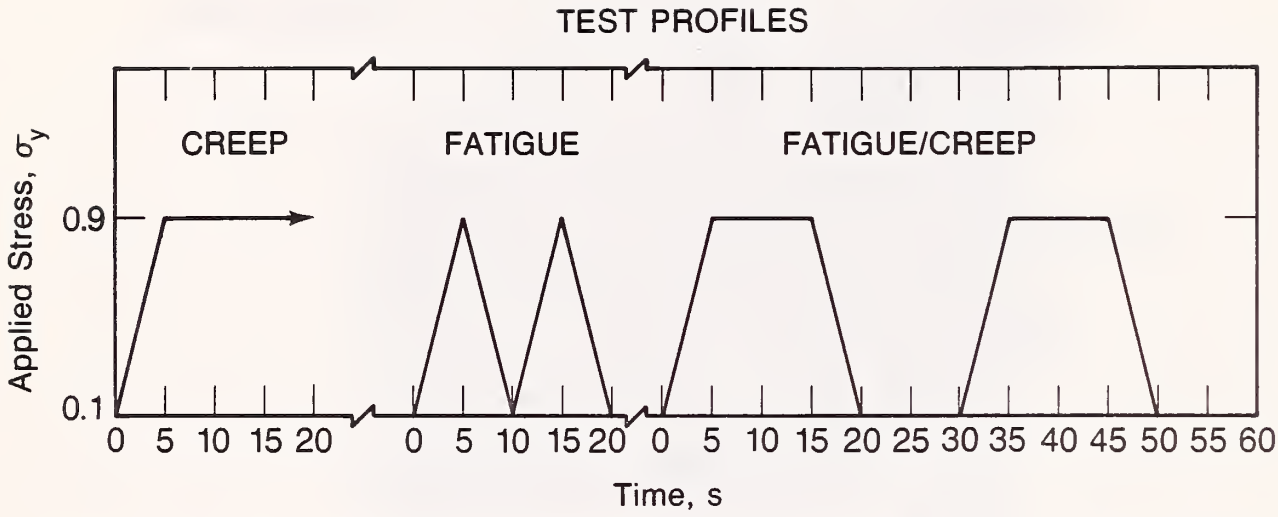

Fig. 9. Stress profiles for fatigue, creep, and fatigue-plus-creep tests.

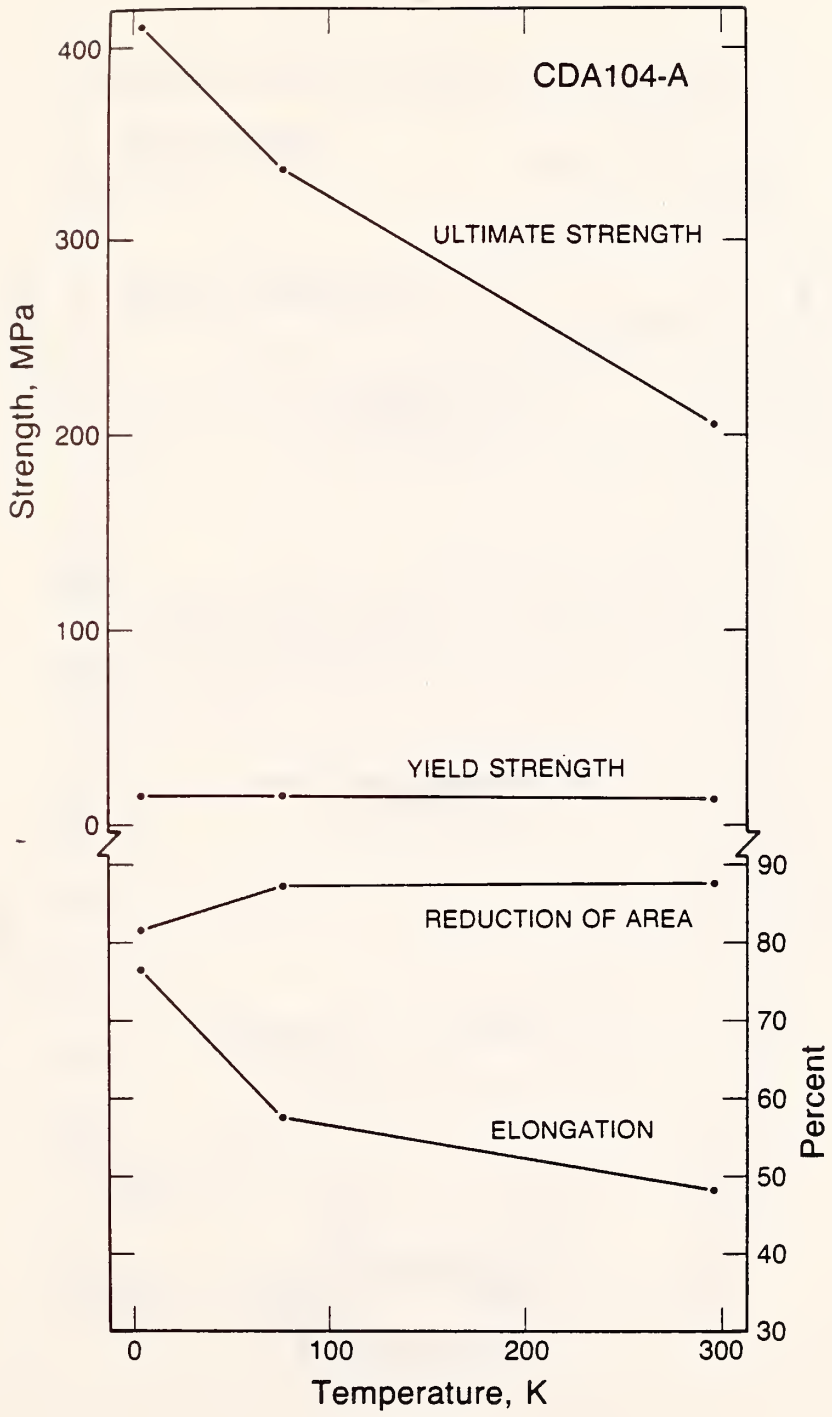

Fig. 10. The tensile properties of alloy CDA 104-A.

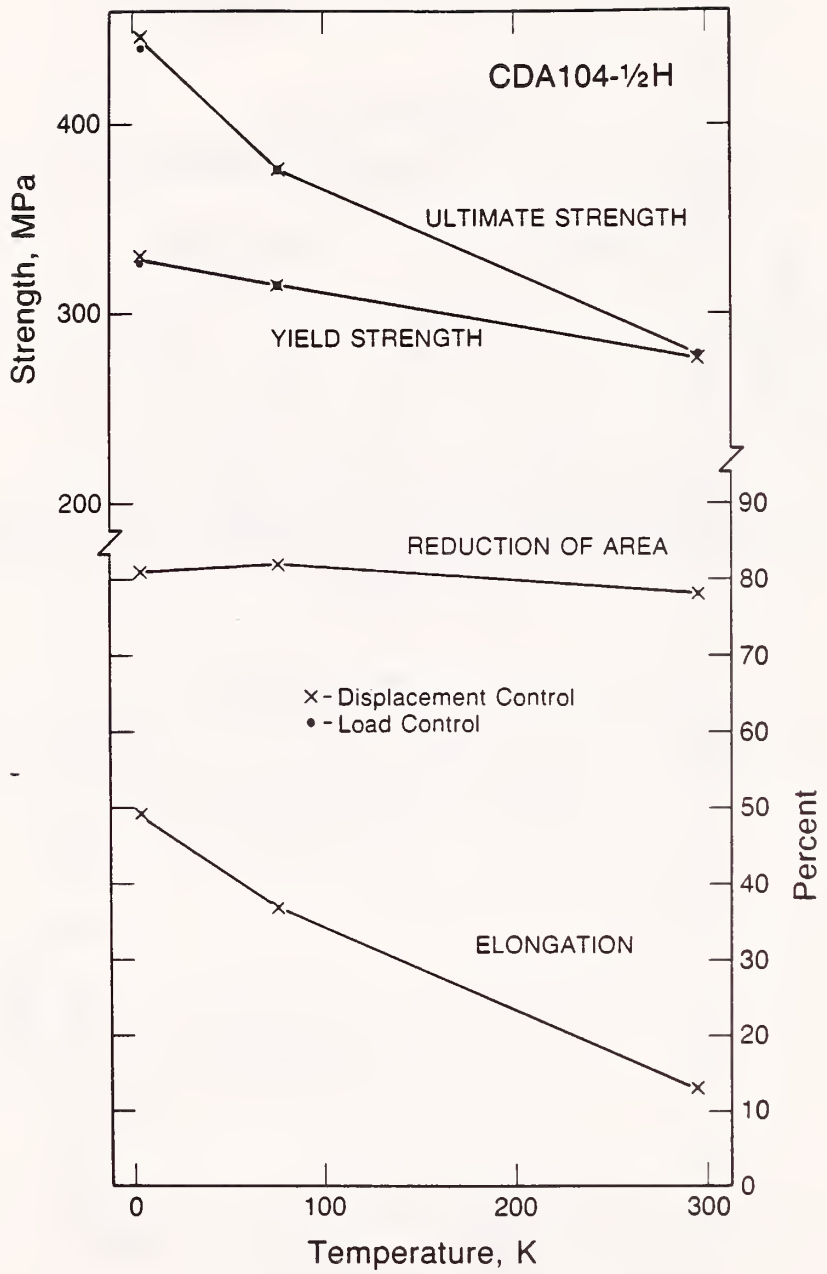

Fig. 11. The tensile properties of alloy CDA 104–1/2 H.

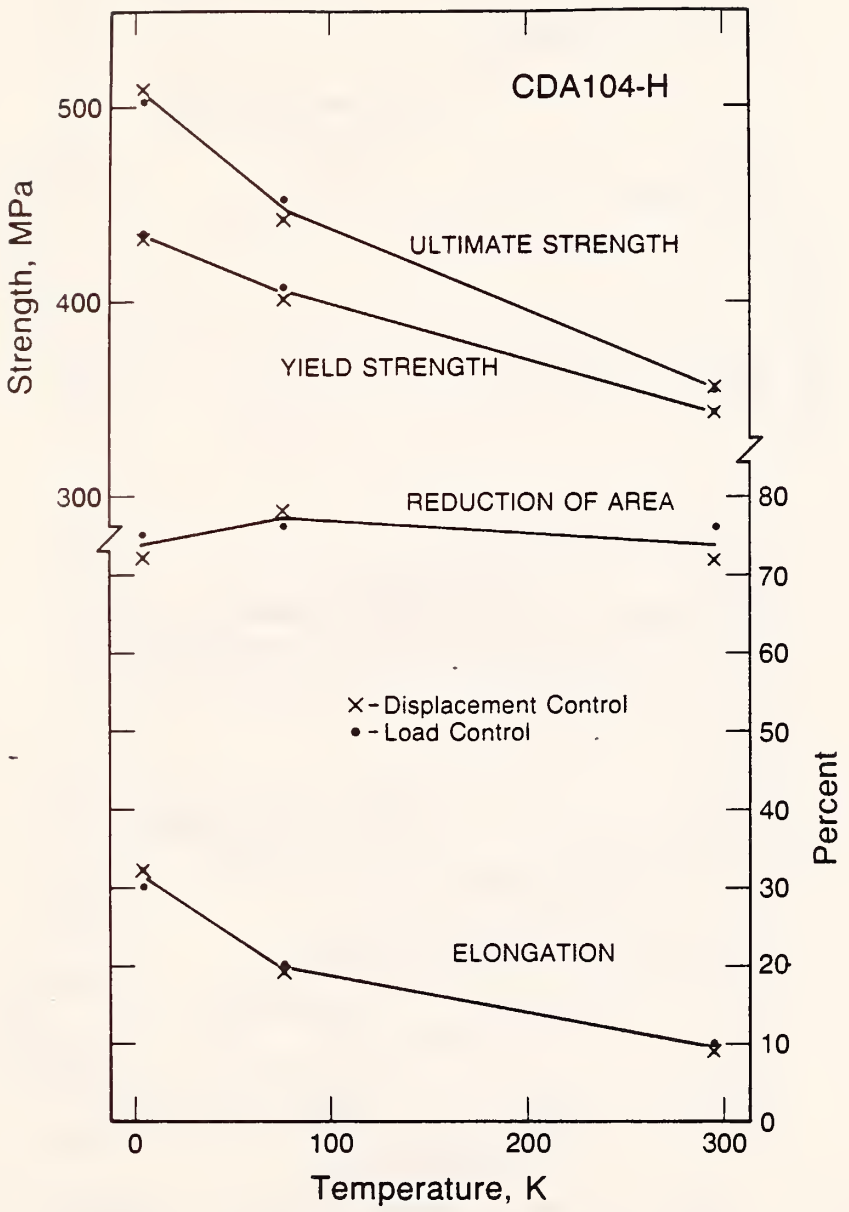

Fig. 12. The tensile properties of alloy CDA 104-H.

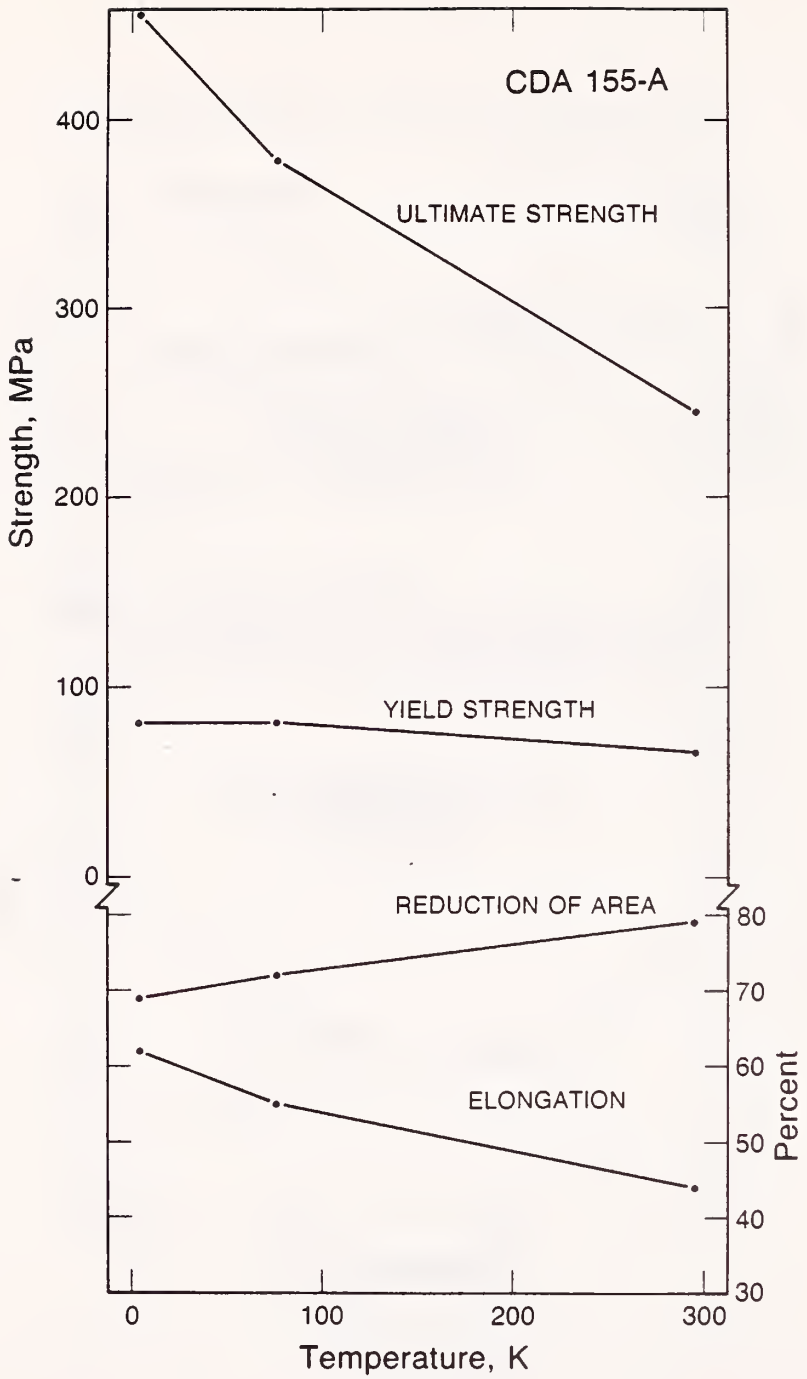

Fig. 13. The tensile properties of alloy CDA 155-A.

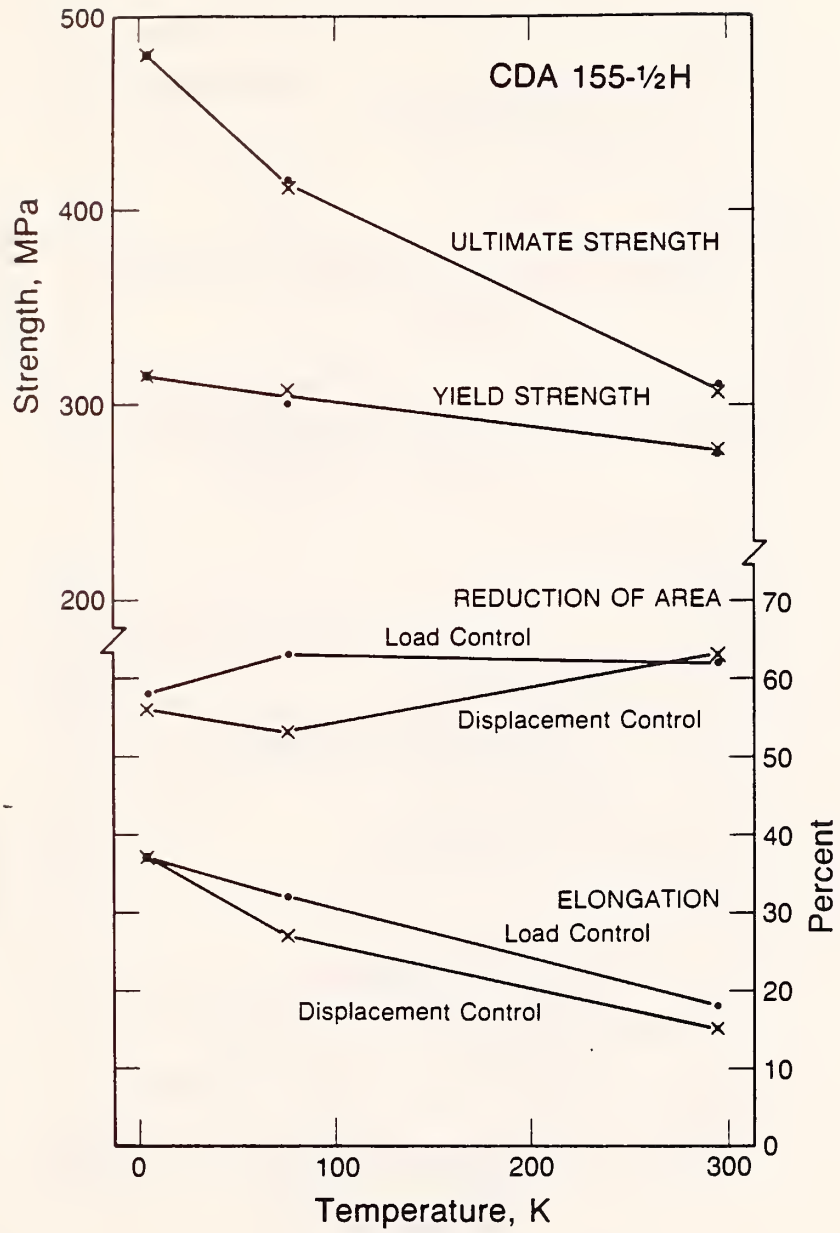

Fig. 14. The tensile properties of alloy CDA 155–1/2 H.

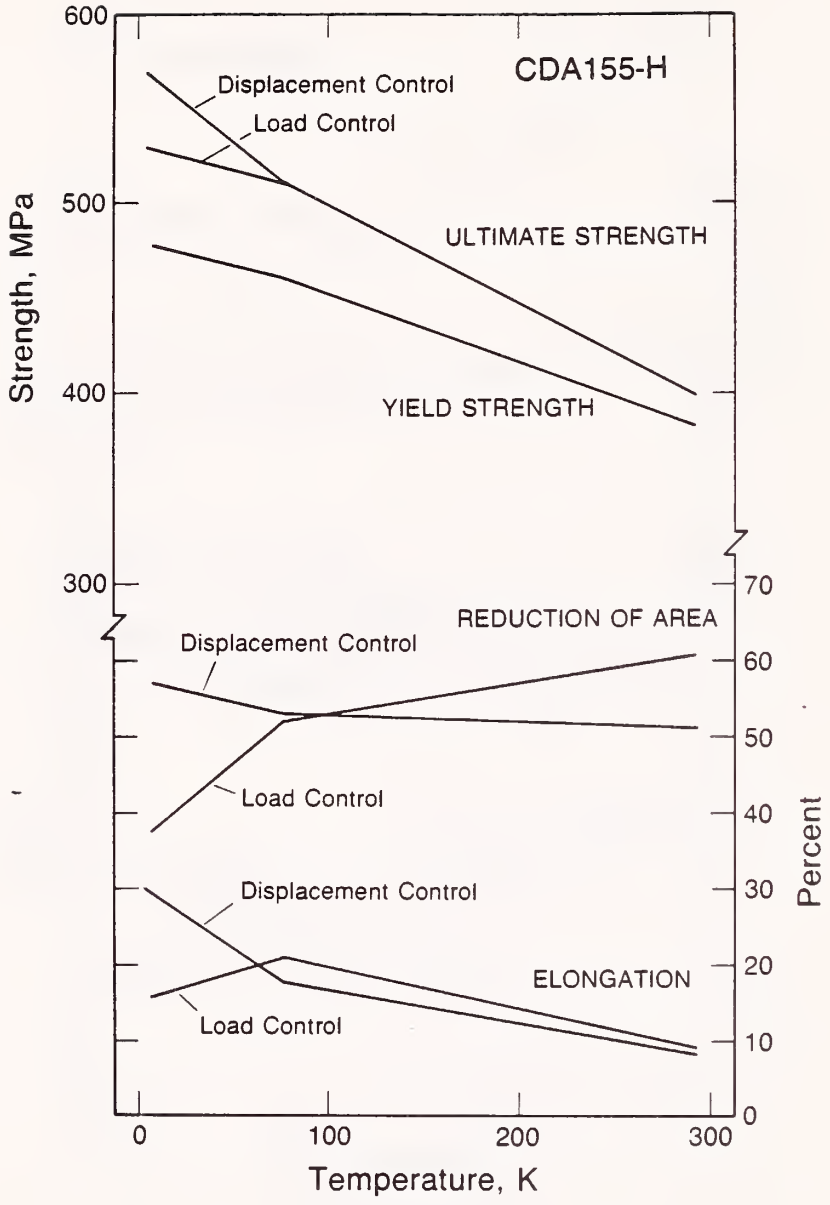

Fig. 15. The tensile properties of alloy CDA 155-H.

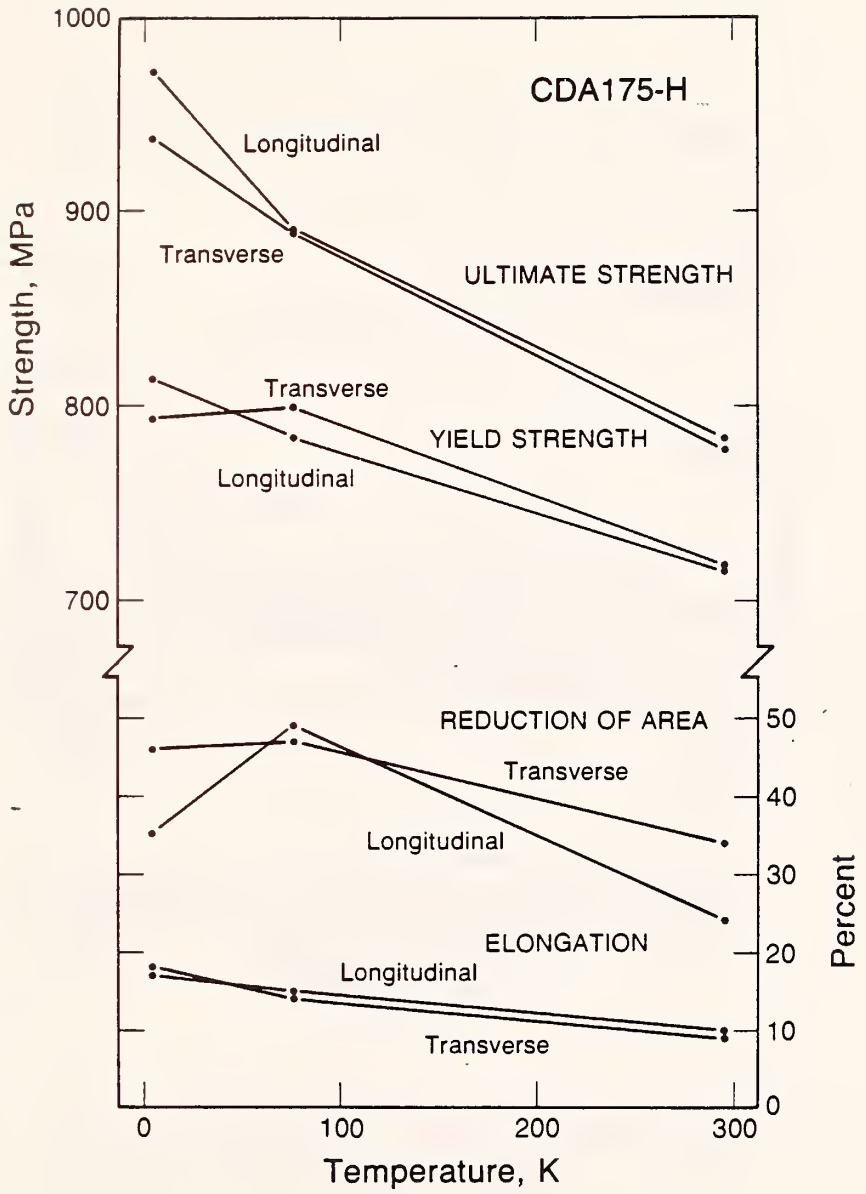

Fig. 16. The tensile properties of alloy CDA 175-H.

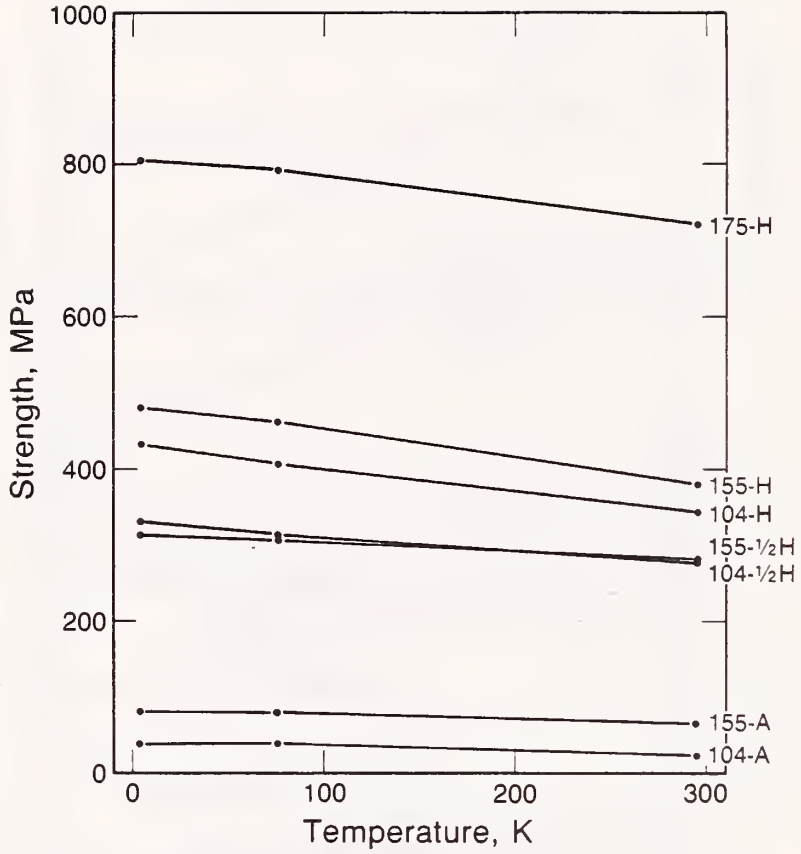

Fig. 17. Tensile yield strength summary.

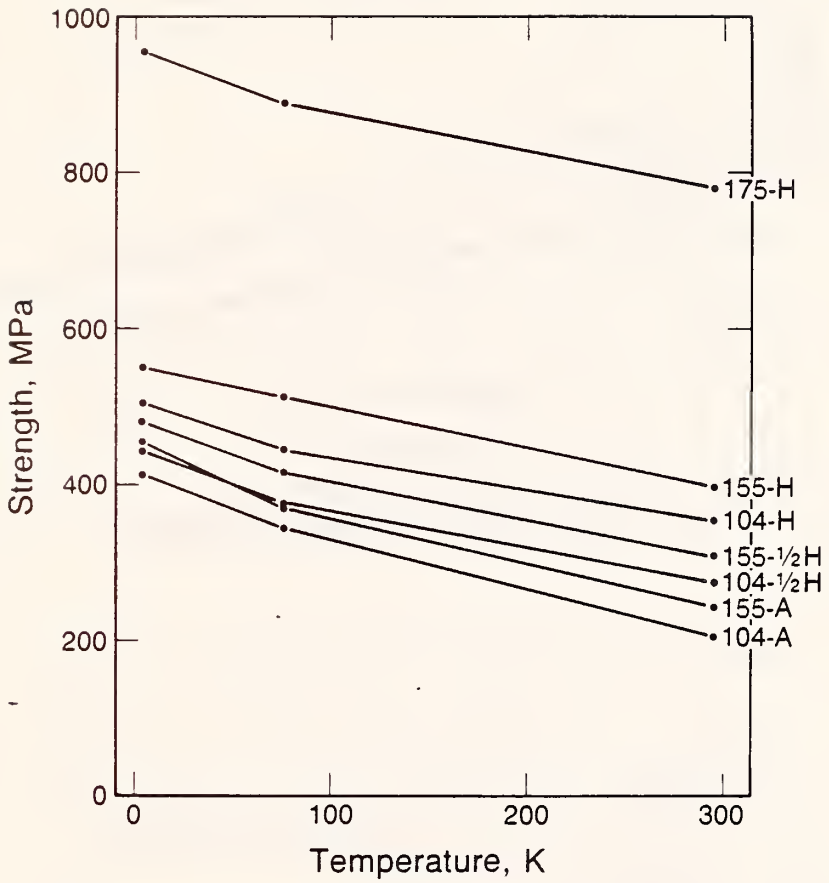

Fig. 18. Tensile ultimate strength summary.

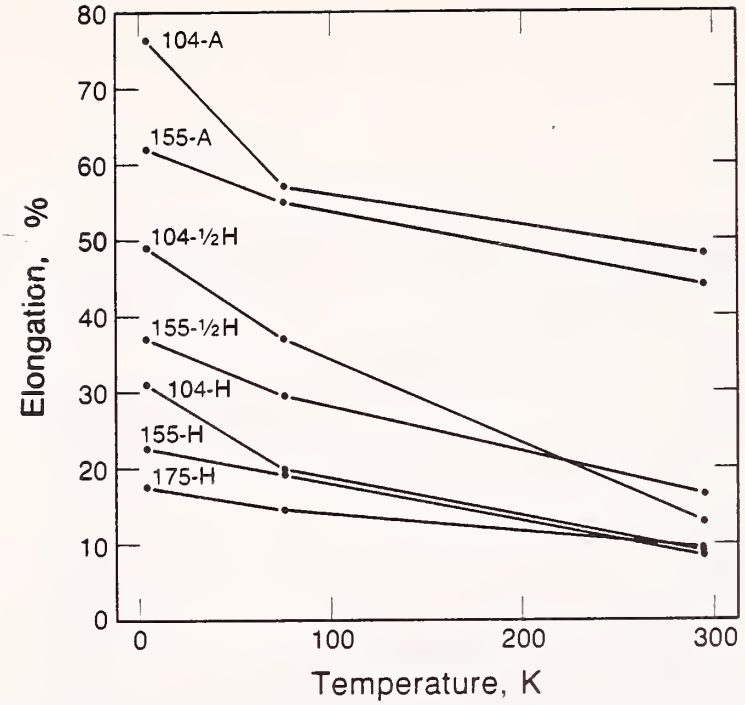

Fig. 19. Tensile elongation summary.

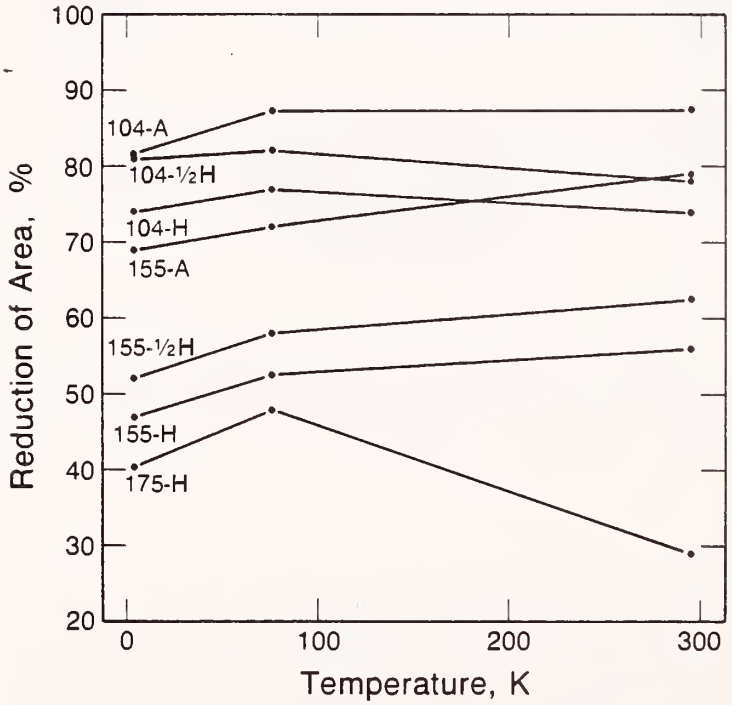

Fig. 20. Tensile reduction of area summary.

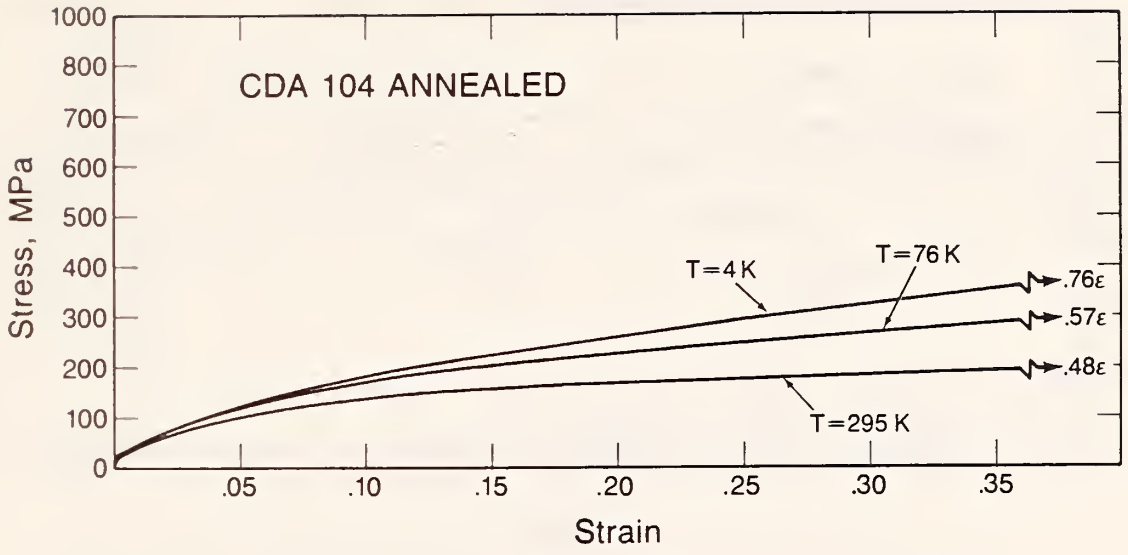

Fig. 21. Stress–strain curves for alloy CDA 104–A; displacement-control test.

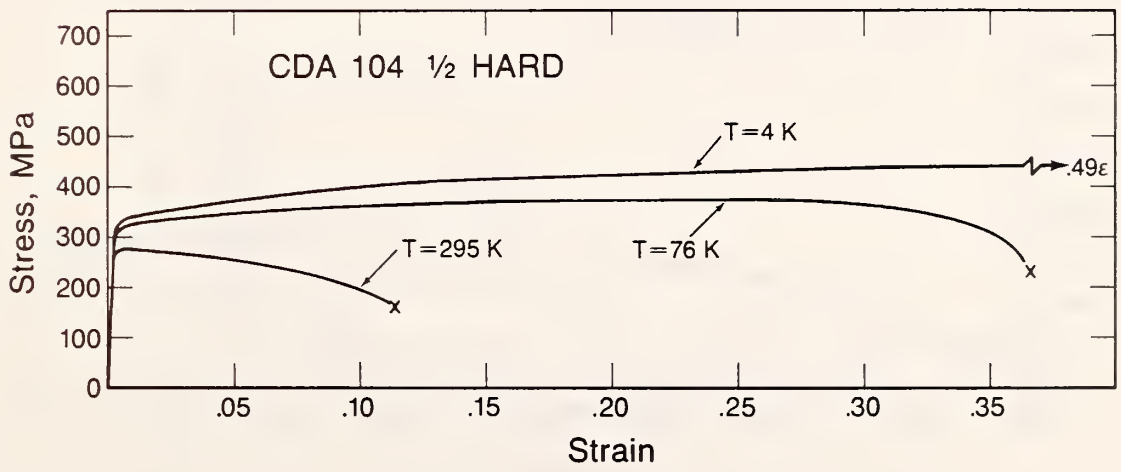

Fig. 22. Stress–strain curves for alloy CDA 104–1/2 H; displacement-control test.

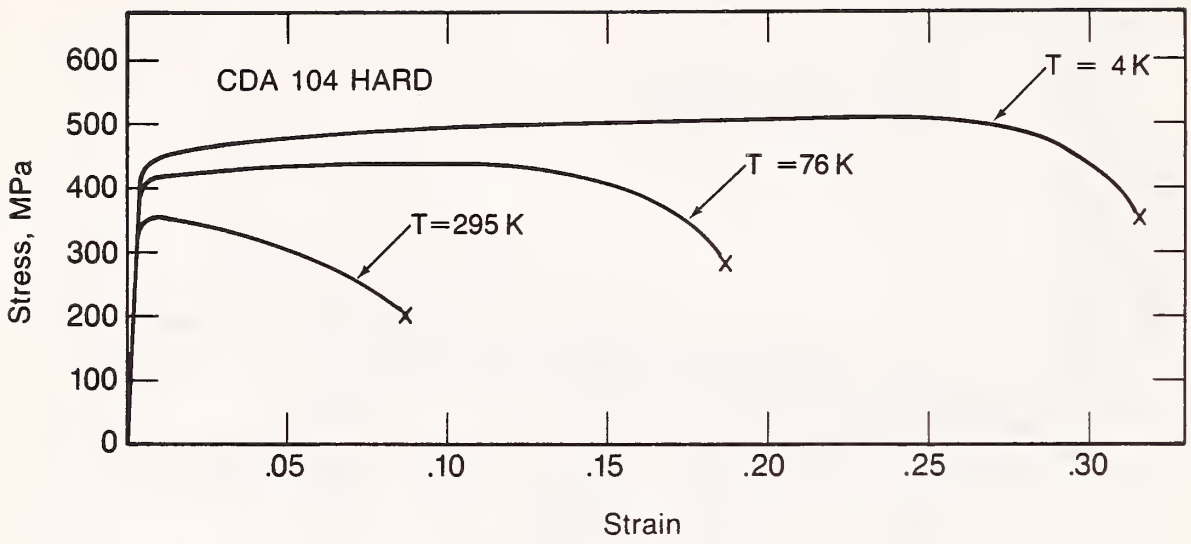

Fig. 23. Stress–strain curves for alloy CDA 104–H; displacement-control test; transverse orientation.

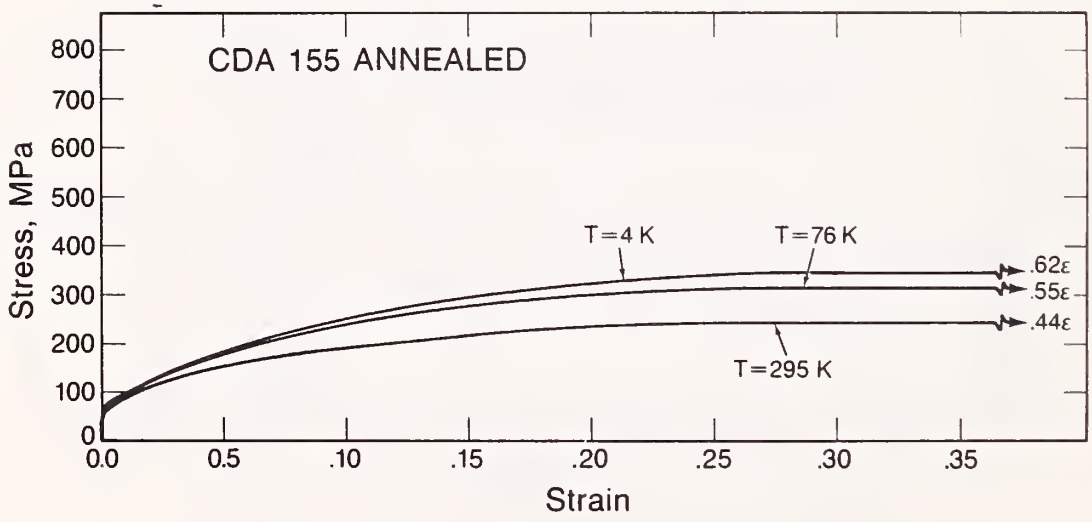

Fig. 24. Stress–strain curves for alloy CDA 155–A; displacement-control test.

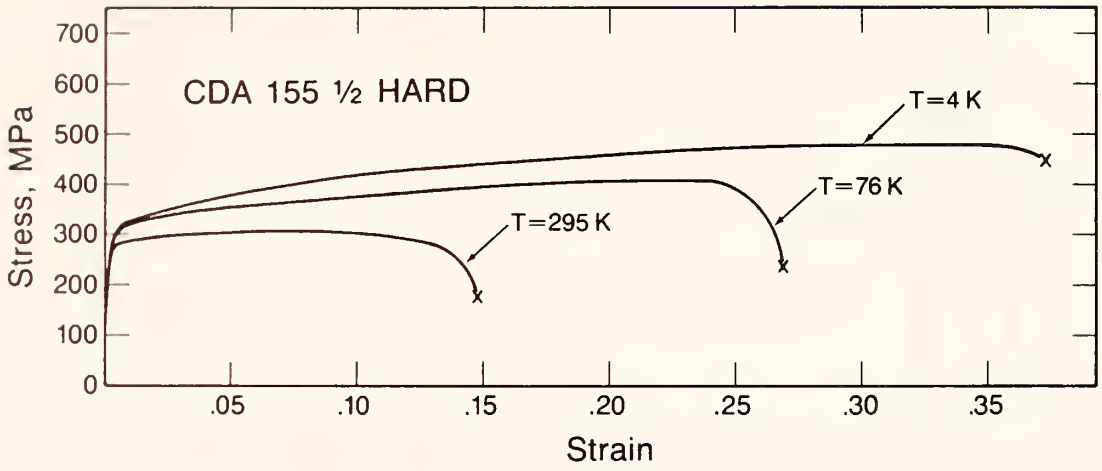

Fig. 25. Stress–strain curves for alloy CDA 155–1/2 H; displacement-control test; longitudinal orientation.

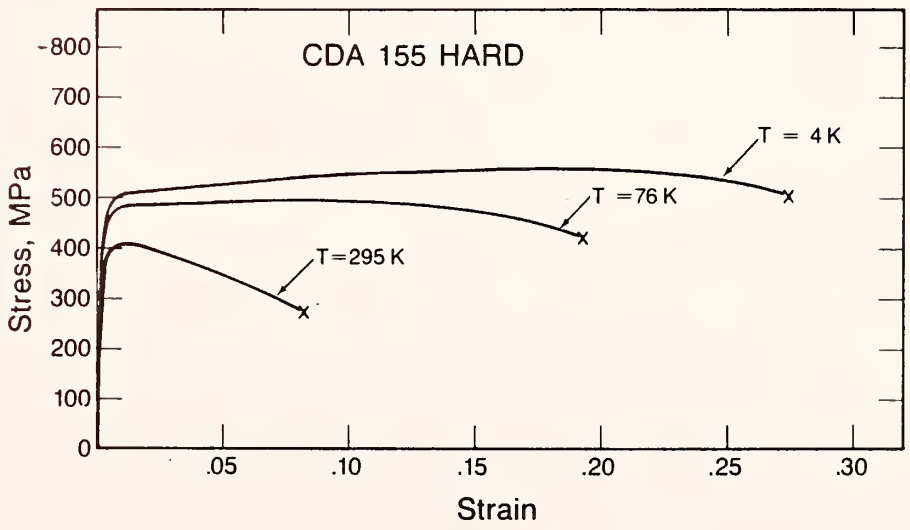

Fig. 26. Stress–strain curves for alloy CDA 155–H; displacement-control test; transverse orientation.

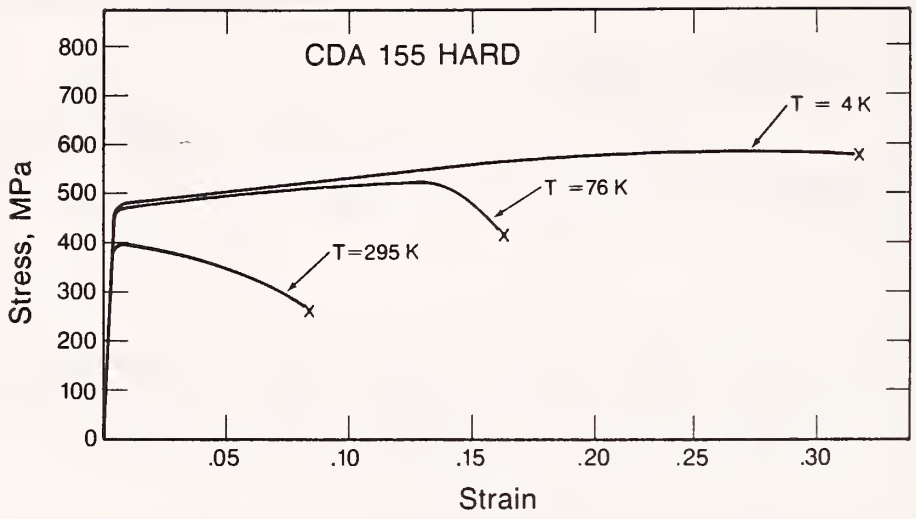

Fig. 27. Stress–strain curves for alloy CDA 155–H; displacement-control test; longitudinal orientation.

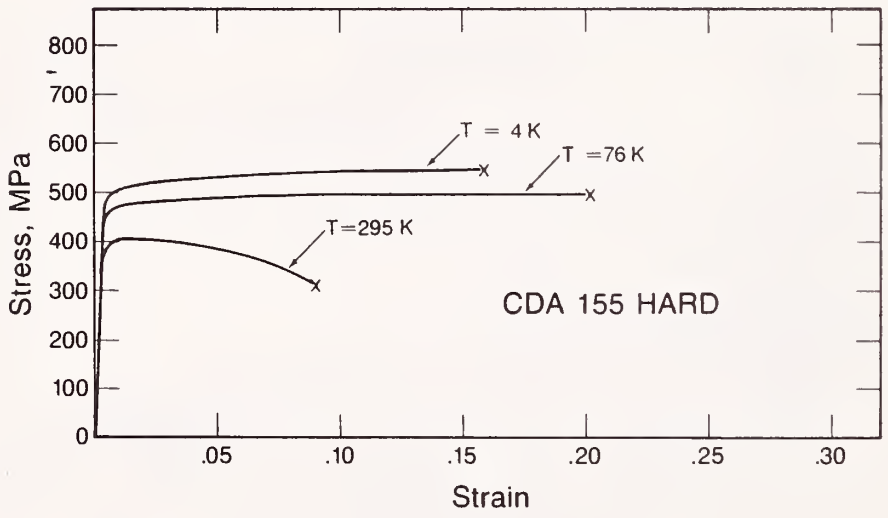

Fig. 28. Stress–strain curves for alloy CDA 155–H; load-control test; transverse orientation.

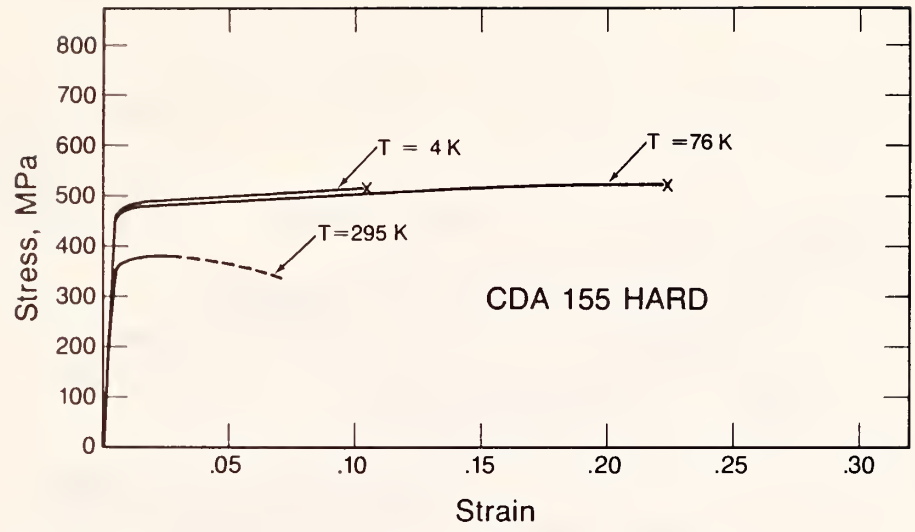

Fig. 29. Stress-strain curves for CDA 155-H; load-control test; longitudinal orientation.

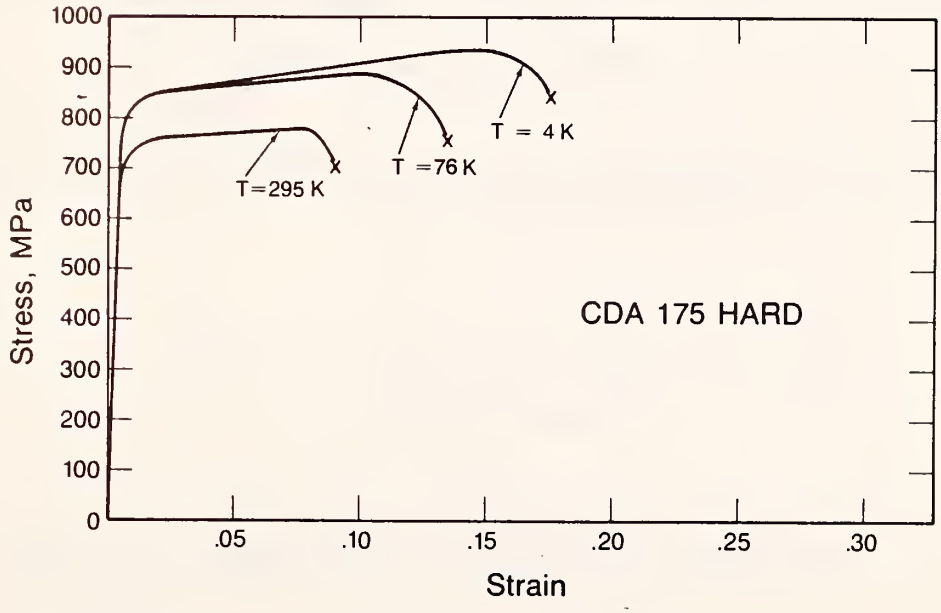

Fig. 30. Stress-strain curves for CDA 175-H; displacement-control test; transverse orientation.

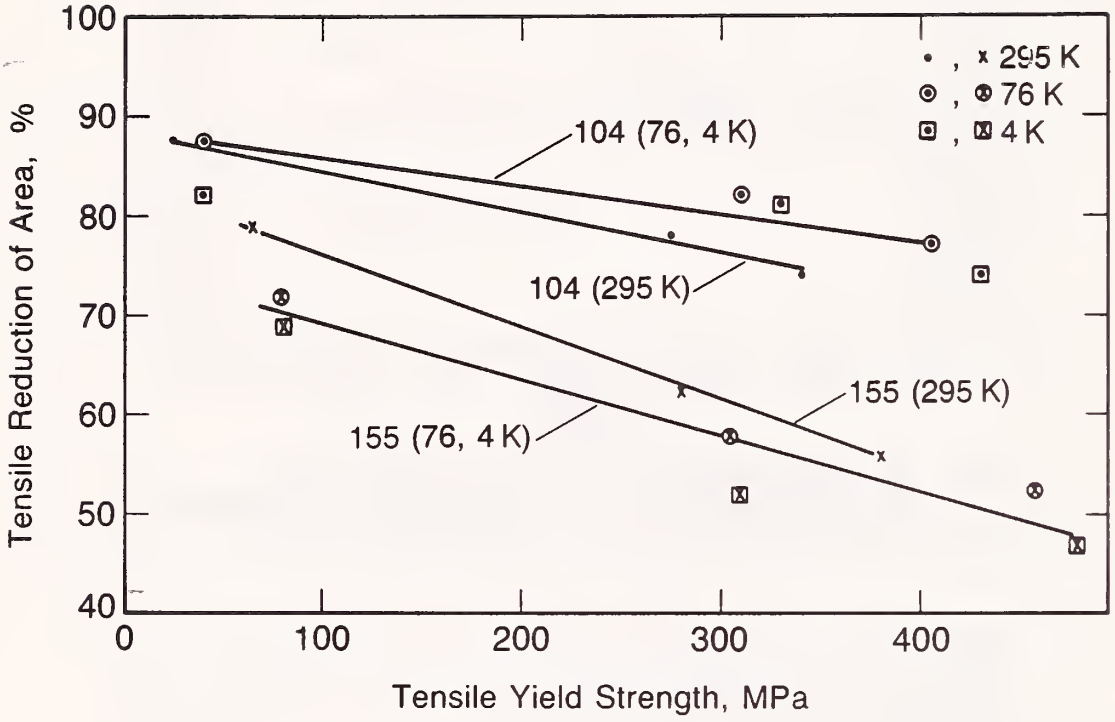

Fig. 31. Reduction of area as a function of yield strength for alloys 104 and 155.

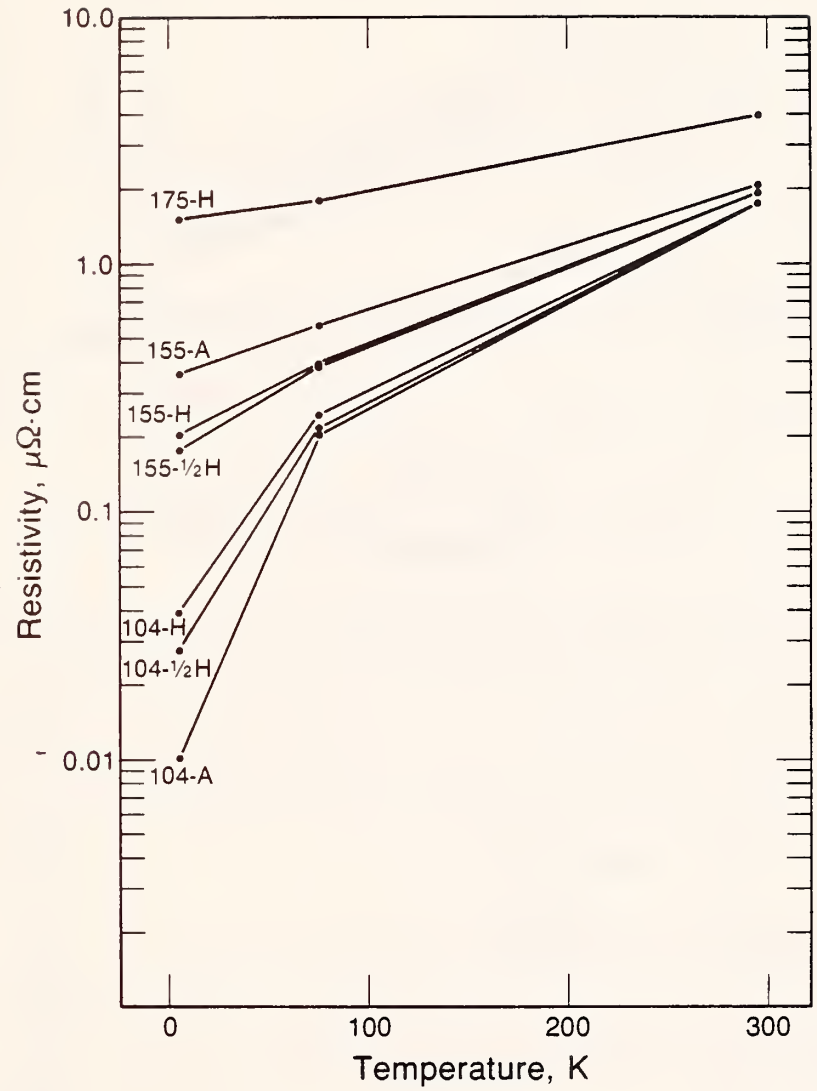

Fig. 32. Resistivity as a function of temperature.

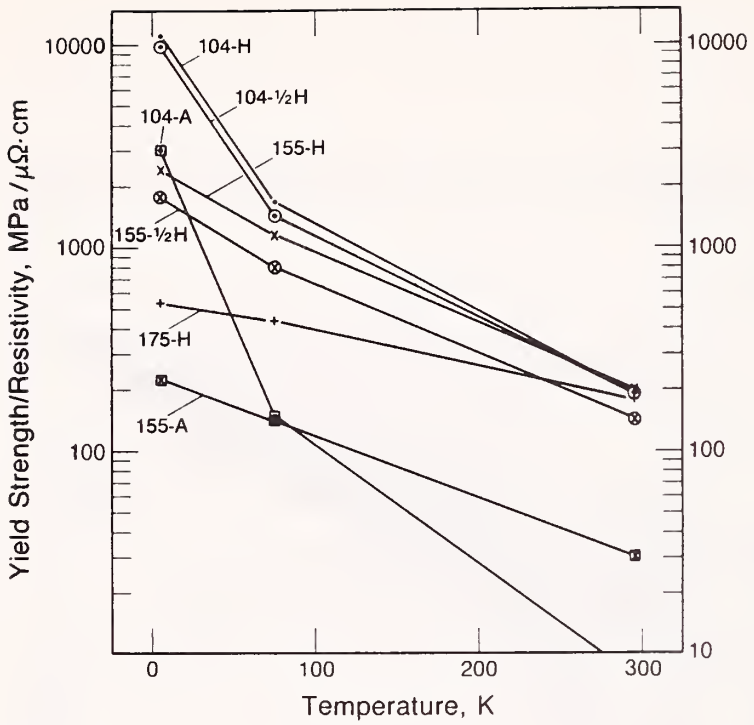

Fig. 33. Ratio of yield strength to resistivity as a function of temperature.

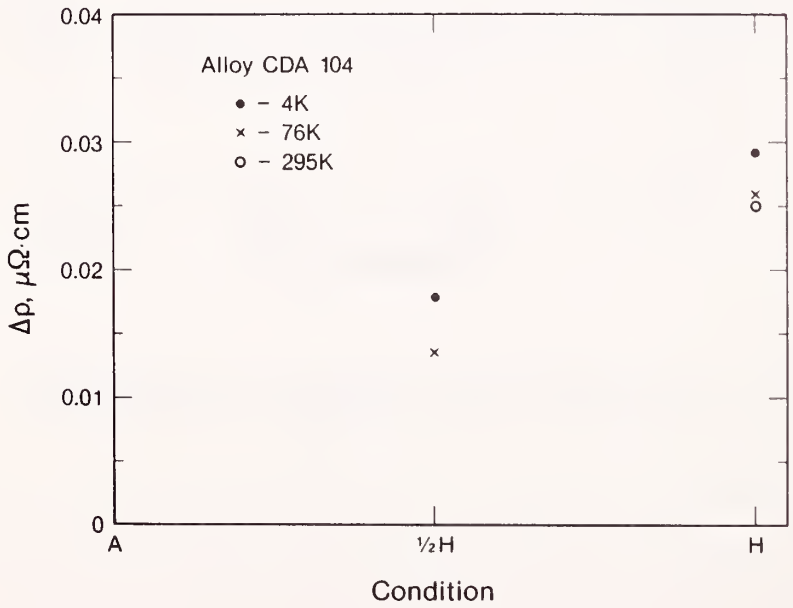

Fig. 34. Changes in resistivity due to changes in alloy condition.

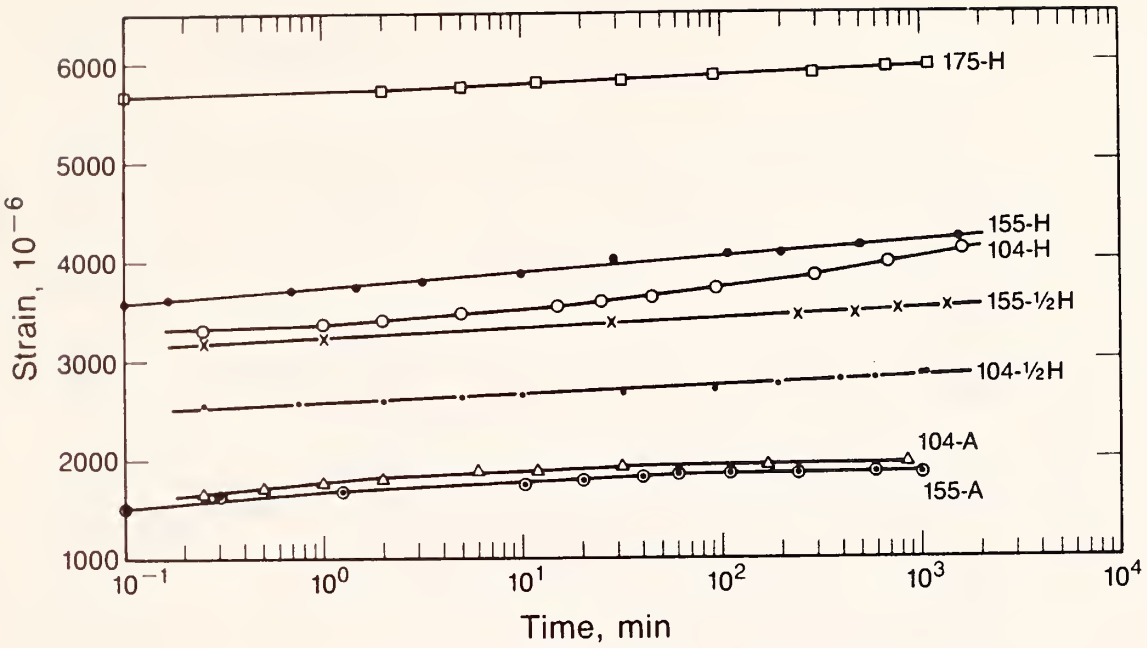

Fig. 35. Summary of creep data at 295 K; $\sigma = 0.9\ \sigma_y$.

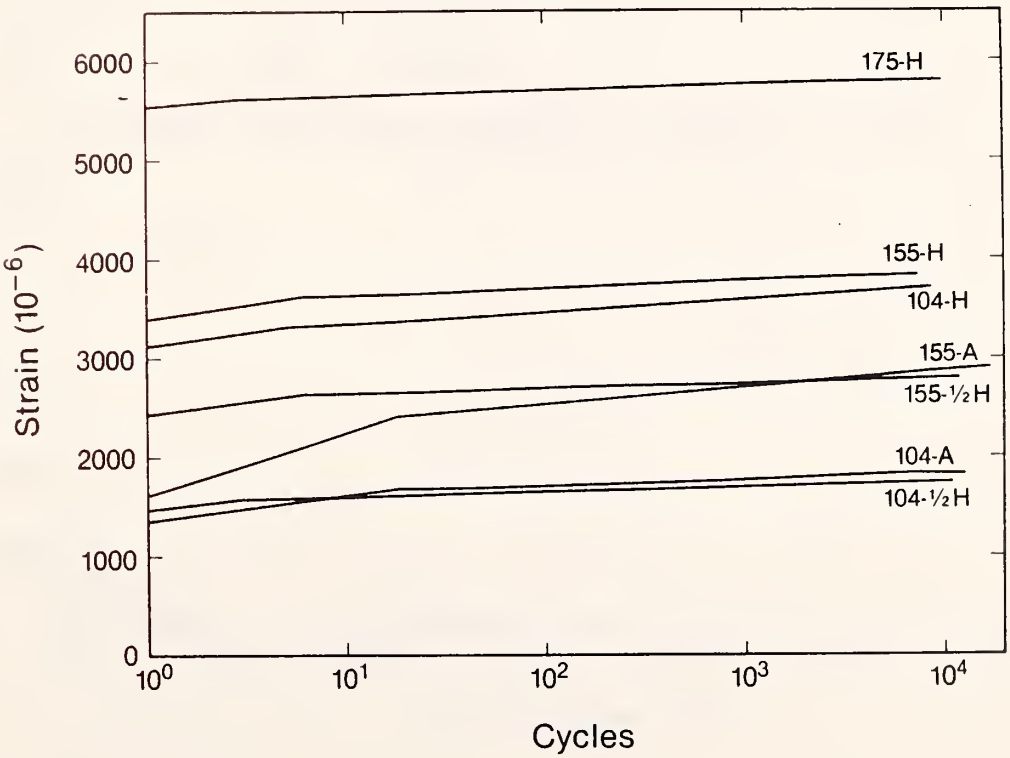

Fig. 36. Summary of fatigue data at 295 K; $\sigma = 0.9\ \sigma_y$.

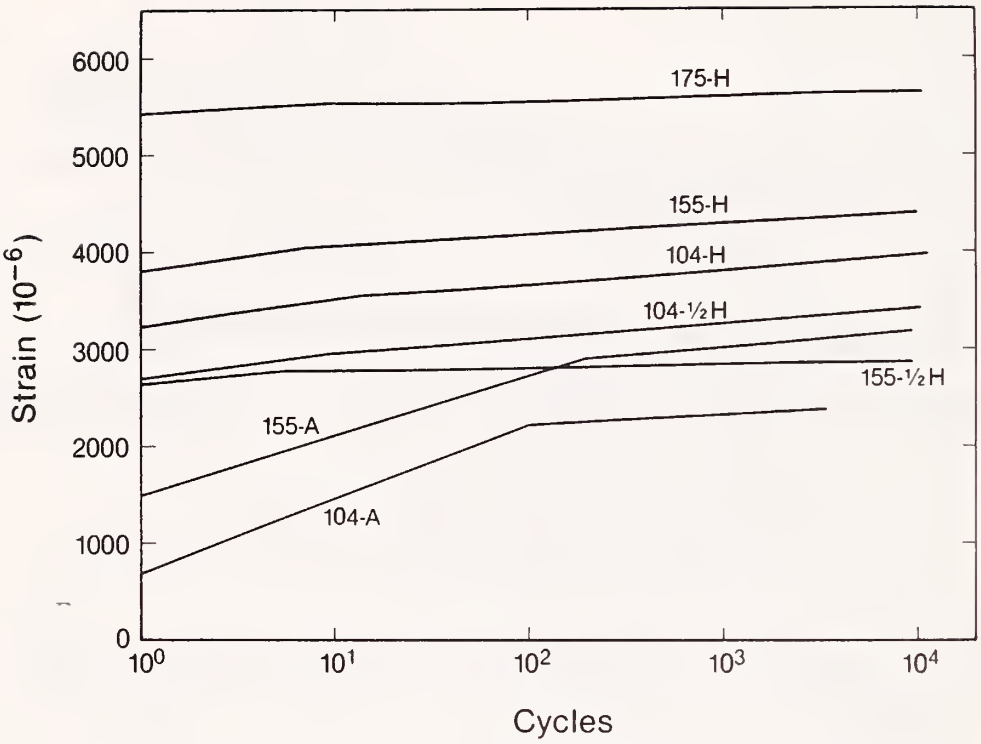

Fig. 37. Summary of combined creep and fatigue data at 295 K; $\sigma = 0.9\ \sigma_y$.

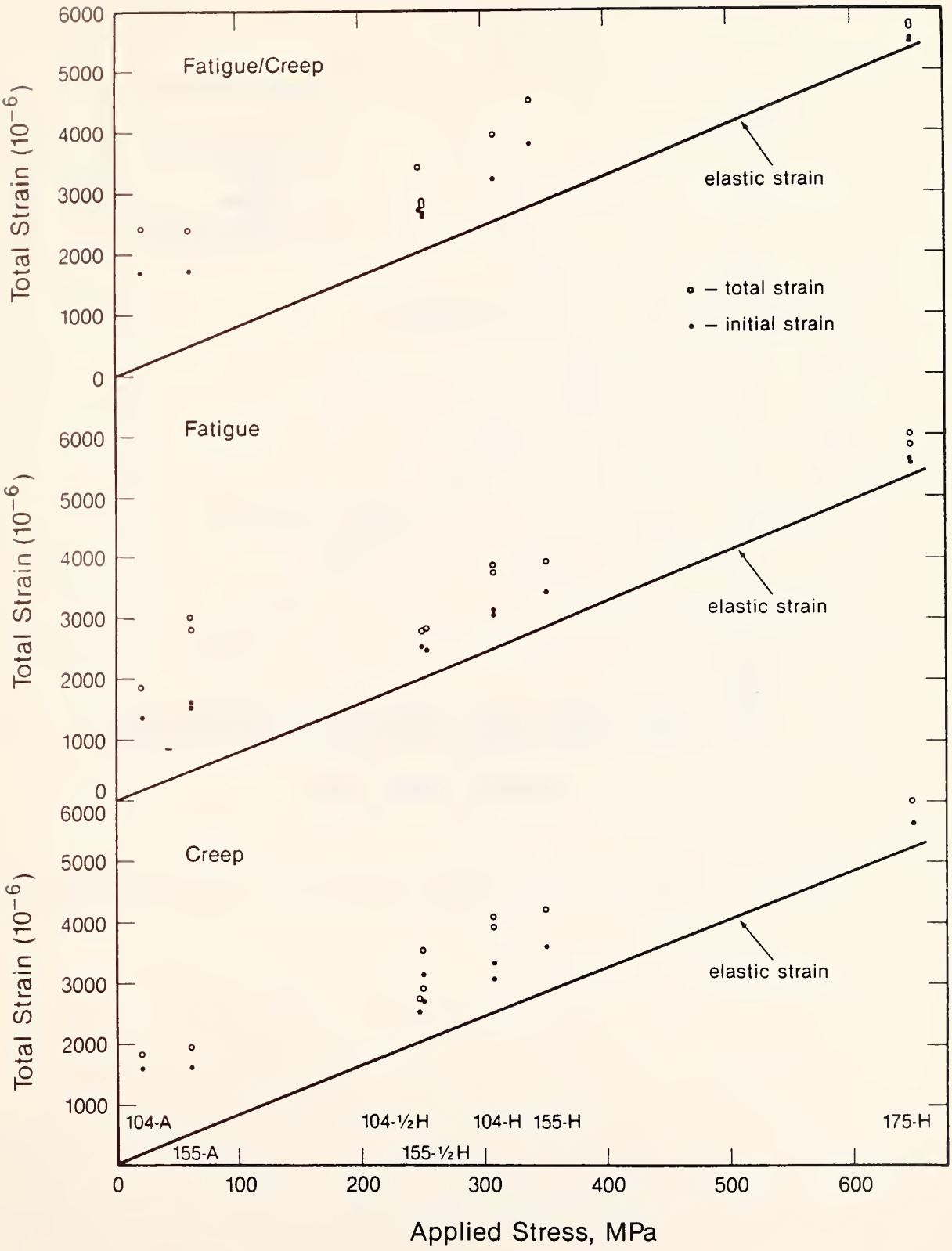

Fig. 38. Summary of all creep and fatigue data at 295 K.

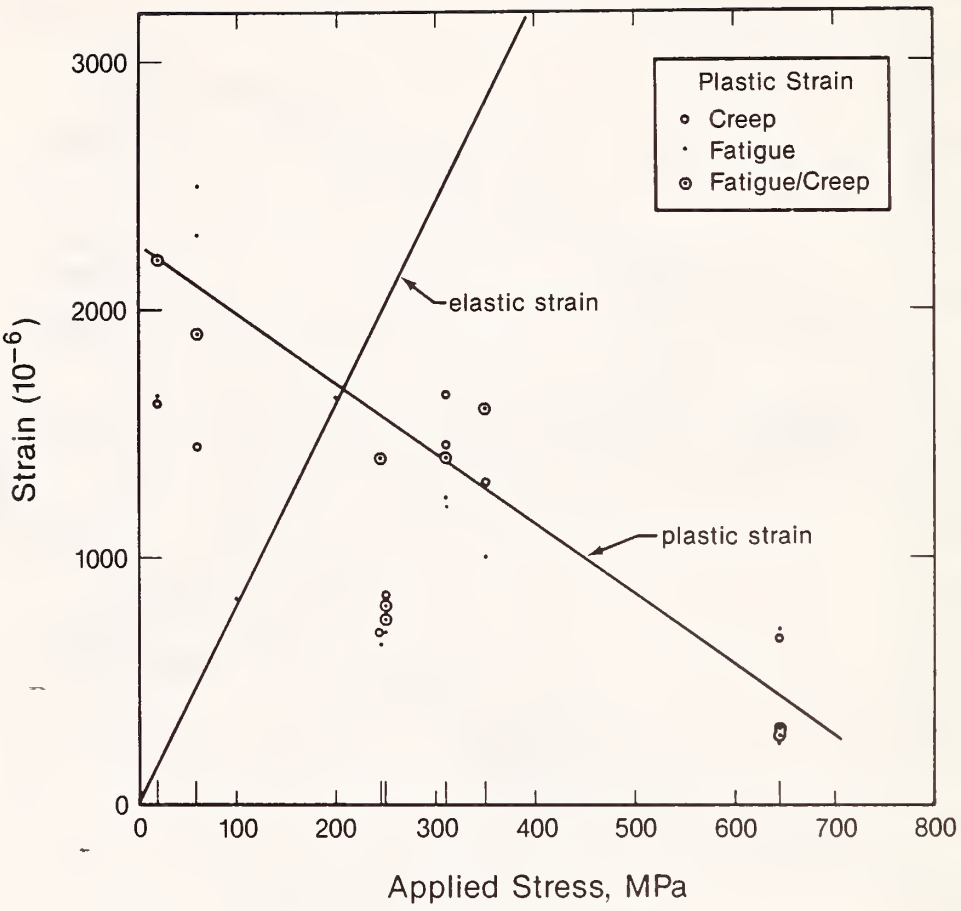

Fig. 39. Relative contributions of elastic and plastic strain versus stress.

DEFORMED-POLYCRYSTALLINE-COPPER ELASTIC CONSTANTS*

H. M. Ledbetter and M. W. Austin
Fracture and Deformation Division
Institute for Materials Science and Engineering
National Bureau of Standards
Boulder, Colorado

By ultrasonic methods, we studied the principal macroscopic-orthotropic-symmetry elastic constants of plastically deformed copper plate. By x-ray diffraction, we verified a strong plate texture, which we identified as $(110)[1\bar{1}2, 1\bar{1}\bar{1}]$. From the monocrystal elastic constants, we calculated the macroscopic elastic constants expected for ideal textures. Prediction failed to fit observation; mostly, predicted elastic stiffness was too high. We ascribe this disagreement to a high density of deformation-induced dislocations. To the elastic-constant measurements, these dislocations contribute a reversible plastic strain. For the elastic shear stiffnesses, the usual $C_{ijk\ell} = C_{ij\ell k}$ macroscopic symmetry failed. We ascribe this breakdown to dislocation-array anisotropy. For the elastic constants, the dislocation contribution overwhelms the texture contribution. After plastic deformation, the elastic constants show an ambient-temperature time dependence.

INTRODUCTION

In 1974, Ledbetter and Naimon [1] reviewed copper's elastic constants, both polycrystal and monocrystal. They included effects of temperature and pressure. Plastic-deformation effects they treated only cursorily for two reasons: complexity and dearth of careful systematic studies. Texture effects they omitted.

At least since Grüneisen in 1907 [2], we know that plastic deformation changes apparent elastic moduli, sometimes considerably. Thirty-four years later, Lawson [3] connected the Young-modulus decrease in compressed copper with Taylor dislocations. Models relating elastic-stiffness decrease to dislocation vibrations appeared from several sources: Eshelby [4], Koehler [5], Friedel [6], and Granato and Lücke [7].

---

*Intended for publication in Physica Status Solidi.

We remain uncertain about who first studied texture effects and elastic constants. Probably this occurred a century ago. In 1889, Voigt [8] considered the effective elastic constants of a random polycrystalline aggregate. Probably, nonrandom (textured) aggregates were considered then.

In recent years, Ledbetter [9,10] reported the elastic constants of annealed quasi-isotropic polycrystalline copper. Using various models, he related polycrystal and monocrystal elastic constants and found that Kröner's model [11] works best.

The present study considers the macroscopic elastic constants of polycrystalline copper deformed by rolling. We consider effects of both texture and plastic deformation.

MATERIALS

We studied two commercial copper alloys: CDA104, oxygen-free copper with silver; and CDA155, silver-bearing copper. Including silver, these alloys contain 99.95 and 99.75 percent copper, respectively. We studied three plastic-deformation conditions: the received deformed plate (hardness = 80, 88 R_F), plate deformed by rolling to a 60 percent reduction (hardness = 88, 96 R_F), and plate in the recrystallized-annealed condition (hardness = 53, 63 R_F). From these, we ground parallelepiped specimens measuring approximately 1.5 cm for all three dimensions. Figure 1 shows a typical microstructure. We obtained the annealed condition by heating the received plates for 1 h at 510°C and for 1.3 h at 550°C, respectively.

MEASUREMENT METHODS

Mass density, ρ, we measured by Archimedes's method using distilled water as a standard. We estimated inaccuracy as 0.05 percent.

Sound velocity, v, we measured by a MHz-frequency pulse-echo-superposition method described previously [9,10,12]. From mass density and sound velocities, we computed elastic constants by

$$C_\ell = \rho v_\ell^2 \tag{1}$$

and

$$C_t = \rho v_t^2. \tag{2}$$

Here, subscripts ℓ and t denote longitudinal and transverse. For each of six materials, we measured six sound velocities corresponding to the longitudinal elastic constants C_{11}, C_{22}, and C_{33} and the transverse (shear) elastic constants C_{44}, C_{55}, and C_{66}. Because they contribute little to the present study and because they contain larger errors, we omitted measurements of C_{12}, C_{13}, and C_{23}. For sound velocities, we estimated a 0.2 percent inaccuracy in v_ℓ and a 0.4 percent inaccuracy in v_t. Thus, we estimated C_ℓ errors as 0.45 percent and C_t errors as 0.85 percent.

Texture we studied by x-ray diffraction from surfaces perpendicular to the three principal directions: x_1 = rolling direction, x_3 = direction normal to rolling plane, x_2 = direction orthogonal to x_1 and x_3 (some call x_2 the long-transverse direction). For x-ray diffraction, we used a computer-controlled commercial diffractometer and Cu-Kα radiation.

RESULTS

The study's principal results occur in Table 1. The table shows measurements for two alloys in three plastic-deformation conditions. For one alloy, CDA155, in the high-hardness condition, we show measurements at two post-deformation times: 15 days and 105 days.

Table 1 also shows results calculated from copper's monocrystal elastic constants: C_{11} = 168.4, C_{12} = 121.4, and C_{44} = 75.39 GPa. These calculations include the quasi-isotropic elastic constants by Kröner's method [11] by Voigt's method, elastic constants for three textures: (110)[1$\bar{1}$2], (110)[1$\bar{1}$1], (112)[11$\bar{1}$]. The fourth texture, (110)[1$\bar{1}$2, 1$\bar{1}\bar{1}$], equals an arithmetic average of the first two.

Figure 2 shows a set of four typical x-ray-diffraction patterns: standard copper and patterns from the x_1, x_2, x_3 faces. Study of these patterns led to the following interpretation. With respect to annealed copper, diffraction lines are broadened but little shifted. For the x_1 and x_2 faces, one sees essentially identical patterns. These differ dramatically from the x_3-surface pattern. It shows no (111) line and a strong (220) line. Unambiguously, this shows that {110} corresponds to the rolling plane. We expect a rolling direction of either <111> or <112>. Diffraction patterns from the x_1 and x_2 surfaces suggest a mixture of both, favoring <111>.

PLATE-TEXTURE ELASTIC CONSTANTS

We denote a plate texture by the notation (hkℓ)[uvw], where (hkℓ) denotes the rolling plane and [uvw] the orthogonal rolling direction. Here, we take x_1 = rolling direction, x_2 = transverse direction, x_3 = rolling-plane normal. In an ideal plate texture, only [uvw] directions are parallel to x_1 and only (hkℓ) plane normals are parallel to x_3. Thus, in many ways, an ideal plate texture behaves like a monocrystal. To obtain the plate-texture elastic constants, $D_{ijk\ell}$, we perform the usual tensor-property co-ordinate transformation:

$$D_{ijk\ell} = a_{im}a_{jn}a_{ko}a_{\ell p}C_{mnop}. \qquad (3)$$

Here, C_{mnop} denotes the usual fourth-order monocrystal elastic constants and the a_{im} denote the direction cosines between the new (plate) co-ordinates and the old (crystal) co-ordinates.

For (110)[1$\bar{1}$2] plate texture, the new base vectors are $\underset{\sim}{x}_1$ = [1$\bar{1}$2], $\underset{\sim}{x}_2$ = [$\bar{1}$11], and $\underset{\sim}{x}_3$ = [110]. In Voigt's contracted notation, for this case, one obtains the six-by-six matrix (for simplicity, we show only indices):

$$D_{ij} = \begin{bmatrix} 11 & 12 & 13 & 0 & 0 & 16 \\ 12 & 22 & 12 & 0 & 0 & 0 \\ 13 & 12 & 11 & 0 & 0 & -16 \\ 0 & 0 & 0 & 44 & -16 & 0 \\ 0 & 0 & 0 & -16 & (11-13)/2 & 0 \\ 16 & 0 & -16 & 0 & 0 & 44 \end{bmatrix} . \quad (4)$$

Here,

$$\begin{aligned} D_{11} &= (C_{11} + C_{12} + 2C_{44})/2 \\ D_{22} &= (C_{11} + 2C_{12} + 4C_{44})/3 \\ D_{12} &= (C_{11} + 2C_{12} - 2C_{44})/3 \\ D_{13} &= (C_{11} + 5C_{12} - 2C_{44})/6 \\ D_{16} &= (C_{11} - C_{12} - 2C_{44})/\sqrt{18} \\ D_{44} &= (C_{11} - C_{12} + C_{44})/3. \end{aligned} \quad (5)$$

For (112)[11$\bar{1}$] plate texture, x_1 = [11$\bar{1}$], x_2 = [1$\bar{1}$0], x_3 = [112], and one obtains

$$D_{ij} = \begin{bmatrix} 22 & 12 & 12 & 0 & 0 & 0 \\ 12 & 11 & 13 & 0 & 16 & 0 \\ 12 & 13 & 11 & 0 & -16 & 0 \\ 0 & 0 & 0 & (11-13)/2 & 0 & 16 \\ 0 & 16 & -16 & 0 & 44 & 0 \\ 0 & 0 & 0 & 16 & 0 & 44 \end{bmatrix} . \quad (6)$$

Here, the D_{ij} elements are given by Eq. (5). To compute the D_{ij} elements, for copper's monocrystal elastic constants we used $C_{11} = 168.4$, $C_{12} = 121.4$, and $C_{44} = 75.39$ GPa [1].

For these two texture cases—(110)[1$\bar{1}$2] and (112)[11$\bar{1}$], the D_{ij} results are given in Table 1. Also, the table shows results for a (110)[1$\bar{1}$2, 1$\bar{1}\bar{1}$] texture suggested by our x-ray-diffraction results: a (110) rolling plane and a rolling direction consisting of an approximately equal mix of [1$\bar{1}$2] and [1$\bar{1}$1] directions. To make this mixed-case prediction, we averaged the (110)[1$\bar{1}$2] case with the (110)[1$\bar{1}$1] case where $x_1 = [1\bar{1}\bar{1}]$, $x_2 = [1\bar{1}2]$, $x_3 = [110]$, and

$$D_{ij} = \begin{bmatrix} 22 & 12 & 12 & 0 & 0 & 0 \\ 12 & 11 & 13 & 0 & 0 & -16 \\ 12 & 13 & 11 & 0 & 0 & 16 \\ 0 & 0 & 0 & (11-13)/2 & 16 & 0 \\ 0 & 0 & 0 & 16 & 44 & 0 \\ 0 & -16 & 16 & 0 & 0 & 44 \end{bmatrix} . \quad (7)$$

The D_{ij} elements are given by Eq. (5).

DISCUSSION

Results in Table 1 show several features:

1. For a rolled plate, the C_{ij} show the expected orthotropic symmetry: $C_{11} \neq C_{22} \neq C_{33}$ and $C_{44} \neq C_{55} \neq C_{66}$.

2. Excepting C_{2323} and C_{2121}, all the principal-diagonal elastic stiffnesses are lower than those predicted for (110)[1$\bar{1}$2, 1$\bar{1}\bar{1}$] texture.

3. For the elastic shear stiffnesses, the usual $C_{ijk\ell} = C_{k\ell ij}$ symmetry fails.

4. With time, all the C_{ij} increase: over three months, 1 percent in the C_{ii} (i = 1,2,3), and 2 percent in the C_{ii} (i = 4,5,6).

The first feature, macroscopic anisotropy, results from texture; and, as described below, from anisotropic dislocation arrays.

We explain the unexpected second and third features by a single hypothesis: an anisotropic high-density dislocation array. Dislocations arise

naturally during plastic deformation; heavy deformation induces large numbers. In fcc metals, the principal dislocations lie on {111} planes in <110> directions. Because of texture, these planes and directions orient preferredly rather than randomly. For the present case, we expect {111} planes perpendicular to both x_1 and x_2 and <110> directions parallel to x_3.

Perhaps Lawson [3] first discovered the relationship between dislocations and elastic constants. He applied compressive stress to polycrystalline copper and found a Young-modulus decrease of six to seven percent. A theoretical basis for dislocation-lowered elastic constants arose from Eshelby [4]. He showed that the shear-modulus varies according to

$$\frac{\delta G^{-1}}{G^{-1}} = naG \frac{d}{\sigma_o}. \tag{8}$$

Here, n denotes dislocation density, a unit-cell dimension; d, dislocation-motion distance, and σ_o, elastic shear stress. For a pinned dislocation under oscillating stress, Koehler [5] gave a detailed calculation. He showed that reversible plastic dislocation motion creates a small extra strain that lowers the Young modulus. In measurements on copper monocrystals, Thompson and Holmes [13] found that mechanical deformation reduces the Young modulus up to ten percent. Calculations by Koehler and deWit [14] produced three conclusions: (1) elastic anisotropy increases the dislocation-network elastic-constant lowering; (2) for annealed copper, the effect equals a few percent; (3) for slightly deformed copper, the effect may reach ten percent. Extending Koehler's vibrating-string model, Granato and Lücke [7] gave a detailed dislocation-damping model that contains an associated modulus change, $\Delta E/E$, with each loss mechanism involved in dislocation motion. These authors showed that $\Delta E/E$ depends on both strain amplitude and frequency (at high frequencies).

From these five studies, both experimentally and theoretically, we expect unpinned dislocations to lower the elastic stiffness, C. The following relationship summarizes the main idea:

$$C = \frac{\sigma}{\epsilon} = \frac{\sigma}{\epsilon_e + \epsilon_p}. \tag{9}$$

Here, σ denotes stress; ϵ, strain; e, elastic; and p, plastic. For well-pinned dislocations, ϵ_p equals zero. Pinning results from many mechanisms that include impurities, irradiation-induced defects, and dislocation nodes.

We now consider whether basic physical relationships allow such a large modulus decrease. For low strain amplitudes, Koehler [5] derived an expression for the shear-modulus change

$$\frac{dG}{G} = -\frac{NGa^5}{2CL^3c^2}. \tag{10}$$

Here, N denotes atomic lengths of dislocation line; G, shear modulus; a, interatomic spacing; L^3, specimen volume; c, concentration of pinning points

along dislocation line (n/N); and πC, the line tension that tends to decrease dislocation length. According to Mott and Nabarro [15]

$$\pi C = \frac{2Ga^2}{(1 - \nu)}. \tag{11}$$

Here, ν denotes Poisson ratio. Combining Eqs. (10) and (11) gives

$$\frac{dG}{G} = -\frac{\pi Da^2(1 - \nu)}{4c^2}. \tag{12}$$

We substituted $D = Na/L^3$, D being the usual dislocation density (total length per unit volume, cm/cm^3). From Eq. (12), we can compute the dislocation density required to give a ten-percent shear-modulus decrease. For copper, we take $a = 2.56$ Å and $\nu = 0.345$. We assume $c = 10^{-2}$, one pinning point per hundred atoms. Then, we obtain a reasonable number:

$$D = 3 \cdot 10^{10} \text{ cm/cm}^3. \tag{13}$$

According to Hull and Bacon [16], well-annealed metal crystals show a D of 10^6 to 10^8 cm^{-2} and heavily deformed metals show D values up to $5 \cdot 10^{13}$ cm^{-2}. We conclude that the observed modulus decrease agrees with existing models.

By using a model of Seeger and Haasen [17], we can estimate the dislocation density in our deformed materials. For nondeformed crystals, these authors concluded that dislocations increase volume by one atomic volume, Ω, per length of dislocation equal to the Burgers-vector magnitude, b. Thus,

$$D = -\frac{d\rho}{\rho} \frac{b}{\Omega}. \tag{14}$$

Here, ρ denotes mass density, and we found $-d\rho/\rho = 2.5 \cdot 10^{-4}$. Taking $b = 2.56$ Å and $\Omega = 11.81$ Å^3, we obtain $D = 5 \cdot 10^{11}$ cm/cm^3. This agrees within one order of magnitude with the estimate of Eq. (13). Considering contributions from point defects would give closer agreement.

It remains to consider the dislocation-array anisotropy. In fcc crystals such as Cu, Ag, and Au, the principal dislocation is an (a/2)<110> Burgers-vector edge dislocation that glides on {111} planes and lies along <112> directions [18]. In a nontextured aggregate, all these vectors are distributed randomly, and the ϵ_p term in Eq. (9) is isotropic. Texture causes a nonrandom distribution of these dislocation vectors and makes ϵ_p anisotropic. Figure 3 shows the source of this anisotropy by considering a single edge dislocation in an isotropic block. If we assume that the pinned dislocation can move easily in its glide plane, but not otherwise, then it follows for the longitudinal elastic moduli that

$$C_{1111} = C_{3333} > C_{2222}. \tag{15}$$

Similarly, for the shear moduli, it follows that

$$C_{2323} > C_{3232}, \tag{16}$$

$$C_{2121} > C_{1212}, \tag{17}$$

and

$$C_{1313} = C_{3131}. \tag{18}$$

Here, the first index indicates shear-plane normal and the second index indicates shear direction. For this simple case, Eqs. (15) through (17) represent an anisotropic dislocation contribution to the elastic constants through an anisotropic ϵ_p. By considering screw dislocations and partial dislocations, one finds corresponding anisotropies that break the usual $C_{ijij} = C_{ijji}$ symmetry for shear elastic constants and the $C_{1111} = C_{2222} = C_{3333}$ symmetry for longitudinal elastic constants. We expect the largest symmetry breaking for the shear constants. The shear constant showing the largest effect corresponds to the shear-wave polarization direction containing the Burgers vector, x_2 in Fig. 3.

Results in Table 1 for the shear constants show that symmetry breaking occurs for C_{44} and C_{66}, but not for C_{55}. This requires that the Burgers vectors favor x_2, which is consistent with the texture result that <110> directions lie along x_2. The remarkably low C_{22} value for the CDA155 alloy also supports the suggestion that Burgers vectors lie along x_2.

Although we failed to study the phenomenon systematically, we found that after plastic deformation all the C_{ij} increased with time. Over three months, the increase was 1 to 2 percent, being larger for the shear constants C_{44}, C_{55}, and C_{66}. We interpret this recovery to result from impurity atoms diffusing to and pinning dislocations, thus reducing ϵ_p in Eq. (9).

Finally, we discuss texture effects. As described in the results section, x-ray-diffraction results from the three faces orthogonal to x_1, x_2, and x_3, when compared with those of nontextured copper, show a strong texture: a {110} rolling plane and a rolling direction that combines <110> and <112>. From the calculated results in Table 1, we expect this texture to increase C_{11}, C_{22}, and C_{33}, decrease C_{66}, and leave C_{44} and C_{55} unaffected. Observation fails to confirm these expectations. No other reasonable texture model gives results that agree with observation. We conclude that texture effects obscure the dislocation effects described above. In studying deformed-copper-rod elastic constants, Wawra [19] reached a similar conclusion: "texture ... is not decisive in our problem."

CONCLUSIONS

From this study, there emerged six conclusions:

1. In rolled copper plate, elastic constants depend on two conditions: texture and plastic deformation.

2. For heavily deformed materials, plastic-deformation effects can obscure texture effects. For both longitudinal and transverse elastic constants, plastic deformation may lower the elastic stiffness by up to 15 percent.

3. Elastic stiffness is lowered by a high density of nonpinned dislocations, that is, a reversible plastic strain.

4. The $C_{ijk\ell} = C_{ij\ell k}$ macroscopic symmetry breaks because of an anisotropic dislocation array.

5. After plastic deformation, elastic stiffness increases with time because the density of nonpinned dislocations decreases, caused perhaps by impurity diffusion to dislocations.

6. Annealing restores elastic constants that typify the nondeformed texture-free quasi-isotropic state.

ACKNOWLEDGMENT

The U.S. Department of Energy, Office of Fusion Energy, provided support. S. A. Kim made the velocity measurements. L. Scull and R. Walsh furnished samples and metallography. Professor E. Kröner (Stuttgart) made many valuable comments. M. Lei, guest worker from Institute for Metal Research (Shenyang) verified the matrix equations.

REFERENCES

1. H. M. Ledbetter and E. R. Naimon, J. Phys. Chem. Ref. Data 3, 897 (1974).
2. E. Grüneisen, Ann. Phys. 22, 801 (1907).
3. A. W. Lawson, Phys. Rev. 60, 330 (1941).
4. J. D. Eshelby, Proc. Roy. Soc. Lond. 197, 396 (1949).
5. J. S. Koehler, in Imperfections in Nearly Perfect Crystals, Wiley, New York (1952), p. 197.
6. J. Friedel, Philos. Mag. 44, 444 (1953).
7. A. Granato and K. Lücke, J. Appl. Phys. 27, 789 (1956).
8. W. Voigt, Ann. Phys. 38, 573 (1989).
9. H. M. Ledbetter, J. Phys. D: Appl. Phys. 13, 1879 (1980).
10. H. M. Ledbetter, Phys. Status Solidi (a) 66, 477 (1981).
11. E. Kröner, Z. Phys. 151, 504 (1958).
12. H. M. Ledbetter, N. V. Frederick, and M. W. Austin, J. Appl. Phys. 51, 305 (1980).
13. D. O. Thompson and D. K. Holmes, J. Appl. Phys. 27, 191 (1956).
14. J. S. Koehler and G. DeWit, Phys. Rev. 116, 1121 (1959).
15. N. F. Mott and F. R. N. Nabarro, in Report on a Conference on the Strength of Solids, Physical Society, London (1948), p. 8.
16. D. Hull and D. J. Bacon, Introduction to Dislocations, Pergamon, Oxford (1984), p. 22.
17. A. Seeger and P. Haasen, Philos. Mag. 3, 470 (1958).
18. A. Seeger, in Dislocations and Mechanical Properties of Crystals, General Electric, Schenectady (1957), p. 243.
19. H. Wawra, Phys. Status Solidi (a) 54, 291 (1979).

Table 1. Calculated and measured elastic constants of annealed and deformed copper alloys, units GPa

Voigt Elastic Stiffness	Calculated Results* Isotropic	(110) [1$\bar{1}$2] Texture	(110) [11$\bar{1}$] Texture	(112) [11$\bar{1}$] Texture	(110) [1$\bar{1}$2, 1$\bar{1}\bar{1}$] Texture	Measured Results CDA104 53	CDA104 80	CDA104 88	CDA155 63	CDA155 88	CDA155 96-1	CDA155 96-2**
C_{11}	201	220	238	238	229	202	201	203	201	204	204	205
C_{22}	201	238	220	220	229	202	200	199	201	200	188	189
C_{33}	201	220	220	220	220	202	197	192	201	194	201	202
C_{44} (3232)	48.2	40.8	58.1	58.1	49.5	48.3	47.5	48.8	48.1	51.9	43.7	44.9
(2323)						48.4	48.1	44.1	48.1	54.5	51.0	52.4
C_{55} (3131)	48.2	58.1	40.8	40.8	49.5	48.0	46.6	45.7	48.6	47.1	41.5	42.5
(1313)						48.0	46.9	43.6	48.5	48.1	41.8	42.7
C_{66} (1212)	48.2	40.8	40.8	40.8	40.8	48.4	46.3	44.8	48.2	45.5	39.1	40.0
(2121)						48.4	46.3	45.0	48.2	45.1	46.3	47.2

*Based on C_{11} = 168.4, C_{12} = 121.4, C_{44} = 75.39.

**First number indicates R_F hardness. Second number indicates different times after plastic deformation. The hardnesses represent three mechanical-deformation states: annealed, half-hard, and hard.

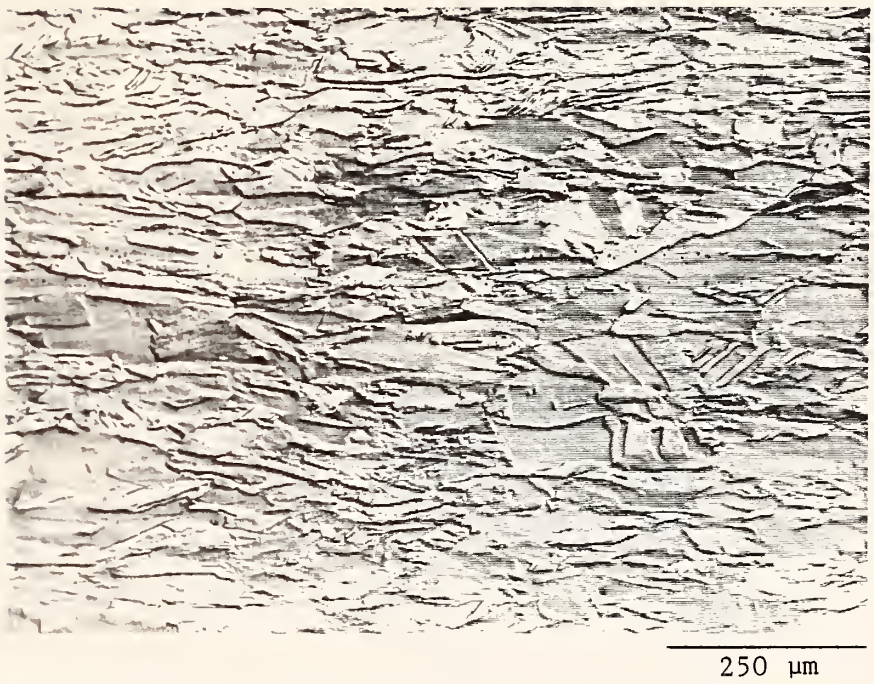

Fig. 1. Microstructure of CDA104 alloy in R_F = 88 hardness condition.

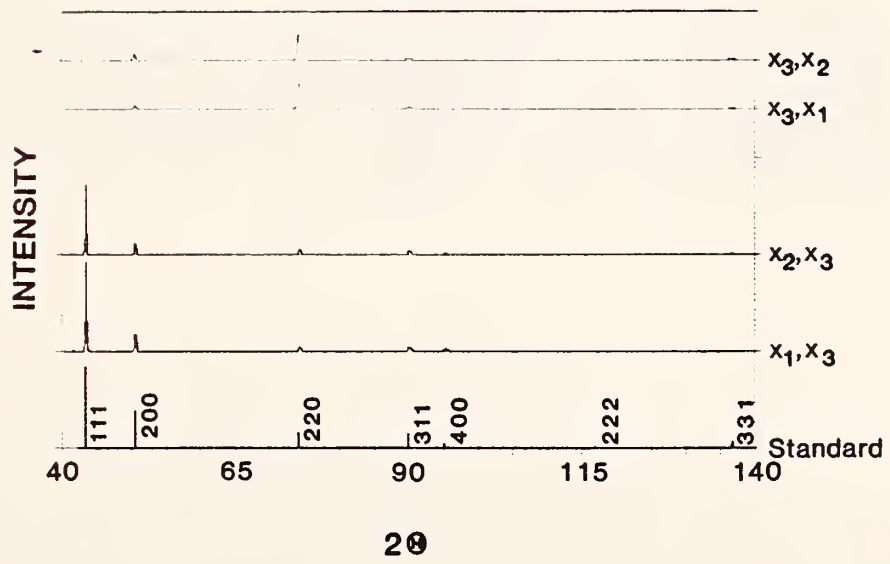

Fig. 2. X-ray-diffraction patterns for CDA104 alloy in R_F = 88 hardness condition. Top two patterns represent x_3 face, rotated around x_2 and rotated around x_1. Third and fourth patterns represent x_2 and x_1 faces, both rotated around x_3. At the bottom, we show a standard pattern for annealed isotropic copper.

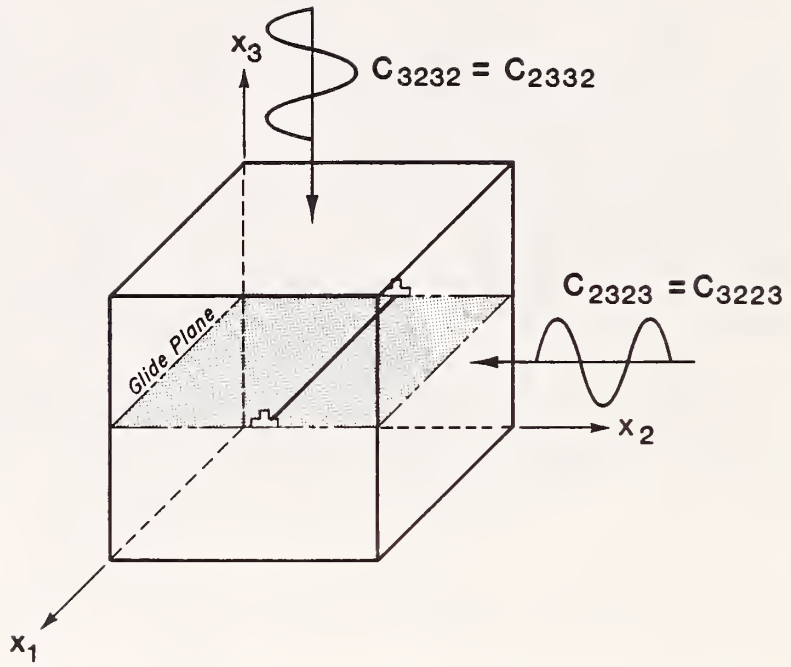

Fig. 3. An ideal block containing a single edge dislocation and showing propagation directions and polarization directions for various elastic shear waves corresponding to C_{2323} and C_{3232}. For the six principal elastic constants, the dislocation breaks usual macroscopic symmetries, causing $C_{1111} = C_{3333} > C_{2222}$ and $C_{1221} = C_{1313} = C_{1331} = C_{3223} > C_{3232} = C_{1212}$.

LOW-TEMPERATURE ELASTIC CONSTANTS OF DEFORMED POLYCRYSTALLINE COPPER*

H. M. Ledbetter and S. A. Kim

Fracture and Deformation Division
Institute for Materials Science and Engineering
National Bureau of Standards
Boulder, Colorado

By ultrasonic methods, we studied copper's elastic constants between 295 and 4 K. The specimens consisted of polycrystals deformed by rolling. At ambient temperature, compared with annealed texture-free copper, the deformed specimens usually showed lower elastic stiffness: up to 11 percent in Young modulus and 19 percent in shear modulus. The Poisson ratio increased up to 14 percent. These softenings reflect three internal-structure changes: texture, nonpinned dislocation density, and anisotropic dislocation array. Cooling to 4 K showed regular behavior: nearly the same as that of annealed texture-free copper. After plastic deformation, at ambient temperatures, the elastic constants showed time-dependent recovery.

INTRODUCTION

Elastic constants vary measurably with common metallurgical variables: temperature, stress (or pressure), and alloying. Unless a phase transformation intervenes, a material's physical properties usually vary smoothly and monotonically. Often, one can successfully model physical-property changes associated with these variables.

Plastic deformation presents another case. It changes the internal structure: texture, dislocation density, dislocation arrangement, point-defect density, internal strain, and so on. These internal variables may vary nonmonotonically with plastic deformation. They may depend on secondary factors: deformation mode (tension, compression, rolling, and so on), deformation rate, and time after deformation (recovery). Unlike the variables listed above, microscopic plastic deformation is difficult to specify. Usually, we resort to macroscopic average specifications: elongation, reduction-in-area, hardness, and so on.

---

*Intended for Materials Science and Engineering.

Experimentally, plastic-deformation effects on elastic constants are well-known. Lawson [1] applied compressive stress to polycrystalline copper and found a Young-modulus decrease of 7 percent. On copper monocrystals, Thompson and Holmes [2] found Young-modulus decreases up to 10 percent. In copper deformed at 78 K, van den Beukel and Brouwer [3] found a shear-modulus decrease of 18 percent. There have been numerous similar studies, too many to describe (for examples, see references in reference 4).

Many theoretical models based on dislocations predict that the apparent elastic stiffness decreases as the density of nonpinned dislocations increases. Sources of these models include Eshelby [5], Koehler [6], Friedel [7], and Granato and Lücke [8]. Calculations by Koehler and deWit [9] produced three conclusions: (1) elastic anisotropy increases the dislocation-induced elastic-constant lowering; (2) for annealed copper, the effect equals a few percent; (3) for slightly deformed copper, the effect ranges up to ten percent.

From the above experimental and theoretical studies, we expect nonpinned dislocations to lower elastic stiffness, C. The following relationship summarizes the main idea:

$$C = \frac{\sigma}{\epsilon} = \frac{\sigma}{\epsilon^{(e)} + \epsilon^{(p)}} . \qquad (1)$$

Here, σ denotes stress; ϵ, strain; e, elastic; and p, plastic. The plastic strain is reversible, resulting from dislocations bowing between pinning points. For well-pinned dislocations, $\epsilon^{(p)}$ equals zero. Pinning results from many mechanisms that include impurities, irradiation-induced defects, and dislocation nodes.

This study considers the effects of ambient-temperature plastic deformation (rolling) on the elastic constants of polycrystalline copper. By ultrasonic methods, we measured the six principal C_{ij} (C_{ii}, i = 1,6) between 295 and 4 K. We report values for the three principal Young moduli (E_1, E_2, E_3) and the principal shear moduli (G_{23}, G_{13}, G_{12}).

MEASUREMENTS

Materials

We studied two commercial copper alloys: CDA104 and CDA155. Including silver, these alloys contain 99.95 and 99.75 percent copper, respectively. For each alloy, we studied three plastic-deformation conditions: the received deformed plate (hardness = 80, 88 R_F), a plate deformed by rolling to a 60 percent reduction (hardness = 88, 96 R_F), and the recrystallized-annealed condition (hardness = 53, 63 R_F). From these, by grinding, we prepared parallelepiped specimens measuring 1.5 to 2 cm. Figure 1 shows a typical microstructure. We obtained the annealed condition by heating the received plates for 1 h at 510°C and for 1.3 h at 550°C, respectively.

Ambient-Temperature Methods

Mass density, ρ, we measured by Archimedes's method using distilled water as a standard. We estimate inaccuracy as 0.05 percent.

Sound velocity, v, we measured by a MHz-frequency pulse-echo-superposition method described previously [10]. From mass density and sound velocities, we computed elastic constants by

$$C_\ell = \rho v_\ell^2 \tag{2a}$$

and

$$C_t = \rho v_t^2. \tag{2b}$$

Here, subscripts ℓ and t denote longitudinal and transverse. For each of six materials (two alloys, three hardnesses), we measured six sound velocities corresponding to the longitudinal elastic constants C_{11}, C_{22}, and C_{33} and the transverse (shear) elastic constants C_{44}, C_{55}, and C_{66}. Because they contribute little to the present study and because they contain larger errors, we omitted measurements of C_{12}, C_{13}, and C_{23}. For sound velocities, we estimated a 0.2 percent inaccuracy in v_ℓ and a 0.4 percent inaccuracy in v_t. Thus, we estimated C_ℓ errors as 0.45 percent and C_t errors as 0.85 percent.

Low-Temperature Methods

We achieved measurements at liquid-helium temperature by methods described previously [11]. At each temperature, at approximately 5-K intervals, we made absolute v_ℓ and two v_t measurements in three coolings of the same specimen. The two v_t measurements correspond to shear-wave polarization along the two principal directions.

Texture

Texture we studied by x-ray diffraction from surfaces perpendicular to the three principal directions: x_1 = rolling direction, x_3 = direction normal to rolling plane, x_2 = direction orthogonal to x_1 and x_3 (some call x_2 the long-transverse direction). For x-ray diffraction, we used a computer-controlled commercial diffractometer and Cu-Kα radiation.

RESULTS

The study's principal results occur in Table 1. The table shows results for two alloys in three plastic-deformation conditions. For one alloy, CDA155, for the high-hardness condition, we show measurements at two post-deformation times: 15 days and 105 days. For comparison, Table 1 shows results for annealed texture-free copper. For each material, we measured the principal C_{ij} (C_{ii}, i = 1–6). To compute the Young moduli, E_i, and the Poisson ratios ν_{ij}, we inverted the six-by-six C_{ij} matrix to obtain the S_{ij} matrix. This requires knowing the three off-diagonal C_{ij}, which we

did not measure. We estimated them under the assumptions that neither texture nor dislocations affect the bulk modulus

$$B = (C_{11} + 2C_{12})/3. \tag{3}$$

Then, one can compute the Young moduli by

$$E_i = 1/S_{ii} \tag{4}$$

and the Poisson ratios by

$$\nu_{ij} = -\frac{S_{ij}}{S_{ii}}. \tag{5}$$

Figure 2 shows the temperature variation of two of the elastic constants, a longitudinal and a shear. We fit these results to Varshni's [12] relationship:

$$C(T) = C(0) - s/[\exp(t/T) - 1]. \tag{6}$$

Equation (6) contains three adjustable parameters: C(0), the elastic stiffness at zero temperature; s, which relates to zero-point energy; and t, the Einstein temperature. Compared with reference copper, we found that the deformed coppers showed essentially identical C(T) behavior when one superimposes the curves.

For T = 4 K, Table 2 nearly replicates Table 1. Table 3 gives the Varshni-fit parameters, together with those reported previously for oxygen-free high-conductivity copper [13].

Figure 3 shows a typical set of four x-ray-diffraction patterns: standard copper and patterns from the x_1, x_2, x_3 faces. Study of these patterns led to the following interpretation. Diffraction lines are broadened but little shifted. From the x_1 and x_2 faces, one sees essentially identical patterns. These differ dramatically from the x_3-surface pattern. It shows no (111) line and a strong (220) line. Unambiguously, this shows that {110} corresponds to the rolling plane. We expect a rolling direction of either <111> or <112>. Diffraction patterns from the x_1 and x_2 surfaces suggest a mixture of both, favoring <111>.

DISCUSSION

To begin, we consider the results in Table 1. For the Young moduli, E_i, and the shear moduli, G_{ij}, almost always, the deformed elastic stiffness is less than the annealed-recrystallized value (hardnesses 53 and 63). For the Young modulus, the elastic softening ranges up to 11 percent; for the shear modulus up to 19 percent. This softening results from a high density of nonpinned dislocations. These dislocations contribute a reversible plastic component to the strain.

Unlike the quasi-isotropic cases where E_i and G_{ij} are independent of direction, in the deformed material, $E_1 \neq E_2 \neq E_3$, and $G_{23} \neq G_{13} \neq G_{12}$. This emphasizes the orthotopic macroscopic symmetry of the deformed material: a rolled parallelepiped.

Although we failed to study time effects systematically, we found that at ambient temperatures, the softening tends to disappear and elastic stiffness tends to approach the reference values. Several studies [4] found such recovery, usually ascribed to dislocation pinning by point defects. For our few measurements, we observe that the dilatational elastic constants recover more than the shear elastic constants.

Concerning texture, which we verified by x-ray diffraction, we gave a thorough analysis elsewhere [14]. The effect of (110) [$\bar{1}12$, $\bar{1}11$] texture is to increase E_1, E_2, G_{23}, and G_{13}. It decreases E_3 and G_{12}. Because these effects disagree with observation, we concluded that texture affected anisotropic elastic stiffness only secondarily.

The most remarkable result shown in Table 1 is the breaking of the usual symmetry

$$C_{ijkl} = C_{ijlk}. \tag{7}$$

We see that $G_{2323} \neq G_{2332}$, $G_{1313} \neq G_{1331}$, and $G_{1212} \neq G_{1221}$. With a measurement uncertainty of less than 1 percent, we found differences up to 17 percent that averaged 5 percent. This symmetry breaking means a nonsymmetry of C_{ijkl} in the usual expression for Hooke's law:

$$\sigma_{ij} = C_{ijkl}\epsilon_{kl}. \tag{8}$$

In Eq. (1), we wrote that the total strain consists of two parts:

$$\epsilon_{kl} = \epsilon_{kl}^{(e)} + \epsilon_{kl}^{(p)}. \tag{9}$$

This nonsymmetry arises naturally if we consider a single edge dislocation (Fig. 4) lying along x_1 with Burgers vector, $\underset{\sim}{b}$, along x_2. When shear waves pass the dislocation, it can bow between pinning points, bow in the glide plane, but not out of the plane. If a shear wave passes that propagates along x_3 and is polarized along x_2, the dislocation contributes to $\epsilon_{32}^{(p)}$. If a shear wave passes that propagates along x_2 and is polarized along x_3, the dislocation contributes nothing to ϵ_{23}. Dislocations contribute zero strain when $\underset{\sim}{b}\cdot\underset{\sim}{p} = 0$, where $\underset{\sim}{p}$ denotes the polarization vector. In terms of elastic constants, this means $C_{2323} > C_{2332}$. In the notation in Table 1, $G_{23} > G_{32}$.

Thus, we understand the shear-modulus symmetry breaking when the deformed polycrystalline materials contain anisotropic dislocation arrays: arrays where $\underset{\sim}{b}$ fails to average to zero over direction. Elsewhere [15], we gave further analysis on this point. There, we emphasized the importance of the present results for acoustoelastic residual-stress measurements.

Measuring residual stress typically requires detecting a shear-wave velocity difference of 1 in 10^5. Obviously, anisotropic dislocation arrays caused by plastic deformation could obscure and confuse shear-wave-birefringence residual-stress measurements.

Interestingly, in all the deformed materials the Poisson ratio increased, up to 13 percent. For an isotropic material, the Poisson ratio ν relates simply to shear modulus G and bulk modulus B:

$$\nu = \frac{1}{2}\,\frac{3B - 2G}{3B + G}. \tag{10}$$

By taking $\nu \approx 1/3$ and differentiating, one obtains

$$\frac{d\nu}{\nu} \approx \frac{4}{9}\left(\frac{dB}{B} - \frac{dG}{G}\right). \tag{11}$$

Thus, accompanying a large decrease in G and a small change in B, we expect a large increase in ν. Usually, changes in ν reflect changes in interatomic bonding [16]. In the present study, ν increases reflect increased nonpinned dislocation density.

CONCLUSIONS

From this study, there emerge five principal conclusions:

1. In copper deformed heavily by rolling, elastic constants softened considerably: up to 11 percent in the Young modulus. The softening resulted principally from an increased density of nonpinned dislocations.

2. The (110) [$\bar{1}12$, $\bar{1}11$] texture, which increases six of the nine principal Young and shear moduli, played a secondary role.

3. Shear-modulus symmetry breaking, for example $G_{2323} \neq G_{2332}$, occurred for all the shear moduli. We hypothesize that this asymmetry arises from an anisotropic dislocation array. This array contributed a reversible plastic strain that varied with deformation mode.

4. At ambient temperature, the elastic stiffnesses recovered toward their annealed, texture-free values. We ascribe this time dependence to dislocation pinning by point defects.

5. The low-temperature results presented no surprises. The various $E_i(T)$ and $G_{ij}(T)$ curves almost superimpose on those for nondeformed copper.

ACKNOWLEDGMENT

For this study, the DoE Office of Fusion Energy provided financial support. Using materials provided by Lawrence Livermore National Laboratory and Princeton Plasma Physics Laboratory, L. Scull and R. Walsh provided material preparation. M. Austin provided elastic-constant-measurement guidance.

REFERENCES

1. A. W. Lawson, Phys. Rev., 60 (1941) 330.
2. D. O. Thompson and D. K. Holmes, J. Appl. Phys., 27 (1956) 191.
3. A. van den Beukel and C. Brouwer, Philos. Mag., 17 (1968) 453.
4. G. Fantozzi, D. Boulanger, and P. Gobin, J. Inst. Met., 96 (1968), 236.
5. J. D. Eshelby, Proc. Roy. Soc. Lond., 197 (1949) 396.
6. J. S. Koehler, in Imperfections in Nearly Perfect Crystals, Wiley, New York, 1952, p. 197.
7. J. Friedel, Philos. Mag., 44 (1953) 444.
8. A. Granato and K. Lücke, J. Appl. Phys., 27 (1956) 789.
9. J. S. Koehler and G. deWit, Phys. Rev., 116 (1959) 1121.
10. H. M. Ledbetter, N. V. Frederick, and M. W. Austin, J. Appl. Phys., 51 (1980) 305.
11. E. R. Naimon, W. F. Weston, and H. M. Ledbetter, Cryogenics, 14 (1974) 246.
12. Y. P. Varshni, Phys. Rev. B, 10 (1970) 3952.
13. H. M. Ledbetter, Phys. Stat. Solidi (a), 66 (1981) 477.
14. H. M. Ledbetter and M. W. Austin, submitted to Physica Status Solidi.
15. H. M. Ledbetter, submitted to Journal of Applied Physics.
16. W. Köster and H. Franz, Metall. Rev., 6 (1961) 1.

TABLE 1. Engineering elastic constants at 295 K

	Reference Copper	Copper CDA104			Copper CDA155			
		53*	80	88	63	88	96	96**
E_1	129	128	124	124	125	126	125	127
E_2		128	123	121	125	123	111	113
E_3		128	121	115	125	117	122	125
G_{23}	47.9	48.4	48.1	44.1	48.1	54.5	51.0	52.4
G_{32}		48.3	47.5	48.8	48.1	51.9	43.7	44.9
G_{13}		48.0	46.9	43.6	48.5	48.1	41.8	42.7
G_{31}		48.1	46.6	45.8	48.6	47.1	41.5	42.5
G_{12}		48.4	46.3	44.8	48.3	45.5	39.1	40.0
G_{21}		48.4	46.3	45.0	48.2	45.1	46.3	47.2
ν_{23}	0.345	0.346	0.360	0.380	0.349	0.375	0.357	0.354
ν_{32}		0.348	0.354	0.361	0.349	0.358	0.393	0.389
ν_{13}		0.346	0.359	0.374	0.350	0.369	0.334	0.331
ν_{31}		0.346	0.350	0.345	0.350	0.343	0.326	0.325
ν_{12}		0.348	0.349	0.345	0.349	0.344	0.389	0.385
ν_{21}		0.347	0.347	0.335	0.350	0.334	0.346	0.343

E = Young modulus (GPa)
G = shear modulus (GPa)
ν = Poisson ratio
1 = rolling direction
3 = direction normal to rolling plane
* = hardness (Rockwell F)
** = remeasured after 90 days

TABLE 2. Engineering elastic constants at 4 K

	Reference Copper	Copper CDA104			Copper CDA155			
		53*	80	88	63	88	96	96**
E_1	140	146	142	143	143	144	142	146
E_2		146	141	139	143	140	127	146
E_3		146	139	133	143	134	139	146
G_{23}	52.4	52.6	52.4	48.1	52.4	59.4	55.6	57.1
G_{32}		52.6	51.7	53.2	52.4	56.6	47.6	49.0
G_{13}		52.3	51.0	47.5	52.9	52.5	45.6	46.6
G_{31}		52.3	50.8	49.8	53.0	51.4	45.3	46.3
G_{12}		52.7	50.4	48.8	52.6	49.7	42.6	43.6
G_{21}		52.7	50.4	49.0	52.6	49.2	50.5	51.5
ν_{23}	0.336	0.324	0.337	0.354	0.329	0.351	0.336	0.324
ν_{32}		0.325	0.331	0.338	0.328	0.336	0.367	0.325
ν_{13}		0.324	0.336	0.349	0.329	0.346	0.317	0.324
ν_{31}		0.324	0.329	0.324	0.329	0.323	0.311	0.324
ν_{12}		0.326	0.328	0.325	0.328	0.325	0.364	0.326
ν_{21}		0.325	0.326	0.316	0.329	0.316	0.326	0.325

E = Young modulus (GPa)
G = shear modulus (GPa)
ν = Poisson ratio
1 = rolling direction
3 = direction normal to rolling plane
* = hardness (Rockwell F)
** = remeasured after 90 days

TABLE 3. Fitting parameters for Varshni equation*

	Reference Copper		CDA104-88		CDA155-96	
	C_ℓ	G	C_ℓ	G	C_ℓ	G
C(0) (GPa)	213.4	51.7	208.0	49.4	207.2	215.6
s (GPa)	7.42	2.41	6.82	2.24	7.97	1.97
t (K)	161.5	135.1	152.2	129.5	179.9	115.9

* See Eq. (6)

Fig. 1. Microstructure of CDA104 alloy in R_F = 88 hardness condition. View of x_2 plane: x_1 is horizontal and x_3 is vertical.

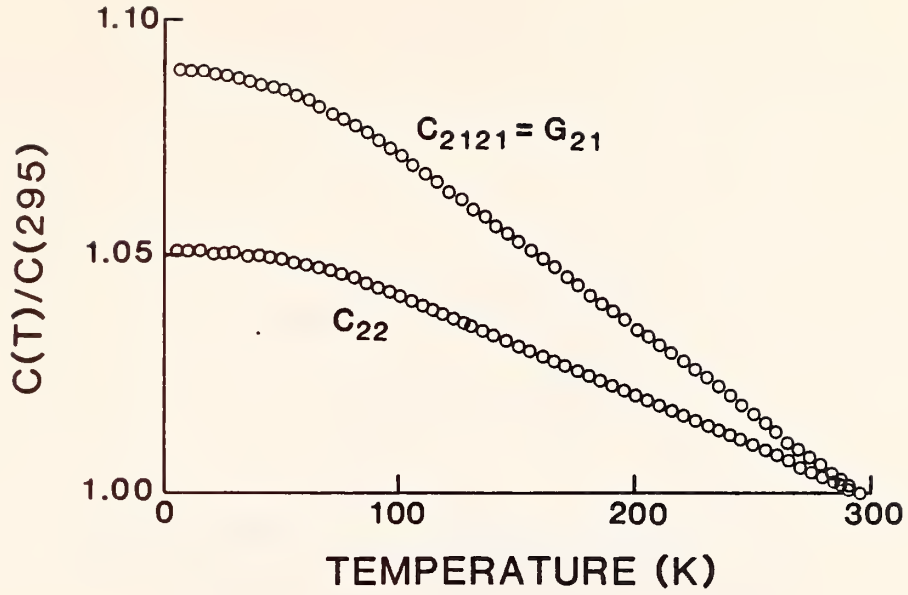

Fig. 2. Temperature behavior of two typical elastic-stiffness constants: C_{22} and G_{21}. The behavior is regular. For reference copper, the intercepts at T = 0 K are 1.084 and 1.049. Thus, deformed copper and reference copper show essentially identical C(T) behavior. These results represent CDA104 copper in the hardness-80 condition.

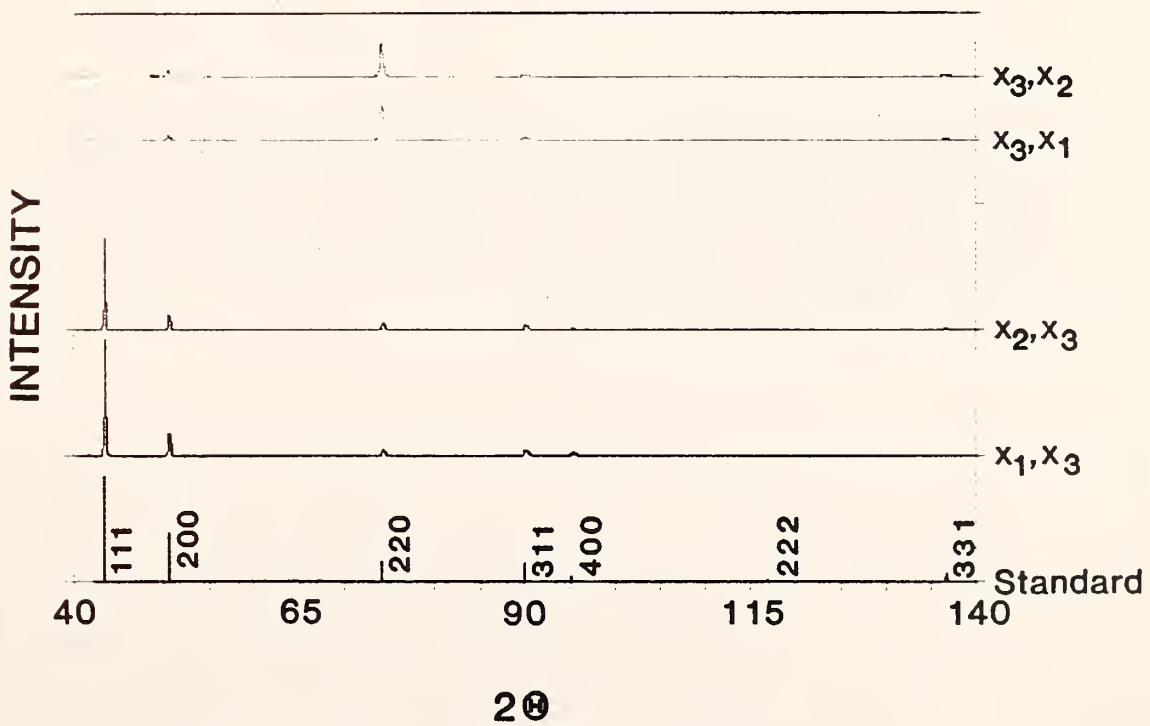

Fig. 3. X-ray-diffraction patterns for CDA104 alloy in R_F = 88 hardness condition. Top two patterns represent x_3 face, rotated around x_2 and rotated around x_1. Third and fourth patterns represent x_2 and x_1 faces, both rotated around x_3. At the bottom, we show a standard pattern for annealed isotropic copper.

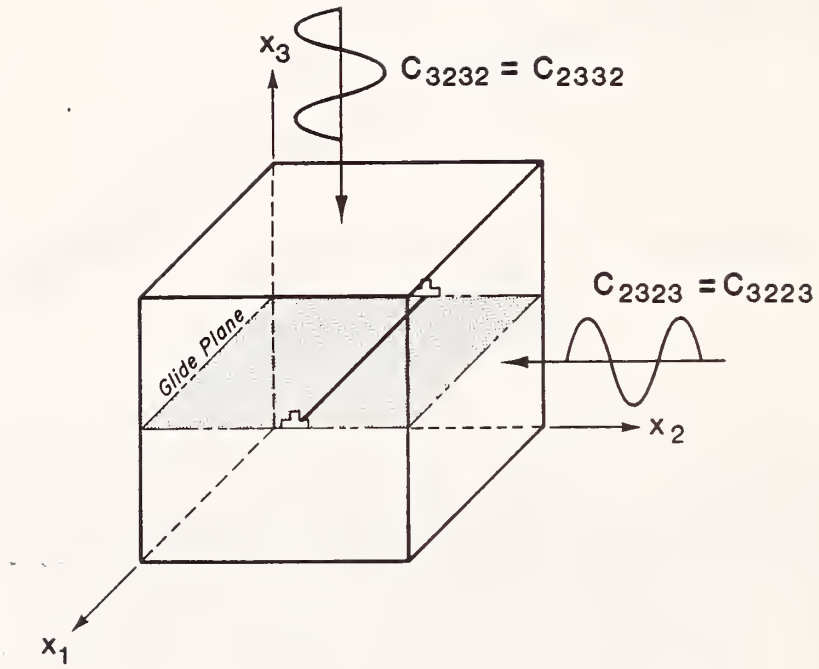

Fig. 4. An ideal block containing a single edge dislocation showing propagation directions and polarization directions for elastic shear waves corresponding to C_{2323} and C_{2332}. For the six principal elastic constants, the dislocation breaks usual macroscopic symmetries, causing $C_{1111} = C_{3333} > C_{2222}$ and $C_{1221} = C_{1313} = C_{1331} = C_{2323} > C_{1212} = C_{2332}$.

ACOUSTOELASTIC RESIDUAL-STRESS MEASUREMENTS: ROLE OF ANISOTROPIC DISLOCATION ARRAYS*

H. M. Ledbetter

Fracture and Deformation Division
Institute for Materials Science and Engineering
National Bureau of Standards
Boulder, Colorado

We consider how an anisotropic dislocation array affects sound velocities and elastic constants. Assuming isotropic dislocation arrays, existing models predict that dislocations reduce elastic stiffness up to approximately 10 percent. Measurements show larger reductions. For an anisotropic dislocation array, where the Burgers vectors do not average to zero over the material volume, elastic softening is anisotropic. This means nonsymmetry in the effective fourth-order elastic-stiffness tensor: $C_{ijkl} \neq C_{ijlk}$. And, in general, $C_{ijkl} \neq C_{klij}$. We studied this effect experimentally by measuring sound velocities in deformed (rolled) copper plate. We estimated sound-velocity measurement uncertainty as less than 0.2 percent. We found that C_{2323} exceeds C_{2332} by 17 percent, C_{3131} approximately equals C_{3113}, and C_{2121} exceeds C_{2112} by 18 percent. Such large differences indicate an enormous fictitious internal strain or residual stress when measured acoustoelastically.

INTRODUCTION

Among various methods used to measure internal strain or residual stress, acoustoelasticity ranks after x-ray diffraction. For an isotropic medium, this method depends on the sound-velocity dependence on the stress direction: a shear wave vibrating parallel to the stress axis travels with a velocity different from a wave vibrating perpendicular to the stress axis. The situation is equivalent to shear waves in a stress-free medium containing elastic anisotropy. Such anisotropy occurs, for example, in monocrystals and in textured polycrystalline aggregates. (By texture, we mean a nonrandom distribution of crystallite orientations.) Thus, any internal irregularity that causes effective elastic-constant anisotropy appears as an internal stress.

---

*Intended for Journal of Applied Physics.

To determine internal stress acoustoelastically, one usually uses the approximate relationship:[1]

$$\sigma_i - \sigma_j = \frac{8G^2}{4G + n} \frac{v_{ki} - v_{kj}}{v_k}. \tag{1}$$

Here, σ_i denotes the stress component along the i axis, G denotes the usual isotropic-symmetry shear modulus, n denotes one of the Murnaghan isotropic-symmetry third-order elastic-stiffness constants ($n = 4C^0_{456}$), v denotes acoustic-wave velocity, subscript k denotes the shear-wave propagation direction, and subscripts i and j denote the shear-wave polarization (vibration) direction. For copper,[2] G equals 48.2 GPa and n equals −49.1. The exact value of n remains uncertain. Here, we take the arithmetic average of the Voigt and Reuss bounds computed from the monocrystal C_{ijklmn} by Chang and Graham.[3] Thus, for copper

$$\sigma_i - \sigma_j = 129.3\ (\Delta v/v)\ \text{GPa}. \tag{2}$$

A stress of 350 MPa, an upper-bound yield strength for work-hardened copper, produces a $\Delta v/v$ of only $2.7 \cdot 10^{-3}$. To achieve the sometimes-quoted ± 10 MPa within 10 percent requires a $\Delta v/v$ measurement error less than $0.8 \cdot 10^{-6}$!

Texture causes a large velocity difference. The largest possible velocity difference depends on the Zener elastic-anisotropy ratio:

$$A = 2C_{44}/(C_{11} - C_{12}). \tag{3}$$

For copper, with $C_{11} = 169.6$, $C_{12} = 122.4$, and $C_{44} = 75.4$ GPa, we obtain

$$v_{max}/v_{min} = A^{1/2} = 1.79. \tag{4}$$

In practice, lower ratios occur. For example, for <100>, <110>, and <111> rod textures in copper, Gairola[4] found $v_{max}/v_{min} = 1.32$, 1.07, and 1.22, respectively. If we take the lowest value, that for the <110> case, and assume only 1 percent texture, then Eq. (1) predicts a fictitious internal stress of 90 MPa! Thus, for acoustoelastic internal-stress measurements, texture remains a large, unsolved problem.

This study considers another large, unsolved problem: anisotropic dislocation arrays. We know that many engineering materials contain large numbers of dislocations. Hull and Bacon[5] estimated that well-annealed metals contain a dislocation density of 10^6 to 10^8 cm^{-2} and that heavily deformed metals contain up to $5 \cdot 10^{13}$ cm^{-2}. We expect dislocations to lower the elastic stiffness, C, by contributing an extra strain to the usual elastic strain:

$$C = \frac{\sigma}{\epsilon} = \frac{\sigma}{\epsilon^e + \epsilon^d}. \tag{5}$$

This extra strain arises because, when stressed, dislocations bow out in their glide plane. Several authors[6-9] gave models for dislocation-induced elastic-stiffness softening. Several experimental studies[10-13] confirm the effect. For slightly deformed copper, Koehler and deWit[14] estimated that the elastic-softening might reach 10 percent. All the models depend on non-pinned dislocations. For well-pinned dislocations, ϵ^d in Eq. (5) equals zero and no elastic softening occurs. Implicitly, all the models assume an isotropic dislocation array: dislocation Burgers vectors occur in all directions with equal probability.

This study goes a step further: it invokes an anisotropic dislocation array. One imagines such arrays to arise usually during plastic deformation. Mughrabi[15] reviewed the topic of dislocation structures that arise in copper during low-temperature unidirectional deformation. He described many anisotropic dislocation arrangements: bundles, grids, and three-dimensional cells. Their usually rectilinear geometry relates to the co-ordinates of the externally applied deformation forces.

To confirm the basic idea that anisotropic dislocation arrays cause strong shear-wave-velocity birefringence, we measured sound velocities in a copper deformed heavily by rolling. By ultrasonic methods, we measured sound velocities corresponding to the six principal elastic stiffnesses: C_{11}, C_{22}, C_{33}, C_{44}, C_{55}, and C_{66}. We especially focused on the differences between C_{2323} and C_{2332}, C_{1313} and C_{1331}, and C_{1212} and C_{1221}. For a well-behaved material, even one with strong texture, these C_{ijkl} are equal in pairs, that is

$$C_{ijkl} = C_{ijlk}. \tag{6}$$

As described below, this relationship fails for the studied material.

MEASUREMENTS

Material

For study, we chose a commercial copper alloy: CDA155. Including silver, this alloy contains 99.75 percent copper. We studied three plastic-deformation conditions: the received deformed plate (hardness = 88 R_F), a plate deformed by rolling to a 60 percent reduction (hardness = 96 R_F), and the recrystallized-annealed condition (hardness = 63 R_F). From these, we ground parallelepiped specimens measuring approximately 1.5 cm for all three dimensions. Figure 1 shows a typical microstructure. We obtained the annealed condition by heating the received plate for 1.3 h at 550°C. We adopted the following co-ordinate system: x_1 = rolling direction, x_3 = normal to rolling plane, x_2 = third orthogonal direction.

Methods

Mass density, ρ, we measured by Archimedes's method using distilled water as a standard. We estimated inaccuracy as 0.05 percent.

Sound velocity, v, we measured by a MHz-frequency pulse-echo-superposition method described previously.[16] From mass density and sound velocities, we computed elastic constants by the general relationship

$$C_{ijij} = \rho v_{ij}^2. \tag{7}$$

Here, subscripts i and j denote wave-propagation and wave-polarization directions, respectively. For four states of the material, we measured six sound velocities corresponding to the longitudinal elastic constants C_{11}, C_{22}, and C_{33} and the transverse, or shear, elastic constants C_{44}, C_{55}, and C_{66}. Because they contribute little to this study and because they contain larger errors, we omitted measurements of C_{12}, C_{13}, and C_{23}. For sound velocities, we estimated a 0.2 percent inaccuracy in v_ℓ and a 0.4 percent inaccuracy in v_t. Thus, we estimated C_ℓ errors as 0.45 percent and C_t errors as 0.85 percent. (Subscripts ℓ and t denote longitudinal and transverse waves.)

Texture we studied by x-ray diffraction from surfaces perpendicular to the three principal directions: x_1 = rolling direction, x_3 = direction normal to rolling plane, x_2 = direction orthogonal to x_1 and x_3 (some call x_2 the long-transverse direction). For x-ray diffraction, we used a computer-controlled commercial diffractometer and Cu-Kα radiation.

RESULTS

The study's principal results appear in Table I. The table shows measurements for three plastic-deformation conditions. The lowest hardness represents the recrystallized-annealed condition. For the high-hardness condition, we show measurements at two post-deformation times: 15 days and 105 days. For brevity, we report only sound velocities and not the C_{ijkl}. The velocities correspond more closely to measurement and to any acousto-elasticity study.

Table I also shows results calculated from copper's monocrystal elastic constants: C_{11} = 168.4, C_{12} = 121.4, and C_{44} = 75.39 GPa. We calculated the quasi-isotropic elastic constants by Kröner's method.[17] Figure 2 shows a typical set of four x-ray-diffraction patterns: standard copper and patterns from the x_1, x_2, x_3 faces. Study of these patterns led to the following interpretation. With respect to annealed copper, diffraction lines are broadened but little shifted. For the x_1 and x_2 faces, one sees essentially identical patterns. These differ dramatically from the x_3-surface pattern. It shows no (111) line and a strong (220) line. Unambiguously, this shows that {110} corresponds to the rolling plane. We expect a rolling direction of either <111> or <112>. Diffraction patterns from the x_1 and x_2 surfaces suggest a mixture of both, favoring <111>.

DISCUSSION

As shown by the x-ray diffraction results, the deformed material contains texture. Elsewhere,[18] we consider the texture effect and show that it is small compared with dislocation effects.

As mentioned in the introduction, previous studies show large elastic-constant decreases caused by plastic deformation. For example, van den Beukel and Brouwer[12] reported that deforming copper at 78 K decreases the shear modulus 18 percent. It remains to determine the maximum decrease.

Since elastic-stiffness decreases are well documented and well understood, in this study we focus on symmetry breaking caused by anisotropic dislocation arrays. Table I provides ample evidence of this phenomenon. We see that $C_{11} \neq C_{22} \neq C_{33}$ is not explained by texture.[18] More surprisingly, we see that $C_{3232} \neq C_{3223}$ and $C_{1212} \neq C_{1221}$. (For another copper material, reported elsewhere,[18] we also found that $C_{1313} \neq C_{1331}$.)

For a better understanding of the symmetry-breaking effect, consider the usual equation of motion:

$$-\rho \frac{\partial^2 u_j}{\partial t^2} + \partial_i \sigma_{ij} = 0. \tag{8}$$

Here, ρ denotes mass density; u_j, displacement; t, time; and σ_{ij}, the stress tensor. Separate the displacement into elastic and dislocation parts:

$$u_j = u_j^e + u_j^d, \tag{9}$$

and write Hooke's law:

$$\sigma_{ij} = C_{ijk\ell}\, \partial_k u_\ell^e = C_{ijk\ell}\, \partial_k (u_\ell - u_\ell^d). \tag{10}$$

For small dislocation motions,

$$\partial_k u_\ell^d = t_{k\ell mn}\, \partial_m u_n, \tag{11}$$

where $t_{k\ell mn}$ amounts to an elastic polarizability.[19] Combining Eqs. (8), (10), and (11), one obtains

$$-\rho \frac{\alpha^2 u_j}{\alpha t^2} + A_{ijk\ell}\, \partial_i \partial_k u_\ell = 0, \tag{12}$$

where

$$A_{ijk\ell} = C_{ijk\ell} - C_{ijmn}\, t_{mnk\ell}. \tag{13}$$

We see that $A_{ijk\ell}$, the effective elastic-stiffness tensor, is symmetric in i and j, the indices related to the stress tensor σ_{ij}, but $A_{ijk\ell}$ is nonsymmetric in k and ℓ.

In Fig. 3, the two shear-wave velocities correspond to

$$v^2 = \omega^2/k^2 = A_{3232}/\rho \tag{14}$$

and

$$v^2 = \omega^2/k^2 = A_{3223}/\rho. \tag{15}$$

Experiment shows that $A_{3232} \neq A_{3223}$. We understand this because in the first case the dislocation moves through the lattice and contributes a strain corresponding to the displacement u_2^d. In the second case, when the shear wave passes, the dislocation moves only with the lattice, $u_3^d = 0$. Because $A_{ijkl} = A_{jikl}$, we can write these two effective elastic moduli as A_{2332} and A_{2323}. In general, we conclude that

$$A_{ijk\ell} \neq A_{k\ell ij}. \tag{16}$$

The present study relates also to ideas of Laval[20] questioning Cauchy's classical concept of a symmetrical stress tensor: $\sigma_{ij} = \sigma_{ji}$. Laval suggested that in dynamic elastic-constant measurements, where the passing ultrasonic wave might cause torques and rotations, the stress tensor is nonsymmetric. If so, then

$$C_{ijkl} \neq C_{jikl}. \tag{17}$$

Thus, a triclinic crystal, with no point-group symmetry, would exhibit forty-five rather than twenty-one independent elastic constants. Raman and Viswanathan[21] studied the wave-propagation relationships and concluded that orthorhombic symmetry would exhibit fifteen, rather than nine, independent elastic constants. In Hooke's law, the strain tensor is mathematically the same as the stress tensor. Thus, an orthorhombic-symmetry material with a displacement described by Eq. (8) would also exhibit fifteen independent elastic constants. Although subsequent theoretical[22] and experimental[23] studies disprove Laval's hypothesis, his symmetry ideas relate to this study, where dislocations contribute anisotropically to displacement and displacement gradient.

Finally, we note that acoustoelasticians have allowed formally for permanent plastic strain. In reviewing this subject, Pao, Sachse, and Fukuoka[24] wrote the following relationship corresponding to Eq. (1) [their Eq. (124)]:

$$\frac{V_{ki} - V_{kj}}{V_k} = \epsilon_i^p - \epsilon_j^p + \frac{4G + n}{8G^2}(\sigma_i - \sigma_j). \tag{18}$$

Here, $\epsilon_i^p - \epsilon_j^p$ denotes the difference in principal plastic strains. Pao et. al. call this effect acoustoelastic-plastic birefringence and point out that the "relative change of wave speed is of the order of the permanent plastic strain (residual strain), which can be very large." The present study

identifies a mechanism that can contribute to $\varepsilon_j^p - \varepsilon_j^p$ an amount far exceeding the maximum residual strain, which corresponds to the work-hardened yield strength.

CONCLUSIONS

From this study, we draw five conclusions:

1. Copper deformed heavily by rolling shows large elastic-constant changes. Texture, which increases some elastic stiffnesses and decreases others, is not the principal cause.

2. In agreement with many previous studies, both experimental and theoretical, the nonpinned dislocation density lowers the elastic stiffnesses.

3. C_{11}, C_{22}, and C_{33} differ in a way not explained by texture. More important, the macroscopic symmetry of the shear moduli $C_{ijij}(i \neq j)$ breaks. We ascribe these results to anisotropic dislocation arrays.

4. At ambient temperatures, after deformation, all the elastic stiffness values increase with time. As in previous studies, we ascribe this recovery to dislocation pinning by point defects.

5. For acoustoelastic studies of internal strain (residual stress), the specter of anisotropic dislocation arrays hangs heavily. Even a small dislocation-array anisotropy suggests large fictitious internal strains. Clearly, such arrays exist in deformed materials. It remains to be seen whether they exist also in annealed materials.

ACKNOWLEDGMENT

Partial support for this study came from the U.S. DoE Office of Fusion Energy. S. Kim made the sound-velocity measurements. L. Scull and R. Walsh provided samples. Both Professor E. Kröner (Stuttgart) and Professor S. K. Datta (Boulder) made many valuable comments.

REFERENCES

1. R. E. Green, Ultrasonic Investigation of Mechanical Properties (Academic, New York, 1973), p. 131.
2. H. M. Ledbetter, J. Phys. D: Appl. Phys. 13, 1879 (1980).
3. R. Chang and L. J. Graham, Mater. Res. Bull. 3, 745 (1968).
4. B. K. D. Gairola, in Continuum Models of Discrete Systems (U. Waterloo Press, Waterloo, 1980), p. 387.
5. D. Hull and D. J. Bacon, Introduction to Dislocations (Pergamon, Oxford, 1984), p.22.
6. J. D. Eshelby, Proc. Roy. Soc. Lond. 197, 396 (1949).

7. J. S. Koehler, in Imperfections in Nearly Perfect Crystals (Wiley, New York, 1952), p. 197.
8. J. Friedel, Philos. Mag. 44, 444 (1953).
9. A. Granato and K. Lücke, J. Appl. Phys. 27, 789 (1956).
10. D. O. Thompson and D. K. Holmes, J. Appl. Phys. 27, 191 (1956).
11. W. Lems, Physica 28, 445 (1962).
12. A. van den Beukel and C. Brouwer, Philos. Mag. 17, 453 (1968).
13. G. Fantozzi, D. Boulanger, and P. Gobin, J. Inst. Met. 96, 236 (1968).
14. J. S. Koehler and G. deWit, Phys. Rev. 116, 1121 (1959).
15. H. Mughrabi, in Constitutive Equations in Plasticity (MIT Press, Cambridge, 1975), p. 199.
16. H. M. Ledbetter, N. V. Frederick, and M. W. Austin, J. Appl. Phys. 51, 305 (1980).
17. E. Kröner, Z. Phys. 151, 504 (1958).
18. H. M. Ledbetter, submitted to Phys. Status. Solidi.
19. E. Kröner, in Theory of Crystal Defects (Academic, New York, 1966), p. 215.
20. J. Laval, Compt. Rend. 232, 1947 (1951).
21. C. V. Raman and K. S. Viswanathan, Proc. Indian Acad. Sci. 42, 51 (1955).
22. M. Lax, in Lattice Dynamics (Pergamon, Oxford, 1965), p. 583.
23. K. D. Schwartz and A. V. Granato, J. Acoust. Soc. Amer. 38, 824 (1965).
24. Y-H. Pao, W. Sachse, and H. Fukuoka, Physical Acoustics 17, 61 (1984).

TABLE I. Sound velocities in units of cm/μs.

Hardness (Rockwell F)	63	88	96-1[a]	96-2[b]	Annealed Pure Cu
Mass Density (g/cm^3)	8.897	8.895	8.893	8.893	8.935
v_{11}	0.4750	0.4786	0.4787	0.4803	0.4724
v_{22}	0.4753	0.4738	0.4596	0.4613	
v_{33}	0.4751	0.4664	0.4751	0.4769	
v_{32}	0.2324	0.2415	0.2216	0.2246	0.2318
v_{23}	0.2324	0.2474	0.2395	0.2426	
v_{31}	0.2336	0.2302	0.2161	0.2186	
v_{13}	0.2335	0.2326	0.2169	0.2192	
v_{12}	0.2329	0.2263	0.2096	0.2121	
v_{21}	0.2328	0.2253	0.2281	0.2303	

[a] Measured 15 days after deformation.
[b] Measured 105 days after deformation.

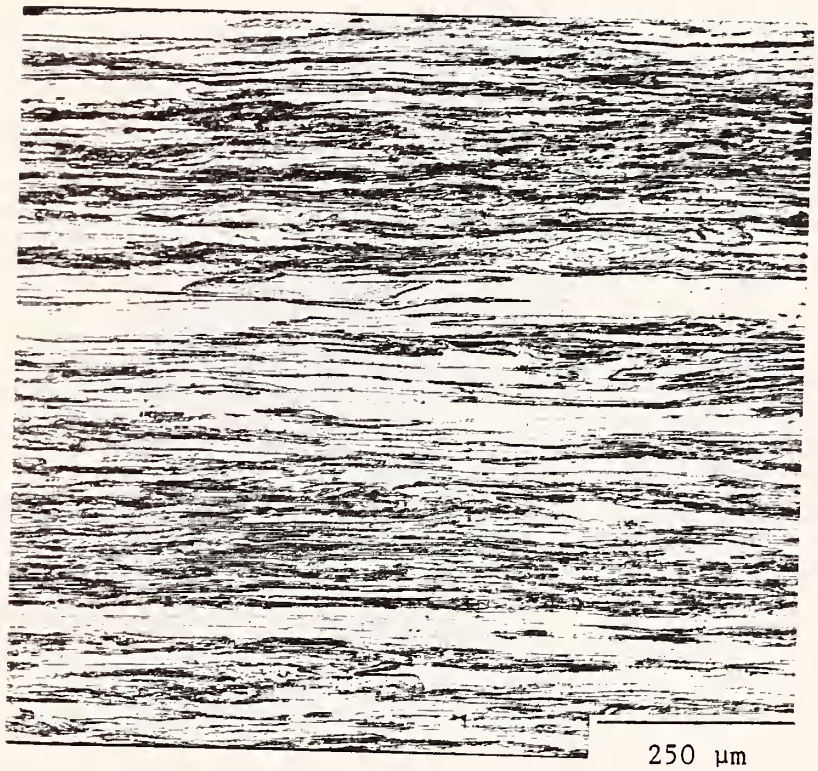

Fig. 1. Microstructure of heavily deformed copper plate (hardness equals R_F96). View is x_1 plane, or along rolling direction. Vertical direction is x_3, the through-plate direction.

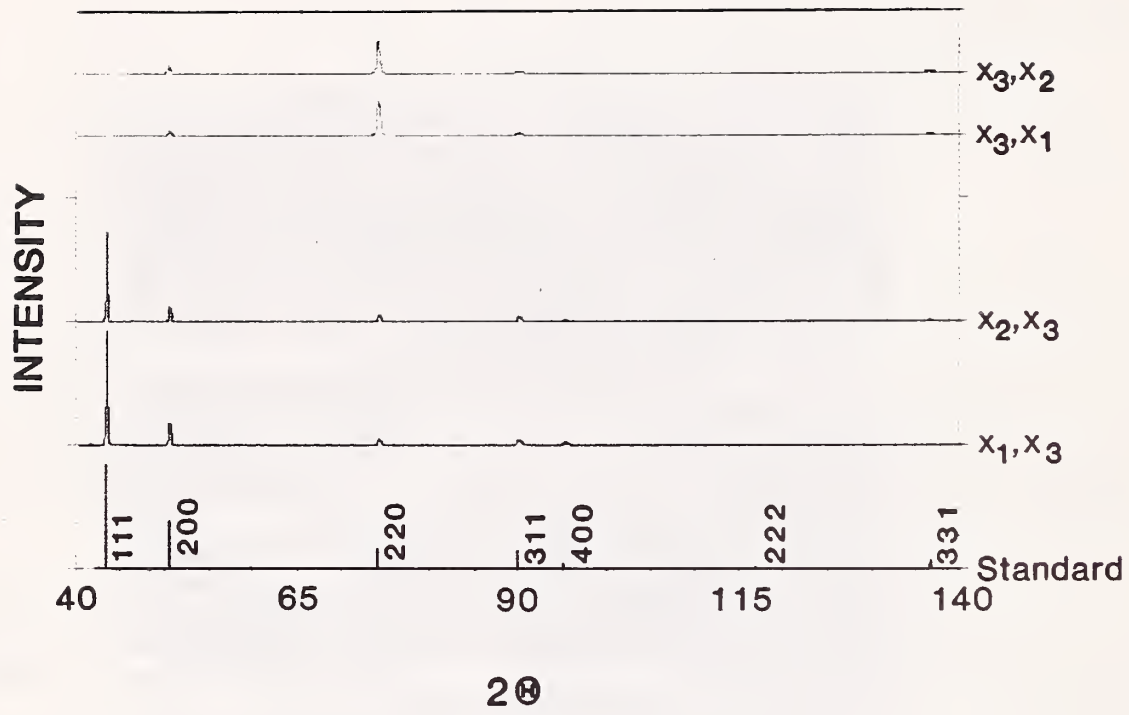

Fig. 2. X-ray diffraction patterns for deformed copper (hardness equals R_F88). Top two patterns represent x_3 face, rotated around x_2 and rotated around x_1. Third and fourth patterns represent x_2 and x_1 faces, both rotated around x_3. At the bottom, we show a standard pattern for annealed isotropic copper.

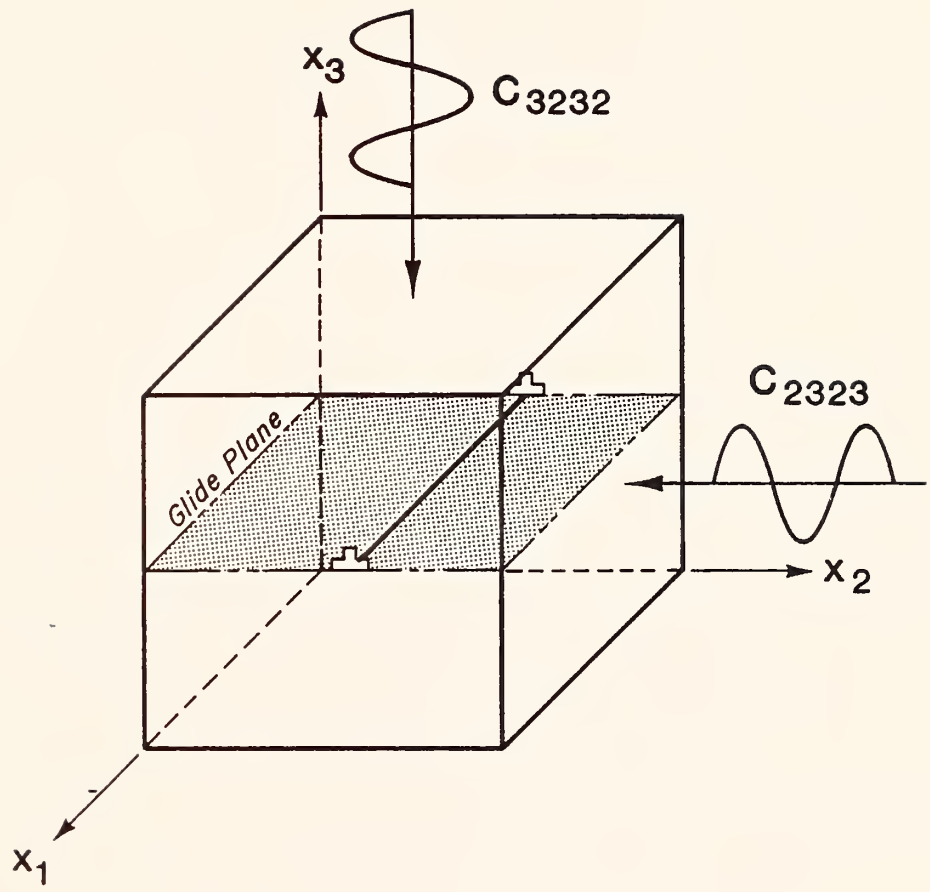

Fig. 3. Schematic to illustrate a dislocation's role in breaking elastic-constant symmetry. Under stress, the dislocation can bow in the glide plane, but not out of the glide plane. The anisotropic reversible plastic displacement and strain causes $C_{1111} = C_{3333} > C_{2222}$. For the shear elastic-stiffness constants, it causes $C_{2323} = C_{1313} = C_{1331} = C_{1221} > C_{2332} = C_{1212}$.

To be submitted to AIAA Journal

Temperature Variation of the Elastic Constants of Aluminum Alloy 2090-T81

J. Glazer and J.W. Morris, Jr.
Center for Advanced Materials,
Lawrence Berkeley Laboratory, and
Department of Materials Science and Mineral Engineering,
University of California, Berkeley,
Berkeley, California

S.A. Kim, M.W. Austin, and H.M. Ledbetter
Fracture and Deformation Division,
Institute for Materials Science and Engineering,
National Bureau of Standards,
Boulder, Colorado

Aluminum is often the material of choice for weight-critical structures used at cryogenic temperatures. Current aerospace applications include the external tank of the space shuttle, currently manufactured from aluminum alloy 2219. Future applications might include tanks for proposed hypersonic vehicles. Aluminum-lithium alloys have been proposed for these applications because they provide mechanical properties comparable or superior to those of existing aerospace aluminum alloys at 7-10% lower density and higher stiffness. Since stiffness is an important design criterion for structures like tanks, the elastic constants for these materials at low temperature are important design properties. This note focuses on a particular aluminum-lithium alloy, 2090-T81, that may see cryogenic service.

Aluminum-lithium alloys of commercial compositions have elastic moduli at room temperature approximately 7-12% higher than those of conventional aluminum alloys. The increase in elastic modulus is related primarily to the amount of lithium in the alloy, so it can vary significantly even within the specified composition ranges of commercial alloys [1,2].

The temperature variation of the elastic constants of various commercial aluminum alloys has been studied previously [3,4]. All aluminum alloys behave similarly, displaying an increase in elastic modulus of about 12% between room temperature and 4 K. This note confirms this trend for the aluminum-lithium alloy 2090-T81. Titanium alloys, which are also used for cryogenic tanks, show a smaller increase in stiffness at low temperatures [4].

The alloy studied in this investigation, 2090-T81, has a nominal chemical composition of Al-2.7Cu-2.2Li-0.12Zr in weight percent. The chemical composition limits and the actual chemical composition, as determined by atomic absorption spectroscopy, are given in Table 1. This alloy shows improved strength, elongation, and fracture toughness at low temperatures. The mechanical properties at 298 K, 77 K, and 4 K are given in reference 5.

The elastic-constant measurements were performed using ultrasonic (10 MHz) pulse techniques. The experimental procedure is described in detail elsewhere [4,6]. Except for high-strain cases, dynamic elastic constants equal static elastic constants within the usual uncertainty of the latter. For the dynamic values, we estimate the uncertainty as 0.1%. Static and dynamic values should show essentially identical temperature behavior.

Figure 1 shows the Young's modulus and Poisson's ratio of 2090-T81 alloy as a function of temperature between 295 K and 4 K. The values at selected temperatures are listed in Table 2. The room-temperature value of the Young's modulus lies close to the reported average values from static tensile tests [2]. The temperature variation is similar to that observed for other aluminum alloys [4].

Acknowledgment: The authors thank the Aluminum Company of America for supplying the material used in these measurements. This study was supported at the Lawrence Berkeley Laboratory by the Director, Office of Energy Research, Office of Basic Energy Science, Material Sciences Division of the U.S. Department of Energy under Contract No. DE-AC03-76SF00098.

References

1. Muller, W., Bubeck, E., and Gerold, V., "Elastic Constants of Al-Li Solid Solutions and δ' Precipitates," *Aluminium-Lithium Alloys III*, eds. C. Baker, P.J. Gregson, S.J. Harris, and C.J. Peel, The Institute of Metals, London, 1986, pp. 435-441.

2. Bretz, P.E. and Sawtell, R.R., "'Alithalite' Alloys: Progress, Products and Properties," *Aluminium-Lithium Alloys III*, eds. C. Baker, P.J. Gregson, S.J. Harris, and C.J. Peel, The Institute of Metals, London, 1986, pp. 47-56.

3. Read, D.T. and Ledbetter, H.M., "Temperature Dependences of the Elastic Constants of Precipitation-Hardened Aluminum Alloys 2014 and 2219," *Journal of Engineering Materials and Technology*, Vol. 99, 1977, pp. 181-184.

4. Naimon, E.R., Ledbetter, H.M., and Weston, W.F., "Low-Temperature Elastic Properties of Four Wrought and Annealed Aluminum Alloys," *Journal of Materials Science*, Vol. 10, 1975, pp. 1309-1316.

5. Glazer, J., Verzasconi, S.L., Dalder, E.N.C., Yu, W., Emigh, R.A., Ritchie, R.O., and Morris, Jr., J.W., "Cryogenic Mechanical Properties of Al-Cu-Li-Zr Alloy 2090," *Advances in Cryogenic Engineering*, Vol. 32, 1986, pp. 397-404.

6. Ledbetter, H.M., Frederick, N.V., and Austin, M.W., "Elastic-constant Variability in Stainless-Steel 304," *Journal of Applied Physics,* Vol. 51, 1980, pp. 305-309.

Table 1 Chemical composition limits for 2090 alloy and actual composition of the material used in this study (in weight percent)

element	Al	Cu	Li	Zr	Fe	Si	Mg	Mn	Ti
composition limits	bal	2.4-3.0	1.9-2.6	0.08-0.15	0.10	0.12	0.25	0.05	0.15
actual composition	bal	2.86	2.05	0.12	0.02	< 0.01	< 0.01	< 0.005	0.02

Table 2 Elastic constants of 2090-T81 alloy

Elastic constant	Temperature			
	295 K	77 K	20 K	4 K
E (GPa)	78.3	86.9	87.6	87.6
(10^6 psi)	11.36	12.60	12.70	12.70
ν	0.320	0.308	0.307	0.307

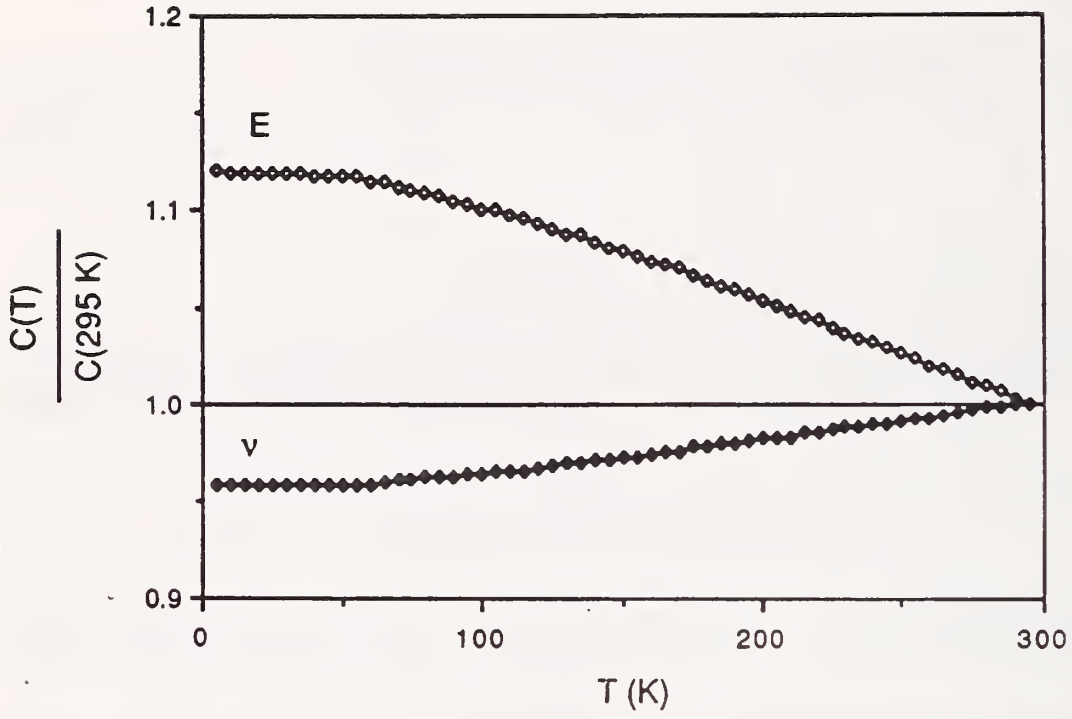

Fig. 1 Young's modulus (E) and Poisson's ratio (ν) of 2090-T81 alloy as functions of temperature. The plotted values are ratios between the actual values and the room-temperature values given in Table 2.

WELDING

WELDING PROGRAM

LEADER: T. A. Siewert
CONTRIBUTORS: C. N. McCowan, D. P. Vigliotti

OBJECTIVES

- Investigation of the metallurgical factors that affect the mechanical properties of stainless-steel weldments at cryogenic temperatures
- Contribution to the development of improved filler metals for welding stainless steels for use at 4 K
- Evaluation of the mechanical properties of weldments at 4 K
- Development of methods for detecting defects and evaluation of their significance in stainless steel weldments

RESEARCH HIGHLIGHTS

- High toughness, 262 MPa·$m^{½}$, at 4 K was achieved in a fully austenitic shielded-metal-arc weld that contained exceptionally high nickel content (Fe–6Cr–43Ni). However, its 559-MPa yield strength was relatively low. This indicates that the improvement in the strength–toughness combination, which had been observed previously when the nickel content was increased to 20 wt.%, may not extend beyond this value.

- Electron beam and laser welds in 25-mm-thick base metal produced 4-K fracture toughness values near 150 MPa·$m^{½}$, slightly less than the 170 to 200 MPa·$m^{½}$ values measured in previous tests of the AISI type 316LN base metal. Transverse tensile specimens for both the electron beam and laser welds fractured in the base metal, indicating that the weld did not reduce the joint efficiency. Specimens had ductile dimple densities near 1.5×10^4 dimples/mm^2, a value higher than that for the base metal but lower than that for conventional welds.

- The effect of inclusion spacing on the strength–toughness combination was described by an equation that is applicable to both weld and base metal. The equation was developed by a regression technique that chose the best combination of twenty variables in a large data base. Small spacing between inclusions results in a poor strength–toughness combination.

- Molybdenum and nickel interact in determining the strength and CVN absorbed energy of welds. Welds with 9- and 14-wt.% nickel and various molybdenum contents were studied. Overall, molybdenum had a strengthening coefficient of 33 MPa per wt.%, but its effect decreased to 25 MPa per wt.% in combination with 14-wt.% nickel. Molybdenum at the 4-wt.% level substantially degraded the toughness when the nickel content was 9 wt.%, but had no effect in combination with 14-wt.% nickel.

SUMMARY OF MECHANICAL PROPERTY MEASUREMENTS OF WELDS

Weld Alloy [designation]	Welding Process	Tensile	Charpy Impact	Fracture Toughness	Fatigue Crack Growth Rate	Report Volume* (page)
AUSTENITIC STAINLESS STEELS						
Fe-13Cr-20Ni-9Mn-2Nb	SMAW	I,II	I,II, VIII			I (159,169) II (299) VIII (29)
Fe-15Cr-12Ni-10Mn	SMAW	IV	IV,VIII			IV (453) VIII (29)
Fe-16Cr-15Ni-4Mo	SMAW	IV		IV		IV (275)
Fe-16Cr-16Ni-2Mo	FCAW	II		III	III,VI	III (155) VI (199)
Fe-16Cr-16Ni-4Mo	FCAW	IV	IV,VIII	IV		IV (275) VIII (29)
Fe-16Cr-35Ni-4Mn [330 modified]	SMAW	I	I,VIII	II		I (159) II (299) VIII (29)
Fe-17Cr-9Ni-Mn-N	SMAW	IX	IX			IX (217)
Fe-17Cr-16Ni-4Mo	SMAW	IV		IV		IV (275)
Fe-18Cr-16Ni-6.5Mn-2Mo	SMAW	IX	IX			IX (257)
Fe-18Cr-16Ni-9Mn-N	GMAW	III,IV	IV	III,IV	III,VI	III (155) IV (275,453) V (199)
Fe-18Cr-18Ni-2Mo-5Mn-N	SMAW	IV	IV			IV (453)
Fe-18Cr-20Ni-5Mn-N	GMAW	IX	IX			IX (247)
Fe-18Cr-20Ni-6Mn-0.3Nb	GMAW	IV	IV	IV		IV (275)
Fe-18Cr-20Ni-6Mn-0.2Ti	GMAW	IV	IV	IV		IV (275)
Fe-19Cr-12Ni-2Mo [316]	SMAW	II	II,VIII	II		II (315) VIII (29)
Fe-19Cr-12Ni-2Mo [316L]	ESW	IV		IV	IV,VI	IV (275,415) VI (199)
	GMAW	III,IV	III,IV, VIII	IV		III (155,195) IV (275) VIII (29)
	GTAW	III,IV	III,IV, VIII	IV		III (155,195) IV (275) VIII (29)
	SAW	III,IV, V	III,IV, V	III,IV	III,VI	III (155,195) IV (275,415) V (233) VI (199)

*MATERIALS STUDIES FOR MAGNETIC FUSION ENERGY APPLICATIONS AT LOW TEMPERATURES: NBSIR 78-884 (I); NBSIR 79-1609 (II); NBSIR 80-1627 (III); NBSIR 81-1645 (IV); NBSIR 82-1667 (V); NBSIR 83-1690 (VI); NBSIR 84-3000 (VII); NBSIR 85-3025 (VIII); NBSIR 86-3050 (IX).

SUMMARY OF MECHANICAL PROPERTY MEASUREMENTS OF WELDS, continued

Weld Alloy [designation]	Welding Process	Tensile	Charpy Impact	Fracture Toughness	Fatigue Crack Growth Rate	Report Volume* (page)
Fe-19Cr-12Ni-2Mo [316L], continued	SMAW	II,III, IV	II,VIII	II,III, IV	III,IV,VI	II (299,315) III (155,167) VI (199) VIII (29)
Fe-19Cr-12Ni-2Mo-N [316LN]	SMAW	II	II,VIII	II		II (299) VIII (29)
Fe-19Cr-16Ni-7Mn	GMAW	IV	IV			IV (453)
Fe-20Cr-10Ni [308]	SMAW	I	I,VIII			I (169) VIII (29)
Fe-20Cr-10Ni [308L]	FCAW	III		III	III,VI	III (155) VI (199)
	GMAW	III		III	III,VI	III (155) VI (199)
	SMAW	II,III	II,VIII	II,III	III,VI	II (299) III (155) VI (199) VIII (29)
Fe-20Cr-10Ni-N [308LN]	FCAW	IV		IV	IV,VI	IV (275,415) V (199)
Fe-20Cr-10Ni-9Mn-N	SMAW	I	I			I (159,169)
Fe-20Cr-16Ni-7Mo-2W	SAW	IV		IV		IV (275)
Fe-20Cr-34Ni-2Mo-Nb	SMAW	VII		VII		VII (253)
Fe-21Cr-6Ni-9Mn-N	SMAW	I,II	I,II			I (159,169) II (299)
AUSTENITIC STEELS						
Fe-15Mn-8Ni-1Mo-0.7C	SAW	VIII		VIII		VIII (15)
Fe-5Cr-25Mn-1Ni		V		V,VII	V,VI	V (233) VI (199) VII (245)
Fe-6.5Cr-25Mn-3Ni-1Mo	SMAW	V		V	V,VI	V (233,245) VI (199)
ALUMINUM ALLOYS						
Al-5Mg [5183]	GMAW	III		IV	IV	III (155,217) IV (323)
Al-5Mg-0.12Ti [5556]	GMAW	III		IV	IV	III (155, 217) IV (323)

*MATERIALS STUDIES FOR MAGNETIC FUSION ENERGY APPLICTIONS AT LOW TEMPERATURES: NBSIR 78-884 (I); NBSIR 79-1609 (II); NBSIR 80-1627 (III); NBSIR 81-1645 (IV); NBSIR 82-1667 (V); NBSIR 83-1690 (VI); NBSIR 84-3000 (VII); NBSIR 85-3025 (VIII); NBSIR 86-3050 (IX).

THE ROLE OF INCLUSIONS IN THE FRACTURE OF AUSTENITIC STAINLESS STEEL WELDS AT 4 K*

T. A. Siewert and C. N. McCowan
Fracture and Deformation Division
National Bureau of Standards
Boulder, Colorado

Inclusion densities were measured for three types of austenitic stainless steel welds and compared to the 4-K yield strengths, 76-K Charpy V-notch absorbed energies, and the ductile dimple densities on the respective fracture surfaces. The welds included shielded metal arc (SMA) welds and gas metal arc (GMA) welds. The inclusion density was consistently a factor of 8 to 10 less than the fracture surface dimple density. Inclusion and dimple densities ranged from 3.9×10^4 inclusions$\cdot$mm^{-2} and 3.2×10^5 dimples$\cdot$mm^{-2} for one SMA specimen to 1.1×10^4 inclusions$\cdot$mm^{-2} and 1.2×10^5 dimples$\cdot$mm^{-2} for the fully austenitic GMA specimen. Both ductile dimple density and dimple morphology varied with specimen type. The inclusion data for the welds agreed with a linear relationship between fracture toughness and inclusion spacing that had been developed for base metals.

INTRODUCTION

Type 316LN stainless steel is emerging as the preferred structural material for superconducting magnet casings designed to operate at 4 K because it has a higher strength than the older 316L grade and comparable toughness at cryogenic temperatures.[1-3] Unfortunately, welding electrodes matching this composition and strength have substantially poorer toughness at 4 K than the stainless steel plate. This is illustrated in figure 1 for type 304LN stainless steel (similar in strength and toughness to type 316LN) and various welds produced with type 308LN and type 316LN electrodes.[4] Matching the electrode strength to the base metal strength results in much lower toughness. This forces the designer to move the welds into regions of the structure where the lower toughness can be tolerated. Where high toughness welds are required, the corresponding weld strength is substantially reduced, and the structural design becomes less efficient. This study sought the reason for the lower weld toughness and also looked at parameters that can be used to predict the 4-K fracture toughness.

*Submitted to Advances in Cryogenic Engineering—Materials, vol. 34.

EXPERIMENTAL PROCEDURES

Two shielded metal arc (SMA) welds and a gas metal arc (GMA) weld were selected for detailed microstructural evaluation. These welds were specifically selected on the basis of previous mechanical property evaluations, so that their range of toughness and strength would reveal any microstructural basis for variations in toughness.[5,6] Table 1 lists the mechanical property data and composition of these welds. Welds SMA-1 and SMA-21 differ primarily in nitrogen and manganese content. Data from previous studies indicate a reduction in Charpy V-notch (CVN) absorbed energy as nitrogen additions increase the strength.[6] Because GMA has twice the nickel content of SMA-21, the importance of the nickel content in increasing the CVN absorbed energy and its effect on the fracture surface appearance could be examined. The delta-ferrite content is also known to affect toughness, but the compositions in this study vary over a small range (0–4 FN), and Szumachowski and Reid have shown that the effect of delta-ferrite content is less than that of the nitrogen content.[7]

Specimens for microstructural evaluation were selected from the 25-mm-thick butt welds used for mechanical property tests. Fracture surfaces that were analyzed were those of specimens fractured at 4 K, CVN specimens fractured at 76 K, and compact tension (CT) specimens fractured at 4 K. The surfaces chosen to be polished were parallel to the direction of the welding and normal to the plate surface, at least 1 cm in each dimension, and they included several weld passes. They were polished until scratches were no longer visible at 3000X, but the polishing time was minimized to reduce relief effects and selective removal of inclusions. This finish enabled measurement of the inclusion size and density with a scanning electron microscope (SEM) having a quantitative image analyzer.

Examination of both the fractured and polished surfaces at 3000X enabled easy identification of the micrometer-scale inclusions characteristic of these welds. This magnification was quite useful measuring the surface dimple dimensions and densities. At least 500 inclusions and dimples were counted to provide statistically significant data.

The all-weld-metal specimens for tensile testing were 6 mm in diameter and oriented parallel to the direction of welding; their fracture surfaces were, therefore, normal to the direction of welding. Tensile tests were performed in accordance with ASTM standard A370 at a strain rate of 2×10^{-4} s^{-1}. Details of the fixture and the procedure for tensile testing at 4 K have been described elsewhere.[8]

Specimens for CVN tests were standard 10-mm square, centered in the weld and notched so that the crack propagated in the weld direction; they were prepared according to ASTM E23. Because physical property constraints (adiabatic heating and low heat capacity) preclude obtaining meaningful data at 4 K, the CVN testing was performed at 76 K.

The 25-mm-thick CT specimens were notched so that the fatigue crack propagated down the center of the weld in the direction of the welding; they were prepared according to ASTM E813. The $K_{Ic}(J)$ value was calculated from

the fracture energy, J, using the single-specimen unloading-compliance technique. Details of the fixture and testing procedure have been described elsewhere.[9] The CT data (average of two specimens) were available for only the GMA weld.

RESULTS AND DISCUSSION

Role of Inclusions

Neither inclusion density nor the average inclusion size was affected by the differences in nitrogen content of the SMA-21 and SMA-1 welds (see table 2). The SMA-21 weld had greater yield strength owing to its higher nitrogen content, but the inverse relationship between strength and toughness observed in a previous study[6] is not evident here. The similar inclusion densities and sizes of SMA-21 and SMA-1 may be the reason for the similarity in their CVN absorbed energies. This suggests that the factors controlling strength and toughness might be considered independently, at least for these two welds.

The GMA weld metal has more than twice the CVN absorbed energy of the SMA welds, yet its strength is similar to SMA-21. Therefore, the difference in toughness is due to another factor, possibly the nickel content, inclusion content, inclusion size, or a combination of these factors. Unfortunately, these factors are confounded in these data.

A study by Reed and Simon separated the two factors of nickel content and inclusion size.[3] Although their study was of base metals, the stainless steel compositions were similar to these weld-metal compositions. Through a statistical regression analysis of NBS test data, they determined that the fracture toughness at 4 K could be predicted by a linear combination of strength, nickel content, and inclusion spacing (calculated from inverting and taking the square root of the inclusion density):

$$K_{Ic}(MPa \cdot m^{1/2}) = 130 - 0.34\sigma_y + 20[Ni] + 2.25\lambda, \qquad (1)$$

where σ_y is the yield strength (MPa), [Ni] is the nickel content (wt.%) and λ is the inclusion spacing. The standard deviation for the fit of this equation to 19 data points was 31 $MPa \cdot m^{1/2}$. This equation was developed from data with a range of 550 to 1100 MPa, a [Ni] range of 8 to 12 wt.%, and a λ range of 40 to 110 μm.

The 4-K fracture toughness of the GMA weld (table 1) is predicted well by equation 1, even though it was developed from data on alloy 316-type base metals. Since fracture toughness data at 4 K are not available for the SMA welds in table 1, they cannot be used to evaluate the fit of the equation. However, 4-K fracture toughness has been evaluated in previous studies of austenitic stainless steel welds.[10-12] Therefore, inclusion densities were measured on three of these welds. These data, listed in table 3, also fit the equation fairly well, although they are outside the range of composition (Ni, Mn) of alloy 316 for which the equation was developed. This is surprising because welds and base metal have different cooling rates and

solidification structures and an order-of-magnitude difference in inclusion density. This emphasizes the importance of inclusion density in controlling fracture toughness. When the weld metal data are added to the base metal data, the predictive equation for fracture toughness can be revised to cover this expanded inclusion density range.

When revising this predictive equation, it is also appropriate to reassess the form. Because the fundamental relationships among toughness, strength, and composition are only beginning to be developed, it is difficult to choose the optimum form for a predictive equation. For this reason, a stepwise multiple linear regression program was used to choose the statistically most significant form from a selection of over thirty combinations of strength, nickel content, and inclusion spacing. The combinations included linear, product, and quotient forms with various exponents. The revised predictive equation selected by the regression program is

$$K_{Ic} = 30 + 6000 \frac{[Ni]}{\sigma_y}(1 + 0.02\lambda), \qquad (2)$$

where the units are the same as in equation 1. This equation, predicting the toughness for both weld and base metal compositions, was developed from the data used for equation 1 and four weld data with a σ_y range of 550 to 1100 MPa, a [Ni] range of 8 to 20 wt.%, and a λ range of 5 to 110 μm. It has a standard deviation of 27 MPa·m$^{\frac{1}{2}}$, an R^2 of 0.87, and an F ratio of 159. This standard deviation is comparable to that found for equation 1, which was developed for the restricted data set of alloy 316-type base metals.

Role of Dimple Density

All fracture surfaces were composed of ductile dimples. The inclusions that nucleated the dimples were still at the bottom of some of the dimples. Microprobe analysis indicated they were all of the manganese silicate type. The fracture-surface dimple measurements are given in table 4. For each weld, we see less than 25 percent variation when the dimple densities were measured on tensile, CVN, and CT (for one weld) fracture surfaces. This variation is small considering that testing was done at two temperatures, at strain rates ranging from 2×10^{-4} s^{-1} for the tensile and CT specimens to approximately 1×10^{-3} s^{-1} for the CVN specimens, and that the specimen types had different loading configurations. However, the CVN data are consistently higher than those for the other fracture surfaces, which may indicate a small effect. More detailed studies are needed to confirm this trend. The good agreement found here indicates that the dimple densities of the various welds can be characterized with any of these specimen types.

The higher CVN absorbed energy of the GMA weld could be explained by the lower density of inclusions measured on the polished surface section. Assuming all ductile dimples observed on fracture surfaces were nucleated at inclusions, one can correlate the higher CVN absorbed energy to the lower dimple density.

In a study of C–Mn welds, Passoja and Hill found very good agreement between the inclusion density measured on an electropolished planar surface

and the number of dimples on a fracture surface.[13] In fact, they found that the 1.18 factor in an equation by Kochs,

$$D_S = 1.18\ N_S^{-\frac{1}{2}}, \qquad (3)$$

was sufficient to correct the results when the inclusion density was calculated in terms of a three-dimensional nearest-neighbor spacing.[14] Here D_S is the nearest-neighbor spacing, and N_S is the average planar surface inclusion density.

Comparison of tables 2 and 4 reveals about an order-of-magnitude difference between the inclusion density on planar surfaces and the fracture surface dimple density for this study. This difference in density is clearly visible in figures 2 and 3. The largest difference predicted by the fracture models for these two surfaces (corrected for the difference between plan views of a 2- and 3-dimensional surface) is about a factor of 2.[15] The unexplained difference (about a factor of 5) could be due to undercounting the inclusions on the polished surface, overcounting the dimples on the fracture surface, or a surface roughness greater than that predicted by general fracture models.

The first possible cause, undercounting inclusions on the polished surface, is unlikely since the surfaces were polished with care and the final polishing time was minimized. Pits indicating that inclusions had been removed from the surface were not evident. The electropolishing technique employed by Passoja and Hill, may, in fact, have led to an overestimate of inclusion content in their study owing to selective removal of the matrix material. The second possible cause, overcounting of the dimples, is also unlikely. Whether the small indentations in figure 3 are facets of one large inclusion or several smaller inclusions is somewhat uncertain, but the possibility of miscounting by a factor of 5 is very small. This leaves the roughness of the fracture surface as the most likely reason for the differences between inclusion counts and dimple density. Grain orientations that favor shear on other than a 45-degree angle, nonuniform inclusion distribution, and other microstructural heterogeneity could cause increased surface roughness.

Comparison of the inclusion sizes of the polished and fracture surfaces provides further insight into the fracture process. Table 2 includes average inclusion diameters measured on the polished surfaces. Figures 4 through 6 are plots of inclusion diameters measured on the fracture surfaces of these three welds versus the average dimple diameters. In some cases, the dimples had major and minor axes, and the data are represented with a bar. In other cases, the dimples were circular and are represented by an X within a circle. Notice that there were relatively few inclusion–ductile dimple pairs that could be measured. Many dimples had lost their inclusions during the fracture process. Also, notice that the average diameter of the fracture-surface inclusions is much greater than that of the polished-surface inclusions. This may indicate that the small inclusions were lost more frequently than the large ones or that large inclusions are more likely to initiate fracture and, therefore, they are more commonly observed on the

fracture surface. We found that another possibility, the correction to the true inclusion diameter from random sections of a polished surface, increased the average inclusion diameter only slightly.

The measurements shown in figures 4 through 6 also indicate that larger inclusions form larger dimples. Since the higher toughness GMA weld had larger dimples, perhaps further improvements in toughness can be achieved by reducing the inclusion density through better refining or agglomeration of the manganese silicate into larger, widely spaced inclusions.

CONCLUSIONS

1. The fracture-surface dimple density and inclusion density were inversely related to the Charpy V-notch absorbed energy, indicating that inclusion spacing is a primary factor in determining the toughness.

2. The fracture-surface dimple density was found to be almost independent of the strain rate during fracture and specimen type. It varied less than 25 percent when measured on a tensile specimen fractured at 4 K, a Charpy V-notch specimen fractured at 76 K, and a compact tension specimen fractured at 4 K.

3. The fracture-surface dimple density was a factor of 5 greater than that predicted by fracture models based on inclusion density. This indicates either shear on an angle other than 45 degrees, a nonuniform inclusion distribution, or microstructural inhomogeneity.

4. The weld metal fracture toughness can be predicted from an equation developed for the base metal. The applicability of one equation for both weld and base metal indicates a role of strength, Ni content, and inclusion density in determining the toughness of the austenitic stainless steels.

ACKNOWLEDGMENT

This study was supported by the Office of Fusion Energy, U.S. Department of Energy.

REFERENCES

1. G. M. Goodwin: Weld. J., vol. 64, 1985, pp. 19–25.
2. S. Yamamoto, N. Yamagami, and C. Ouichi: Advances in Cryogenic Engineering—Materials, vol. 32, Plenum Press, New York, 1985, pp. 57–64.
3. N. J. Simon and R. P. Reed: J. Nucl. Mater., in press.
4. R. L. Tobler, T. A. Siewert, and H. I. McHenry: Cryogenics, 1986, vol. 26, pp. 392–396.
5. C. N. McCowan, T. A. Siewert, and R. L. Tobler: Trans ASME, 1986, vol. 108, pp. 340–343.

6. C. N. McCowan, T. A. Siewert, R. P. Reed, and F. B. Lake: Weld. J., in press.
7. E. R. Szumachowski and H. F. Reid: Welding J., 1979, vol. 58, pp. 34–44.
8. D. T. Read and R. L. Tobler: Advances in Cryogenic Engineering—Materials, vol. 28, Plenum Press, New York, 1982, pp. 17–28.
9. R. L. Tobler, D. T. Read, and R. P. Reed: Fracture Mechanics: Thirteenth Conference, Richard Roberts, Ed., ASTM STP 743, American Society for Testing and Materials, Philadelphia, 1981, pp. 250–268.
10. D. J. Kotecki: Materials Studies for Magnetic Fusion Energy Applications at Low Temperatures—III, R. P. Reed, Ed., NBSIR 80-1627, National Bureau of Standards, Washington, 1980, pp. 197–204.
11. T. A. Whipple and D. J. Kotecki: Materials Studies for Magnetic Fusion Energy Applications at Low Temperatures—IV, R. P. Reed, Ed., NBSIR 81-1645, National Bureau of Standards, Washington, 1981, pp. 303–321.
12. H. I. McHenry and T. A. Whipple: Materials Studies for Magnetic Fusion Energy Applications at Low Temperatures—III, R. P. Reed, Ed., NBSIR 80-1627, National Bureau of Standards, Washington, 1980, pp. 155–165.
13. E. Passoja and D. C. Hill: Fractography—Microscopic Cracking Processes, ASTM STP 600, American Society for Testing and Materials, Philadelphia, 1976, pp. 30–46.
14. U. F. Kochs: Philos. Mag., 1966, vol. 13, pp. 541–544.
15. E. E. Underwood: J. Met., 1986, vol. 38, pp. 30–32.

Table 1. Selected Data for the Welds*

	SMA-1	SMA-21	GMA
Yield Strength (MPa at 4 K)	460	880	1020
CVN Absorbed Energy (J at 76 K)	45	42	102
$K_{Ic}(J)$ ($MPa \cdot m^{1/2}$)	—	—	203
Ferrite Number (FN)	4	0.5	0
Composition (wt.%)			
C	0.03	0.03	0.03
Mn	1.6	3.5	5.4
Si	0.29	0.37	0.26
Cr	17.6	17.8	18.1
Ni	9.2	9.1	20.4
N	0.05	0.15	0.16

*This study.

Table 2. Inclusion Measurements on Polished Surfaces

Measurement	Weld		
	SMA-1	SMA-21	GMA
Inclusion Density, n (mm^{-2})	3.9×10^4	4.0×10^4	1.1×10^4
Average Diameter (μm)	0.36	0.37	0.45
Volume Fraction	4.8×10^{-3}	4.9×10^{-3}	2.3×10^{-3}
Mean Spacing, λ (μm)	5.1	5.0	9.5

Table 3. SMA Fracture Toughness Data at 4 K Developed in Previous Studies

Weld Identification	K_{Ic} ($MPa \cdot m^{1/2}$)	σ_y (MPa)	Ni (wt.%)	n (mm^{-2})	λ^* (μm)	Reference
497-5 FCA	159	608	15.2	4×10^4	5	10,11
508-2 GMA	163	779	11.8	4.2×10^4	4.9	10,11
1616-2 FCA	235	607	16	3.2×10^4	5.6	12

*λ (the inclusion spacing) is defined as the inverse root of n (the inclusion density).

Table 4. Dimple Measurement on the Fracture Surfaces

Specimen	Weld		
	SMA-1	SMA-21	GMA
4-K Tensile Specimen			
Dimple Density (mm^{-2})	3.2×10^5	3.5×10^5	1.2×10^5
76-K CVN Specimen			
Dimple Density (mm^{-2})	4.1×10^5	4.6×10^5	1.6×10^5
4-K CT Specimen			
Dimple Density (mm^{-2})	—	—	1.2×10^5

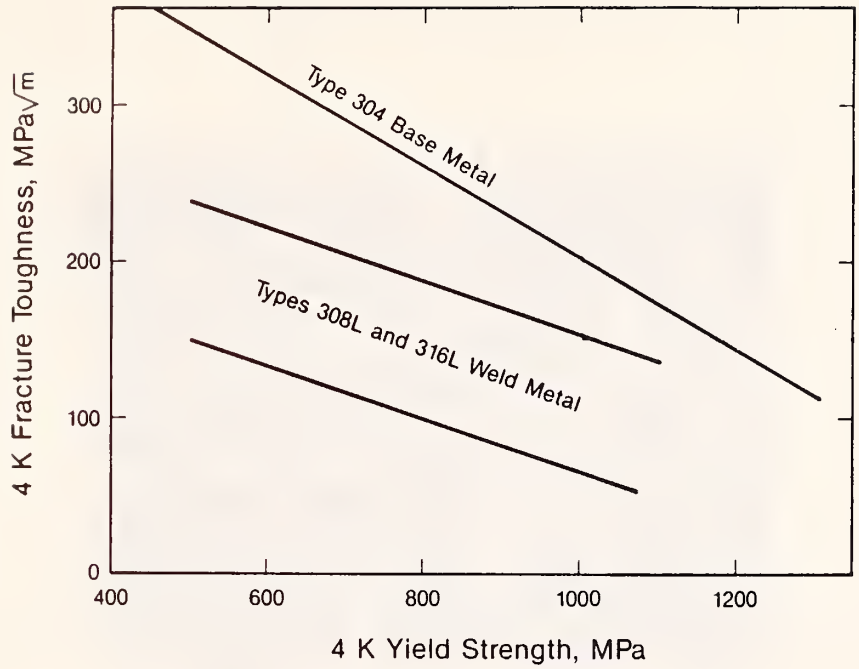

Figure 1. Comparison of the strength–toughness relationships for type 304LN austenitic stainless steel and type 308LN and 316LN welds.

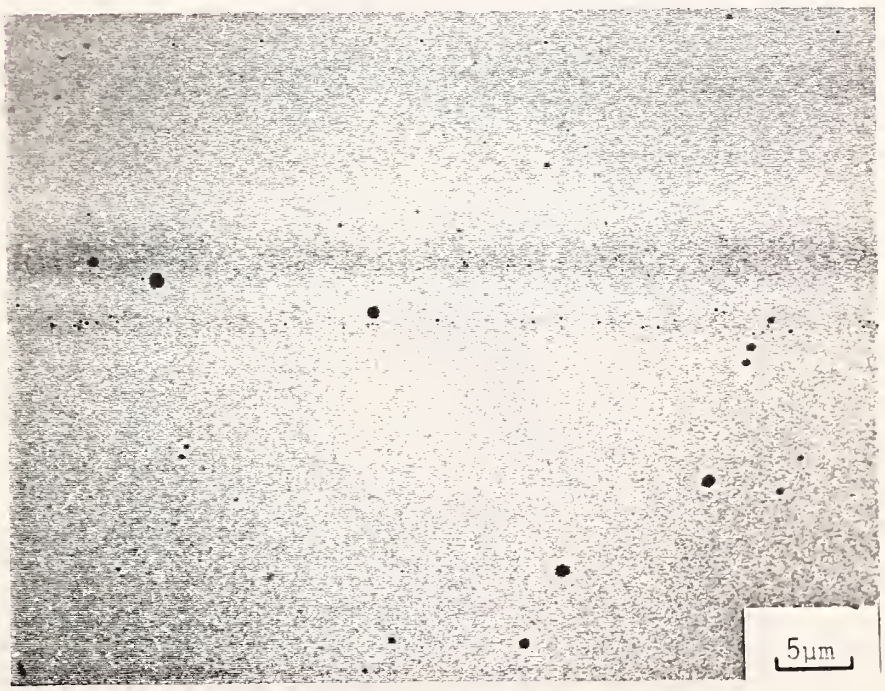

Figure 2. Polished surface of GMA weld.

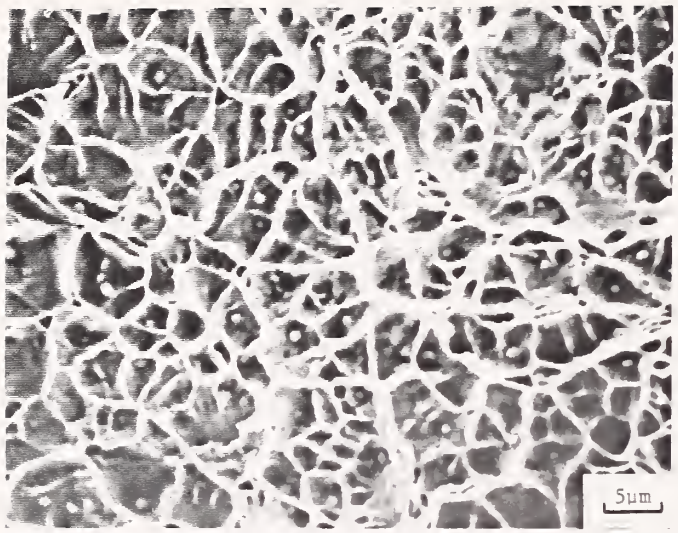

Figure 3. Fracture surface of GMA tensile specimen.

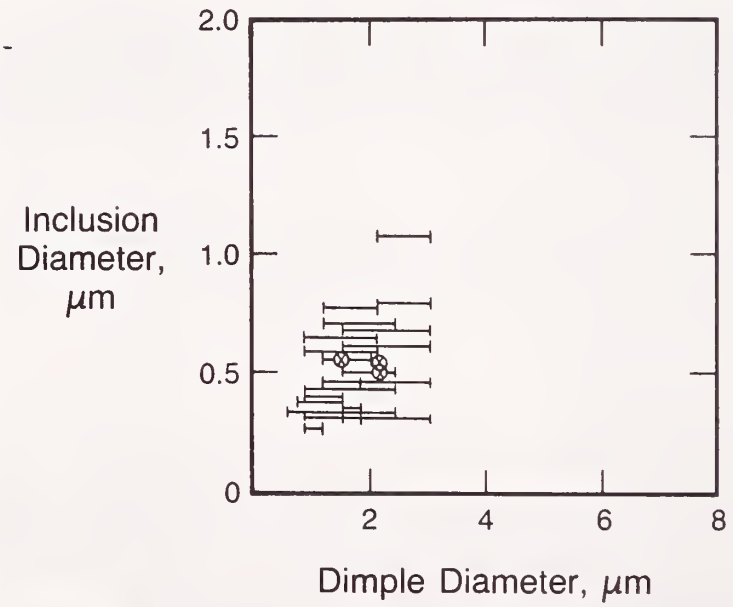

Figure 4. Dimple diameter versus inclusion diameter for weld SMA-1.

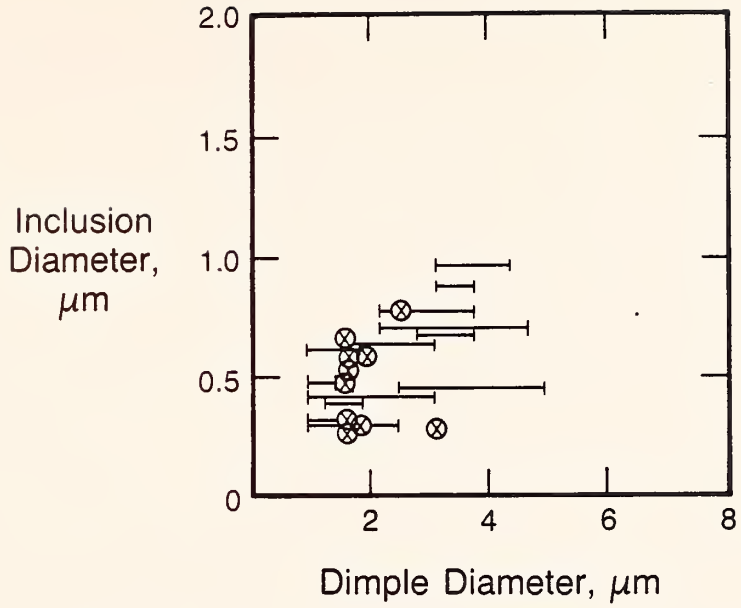

Figure 5. Dimple diameter versus inclusion diameter for weld SMA-21.

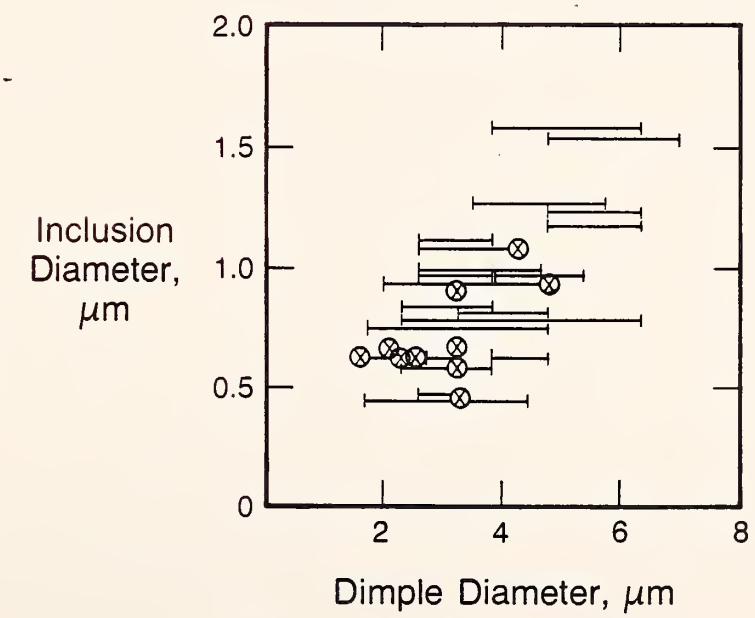

Figure 6. Dimple diameter versus inclusion diameter for GMA weld.

CRYOGENIC STRENGTH, TOUGHNESS, AND FERRITE CONTENT OF STAINLESS STEEL WELDS*

Christopher N. McCowan

To study the effect of alloy content on the strength, toughness, and ferrite content of shielded metal arc (SMA) stainless steel welds, two test matrices were evaluated.

Evaluation of a SMA weld test matrix in which manganese (1.5 to 10 wt.%) and nitrogen (0.04 to 0.26 wt.%) were varied independently has clarified the effect of these elements on the cryogenic mechanical properties. Several molybdenum and boron additions were also made. The matrix was based on a type-308L stainless steel weld metal composition. Desired compositions and constant FN were attained through alloy additions to the electrode coating. For each weld, one all-weld-metal 4-K tensile specimen and five 76-K Charpy V-notch (CVN) impact specimens were tested.

The addition of nitrogen linearly increased the 4-K yield strength from 600 to 1300 MPa and decreased the 76-K lateral expansion from 0.7 to 0.1 mm. Nitrogen reduced the 76-K CVN absorbed energy but not linearly. The addition of manganese and molybdenum slightly increased the yield strength and slightly decreased the lateral expansion. The solid-solution strengthening of molybdenum was greater than that of manganese and the 3.84 wt.% molybdenum alloy had substantially lower toughness than other similar compositions. The 4-K tensile strength was relatively unaffected by alloy additions; values varied between 1300 and 1500 MPa.

The second SMA test matrix was evaluated using stepwise linear regression techniques to determine more accurate equations for predicting the ferrite number (FN) in welds having high alloy contents. This test matrix contained the weld compositions and associated FN values of the manganese—nitrogen test matrix plus those of approximately 850 other SMA welds.

---

*M.S. Thesis, No. T3449, Publication of Colorado School of Mines, Golden, Colorado, 1987.

The simplest predictive equation (FN1) developed had chromium and nickel equivalents similar in complexity to the DeLong equivalents. The coefficients for chromium, nitrogen, and silicon, however, were lowered with respect to the DeLong coefficients while those for carbon and nickel remained approximately the same. When using the FN1 equation, approximately 70 percent of the welds analyzed had predicted FN values within 2FN of the measured values. When the DeLong-type equation was used, only around 50 percent of the predicted FN values fell within this error range.

Several alternative predictive equations were also developed. A modification of the "pseudo polar" Schaeffler equation predicted FN with accuracy close to that of the FN1 equation. Another, more complex, predictive equation developed included interaction terms, such as molybdenum–chromium and manganese–nitrogen. The results indicated that more accurate prediction of FN requires: (1) better understanding of the interactions between compositional elements, (2) development of nonlinear predictive equations forms, and (3) development of separate FN predictive equations for welds with primarily ferritic solidification modes and welds with primarily austenitic solidification modes.

I. INTRODUCTION

A. Overview

Toughness values for 300-series stainless steel welds at cryogenic temperatures have consistently been lower than those for base materials of equal strength.[1,2] Several studies have attempted to understand this phenomenon by statistically determining predictive equations for Charpy V-notch (CVN) toughness on the basis of the weld composition.[3-5] Although these studies have resulted in tougher welds through optimized electrode compositions, the welds still do not match the toughness of the base material. Recently, controlled additions of nitrogen (along with additions of manganese to reduce the tendency to form porosity) have increased the plate strength at cryogenic temperatures with little loss in toughness.[6]

Typical mechanical properties for nitrogen-strengthened base materials are reflected by the properties reported for an as-received hot-rolled 316LN stainless steel plate.[7] A 4-K yield strength and fracture toughness [$K_{Ic}(J)$] of 1020 MPa and 224 MPa$\sqrt{m}$, respectively, were reported, with an associated 76-K CVN absorbed energy of 89 J and a lateral expansion of 1.03 mm. This increased base materials strength, however, cannot be totally utilized until welds of comparable toughness at these elevated strengths are developed.

To guide electrode development projects, the 1984 NBS–DOE Workshop on Materials at Low Temperatures established a 4-K fracture toughness goal of

160 MPa$\sqrt{m}$ [$K_{Ic}(J)$] for weld metals having a yield strength of 1000 MPa.[8] As an economical means of screening promising alloy compositions, the workshop suggested 76-K Charpy V-notch testing.

In addition to mechanical property goals to guide electrode development, more accurate methods for predicting ferrite content in these highly alloyed welds are needed. Unlike the fully austenitic 300-series base materials, the welds normally have microstructures containing 3 to 7 percent ferrite. The presence of the more brittle ferritic phase reduces toughness at low temperatures. Small amounts of ferrite, however, are generally desirable to reduce microfissuring tendencies in the weld that would more severely degrade the toughness. To achieve an accurate, optimum ferrite content of experimental alloys, new ferrite predictive equations must be developed.

B. Objective

The test matrices evaluated in this study were designed to help clarify the effects of nitrogen, manganese, and molybdenum on the strength and toughness of shielded metal arc (SMA) weld metals at low temperature, and the ferrite content of weld metals. The study was intended to contribute to the development of welds having mechanical properties comparable to those of the nitrogen-strengthened base materials and to develop equations that better predict the ferrite content of these more highly alloyed weld metals.

C. Literature Review

In this review, emphasis is placed on the effect that ferrite, nitrogen, manganese, and molybdenum have on the strength and toughness of 300-series stainless steels at low temperature and on the prediction of weld metal ferrite content. In addition, the deformation behavior of stainless steels during tensile testing at 4 K and the difficulties of comparing Charpy V-notch absorbed energy to lateral expansion results for materials of differing strengths is discussed.

1. Strength

The strengthening potential of nitrogen in stainless steel increases with decreasing temperature.[5,9-12] Nitrogen occupies the octahedral interstitial sites in the face centered cubic structure and expands the lattice in a manner similar to that of carbon. The carbon-atom size is larger than that of nitrogen, but when the temperature is decreased from room temperature to 4 K, interstitial nitrogen increases the yield strength by approximately sixfold compared with the twofold yield strength increase associated with carbon.[6]

It is clear that the traditional "hard-ball-model"[13,14] for strengthening by lattice expansion does not adequately address the differences between carbon and nitrogen strengthening in stainless steels at low temperatures. Stronger metal–nonmetal bonding occurs in Fe–C than in Fe–N,

because the extra electron associated with the nitrogen atom may result in an increased elastic misfit for the nitrogen atom, which would partially explain this difference.[15,16] The solute atom–dislocation interaction would increase and result in an increased yield strength.

Unlike high carbon contents, high nitrogen contents do not result in sensitization problems. Nitrogen content can be increased until porosity occurs at the solubility limit. For a liquid Fe–18Cr–11Ni alloy, solubility is not reached until approximately 0.2 wt.% nitrogen.[17] Nitrogen solubility increases as the chromium content in the alloy increases. The absorption of nitrogen obeys Severts law in alloys of up to 57 wt.% chromium.[18,19] In commercial alloys, the manganese additions also increase nitrogen solubility so that nitrogen contents greater the 0.2 wt.% are attainable. Clearly, the high solubility limit, lack of sensitization, and its greater strengthening power make nitrogen an attractive interstitial alloying element.

Further increasing its attractiveness is the ability to add nitrogen to weld metal deposits easily and economically. Nitrogen can be introduced to the weld through shielding-gas mixtures with the gas metal arc (GMA) and gas tungsten arc (GTA) processes or through nitrogen-containing alloy additions to the coating with the shielded metal arc (SMA) process.

The increase in yield strength at low temperatures due to nitrogen alloying in type-308 stainless steel composition is well known. To simplify comparisons of studies done within differing nitrogen content ranges, a linear relationship is assumed between nitrogen and yield strength and the effect of nitrogen is expressed as an approximate function of nitrogen content. With increases in nitrogen contents of 0.05 wt.% at 76 K, increases in yield strengths of 150 and 175 MPa were reported by Enjo et al.[11] and Onishi et al.,[12] respectively. At 111 K, Mukai et al. reported an increase in yield strength of 120 MPa.[20] In comparison, only slight increases in weld metal yield strengths have been found at room temperature.[11,12,20,21]

The influence of nitrogen on the tensile strength is disputed. Enjo et al. found tensile strength increases of less than 10 MPa per 0.05 wt.% nitrogen, implying a nearly constant tensile strength at 76 K with respect to nitrogen content.[11] Onishi et al. found increases in the tensile strength of approximately 25 MPa per 0.05 wt.% nitrogen.[12] In all cases, the increases in tensile strength reported were much less than those observed for yield strength.

The effects of manganese, molybdenum, and boron on cryogenic weld metal strength have not been published. For 300-series-base materials, however, some data on the effects of manganese and molybdenum are available. Manganese has been reported to increase the 76-K yield strength slightly in Fe–12Cr–12Ni–Mo–N alloys by Mukai et al.[20] and by Sakamoto et al.[22] in a wide range of stainless steel compositions. Yamamoto et al.[23] report that manganese had no effect on strength, but that molybdenum increased the yield strength at 4 K by 80 MPa for each wt.%. Purtscher and Read[24] report a 40-MPa yield strength increase per wt.% molybdenum at 4 K. Mukai et al.[20] report a 50-MPa increase in yield strength per wt.% molybdenum at 77 K.

2. Toughness

The cryogenic toughness of type-308L and -316L stainless steel welds is determined by the interrelated and sometimes opposing effects of the individual alloying elements and the ferrite content. The ferrite content is often represented by a ferrite number (FN), which is approximately equivalent to percent ferrite within the range of 0 to 20 FN.[25]

The FN was found to be a dominant factor in determining Charpy V-notch (CVN) toughness for these 300-series stainless steels.[26-29] Lower FN tends to raise the toughness. On the other hand, increased nitrogen contents, which lower the FN, have been reported to lower the CVN absorbed energy (AE) and lateral expansion (LE) values in SMA welds.[4] Contradicting this reported nitrogen effect, Enjo et al.[11] found that CVN absorbed energies increased with increasing nitrogen content (decreasing FN) in his GMA study of type-308 stainless steel welds. Whether increasing nitrogen content lowers the CVN toughness more than decreasing FN raises it is still unclear. Separating these factors to evaluate their individual effects on toughness is difficult. To evaluate the effect of nitrogen, for example, FN must be held constant by concurrently raising the chromium content or that of some other ferritizing element. Past research indicates, however, that increased chromium and carbon contents can reduce toughness.[4,20,28] The effects of molybdenum are not clear, but Miura[30] reports a dramatic drop in CVN absorbed energy in a Fe–12Cr–12Ni–0.1N base metal alloy for molybdenum contents of approximately 7 to 9 wt.%. This type of loss in toughness has been reported at molybdenum contents as low as 3.5 wt.% in 25Cr–16Ni–0.34N–Mo welds.[31] Manganese has been reported to decrease the 77-K CVN absorbed energy in stainless steel base material but to slightly increase fracture toughness at 4 K.[24] Nickel is the only compositional element common to stainless steels that is generally agreed to increase CVN toughness.

Charpy V-notch test results for type-308L stainless steel welds at 76 K show substantial scatter. To reduce the scatter, only weld deposits having FN less than eight and low nitrogen contents are reported here. For SMA weld deposits, absorbed energy values ranging from 16 to 34 J and lateral expansions from 0.15 to 0.46 mm have been reported.[5,11,32] When GMA and GTA 308L stainless steel welds are included absorbed energies of 29 to greater than 100 J have been reported.[5,11] The principal differences in toughness values of welds produced with different processes is attributed to the lower inclusion content associated with the GMA and GTA welds.

3. Ferrite-Number Prediction

The strong influence of ferrite content on cryogenic toughness dictates the use of an accurate method for predicting the FN in the new high nitrogen and manganese stainless steel electrodes. The diagrams developed by Schaeffler[33] and DeLong et al.[34,35] are the most common methods for the prediction of FN (figures 1 and 2).

The basis for these diagrams can most easily be seen from the Fe–Cr–Ni isothermal diagram at 1000°C (figure 3a). In figure 3b a portion of this

isothermal diagram is shown in an orientation similar to the Schaeffler and DeLong diagrams. It is apparent that the general shape of the austenite-plus-ferrite ($\gamma + \alpha$) two-phase region and the orientations of the single-phase (γ and α) regions with respect to it are carried over to the FN predictive diagrams. The FN predictive diagrams are, however, nonequilibrium constitutional diagrams that were empirically developed from alloys having more complex compositions than those of the Fe–Cr–Ni ternary diagram alloys. These differences make further comparisons between the two types of diagrams difficult.

Although both the Schaeffler and DeLong diagrams have proven quite successful and useful in predicting the FN, recent studies[36,37] indicate that several of the coefficients used with these diagrams do not accurately reflect the appropriate trends. Also, alloys are being developed with compositions outside the ranges of applicability for these diagrams.

The Schaeffler diagram has been found to be an accurate predictor of FN for type-308 and -347 stainless steels. DeLong et al.[34,35] refined the Schaeffler diagram to better predict FN for type-309 and -316 stainless steel compositions. These compositions have higher chromium and nickel equivalents than the type-308 and -347 stainless steel welds for which the Schaeffler diagram is best suited. Whether the respective FN diagrams or the corresponding mathematical expressions for these diagrams are used, nickel and chromium equivalents are commonly used to represent the relative austenitizing and ferritizing tendencies for a given alloy composition. The Schaeffler equivalents are:

$$Ni_{eq} = Ni + 30(C) + 0.5(Mn); \tag{1}$$

$$Cr_{eq} = Cr + Mo + 1.5(Si) + 0.5(Nb); \tag{2}$$

where the elements are given in wt.%

DeLong added a nitrogen term with a coefficient of 30 to the Schaeffler nickel equivalent and refined his diagram to represent only those alloy compositions of more common commercial interest. The constant FN lines on both diagrams, however, vary in slope and spacing. Therefore, both diagrams would best be represented by a polar-type equation form that would allow both the slope and the spacing changes of the constant FN lines to be modeled. The Schaeffler diagram is expressed mathematically by a "pseudo polar" equation form:[38]

$$FN\ (Schaeffler) = -39.1 + 43.5\ \frac{Cr_{eq} - 5.5}{Ni_{eq} + 2.0}\ . \tag{3}$$

Presently, however, the best representation of the DeLong diagram is by an equation having a linear form:[38]

$$FN\ (DeLong) = 30.64 + 3.49[Cr_{eq}] - 2.5[Ni_{eq}]. \tag{4}$$

This linear FN predictive equation is a reasonably accurate representation of the DeLong diagram at low FN, but at FN values of greater than ten, the predictive error increases.

Two important advantages of the linear representation of the DeLong diagram and the respective chromium and nickel equivalents used within it are simplicity and clarity. Alloy elements that promote the formation of ferrite, such as chromium, molybdenum, niobium, and silicon, are grouped together in the chromium equivalent. Austenitizing elements, which include nickel, carbon, nitrogen, and manganese, make up the nickel equivalent. Each elemental variable within the respective equivalent expressions is weighted and the difference between the equivalents determines the FN. Chromium and molybdenum are shown to have equivalent ferrite-forming powers on a weight percent basis. Niobium promotes ferrite formation only half as well. Nickel is approximately 28 percent less effective in preventing ferrite formation as chromium is in promoting it, and so on. The problem with making these empirical interpretations is that all the FN predictive equations are designed around specific alloy compositions.

Thermodynamics would predict an FN predictive equation of a more complex form:[39]

$$FN = K_{Ni}\,Ni + K_{Mn}\,Mn + K_{Cr}\,Cr + K_{N}\,N + K_{i}\,i + K_{Ni-Mn}\,MnNi + K_{Ni-Cr}\,NiCr + K_{i-j}\,i_j. \quad (5)$$

This solution form implies that, in addition to the effect on ferrite formation by individual alloying elements, interaction terms between these elements need consideration to more accurately predict FN over a wide range of alloy compositions. Support can be found for the need to include interaction terms in FN predictive equations. For example, the austenitizing power of manganese has been observed to decrease when concentrations exceed 4 to 5 wt.%[40] The indication of a chromium–nickel interaction is found as far back as 1939 in the Maurer diagram.[41] Nitrogen–manganese interactions have been suspected.[42,43]

The struggle for better definition of coefficients in the FN predictive equations is indicated by the various coefficients and constants that have been proposed to model the effects of nitrogen and manganese (table 1).[44-48] At high nitrogen contents, Espy found that the nitrogen coefficient decreases.[37] Most studies involving high manganese contents have proposed constants to represent the effect of manganese and replace the 0.5 term of DeLong et al.[36,37] The Hull study[43] was the only high manganese test matrix to yield a manganese coefficient. However, its second-order term does reduce the influence of manganese on the nickel equivalent at high concentrations. A review of the alloy ranges used in the various studies did not disclose the reason for proposing different terms to model the influences of manganese or nitrogen in the nickel equivalent expression. The specifics of any possible interactions remain undefined.

In addition to the need of defining the appropriate variables and coefficients for better predicting FN, the ambiguity of predicting ferrite

formed via primary ferritic versus primary austenitic or mixed solidification modes from the same function of composition must be addressed. The DeLong diagram, for example, was developed empirically from types 308, 309, 310, 316, 410, and 502 stainless steel alloys. These alloys solidify via a primary ferritic solidification mode. So the Delong diagram, by the nature of its development, has empirically incorporated the kinetic factors associated with primary ferritic solidification into the positioning of the constant FN lines. For weld deposits having FN values near zero, however, fully austenitic or mixed mode solidification may have been involved in the freezing process. It might be speculated that the quantity of ferrite formed by either of these processes could not be accurately predicted by constant FN lines representing the primary ferritic solidification process. For clear and accurate definition of the constant FN lines from zero to five, it may be necessary to separate weld data by solidification mode. Although there are several proposed mathematical expressions to predict whether primary austenitic or ferritic solidification will occur, as yet, these types of expressions have not been integrated into the process of predicting FN.[49]

D. Testing

1. Tensile Testing at 4 K

The 4-K stress–strain curves, shown in figures 4 and 5, illustrate several characteristic changes in the curves that take place as either the test temperature is decreased or the austenitic alloying element concentrations are increased in metastable 18Cr–8Ni stainless steels. Considering the test temperature effects first, figure 4 shows the occurrence of sudden load drops or serrations that are associated with the 4-K stress–strain curves. Serrated curves are common in Fe–18Cr–8Ni alloys at this temperature and have also been observed in other austenitic stainless steels, brasses, bronzes, coppers, and aluminum alloys. The occurrence of these serrations is a low-temperature phenomenon with the exception of materials undergoing strain aging at ambient temperatures.[50]

One explanation of the serration process is that a nucleation deformation event occurs as a result of local stress concentrations, thermal fluctuations within the sample, or both. This event produces heat that is not easily dissipated because of the low thermal conductivity of impure metals at low temperatures. This results in a lowering of the local flow stress, and deformation can continue at the applied stress level. This produces more heat, and deformation continues until some undefined equilibrium is reached with respect to local heat generation, the absorption of heat by the bulk specimen, and the applied stress. At this point a seemingly elastic reloading of the sample begins until another load drop takes place. This adiabatic heating explanation is supported by the measured mechanical energy dissipated in load drops, by correlations to thermal energy required for the process, and by the ability to predict the temperature increase using specific heat, the temperature dependance of the flow stress, and volume strained.[51]

The character of the stress–strain for these metastable 18Cr–8Ni stainless steels is also dramatically altered by increasing the nitrogen and manganese alloy contents. As the concentration for either of these austenitizing elements is increased, the alloy becomes more stable against stress-induced martensitic transformations. In figure 5, stress–strain curves characteristic of an 18Cr–8Ni base material are shown. As the manganese content increased from 1 to 6 wt.%, the yield strength increased and the work-hardening rate decreased.

2. Charpy V-notch Testing

The Charpy V-notch impact test is commonly used to measure the ability of a material to absorb energy in the presence of a flaw. The absorbed energy is the sum of the crack initiation and propagation energies. It is controlled by strength and ductility. The strength of the material regulates the force required to deform the specimen during testing. The ductility of the material determines the distance through which the force acts. The absorbed energy (AE) is a product of force times distance and represents toughness in a manner similar to the area under a stress–strain curve. Lateral expansion (LE), on the other hand, is a direct measure of notch ductility. So, since the area under the stress–strain curve may not change substantially for materials of varying strengths, a loss in notch ductility measured directly by a loss in lateral expansion may not result in a measurable loss in the absorbed energy. For example, in a higher strength material, an increased absorbed energy value is required to obtain the same lateral expansion. This fact is illustrated by figure 6.[52] By replotting this data as LE versus strength it is found that LE can decrease linearly as strength increases at a constant AE. Thus, lateral expansion and absorbed energy measurements from Charpy V-notch tests may imply seemingly contradictory results for materials of different strengths.

II. EXPERIMENTAL PROCEDURES

A. Materials

Two SMA weld metal test matrices were evaluated in this study. The first test matrix, referred to as the manganese–nitrogen matrix, was used for mechanical testing. The second test matrix was used to evaluate the effects of compositional components on the weld metal ferrite content.

The test welds for the manganese–nitrogen test matrix were produced using a series of 3.2-mm (0.13-in) diameter electrodes that had core wires from a single heat of type-308 stainless steel. Alloy additions were made to the SMA electrode coating. The chemical compositions of the individual weld deposits tested in this study are given in table 2. These compositions represent a test matrix, based on 18Cr–8Ni stainless steels, in which manganese (1.5 to 10 wt.%) and nitrogen (0.04 to 0.26 wt.%) were the principal

variants of interest. Several molybdenum (2 and 4 wt.%) and boron (0.006 and 0.015 wt.%) additions were also made to the matrix. The chromium content of the matrix was varied (15 to 21 wt.%) to compensate for the manganese, molybdenum, and nitrogen additions so that welds with a nearly constant ferrite content were produced.

The weld metal carbon and nitrogen contents were determined with individual element analyses. The phosphorus and sulfur contents were determined by optical emission spectrophotometry. The remaining element contents were determined by using conventional analytical techniques. The ferrite contents of weld pads and the welds were measured magnetically. The FN measurement device was calibrated with the ANSI/AWS standard A4.2-74.[53]

The second test matrix consisted of 929 SMA stainless steel weld compositions (Appendix 1). Most of these data were supplied by electrode manufacturers in cooperation with the Welding Research Council. The remainder of the data was collected from the literature. The nitrogen–manganese test matrix is included in these data. The FN values used for all welds in this test matrix were those measured magnetically. The FN values ranged from approximately zero to the very high values associated with duplex stainless steels. The welds ranged in composition from commercial types 308, 316, and 310 and duplex stainless steel alloys to experimental compositions. The compositional ranges for the various elements considered in the study are shown in table 3.

The data were divided into four groupings for analysis. Data having FN values of less than one were not used during any of the regressions to eliminate the uncertainties associated with very low FN measurements. The set of data with this restriction was defined as group 1. In addition to this overall limitation, further divisions of the data were made. Data group 2 was limited to FN values between 1 and 30 and to compositions for which molybdenum content did not exceed 2 wt.% when the chromium content was greater than 20 wt.%. This data group excluded experimental alloys of high combined molybdenum–chromium contents and the duplex stainless steel compositions. Several data groups were used to evaluate more specific types of compositional ranges. Data group 3 incorporated the restrictions of group 2 and limited the nitrogen and manganese contents to 0.1 and 3.0 wt.%, respectively. These data groups were used to compare accuracies between FN equations for welds whose compositions were close to those of commercial weld material. Types 308, 309, and 316 stainless steel weld compositions were evaluated separately. Data group 4 was limited to welds having primary ferritic solidification modes, as defined by Suutala.[49]

B. Welding

Mild steel plate cut into 13-mm-thick by 305-mm-long coupons and beveled for a single vee weld joint configuration was used as a base material. To overcome the effect of dilution of the weld deposits by the base metal, the exposed faces and backing strip were buttered with two layers of weld

metal prior to beginning the test weld. This procedure conforms to the AWS A5.4-78 specification.[54] The same welder, power supply, and welding parameters were used to minimize weld variations. Welding was done at 110 A and 22 V using an identical bead sequence. The heat input was approximately 0.6 kJ/mm, and an interpass temperature of approximately 93°C was maintained.

C. Mechanical Test Specimens

Two all-weld-metal 6-mm-diameter tensile specimens, oriented along the axis of the weld, were machined from each weld. The second specimen, reserved as a spare, was tested in a number of cases to check the repeatability of the results. In these cases, the average value is reported. Five Charpy V-notch specimens (ASTM E23 type A) were removed from each weld.[55] Their notches were oriented perpendicular to the plate surface along the weld center line and parallel to the direction of welding.

D. Tensile Testing

The testing apparatus used for the 4-K tensile testing is shown in figures 7 and 8. The upper specimen grip load line connects to a fixed upper crosshead that contains a built-in load cell. The lower specimen grip load line is anchored to the bottom of the compression tube, and as the crosshead moves downward, the specimen is put in tension. A conventional stainless steel Dewar, like the compression tube, is fixed to the moving crosshead and is used as the liquid helium reservoir. Liquid helium is introduced to the reservoir via an inlet passing through the crosshead and measured by a liquid helium superconducting liquid level indicator. The specimens are kept submerged in liquid helium throughout the test.

The extension of the specimen within its gauge length is measured with three cantilever beam extensometers seated on a retaining collar and positioned at 120 degrees with respect to each another. The retaining collars are fixed to the specimen by tungsten-carbide-tipped set screws. A 24.5-mm-long fixture is used during the mounting to help maintain consistent gauge lengths (figure 9). The extensometers are accurate to approximately ten percent strain. They are calibrated individually prior to testing at 76 K with a vertically mounted dial micrometer. The extensometers are wired in parallel so that an average of their outputs is recorded during the test. A strain rate of 9.5×10^{-5} s^{-1} and a gauge length of 24.5 mm was used for all tensile tests.

Two strip chart recorders were used. One recorded a load-time record of the test and one recorded load-displacement up to approximately ten percent strain. After ten percent strain this recorder was also used to record load-time data.

E. Charpy V-notch Testing

Charpy V-notch testing was done at 76 K following the ASTM E23 test standard method. A 163-J (120-ft·lbf) capacity unit was used. The impact velocity was calculated to be approximately 4.8 $m \cdot s^{-1}$.

F. Linear Analysis

Stepwise linear analysis was done on a mainframe computer. Quantities allowed as choices during the regression can generally be categorized into three groupings: (1) simple compositional variables such as carbon (C), nitrogen (N), chromium (Cr), and molybdenum (Mo), (2) interaction variables such as Mn × N, Cr × Mo, and Mo^2, and (3) equation variables. The equation variable grouping in this study was used to submit existing FN predictive equations for evaluation. These equations were "seen" as a single variable during the regression. The three equations included within this category that are of the most interest here were the "DeLong-type FN equations" (FNCD and FNCDK) and the FN predictive equation proposed by Hull (FNCH).[38,39,44] The notations for these equations are defined in table 4.

The program repeatedly evaluated the variable list and added elements and interactive terms to a predictive equation in the order of their statistical significance. In step one, the regression program selected the most highly correlated variable for entry into the model. A coefficient and intercept was then assigned. In step two the process was repeated, and a coefficient was assigned to the variable selected in this step. The coefficient chosen for the variable entered in step one was adjusted at this point and a new intercept value was assigned to the expression. This process was repeated until none of the remaining variables could meet the F-statistic selection criterion. For this study, an F value of 4.0 was chosen as the critical value. The F value is defined as the regression coefficient divided by the standard error squared. This value can also be expressed roughly as a 95 percent confidence level or a ratio of the best parameter estimate to a standard error of 4.0. The program also defined a multiple correlation factor squared (R^2) and a standard error of estimate value to each of the equations.

G. Microscopy

1. Light Microscopy

For making general microstructural observations, samples were taken from test specimens and prepared by standard metallographic techniques. A mixed acid etch containing 55 percent hydrochloric, 22 percent nitric, and 22 percent acetic acids was used as a general etch. To highlight only the delta ferrite phase, samples were electrolytically etched in a potassium hydroxide solution.

2. Scanning Electron Microscopy

After ultrasonic cleaning in methanol, fracture surfaces of broken specimens were characterized using a scanning electron microscope (SEM). Polished surfaces from the specimens were used for inclusion counts.

H. X-ray

Weld samples 6 and 13 were step scanned at intervals of 0.02 degrees, 2θ, for 25 s per step. A tube voltage of 44 kV at 40 mA was used. The radiation was Cu K_β ($\lambda Cu\beta$ = 1.39225 Å). The specimen surfaces were prepared by grinding followed by electropolishing.

III. RESULTS

A. Microscopy

1. Light Microscopy

During light microscope examinations of mechanically polished weld metal samples, all welds were found to have large numbers of inclusions. In figure 10, a micrograph of alloy 1 shows the typical appearance of the unetched weld deposits.

The ferrite morphologies observed after etching the welds were predominately a result of primary ferritic solidification. In figures 11 and 12, micrographs of alloy 6 show the ferrite structures commonly observed in the welds. The two principal ferrite morphologies found were vermicular and lacy. Weld metal having more complex ferrite morphologies and growth orientations, however, was observed in areas located between welding passes. In figure 13, an interpass region from alloy 22 is shown. At higher magnification, this high nitrogen-manganese sample was found to have some areas of weld metal that solidified by primary austenitic solidification. In general, however, most of the welds did not appear to change or have mixed solidification modes, even in these complex interpass areas.

2. Scanning Electron Microscope Inclusion Counts

Inclusion distributions were plotted for several representative welds from data collected at high magnification on the SEM. In figure 14, the inclusion distributions for the welds are represented by an envelope indicating the variations between samples. Alloy 6, the 3.84 wt.% molybdenum alloy, was found to have a large number of small-diameter inclusions. Micrographs of alloys 15 and 6 taken at the magnification used during the counts are shown in figures 15 and 16. The average inclusion diameters were approximately 3.3 μm, however, the variation in size was substantial. Almost all the inclusions were spherical in shape.

B. Strength

Stress–strain curves for five alloys that characterize the observed changes in the curves as a function of alloy content are shown in figure 17. As alloy content increased, the yield strength increased, the work-hardening rate decreased, and the distinctive three-stage curve was lost. These curves are shown without serrations for simplicity. In figure 18, a representative serrated curve is shown.

The specific yield and tensile strengths determined for the various welds at 4 K are given in table 5 and plotted versus nitrogen content in figure 19. The tensile strength remained nearly constant at an average of 1400 MPa for nitrogen contents up to 0.16 wt.% and increased slightly to an average of 1500 MPa for the three alloys having about 0.26 wt.% nitrogen. The differences in tensile strength among welds were not statistically related to alloy content. The yield strength, however, was clearly related to the alloy content of the welds. The dominant strengthener was nitrogen. The equation expressing the yield strength solely as a function of nitrogen content was:

$$\text{Weld Yield Strength (MPa at 4 K)} = 400 + 3600(\text{wt.\% N}) \qquad (6)$$

The F value (a test of the significance of the model) was 265. The coefficient of determination (R^2, a measure of the quality of the regression) was 0.92. The standard error of the prediction (STD) was 83 MPa.

Increases in yield strength due to manganese additions are shown in figure 20. At the 0.05, 0.10, and the 0.15 wt.% nitrogen concentrations, an approximate 15 MPa increase in yield strength per wt.% increase in manganese content was found. This coefficient represents an average of the three individual slopes and assumes no nitrogen–manganese interaction.

A graphical separation of the effects of manganese and nitrogen from factors such as molybdenum content, slight variations in FN, and other compositional elements becomes difficult at this point. Using linear stepwise regression, the equation best able to predict the yield strength was:

$$\text{Weld Yield Strength (MPa at 4 K)} = 334 + 3407(\text{wt.\% N}) + 15(\text{wt.\% Mn}) + 46(\text{wt.\% Mo}). \qquad (7)$$

This equation had an F value of 591, an R^2 of 0.96, and a standard error of estimate of 57 MPa.

C. Toughness

1. Absorbed Energy

The overall CVN absorbed energy at 76 K decreased slightly as the nitrogen content was increased from approximately 0.04 to 0.16 wt.% (figure 21). The average absorbed energy value within this region was 40 J.

Varying effects of nitrogen were found when alloys of otherwise similar composition and FN were compared at 0.04, 0.10, and 0.15 wt.% nitrogen levels. For example, at 1.57 wt.% manganese, alloys 1 and 7 had respective CVN absorbed energies of 46 and 39 J. This implies a loss of approximately 12 J per 0.1 wt.% nitrogen. At 3 wt.% manganese, alloys 18, 17, and 11 showed little reduction in absorbed energy as a function of nitrogen content. At 6 wt.% manganese (alloys 4, 9, and 12), the loss in absorbed energy per 0.1 wt.% nitrogen was approximately 5 J.

Nitrogen contents above 0.16 wt.% caused a substantial decrease in absorbed energy. At 0.25 wt.% nitrogen, the absorbed energy was by reduced by approximately 50 percent with reference to the 40 J average at lower nitrogen contents.

Although some indications of reductions in absorbed energy due to solid-solution alloying additions and FN were present, with the exception of the 3.84 wt.% molybdenum sample, no clear trends were resolvable within the data. Comparing the high molybdenum sample (alloy 6) to the 1.66 wt.% molybdenum sample of similar manganese, nitrogen, and ferrite content (alloy 13), a decrease in absorbed energy of 17 J was found.

2. Lateral Expansion

The lateral expansion decreased linearly as a function of nitrogen content, and to some extent as a function of manganese and molybdenum contents. Slight variations in the ferrite content of the samples could not be correlated to changes in the lateral expansion measurements.

As shown in figure 22, a decrease in lateral expansion of approximately 86 percent occurred when the nitrogen content was increased from 0.03 to 0.26 wt.%. Allowing nitrogen as the only compositional element to be chosen in the stepwise linear regression, the resulting equation was:

$$LE\ (mm) = 0.686 - 2.11(wt.\%\ N) \qquad (8)$$

This equation had an F value of 91, an R^2 value of 0.79, and a standard error of 0.081 mm.

It is apparent from figure 22, however, that manganese also contributes to the loss in lateral expansion at a given nitrogen content. The lateral expansion of alloy 12, for example, is 0.1 mm less than that of alloy 11. Both alloys have 19 wt.% chromium, 0.15 wt.% nitrogen, and 1.5 FN. The loss in lateral expansion is a result of the 3.4 wt.% manganese increase in alloy 12.

The alloys with molybdenum additions generally fit the observed trends; however, the lateral expansion values of alloys with combined high nitrogen, manganese, and molybdenum content (particularly alloys 13 and 16) were low. Allowing all compositional elements and FN as acceptable variables, an equation expressing the effect of molybdenum, manganese, and nitrogen on lateral expansion was found.

$$LE\ (mm) = 0.787 - 1.81(wt.\%\ N) - 0.031(wt.\%\ Mo) - 0.022(wt.\%\ Mn). \quad (9)$$

This equation had an F value of 280, an R^2 value of 0.92, and a standard error of 0.051 mm.

Since the lateral expansion was found to decrease linearly with increasing alloy content, it was inversely proportional to the yield strength.

The strength–toughness relationship is shown in figure 23. The equation found to express lateral expansion in terms of the 4-K yield strength was:

$$LE\ (mm\ at\ 76\ K) = 0.95 - 6 \times 10^{-4}\ (Yield\ Strength,\ MPa) \quad (10)$$

This equation had an F value of 344 and an R^2 value of 0.94.

D. Fractography

Macroscopic examinations of fracture surfaces showed texture differences on Charpy V-notch specimens of varying nitrogen and ferrite contents. In general, the higher nitrogen content samples had coarser, less planar fracture surfaces. At nitrogen contents greater than 0.15 wt.%, the fracture surfaces with the most texture also had the lowest FN (figures 24a and b). Shear lips tended to be present only on a Charpy V-notch specimen having nitrogen contents of greater than 0.15 wt.%. Examination of the tensile specimens at low magnification showed little or no correlation between fracture surface appearance and alloy content. All samples had fine, fibrous, planar fracture surfaces. Little necking took place in the tensile specimens. A narrow shear-lip region was present on many of the samples, but no relationship between shear-lip formation and nitrogen content was observed.

Examinations at high magnifications (SEM) of the Charpy V-notch and tensile specimen fracture surfaces showed the failure mechanism in all samples to be predominantly void nucleation and growth. Typical ductile-dimple tear-ridge networks were observed on all fracture surfaces. The tear-ridge patterns were similar to the two major orientations of ferrite present in the welds (figures 25 and 26). The results of dimple counts taken at 3000× on fracture surfaces showed some variation in dimple densities; however, compositional variations did not alter the inclusion density or size noticeably (table 6). Ductile dimple size was very similar between the various welds and specimen types. Most surfaces had a fine dispersion of small round inclusions and occasional large inclusions. In figure 27 is shown a typical dimple whose size is typical for the welds tested in this study.

The 3.8 wt.% molybdenum sample had a greater number of large inclusions on its Charpy V-notch fracture surfaces. These inclusions had a glassy,

brittle appearance and were found to be rich in calcium, manganese, silicon, and titanium during energy dispersive analysis in the SEM (figure 28).

The ductile dimples of tensile specimens had the same general size and distribution as those observed on the Charpy V-notch specimen surfaces (figure 29). There were, however, several types of characteristic fracture features seen only on Charpy V-notch fracture surfaces (figures 30 and 31). Both types of specimens had isolated areas where fractures of a more brittle nature occurred. Areas clearly fractured by cleavage in both sample types were predominantly ferrite (figures 32 and 33).

E. X-ray Analysis

The types of phases present in the two welds analyzed (alloys 6 and 12) were identical. The relative quantities of the phases differed slightly (figure 34). The principal phase present was austenite.

F. Ferrite-Number Prediction

Four FN predictive equations were developed in this study. These equations (FN1, FN2, FN3, and FN4) are defined in table 7, which also gives the F, R^2, and standard error of estimate values.

Comparing the fits of FN1, FN3, and FN4 equations to those of the DeLong-type equations (FNCD, FNCDK) and to the Hull equation (FNCH), the accuracy of FN prediction was improved for the welds of data group 2. The FN3 equation had an R^2 value of 0.73 and a standard error of estimate of 1.7 FN. This equation more accurately predicted FN than any other equation developed or considered over the wide range of alloy contents present in the group 2 weld data.

Considering only welds having compositions close to those of commercial alloys (group 3), the predictive accuracy of the DeLong-type equation improved. The FN1 equation, however, was a slightly better predictor of FN than the DeLong-type equation for this data group.

The FN2 equation was developed from weld data sorted to include only those welds that had primary solidification modes. It was found that the coefficients within this equation changed with respect to those of the FN1 equation. Most notably, the coefficient for nitrogen increased, and the coefficient for carbon decreased.

IV. DISCUSSION

A. Strength

1. Stress–Strain Curves

The changing character of the stress–strain curves plotted in figure 17 indicates that the 4-K stability of the welds with respect to martensitic transformation is increasing with nitrogen and manganese alloy content. The three-stage curve representing alloy 1 resembles the curve typifying 18Cr–8Ni stainless steel base material (figure 5). At low nitrogen and manganese contents (alloy 1), deformation occurring at low strain required only slight increases in stress to continue. It has been proposed that deformation at nearly constant stress is possible in stainless steel base materials due to the formation of bcc martensite at slip-band intersections.[50] The laths act as "dislocation windows" between slip planes and enable the deformation process to continue without work hardening. The increased work-hardening rates at higher strains are associated with hcp martensitic formation. Although the curves are only approximations and the work hardening rates are somewhat uncertain, it is clear that increasing the manganese content, nitrogen content, or both alters the deformation process in the weld metal. The absence of the "easy glide" region for these alloys would be attributed to the suppression of bcc martensite formation at high interstitial and solid-solution alloy content.

In alloy 1, following the "easy glide" region, the substantially higher rate of work hardening is associated with a higher percentage of austenite to martensite-transformation. In the more stable alloys (10, 12, and 19), however, there is still appreciable martensitic transformation occurring. Alloy 22 (0.259 wt.% nitrogen, 9.7 wt.% manganese) is on the verge of being completely stable. In agreement with the finding on base metals, the work hardening rate decreases with increasing austenite stability.

2. Yield and Tensile Strength

The 4-K yield strength as a function of alloy content was expressed reasonably well by equations 6 and 7. Equation 7, by also including manganese and molybdenum factors, was a better fit to the data.

$$\text{Weld 4-K Yield Strength (MPa)} = 334 + 3407(\text{wt.\% N}) + 15(\text{wt.\% Mn}) + 46(\text{wt.\% Mo}). \quad (7)$$

Large intercept and error values, however, point out that slight variations in ferrite, chromium, and carbon contents are influencing the strength and are beyond the resolution of this study. Nonetheless, it is clear that interstitial nitrogen is the dominant strengthener and that molybdenum has slightly more strengthening power than manganese. The relative magnitude of the nitrogen coefficient proposed in equation 7 is supported by studies on 18Cr–8Ni base material[2] and on 19Cr–14Ni SMA weld metals.[56]

Base Material 4-K Yield Strength (MPa) = 350 + 3400(wt.% N). (20)

19Cr–14Ni SMA Weld Yield Strength (MPa) = 145 + 3441(wt.% N) + 25(wt.% Mo) + 15(wt.% Mn) + 8122(wt.% C). (21)

where F = 2416, R^2 = 0.997, and STD = 12 MPa for equation 21.

The molybdenum coefficient of 46 proposed by this study appears too high when compared to that of equation 21. Because of the limited number of molybdenum alloys tested, it has the most uncertainty associated with it. There is some indication, however, that the strengthening potential of molybdenum decreases as nickel contents increase at 4 K.[57] This would support the finding of a larger coefficient for molybdenum at 9 wt.% nickel than at 14 wt.% nickel.

Other interactions between compositional elements that alter the strengthening character for one alloying element as a function of overall alloy content may also exist. For example, in figure 20 the slopes associated with the strengthening power of manganese appear to decrease as the nitrogen is increased from 0.05 to 0.10 to 0.15 wt.% levels. This implies that the strengthening coefficient of 15 attributed to manganese in equation 7 represents the average effect of manganese throughout the nitrogen range of the test matrix. The actual coefficients may vary depending on nitrogen content. Possibly a more accurate expression of yield strength as a function of composition would need to have manganese–nitrogen, molybdenum–nickel, and additional cross terms associated with it. For a nitrogen SMA weld having approximately 3 wt.% manganese and a low molybdenum content, however, it is felt that equation 7 would predict the 4-K yield strength accurately.

The results showed that variations in the 4-K tensile strength are not statistically related to alloy contents. For example, alloy 1 (1.57 wt.% Mn, 0.047 wt.% N) and alloy 22 (9.72 wt.% Mn, 0.259 wt.% N) had respective tensile strengths of 1586 and 1498 MPa. Inhomogeneities within the weld structures, as shown in figures 32 and 33, and variations in ferrite contents are suspected to be masking any effect that manganese, molybdenum, or nitrogen have on the 4-K tensile strength. Recent studies conducted with fully austenitic weld metals show that tensile strength increases slightly with increasing nitrogen content.[56]

In summation, as the interstitial and solid-solution alloy content increased in the welds, the yield strength increased linearly and the tensile strength remained relatively constant. The fact that the strengthening coefficient defined for nitrogen in this study agrees well with those found in base metals and other stainless steel weld compositions implies that nitrogen additions act principally in an interstitial strengthening capacity. If appreciable amounts of nitrides or other possible forms for nitrogen in the microstructure were being formed, a difference in nitrogen strengthening as a function of overall weld composition might be expected. The relatively small influence of alloy additions on the fracture stress and strain points out that the failure mode (void nucleation and growth) was not altered by increased alloy contents.

B. Toughness

There are two types of questions raised by the Charpy V-notch test results in this study. Questions in the first category are related to the differing results, concerning the effect of nitrogen on toughness, found from absorbed energy versus lateral expansion measurements. Should the relationship between these measurements of toughness be linear? If they should, which alloy compositions deviate from the expected trend and why? Questions within the second category are related to the more specific effects of compositional on the toughness. In particular, is the dramatic decrease in absorbed energy found at high molybdenum contents real?

1. Differences between Measures of Toughness

Addressing the question of linearity between lateral expansion and absorbed energy first, the data from this study are compared with data from a study[27] in which linear relationships were proposed for SMA type-308 and type-316 stainless steel welds at 76 K. In figures 35 and 36 the data sets are shown plotted as absorbed energy versus lateral expansion. Lines representing the expected linear relationships are also shown in the figures. It should be noted that data plotted here from the Szumachowski–Reid studies were selected to correspond to the nickel and ferrite contents of the welds tested in this study (Ni 9 wt.%, FN < 6). The compositions of these welds are given in table 8. From the type-308 and -316 stainless steel trend lines alone, one would suspect that the welds which deviate from the expected trends would be those making up the knee of the curve. In both data sets these welds tend to be of medium nitrogen content (0.08 to 0.15 wt.%) and have substantial manganese content, molybdenum content, or both.

Because both data sets show tendencies toward the same type of deviation from the proposed linear relationship between lateral expansion and absorbed energy, it is concluded that linearity between these two measures of toughness from the Charpy V-notch test should not be expected for highly alloyed welds of varying composition.

It is felt that the differences between these two measures of toughness can be related, at least in part, to the varying strengths of the alloys tested. In steels for example, as discussed in the introduction, material of increasing strengths have similar absorbed energies but decreasing lateral expansion values. This is because absorbed energy is defined by the product of force times distance, whereas lateral expansion is a direct measure of ductility. Although ultimate strength is traditionally used in these arguments, a similar trend might be expected for increasing flow strengths $[(\sigma_y + \sigma_T)/2]$.

Because these two measures of toughness differ for the alloys, both types of results deserve equal attention. Relationships between fracture toughness and impact test results are not known at this time. So even though lateral expansion is a more direct measure of ductility, absorbed energies may relate additional information concerning crack growth.

2. Effects of Alloying on Toughness

The lateral expansion results (figure 22) clearly show that as nitrogen contents increased, notch ductility decreased. At nitrogen levels greater than 0.16 wt.%, the absorbed energy results also show the adverse effect of nitrogen on toughness (figure 21). At lower nitrogen contents, the absorbed energy results are somewhat more difficult to interpret. Considering alloys 1 and 7, for example, which have approximately 1.5 wt.% manganese, a 12-J decrease in absorbed energy per 0.1 wt.% nitrogen was found. This agrees well with the data of Szumachowski and Reid.[4] Trends indicated by alloys 11, 17, and 18 or alloys 4, 9, and 12, however, imply that the detrimental effect of nitrogen on toughness for higher manganese alloy contents was reduced. Similar trends were indicated by the lateral expansion results. The lateral expansion was shown to decrease as manganese contents increased at a given nitrogen level, but at approximately 1 wt.% nitrogen, the increase in manganese content from 1.5 to 3 wt.% did not result in additional notch ductility losses. Increasing manganese contents further at this nitrogen level to increase strength resulted in nearly equivalent losses in toughness on a percentage basis.

In a more general manner, equation 9 can be used to compare the relative effects that nitrogen, manganese, and molybdenum have on notch ductility.

$$\text{LE at } 76\ \text{K (mm)} = 0.78 - 1.8(\text{wt.\% N}) - 0.03(\text{wt.\% Mo}) - 0.02(\text{wt.\% Mn}). \quad (9)$$

For example, losses in lateral expansion of 0.15 and 0.36 mm, respectively, would be predicted if the lowest manganese and nitrogen concentrations in the test matrix were increased by a factor of 5. This translates to approximate losses in lateral expansion of 33 percent for the 7.5 wt.% manganese alloy and 51% for the 0.2 wt.% nitrogen alloy. The significant predicted loss in lateral expansion due to manganese again points out that optimization of solid-solution alloy contents with respect to nitrogen content deserves future consideration. Overall, the equation expresses that nitrogen has the most detrimental effect on lateral expansion, followed by molybdenum, and then manganese. As might be expected, nitrogen effected the greatest increase in strength, followed by molybdenum, and then manganese (equation 7).

Compositional coefficients in equation 9, however, only represent the averaged effects of these elements on toughness. The molybdenum coefficient in particular is somewhat uncertain, since at 3.84 wt.% a sudden decrease in toughness was found and a limited number of molybdenum alloys were tested. This may skew the results and misrepresent the effect of molybdenum on the notch ductility.

The reason for the significantly lower toughness of the 3.84 wt.% molybdenum alloy was not clearly determined. The adverse effect of high molybdenum content, however, was confirmed by testing a second weld whose

composition was similar to that of alloy 6. In an effort to understand the degradation associated with these higher molybdenum alloys, segregation, microstructural, and fractographic studies were conducted.

Welds 6 and 13 had very similar compositions with the exception of their chromium and molybdenum contents. Weld 6, a 15 wt.% chromium and 3.84 wt.% molybdenum alloy, had an absorbed energy of 16 J. Weld 13, a 18 wt.% chromium and 1.66 wt.% molybdenum alloy had an absorbed energy of 33 J. The loss in absorbed energy of approximately 50 percent is attributed to the increase in molybdenum from 1.66 to 3.84 wt.%. Microstructurally, the welds were very similar. During examinations with a light microscope, both welds were found to have roughly equivalent ferrite contents and primary ferritic solidification morphologies. No evidence of intermetallic phases was found. X-ray analyses of chemically polished weld surfaces were inconclusive. Inclusion counts on polished surfaces by SEM did show that the high molybdenum weld had a slightly different inclusion size distribution that of other welds analyzed from the test matrix. It had a larger number of small-diameter inclusions and a higher volume fraction of inclusions. Examination of tensile and Charpy V-notch fracture surfaces showed that all welds failed in a ductile manner by microvoid coalescence. The 3.84 wt.% molybdenum samples, however, had some very large inclusions on their fracture surfaces (figure 28). These inclusions had: diameters ranging from 20 to 100 μm; compositions rich in calcium, manganese, silicon and titanium; and glassy, conchoidal fractures associated with them. It might be speculated that the difference in the 3.84-wt.% molybdenum-sample inclusion-size distributions may be related to changes in the weld pool viscosity. Molybdenum has a high melting point (2610°C). This may increase the solidus temperature of the system and result in an increased weld-pool viscosity. In this case, there would be less opportunity for small inclusions to coalesce and a larger chance for large inclusions to be trapped. Whether the presence of more small- and large-diameter inclusions in alloy 6 was solely responsible for lowering the toughness in these samples is not known.

In these final paragraphs of this section, the strength–toughness relationship determined for the weld metals is summarized. The inverse relationship found between lateral expansion and yield strength at 4 K (see figure 23) was best expressed by equation 10:

$$\text{LE (mm at 76 K)} = 0.95 - 6 \times 10^{-4} \text{ (Yield Strength, MPa)} \qquad (10)$$

Perhaps most importantly, this equation shows that notch ductility is principally a function of strength. Interstitial strengthening elements, such as nitrogen, greatly increase strength and reduce notch ductility proportionately. Solid-solution-strengthening elements, such as molybdenum and manganese, strengthen the weld metal to a much lesser extent. Therefore, they are less detrimental to the notch ductility. Other equations developed in the study (7 and 9) serve to help quantify the relative effect of the alloying elements on strength and toughness. Previous discussions have pointed out that optimizing manganese contents at a given nitrogen level may slightly increase toughness and that molybdenum contents near 4 wt.% may severely decrease toughness in type-18-8 stainless steels weld

deposits. Overall, however, the alloys tested in this study deviate little from the linear relationship between lateral expansion and yield strength defined by equation 10. To significantly improve this relationship, factors other than manganese, nitrogen, and molybdenum alloying effects must be considered.

Comparing the toughness values of the welds tested in this study with those of the typical type-316LN stainless steel base material shows that the strength–toughness relationship determined for these welds is too low. At a 1000-MPa yield strength the base material would be expected to have Charpy V-notch absorbed energy and lateral expansion values of approximately 90 J and 1.0 mm, respectively. The toughest weld (alloy 12) tested in this study, with a yield strength above 1000 MPa, had an absorbed energy value of 37 J and a lateral expansion value of 0.32.

Areas of study that may result in further toughness increases in SMA type-18-8 stainless steel welds include methods to lower the weld metal inclusion contents. Like inclusions, the ferrite content of the weld metal also influences toughness. Although void nucleation did not occur at the ferrite–austenite interface in this study, figures 25 and 26 imply that the ferrite may play an important role during void growth owing to its influence on plastic flow in the matrix.

The importance of controlling and predicting the FN for weld metal alloys is demonstrated by (1) ferrite affected fracture surface appearances for the low FN weld matrix test in this study, and (2) increased ferrite contents reduced toughness in previous studies.

C. Ferrite-Number Prediction

The four FN predictive equations developed in this study (FN1, FN2, FN3, FN4) are discussed in this section. The accuracy of predicting FN using the FN1 linear equation form is compared in detail with the accuracy of FN prediction using previously developed equations. The FN2, FN3, and FN4 equations are discussed to highlight the further improvements in FN prediction that are possible by the use of nonlinear equation forms and the consideration of weld solidification mode prior to analysis. Before beginning the discussion, however, factors complicating the comparisons between the predictive equations need to be identified.

1. Fairness of Comparisons between Equations

Several factors complicate any direct comparisons between equations developed in this study to previously existing equations. As shown in the results (table 7), equations representing the DeLong diagram (FNCD, FNCDK) and the equation incorporating the Hull coefficients (FNCH) are treated as a single variable by the regression program. They are fitted with slopes and intercepts that improve their fit to the data. Therefore, the statistics that characterize the significance of these equations are overestimates.

However, this error is partially balanced by the fact that mathematical expressions representing each diagram differ slightly from the actual diagrams. For example, these equations do not duplicate the slightly decreasing slopes and spacing between increasing constant FN lines of the original DeLong diagram.

Since the error between the DeLong-type equations and the DeLong diagram is small at FN values less than 10 and most of the data in this study have FN values close to or less than 10, the error associated with this factor is believed to be small. For this reason, figures representing the DeLong-type equation are used in this discussion. It is believed that they enable the most direct comparisons between equations to be made. These figures represent the equations without the added complication of the regression program making adjustments to their respective fits.

2. Ferrite-Number Equations

a) Linear Equations

The DeLong nickel and chromium equivalents, developed for low nitrogen-manganese alloys, increased the error associated with FN prediction in more highly alloyed weld metals. The DeLong manganese term (0.5 * Mn) was a major contributor to the errors in FN prediction. In figure 37, a large number of weld compositions having ΔFN errors greater than ± 5 are positioned at the upper left portion of the data. After substitution of the 0.34 constant for the DeLong manganese term, most of the error associated with this region is eliminated (figure 38).

By representing the austenitizing power of manganese as a constant, the tendency to underestimate the predicted FN is reduced for high manganese alloys. Still a substantial number of high ΔFN error exists in figure 38. By using equation FN1, further reductions in the remaining high ΔFN errors were made, as shown in figure 39. Approximately 75 percent of the welds had predicted FN values within 2 ΔFN when the FN1 equation was used. Using either the FNCD or FNCDK expressions, only around 50% of the data fell within this error range (figure 40). The most significant improvement, resulting from the replacement of the DeLong manganese term by the 0.34 constant in the FNCDK expression, was the reduction of the greater than 5 ΔFN error from 20% to almost 10%. Many of the welds that had been in this high ΔFN error group were moved into the $3 < \Delta FN \leq 5$ error group. Since neither the FNCDK nor the FN1 equations have manganese terms, further reductions in ΔFN error found when the FN1 equation was used are attributed to differences between other terms in the two equations.

Comparison of individual compositional coefficients between equations is difficult. The magnitudes of the coefficients within a given equation are relative to one another and the intercept values between equations vary. In table 9, the unfactored coefficients for the various equations are given, however, and interestingly the coefficients for nickel are quite similar. The chromium coefficient, or more importantly the difference between the

chromium and nickel coefficients, is the greatest for the DeLong-type expressions. If the 3.5 chromium coefficient is incorrect, terms within the nickel equivalent expression must have increased magnitudes to offset the error. If the nickel coefficient is approximately correct, this leaves the nitrogen, carbon, and manganese terms responsible for much of the correction.

Examining the compositional coefficients within the various predictive equations showed that many of the DeLong coefficients do not adequately model compositional effects on FN. The 3.5 chromium coefficient, for example, resulted in increasingly positive ΔFN deviation as the chromium content was increased (figure 41). For chromium equivalent components, positive ΔFN error implies that the coefficients are too high. The opposite is true for nickel equivalent terms. The ferritizing power of chromium was modeled better by the FN1 equation in figure 42. In this equation the chromium coefficient is lower and there is less difference between its magnitude and that of the nickel coefficient. These results imply that the FN predictive equations in which the respective ferritizing and austenitizing powers of chromium and nickel are similar in magnitude can more accurately predict FN.

The effects of molybdenum on FN, as modeled by the different predictive equations, were examined in figures 43 through 46. In figures 43 and 44, wt.% molybdenum is plotted versus ΔFN. No clear correlation between molybdenum and ΔFN deviations for either FNCD or FN1 was noted when the duplex stainless steel compositions and other very high molybdenum–chromium contents were ignored (figure 45). When the high molybdenum–chromium alloys were included (figure 46), the nonlinear relationships between ΔFN and molybdenum content could not be modeled by a simple compositional term. It appears that accurate prediction of FN in high chromium–molybdenum alloys requires that nonlinear interaction terms be incorporated into the equation. A final observation with respect to these figures: the DeLong-type expression causes the data to be offset to a relatively constant positive ΔFN value. The FN1 equation positions the data more symmetrically about the 0 ΔFN line. This is evidently due to a difference in intercept values between the two equations.

The nitrogen coefficients in the nickel equivalent terms are evaluated next. A trend toward increasingly negative ΔFN deviations was found when the FNCDK expression was used to predict FN (figure 47). The DeLong nitrogen coefficient of 75 is shown to be too high by this result. Figure 48 shows that the FN1 equation with its lower nitrogen coefficient is a better model of the effect of nitrogen on FN. Again, additional figures to help identify the high chromium–molybdenum (figure 49) and duplex stainless steel data (figure 50) are presented. Probably the most noticeable difference in the nitrogen coefficients of equation FN1 and the DeLong-type of equation is that in the FN1 equation, nitrogen was modeled as being only half as powerful as an austenitizing agent as carbon, and DeLong's coefficients attribute equivalent austenitizing powers to the two elements.

The ΔFN error associated with the use of the (0.5 * Mn) DeLong manganese term is again shown to be significant in figure 51. Clearly, large ΔFN errors result when this coefficient is used in the prediction of FN for alloys having high manganese content. Although the absence of a manganese term in FN1 greatly reduced predicted FN error (figure 52), the true effect of manganese on FN has not been identified by the equation. The modeling of the manganese effect by the Hull equation (FNCH) may come closer to expressing the true effect of manganese on FN. As manganese content increases, the negative manganese-squared term reduces the effect on FN. The change in the austenitizing power of manganese reflected in the FNCH expression is supported by solidification studies.[32] The correct modeling of higher order terms, such as these and interactions between compositonal elements, is difficult. This approach is discussed further when the nonlinear equation forms developed in this study are presented.

The FN1 equation indicated that the DeLong coefficient for silicon is too high and that the effect of titanium on FN may be substantial. For better definition of the effects of these elements on FN, however, additional data would be required.

b) Special Cases

Equation FN1 predicted FN better when only welds of conventional alloy (group 3) content were used to compare fits between it and the DeLong equation. The differences between the predictive abilities of the respective equations, however, were greatly reduced when only low nitrogen and manganese contents were allowed. Two important points were brought out by this comparison: (1) the DeLong diagram is an accurate method of predicting FN for alloys within its suggested compositional range, and (2) that FN1 was developed over and extended compositional range has not lessened the ability for this equation to accurately predict FN in the more commonly used stainless steel alloys.

In figures 53, 54, and 55, the relative accuracies of the FN predictive equations are compared using type-308, -309, and -316 stainless steel welds. For type-308 and -316 stainless steel weld deposits, both the DeLong-type equation and the FN1 equation predicted FN values within 3 FN of the measured values for over 95 percent of the welds considered. For type-309 stainless steel alloys, however, the DeLong-type equation predicted FN within the 3 FN range for only 53 percent of the welds. The FN1 equation remained accurate within the 3 FN range for 95 percent of the type-309 compositions considered. So, the FN1 equation has, to some degree, increased the accuracy of FN prediction for the low alloy compositions.

Welds used to develop the FN1 equation were also separated on the basis of solidification mode by using the Suutala equation. Welds identified as having primary ferritic solidification modes were then used as the data for further linear regression analysis. The FN predictive equation determined using this data (group 4) was FN2. Comparing equation FN2 to FN1: the difference between the chromium and nickel coefficients decreased; the

relative austenitizing power attributed to nitrogen increased; and the austenitizing power attributed to carbon decreased. Although the reported R^2 and F values are similar for the two equations (the lower number of cases analyzed for FN2 tends to lower the F), the decrease in the standard estimate of error and the differences between compositional coefficients are believed to be significant.

The question raised here is: can welds having different modes of solidification have their FN values predicted by the same equation? It seems that FN cannot be singularly defined in terms of composition until this ambiguity is dealt with. Primary ferrite and austenitic solidification modes result in two physically distinct forms of ferrite.

c) Nonlinear Equations

An attempt was made to improve the fit for the extended data (group 1) by allowing nonlinear terms. Equations FN3 and FN4 are discussed here to help identify alternate FN predictive equation forms and possible interaction terms which may be necessary for better prediction of FN.

The FN3 equation was developed after variables expressing interactions between compositional elements and self-interactions were permitted as choices during the regression using data group 1. This equation was the most accurate predictor of FN for both the group 1 and the group 2 data. Although the FN3 equation improves FN prediction, it is presented here only to indicate the types of interaction terms that were consistently deemed significant during the regressions. Principally, titanium–carbon, manganese–nitrogen, nickel–nitrogen, nickel–manganese, chromium–molybdenum, and nickel–chromium interactive variables were chosen during the regression.

Indications of the occurrence of interactions between compositional elements in the literature supports the complex nonlinear form of equation FN3. The work done by Strauss and Maurer[41] shows chromium to behave in a nonlinear manner with respect to nickel and ferrite formation. Previous evaluation of the manganese–nitrogen test matrix used in this study by Lake[42] suggested that including $Mn - Mn^2 - MnN + (MnN)^2$ terms to represent a nitrogen–manganese interaction best enabled FN to be predicted. In figure 56, a contour map of the nickel equivalent incorporating these terms expresses that the austenitizing power of manganese changes at approximately 4 to 5 wt.% and that as nitrogen content increases, the effect of manganese is reduced. Solidification studies done by Suutala[40] support the empirical results of Lake and other similar findings.[44,54]

Inclusion of interaction terms such as these can clearly increase the accuracy of FN prediction. The complexity of equation FN3, however, introduces uncertainty about which terms are truly expressing actual interactions. For example, if an interaction term is added to the equation incorrectly, then other complex terms need to be added to correct for the error. For this reason, the primary element coefficients must first be properly defined and possible interactions existing between primary elements

identified scientifically before the empirical development of more complex FN equations is appropriate.

FN4 was developed using only primary compositional terms. This equation has the pseudo polar form of the Schaeffler equation. This form is of interest because it can model the changing slopes and spacing of constant FN lines found on DeLong- and Schaeffler-type diagrams. Using only simple variables such as FN1, it is suspected that this equation form can improve the accuracy of FN prediction. Although the equation form was difficult to refine using linear regression techniques, by assuming values for the coefficients and constants included in the chromium and nickel equivalent expressions, FN4 predicted FN better for data group 2 than FN1. The analysis indicated that particularly the nitrogen and titanium coefficients required adjustment. However, nonlinear regression analysis can model the coefficients better and develop a better predictive FN equation.

3. Physical Significance

Clearly, it is more difficult to identify the nonlinear equation forms and interaction terms that lead to improved FN prediction. Yet, one anticipates nonlinear behavior in complicated systems, so the eventual development of these complex equations will not only improve the accuracy of FN prediction, but will bring physical significance to these empirical expressions.

Ultimately, FN predictive equations should take on forms suggested by the fundamental thermodynamic and kinetic considerations. A form suggested by Liu et al.[39] to provide more fundamental guidelines for future predictive equation development is:

$$FN = K_{Ni}\,Ni + K_{Mn}\,Mn + K_{Cr}\,Cr + K_{N}\,N + K_{i}\,i + K_{Ni\text{-}Mn}\,MnNi + K_{Ni\text{-}Cr}\,NiCr + K_{i\text{-}j}\,i_j. \quad (5)$$

where the coefficients (K_i) include thermodynamic effects such as the configuration of atoms in the solution and parameters that compare bonding energies between dissimilar and like atoms. In addition to defining the equation coefficients, equation 5 also indicates that both linear and nonlinear contributions are important.

Terms in equation 5, such as K_{Ni} Ni and K_{Cr} Cr, have long been recognized as important to austenite–ferrite stability. Nickel, for example, is an austenitic stabilizer and segregates preferentially to austenitic regions during solidification. In austenitic stainless steel compositions, however, alloy contents exceed those valid for dilute solutions, and therefore, linear behavior should not be expected. Interactions between alloying elements in these complex solid solutions may occur and are indicated by terms in equation 5 like $K_{Ni\text{-}Mn}$ Ni Mn. Proper incorporation of these interactive terms into fundamental equation forms may help indicate the extent of clustering, compound formation, and other types of interactions existing among atoms in these stainless steel compositions.

In this study, the inclusion of interstitial-substitutional interactive terms, such as N Mn and Ti C, improved FN predictive accuracy. From a metallurgical viewpoint, elements such as titanium and carbon can interact to form a new phase by the following reaction:

$$Ti + C = Ti\ C. \qquad (22)$$

The equilibrium constant for this reaction can be represented by:

$$K = \frac{[Ti\ C]}{[Ti][C]}, \qquad (23)$$

where the brackets represent the concentrations of the various components. This indicates that the product of the concentrations of these two elements is directly related to the formation of this phase, and if this phase occurs in stainless steel welds, such an interaction term should be included in an FN predictive equation. Similar interactive terms would be expected for other reactions, intermetallic compounds, and ordered structures.

In ferritic phases, these types of interactions have been confirmed in metallurgical studies.[59] Internal friction studies in commercial steels have shown that carbon and nitrogen interstitial atoms hold manganese, titanium, and other substitutional atoms in close association.[60] Clusters of carbon and nitrogen have been observed about titanium atoms in Fe–0.15 Ti alloys by a field ion microscope atom probe.[61] The improvements in FN prediction found in this study by the inclusion of interstitial-substitutional interactive terms implies that similar associations are present in stainless steel alloys. Suspected interactions between nitrogen and manganese in the mechanical portion of this study support this premise.

In the case of the titanium–carbon interactive term, the precipitation of titanium carbides must be considered in the FN predictive equations. If some portion of the titanium and carbon is removed from their respective roles during solidification by formation of a precipitate, then the effects of these elements on the ferrite content must also be reduced.

Interactions between unlike substitutional atoms were also indicated in this study. Most notably, the chromium–molybdenum interaction. It is difficult to speculate on the specific significance of this interaction. The nonlinear trends observed in figure 46, however, indicate that the interaction has a pronounced effect on FN.

Although the interactive terms developed in this study are not proposed for use at this time, they may identify some of the more important interactions occurring between the alloying elements in stainless steels. Until all the pertinent linear and nonlinear contributions made by these alloying elements are determined and incorporated into a fundamental equation form such as equation 5, more specific information regarding the physical significance of these equations will be unobtainable.

V. CONCLUSIONS

1. The yield strength at 4 K for welds evaluated in this study can be expressed by the equation:

$$\text{Yield Strength (MPa)} = 334 + 3407N + 15Mn + 46Mo \quad (7)$$

2. The notch ductility at 76 K for the welds evaluated in this study was found to be principally a function of strength:

$$LE\ (mm) = 0.95 - 6 \times 10^{-4}\ (\text{Yield Strength, MPa}) \quad (10)$$

3. Molybdenum additions approaching 4 wt.% can severely reduce toughness in type-18-8 nitrogen–manganese stainless steel weld metals.

4. The DeLong diagram was quite accurate in predicting FN for type-308 and 316 stainless steel compositions, but had to have an average error near 2 FN for type-309 alloys.

5. An improved predictive equation was developed having chromium and nickel equivalents similar in complexity and form to the DeLong equivalents.

$$FN1 = -15.2 + 2.2[Cr + Mo + 0.5Si + 15Ti + 0.8Cb] - 1.9[Ni + 17N + 30C]. \quad (14)$$

This equation predicted FN better than the DeLong diagram for common alloy compositions. The equation was substantially better than the DeLong diagram in predicting the FN of alloys with extended manganese and nitrogen contents.

6. The accuracy of FN prediction can be improved further by investigating the following topics:

   a. The grouping of welds by primary solidification modes prior to FN equation development

   b. The development of alternative, nonlinear equation forms

   c. The identification of important interaction terms to be included in predictive equations

   d. The adjustment of principal compositional coefficients, particularly for titanium

VI. ACKNOWLEDGMENTS

I am indebted to many people for guidance, support, and tolerance during the research for and preparation of this manuscript.

For financial support, I acknowledge the United States Department of Commerce, the United States Department of Energy, and the Welding Research Council Subcommittee on Stainless Steel Welding.

For keeping the study on track, I owe much to the guidance of Tom Siewert, Dave Olson, and Dave Matlock.

For tolerance, above and beyond the call of duty, I owe special thanks to: my wife Linda, my daughter Kimberlie, my parents, coworker Bob Walsh, and typist Chris King.

VII. REFERENCES

1. McHenry, H. I., Read, D. T., Steinmeyer, P. A., "Evaluation of Stainless Steel Weld Metals at Cryogenic Temperatures," in Materials Studies for Magnetic Fusion Energy Applications at Low Temperatures—II, NBSIR 79-1609, National Bureau of Standards, Boulder, Colorado, 299 (1979).

2. McHenry, H. I., Elmer, J. W., "Fracture Properties of a 25 Mn Austenitic Steel," in Materials Studies for Magnetic Fusion Energy Applications at Low Temperatures—V, NBSIR 82-1667, National Bureau of Standards, Boulder, Colorado, 245 (1982).

3. Siewert, T. A., "How to Predict Impact Energy from Stainless Steel Composition," Welding Design and Fabrication 51(6), 88–90 (1978).

4. Szumachowski, E. R., Reid, H. F., "Cryogenic Toughness of SMA Austenitic Stainless Steel Weld Metal Part II—Role of Nitrogen," Welding Journal 58(2), 34s–44s (1979).

5. Mori, T., Kuroda, T., "Prediction of Energy Absorbed in Impact for Austenitic Weld Metals at 4.2 K," Cryogenics 25, 243–248 (1985).

6. Reed, R. P., Simon, N. J., "Low Temperature Strengthening of Austenitic Stainless Steels with Nitrogen and Carbon," in Advances in Cryogenic Engineering—Materials 30, Plenum Press, New York, 127–136 (1984).

7. Mazandarany, F. N., Parker, D. M., Koenig, R. F., Read, D. T., "A Nitrogen-Strengthened Austenitic Stainless Steel for Cryogenic Magnet Structures," in Advances in Cryogenic Engineering—Materials 26, Plenum Press, New York, 58–170 (1980).

8. McHenry, H. I., "Strength and Toughness Goals for Cryogenic Steels," in Materials Studies for Magnetic Fusion Energy Applications at Low Temperatures—VIII, NBSIR 85-3025, National Bureau of Standards, Boulder, Colorado, 121 (1981).

9. Peckner, D., Bernstein, I. M., Stainless Steel Handbook, McGraw-Hill, New York, 4-13 (1977).

10. Gunia, R. B., Woodrow, G. R., "Nitrogen Improves Engineering Properties of Chromium-Nickel-Stainless Steel," Journal of Materials 5(2), 413-430 (1970).

11. Enjo, T., Kikuchi, Y., Nagata, H., "Effect of Nitrogen Content on the Low-Temperature Mechanical Properties of Type 304 Stainless Steel Weld Metals," Transactions JWRI 11(2), 35-42 (1982).

12. Onishi, K., Miura, R., et al., "Effect of Carbon and Nitrogen Contents on the Mechanical Properties of SUS 304 and 316 Austenitic Stainless Steel at Low Temperatures Down to 4 K," Tetsu-to-Hagane 67(13), 271 (1981).

13. Fiore, N. F., Bauer, C. L., "The Binding of Solute Atoms to Dislocations," in Progress in Materials Science 16, Pergammon Press, New York, 85-134 (1968).

14. Reed, R. P., Simon, N. J., "Low Temperature Strengthening of Austenitic Stainless Steels with Nitrogen and Carbon," in Advances in Cryogenic Engineering—Materials 30, Plenum Press, New York, 127-136 (1984).

15. Ledbetter, H. M., Austin, M. W., "Dilation of an FCC Fe-Cr-Ni Alloy by Interstitial Carbon and Nitrogen."

16. Ledbetter, H. M., Austin, M. W., Kim, S. A., "Carbon and Nitrogen Effects on the Elastic Constants of a Stainless Steel at 4 K," Materials Science and Engineering, In press.

17. Humbert, J. C., Elliott, J. E., "The Solubility of Nitrogen in Liquid Fe-Cr-Ni Alloys," Metallurgical Transactions 218, 1076-1087 (1960).

18. Erasmus, L. A., Yang, L. J., "Strengthening Welds in Warm Worked Grades of Austenitic Stainless Steel by the Addition of Nitrogen to the Weld Metal," Welding and Metal Fabrication 38(7), 269-275 (1970).

19. Enjo, T., Kikuchi, Y., Kobayashi, T., and Kuwana, T., "Gas Shielded Welding of High-Nitrogen Stainless Steel," Transactions of JWRI 9(2), Osaka University Press, Japan, 12-19 (1980).

20. Mukai, K., Hoshino, K., Fujioka, T, "Tensile and Fatigue Properties of Austenitic Stainless Steel at LNG Temperature," Tetsu-to-Hagane 65(12), 1756-1765 (1979).

21. Ozeki, T., Ogawa, T., "The Solidification and Cryogenic Toughness of High Nitrogen Stainless Steel Weld Metal," in Group Welding Metallurgy Document, Nippon Steel Research Center, Japan, (1985) unpublished.

22. Sakamoto, T., Nakagawa, Y., Yamuchi, I., "Effect of Manganese on the Cryogenic Properties of High Nitrogen Stainless Steels," in Advances in Cryogenic Engineering—Materials 32, Plenum Press, New York, 65–71 (1986).

23. Yamamoto, S., Yamagami, N., Ouchi, C., "Effect of Metallurgical Variables on Strength and Toughness of Mn–Cr and Ni–Cr Stainless Steels at 4.2 K," in Advances in Cryogenic Engineering—Materials 32, Plenum Press, New York, 57–64.

24. Purtscher, P. T., Reed, R. P., "The Toughness of Austenitic Stainless Steels at 4 K," in Materials Studies for Magnetic Fusion Energy Applications at Low Temperatures—IX (NBSIR 86-3050), 53–88 (1986).

25. DeLong, W. T., Ostrom, G. A., Szumachowski, E. R., "Measurement and Calculation of Ferrite in Stainless-Steel Weld Metal," Welding Journal 35(11), 521s–528s (1956).

26. Read, D. T., McHenry, H. I., Steinmeyer, P. A. Thomas, R. D. Jr., "Metallurgical Factors Affecting the Toughness of 316L SMA Weldments at Cryogenic Temperatures," Welding Journal 59(4), 104s–113s (1980).

27. Szumachowski, E. R., Reid, H. F., "Cryogenic Toughness of SMA Austenitic Stainless Steel Weld Metals: Part 1—Role of Ferrite," Welding Journal 57(11), 325s–333s (1978).

28. Siewert, T. A., "Predicting the Toughness of SMA Austenitic Stainless Steel Welds at 77 K," Welding Journal 65(3), 23–28 (1986).

29. Ekstrom, U., Olsson K., "The Influence of Ferrite and Oxygen Contents on Weld Metal Mechanical Properties of Submerged Arc Welded Stainless Steel," in Proceedings of the Welding Institute Conference: Weld Pool Chemistry and Metallurgy, Discussion ISBN 0-85300-138-3, vol. 1, Paper 37, The Welding Institute, Cambridge, England, 80–81, 323–334 (1980).

30. Miura, R., "Development of High Strength Structural Alloys for Superconducting Magnets in Fusion Reactor." Unpublished.

31. Sakamoto, T., Abo, H., Okazaki, T., Ogawa, T., Ogawa, H., Zaizeu, T., "Corrosion Resistant Nitrogen-Containing Stainless Steels for Use by the Chemical Industry," in Alloys for the Eighties, Climax Molybdenum Company, 269–279 (1980).

32. McHenry, H. I., Read, D. T., and Steinmeyer, P. A., "Evaluation of Stainless Steel Weld Metals at Cryogenic Temperatures," in Materials Studies for Magnetic Fusion Energy Applications at Low Temperatures—II, NBSIR 79-1609, National Bureau of Standards, Boulder, Colorado, (1979).

33. Schaeffler, A. L., "Constitution Diagram for Stainless Steel Weld Metal," Metal Progress 85(7), 680 B (1949).

34. DeLong, W. T., "Ferrite in Austenitic Stainless Steel Weld Metal," Welding Journal 66:84p-92p (1987).

35. Long, C. J., DeLong, W. T., "The Ferrite Content of Austenitic Stainless Steel Weld Metal," Welding Journal 52(7), 281s–297s (1973).

36. Szumachowski, E. R., Kotecki, D. J., "Effect of Manganese on Stainless Steel Weld Metal Ferrite," Welding Journal 63(5), 56s–161s (1984).

37. Espy, R. H., "Weldability of Nitrogen-Strengthened Stainless Steel," Welding Journal 61(5), 149s–156s (1982).

38. Johnson, E. W., Hudak, S. J., "H_2 Embrittlement of Austenitic Stainless Steel Weld Metal with Special Consideration Given to Sigma Phase," Welding research bulletin 240, Welding Research Council, New York, (1978).

39. Liu, S., Matlock, D. K., Olson, D. L., "A Thermodynamic and Kinetics Approach in the Development of Expressions for Alloy Behavior Prediction," Colorado School of Mines (1985).

40. Suutala, N., "Effect of Manganese and Nitrogen on the Solidification Mode in Austenitic Stainless Ateel Welds," Metallurgical Transactions A13, 191–197 (1982).

41. Strauss, B., Maurer, E., "Die Hochlegierten Chromnickelstahle als Nichtrostende Stahle," Kruppsche Monatshefte 1(8), 129–146 (1920).

42. McCowan, C. N., Siewert, T. A., Reed, R. P., Lake, F. B., Welding Journal: in press (1986).

43. Hull, F. C., "Delta Ferrite and Martensitic Formation in Stainless Steels," Welding Journal 52(5), 193s–200s (1973).

44. Hammar, O., Svenson, U., Solidification and Casting of Metals, The Metals Society, London, 401–410 (1979).

45. Mel'Kumor, N., Topilin, V. V., "Alloying Austenitic Stainless Steel with Nitrogen," Obrabotka Metallor, 47–51 (August 1969).

46. Okagawa, R. K., Dixon, R. D., Olson, D. L., "The Influence of Nitrogen from Welding on Stainless Steel Weld Metal Microstructures," Welding Journal 62(8), 204s–209s (1983).

47. Olson, D. L., "Prediction of Austenitic Weld Metal Microstructure and Properties," Welding Journal 64(10), 281s–294s (1985).

48. Thielsch, H., "Physical Metallurgy of Austenitic Stainless Steels," Welding Journal 29(12), 577s–621s (1950).

49. Suutala, N., Takalo, T., and Moisio, T., "Ferritic–Austenitic Solidification Mode in Austenitic Stainless Steel Welds," Metallurgical Transactions A 11A, 717–725 (May 1980).

50. Reed, R. P., Tobler, R. L., "Deformation of Metastable Austenitic Steels at Low Temperatures," in Advances in Cryogenic Engineering—Materials 28, Plenum Press, New York, 49–56 (1981).

51. Read, D. T., "Mechanical Properties," Chapter 7 in Materials at Low Temperatures, Reed, R. P., Clark, A. F., Eds., American Soceity for Metals, Metals Park, Ohio, 248–249 (1983).

52. Gross, J. H., "The Effect of Strength and Thickness on Notch Ductility," Welding Journal 48(10), 441s–453s (1969).

53. Standard Procedures for Calibrating Magnetic Instruments to Measure the Delta Ferrite Content of Austenitic Stainless Steel Weld Metal, (ANSI/AWS A4.2-74), American Welding Society, Miami, Florida, (1974).

54. Specification for Corrosion-Resisting Chromium and Chromium–Nickel Steel Covered Welding Electrodes, (AWS A5.4-78), America Welding Society, Miami, Florida (1978).

55. Annual Book of ASTM Standards, Part 10, Metals—Physical, Mechanical, Corrosion Testing (E 23-72), ASTM, 273–293 (1980).

56. McCowan, C. N., Siewert, T. A., Kivineva, E., "Molybdenum in Stainless Steel SMA Welds for Cryogenic Service," Presentation AIME Welding Metallurgy of Structural Steels, Denver, Colorado, February 23–26, (1987), in press.

57. Purtscher, P. T., Reed, R. P., Advances in Cryogenic Engineering—Materials, Plenum Press, New York, To be published (1987).

58. Reed, R. P., "Martensitic Phase Transformations," Chapter 9 in Materials at Low Temperatures, American Society for Metals, Metals Park, Ohio, 303–307 (1983).

59. Leslie, W. C., The Physical Metallurgy of Steels, McGraw–Hill, New York, 136–139 (1981).

60. Dijkstra, L. J., Sladek, R. J., Transactions of the AIME 69, 197 (1953).

61. Hasson, D. T., Arsenault, R. J., Treatise on Materials Science and Technology, Academic Press, New York, 179 (1972).

Table 1. Various Coefficients for Manganese and Nitrogen Determined in Previous Studies

Researcher	Coefficient or Constant		Principal Matrix Variations (wt.%)	Comments
	N	Mn		
Schaeffler [33]	–	0.5 Mn	Ni (0 to 30)	308, 309, 310, 316, 410 and 502 stainless steels
DeLong [35]	30 N	–	N (0.03 to 0.22)	309, 308L, 316, 316L, 347 (low Mn) stainless steels
Hull [43]	18.4 N	0.11 Mn – 0.0086 Mn^2	Ni (0 to 22) Mn (0 to 20) N (0 to 0.15)	70 chill-cast stainless steel alloys. Mo, Si, V, W, Ti, Cb, Ta, Al, Co, Cu, C also varied. Cr = 14 to 20 wt.%
Espy [37]	30 (N-0.045) 22 (N-0.045) 20 (N-0.45)	0.87	Mn (5 to 12.5) N (0.13 to 0.33)	4 nitronic series alloys. N and Mn not varied systematically. The 3 N coefficients are for < 0.20, < 0.25, and < 0.35 wt.% N, respectively.
Hammar and Svenson [44]	14.2 N	0.31	Ni (9.0 to 14) N (0.01 to 0.20) C (0.04 to 0.10)	130 austenitic alloys (ingots). Mn content = 1 to 2 wt.% Cr = 17 to 25 wt.%
Mel'Kumor and Topilin [45]	20 N	–	Ni (10 to 16) N (0.05 to 0.46)	Austenitic stainless steel. 0.5 Mn, 25 Cr, 0.09 C
Szumachowski and Kotecki [36]	–	0.35	Mn (1 to 12)	308, 309L, 316L, 307 stainless steels. Low nitrogen (0.05 wt.%)
Okagawa et al. [46]	13.4 N	–	N (0.04 to 0.29)	GTA weld (no filler metal) on 304L stainless steel base metal. N added through shielding gas.

Table 2. The SMA Weld Metal Compositions for the Manganese–Nitrogen Test Matrix.

Alloy No.	C	Mn	Si	P	S	Cr	Ni	Mo	N	B	FN		
											Pad	Plate+	Calculated DeLong
1	0.033	1.57	0.29	0.013	0.006	17.58	9.19	0.02	0.047	#	2.8	4.9	1.35
2	0.034	1.49	0.34	0.020	0.006	15.37	9.06	2.03	0.034	#	3.4	4.4	2.2
3	0.034	3.23	0.39	0.014	0.006	17.87	9.02	0.02	0.035	#	4.0	4.7	2.07
4	0.036	6.54	0.37	0.015	0.007	17.61	9.13	0.02	0.046	#	2.8	4.2	−4.3
5R**	0.039	6.31	0.34	0.021	0.007	15.39	9.14	1.99	0.047	#	2.8	3.6	−5.4
5	0.039	6.31	0.34	0.021	0.007	15.39	9.14	1.99	0.047	#	2.8	3.6	−5.4
6A	0.036	6.27	0.34	0.027	0.007	15.17	9.14	3.84	0.162	#	2.6	2.9	−8.06
7	0.032	1.66	0.32	0.014	0.006	18.36	8.94	0.02	0.103	#	1.8	3.1	0.6
8	0.033	2.96	0.36	0.013	0.006	18.13	9.12	0.02	0.037	#	3.6	5.1	0.02
9	0.038	6.46	0.35	0.015	0.007	18.51	9.17	0.02	0.098	#	2.6	3.6	−5.35
10	0.037	9.52	0.38	0.017	0.009	17.71	9.10	0.02	0.106	#	1.5	2.7	−12.16
11	0.031	3.18	0.34	0.015	0.006	18.99	9.95	0.02	0.153	#	1.4	1.9	−2.93
12.	0.037	6.62	0.38	0.016	0.008	19.51	9.06	0.02	0.151	#	2.2	3.6	−5.53
13	0.035	6.61	0.32	0.021	0.007	17.77	9.10	1.66	0.166	#	2.5	3.5	−7.25
14	0.038	9.38	0.35	0.017	0.009	18.98	9.14	0.02	0.163	#	1.7	2.8	−12.16
15	0.032	6.11	0.36	0.016	0.007	20.90	9.29	0.02	0.252	#	1.6	2.0	−7.92
16	0.038	9.56	0.37	0.019	0.009	20.22	9.07	0.02	0.252	#	1.2	1.8	2.83
17	0.031	2.90	0.30	0.013	0.006	18.79	9.12	0.02	0.104	#	2.0	3.8	2.83
18	0.033	3.25	0.39	0.014	0.006	17.58	9.00	0.02	0.032	0.015	3.2	3.7	1.38
18R**	0.032	3.16	0.42	0.013	0.006	17.90	9.05	0.02	0.041	0.006	3.0	4.6	2.04
19	0.039	9.55	0.34	0.017	0.009	17.70	9.26	0.02	0.037	#	3.6	4.8	−7.81
20	0.033	3.10	0.36	0.015	0.006	17.75	9.07	0.02	0.152	#	0.8	1.0	−7.17
21	0.033	3.46	0.37	0.014	0.006	17.82	9.10	0.02	0.150	0.008	0.6	0.5	−7.25
22	0.032	9.72	0.34	0.018	0.009	17.60	9.06	0.02	0.259	#	0.2	0.7	−24.00

*Weight percent.
**Repeated welds.
+FN plate is the average of FN bead surface and FN impact specimen surface.
#Not determined.

Table 3. The Range of Composition for Weld Metals of the FN Test Matrix

Element	Range of Composition, wt.%			
	Min.	Max.	Mean	Standard Deviation
C	0.012	0.200	0.044	0.019
Mn	0.350	12.67	2.317	2.124
Si	0.150	0.940	0.456	0.147
Cr	14.74	26.90	20.31	2.360
Ni	4.610	33.50	11.27	2.286
Mo	0.010	6.850	1.102	1.381
N	0.019	0.300	0.080	0.045
Cb	*	0.880	0.030	0.106
Ti	*	0.540	0.020	0.034

*Not determined

Table 4. Definitions of the Notations Used to Identify the Previously Developed Ferrite-Number Predictive Equations

Equation Abbreviation	Description
FNCD	FN calculated using the DeLong equation form FNCD = − 30.7 + 3.5[Cr + Mo + 1.5(Si)] − 2.5[Ni + 30(n) + 30(C) + 0.5(Mn)]
FNCDK	FN calculated using the DeLong equation form but with the Szumachowski–Kotecki 0.34 constant substituted for the 0.5(Mn) term in the nickel equivalent
FNCH	FN calculated using the Hull equation form, FNCH = +2.88[Cr + 1.1(Mo) + 0.5(Si)] − 3.13[Ni + 18.6(N) + 24.5(C) + 0.11(Mn) − 0.0086(Mn^2)]

Table 5. Mechanical Property Test Results

Alloy	4-K Tensile Properties			76-K CVN Properties		
	σ_y, MPa	σ_T, MPa	Elongation, %	Reduction, %	LE,† mm	AE,‡ J
1	469	1586	26*	16.6	0.686	46
2	527	1570	20	13.5	0.711	39
3	504	1432	25*	23.8	0.584	41
4	455	1341	26	22.7	0.584	42
5R	619	1346	27*	18.0	—	—
5	665	1489	37	29.1	0.533	37
6	1169	1447	12	14.1	0.127	16
7	787	1412	21*	14.3	0.483	39
8	502	1387	24*	14.9	0.686	43
9	864	1410	24*	22.4	0.432	42
10	871	1395	32	23.8	0.406	37
11	932	1376	20	16.8	0.406	40
12	1020	1376	18.8	15.3	0.305	37
13	1129	1410	12.0	13.5	0.229	33
14	1075	1527	28.5	26.6	0.305	34
15	1344	1627	16.5	18.9	0.127	20
16	1306	1622	20.0	13.3	0.127	24
17	748	1438	25*	10.2	0.508	42
18	502	856	6.5	10.8	0.610	43
18R	491	1267	19*	14.5	0.610	38
19	635	1299	27	23.1	0.483	37
20	888	1261	16*	15.1	0.457	42
21	874	1125	11.3	9.6	0.432	41
22	1250	1498	15.5	15.4	0.152	21

*Fractured outside the gauge marks
†LE = lateral expansion
‡AE = absorbed energy

Table 6. The Ductile Dimple Densities of the Fracture Surfaces

Alloy	Specimen Type	Ductile Dimple Density per mm^2
1	4-K tensile	320,000
1	76-K Charpy	410,000
6	4-K tensile	440,000
6	76-K Charpy	440,000
21	4-K tensile	350,000
21	76-K Charpy	460,000

Table 7. Ferrite-Number Predictive Equations

Equation Number	Equation	Statistics			
		Cases	F	R^2	STD
	GROUP 2				
11	$FN = 4.48 + 0.34[FNCD]$	746	582	0.44	2.5
12	$FN = 2.43 + 0.51[FNCDK]$	746	930	0.55	2.2
13	$FN = -5.91 + 0.66[FNCH]$	746	869	0.54	2.2
14	$FN1 = -15.2 + 2.2[Cr + Mo + 15(Ti) + 0.8(Cb) + 0.5(Si)] - 1.9[Ni + 17(N) + 30(C)]$	746	1454	0.66	1.9
	GROUP 3				
15	$FN = 1.8 + 0.65[FNCD]$	582	999	0.63	1.8
16	$FN = 0.12 + 0.98[FN1]$	582	1143	0.66	1.7
	GROUP 4				
17	$FN2 = -14.6 + 2.4[Cr + Mo + 15(Ti) + 0.8(Cb) + 0.7(Si)] - 2.2[Ni + 23(N) + 27(C)]$	—	1215	0.67	1.7
	NONLINEAR				
18	$FN3 = 2.79[Cr + 0.7(Mo) + 15(Ti) + 0.8(Cb)] - 473(Ti \cdot C) - 0.002(Cr \cdot Mo)^2 + 0.0002(Cr)^2(Mo)^3 - 2.36[Ni + 31(C) - 22(N) - 0.05(Mn)] + 1.6(Ni)[C + 4(N) + 0.1(Mn)] - 7.9(Mn)[N - 0.2(Mn \cdot N)]^2 + 0.5(Mn)^{-1/2}$	746	2021	0.73	1.7
19	$FN4 = -45 + 32\left[\frac{2.3(Cr) + 2.4(Mo) + Si + 2(Cb) + 33(Ti) + 32}{2(Ni) + 57(C) + 29(N) + 47}\right]$				

Table 8. The Szumachowski–Reid Weld Compositions[27]

Alloy	C	Mn	Si	Cr	Ni	Mo	N	AE		LE		FN
								J	ft·lbf	μm	mil	
a	0.05	2.21	0.35	15.2	9.1	1.66	0.04	36.6	27.0	610	24.0	2.0
b	0.05	2.17	0.25	15.3	9.2	1.67	0.04	35.9	26.5	526	20.7	2.0
c	0.06	1.97	0.36	16.7	8.7	1.67	0.04	32.5	24.0	457	18.0	5.8
d	0.05	2.23	0.41	15.3	9.2	1.70	0.08	28.6	21.1	312	12.3	0.8
e	0.05	2.00	0.43	17.8	8.7	1.72	0.08	30.2	22.3	271	10.7	3.2
f	0.04	2.15	0.35	15.3	9.4	1.73	0.08	31.6	23.3	305	12.0	0.6
g	0.06	1.62	0.38	19.5	9.8	0.20	0.06	18.4	13.6	160	6.3	4.0
h	0.06	2.26	0.36	21.1	9.5	0.20	0.08	12.7	9.4	84	3.3	0.0

Table 9. The Unfactored Coefficients for the FN Predictive Equations

DeLong	3.5	3.5	5.2	1.7	—	−2.5	−75	−75	−1.3
FNCH	1.9	2.1	0.9	—	—	−2.1	−38	−50	$+0.2(\overline{Mn}) - 0.018(\overline{Mn})^2$
FN1	2.2	2.2	1.1	1.8	33	−1.9	−32	−65	—
FN2	2.4	2.4	1.6	1.9	35	−2.2	−50	−60	—

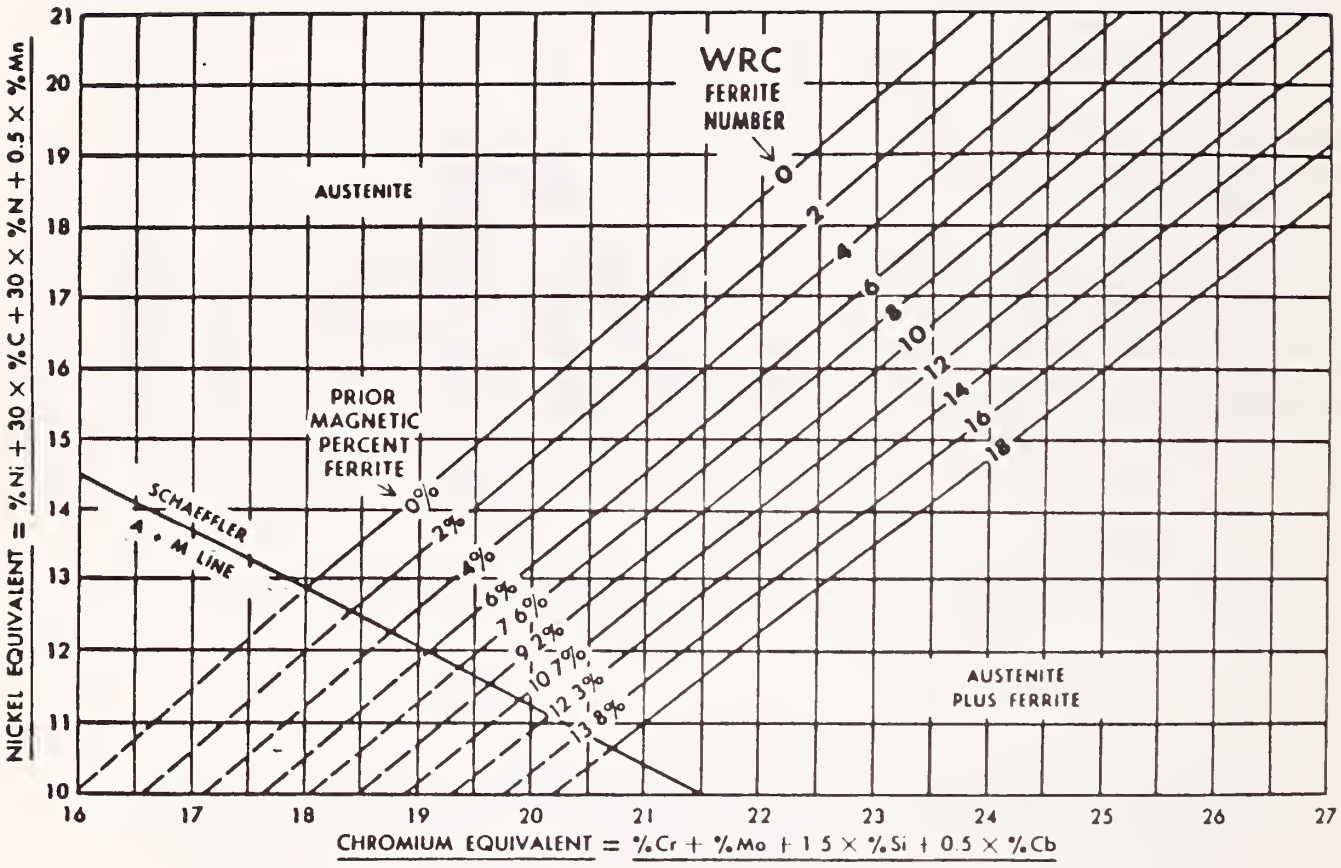

Figure 1. The Schaeffler constitutional diagram for stainless steel weld metal.[33]

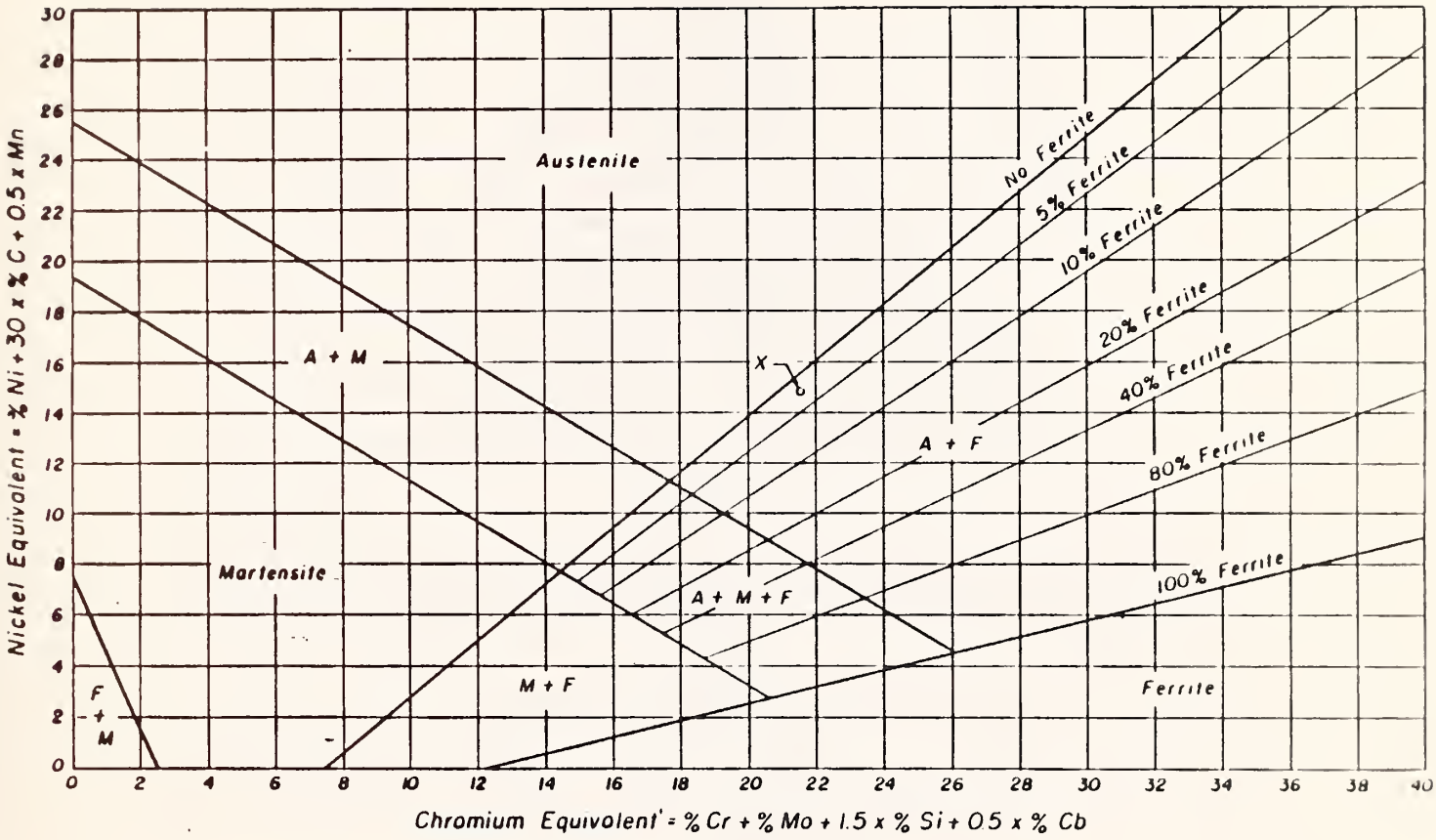

Figure 2. The DeLong constitutional diagram for stainless steel weld metal.[34,35]

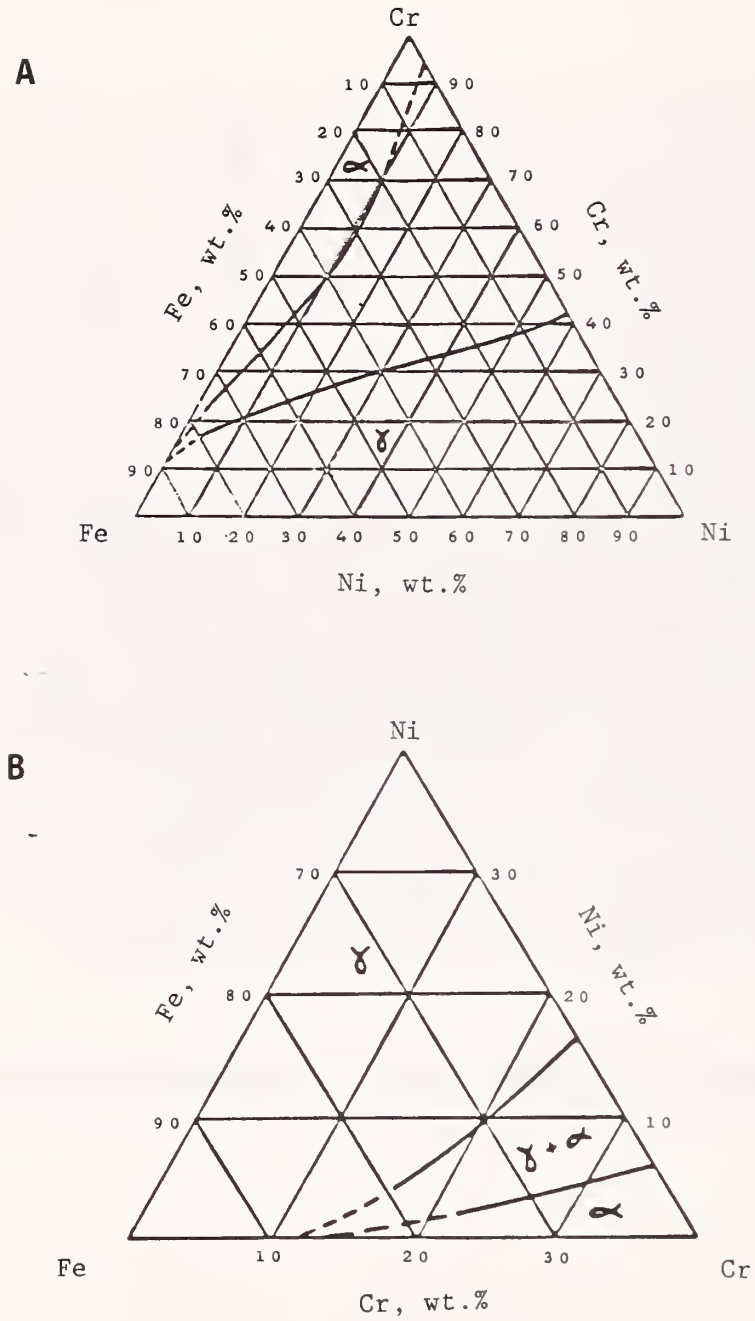

Figure 3. Isothermal diagrams at 1000°C from the Fe—Cr—Ni ternary diagram.

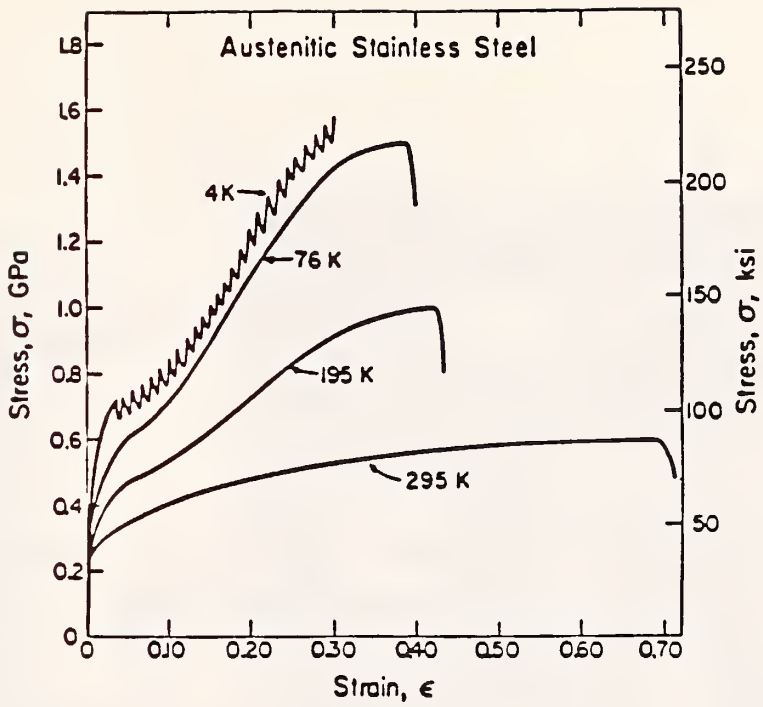

Figure 4. Stress–strain behavior of an 18Cr–8Ni austenitic stainless steel as a function of temperature.[50]

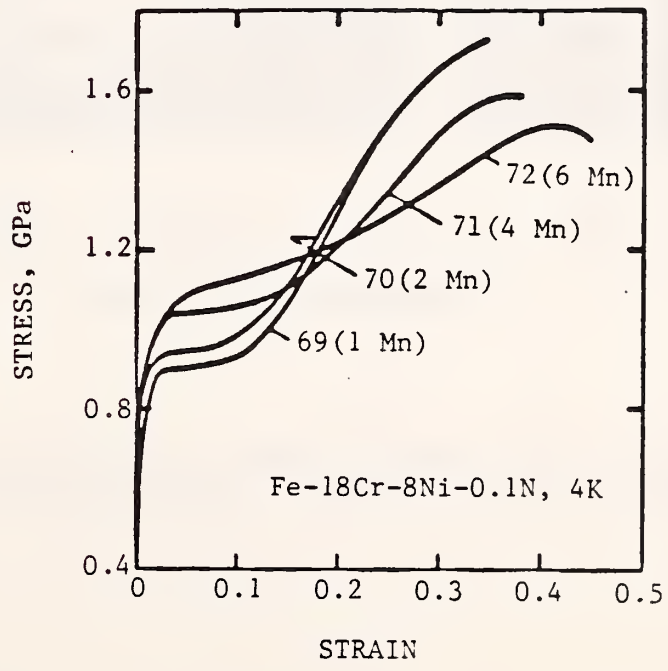

Figure 5. Stress–strain behavior of an 18Cr–8Ni austenitic stainless steel at 4 K as a function of alloy content.[50]

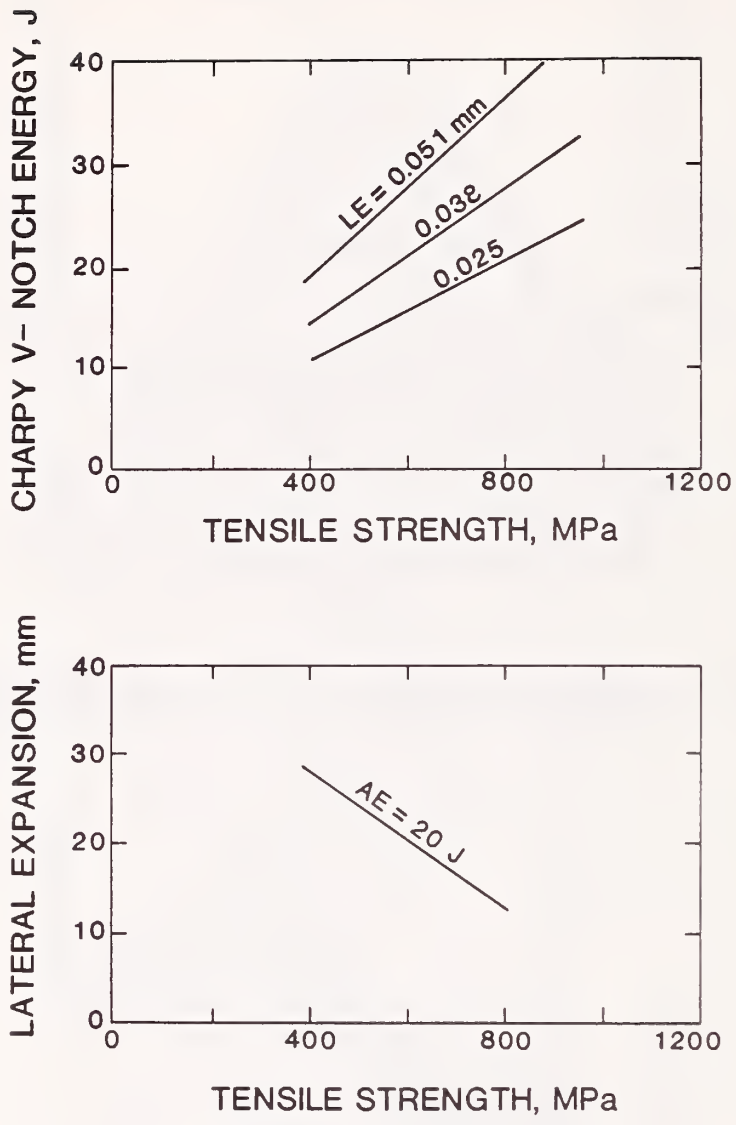

Figure 6. Charpy V-notch absorbed energy versus lateral expansion measurements in materials of varying strength levels.[52]

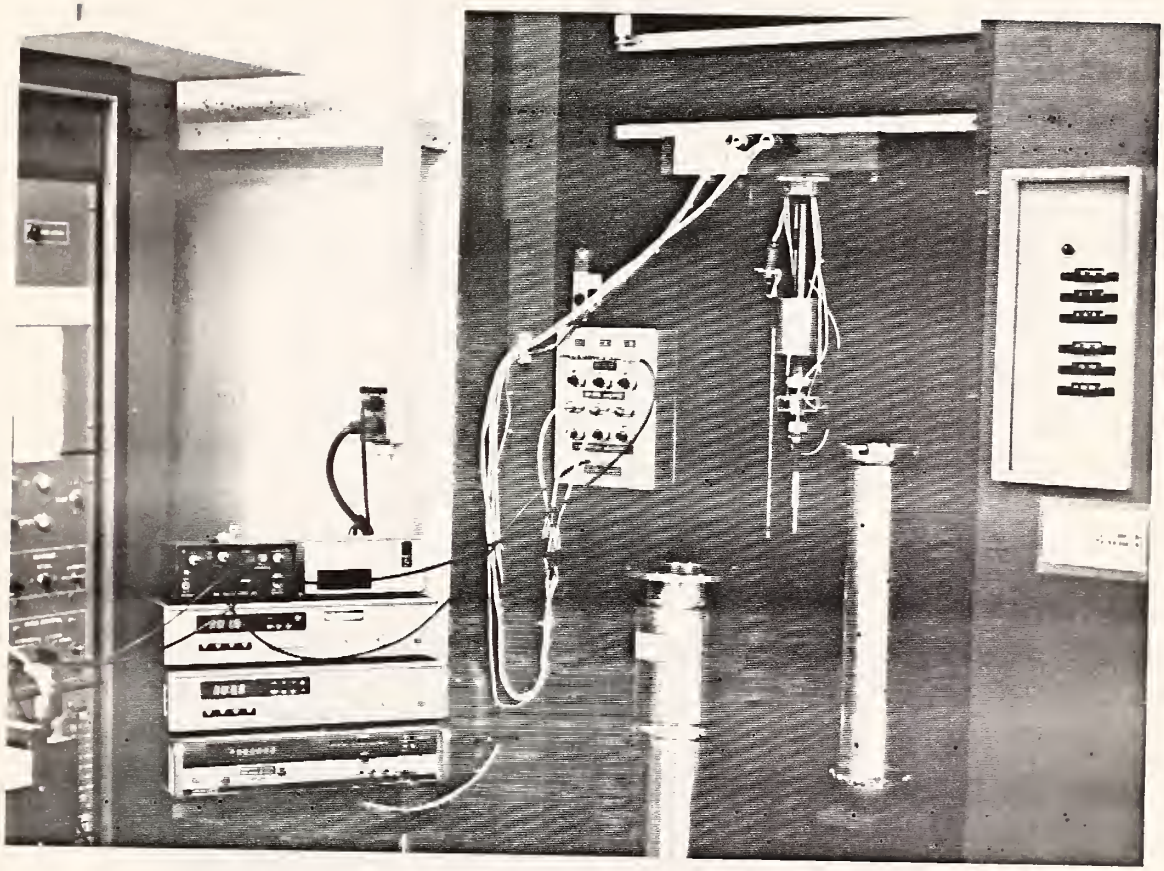

Figure 7. The 4-K tensile testing apparatus.

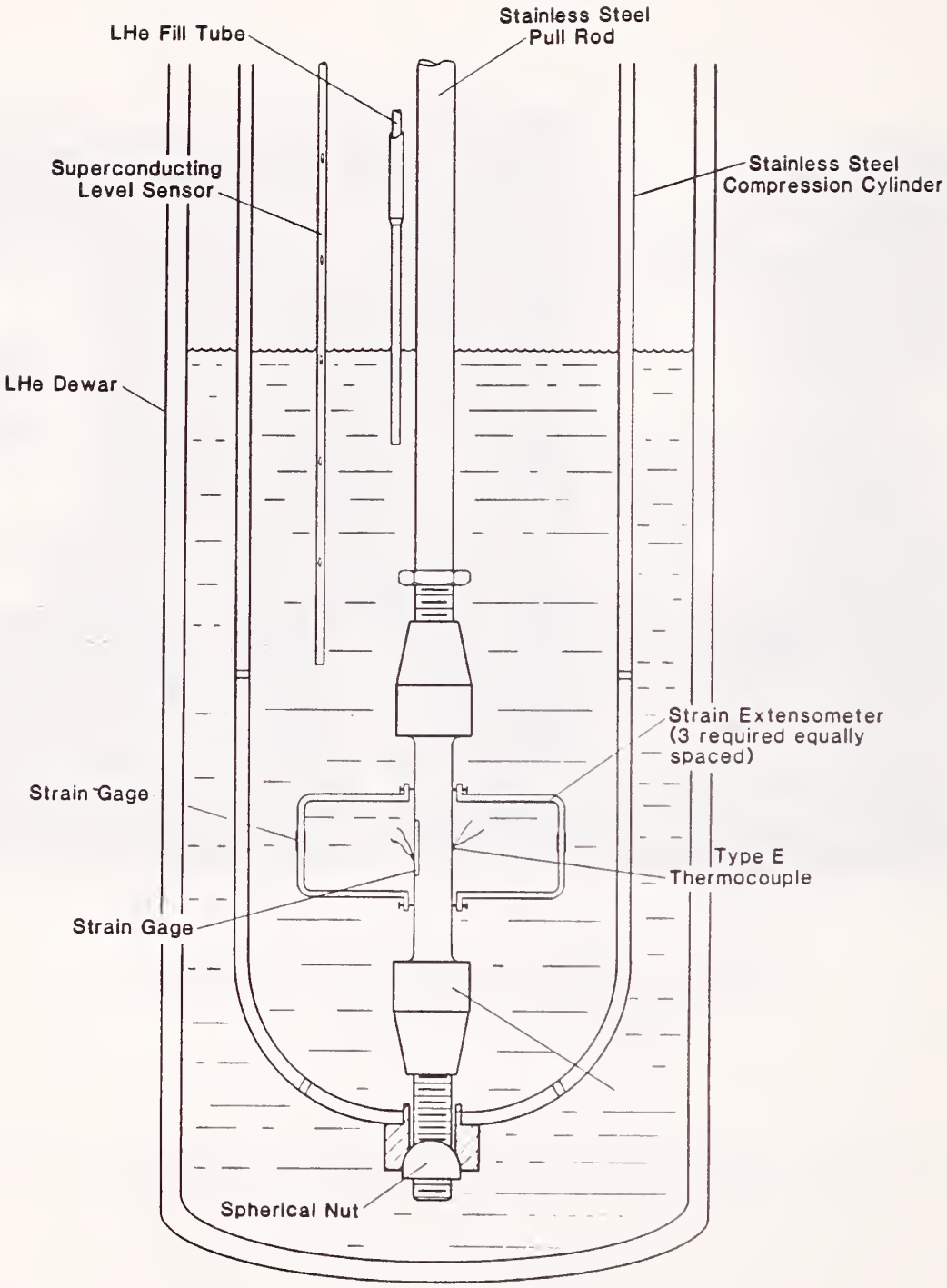

Figure 8. Detail of the load train and specimen configuration during tensile testing.

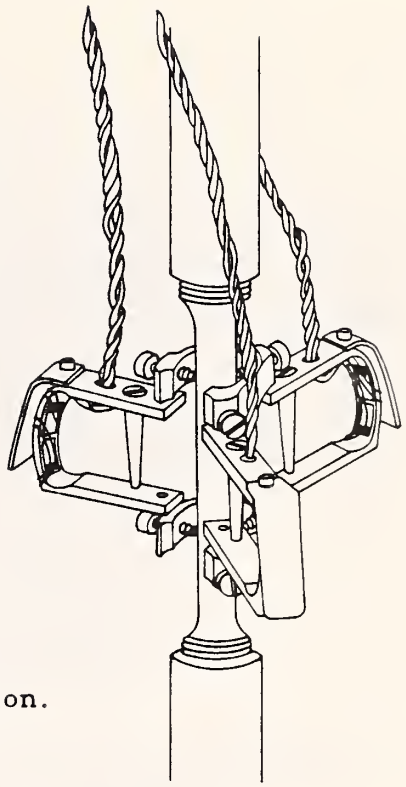

Figure 9. Detail of the extensometer configuration.

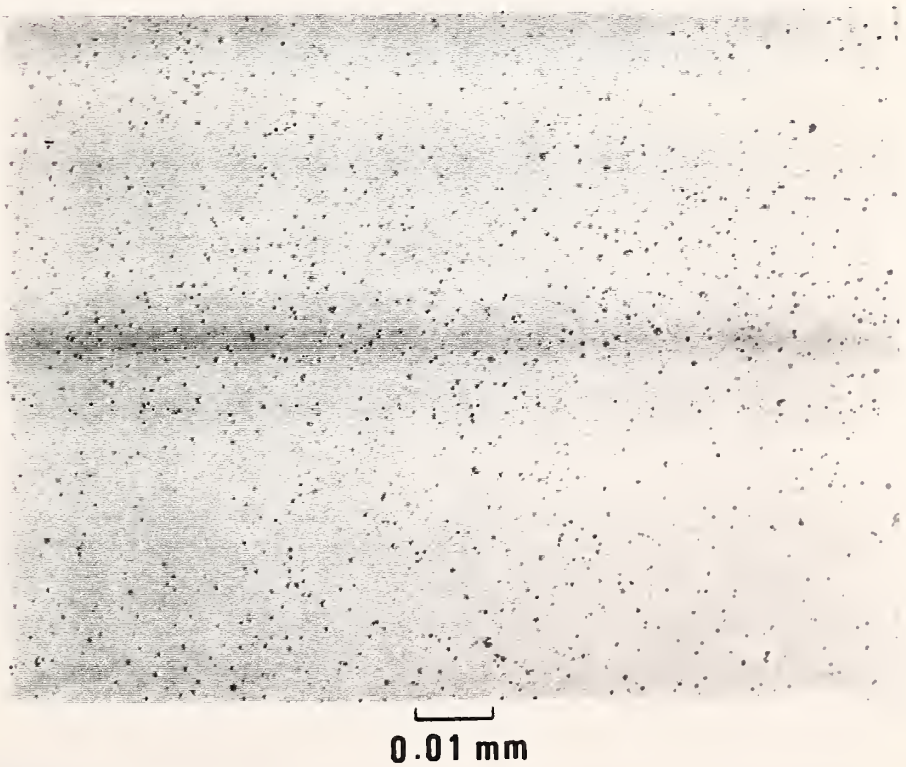

Figure 10. Optical micrograph showing inclusions on a mechanically polished cross section of weld 1. This inclusion morphology and distribution is representative of all the welds.

Figure 11. Optical micrograph of the microstructure of weld 6. Vermicular and lacy ferrite morphologies were commonly observed. A hydrochloric-nitric-acetic acid etch was used.

Figure 12. Optical micrograph of the microstructure of weld 6. The weld was etched in a potassium hydroxide solution.

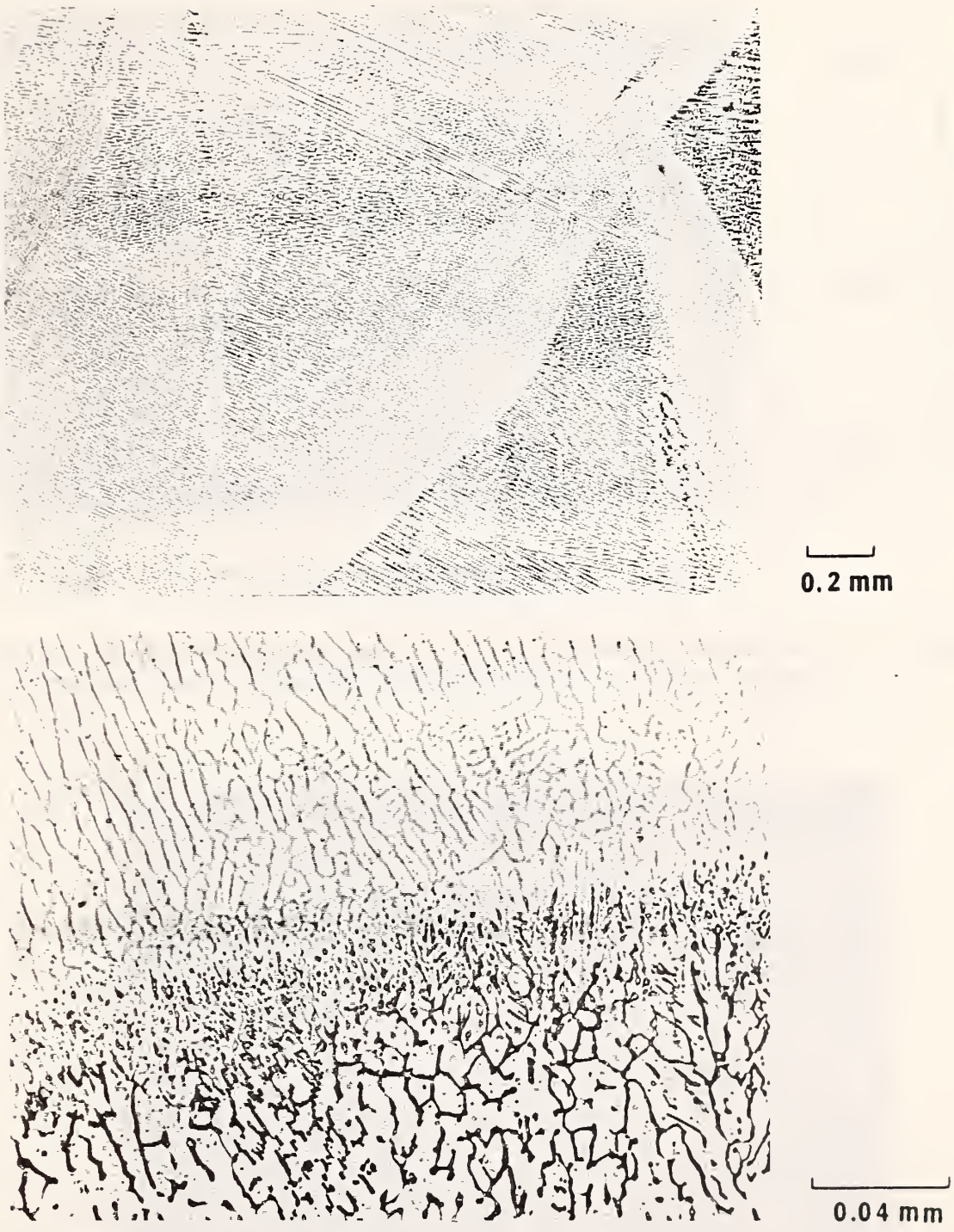

Figure 13. Optical micrograph of the microstructure near an interpass region in weld 22. The weld was etched in a 33 percent nital solution.

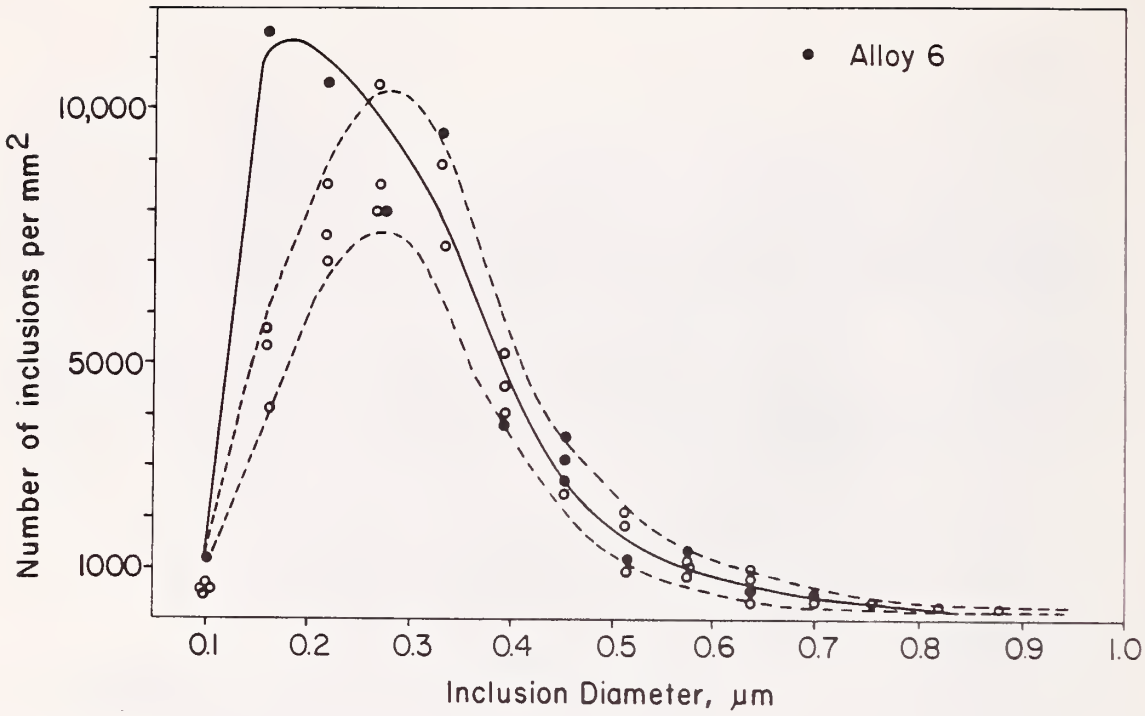

Figure 14. Inclusion distributions found for four of the weld deposits. Weld 6 had more small diameter inclusions than the other welds.

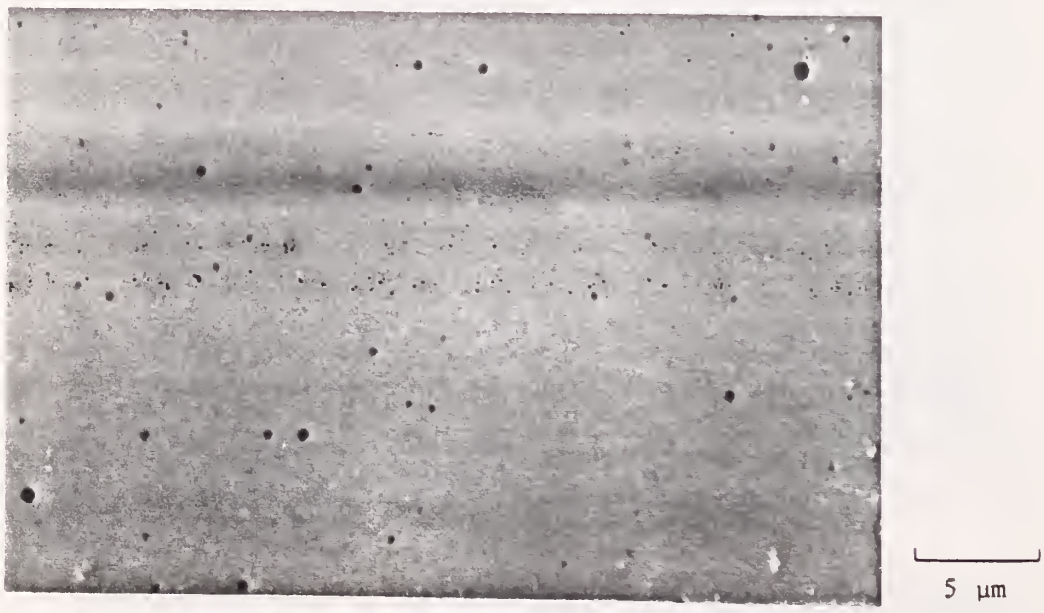

Figure 15. SEM micrograph showing the inclusion morphology observed for alloy 15.

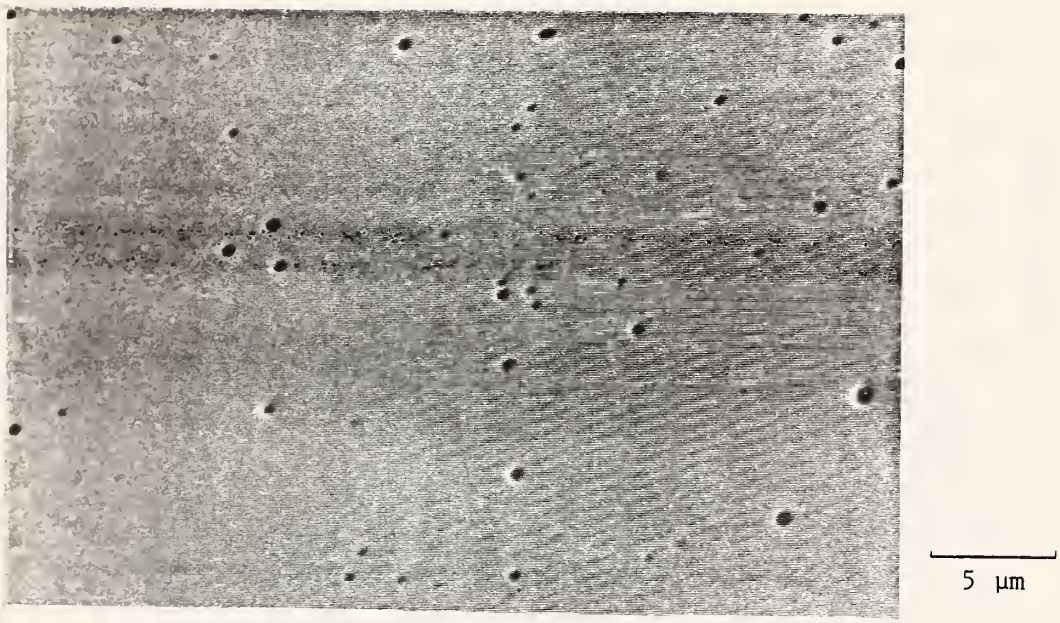

Figure 16. SEM micrograph showing the inclusion morphology observed for alloy 6.

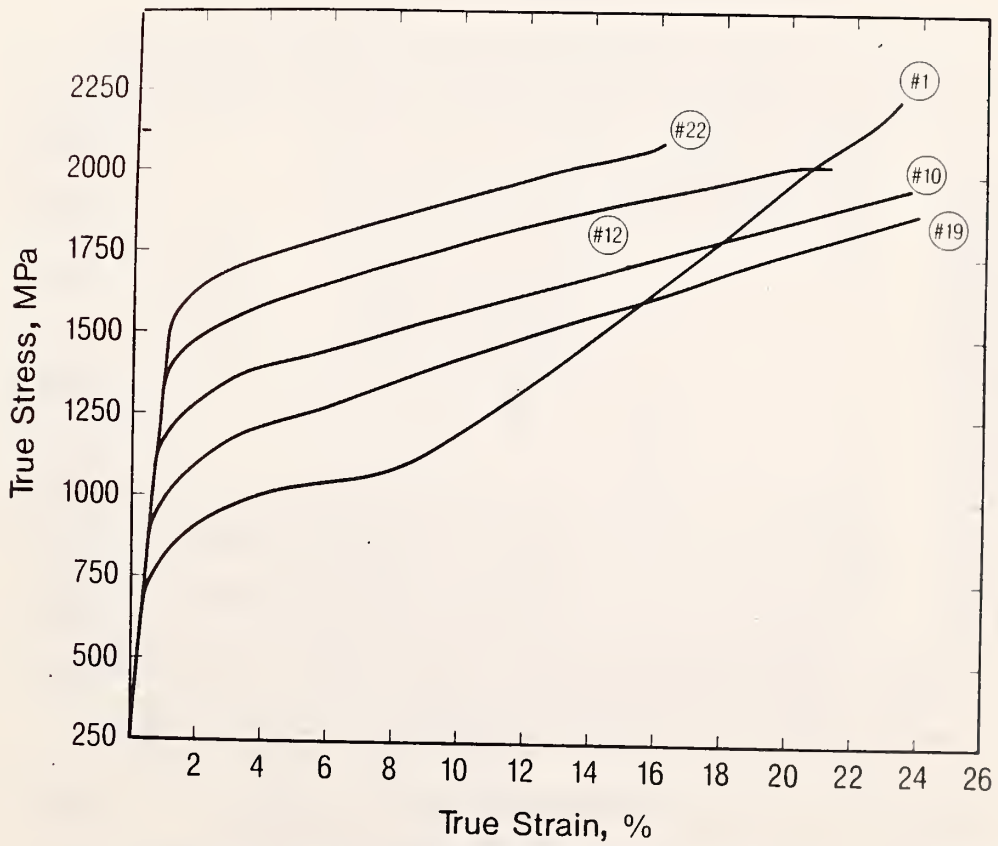

Figure 17. Stress-strain curves characterizing the deformation behavior of the welds.

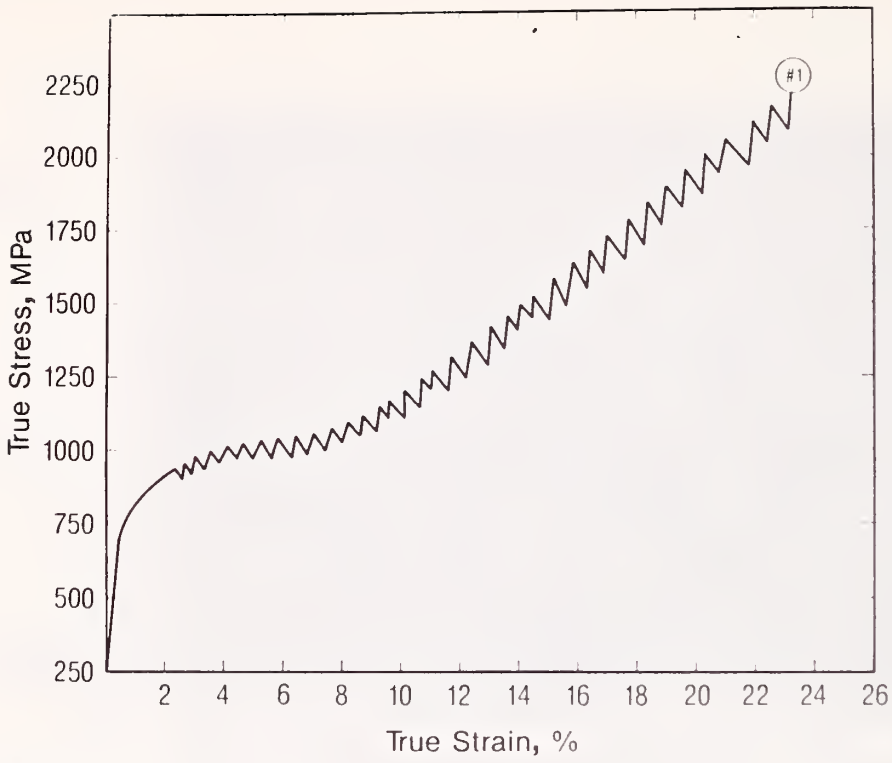

Figure 18. Serrated stress-strain curve characteristic of the welds tested at 4 K.

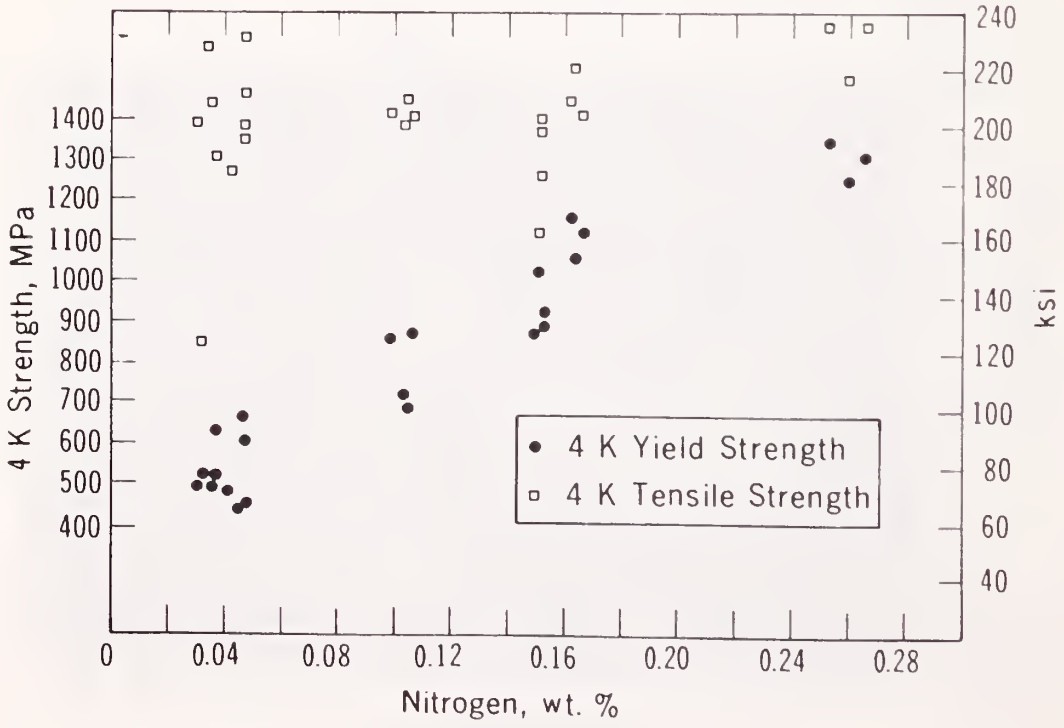

Figure 19. Strength versus nitrogen content of the welds.

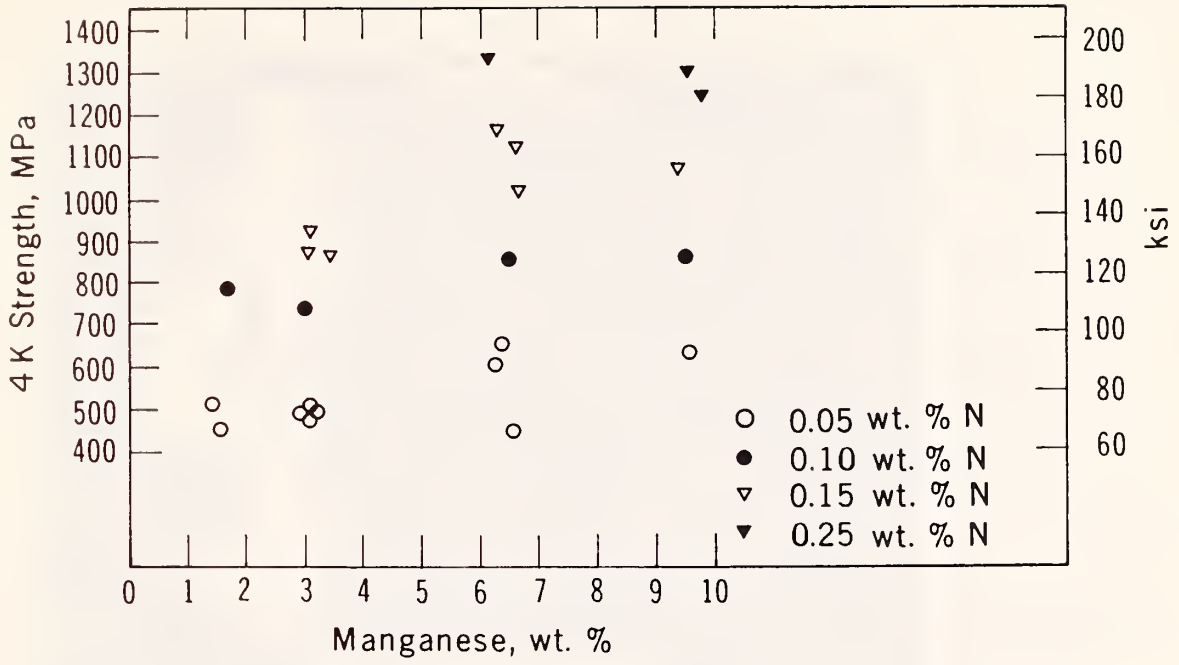

Figure 20. Yield strength versus manganese content of the welds.

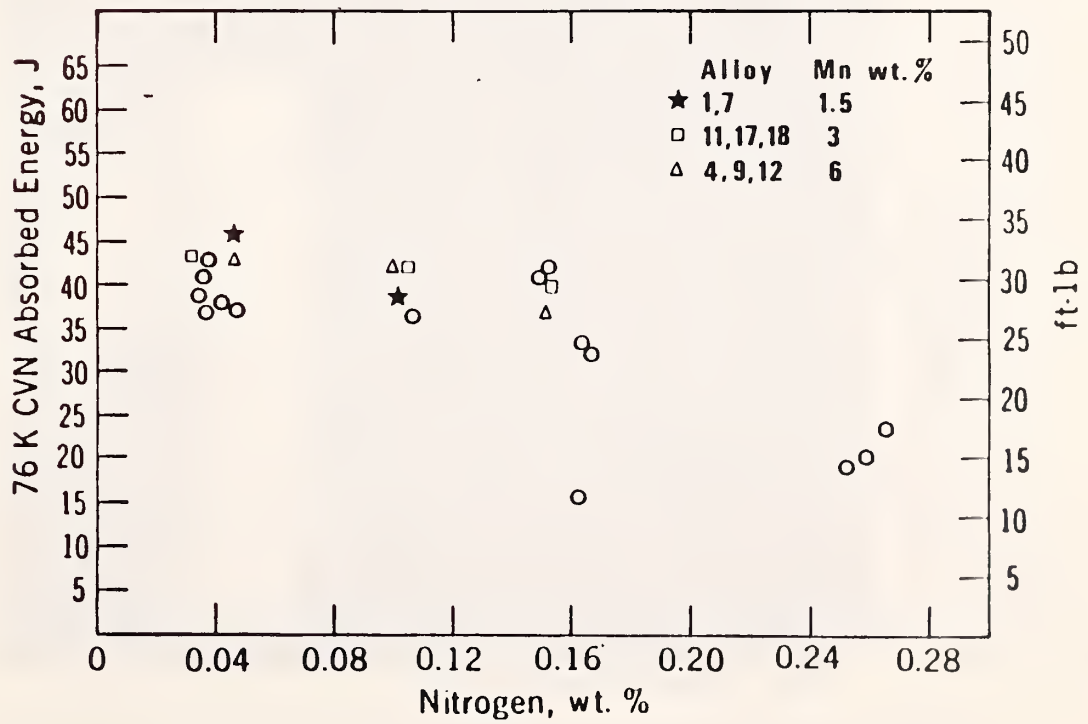

Figure 21. Charpy V-notch absorbed energy versus nitrogen content in the welds.

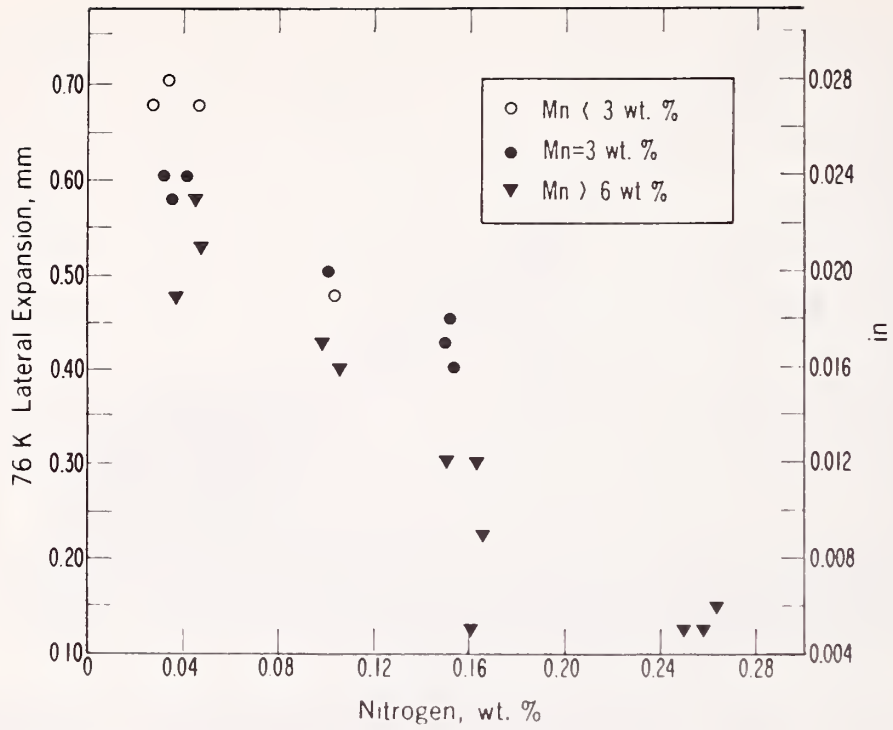

Figure 22. Lateral expansion versus nitrogen content in the welds.

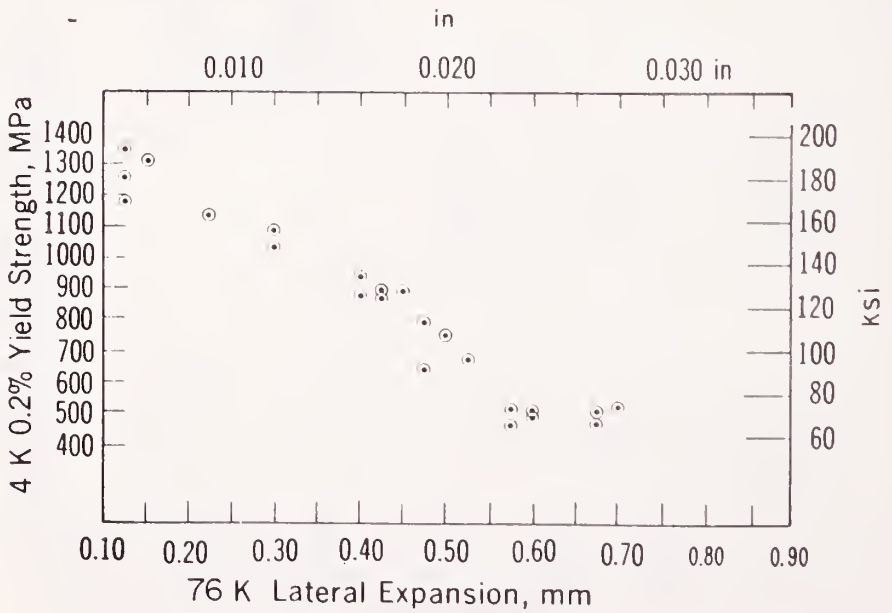

Figure 23. The relationship between 4-K yield strength and 76-K lateral expansion.

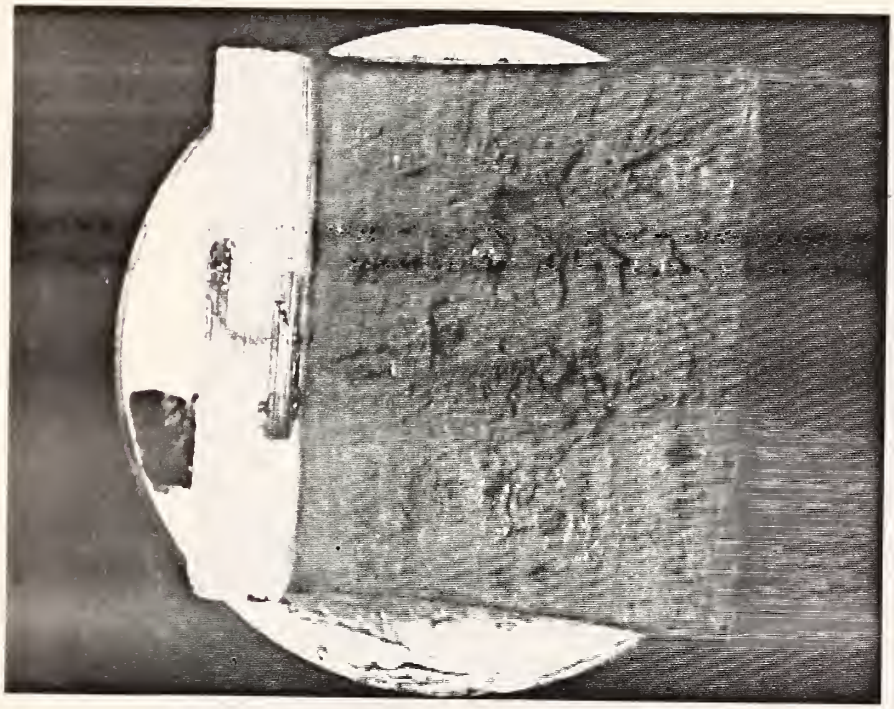

Alloy 1

low nitrogen

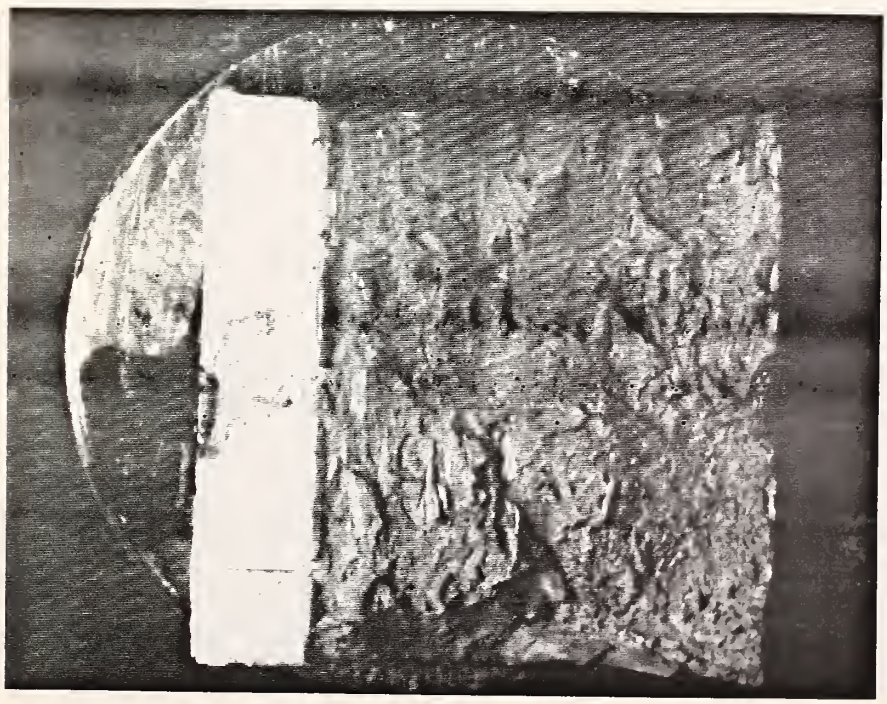

Alloy 22

high nitrogen

Figure 24. The effect of nitrogen on the fracture surface appearance of Charpy V-notch specimens.

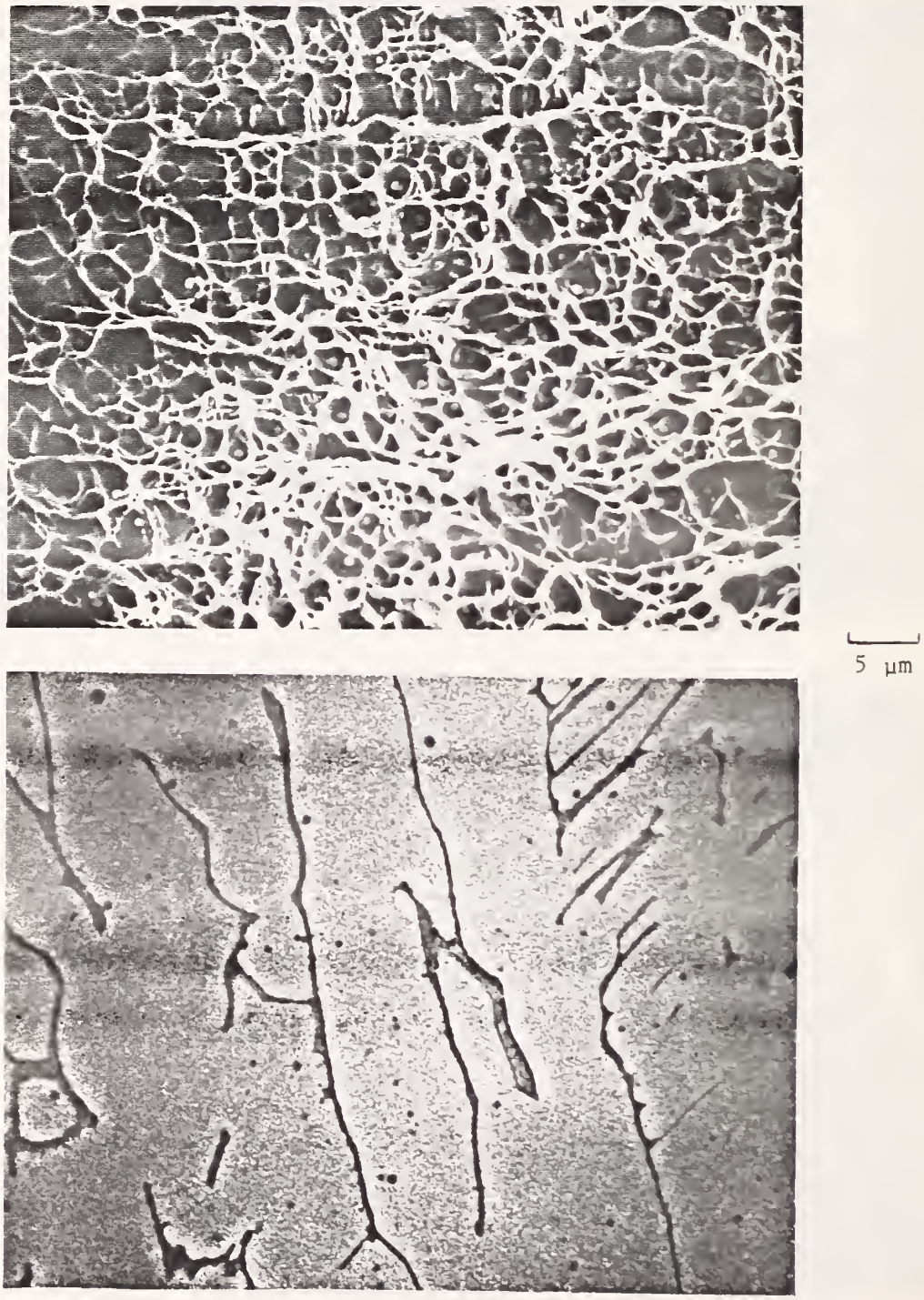

Figure 25. Similarities in the shape and spacing of ferrite morphologies of polished specimens and the tear-ridge networks on the fracture surface for weld 12.

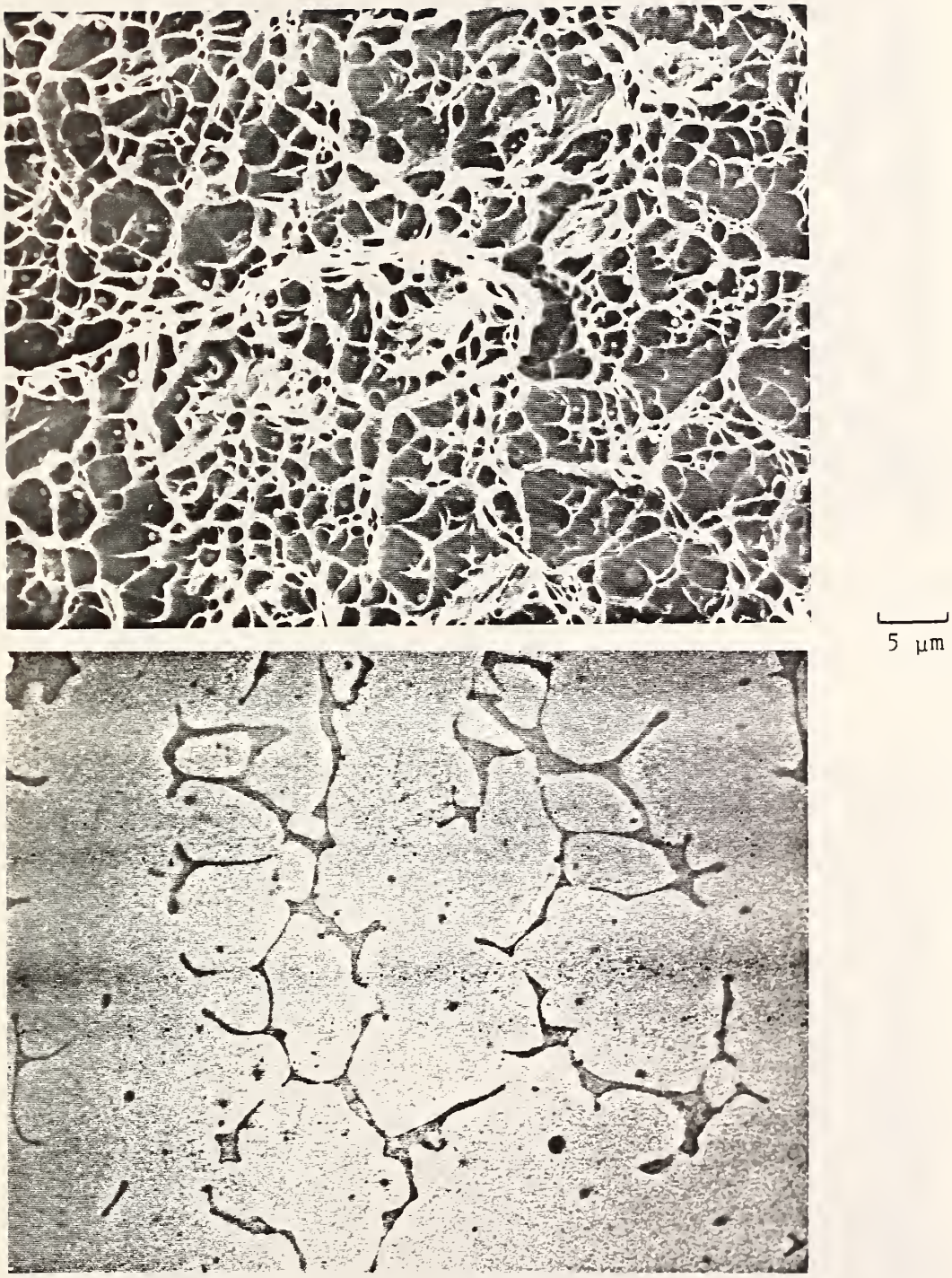

Figure 26. Similarities in the shape and spacing of ferrite morphologies of polished specimens and the tear-ridge networks on thefracture surface for weld 12.

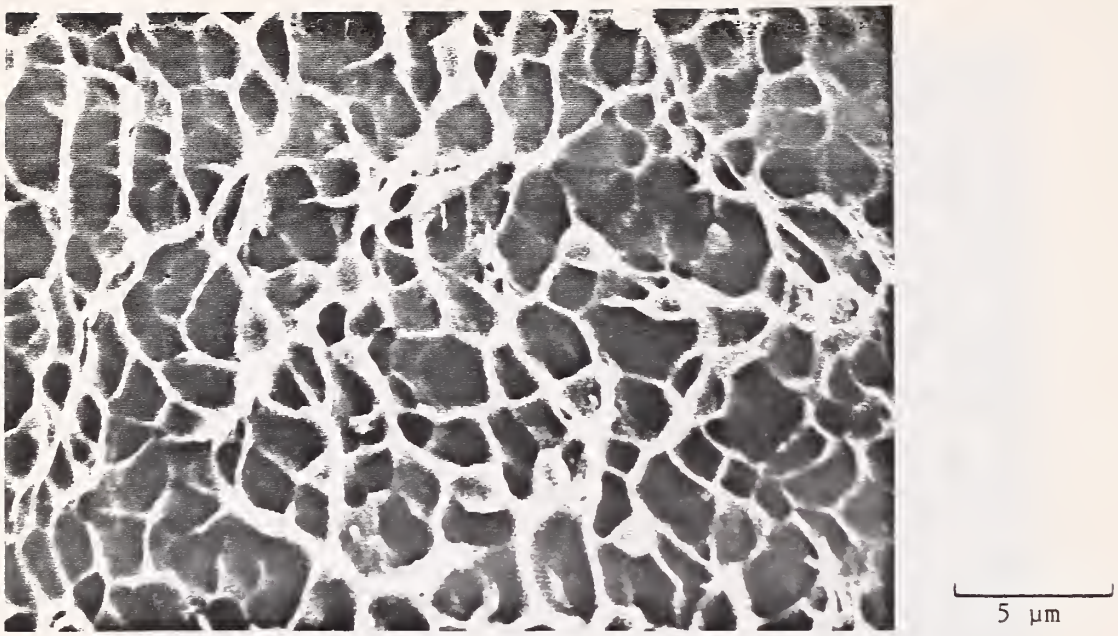

Figure 27. Fractograph of Charpy V-notch specimen, taken near the notch of weld 6. The ductile dimple density shown here is similar to those observed on tensile specimen fracture surfaces.

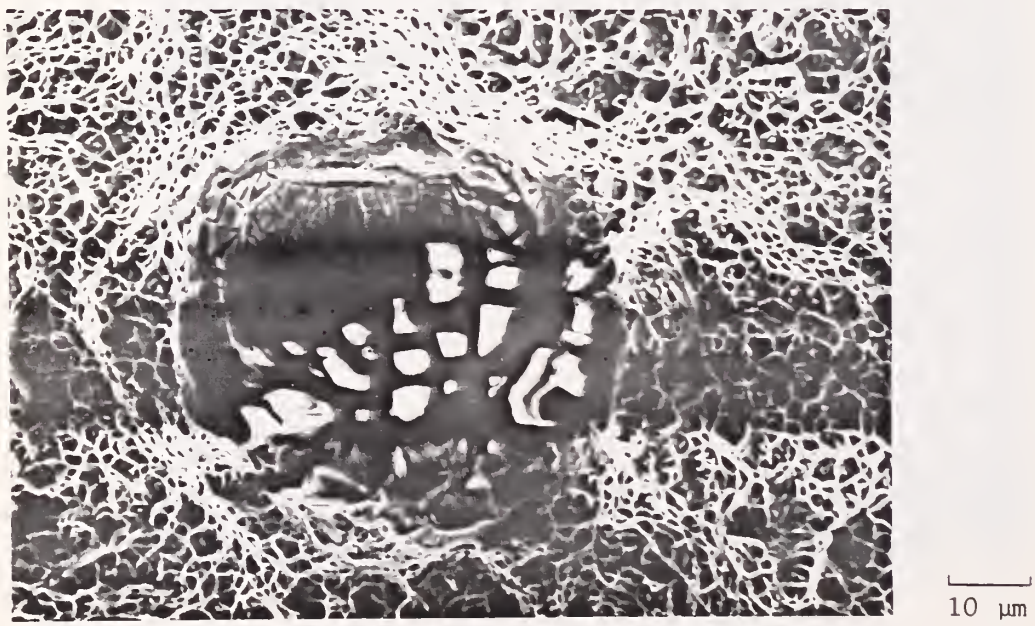

Figure 28. Fractograph showing one of the large inclusions found in the 3.84 wt. pct. molybdenum alloy (weld 6).

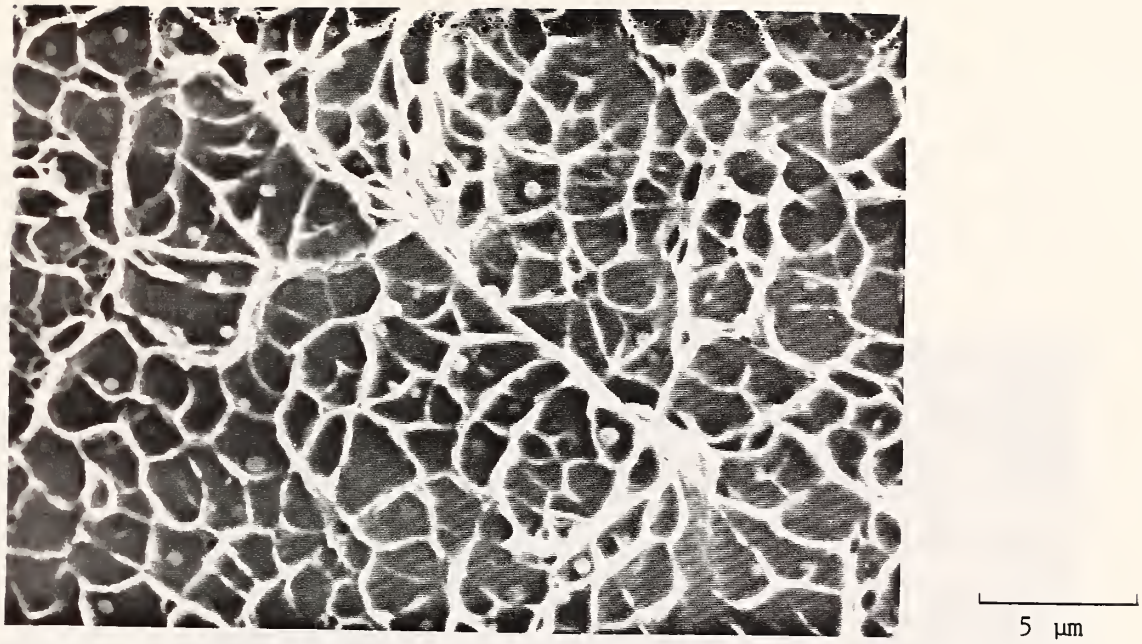

Figure 29. Fractograph taken near the center of a weld 1 tensile specimen. It is representative of the dimple size and morphologies commonly observed.

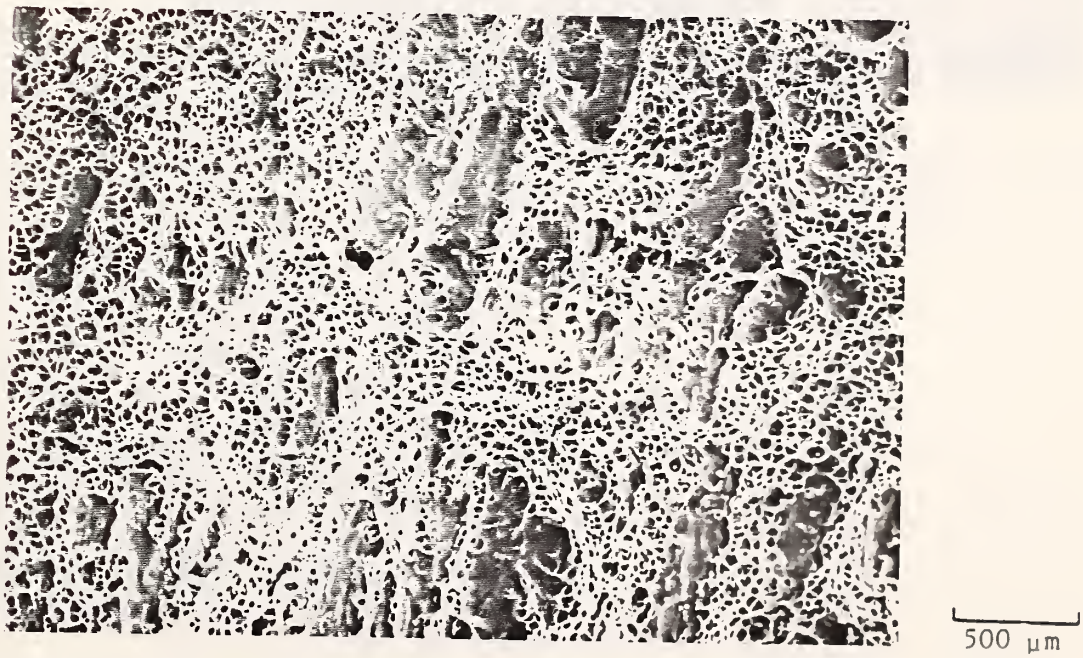

Figure 30. Fracture surface features on a Charpy V-notch specimen near the notch of a weld 1 specimen. Similar markings were observed in other welds.

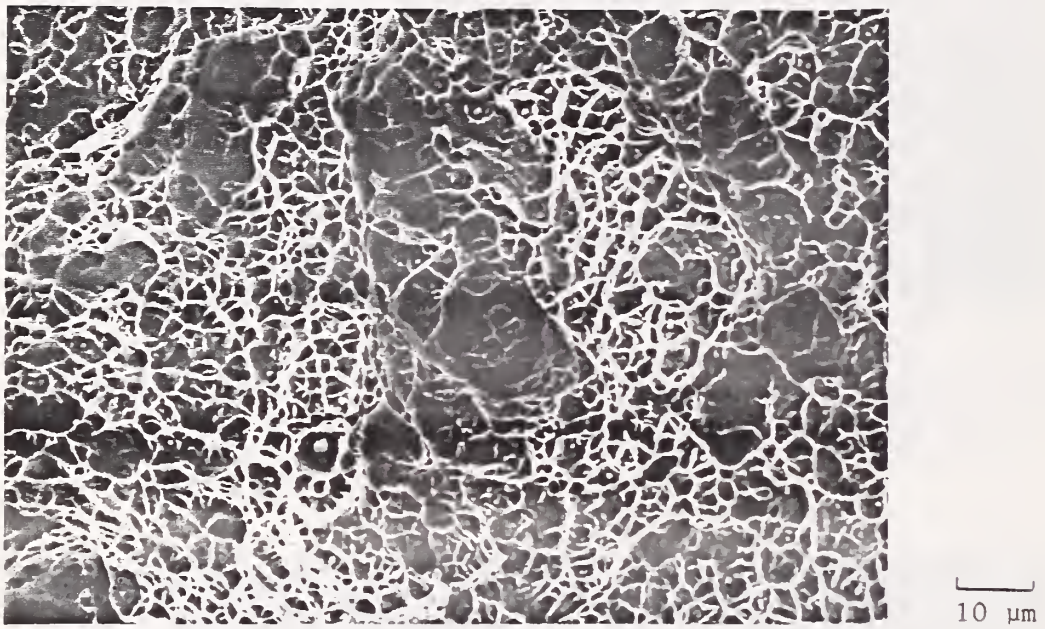

Figure 31. Fracture surface features observed near the center of a weld 13 Charpy V-notch specimen. Similar features were observed in this area for the other welds.

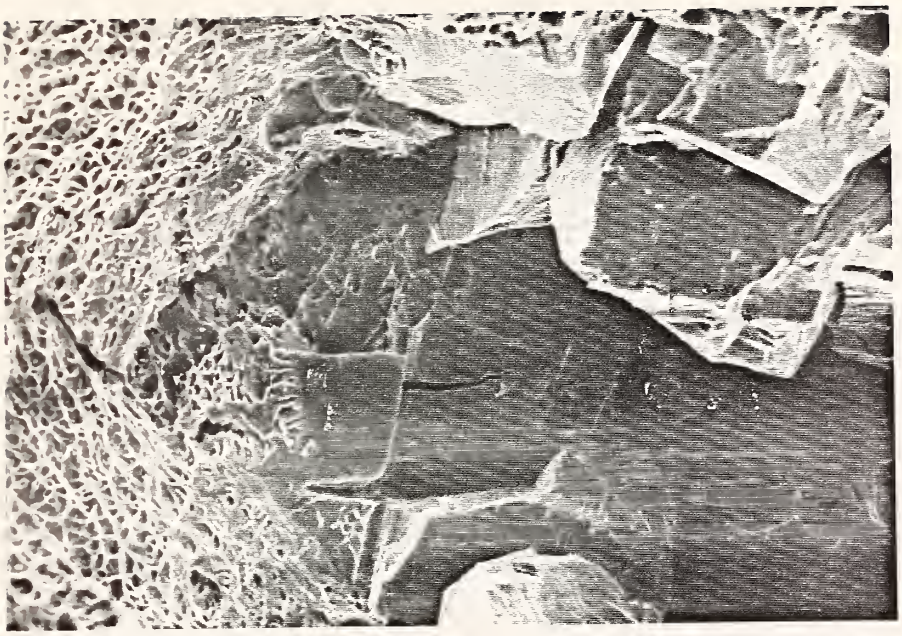

Figure 32. Isolated ferritic area of a weld metal tensile specimen that fractured by cleavage.

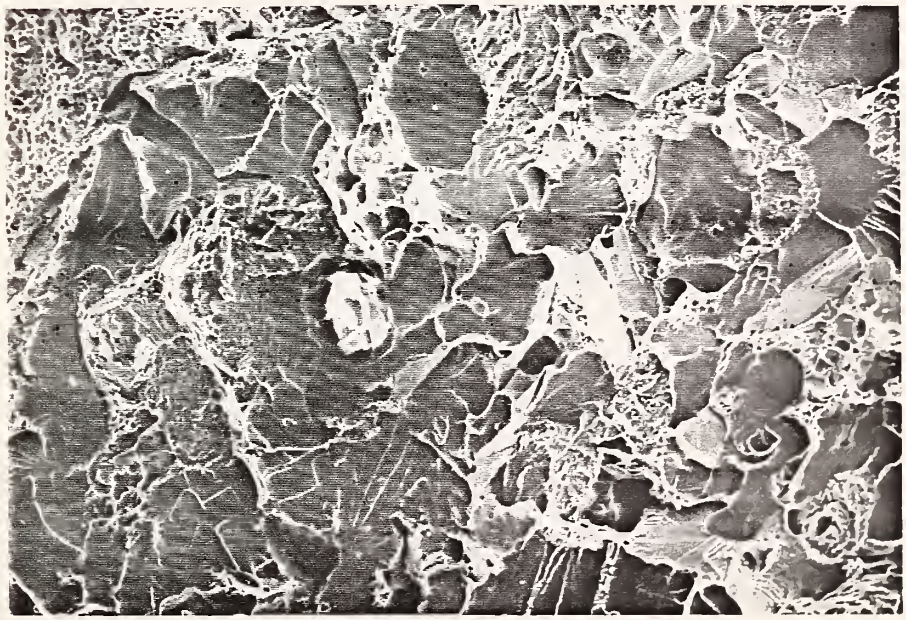

Figure 33. Isolated ferritic area of a weld metal tensile specimen that fractured by cleavage.

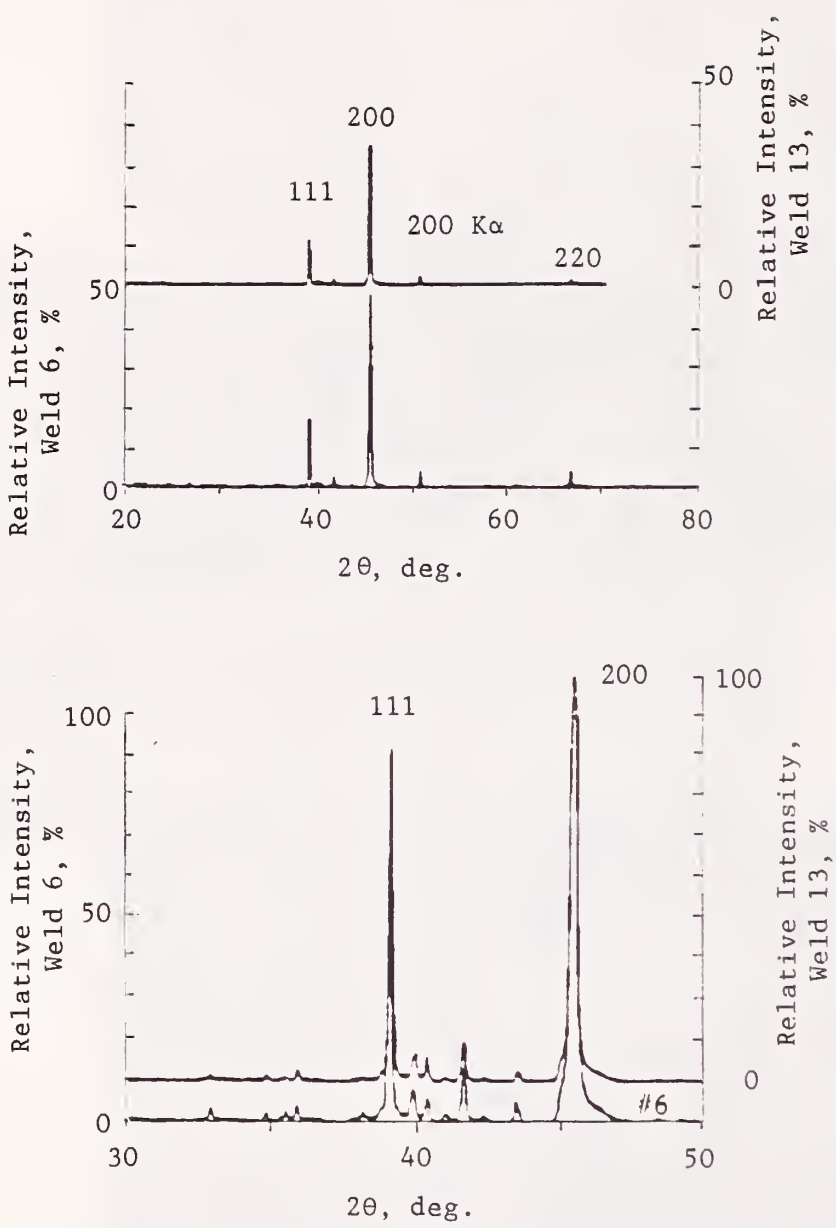

Figure 34. X-ray determination of the phases present in welds 6 and 13. The principal phase present in the welds was austenite.

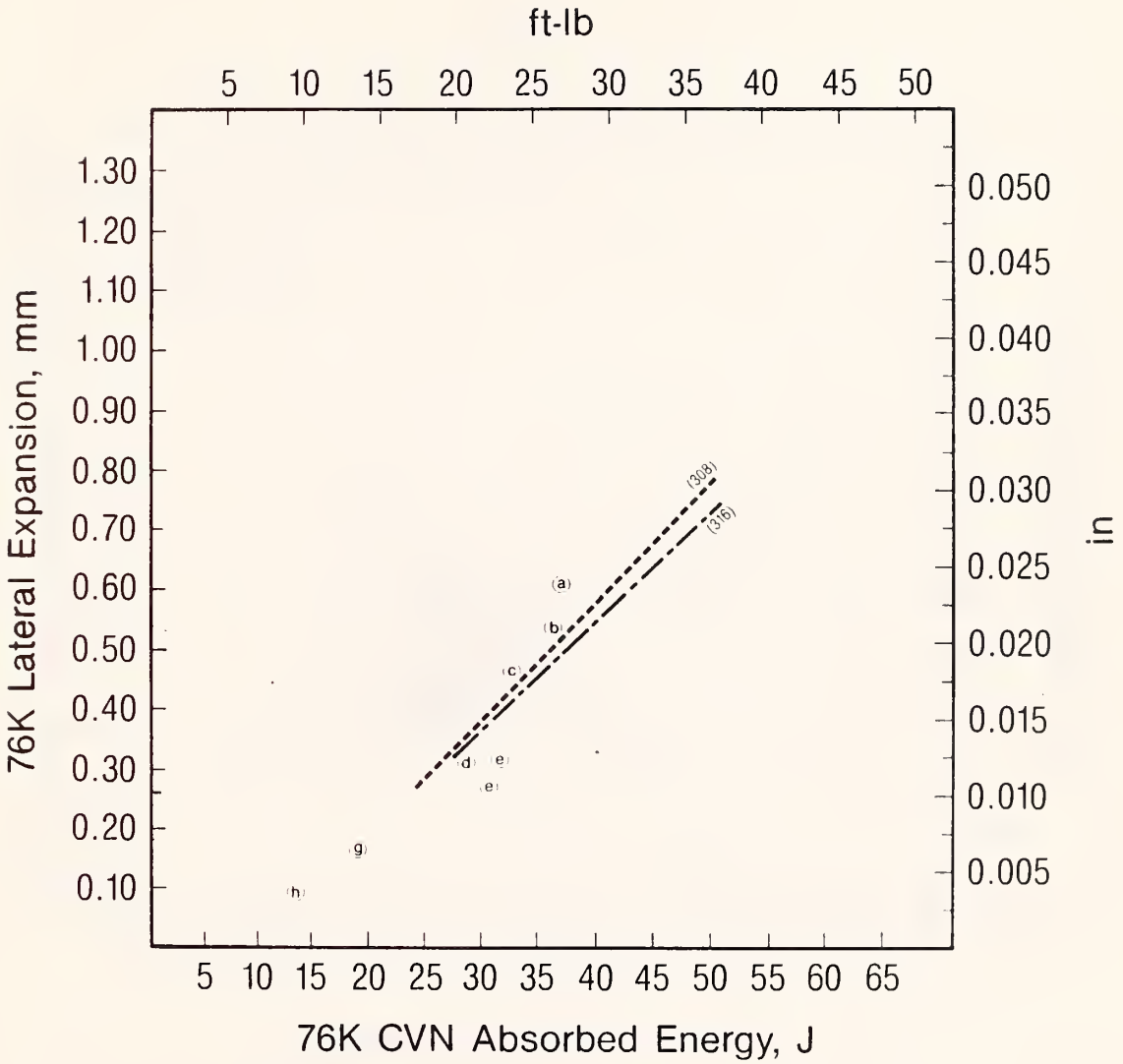

Figure 35. The relationship between lateral expansion and absorbed energy for the Szumakowski-Reid data.[27]

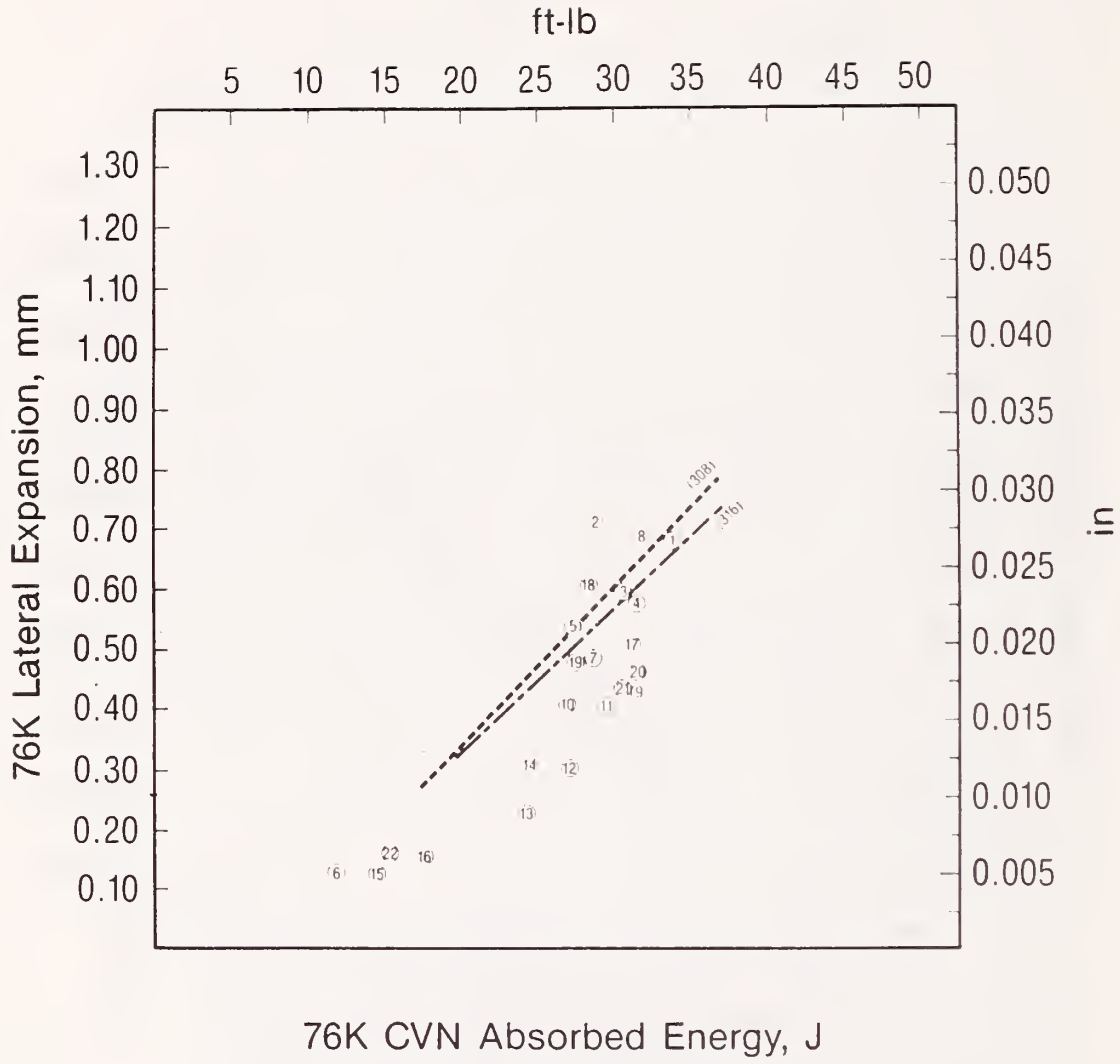

Figure 36. The relationship between lateral expansion and absorbed energy for the welds in this study.

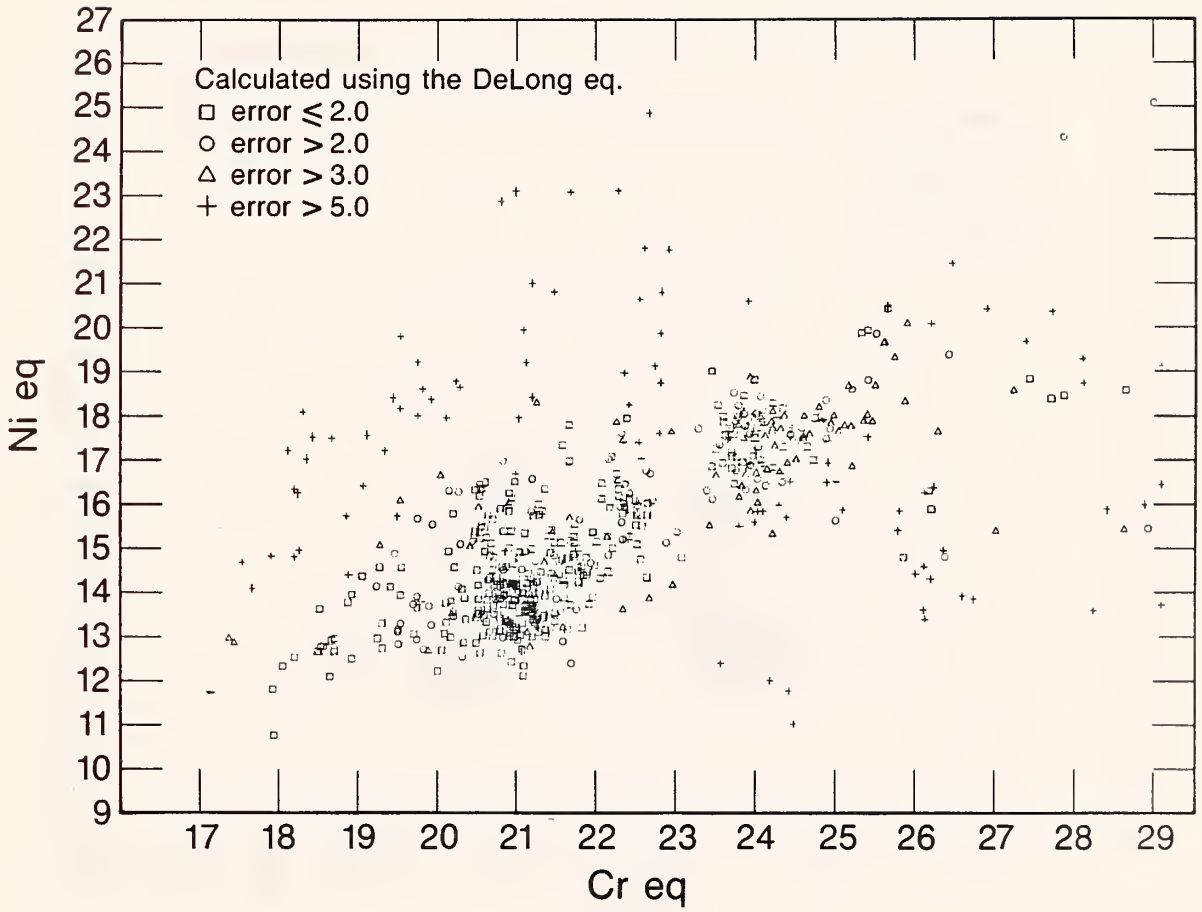

Figure 37. Predicted error of FN for data group 1 using the DeLong-type equation (FNCD).

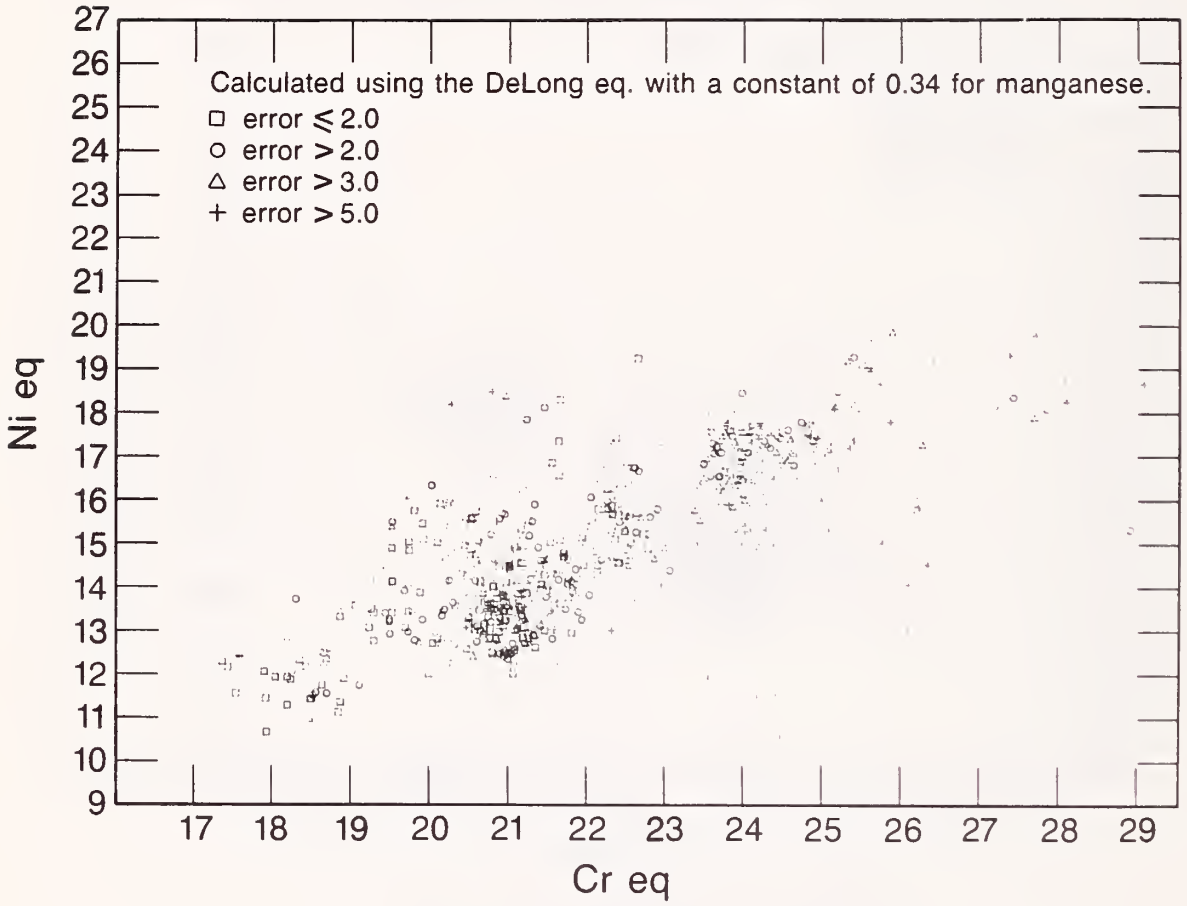

Figure 38. Predicted error of FN for data group 1 using the 0.34 constant for the manganese term in the DeLong type equation (FNCDK).

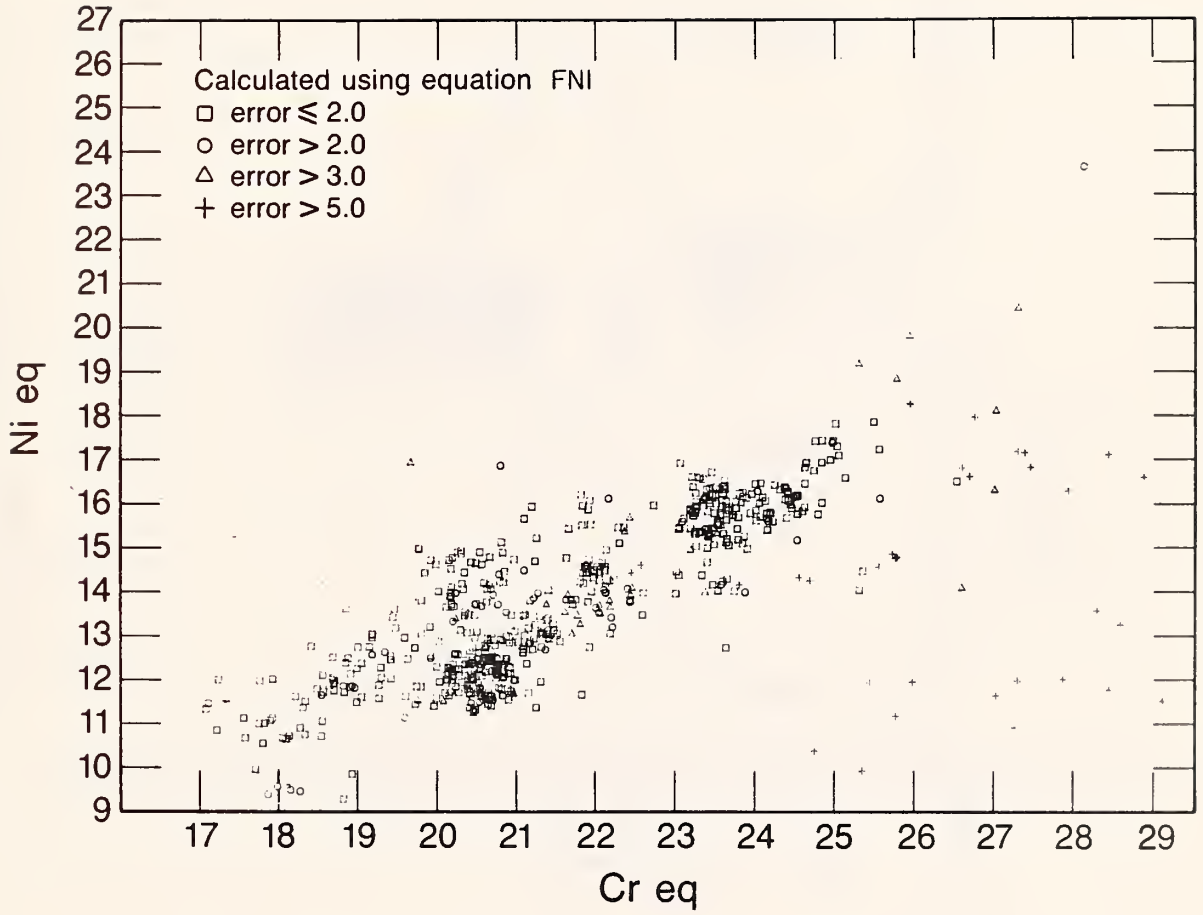

Figure 39. Predicted error of FN for data group 1 using the FN1 equation.

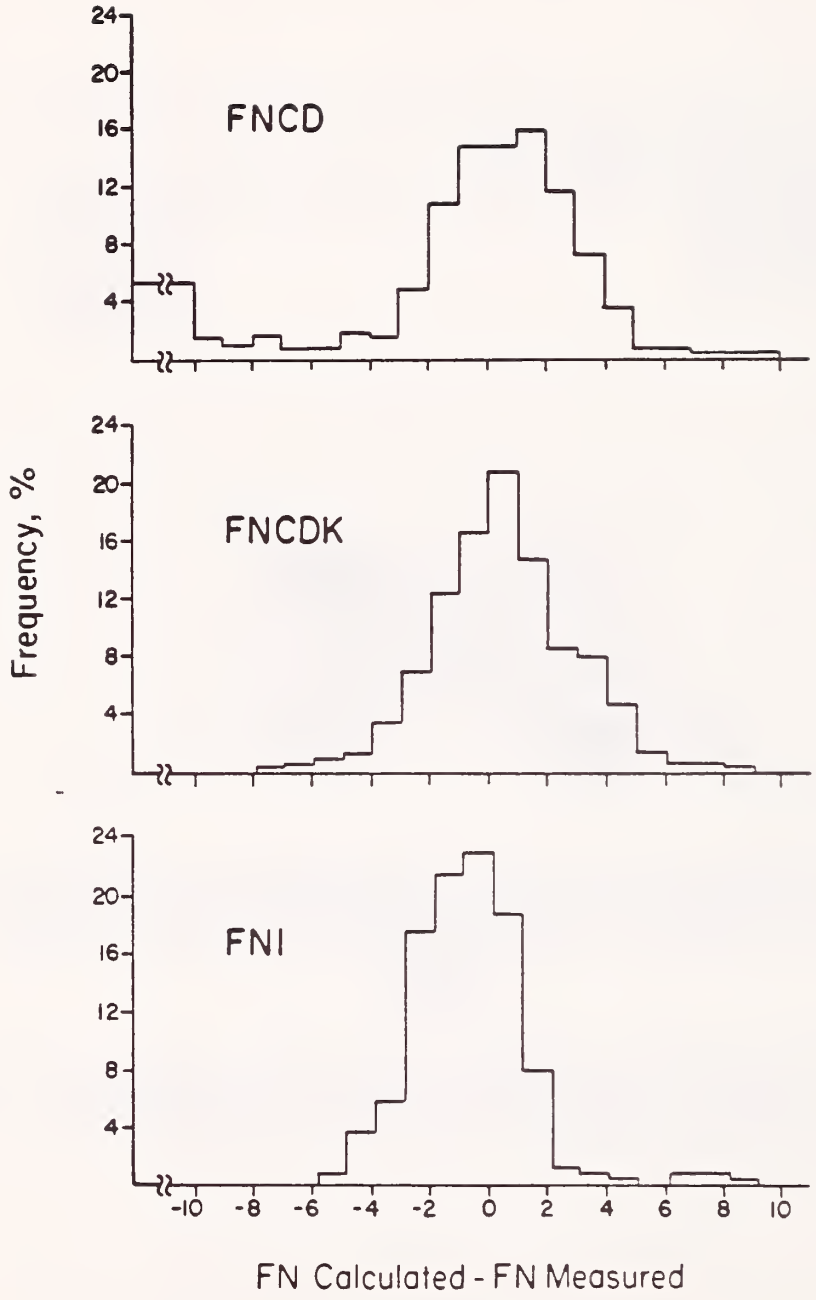

Figure 40. The frequency (%) versus FN predicted error for group 1 when the FNCD, FNCDK, and FN1 equations were used.

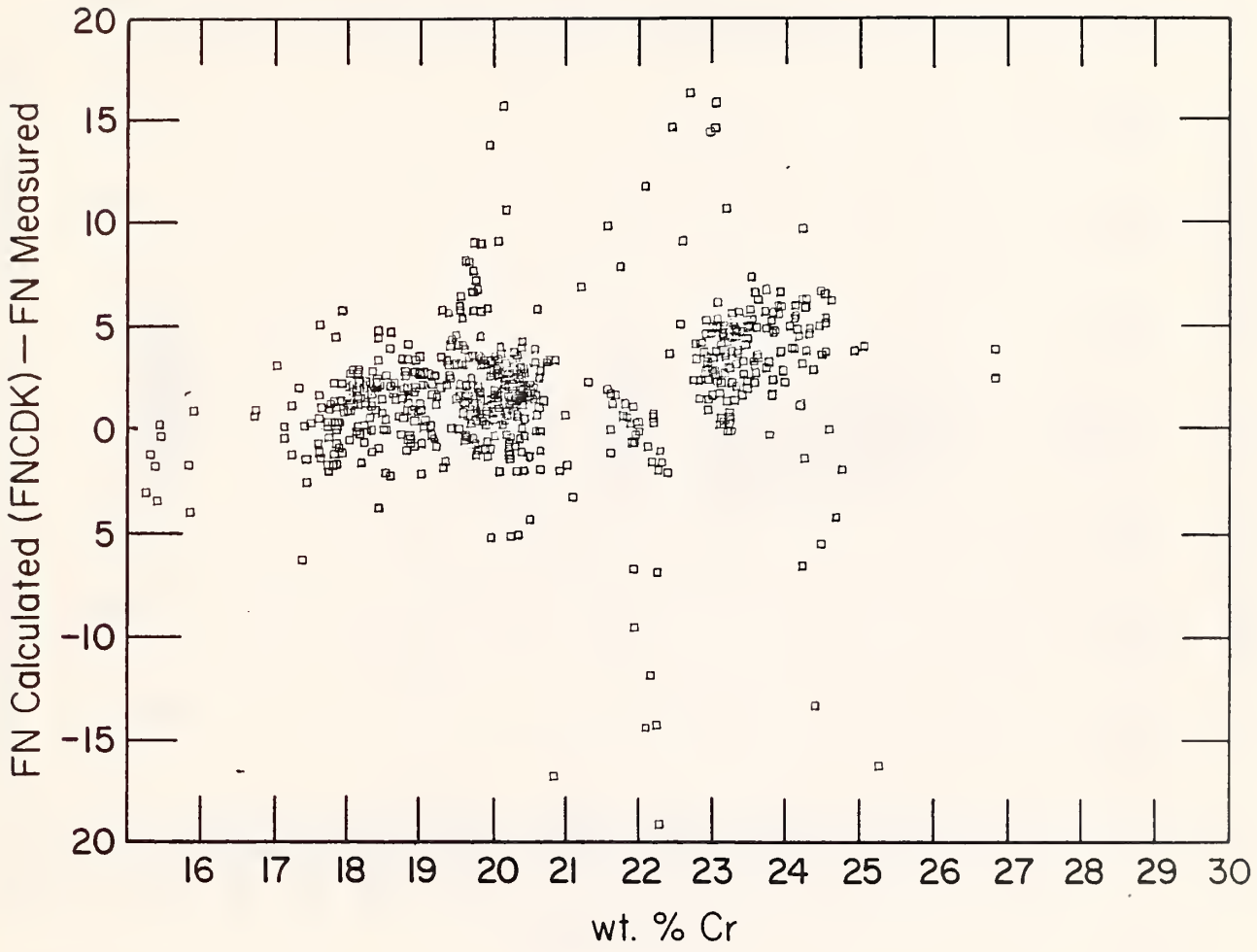

Figure 41. FN predicted error versus chromium content for data group 1 using the 0.34 constant for the manganese term in the DeLong-type equation (FNCDK).

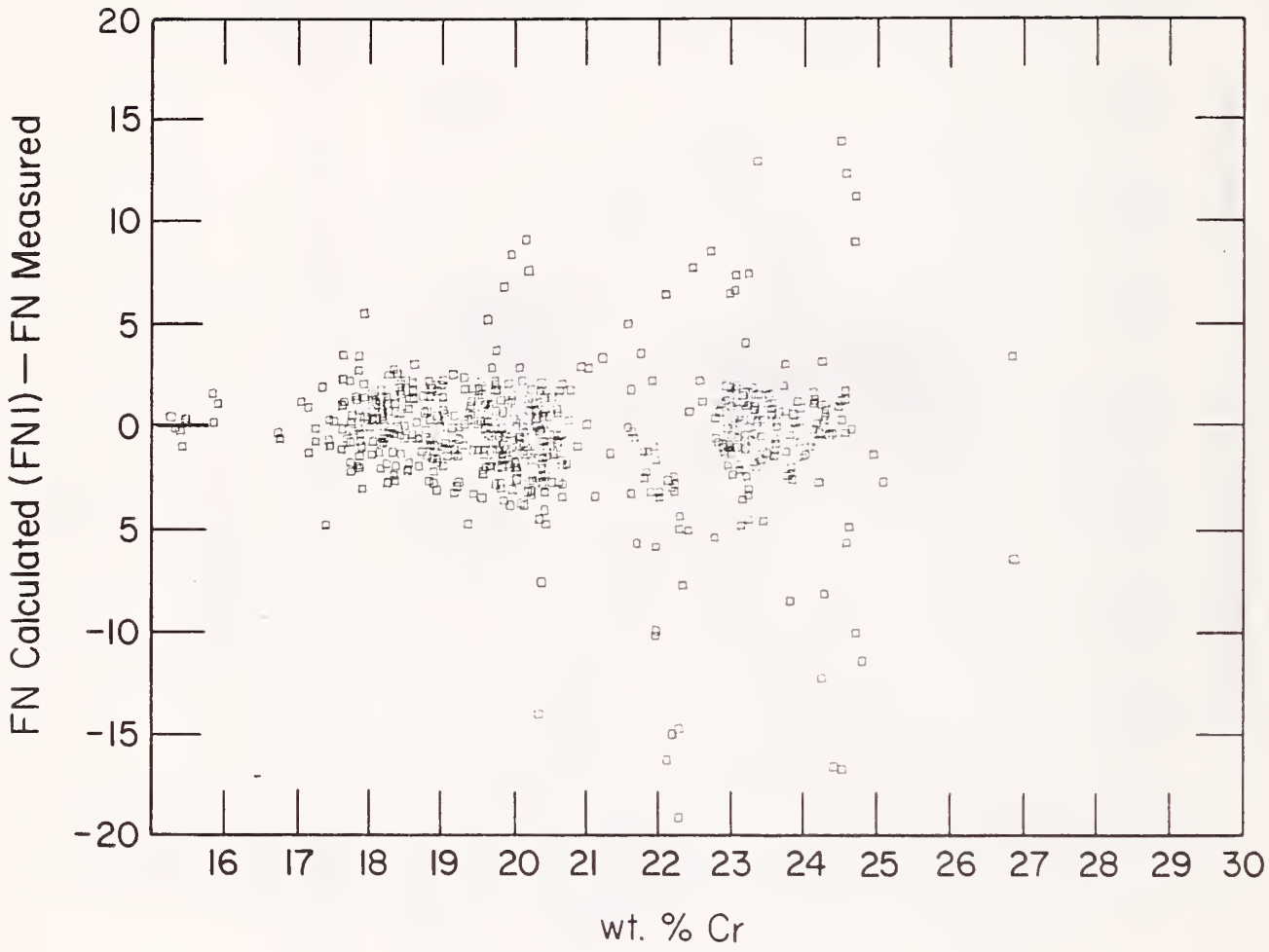

Figure 42. FN predicted error versus chromium content for data group 1 when the FN1 equation was used.

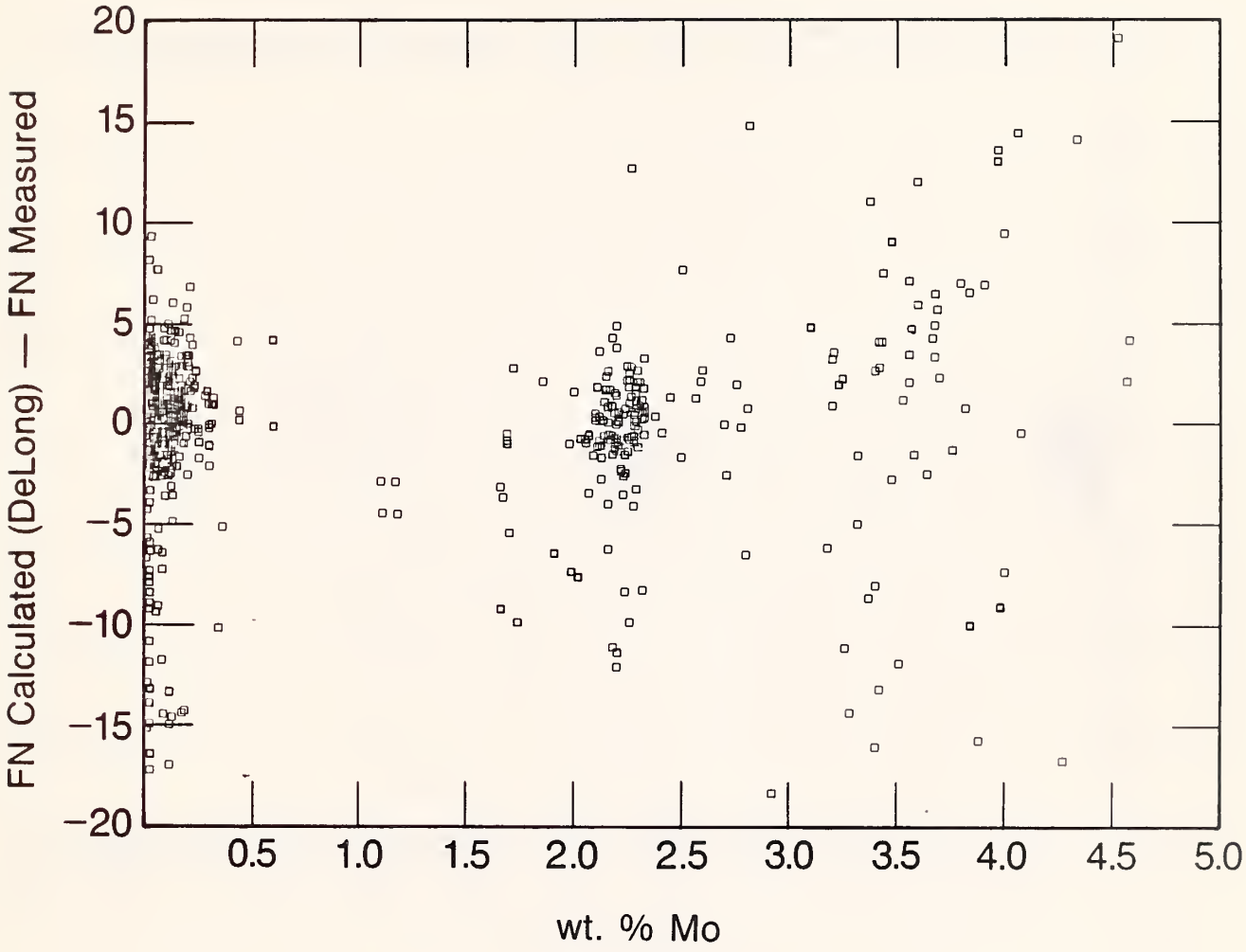

Figure 43. FN predicted error versus molybdenum content for data group 1 when the FNCD equation was used.

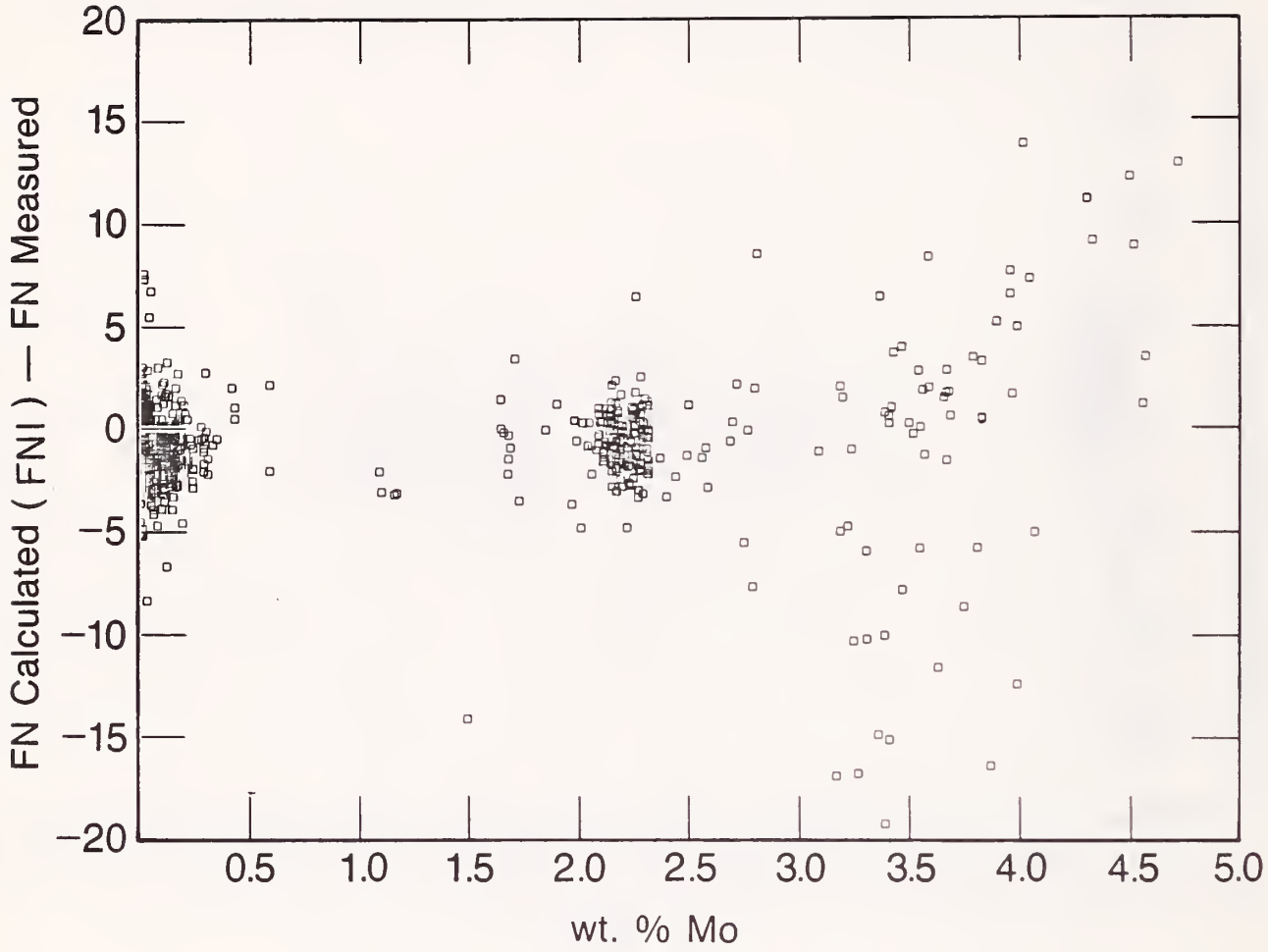

Figure 44. FN predicted error versus molybdenum content for data group 1 when the FN1 equation was used.

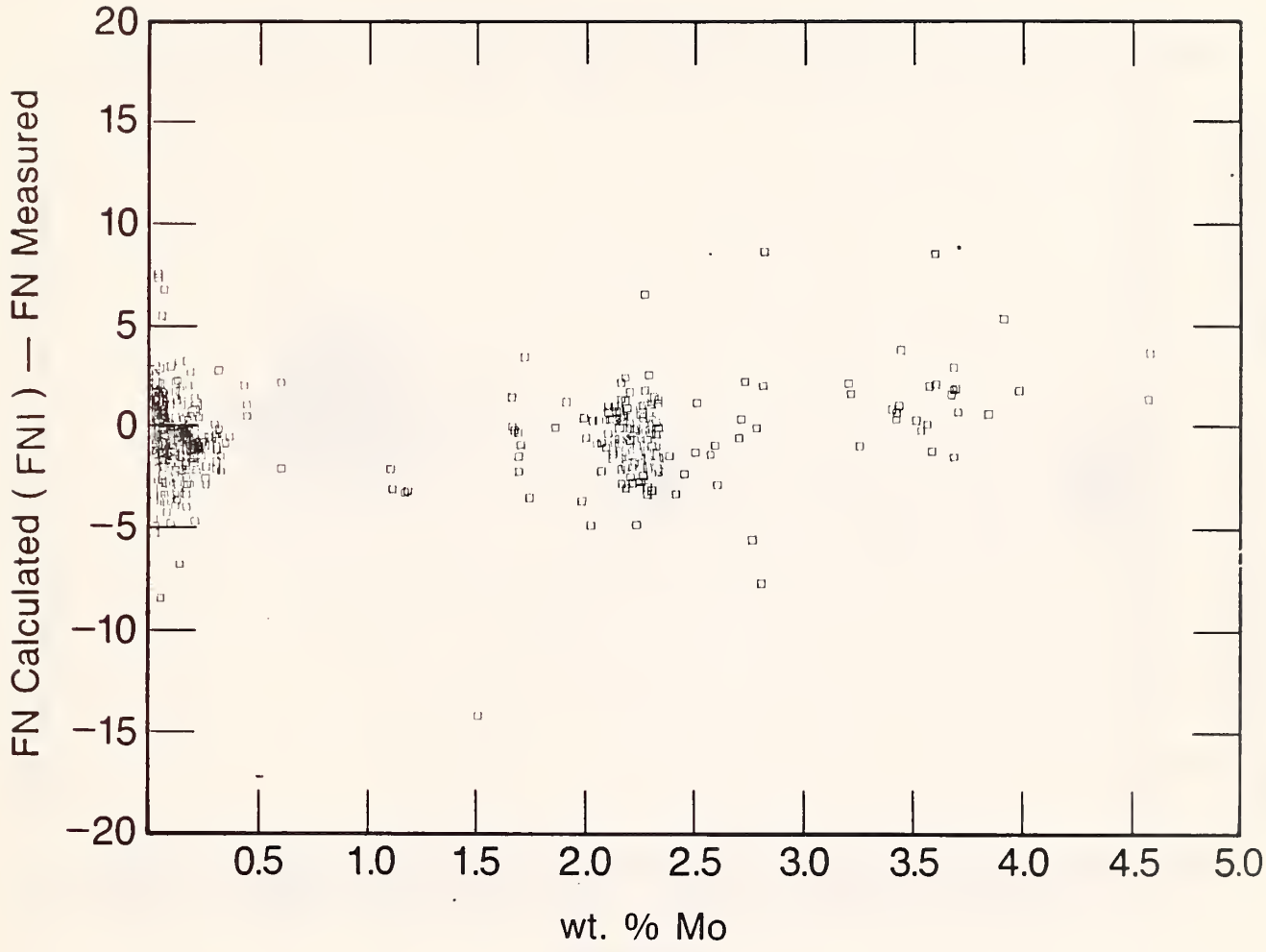

Figure 45. FN predicted error versus molybdenum content for data group 2 when the FN1 equation was used.

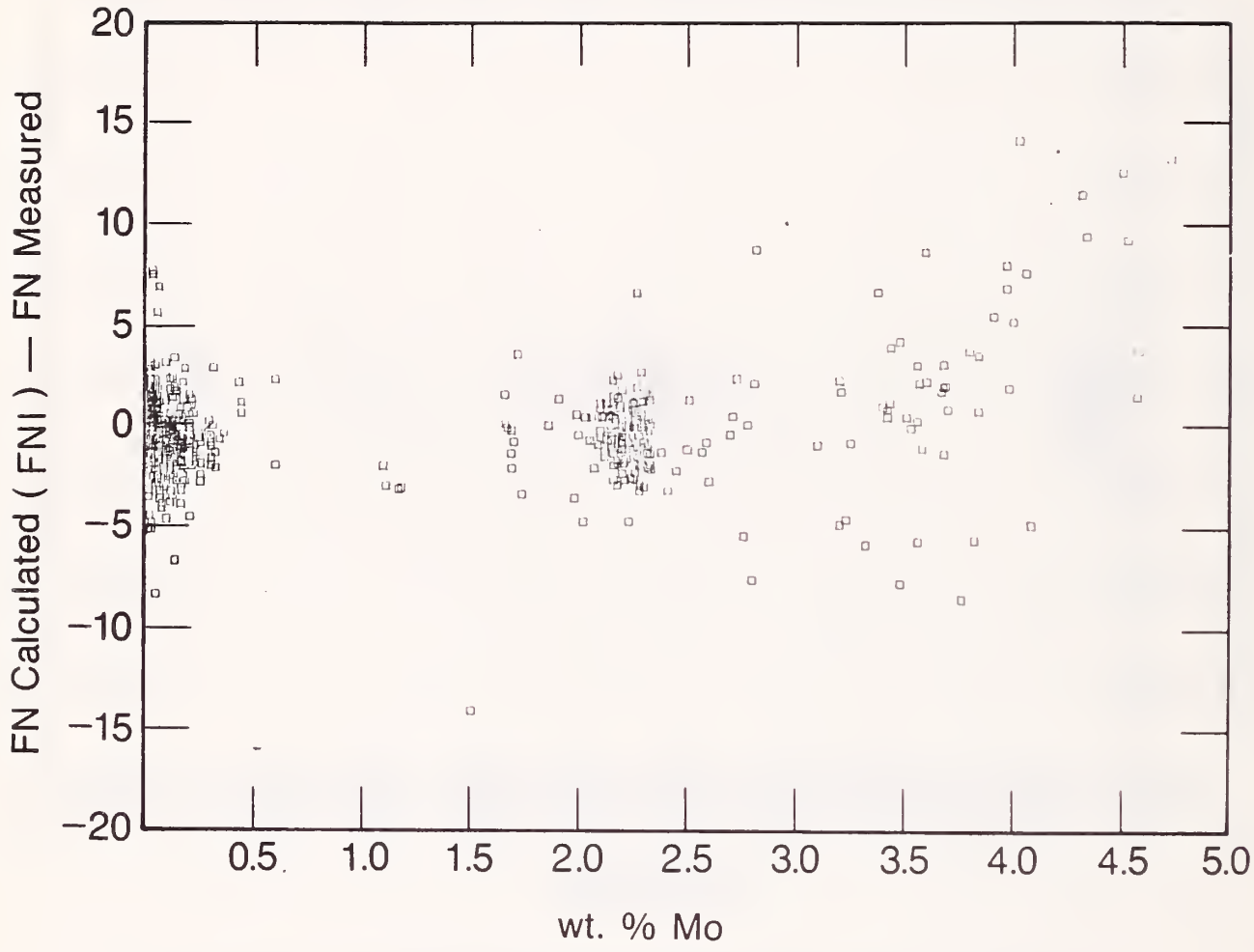

Figure 46. FN predicted error versus molybdenum content for weld data having FN values between 1 and 30 (FN1).

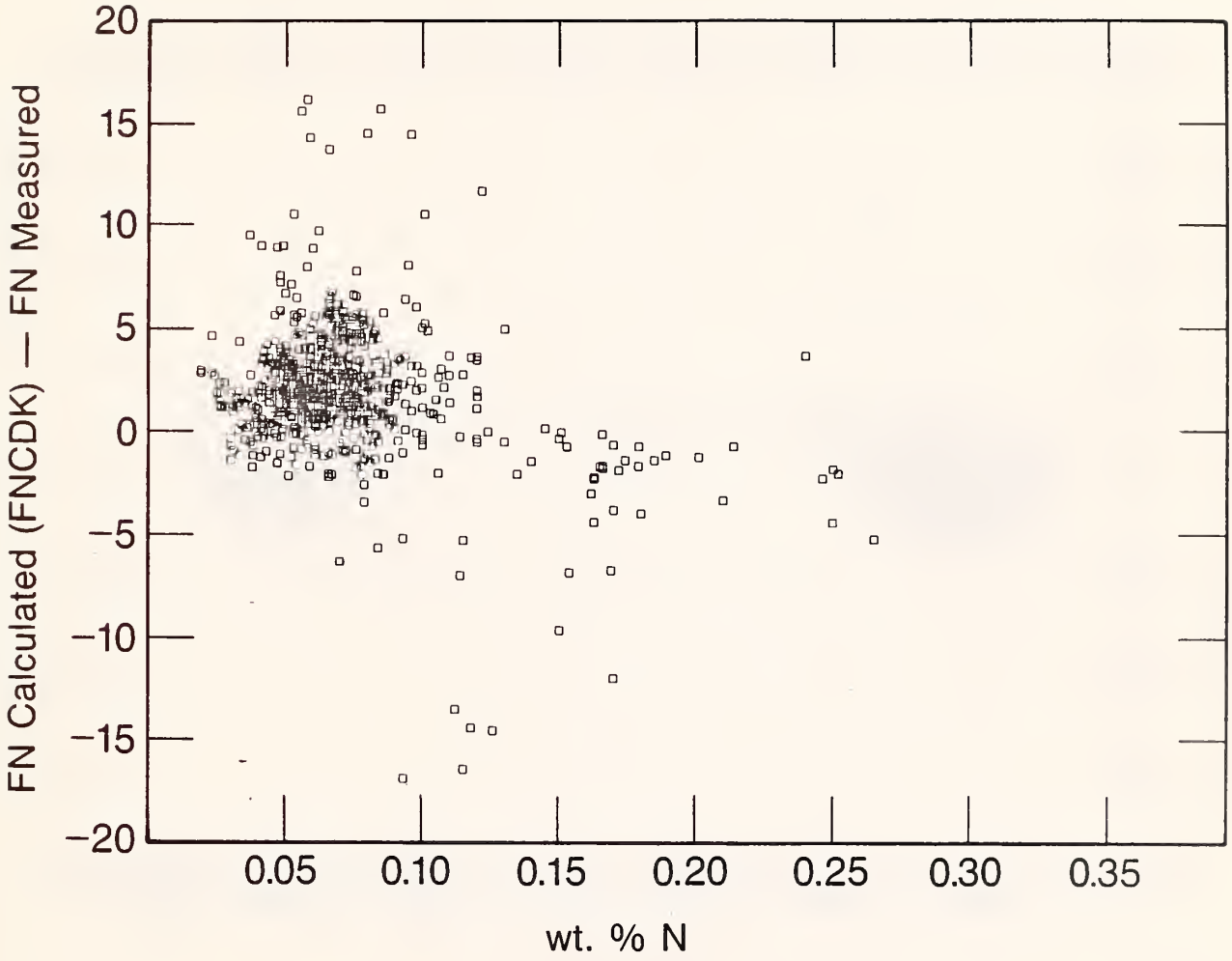

Figure 47. FN predicted error versus nitrogen content for data group 1 when the FNCDK equation was used.

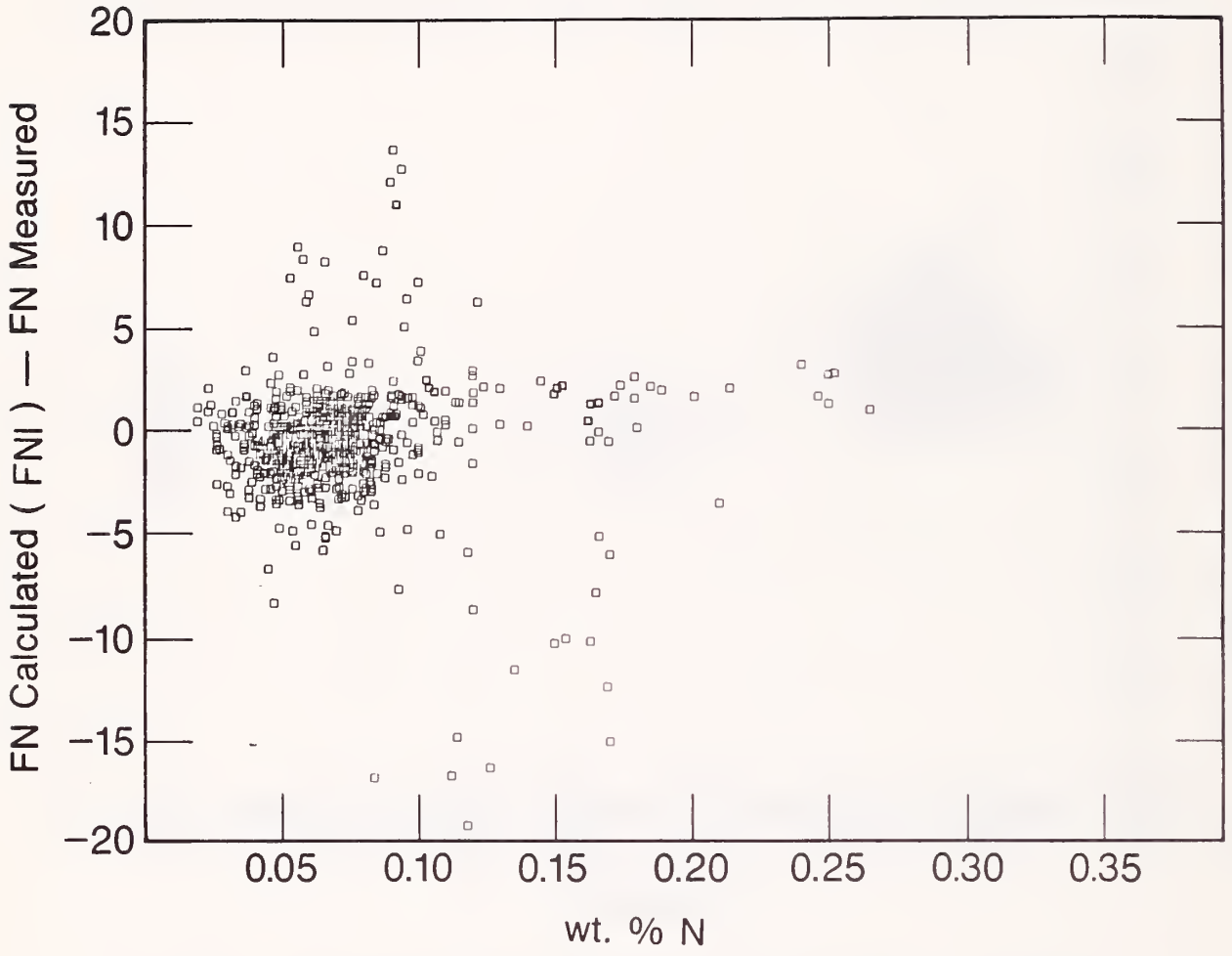

Figure 48. FN predicted error versus nitrogen content for data group 1 when the FN1 equation was used.

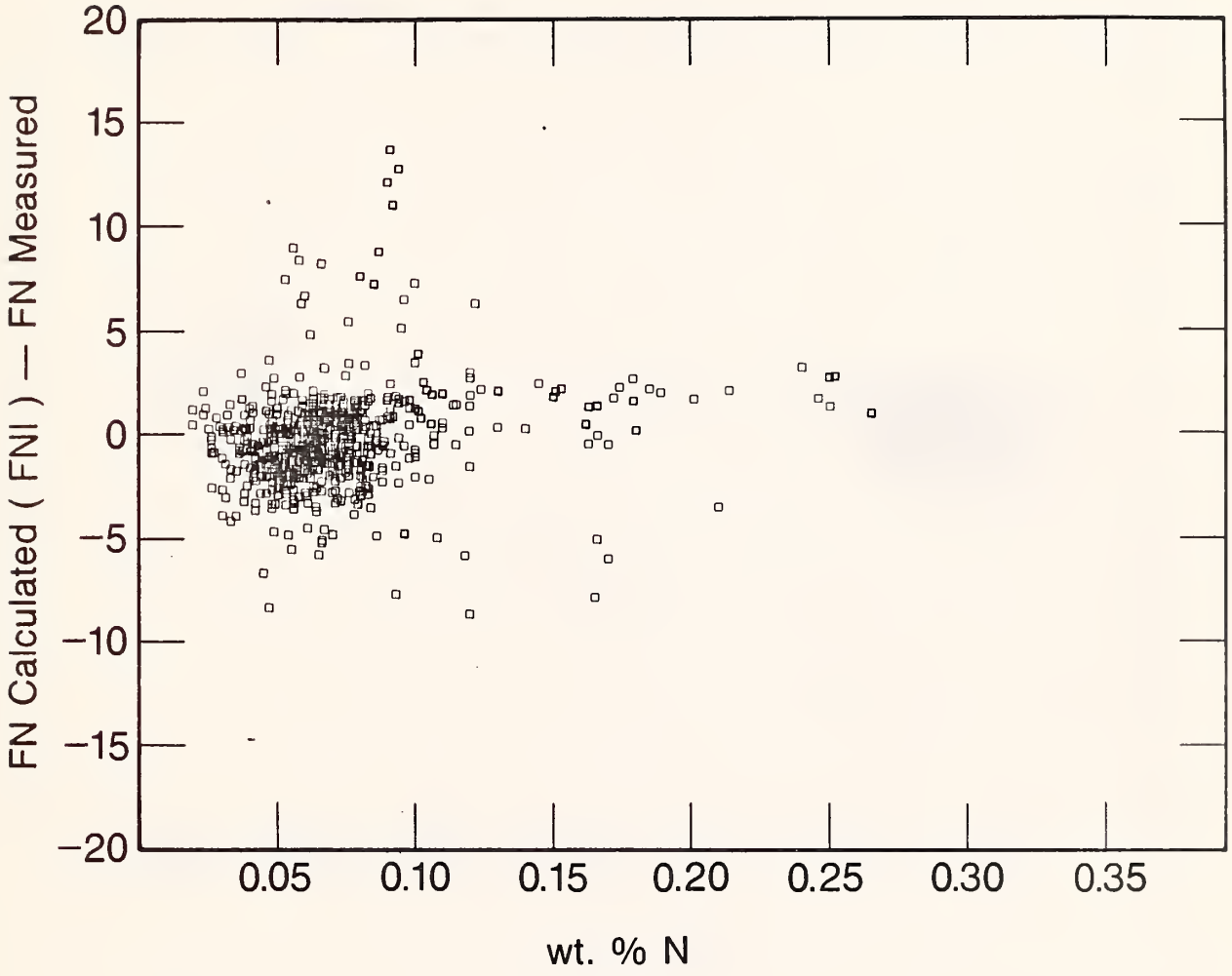

Figure 49. FN predicted error versus nitrogen content for welds having FN values between 1 and 30 (FN1).

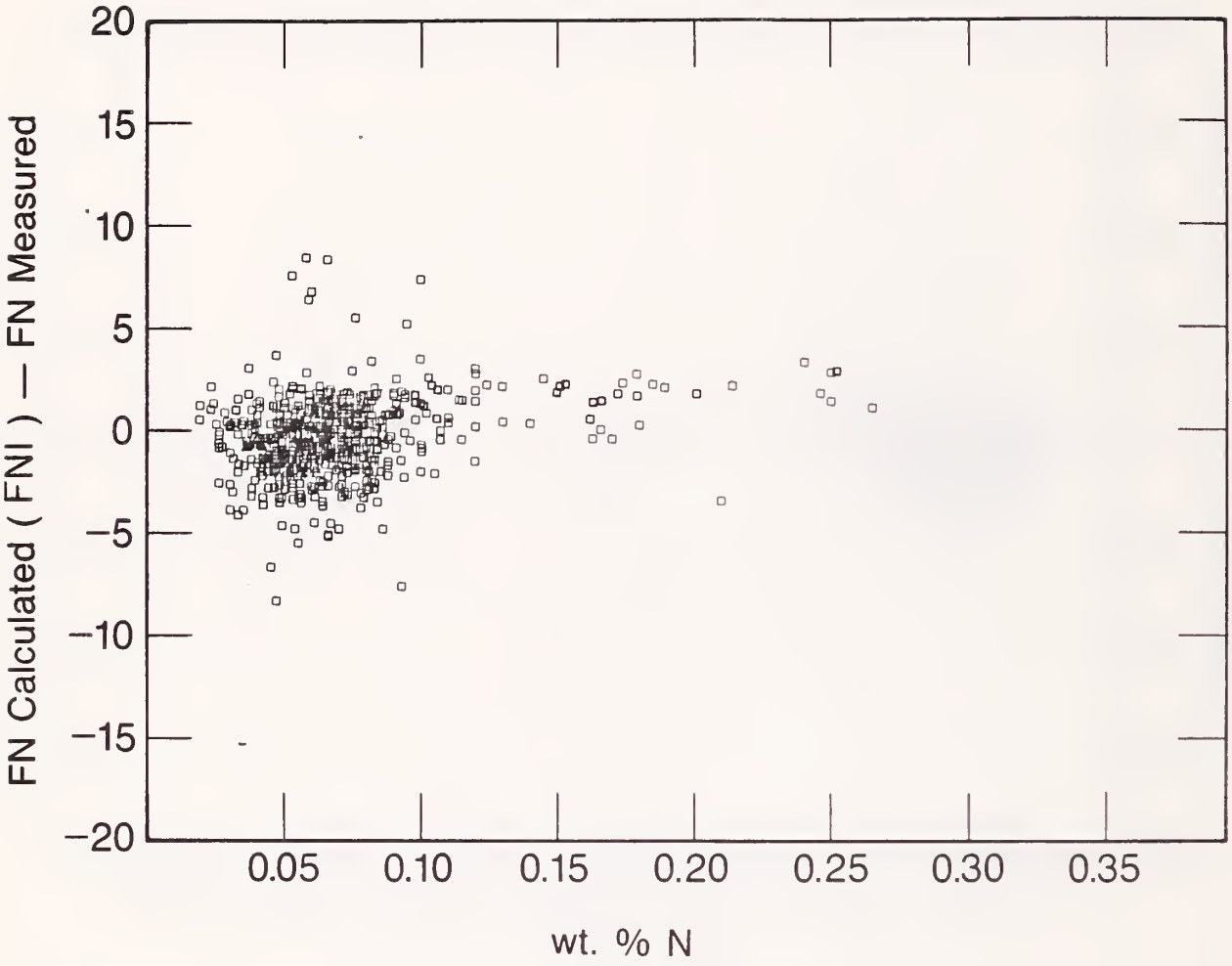

Figure 50. FN predicted error versus nitrogen content for data group 2 when the FN1 equation was used.

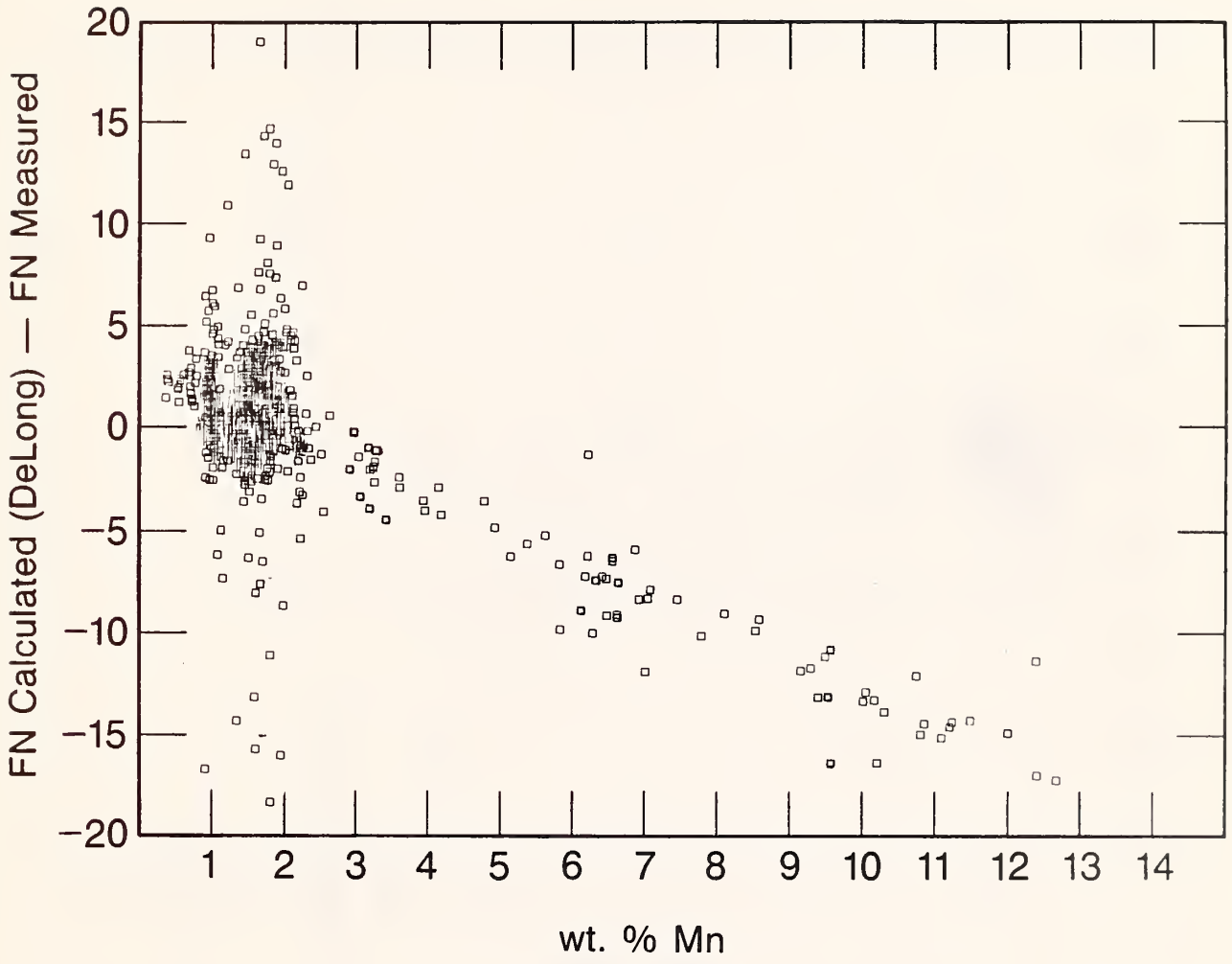

Figure 51. FN predicted error versus manganese content for data group 1 when the FNCD equation was used.

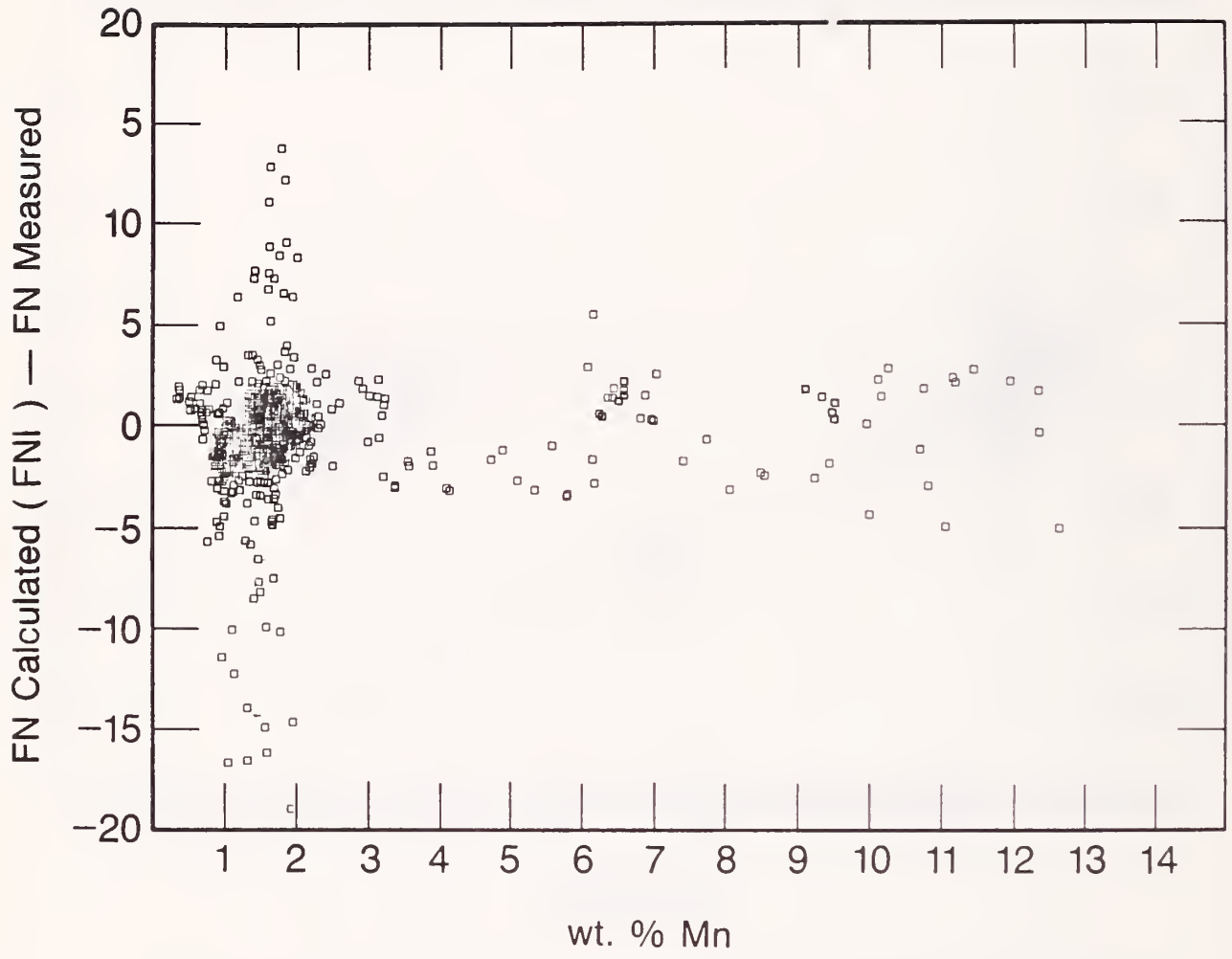

Figure 52. Predicted error versus manganese content for data group 1 when the FN1 equation was used.

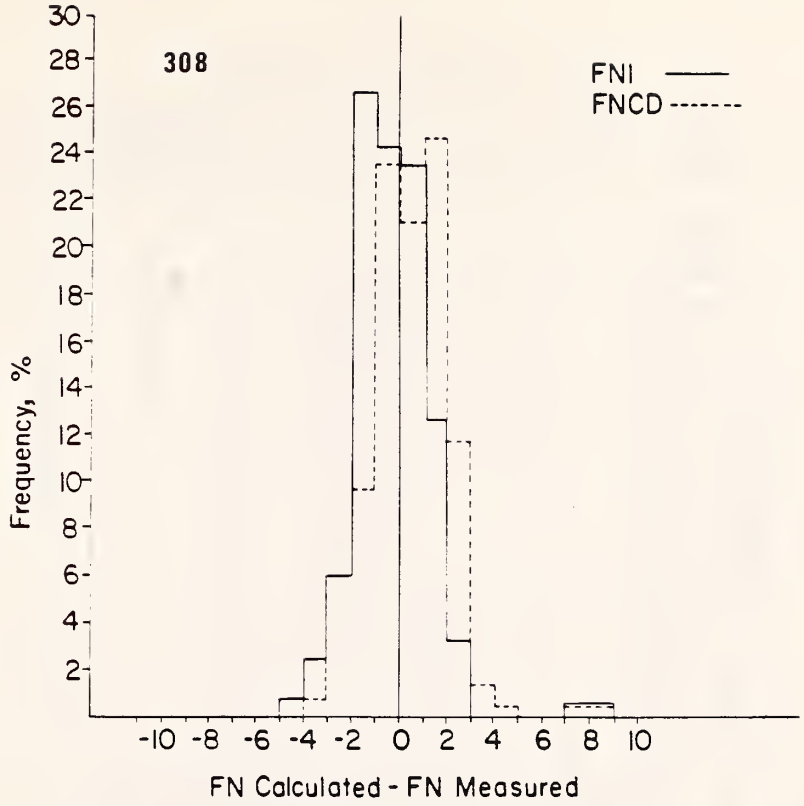

Figure 53. The frequency (%) versus FN predicted error for type 308 stainless steels.

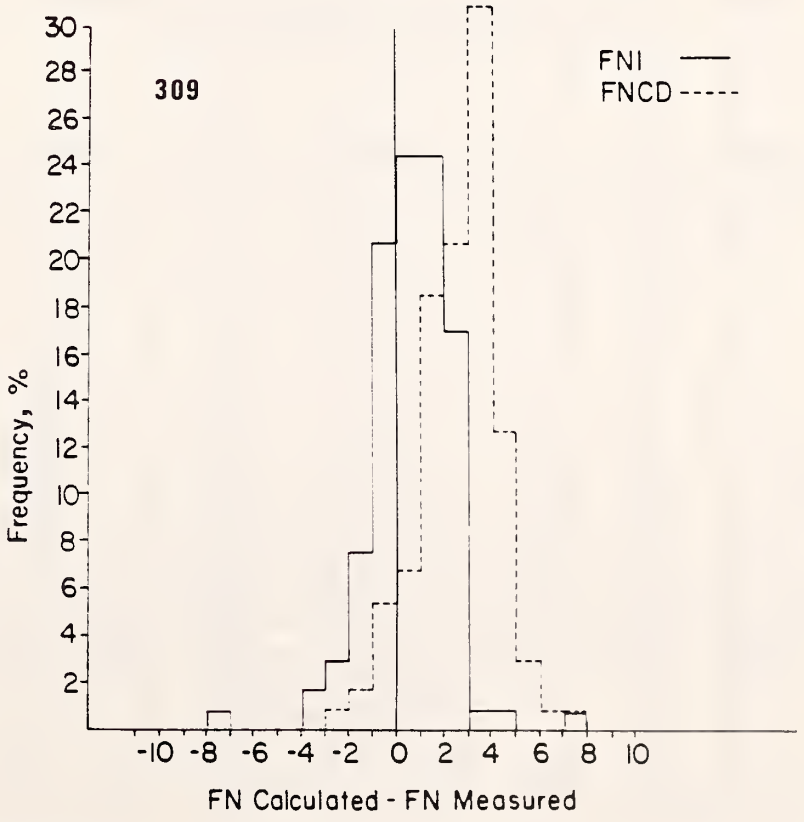

Figure 54. The frequency (%) versus FN predicted error for type 309 stainless steels.

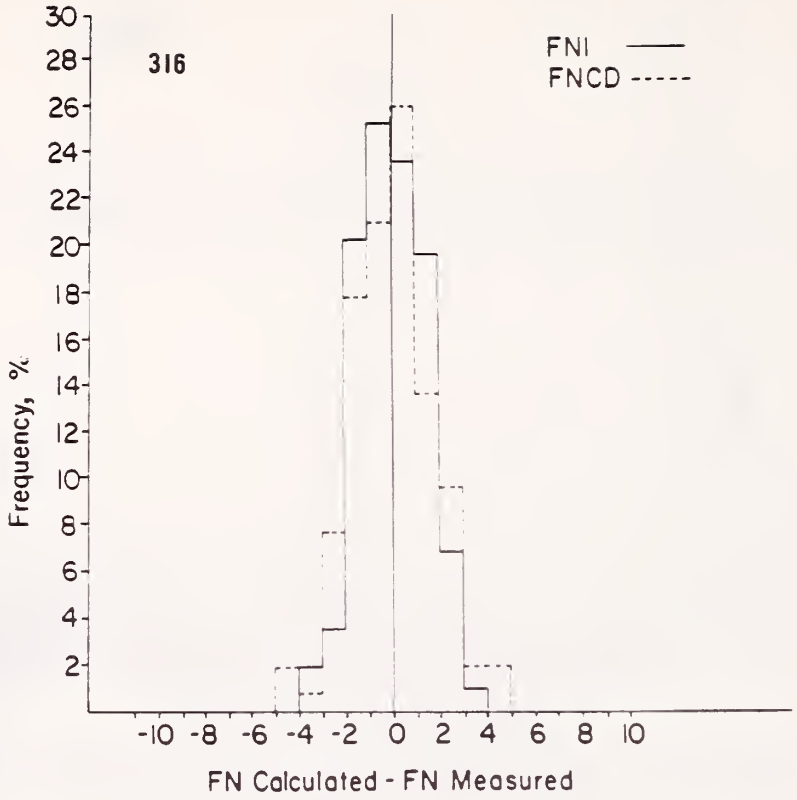

Figure 55. The frequency (%) versus FN predicted error for type 316 stainless steels.

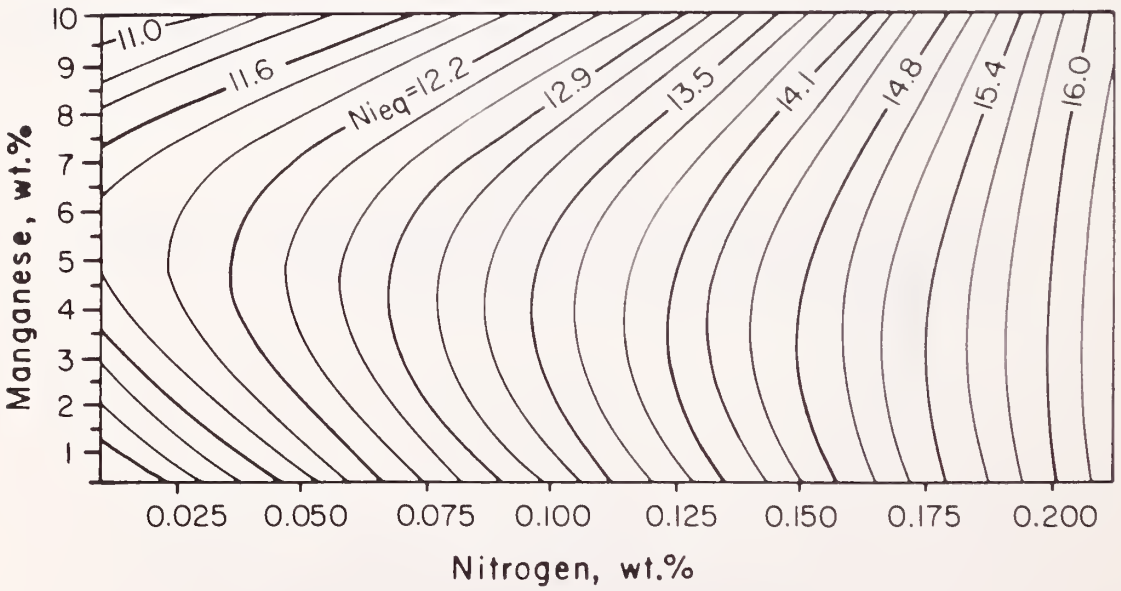

Figure 56. The manganese-nitrogen interaction.

Appendix I. FN Data Base

The weld metal compositions and FN values collected for the data base to develop and evaluate equations predicting ferrite content.

C	Mn	Si	Cr	Ni	N	Mo	Cb	Ti	FN
.04	1.54	.50	18.00	10.80	.16	.13	.00	.00	.2
.02	1.49	.46	18.20	10.40	.49	.21	.00	.00	.2
.05	1.43	.45	16.70	10.20	.15	.05	.00	.00	.3
.04	1.55	.60	18.40	11.70	.15	.04	.00	.00	2.2
.02	1.51	.47	18.60	9.10	.09	.22	.00	.03	.5
.04	1.54	.50	18.00	10.80	.16	.04	.00	.00	2.4
.02	1.49	.46	18.20	10.40	.49	.10	.00	.00	.5
.02	1.53	.41	18.30	9.10	.31	.18	.00	.00	.4
.02	1.65	.48	18.40	9.20	.36	.17	.00	.01	3.2
.02	1.53	.41	18.30	9.10	.31	.12	.00	.00	1.6
.03	1.61	.35	18.00	9.40	.13	.06	.00	.00	2.6
.02	1.51	.47	18.60	9.10	.09	.12	.00	.03	1.9
.03	1.72	.57	17.50	13.40	2.72	.25	.00	.01	.2
.03	1.72	.57	17.50	13.40	2.72	.14	.00	.01	.2
.04	1.06	.78	18.60	14.50	2.07	.02	.02	.02	.5
.03	1.53	.47	17.40	11.20	2.71	.19	.00	.00	.3
.03	1.53	.47	17.40	11.20	2.71	.14	.00	.00	2.0
.05	1.73	.36	17.20	11.80	2.78	.04	.00	.00	3.7
.02	1.63	.54	17.30	10.40	2.81	.20	.00	.00	.6
.04	1.64	.40	17.10	10.80	2.50	.06	.00	.00	5.2
.02	1.63	.54	17.30	10.40	2.81	.12	.00	.00	3.5
.03	1.90	.61	18.40	14.10	3.20	.05	.00	.00	1.8
.03	1.34	.43	18.40	14.20	3.21	.03	.00	.00	2.5
.01	1.55	.46	19.50	24.80	4.45	.06	.00	.01	.2
.02	1.40	.50	19.60	24.80	4.33	.04	.00	.00	.2
.02	1.59	.51	16.80	14.50	4.43	.30	.00	.02	.3
.02	1.59	.51	16.80	14.50	4.43	.11	.00	.02	.2
.03	1.47	.40	17.00	15.50	4.47	.03	.00	.01	.6
.02	1.41	.50	17.60	13.50	4.58	.20	.00	.00	.2
.02	1.49	.49	17.00	14.70	4.57	.06	.00	.02	1.1
.02	1.41	.50	17.60	13.50	4.58	.10	.00	.00	1.9
.08	5.79	.64	26.10	20.00	.57	.05	.02	.02	.5
.04	6.33	.37	18.00	15.00	2.61	.05	.01	.04	.2
.07	7.77	.43	17.20	9.30	.34	.04	.00	.04	2.4
.01	6.20	.37	17.90	7.90	.05	.08	.00	.00	1.1
.05	1.63	.46	17.10	10.70	2.13	.23	.00	.00	.1
.05	1.47	.48	21.30	11.50	.17	.24	.00	.00	.3
.05	1.50	.48	17.80	9.40	.17	.18	.00	.00	.1
.04	1.59	.54	23.80	13.50	.10	.20	.00	.00	.5
.04	1.48	.55	26.90	15.20	.13	.24	.00	.00	3.7
.04	1.33	.43	16.80	12.90	2.71	.06	.00	.00	.3
.04	1.42	.46	17.00	13.00	2.71	.06	.00	.00	.9
.05	1.63	.46	17.10	10.70	2.13	.09	.00	.00	1.6
.04	1.59	.54	23.80	13.50	.10	.05	.00	.00	11.6
.05	1.50	.48	17.80	9.40	.17	.05	.00	.00	3.0
.04	1.48	.55	26.90	15.20	.13	.05	.00	.00	19.3
.05	1.47	.48	21.30	11.50	.17	.05	.00	.00	8.4
.03	1.42	.46	16.70	10.70	2.70	.05	.00	.00	5.5
.06	1.62	.38	19.53	9.84	.20	.06	.00	.00	4.0
.05	1.65	.35	18.81	10.40	.20	.06	.00	.00	1.8
.05	1.19	.35	19.69	10.02	.13	.04	.00	.00	7.7
.05	1.19	.32	19.13	10.35	.12	.04	.00	.00	5.4
.05	1.13	.41	18.91	11.29	.13	.04	.00	.00	.1
.04	2.27	.31	18.97	12.30	2.28	.03	.00	.00	7.2
.04	2.32	.36	18.37	12.50	2.29	.03	.00	.00	4.8
.04	2.37	.33	18.08	13.52	2.22	.03	.00	.00	.8
.04	2.27	.38	17.53	14.25	2.23	.03	.00	.00	.1
.04	2.26	.37	17.36	16.70	2.15	.03	.00	.00	.1
.03	2.54	.27	17.82	11.98	2.28	.06	.00	.00	5.4
.03	2.52	.35	17.81	12.61	2.19	.06	.00	.00	1.8

Appendix I. FN Data Base, continued

C	Mn	Si	Cr	Ni	N	Mo	Cb	Ti	FN
.04	2.51	.30	17.80	12.90	2.25	.05	.00	.00	.4
.03	2.64	.32	17.74	15.60	2.12	.05	.00	.00	.0
.03	2.44	.30	18.22	11.63	2.29	.09	.00	.00	1.8
.03	2.42	.34	17.91	12.50	2.18	.10	.00	.00	.2
.03	2.42	.29	17.57	13.03	2.18	.10	.00	.00	.0
.03	2.46	.31	17.36	15.48	2.14	.09	.00	.00	.0
.05	1.16	.40	17.70	8.80	1.69	.04	.00	.00	9.9
.06	1.97	.36	16.68	8.74	1.69	.04	.00	.00	5.8
.05	2.21	.35	15.24	9.09	1.66	.04	.00	.00	1.5
.05	2.17	.25	15.31	9.19	1.67	.04	.00	.00	1.4
.05	2.18	.30	15.00	11.47	1.60	.03	.00	.00	.0
.05	1.30	.43	17.82	8.75	1.69	.07	.00	.00	8.2
.05	2.00	.43	17.82	8.72	1.72	.08	.00	.00	3.1
.05	2.23	.41	15.33	9.19	1.70	.08	.00	.00	1.4
.04	2.15	.35	15.28	9.36	1.73	.08	.00	.00	.6
.05	2.10	.31	14.93	11.52	1.64	.07	.00	.00	.3
.03	1.12	.33	21.60	11.45	.04	.05	.00	.00	11.1
.03	2.16	.36	21.81	11.60	.05	.06	.00	.00	10.4
.03	3.24	.34	21.78	11.67	.05	.06	.00	.00	10.6
.04	4.17	.36	21.87	11.49	.01	.06	.00	.00	11.5
.04	5.36	.37	21.99	11.56	.01	.06	.00	.00	11.3
.04	5.81	.35	21.99	11.76	.01	.06	.00	.00	11.3
.04	6.20	.35	22.20	11.65	.06	.06	.00	.00	11.5
.04	8.09	.36	22.20	11.75	.06	.06	.00	.00	11.4
.04	8.57	.32	22.19	11.85	.05	.06	.00	.00	10.9
.04	10.04	.34	22.28	11.88	.01	.06	.00	.00	12.6
.04	11.09	.36	22.26	12.00	.01	.07	.00	.00	12.0
.04	12.67	.33	22.39	12.18	.02	.07	.00	.00	12.1
.07	1.50	.27	23.08	12.28	.09	.07	.00	.00	8.8
.06	2.00	.27	23.19	12.18	.09	.07	.00	.00	8.3
.07	3.59	.24	23.32	12.41	.09	.07	.00	.00	9.2
.07	4.76	.27	23.42	12.41	.09	.07	.00	.00	9.6
.06	5.61	.28	21.92	11.51	.06	.07	.00	.00	7.6
.07	6.17	.21	21.95	11.60	.08	.08	.00	.00	7.3
.07	9.28	.23	22.11	11.74	.08	.07	.00	.00	8.0
.08	10.85	.23	22.17	11.82	.08	.08	.00	.00	8.2
.07	4.92	.23	21.77	11.40	.13	.07	.00	.00	7.6
.06	3.92	.24	21.83	11.63	.13	.07	.00	.00	7.0
.07	3.19	.25	21.64	11.52	.13	.07	.00	.00	6.5
.06	2.20	.25	21.55	11.30	.13	.06	.00	.00	6.5
.06	1.40	.27	21.61	11.60	.14	.06	.00	.00	6.0
.04	1.15	.41	17.85	11.80	2.18	.03	.00	.00	7.1
.04	2.07	.39	17.98	11.55	2.12	.03	.00	.00	6.9
.03	3.03	.39	18.11	11.45	2.20	.04	.00	.00	6.9
.05	3.94	.41	18.11	11.80	2.16	.03	.00	.00	6.8
.05	5.13	.41	18.20	11.68	2.16	.04	.00	.00	7.1
.04	7.44	.39	18.19	11.75	2.24	.04	.00	.00	6.6
.04	8.52	.42	18.30	11.73	2.26	.04	.00	.00	7.8
.05	9.48	.40	18.33	11.80	2.18	.05	.00	.00	6.9
.05	10.74	.40	18.28	11.88	2.20	.04	.00	.00	5.4
.05	12.39	.39	18.40	11.90	2.20	.05	.00	.00	2.6
.05	1.33	.22	19.90	9.49	.07	.03	.00	.00	11.2
.05	1.77	.24	20.38	9.65	.07	.03	.00	.00	12.2
.05	2.36	.25	20.98	9.52	.07	.11	.00	.00	7.9
.09	3.60	.47	19.97	9.49	1.10	.06	.00	.00	9.9
.08	3.40	.35	19.95	9.51	1.18	.07	.00	.00	10.1
.08	3.41	.37	19.77	9.18	1.11	.07	.00	.00	10.1
.04	1.92	.52	19.20	13.20	2.20	.06	.00	.04	4.0
.13	2.15	.54	26.40	20.50	.22	.06	.00	.05	.0
.06	1.95	.59	19.80	9.50	.09	.04	.00	.01	8.0
.03	1.81	.50	19.20	9.50	.15	.07	.00	.01	6.0
.03	1.68	.42	19.40	9.50	.13	.09	.00	.03	4.0
.04	1.73	.49	20.00	9.90	.12	.07	.00	.03	6.0

Appendix I. FN Data Base, continued

C	Mn	Si	Cr	Ni	N	Mo	Cb	Ti	FN
.04	1.99	.64	19.90	9.70	.43	.06	.00	.01	6.0
.04	2.14	.31	19.60	9.70	.44	.06	.00	.01	6.0
.05	2.63	.23	19.90	9.80	.44	.05	.00	.01	6.0
.05	1.78	.58	19.80	9.60	.11	.07	.00	.01	6.0
.03	1.52	.49	18.90	9.70	.15	.09	.00	.01	4.0
.20	1.83	.49	25.90	20.40	.21	.07	.00	.02	.0
.11	1.62	.86	25.10	19.70	2.60	.05	.00	.01	5.0
.05	1.56	.51	18.00	13.30	2.20	.08	.00	.00	.0
.03	1.57	.54	17.90	13.50	2.20	.05	.00	.00	.0
.20	1.63	.45	15.10	33.50	.72	.04	.00	.03	.0
.06	1.93	.47	19.90	9.70	.13	.06	.00	.02	6.0
.03	.90	.71	20.40	10.00	.02	.09	.00	.03	12.0
.03	2.20	.26	17.92	13.35	2.16	.03	.04	.06	.9
.04	2.15	.28	18.00	13.55	2.12	.02	.04	.06	.7
.06	1.11	.36	20.06	9.90	.14	.05	.02	.05	6.6
.03	2.22	.38	17.79	13.18	2.14	.03	.04	.06	1.2
.03	2.12	.37	18.13	13.48	2.19	.03	.04	.06	1.0
.03	2.13	.29	18.01	13.15	2.16	.02	.04	.07	1.7
.03	2.12	.31	18.12	13.42	2.18	.02	.04	.08	1.5
.04	5.82	.71	21.08	10.15	1.74	.21	.03	.04	11.9
.04	1.80	.46	18.09	13.60	3.58	.08	.03	.03	4.4
.04	11.20	.25	17.60	5.21	.12	.17	.02	.02	4.8
.02	1.08	.33	19.69	9.81	.12	.06	.02	.04	7.3
.08	1.00	.39	24.11	12.86	.19	.07	.03	.05	9.2
.02	1.02	.78	19.56	11.63	2.20	.05	.04	.06	9.8
.03	.88	.59	18.62	11.53	2.00	.07	.03	.05	6.5
.02	.94	.62	20.00	10.12	.12	.03	.03	.05	11.1
.05	1.00	.68	20.06	10.00	.14	.05	.03	.06	7.8
.05	.98	.68	20.37	9.96	.13	.06	.03	.05	8.8
.03	1.13	.39	20.47	9.97	.08	.08	.03	.04	8.8
.06	1.05	.39	19.84	9.60	.11	.06	.03	.05	7.8
.03	.94	.43	20.85	9.66	.16	.05	.03	.05	11.9
.03	1.04	.48	20.69	9.60	.20	.08	.03	.05	11.4
.03	.96	.38	19.88	9.52	.18	.07	.03	.05	8.5
.04	1.74	.40	18.31	12.47	2.24	.05	.04	.05	6.4
.03	.93	.33	18.78	11.71	2.25	.07	.03	.05	8.3
.04	.91	.33	18.89	11.70	2.30	.06	.03	.05	9.0
.04	.96	.43	23.63	13.35	.20	.07	.03	.05	9.3
.08	1.00	.42	23.76	12.67	.04	.08	.03	.05	4.2
.08	4.13	.61	20.21	9.92	1.17	.04	.02	.02	11.6
.07	.99	.73	23.56	12.60	.21	.05	.03	.06	8.1
.03	.74	.32	18.22	13.61	3.53	.06	.03	.04	4.2
.03	.76	.34	18.39	13.37	3.70	.07	.03	.04	4.8
.04	1.05	.42	24.02	13.64	.07	.09	.02	.03	9.0
.05	.98	.42	20.35	9.57	.18	.07	.03	.05	10.3
.04	1.00	.35	19.17	11.86	2.28	.06	.03	.05	9.8
.03	1.55	.48	19.99	11.82	2.33	.05	.04	.06	11.1
.04	.91	.33	18.89	11.70	2.30	.06	.03	.05	9.0
.05	1.01	.44	20.29	9.77	.12	.06	.03	.05	10.6
.03	1.05	.42	19.52	11.56	2.45	.05	.04	.05	11.8
.07	1.08	.81	23.86	12.61	.11	.05	.03	.07	10.5
.03	2.25	.21	17.78	11.54	2.29	.05	.03	.04	6.5
.03	.90	.37	18.98	11.39	2.21	.06	.03	.05	9.5
.05	1.01	.48	19.40	12.36	2.41	.05	.04	.05	9.6
.07	.93	.35	23.50	12.94	.16	.08	.02	.04	8.5
.03	.99	.40	20.39	9.79	.08	.05	.03	.05	10.8
.02	.97	.74	19.40	11.29	2.12	.06	.04	.05	10.3
.03	.96	.36	19.13	11.90	2.28	.05	.03	.05	10.6
.02	1.22	.36	19.78	11.70	2.21	.06	.03	.05	11.4
.03	.83	.32	18.85	11.35	2.12	.06	.03	.04	8.9
.03	1.21	.33	19.19	11.69	2.24	.08	.04	.05	9.1
.04	1.22	.37	19.63	11.61	2.28	.08	.04	.04	9.3
.03	.95	.40	18.84	12.06	2.21	.06	.03	.05	8.7

Appendix I. FN Data Base, continued

C	Mn	Si	Cr	Ni	N	Mo	Cb	Ti	FN
.03	.96	.36	19.56	12.00	2.38	.08	.03	.05	8.7
.05	.98	.66	20.62	10.29	.11	.04	.03	.06	9.0
.03	.83	.39	20.16	9.84	.16	.04	.03	.05	11.1
.03	1.46	.37	20.19	9.82	.12	.06	.02	.04	11.6
.06	1.56	.33	24.22	12.87	.09	.08	.02	.03	11.4
.03	.98	.73	20.13	10.25	.17	.08	.03	.04	8.2
.03	.95	.68	20.21	10.26	.17	.06	.03	.05	9.6
.02	.89	.67	20.01	10.29	.15	.05	.03	.05	10.9
.03	1.01	.65	20.38	10.49	.20	.05	.03	.06	8.9
.03	.92	.62	20.01	10.25	.20	.05	.03	.04	8.7
.02	.90	.68	20.37	10.21	.16	.05	.03	.05	10.7
.08	1.00	.82	23.82	12.87	.12	.07	.03	.08	8.5
.06	.94	.68	23.67	12.79	.20	.07	.02	.05	8.7
.07	1.07	.82	24.09	13.18	.12	.07	.02	.08	9.6
.05	.95	.43	19.13	11.61	2.57	.06	.04	.05	8.5
.05	.86	.60	19.87	9.84	.16	.05	.03	.04	8.4
.05	.87	.58	20.35	9.96	.23	.05	.03	.04	9.4
.04	1.22	.37	19.63	11.61	2.28	.08	.04	.04	9.3
.04	1.38	.39	19.19	11.70	2.33	.06	.04	.05	8.8
.03	1.43	.38	19.32	11.57	2.23	.05	.04	.04	12.1
.02	.92	.31	18.85	11.20	2.33	.05	.04	.04	10.4
.03	.95	.33	19.05	11.35	2.16	.08	.03	.04	8.2
.03	1.00	.37	20.02	10.00	.18	.06	.03	.05	9.1
.03	.94	.36	20.16	9.53	.18	.07	.03	.04	9.9
.05	.92	.35	20.26	10.03	.22	.05	.03	.04	8.7
.06	.94	.36	20.06	9.90	.16	.04	.03	.06	8.5
.05	1.05	.42	20.38	9.89	.14	.07	.03	.05	9.1
.04	.96	.41	20.50	10.22	.17	.05	.03	.05	9.3
.03	.92	.39	20.58	10.24	.17	.05	.03	.05	11.1
.02	1.13	.41	20.20	9.73	.11	.08	.03	.04	11.6
.03	.94	.31	20.04	10.07	.17	.06	.02	.04	8.7
.02	1.08	.38	20.21	9.71	.11	.08	.03	.05	10.8
.03	1.04	.42	20.27	9.91	.25	.08	.03	.04	10.5
.03	.86	.36	19.80	10.03	.17	.04	.03	.05	9.7
.04	1.06	.45	20.31	9.76	.20	.09	.03	.05	7.9
.04	1.00	.43	20.32	9.97	.20	.07	.03	.04	12.6
.03	1.01	.40	20.06	9.70	.11	.08	.03	.04	11.3
.03	1.07	.44	20.35	9.92	.15	.08	.03	.05	8.0
.03	1.07	.43	20.53	9.95	.15	.09	.03	.04	8.2
.03	1.02	.38	20.32	10.07	.17	.03	.03	.05	11.9
.07	.95	.46	24.25	12.75	.24	.11	.03	.05	8.5
.07	.93	.41	23.60	12.47	.23	.08	.03	.06	9.9
.07	.98	.43	23.99	12.64	.22	.08	.03	.06	10.6
.08	.96	.35	23.95	13.22	.10	.05	.03	.05	8.3
.03	1.06	.44	22.78	13.62	.04	.06	.02	.07	6.6
.07	.92	.40	23.49	12.39	.23	.08	.03	.05	9.6
.07	.97	.47	23.60	12.74	.24	.09	.03	.06	8.8
.06	.96	.42	23.35	12.29	.21	.07	.02	.05	10.1
.06	1.15	.38	20.28	9.71	.12	.08	.02	.05	6.9
.05	.99	.37	20.21	9.49	.08	.08	.03	.05	9.3
.03	1.70	.53	20.88	17.45	3.82	.07	.15	.03	.9
.03	1.15	.44	21.64	17.25	3.52	.07	.13	.03	.8
.03	1.26	.39	21.72	17.45	3.64	.07	.08	.03	.7
.03	1.29	.44	21.78	17.23	3.92	.07	.17	.03	.8
.15	1.42	.70	23.80	9.95	3.76	.12	.03	.04	24.7
.03	2.23	.31	18.12	12.25	2.05	.03	.03	.04	5.9
.02	2.31	.31	18.02	13.65	2.06	.03	.03	.04	1.6
.02	2.25	.25	18.19	13.60	2.14	.03	.03	.04	.9
.02	2.04	.38	18.00	12.80	2.10	.04	.03	.04	2.2
.02	2.03	.22	18.10	12.80	2.10	.04	.03	.03	2.4
.02	2.31	.24	18.57	12.50	2.16	.02	.03	.04	3.4
.02	2.31	.24	18.05	12.50	2.16	.02	.03	.04	3.7
.02	2.33	.24	18.00	13.70	2.16	.03	.03	.04	1.0

Appendix I. FN Data Base, continued

C	Mn	Si	Cr	Ni	N	Mo	Cb	Ti	FN
.02	2.06	.31	18.15	12.30	2.07	.03	.03	.03	5.8
.02	2.36	.25	18.07	13.75	2.04	.02	.03	.04	.9
.04	12.40	.29	18.56	5.26	.11	.16	.00	.00	9.8
.03	10.80	.51	18.56	4.88	.11	.25	.00	.00	6.2
.05	10.16	.36	17.69	5.00	.11	.19	.00	.00	4.9
.04	10.00	.38	18.16	4.61	.11	.17	.00	.00	9.3
.04	1.35	.56	21.75	17.50	3.80	.08	.14	.03	1.4
.03	1.30	.44	21.67	12.80	3.82	.07	.02	.03	19.0
.03	.93	.44	22.76	12.90	2.76	.06	.03	.01	19.0
.03	.95	.41	21.57	17.00	4.00	.06	.01	.03	1.0
.03	.90	.36	21.20	17.20	3.84	.07	.11	.03	1.0
.03	2.19	.42	17.85	12.30	2.09	.04	.03	.04	4.7
.03	2.17	.44	17.73	12.05	2.20	.04	.04	.04	4.9
.04	2.09	.29	18.10	13.60	2.04	.05	.04	.04	.7
.03	2.21	.27	18.30	13.50	2.02	.06	.03	.04	.7
.03	2.37	.27	18.02	13.50	2.07	.04	.03	.04	.7
.03	1.37	.27	17.66	12.60	2.20	.04	.03	.05	3.1
.03	1.40	.28	17.83	12.60	2.18	.04	.04	.05	3.4
.03	2.22	.32	17.71	12.09	2.22	.04	.03	.04	5.4
.03	2.26	.30	17.74	12.63	2.26	.03	.03	.04	3.6
.03	1.64	.37	18.04	12.77	2.31	.06	.04	.05	1.2
.04	1.67	.37	18.41	12.75	2.29	.10	.04	.05	.6
.03	1.64	.38	18.42	12.67	2.33	.07	.04	.05	2.1
.03	2.15	.20	18.28	11.45	2.23	.03	.03	.03	6.6
.03	2.05	.31	18.10	11.60	2.20	.03	.03	.04	6.4
.04	2.16	.25	18.25	11.21	2.30	.04	.02	.04	6.6
.04	2.18	.34	17.97	11.80	2.33	.05	.03	.04	4.9
.05	4.70	.50	19.54	13.10	4.77	.19	.09	.01	.9
.04	2.22	.28	17.95	13.10	2.21	.04	.03	.04	.9
.03	1.67	.42	18.45	12.60	2.16	.06	.04	.06	4.2
.03	1.72	.52	19.65	12.10	2.18	.06	.04	.07	8.8
.03	2.21	.28	17.92	13.09	2.11	.04	.03	.04	1.0
.04	-2.25	.30	18.01	13.17	2.12	.04	.03	.04	1.1
.15	1.42	.49	20.45	10.00	.11	.02	.03	.08	2.6
.05	11.23	.39	17.89	4.82	.17	.19	.02	.02	5.4
.04	11.49	.28	17.81	5.14	.18	.18	.02	.02	4.9
.04	1.45	.28	17.69	12.25	2.13	.08	.03	.04	2.0
.04	1.51	.36	17.46	12.51	2.17	.05	.04	.05	1.0
.06	1.59	.41	18.74	12.10	2.27	.08	.05	.06	3.3
.03	1.10	.36	23.35	13.25	.09	.05	.03	.04	8.1
.05	1.29	.34	19.69	9.43	.25	.05	.05	.04	9.8
.05	1.36	.40	19.70	9.84	.25	.05	.05	.04	9.0
.05	1.33	.37	19.64	9.75	.25	.05	.05	.04	8.5
.05	1.35	.38	19.66	9.65	.25	.06	.05	.04	7.3
.12	1.70	.46	19.82	9.56	1.98	.04	.02	.04	11.3
.07	1.64	.53	23.97	13.09	.16	.07	.02	.05	7.5
.03	1.08	.46	23.19	13.55	.10	.06	.03	.07	7.4
.04	1.05	.45	23.08	13.38	.09	.06	.03	.06	6.3
.05	.98	.36	20.16	9.30	.08	.04	.03	.06	11.2
.06	1.27	.42	20.15	9.43	.14	.07	.03	.06	8.3
.06	1.15	.38	20.28	9.71	.12	.08	.02	.05	6.9
.02	.90	.68	20.37	10.21	.16	.05	.03	.05	10.7
.07	1.02	.87	23.95	12.94	.13	.07	.03	.06	8.8
.05	1.03	.65	20.11	10.17	.16	.04	.03	.05	11.3
.03	.79	.32	18.77	13.44	3.40	.07	.03	.02	4.8
.06	.95	.61	19.77	10.00	.12	.06	.03	.05	6.3
.03	1.45	.34	17.38	12.31	2.22	.04	.04	.04	3.3
.08	.92	.36	23.76	13.30	.11	.05	.03	.06	8.7
.04	1.17	.49	23.63	13.41	.12	.07	.03	.06	8.8
.06	1.03	.46	20.32	10.08	.16	.06	.03	.05	8.8
.06	1.34	.42	19.58	9.83	.11	.06	.02	.04	7.3
.05	1.25	.47	19.66	10.12	.11	.08	.02	.04	5.5
.03	1.40	.38	18.31	13.13	2.29	.06	.03	.03	1.3

Appendix I. FN Data Base, continued

C	Mn	Si	Cr	Ni	N	Mo	Cb	Ti	FN
.04	1.12	.43	19.59	9.84	.11	.07	.54	.05	6.3
.07	.91	.83	23.39	13.11	.18	.08	.03	.09	6.8
.05	1.05	.41	19.87	9.81	.08	.05	.57	.05	9.0
.06	1.12	.36	19.63	9.52	.31	.06	.03	.05	6.0
.07	1.20	.57	20.00	9.59	.32	.05	.04	.06	8.2
.06	1.35	.77	20.40	9.51	.32	.06	.04	.07	10.9
.04	.92	.45	19.02	9.47	.11	.06	.55	.05	7.2
.04	1.15	.56	19.80	9.45	.12	.05	.58	.06	10.2
.06	1.47	.53	20.18	9.64	.11	.08	.67	.04	8.8
.05	1.75	.46	19.78	11.50	.18	.05	.03	.04	3.0
.05	1.67	.42	19.81	11.45	1.86	.05	.03	.04	7.3
.05	1.65	.41	19.78	11.60	2.59	.05	.03	.04	9.6
.06	1.55	.46	19.81	11.60	3.68	.05	.03	.04	12.0
.06	1.53	.46	19.77	11.55	5.29	.05	.03	.04	15.8
.06	1.45	.41	19.52	11.60	6.85	.05	.03	.04	20.5
.03	1.57	.29	17.58	9.19	.02	.05	.00	.00	2.8
.03	1.49	.34	15.37	9.06	2.03	.03	.00	.00	3.4
.03	3.23	.39	17.89	9.02	.02	.04	.00	.00	4.0
.04	6.54	.37	17.61	9.13	.02	.05	.00	.00	2.8
.04	6.31	.34	15.39	9.14	1.99	.05	.00	.00	2.8
.04	6.31	.34	15.39	9.14	1.99	.05	.00	.00	2.8
.04	6.27	.34	15.17	9.14	3.84	.16	.00	.00	2.6
.03	1.66	.32	18.36	8.94	.02	.10	.00	.00	1.8
.03	2.96	.36	18.13	9.12	.02	.04	.00	.00	3.6
.04	6.46	.35	18.51	9.17	.02	.10	.00	.00	2.6
.04	9.52	.38	17.71	9.10	.02	.11	.00	.00	1.5
.03	3.18	.34	18.99	9.05	.02	.15	.00	.00	1.4
.04	6.62	.38	19.51	9.06	.02	.15	.00	.00	2.2
.04	6.61	.32	17.77	9.10	1.66	.17	.00	.00	2.5
.04	9.38	.35	18.98	9.14	.02	.16	.00	.00	1.7
.03	6.11	.36	20.90	9.29	.02	.25	.00	.00	1.6
.04	9.56	.37	20.22	9.07	.02	.27	.00	.00	1.2
.03	- 2.90	.30	18.79	9.12	.02	.10	.00	.00	2.0
.03	3.25	.39	17.58	9.00	.02	.03	.00	.00	3.2
.03	3.16	.42	17.90	9.05	.02	.04	.00	.00	3.0
.04	9.55	.34	17.70	9.26	.02	.04	.00	.00	3.6
.03	3.10	.36	17.75	9.07	.02	.15	.00	.00	.8
.03	3.46	.37	17.82	9.10	.02	.15	.00	.00	.6
.03	9.72	.34	17.60	9.06	.02	.26	.00	.00	.2
.04	1.29	.26	21.02	5.37	3.00	.15	.00	.15	49.0
.02	1.63	.26	20.99	6.75	3.09	.10	.00	.13	51.0
.03	1.80	.30	20.80	7.45	2.92	.09	.00	.13	42.0
.03	1.70	.28	20.33	7.90	2.80	.09	.00	.13	27.0
.03	1.95	.32	22.23	7.96	3.40	.12	.00	.13	43.0
.03	1.98	.32	22.24	8.40	3.37	.11	.00	.08	35.0
.02	1.60	.42	22.07	8.70	3.88	.13	.00	.23	43.0
.02	1.80	.61	21.92	8.55	3.26	.15	.00	.23	35.0
.02	1.75	.62	22.29	8.55	3.50	.13	.00	.33	62.0
.03	1.90	.62	21.85	8.55	3.40	.14	.00	.54	83.0
.02	1.60	.44	21.93	8.35	3.40	.15	.00	.13	32.0
.02	1.59	.52	22.14	8.45	3.42	.17	.00	.13	37.0
.02	1.49	.38	22.31	8.50	3.48	.17	.00	.05	27.0
.02	1.38	.39	21.93	8.40	3.32	.17	.00	.05	24.0
.04	1.33	.47	24.41	10.60	3.28	.11	.00	.21	43.0
.05	1.12	.56	24.71	9.10	3.32	.16	.00	.11	35.0
.05	1.14	.56	24.24	9.45	4.00	.17	.00	.11	37.0
.05	.95	.42	24.62	10.80	4.08	.17	.00	.11	28.0
.02	.90	.21	25.28	9.20	4.27	.12	.00	.13	56.0
.03	.91	.17	25.22	9.35	4.27	.11	.00	.01	67.0
.02	1.00	.25	25.25	9.30	3.46	.11	.00	.13	57.0
.02	.97	.32	24.79	10.25	3.64	.14	.00	.02	34.0
.02	.77	.31	24.58	10.95	3.56	.12	.00	.02	27.0
.01	1.06	.36	24.51	10.17	3.18	.08	.00	.02	40.0

Appendix I. FN Data Base, continued

C	Mn	Si	Cr	Ni	N	Mo	Cb	Ti	FN
.06	1.53	.40	20.57	9.29	.05	.05	.02	.02	7.0
.06	1.44	.39	20.57	9.31	.05	.06	.02	.02	7.0
.06	1.51	.40	20.48	9.35	.05	.07	.02	.02	7.0
.07	1.45	.39	20.19	9.41	.04	.06	.02	.02	6.0
.06	1.40	.39	20.09	9.38	.04	.06	.02	.02	4.0
.07	1.49	.40	20.38	9.41	.04	.09	.02	.02	5.0
.06	1.48	.41	20.19	9.33	.04	.09	.02	.02	5.0
.06	1.45	.42	20.47	9.34	.05	.07	.02	.02	8.0
.06	1.35	.31	20.20	9.37	.03	.06	.01	.02	5.0
.06	1.48	.39	20.31	9.32	.03	.07	.01	.02	6.0
.06	1.44	.36	20.37	9.37	.03	.07	.01	.02	6.0
.06	1.58	.42	20.73	9.26	.03	.06	.02	.02	8.0
.06	1.33	.29	20.27	9.41	.03	.09	.01	.01	6.0
.06	1.49	.39	20.36	9.37	.03	.08	.02	.02	6.0
.06	1.55	.36	20.42	9.45	.12	.10	.01	.02	7.0
.06	1.60	.37	20.58	9.35	.03	.10	.01	.02	7.0
.06	1.49	.37	20.64	9.39	.04	.08	.02	.02	10.0
.06	1.50	.37	20.64	9.34	.03	.08	.02	.02	9.0
.06	1.51	.38	20.63	9.81	.12	.08	.02	.02	10.0
.06	1.53	.40	20.49	9.76	.12	.08	.02	.02	9.0
.06	1.50	.40	20.33	9.72	.12	.06	.02	.03	7.0
.06	1.47	.38	20.31	9.75	.12	.09	.02	.02	6.0
.06	1.51	.42	20.41	9.71	.12	.05	.02	.02	7.0
.06	1.50	.40	20.33	9.72	.12	.06	.02	.03	7.0
.06	1.50	.41	20.39	9.70	.12	.05	.02	.02	6.0
.05	1.51	.43	20.41	9.73	.12	.05	.02	.02	8.0
.07	1.38	.41	20.16	9.32	.03	.08	.02	.02	5.0
.06	1.42	.38	20.17	9.45	.03	.06	.02	.02	5.0
.06	1.49	.43	20.32	9.40	.03	.07	.02	.02	5.0
.07	1.53	.43	20.25	9.39	.04	.07	.02	.03	5.0
.07	1.52	.42	20.28	9.31	.04	.06	.02	.02	6.0
.07	1.48	.40	20.26	9.33	.05	.07	.02	.02	5.0
.06	1.52	.45	20.48	9.32	.05	.07	.02	.02	8.0
.06	1.47	.42	20.42	9.39	.05	.08	.02	.02	6.0
.06	1.47	.43	20.57	9.31	.05	.07	.02	.02	8.0
.03	1.69	.46	23.14	13.44	.02	.04	.02	.03	9.0
.03	1.71	.46	23.00	13.41	.02	.05	.02	.03	9.0
.03	1.69	.48	23.20	13.57	.02	.07	.02	.03	8.0
.04	1.69	.43	22.94	13.64	.02	.07	.02	.02	6.0
.03	1.70	.47	22.94	13.78	.06	.07	.02	.00	7.0
.03	1.71	.45	22.93	13.73	.06	.07	.02	.03	5.0
.02	1.57	.42	23.10	13.85	.05	.09	.02	.02	8.0
.06	1.46	.44	20.43	9.33	.03	.08	.02	.03	8.0
.06	1.48	.44	20.35	9.45	.03	.08	.02	.02	4.0
.06	1.55	.43	20.34	9.42	.02	.10	.03	.03	4.0
.06	1.40	.42	20.22	9.40	.03	.13	.02	.02	4.0
.07	1.67	.50	20.62	9.28	.02	.10	.03	.03	7.0
.07	1.68	.44	20.76	9.31	.02	.09	.03	.03	5.0
.06	1.54	.48	20.41	9.18	.02	.09	.02	.03	6.0
.06	1.48	.46	20.64	9.46	.04	.11	.03	.05	4.0
.06	1.33	.40	20.29	9.33	1.50	.09	.20	.20	5.0
.03	1.80	.48	23.24	13.88	.09	.05	.02	.03	12.0
.03	1.79	.48	23.50	13.50	.09	.04	.02	.05	10.0
.03	1.79	.50	22.89	13.70	.09	.04	.02	.04	8.0
.03	1.84	.50	23.43	13.49	.09	.05	.03	.05	9.0
.03	1.75	.40	22.79	13.75	.04	.05	.02	.03	7.0
.03	1.56	.41	22.83	13.58	.03	.07	.03	.02	7.0
.03	1.72	.44	22.98	13.64	.04	.05	.02	.03	8.0
.03	1.73	.49	23.84	13.61	.05	.06	.02	.03	11.0
.03	1.76	.47	23.12	13.49	.06	.06	.02	.02	7.0
.03	1.73	.44	23.23	13.39	.06	.06	.02	.02	11.0
.03	1.69	.44	23.38	13.38	.06	.04	.02	.03	10.0
.04	1.71	.44	23.24	13.33	.06	.07	.02	.03	10.0

Appendix I. FN Data Base, continued

C	Mn	Si	Cr	Ni	N	Mo	Cb	Ti	FN
.03	1.57	.30	23.46	13.78	.10	.06	.02	.02	7.0
.03	1.51	.44	24.28	12.71	.04	.05	.02	.03	20.0
.04	1.78	.54	22.42	13.75	.03	.07	.02	.03	4.0
.03	1.85	.53	23.18	13.33	.02	.05	.03	.03	9.0
.03	1.80	.50	22.91	13.45	.02	.06	.02	.03	8.0
.03	1.68	.46	22.95	13.45	.02	.09	.02	.03	8.0
.03	1.75	.50	23.03	13.43	.02	.06	.02	.03	8.0
.03	1.79	.44	22.61	12.75	2.51	.04	.02	.02	12.0
.03	1.97	.55	23.00	12.72	2.27	.06	.02	.04	7.0
.04	1.79	.44	22.73	12.75	2.82	.06	.02	.03	5.0
.07	1.76	.39	23.44	12.61	.02	.07	.02	.02	8.0
.07	1.78	.42	23.34	12.66	.02	.07	.02	.03	7.0
.07	1.83	.41	23.61	12.94	.02	.07	.02	.02	8.0
.07	1.81	.48	23.33	12.90	.02	.08	.02	.03	5.0
.07	1.79	.39	23.74	12.98	.01	.07	.02	.03	5.0
.07	1.46	.41	23.06	13.02	.03	.09	.02	.02	3.0
.07	1.34	.31	23.01	13.25	.03	.08	.02	.02	5.0
.07	1.34	.33	23.05	12.99	.03	.08	.02	.02	5.0
.03	1.63	.40	23.16	13.34	.06	.06	.02	.03	11.0
.03	1.57	.38	23.11	13.33	.06	.07	.02	.02	9.0
.07	1.43	.39	23.26	13.14	.03	.10	.20	.20	4.0
.07	1.29	.34	23.05	12.88	.03	.07	.02	.02	6.0
.08	1.43	.39	23.21	13.12	.03	.08	.03	.02	6.0
.07	1.33	.39	23.23	12.90	.03	.07	.02	.02	6.0
.07	1.39	.40	23.27	12.87	.03	.07	.02	.02	6.0
.07	1.26	.33	23.22	12.91	.03	.08	.02	.02	8.0
.06	1.37	.40	23.32	12.87	.03	.06	.02	.02	6.0
.08	1.97	.44	23.35	12.68	.03	.08	.02	.03	5.0
.07	1.73	.41	23.90	12.61	.03	.06	.02	.03	8.0
.07	1.75	.42	23.93	12.52	.03	.07	.02	.03	7.0
.07	1.71	.41	23.77	12.57	.02	.07	.02	.03	7.0
.07	1.98	.44	23.63	12.56	.03	.08	.02	.03	7.0
.07	1.79	.46	24.21	12.52	.01	.07	.02	.03	9.0
.07	1.83	.48	24.36	12.54	.01	.08	.02	.03	9.0
.07	1.29	.36	22.96	12.92	.07	.08	.02	.02	6.0
.08	1.50	.46	23.08	13.04	.03	.07	.02	.02	3.0
.08	1.55	.59	23.28	13.08	.03	.07	.02	.03	4.0
.07	1.38	.38	23.16	13.19	.03	.06	.02	.02	4.0
.07	1.36	.38	22.84	12.90	.02	.11	.02	.02	3.0
.07	1.61	.48	23.54	12.90	.03	.07	.02	.03	6.0
.07	1.61	.47	23.33	12.77	.06	.07	.02	.03	6.0
.06	1.47	.40	23.02	12.50	.02	.08	.02	.02	6.0
.06	1.63	.47	23.22	12.51	.02	.08	.02	.02	5.0
.07	1.50	.43	22.86	12.48	.02	.07	.02	.02	5.0
.07	1.58	.51	23.12	12.28	.03	.06	.01	.02	8.0
.06	1.66	.49	23.36	12.25	.03	.06	.02	.02	8.0
.07	1.00	.52	23.28	12.29	.03	.10	.02	.02	7.0
.06	1.66	.52	23.56	12.25	.03	.07	.02	.03	8.0
.06	1.50	.46	23.33	12.30	.03	.07	.02	.02	7.0
.06	1.72	.52	23.60	12.16	.03	.05	.02	.03	8.0
.06	1.63	.40	23.58	12.88	.02	.10	.01	.02	6.0
.06	1.63	.42	23.19	12.85	.02	.09	.01	.02	5.0
.06	1.54	.41	23.12	12.87	.02	.09	.02	.02	5.0
.06	1.61	.43	23.17	12.87	.02	.07	.01	.02	5.0
.06	1.66	.44	23.54	12.82	.02	.07	.02	.03	6.0
.06	1.70	.43	23.38	12.80	.03	.08	.02	.03	5.0
.06	1.71	.43	23.50	12.81	.03	.08	.02	.03	5.0
.07	1.60	.44	23.36	13.00	.03	.07	.02	.02	5.0
.07	1.55	.42	23.30	13.09	.03	.07	.02	.02	4.0
.07	1.58	.46	23.24	12.96	.03	.07	.02	.02	4.0
.07	1.87	.44	23.51	12.69	.02	.07	.02	.02	6.0
.07	1.88	.44	23.89	12.46	.02	.07	.02	.02	8.0
.08	1.92	.47	23.86	12.49	.02	.08	.02	.03	7.0

Appendix I. FN Data Base, continued

C	Mn	Si	Cr	Ni	N	Mo	Cb	Ti	FN
.08	1.93	.47	23.93	12.41	.02	.07	.02	.03	7.0
.07	1.96	.46	24.15	12.72	.02	.09	.02	.03	8.0
.07	2.09	.50	24.26	12.49	.01	.07	.02	.03	8.0
.07	2.14	.51	24.32	12.47	.01	.07	.02	.03	8.0
.07	2.12	.56	24.52	12.69	.02	.08	.03	.03	8.0
.08	1.75	.43	24.17	12.45	.02	.08	.02	.03	7.0
.08	1.75	.40	24.15	12.69	.02	.08	.02	.03	6.0
.08	1.76	.43	24.14	12.57	.01	.08	.02	.03	7.0
.08	1.79	.44	24.28	12.63	.02	.08	.02	.03	8.0
.07	1.76	.46	24.27	12.44	.02	.04	.02	.03	7.0
.07	1.59	.45	23.12	12.68	.02	.09	.02	.02	8.0
.07	1.64	.46	23.17	12.65	.02	.08	.02	.02	5.0
.07	1.68	.49	23.23	12.67	.02	.08	.02	.03	5.0
.07	1.67	.45	22.93	12.72	.02	.07	.02	.02	4.0
.06	1.55	.44	23.00	12.63	.02	.08	.02	.02	4.0
.06	1.55	.46	23.00	12.57	.03	.09	.02	.03	5.0
.03	1.65	.43	18.64	11.33	2.29	.04	.02	.02	9.0
.02	1.62	.41	18.65	11.41	2.28	.06	.02	.02	7.0
.02	1.63	.43	18.80	11.37	2.30	.06	.02	.02	8.0
.02	1.69	.38	18.80	11.62	2.24	.06	.01	.02	7.0
.02	1.68	.35	18.68	11.70	2.25	.07	.01	.02	7.0
.02	1.32	.31	18.62	11.37	2.20	.06	.01	.01	6.0
.02	1.46	.38	18.83	11.37	2.18	.04	.01	.02	9.0
.03	1.52	.36	19.17	11.35	2.15	.05	.02	.02	8.0
.02	1.42	.34	18.94	11.42	2.19	.06	.01	.02	7.0
.02	1.46	.37	18.50	11.39	2.18	.06	.01	.02	8.0
.02	1.43	.35	18.86	11.42	2.18	.05	.01	.02	8.0
.06	1.70	.48	19.27	11.39	2.32	.06	.02	.02	7.0
.06	1.61	.43	19.47	11.59	2.28	.07	.02	.02	7.0
.06	1.70	.47	19.53	11.35	2.32	.05	.02	.02	9.0
.06	1.64	.46	19.47	11.47	2.33	.06	.02	.02	5.0
.06	1.57	.43	19.14	11.64	2.26	.07	.02	.02	4.0
.02	1.58	.42	18.90	11.48	2.17	.07	.02	.02	8.0
.02	1.57	.38	19.01	11.41	2.17	.06	.02	.02	8.0
.02	1.65	.42	19.02	11.30	2.15	.06	.01	.02	8.0
.02	1.49	.39	19.00	11.43	2.17	.07	.02	.02	6.0
.03	1.32	.33	18.76	11.60	2.15	.07	.02	.01	5.0
.02	1.51	.42	18.73	11.39	2.15	.05	.02	.02	6.0
.02	1.52	.40	19.10	11.54	2.15	.06	.02	.02	7.0
.02	1.80	.45	18.91	11.51	2.27	.05	.02	.02	9.0
.02	1.76	.49	19.02	11.34	2.27	.05	.02	.02	9.0
.02	1.69	.43	18.89	11.46	2.28	.05	.02	.02	9.0
.02	1.68	.45	18.92	11.42	2.31	.06	.02	.02	7.0
.02	1.65	.46	18.75	11.19	2.32	.05	.02	.02	9.0
.06	1.42	.46	19.38	11.41	2.26	.07	.01	.01	5.0
.05	1.39	.46	19.62	11.25	2.32	.09	.01	.02	7.0
.07	1.59	.46	19.56	11.39	2.25	.06	.01	.02	5.0
.07	1.51	.46	19.34	11.43	2.25	.06	.02	.02	5.0
.06	1.50	.45	19.48	11.43	2.26	.07	.01	.02	6.0
.06	1.40	.37	19.66	11.49	2.26	.07	.01	.01	5.0
.03	1.79	.36	19.27	12.35	3.56	.08	.01	.01	8.0
.02	1.87	.40	19.73	12.49	3.44	.05	.01	.01	6.0
.03	1.93	.45	19.82	12.38	3.42	.06	.01	.02	9.0
.03	1.87	.40	19.37	12.29	3.43	.05	.01	.01	8.0
.03	1.86	.40	19.42	12.42	3.42	.07	.01	.02	8.0
.05	1.80	.44	19.28	11.46	2.18	.05	.01	.01	4.0
.06	1.64	.43	19.48	11.37	2.27	.07	.02	.03	4.0
.06	1.50	.40	19.37	11.53	2.29	.07	.02	.02	5.0
.06	1.48	.41	19.34	11.40	2.30	.08	.02	.02	5.0
.06	1.69	.47	19.72	11.19	2.26	.08	.02	.03	6.0
.06	1.67	.44	19.37	11.55	2.29	.06	.02	.02	5.0
.07	1.63	.44	19.38	11.56	2.30	.07	.02	.02	4.0
.06	1.62	.42	19.59	11.53	2.30	.07	.02	.03	5.0

Appendix I. FN Data Base, continued

C	Mn	Si	Cr	Ni	N	Mo	Cb	Ti	FN
.03	1.63	.39	19.97	9.74	.08	.05	.54	.02	10.0
.03	1.50	.34	19.95	9.86	.08	.12	.60	.20	11.0
.03	1.66	.36	19.65	9.93	.06	.06	.52	.02	7.0
.03	1.55	.34	19.75	10.05	.05	.06	.54	.02	8.0
.04	1.82	.41	19.52	12.46	3.67	.07	.01	.01	7.0
.03	1.84	.43	19.74	12.48	3.69	.05	.01	.02	8.0
.03	2.24	.50	20.06	12.41	3.56	.05	.01	.02	8.0
.02	2.00	.44	19.71	12.52	3.60	.05	.01	.02	8.0
.02	2.05	.48	19.95	12.31	3.60	.07	.02	.02	2.0
.02	1.94	.44	19.66	12.49	3.68	.06	.02	.02	7.0
.02	2.03	.42	19.70	12.40	3.68	.07	.01	.02	8.0
.03	2.02	.44	19.54	12.51	3.57	.07	.01	.02	7.0
.03	1.66	.38	19.61	13.23	3.91	.10	.01	.02	2.0
.03	1.89	.39	20.15	12.40	4.34	.06	.01	.02	3.0
.03	1.60	.42	19.58	9.79	.04	.09	.50	.02	7.0
.02	1.63	.41	19.84	9.89	.06	.06	.46	.02	1.0
.03	1.65	.49	20.18	9.91	.03	.05	.59	.02	1.0
.02	1.84	.21	20.20	10.25	.03	.05	.71	.02	9.0
.02	1.61	.36	19.74	10.20	.05	.09	.59	.02	8.0
.02	1.80	.40	19.94	10.18	.05	.08	.64	.02	6.0
.02	1.73	.39	19.87	10.22	.05	.09	.63	.02	8.0
.02	1.76	.42	19.71	10.19	.05	.08	.63	.02	8.0
.02	1.90	.43	20.01	10.12	.05	.07	.70	.03	10.0
.04	1.89	.68	23.21	15.27	3.48	.10	.00	.00	6.0
.04	1.85	.70	23.07	14.29	3.97	.10	.00	.00	6.8
.04	1.87	.73	24.61	14.34	4.51	.09	.00	.00	5.6
.04	1.82	.63	24.54	13.85	4.03	.09	.00	.00	3.6
.03	1.45	.62	22.48	15.78	3.97	.08	.00	.00	2.4
.02	1.22	.39	22.57	14.97	2.73	.13	.00	.00	5.2
.03	1.35	.64	21.94	16.38	5.31	.08	.00	.00	.6
.02	1.20	.94	22.10	15.52	3.38	.12	.00	.00	1.0
.04	1.62	.65	24.37	16.31	5.02	.10	.00	.00	.0
.03	1.64	.68	24.74	14.02	4.32	.09	.00	.00	7.4
.04	1.66	.64	23.39	14.46	4.73	.09	.00	.00	2.0
.03	1.71	.64	23.08	14.41	4.06	.09	.00	.00	6.0
.04	1.69	.73	23.13	13.73	3.20	.11	.00	.00	17.0
.04	1.68	.68	23.44	13.64	3.23	.10	.00	.00	18.2
.03	1.70	.69	23.09	13.93	3.10	.10	.00	.00	13.7
.03	1.65	.72	24.73	14.43	4.53	.09	.00	.00	9.2
.03	1.64	.68	24.74	14.02	4.32	.09	.00	.00	7.4
.04	2.00	.56	19.85	9.77	.28	.04	.00	.00	8.0
.05	1.91	.51	19.68	9.30	.16	.06	.00	.00	7.8
.05	1.85	.49	19.95	9.40	.19	.05	.00	.00	7.6
.03	2.13	.55	24.30	13.41	.22	.09	.00	.00	9.4
.02	1.87	.54	19.98	9.70	.16	.06	.00	.00	10.0
.02	1.89	.54	20.03	9.62	.16	.06	.00	.00	9.4
.02	1.87	.55	20.05	9.62	.16	.06	.00	.00	9.6
.04	1.99	.57	19.84	9.77	.29	.04	.00	.00	8.7
.03	1.87	.53	18.80	12.28	2.11	.05	.00	.00	5.5
.02	1.79	.53	20.51	9.80	.16	.07	.00	.00	10.0
.03	1.91	.68	18.11	12.46	2.14	.05	.00	.00	3.9
.03	1.95	.60	19.51	9.60	.15	.05	.00	.00	7.8
.10	1.85	.61	24.49	12.89	.19	.10	.00	.00	6.8
.06	1.88	.57	19.76	9.34	.19	.08	.00	.00	6.8
.09	2.04	.55	24.40	12.85	.17	.12	.00	.00	7.8
.10	2.16	.57	24.58	12.78	.17	.10	.00	.00	6.6
.05	1.94	.50	20.13	9.26	.18	.06	.00	.00	9.8
.05	1.93	.52	20.01	9.34	.18	.07	.00	.00	8.4
.09	2.07	.56	24.31	12.87	.17	.11	.00	.00	6.0
.05	1.93	.52	20.36	9.17	.19	.06	.00	.00	9.2
.03	2.08	.59	20.27	9.42	.08	.07	.00	.00	8.5
.03	1.95	.53	20.12	9.18	.30	.08	.00	.00	9.2
.03	1.85	.52	20.04	9.27	.30	.08	.00	.00	9.2

Appendix I. FN Data Base, continued

C	Mn	Si	Cr	Ni	N	Mo	Cb	Ti	FN
.03	1.84	.53	19.99	9.33	.30	.08	.00	.00	10.6
.10	2.11	.63	24.53	12.83	.17	.12	.00	.00	6.8
.03	1.79	.50	19.90	9.47	.30	.10	.00	.00	9.8
.07	2.04	.53	20.04	9.35	.30	.07	.00	.00	7.0
.06	2.01	.53	19.89	9.38	.30	.07	.00	.00	8.2
.08	1.22	.84	24.97	12.86	.18	.12	.00	.00	10.1
.04	1.86	.54	19.71	9.53	.60	.05	.00	.00	6.6
.05	1.92	.53	19.86	9.37	.30	.07	.00	.00	8.0
.04	1.76	.52	19.57	9.40	.60	.05	.00	.00	10.4
.06	1.82	.49	19.80	9.29	.16	.06	.00	.00	7.4
.06	1.78	.49	19.72	9.33	.16	.06	.00	.00	7.4
.06	1.78	.50	19.73	9.39	.16	.07	.00	.00	7.8
.10	1.92	.54	24.58	13.12	.10	.06	.00	.00	8.6
.09	1.94	.56	24.36	13.04	.20	.07	.00	.00	8.2
.06	1.75	.55	19.79	9.44	.21	.07	.00	.00	5.6
.06	1.73	.56	19.71	9.32	.20	.07	.00	.00	7.3
.09	1.82	.51	24.19	13.08	.20	.07	.00	.00	7.0
.05	1.83	.54	20.35	9.29	.16	.06	.00	.00	10.9
.06	1.90	.61	19.77	9.29	.16	.05	.00	.00	8.0
.06	1.92	.54	20.01	9.34	.29	.05	.00	.00	7.2
.06	1.84	.51	19.82	9.29	.16	.08	.00	.00	7.0
.08	1.83	.72	24.66	13.13	.12	.07	.00	.00	9.0
.05	1.82	.52	20.41	9.20	.16	.05	.00	.00	11.6
.08	1.50	.70	23.02	12.65	2.20	.06	.00	.00	13.4
.03	2.01	.76	20.60	9.50	.14	.08	.88	.00	9.8
.09	2.22	.78	23.83	12.83	.08	.11	.84	.00	9.2
.09	2.09	.67	24.58	12.96	.14	.09	.00	.00	6.8
.09	1.93	.52	24.16	12.98	.21	.07	.00	.00	6.4
.04	1.23	.84	20.39	9.27	.16	.07	.00	.00	12.5
.05	1.62	.45	18.84	13.05	2.13	.08	.00	.00	2.4
.05	1.70	.46	18.73	13.00	2.14	.07	.00	.00	1.5
.03	1.91	.61	18.15	13.54	2.10	.05	.00	.00	.4
.03	1.82	.50	20.21	9.58	.23	.07	.00	.00	10.2
.03	1.61	.46	18.30	12.55	2.10	.04	.00	.00	4.4
.03	1.67	.43	18.97	12.28	3.25	.04	.00	.00	9.8
.03	2.02	.89	20.04	9.75	.13	.08	.87	.00	10.0
.03	1.82	.50	20.21	9.58	.23	.07	.00	.00	10.2
.03	1.32	.21	17.33	12.37	1.85	.08	.01	.00	.2
.04	1.54	.22	17.58	12.47	2.22	.07	.01	.00	1.5
.03	1.78	.22	17.73	12.82	2.28	.06	.01	.00	.7
.03	2.33	.35	17.75	12.78	2.39	.08	.02	.00	.8
.03	2.43	.22	17.79	12.96	2.56	.06	.01	.00	.7
.03	2.25	.16	17.65	12.75	2.25	.06	.01	.00	.4
.03	1.43	.26	17.40	12.74	2.23	.08	.01	.00	1.6
.03	1.56	.42	17.48	12.59	2.14	.08	.02	.00	.4
.02	1.63	.46	17.46	13.04	2.10	.07	.02	.00	.2
.03	1.56	.43	17.54	13.78	2.11	.06	.02	.00	.2
.03	1.74	.46	17.42	12.20	2.08	.08	.01	.00	.5
.03	1.65	.23	17.34	12.42	2.13	.08	.01	.00	.7
.03	1.70	.15	17.30	12.54	2.16	.07	.01	.00	.5
.03	1.62	.51	17.48	14.31	2.04	.07	.00	.00	.5
.03	1.67	.61	17.34	14.84	2.02	.07	.00	.00	1.0
.03	1.60	.35	17.42	14.45	2.05	.07	.00	.00	.0
.03	1.66	.40	17.44	14.89	2.06	.07	.00	.00	.5
.03	1.56	.50	17.54	14.41	2.08	.07	.00	.00	.5
.03	1.56	.47	18.21	13.80	2.17	.07	.03	.00	.8
.03	1.68	.44	18.49	15.16	2.07	.05	.03	.00	1.0
.03	1.75	.43	18.03	14.20	2.15	.07	.02	.00	.6
.03	1.63	.44	17.97	13.68	2.21	.05	.02	.00	.7
.02	.71	.78	18.81	9.92	.05	.06	.02	.00	6.4
.02	.35	.84	18.21	10.15	.04	.10	.02	.00	1.4
.02	.37	.84	18.57	10.16	.04	.09	.02	.00	2.0
.02	.37	.84	18.37	10.11	.04	.09	.02	.00	1.6

Appendix I. FN Data Base, continued

C	Mn	Si	Cr	Ni	N	Mo	Cb	Ti	FN
.02	.39	.86	18.39	10.16	.04	.10	.02	.00	1.4
.02	.70	.84	18.96	10.11	.02	.11	.02	.00	2.5
.02	.69	.78	18.98	9.92	.03	.09	.02	.00	4.8
.02	.77	.65	18.90	9.89	.03	.08	.01	.00	3.4
.02	.55	.80	18.24	10.07	.05	.07	.01	.00	3.2
.02	.55	.80	18.23	10.05	.05	.08	.02	.00	2.2
.02	.53	.74	18.12	10.17	.05	.08	.02	.00	2.3
.02	.70	.87	19.55	10.03	.03	.08	.02	.00	6.6
.02	.72	.79	18.45	10.01	.05	.07	.01	.00	4.2
.02	.69	.73	18.14	10.15	.05	.06	.01	.00	3.7
.02	.67	.90	18.32	9.94	.05	.07	.01	.00	3.7
.02	.67	.83	18.57	9.92	.05	.06	.01	.00	3.9
.03	.89	.88	18.82	10.35	.02	.07	.01	.00	2.9
.02	.60	.83	18.51	9.63	.05	.08	.01	.00	4.8
.02	.50	.81	18.20	9.95	.05	.11	.01	.00	.9
.02	.55	.85	18.15	10.00	.05	.08	.02	.00	2.6
.02	.52	.84	18.20	10.11	.05	.08	.02	.00	2.1
.02	.52	.75	18.05	9.98	.05	.07	.01	.00	2.3
.03	1.57	.29	17.58	9.19	.02	.05	.00	.00	2.8
.03	.95	.22	17.57	8.67	.02	.03	.00	.00	6.0
.03	3.23	.39	17.87	9.02	.02	.04	.00	.00	4.0
.03	3.25	.39	17.58	9.00	.02	.03	.00	.00	3.2
.04	9.55	.34	17.70	9.26	.02	.04	.00	.00	3.6
.04	6.54	.37	17.61	9.13	.02	.05	.00	.00	2.8
.03	9.14	.43	21.60	11.67	.02	.20	.00	.00	1.0
.03	12.00	.49	21.90	11.56	.02	.21	.00	.00	1.8
.03	8.79	.33	18.61	8.69	.02	.25	.00	.00	.4
.03	5.61	.21	18.31	8.65	.02	.25	.00	.00	.4
.03	3.25	.22	18.04	8.50	.02	.23	.00	.00	.4
.04	10.20	.31	20.49	9.38	.02	.25	.00	.00	1.0
.05	10.30	.42	21.01	9.14	.02	.25	.00	.00	1.6
.04	1.45	.36	18.07	9.10	.02	.04	.00	.00	4.0
.03	1.45	.35	18.14	9.88	.02	.04	.00	.00	4.0
.03	2.04	.59	18.83	9.22	.02	.15	.00	.00	1.0
.04	6.85	.33	18.35	9.19	.02	.03	.00	.00	5.5
.03	7.07	.40	19.12	9.15	.02	.15	.00	.00	1.5
.03	7.02	.37	20.08	9.22	.02	.23	.00	.00	.5
.04	7.03	.31	14.74	9.18	2.32	.03	.00	.00	2.7
.03	6.96	.28	14.82	9.20	5.42	.20	.00	.00	.8
.04	6.91	.34	18.80	9.14	.02	.12	.00	.00	2.4
.04	6.47	.33	19.29	9.16	.02	.17	.00	.00	1.6
.03	6.11	.36	20.90	9.29	.02	.25	.00	.00	1.6
.04	6.54	.33	15.84	9.09	1.91	.05	.00	.00	2.7
.04	7.00	.30	15.78	9.18	3.51	.18	.00	.00	2.0
.03	1.66	.32	18.36	8.94	.02	.10	.00	.00	1.8
.03	3.18	.34	18.99	9.05	.02	.15	.00	.00	1.4
.03	3.27	.47	17.79	9.02	.02	.04	.00	.00	3.0
.04	6.40	.35	18.51	9.17	.02	.10	.00	.00	2.6
.04	6.62	.38	19.51	9.06	.02	.15	.00	.00	2.2
.04	6.31	.34	15.39	9.14	1.99	.05	.00	.00	2.8
.04	6.27	.34	15.17	9.14	3.84	.16	.00	.00	2.6
.04	9.56	.37	20.22	9.07	.02	.27	.00	.00	1.2
.04	9.38	.35	18.98	9.14	.02	.16	.00	.00	1.7
.04	9.52	.38	17.71	9.10	.02	.11	.00	.00	1.5
.03	3.10	.36	17.75	9.07	.02	.15	.00	.00	.8
.03	3.28	.47	17.63	9.05	.02	.15	.00	.00	.3
.03	3.14	.42	17.70	9.08	.02	.15	.00	.00	.5
.03	1.49	.34	15.37	9.06	2.03	.03	.00	.00	3.4
.04	3.05	.35	18.71	9.09	.02	.11	.00	.00	2.1
.04	6.61	.32	15.77	9.07	3.98	.18	.00	.00	2.6
.04	6.61	.32	17.77	9.10	1.66	.17	.00	.00	2.5
.03	3.46	.37	17.82	9.10	.02	.15	.00	.00	.6
.03	3.20	.34	17.72	9.07	.02	.15	.00	.00	.4

Appendix I. FN Data Base, continued

C	Mn	Si	Cr	Ni	N	Mo	Cb	Ti	FN
.03	2.96	.36	18.13	9.12	.02	.04	.00	.00	3.6
.03	2.90	.30	18.79	9.12	.02	.10	.00	.00	2.0
.03	3.16	.42	17.90	9.05	.02	.04	.00	.00	3.0
.03	1.60	.37	18.47	9.03	.02	.12	.00	.00	1.3
.03	1.70	.39	19.55	9.10	.02	.20	.00	.00	.5
.04	1.89	.68	23.21	15.27	3.48	.10	.00	.00	6.0
.04	1.85	.70	23.07	14.29	3.97	.10	.00	.00	6.8
.04	1.87	.73	24.61	14.34	4.51	.09	.00	.00	5.6
.04	1.82	.63	24.54	13.85	4.03	.09	.00	.00	3.6
.03	1.45	.62	22.48	15.78	3.97	.08	.00	.00	2.4
.02	1.22	.39	22.57	14.97	2.73	.13	.00	.00	5.2
.03	1.35	.64	21.94	16.38	5.31	.08	.00	.00	.6
.02	1.20	.94	22.10	15.52	3.38	.12	.00	.00	1.0
.04	1.62	.65	24.37	16.31	5.02	.10	.00	.00	.0
.03	1.64	.68	24.74	14.02	4.32	.09	.00	.00	7.4
.04	1.66	.64	23.39	14.46	4.73	.09	.00	.00	2.0
.03	1.71	.64	23.08	14.41	4.06	.09	.00	.00	6.0
.04	1.69	.73	23.13	13.73	3.20	.11	.00	.00	17.0
.04	1.68	.68	23.44	13.64	3.23	.10	.00	.00	18.2
.03	1.70	.69	23.09	13.93	3.10	.10	.00	.00	13.7
.03	1.65	.72	24.73	14.43	4.53	.09	.00	.00	9.2
.03	1.64	.68	24.74	14.02	4.32	.09	.00	.00	7.4
.04	2.00	.56	19.85	9.77	.28	.04	.00	.00	8.0
.05	1.91	.51	19.68	9.30	.16	.06	.00	.00	7.8
.05	1.85	.49	19.95	9.40	.19	.05	.00	.00	7.6
.03	2.13	.55	24.30	13.41	.22	.09	.00	.00	9.4
.02	1.87	.54	19.98	9.70	.16	.06	.00	.00	10.0
.02	1.89	.54	20.03	9.62	.16	.06	.00	.00	9.4
.02	1.87	.55	20.05	9.62	.16	.06	.00	.00	9.6
.04	1.99	.57	19.84	9.77	.29	.04	.00	.00	8.7
.03	1.87	.53	18.80	12.28	2.11	.05	.00	.00	5.5
.02	1.79	.53	20.51	9.80	.16	.07	.00	.00	10.0
.03	- 1.91	.68	18.11	12.46	2.14	.05	.00	.00	3.9
.03	1.95	.60	19.51	9.60	.15	.05	.00	.00	7.8
.10	1.85	.61	24.49	12.89	.19	.10	.00	.00	6.8
.06	1.88	.57	19.76	9.34	.19	.08	.00	.00	6.8
.09	2.04	.55	24.40	12.85	.17	.12	.00	.00	7.8
.10	2.16	.57	24.58	12.78	.17	.10	.00	.00	6.6
.05	1.94	.50	20.13	9.26	.18	.06	.00	.00	9.8
.05	1.93	.52	20.01	9.34	.18	.07	.00	.00	8.4
.09	2.07	.56	24.31	12.87	.17	.11	.00	.00	6.0
.05	1.93	.52	20.36	9.17	.19	.06	.00	.00	9.2
.03	2.08	.59	20.27	9.42	.08	.07	.00	.00	8.5
.03	1.95	.53	20.12	9.18	.30	.08	.00	.00	9.2
.03	1.85	.52	20.04	9.27	.30	.08	.00	.00	9.2
.03	1.84	.53	19.99	9.33	.30	.08	.00	.00	10.6
.10	2.11	.63	24.53	12.83	.17	.12	.00	.00	6.8
.03	1.79	.50	19.90	9.47	.30	.10	.00	.00	9.8
.07	2.04	.53	20.04	9.35	.30	.07	.00	.00	7.0
.06	2.01	.53	19.89	9.38	.30	.07	.00	.00	8.2
.08	1.22	.84	24.97	12.86	.18	.12	.00	.00	10.1
.04	1.86	.54	19.71	9.53	.60	.05	.00	.00	6.6
.05	1.92	.53	19.86	9.37	.30	.07	.00	.00	8.0
.04	1.76	.52	19.57	9.40	.60	.05	.00	.00	10.4
.06	1.82	.49	19.80	9.29	.16	.06	.00	.00	7.4
.06	1.78	.49	19.72	9.33	.16	.06	.00	.00	7.4
.06	1.78	.50	19.73	9.39	.16	.07	.00	.00	7.8
.10	1.92	.54	24.58	13.12	.10	.06	.00	.00	8.6
.09	1.94	.56	24.36	13.04	.20	.07	.00	.00	8.2
.06	1.75	.55	19.79	9.44	.21	.07	.00	.00	5.6
.06	1.73	.56	19.71	9.32	.20	.07	.00	.00	7.3
.09	1.82	.51	24.19	13.08	.20	.07	.00	.00	7.0
.05	1.83	.54	20.35	9.29	.16	.06	.00	.00	10.9

Appendix I. FN Data Base, continued

C	Mn	Si	Cr	Ni	N	Mo	Cb	Ti	FN
.06	1.90	.61	19.77	9.29	.16	.05	.00	.00	8.0
.06	1.92	.54	20.01	9.34	.29	.05	.00	.00	7.2
.06	1.84	.51	19.82	9.29	.16	.08	.00	.00	7.0
.08	1.83	.72	24.66	13.13	.12	.07	.00	.00	9.0
.05	1.82	.52	20.41	9.20	.16	.05	.00	.00	11.6
.08	1.50	.70	23.02	12.65	2.20	.06	.00	.00	13.4
.03	2.01	.76	20.60	9.50	.14	.08	.88	.00	9.8
.09	2.22	.78	23.83	12.83	.08	.11	.84	.00	9.2
.09	2.09	.67	24.58	12.96	.14	.09	.00	.00	6.8
.09	1.93	.52	24.16	12.98	.21	.07	.00	.00	6.4
.04	1.23	.84	20.39	9.27	.16	.07	.00	.00	12.5
.05	1.62	.45	18.84	13.05	2.13	.08	.00	.00	2.4
.05	1.70	.46	18.73	13.00	2.14	.07	.00	.00	1.5
.03	1.91	.61	18.15	13.54	2.10	.05	.00	.00	.4
.03	1.82	.50	20.21	9.58	.23	.07	.00	.00	10.2
.03	1.61	.46	18.30	12.55	2.10	.04	.00	.00	4.4
.03	1.67	.43	18.97	12.28	3.25	.04	.00	.00	9.8
.03	2.02	.89	20.04	9.75	.13	.08	.87	.00	10.0
.03	1.82	.50	20.21	9.58	.23	.07	.00	.00	10.2
.03	1.32	.21	17.33	12.37	1.85	.08	.01	.00	.2
.04	1.54	.22	17.58	12.47	2.22	.07	.01	.00	1.5
.03	1.78	.22	17.73	12.82	2.28	.06	.01	.00	.7
.03	2.33	.35	17.75	12.78	2.39	.08	.02	.00	.8
.03	2.43	.22	17.79	12.96	2.56	.06	.01	.00	.7
.03	2.25	.16	17.65	12.75	2.25	.06	.01	.00	.4
.03	1.43	.26	17.40	12.74	2.23	.08	.01	.00	1.6
.03	1.56	.42	17.48	12.59	2.14	.08	.02	.00	.4
.02	1.63	.46	17.46	13.04	2.10	.07	.02	.00	.2
.03	1.56	.43	17.54	13.78	2.11	.06	.02	.00	.2
.03	1.74	.46	17.42	12.20	2.08	.08	.01	.00	.5
.03	1.65	.23	17.34	12.42	2.13	.08	.01	.00	.7
.03	1.70	.15	17.30	12.54	2.16	.07	.01	.00	.5
.03	1.62	.51	17.48	14.31	2.04	.07	.00	.00	.5
.03	1.67	.61	17.34	14.84	2.02	.07	.00	.00	1.0
.03	1.60	.35	17.42	14.45	2.05	.07	.00	.00	.0
.03	1.66	.40	17.44	14.89	2.06	.07	.00	.00	.5
.03	1.56	.50	17.54	14.41	2.08	.07	.00	.00	.5
.03	1.56	.47	18.21	13.80	2.17	.07	.03	.00	.8
.03	1.68	.44	18.49	15.16	2.07	.05	.03	.00	1.0
.03	1.75	.43	18.03	14.20	2.15	.07	.02	.00	.6
.03	1.63	.44	17.97	13.68	2.21	.05	.02	.00	.7
.02	.71	.78	18.81	9.92	.05	.06	.02	.00	6.4
.02	.35	.84	18.21	10.15	.04	.10	.02	.00	1.4
.02	.37	.84	18.57	10.16	.04	.09	.02	.00	2.0
.02	.37	.84	18.37	10.11	.04	.09	.02	.00	1.6
.02	.39	.86	18.39	10.16	.04	.10	.02	.00	1.4
.02	.70	.84	18.96	10.11	.02	.11	.02	.00	2.5
.02	.69	.78	18.98	9.92	.03	.09	.02	.00	4.8
.02	.77	.65	18.90	9.89	.03	.08	.01	.00	3.4
.02	.55	.80	18.24	10.07	.05	.07	.01	.00	3.2
.02	.55	.80	18.23	10.05	.05	.08	.02	.00	2.2
.02	.53	.74	18.12	10.17	.05	.08	.02	.00	2.3
.02	.70	.87	19.55	10.03	.03	.08	.02	.00	6.6
.02	.72	.79	18.45	10.01	.05	.07	.01	.00	4.2
.02	.69	.73	18.14	10.15	.05	.06	.01	.00	3.7
.02	.67	.90	18.32	9.94	.05	.07	.01	.00	3.7
.02	.67	.83	18.57	9.92	.05	.06	.01	.00	3.9
.03	.89	.88	18.82	10.35	.02	.07	.01	.00	2.9
.02	.60	.83	18.51	9.63	.05	.08	.01	.00	4.8
.02	.50	.81	18.20	9.95	.05	.11	.01	.00	.9
.02	.55	.85	18.15	10.00	.05	.08	.02	.00	2.6
.02	.52	.84	18.20	10.11	.05	.08	.02	.00	2.1
.02	.52	.75	18.05	9.98	.05	.07	.01	.00	2.3

Appendix I. FN Data Base, continued

C	Mn	Si	Cr	Ni	N	Mo	Cb	Ti	FN
.03	1.57	.29	17.58	9.19	.02	.05	.00	.00	2.8
.03	.95	.22	17.57	8.67	.02	.03	.00	.00	6.0
.03	3.23	.39	17.87	9.02	.02	.04	.00	.00	4.0
.03	3.25	.39	17.58	9.00	.02	.03	.00	.00	3.2
.04	9.55	.34	17.70	9.26	.02	.04	.00	.00	3.6
.04	6.54	.37	17.61	9.13	.02	.05	.00	.00	2.8
.03	9.14	.43	21.60	11.67	.02	.20	.00	.00	1.0
.03	12.00	.49	21.90	11.56	.02	.21	.00	.00	1.8
.03	8.79	.33	18.61	8.69	.02	.25	.00	.00	.4
.03	5.61	.21	18.31	8.65	.02	.25	.00	.00	.4
.03	3.25	.22	18.04	8.50	.02	.23	.00	.00	.4
.04	10.20	.31	20.49	9.38	.02	.25	.00	.00	1.0
.05	10.30	.42	21.01	9.14	.02	.25	.00	.00	1.6
.04	1.45	.36	18.07	9.10	.02	.04	.00	.00	4.0
.03	1.45	.35	18.14	9.88	.02	.04	.00	.00	4.0
.03	2.04	.59	18.83	9.22	.02	.15	.00	.00	1.0
.04	6.85	.33	18.35	9.19	.02	.03	.00	.00	5.5
.03	7.07	.40	19.12	9.15	.02	.15	.00	.00	1.5
.03	7.02	.37	20.08	9.22	.02	.23	.00	.00	.5
.04	7.03	.31	14.74	9.18	2.32	.03	.00	.00	2.7
.03	6.96	.28	14.82	9.20	5.42	.20	.00	.00	.8
.04	6.91	.34	18.80	9.14	.02	.12	.00	.00	2.4
.04	6.47	.33	19.29	9.16	.02	.17	.00	.00	1.6
.03	6.11	.36	20.90	9.29	.02	.25	.00	.00	1.6
.04	6.54	.33	15.84	9.09	1.91	.05	.00	.00	2.7
.04	7.00	.30	15.78	9.18	3.51	.18	.00	.00	2.0
.03	1.66	.32	18.36	8.94	.02	.10	.00	.00	1.8
.03	3.18	.34	18.99	9.05	.02	.15	.00	.00	1.4
.03	3.27	.47	17.79	9.02	.02	.04	.00	.00	3.0
.04	6.40	.35	18.51	9.17	.02	.10	.00	.00	2.6
.04	6.62	.38	19.51	9.06	.02	.15	.00	.00	2.2
.04	6.31	.34	15.39	9.14	1.99	.05	.00	.00	2.8
.04	6.27	.34	15.17	9.14	3.84	.16	.00	.00	2.6
.04	9.56	.37	20.22	9.07	.02	.27	.00	.00	1.2
.04	9.38	.35	18.98	9.14	.02	.16	.00	.00	1.7
.04	9.52	.38	17.71	9.10	.02	.11	.00	.00	1.5
.03	3.10	.36	17.75	9.07	.02	.15	.00	.00	.8
.03	3.28	.47	17.63	9.05	.02	.15	.00	.00	.3
.03	3.14	.42	17.70	9.08	.02	.15	.00	.00	.5
.03	1.49	.34	15.37	9.06	2.03	.03	.00	.00	3.4
.04	3.05	.35	18.71	9.09	.02	.11	.00	.00	2.1
.04	6.61	.32	15.77	9.07	3.98	.18	.00	.00	2.6
.04	6.61	.32	17.77	9.10	1.66	.17	.00	.00	2.5
.03	3.46	.37	17.82	9.10	.02	.15	.00	.00	.6
.03	3.20	.34	17.72	9.07	.02	.15	.00	.00	.4
.03	2.96	.36	18.13	9.12	.02	.04	.00	.00	3.6
.03	2.90	.30	18.79	9.12	.02	.10	.00	.00	2.0
.03	3.16	.42	17.90	9.05	.02	.04	.00	.00	3.0
.03	1.60	.37	18.47	9.03	.02	.12	.00	.00	1.3
.03	1.70	.39	19.55	9.10	.02	.20	.00	.00	.5

INFLUENCE OF MOLYBDENUM ON THE STRENGTH AND TOUGHNESS OF STAINLESS STEEL WELDS FOR CRYOGENIC SERVICE*

C. N. McCowan and T. A. Siewert

Fracture and Deformation Division
National Bureau of Standards
Boulder, Colorado

E. Kivineva

Department of Metallurgy
University of Oulu
Oulu, Finland

Molybdenum additions to austenitic stainless welds were found to increase the 4-K yield strength by approximately 30 MPa/wt.%. Molybdenum additions had little effect on the 76-K Charpy V-Notch impact energy, with one exception: when the molybdenum content was raised from 1.7 to 3.8 wt.% in an otherwise equivalent stainless steel composition of approximately 17Cr–9Ni–6.6Mn–0.17N, the absorbed energy decreased from 33 to 16 J. At a nickel content of 14 wt.%, the higher molybdenum contents did not reduce the impact toughness. The loss in impact toughness for the 9-wt.% nickel, 3.8-wt.% molybdenum composition was linked to an increase in both small and large inclusions in the weld. The effects of nickel and manganese on the cryogenic strength and toughness are also reported.

INTRODUCTION

Recently there has been an interest in the development of higher strength austenitic stainless steels for lower cost and more compact magnetic fusion structural designs. Fusion magnet components are expected to operate at temperatures near 4 K. Austenitic stainless steels are one of the common structural materials chosen for service in this environment because, unlike many high strength materials, these alloys have good toughness at temperatures approaching absolute zero. For example, high

*Accepted for publication in Welding Metallurgy of Structural Steels, Metallurgical Society of AIME, Warrendale, Pennsylvania.

strength type 316LN stainless steel base materials have 4-K yield strengths of 1020 MPa, 76-K Charpy V-notch absorbed energies of 89 J, and 4-K fracture toughness [$K_{Ic}(J)$] values of 224 MPa$\sqrt{m}$.[1] The properties of these nitrogen-strengthened base materials cannot be totally utilized, however, until welds of comparable toughness at these elevated strengths are also developed.

Nitrogen additions can increase the yield strength of 300-series stainless steel weld metals to levels comparable to those of the nitrogen-strengthened base materials. The problem is that toughness values for the welds at cryogenic temperatures have been consistently lower than those for base materials of equal strength.[2] For this reason, other strengthening elements that have a less detrimental effect than nitrogen on toughness are being investigated.

The effect of molybdenum on the strength and toughness in shielded metal arc (SMA) welds is reported in this study, and interactive effects with nickel, nitrogen, and manganese are also investigated.

BACKGROUND

Much of the data pertaining to the effects of alloying element additions on the strength and toughness of austenitic stainless steels at 4 K are from studies of base materials. In types 304 and 316 stainless steel base materials, the strength–toughness relationship remains essentially the same, whether the strength is increased by nitrogen, carbon, or molybdenum additions.[3,4] The toughness decreases as the strength increases. From this perspective, nitrogen, which increases the 4-K yield strength in both 300-series weld and base metal by approximately 3000 MPa/wt.%, would therefore be expected to have a more detrimental effect on toughness than molybdenum.[5-8] Molybdenum reportedly increases the yield strength at 4 K by only 40 to 80 MPa/wt.% in 300 series base materials.[3,6,9] The only alloying element that has been found to improve the strength–toughness relationship in 300 series stainless steels at cryogenic temperatures is nickel. Increased nickel contents increase the toughness while having very little effect on the strength.[10]

Although, substitutional alloying by molybdenum in 300-series stainless steel base materials has been found to increase strength and decrease toughness, as molybdenum contents are increased, unexpected decreases in toughness have been observed.[3] One cause for the loss of toughness in molybdenum-alloyed stainless steels is the formation of molybdenum-rich chi and laves phases. Formation of these brittle intermetallic phases reduced the 76-K Charpy V-notch energy by more than 100 J in a 12Cr–12Ni–0.1N–Mo base metal alloy when the molybdenum content was increased from 5 to 7 wt.%.[9] However, not all reported toughness losses for molybdenum-alloyed stainless steels can be clearly related to embrittlement by these intermetallic phases. A type 316 stainless steel base metal, for example, had unexpectedly low 4-K fracture toughness values at 3.8-wt.% molybdenum contents.[3] Presumably, the molybdenum had not been uniformly distributed in this alloy. A second phase was present in the microstructure, but it was not rich in molybdenum.

In welds, nonuniform distributions of alloying elements are common owing to the dendritic solidification process. Molybdenum, in particular, segregates extensively in austenitic stainless steel welds.[11] Therefore, decreases in weld metal toughness, similar to the decreases observed in base metals, may also result from an inhomogeneous distribution of molybdenum. In the case of a 25Cr–16Ni–0.34N–Mo weld, ductilities were found to decrease rapidly after the molybdenum content exceeded 3.5 wt.%.[12]

MATERIALS AND PROCEDURE

The test matrix was designed to evaluate welds with molybdenum contents of approximately 0.02, 2, and 3.8 wt.%. At each level of molybdenum content, there were two possible nickel and nitrogen levels. In addition, several manganese additions were included in the test matrix. The alloying elements were added to the shielded metal arc (SMA) electrode coatings. The weld compositions were determined by optical emission spectroscopy, and the ferrite number (FN) of the weld deposits was measured magnetically; both are given in table 1.

Test welds were produced by using a series of 3.2-mm-diameter electrodes that had core wires from a single heat of type 308 stainless steel. The base material was 13-mm-thick by 305-mm-long mild steel plate. To overcome the effect of dilution by the base material, the exposed faces and backing strip were buttered with two layers of weld metal prior to welding, as specified in AWS A5.4-78. The same welder, power supply, and welding parameters (110 A, 22 V, identical bead sequences, and a heat input of approximately 1.6 kJ/mm) were used to minimize variations in the weldments. The interpass temperature was maintained at 93°C.

Two all-weld-metal 6-mm-diameter tensile specimens, oriented along the axis of the weld, were machined from each weld. The second specimen, reserved as a spare, was tested in a number of cases to check the repeatability of the results; in these cases, the average value is reported. Tensile specimens were tested at 4 K (in liquid helium) with a strain rate of 9.5×10^{-5} s^{-1}. A 25-mm gauge length was used. Specific details on the 4-K tensile testing equipment and procedures have been reported previously.[13]

Five 10-mm-square Charpy V-notch specimens, with their notches oriented perpendicular to the plate surface and located along the weld centerline, were removed from each weld and tested at 76 K (in liquid nitrogen).

Scanning electron microscopy was employed in the acquisition of inclusion distribution data from polished weld metal samples. In addition, wavelength dispersive spectroscopy (WDS) was used to evaluate molybdenum segregation between the ferrite and austenite phases, and energy dispersive spectroscopy (EDS) was used to evaluate the composition of the inclusions on the fracture surfaces.

Welds 6 and 13 were evaluated with x-ray diffraction techniques. They were step-scanned at 0.02-degree intervals of 2θ for 25 s/step. The tube voltage was 44 kV at 40 mA. The radiation was Cu$K\beta$ ($\lambda Cu\beta$ = 1.39225 Å).

RESULTS AND DISCUSSION

Strength

The yield strength of the weld metal at 4 K increased as a function of molybdenum, manganese, and nitrogen content. Relationships between alloy content and the ultimate strength could not be resolved. The strengths determined for the welds are listed in table 2.

The ultimate strength of the welds had a mean value of 1400 MPa, which is consistent with previous results obtained for SMA weld metals with compositions similar to the 9-wt.% nickel welds tested in this study.[5] Inhomogeneities in the weld structures and variations in ferrite contents evidently contributed to the scatter in the ultimate strength values of this study.

To evaluate the contributions of the alloying elements to the yield strengths of these welds, the data were analyzed with stepwise linear regression techniques. The 4-K yield strength (in MPa) was best predicted by the equation:

$$\text{Yield Strength} = 180 + 3200[N] + 33[Mo] + 32[Mn] + 13[Ni] \qquad (1)$$

This equation (elements in wt.%) had an F value of 920, a coefficient of regression (R^2) of 0.98, and a standard error of estimate of 31 MPa.

As expected, the interstitial strengthening of nitrogen had a much greater effect on the yield strength at 4 K than the solid-solution strengthening contributions of molybdenum, manganese, or nickel. Equation 1 shows the strengthening of nitrogen (3200 MPa/wt.% N) to be two orders of magnitude greater than that of the solid-solution elements. This nitrogen coefficient agrees well with those previously determined for both weld and base metals.[5-8] The effect of nitrogen on the yield strength at 4 K is shown in figure 1.

Much of the variation in yield strength, however, can be attributed to the solid-solution strengthening of molybdenum and manganese. To show the strengthening contributions made by these elements more clearly, the yield strength data were normalized to a 0.05-wt.% nitrogen content using the 3200 MPa/wt.% strengthening coefficient from equation 1 (figure 2). The slopes of the dashed lines in figure 2 indicate the increases in yield strength due to molybdenum additions at the three manganese contents present in this study. The difference in the yield strength between respective lines indicates the strengthening by manganese. Clearly, molybdenum and manganese also contribute to the 4-K yield strength of these welds.

Although both figure 2 and equation 1 indicate the relative magnitude of the strengthening contributions made by the alloying elements, singular strengthening coefficients to represent the effect of molybdenum or manganese could not be defined. The coefficients for these elements did not remain constant over the compositional range considered in this study.

For example, when the 14-wt.% nickel data were evaluated separately, the molybdenum coefficient decreased to 25 and the manganese coefficient decreased to 15. Further manipulation of the data indicated that the substitutional strengthening effects of manganese and molybdenum may decrease as the nickel content, nitrogen content, or both increase. The coefficients in equation 1, therefore, represent the average effects of these elements.

Toughness

The Charpy V-notch absorbed energy (AE) and lateral expansion (LE) values determined for the welds are reported in table 2. Impact toughness at 76 K decreased as the interstitial alloy content of the welds increased. The effects of substitutional alloy content on the impact toughness varied.

Nickel increased both AE and LE for alloys having low nitrogen contents (figures 3 and 4). At higher nitrogen levels (≥ 0.15-wt.% N), however, the beneficial effect of increased nickel content on the impact toughness was reduced.

The effect of molybdenum on the impact energy was related to the nickel content. At nickel contents of 14 wt.%, molybdenum did not adversely affect either the AE or LE. Increased molybdenum contents, in fact, may have been slightly beneficial to the toughness in the higher nickel content welds. In the 9-wt.% nickel welds, however, the AE was much lower for the 3.8-wt.% molybdenum alloy (weld 6). To verify this finding, a new weld was made with another electrode of similar composition. Again, low AE values (17 J) were found for the 4Mo–9Ni type stainless steel weld metal. These AE values are approximately 50 percent lower than that of the 2Mo–9Ni alloy (weld 13). Although the chromium content in welds 6 and 13 also differs, otherwise they have quite similar compositions and the decrease in AE is felt to be directly related to 3.8-wt.% molybdenum content. Lower molybdenum contents had no adverse effect on impact toughness of the 9-wt.% nickel welds. Possible explanations for the decrease in toughness associated with the 3.8-wt.% molybdenum welds are given later in this report.

Regression analysis was applied to the AE and LE data, but equations that were significant at the 99% confidence level could not be developed. Nevertheless, the analysis consistently suggested that: (1) nitrogen reduced the AE and LE, (2) nickel increased the AE and LE, and (3) manganese and ferrite decreased the LE. Because the chromium content was lowered as the molybdenum content was increased to maintain a constant ferrite potential, the effects of these elements on toughness is uncertain. With the exception of the 4Mo–9Ni weld, however, the effect of molybdenum on toughness was small in comparison with the nitrogen effect. The decrease in LE associated with manganese indicated here agrees well with a previous study performed on 9-wt.% nickel SMA welds.[5] In general agreement with past studies, nitrogen[3] and ferrite[14] reduce the toughness, and nickel[10] increases the toughness.

Evaluation of the 3.8-wt.% Molybdenum Alloy

In an effort to determine the reason for the low impact toughness of the 4Mo–9Ni alloy (weld 6), the microstructure of the weld and the fracture surfaces of the test specimens were evaluated and compared with those of weld 13. As previously mentioned, welds 6 and 13 had very similar compositions with the exception of their chromium and molybdenum contents. The reduction in absorbed energy from 33 J (weld 13) to 16 J is attributed to the increase in molybdenum content, from 1.7 wt.% in weld 13 to 3.8 wt.% in weld 6.

The two welds were found to have similar ferrite contents and primary ferritic solidification morphologies during light microscope evaluations of mechanically polished and etched weld metal specimens. The extent of molybdenum segregation between the ferritic and austenitic phases of welds 6 and 13 was also similar. Line scans using wavelength dispersive spectroscopy showed molybdenum contents to be approximately 1 wt.% higher in the ferritic phase than in the austenitic matrix.

Evaluations of the weld metals to determine the presence of intermetallic phases were inconclusive. No evidence of intermetallic phases was found during light microscope examination of the respective weld metals. X-ray analysis showed that both welds 6 and 13 had very similar types and quantities of phases present in their structures. These findings would indicate that the lower absorbed energy found for the 3.8-wt.% molybdenum alloy cannot be attributed to the formation of brittle intermetallic phases.

The only resolvable differences found between the two welds were related to inclusion sizes. Large inclusions were found on the Charpy V-notch fracture surfaces of the 3.8-wt.% molybdenum weld. These inclusions (figure 5) had (a) diameters ranging from 20 to 100 μm; (b) compositions rich in calcium, manganese, silicon, and titanium; and (c) glassy, conchoidal fractures associated with them. Although large inclusions were also found on lower molybdenum content fracture surfaces, they were observed less frequently and generally were not as large. In addition to finding large inclusions on the fracture surfaces of weld 6 specimens, inclusion counts on polished specimens showed a difference between the size distributions for the smaller inclusions in weld 6, figure 6. Weld 6 was had a greater number of small diameter inclusions than the other welds. Whether the presence of more small and large inclusions in alloy 6 was solely responsible for lowering the toughness in these samples is not known.

Inclusions have, however, long been recognized as void nucleation sites in materials having dimpled rupture fracture modes, and they do affect the resistance of engineering alloys to fracture.[15] Attempts to correlate inclusion content and fracture toughness [$K_{Ic}(J)$] at cryogenic temperatures are not directly applicable to the Charpy V-notch toughness results of this study, but they indicate that as inclusion spacing decreases, the toughness decreases.[16] Although more complete investigations of inclusion morphology and spacing were beyond the scope of this study, ductile dimple density counts taken on the fractured tensile specimen surfaces of welds 6 and 1 support the argument that decreased inclusion spacing lowers the toughness.

The weld 6 specimens had a substantially higher dimple density (4.4×10^5 dimples/mm^2) than the weld 1 specimens (3.2×10^5 dimples/mm^2). This indicates that the inclusions nucleating the voids in weld 6 were more closely spaced. Further study is needed to determine the quantitative relation between the presence of the large number of small inclusions (figure 6) observed in weld 6 and inclusion spacing. The very large inclusions, found on weld 6 fracture specimen surfaces, could also be speculated to reduce toughness. As a general observation, when the inclusion size is increased, the strain required to nucleate a void is decreased.[17,18]

CONCLUSIONS

1. The solid-solution strengthening contribution of molybdenum to the welds at 4 K is approximately 30 MPa/wt.%.

2. The effect of molybdenum on the 76-K Charpy V-notch absorbed energy and lateral expansion is small at molybdenum contents of 2 wt.% or less.

3. In 18Cr–9Ni stainless steel SMA welds, molybdenum contents up to 3.8 wt.% cause substantial decreases in Charpy V-notch absorbed energy and lateral expansion at 76 K.

4. In 18Cr–14Ni stainless steel SMA welds, increasing the molybdenum content from approximately 0 to 3.8 wt.% did not adversely affect the Charpy V-notch toughness at 76 K.

ACKNOWLEDGMENT

This work was supported by the U.S. Department of Energy, Office of Fusion Energy.

REFERENCES

1. Mazandarany, F. N., Parker, D. M., Koenig, R. F., Read, D. T., A Nitrogen-Strengthened Austenitic Stainless Steel for Cryogenic Magnet Structures, "Advances in Cryogenic Engineering—Materials," vol. 26, Plenum Press, New York, 58–170 (1980).

2. McHenry, H. I., Read, D. T., Steinmeyer, P. A., Evaluation of Stainless Steel Weld Metals at Cryogenic Temperatures, "Material Studies for Magnetic Fusion Energy Applications at Low Temperatures—II," NBSIR 79-1609, National Bureau of Standards, Boulder, Colorado, 299 (1979).

3. Purtscher, P. T., Reed, R. P., Effect of Molybdenum on the Strength and Toughness of Stainless Steels at Cryogenic Temperatures, to be published in "Advances in Cryogenic Engineering—Materials," vol 34, Plenum Press, New York.

4. Tobler, R. L., Read, D. T., Reed, R. P., Strength/Toughness Relationship for Interstitially Strengthened AISI 304 Stainless Steels at 4 K, "Fracture Mechanics: Thirteenth Conference," Richard Roberts, Ed., ASTM STP 743, American Society for Testing and Materials, Philadelphia, 250–268 (1981).

5. McCowan, C. N., Siewert, T. A., Reed, R. P., Lake, F. B., Manganese and Nitrogen in Stainless Steel SMA Welds for Cryogenic Service, Welding Journal, in press (1987).

6. Yamamoto, S., Yamagami, N., Ouchi, C., Effect of Metallurgical Variables on Strength and Toughness of Mn–Cr and Ni–Cr Stainless Steels at 4.2 K, "Advances in Cryogenic Engineering—Materials, vol. 32, Plenum Press, New York, 57–64 (1986).

7. Reed, R. P., Simon, N. J., Low Temperature Strengthening of Austenitic Stainless Steels with Nitrogen and Carbon, "Advances in Cryogenic Engineering—Materials, vol. 30, Plenum Press, New York, 127–136 (1984).

8. Simon, N. J., Reed, R. P., Strength and Toughness of AISI 304 and 316 at 4 K, "Material Studies for Magnetic Fusion Energy Applications at Low Temperatures—IX," NBSIR 86–3050, National Bureau of Standards, Boulder, Colorado, 27–42 (1986).

9. Miura, R., Development of High Strength Structural Alloys for Superconducting Magnets in Fusion Reactor, unpublished.

10. Reed, R. P., Purtscher, P. T., and Yushchenko, K. A., Nickel and Nitrogen Alloying Effects on the Strength and Toughness of Austenitic Stainless Steels at 4 K, " Advances in Cryogenic Engineering—Materials," vol. 32, Plenum Press, New York, 43–50 (1986).

11. Ogawa, T., Aoki, S., Sakamoto, T., and Zaizen, T., The Weldability of Nitrogen-Containing Austenitic Stainless Steel: Part I—Chloride Pitting Corrosion Resistance, Welding Journal 62(5), 139s–148s (1982).

12. Sakamoto, T., Abo, H., Okazaki, T., Ogawa, T., Ogawa, H., Zaizen, T., Corrosion Resistant Nitrogen-Containing Stainless Steels for Use by the Chemical Industry, "Alloys for the Eighties," Climax Molybdenum Company, Leadville, Colorado, 269–279 (1980).

13. Read, D. T., Tobler, R. L., Mechanical Property Measurements at Low Temperatures, "Advances in Cryogenic Engineering—Materials," vol. 28, Plenum Press, New York, 17–28 (1982).

14. Szumachowski, E. R., Reid, H. F., Cryogenic Toughness of SMA Austenitic Stainless Steel Weld Metals: Part 1—Role of Ferrite, Welding Journal 57(11), 325s–333s (1978).

15. Van Stone, R. H., Cox, J. R., Low, J. R., Jr., Psioda, J. A., Microstructural Aspects of Fracture by Dimpled Rupture, International Metals Reviews 30(4), 157–179 (1985).

16. Reed, R. P., Simon, N. J., Strength and Toughness of AISI 304 and 316 at 4 K, Journal of Nuclear Materials 44, 141–143 (1986).

17. Tauoka, J. P., Pampillo, C. A., Low, J. R., Jr., in "Review of Developments in Plane Strain Fracture Toughness Testing," W. F. Brown Jr., Ed., STP 463, American Society for Testing and Materials, Philadelphia, 191 (1970).

18. Van Stone, R. H., Merchant, R. H., Low, J. R., Jr., in "Fatigue and Fracture Toughness—Cryogenic Behavior," C. F. Hickey and R. G. Broadwell, Eds., STP 556, American Society for Testing and Materials, Philadelphia, 93 (1973).

Table 1. Weld Compositions and Ferrite Contents.

Weld	C	Mn	Si	P	S	Cr	Ni	Mo	N	FN Plate
1	0.033	1.57	0.29	0.013	0.006	17.58	9.19	0.02	0.047	4.9
2	0.034	1.49	0.34	0.013	0.006	15.37	9.06	2.03	0.034	4.4
5	0.039	6.31	0.34	0.013	0.007	15.39	9.14	1.99	0.047	3.6
6	0.036	6.27	0.34	0.013	0.007	15.17	9.14	3.84	0.162	2.9
12	0.037	6.62	0.38	0.013	0.008	19.51	9.06	0.02	0.151	3.6
13	0.035	6.61	0.32	0.013	0.007	17.77	9.10	1.66	0.166	3.5
28	0.028	3.23	0.33	0.014	0.007	19.56	9.31	0.02	0.186	1.4
29	0.029	3.21	0.34	0.019	0.007	18.18	9.24	2.17	0.179	1.8
60	0.036	2.38	0.29	0.024	0.005	19.89	9.40	0.02	0.187	0.9
23	0.037	3.10	0.29	0.012	0.011	19.51	14.61	0.03	0.044	0.4
24	0.038	3.01	0.30	0.016	0.010	14.29	14.29	2.01	0.039	0.5
25	0.040	2.97	0.28	0.020	0.010	15.68	14.33	3.90	0.036	0.4
26	0.040	6.51	0.29	0.017	0.013	17.80	14.49	1.92	0.038	0.0
27	0.044	6.71	0.35	0.021	0.013	15.94	14.57	3.84	0.042	0.4
68	0.028	3.20	0.27	0.012	0.010	19.36	14.67	0.02	0.191	0.3
69	0.031	3.21	0.27	0.013	0.009	18.76	14.69	1.06	0.182	0.3
70	0.028	3.10	0.27	0.015	0.009	18.03	14.70	2.02	0.183	0.3
71	0.027	3.05	0.25	0.018	0.009	16.57	14.74	3.98	0.178	0.4

Table 2. Mechanical Properties of the Welds.

Alloy	Yield Strength MPa (4 K)	Ultimate Strength MPa (4 K)	Absorbed Energy J (76 K)	Lateral Expansion mm (76 K)
1	460	1598	46	0.69
2	523	1570	39	0.71
5	665	1489	37	0.53
6	1169	1432	16	0.13
12	1027	1376	37	0.31
13	1129	1409	33	0.23
28	999	1335	41	0.38
29	1076	1520	41	0.41
60	998	1227	37	0.41
23	638	1152	51	0.84
24	675	1269	60	0.89
25	752	1359	43	0.84
26	758	1299	59	0.91
27	836	1385	56	0.81
68	1093	1413	34	0.36
69	1098	1493	33	0.38
70	1086	1471	37	0.38
71	1124	1453	42	0.43

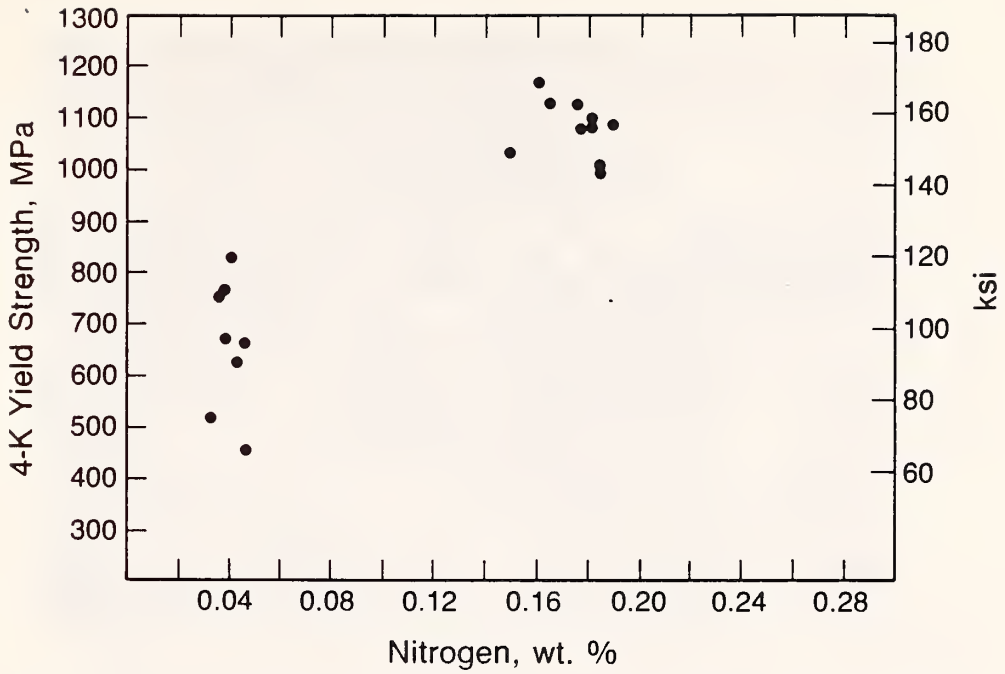

Figure 1. The effect of nitrogen on the 4-K yield strength.

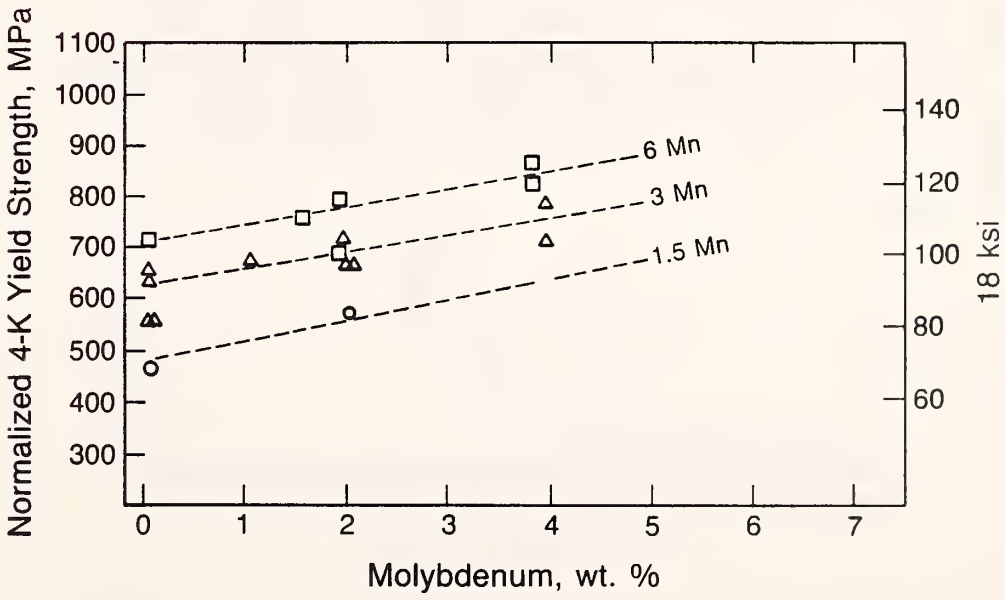

Figure 2. The 4-K yield strength data, normalized (3200 MPa/wt.% nitrogen) to a 0.05-wt.% nitrogen content to show the strengthening contributions of molybdenum and manganese.

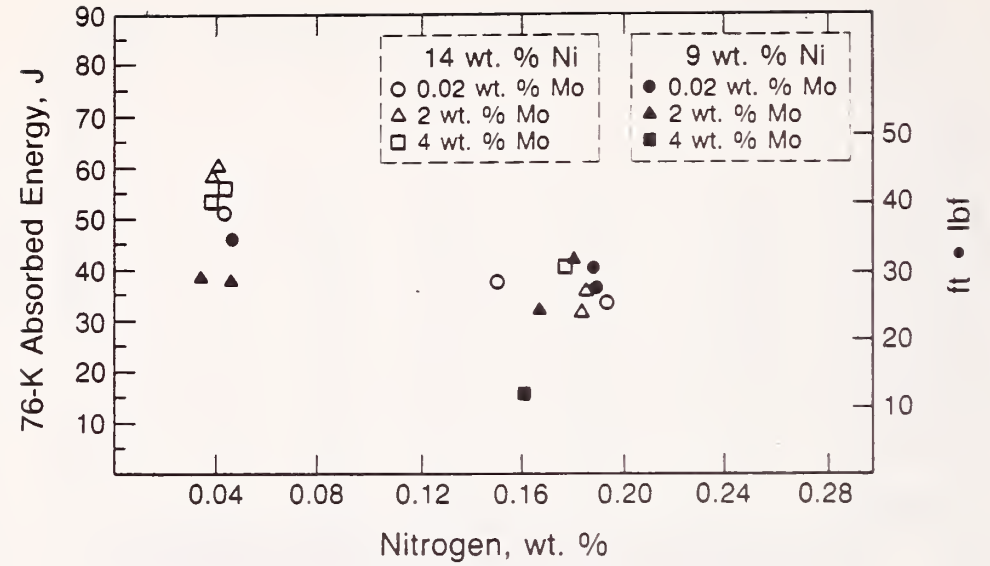

Figure 3. The effect of molybdenum and nickel content on the 76-K Charpy V-notch absorbed energy.

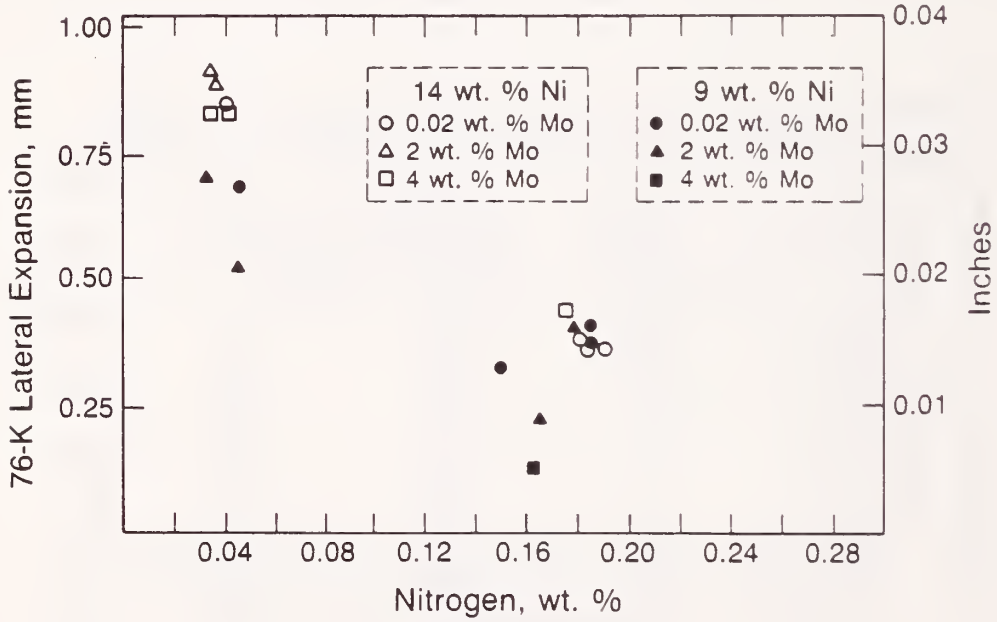

Figure 4. The effect of molybdenum and nickel content on the 76-K Charpy V-notch lateral expansion.

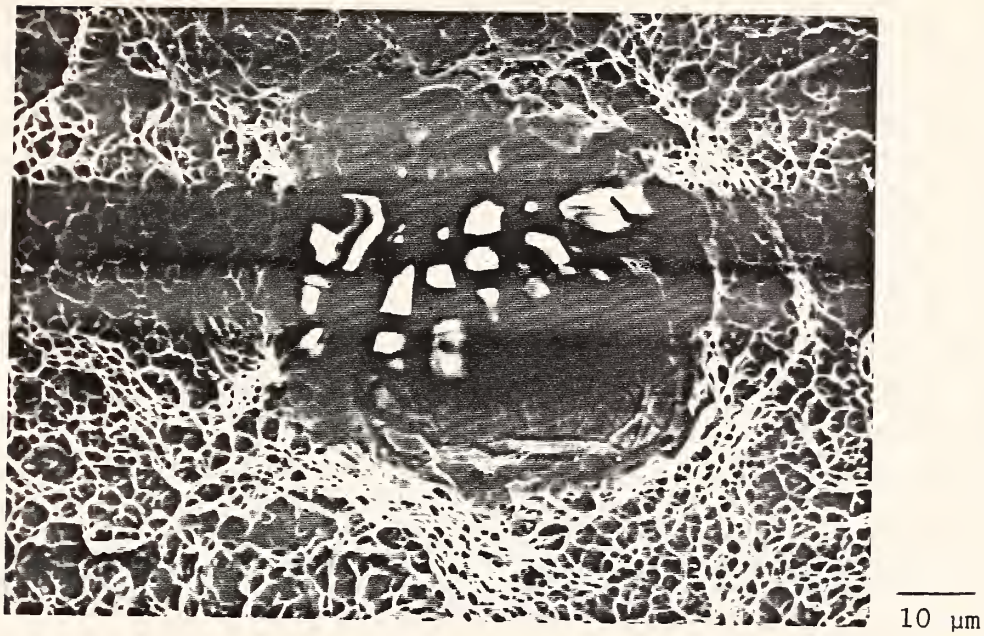

Figure 5. Fractograph (SEM) of a Charpy V-notch specimen from weld 6 showing one of the large inclusions on the fracture surface.

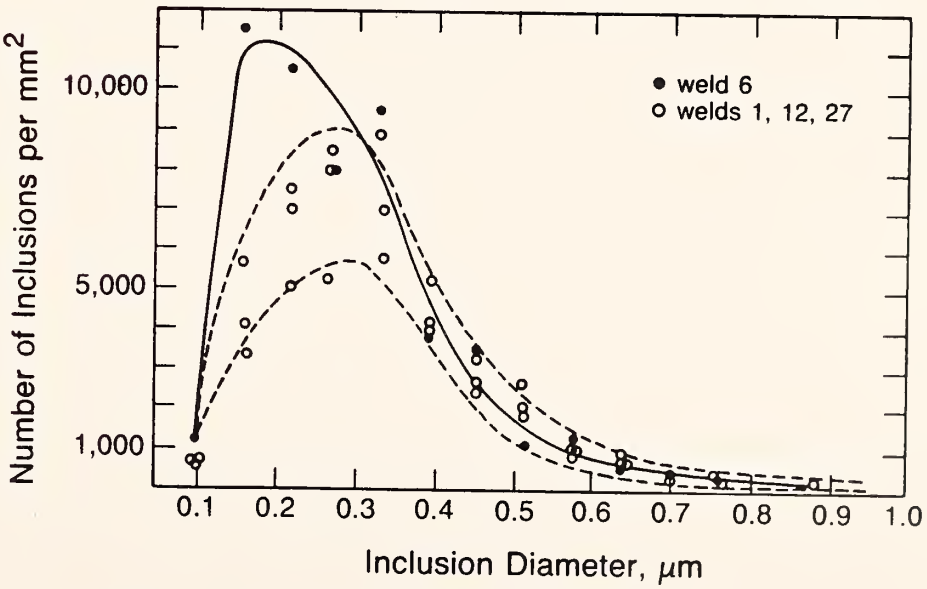

Figure 6. Inclusion size distribution results of welds 1, 6, 12, and 27 acquired at 3000×.

HIGH-ENERGY-BEAM WELDING OF TYPE 316LN STAINLESS STEEL FOR CRYOGENIC APPLICATIONS*

T. A. Siewert, D. Gorni,† and G. Kohn‡
Fracture and Deformation Division
National Bureau of Standards
Boulder, Colorado

Laser and electron-beam welds in 25-mm-thick type 316LN stainless steel containing 0.16 wt.% N were evaluated. Their mechanical properties are compared with those of welds produced with more conventional, lower productivity processes, such as shielded-metal-arc and gas-metal-arc welding. Because these welds are so narrow (about 2 mm), tensile tests were performed on transverse tensile specimens at 4 K. For both welding processes, the fractures occurred in the base metal at a strength level near 950 MPa, indicating that the weld and heat-affected zone has a strength similar to that of the base metal. The 4-K weld fracture toughness averaged near 150 MPa$\sqrt{m}$ for both welding processes, a value only slightly less than that for the base metal and comparable to the best values achieved with conventional welding processes using type 316LN weld metal of similar strength. The Charpy V-notch absorbed energies averaged near 70 J at 76 K. Metallographic analysis revealed cellular, fully austenitic solidification with little porosity and no evidence of hot cracking.

INTRODUCTION

Fusion energy applications demand superior properties from structural materials. For magnet casings, the material must be stable at 4 K and possess high strength and toughness. These requirements are met by type 316LN stainless steel.[1] Unfortunately, matching composition welds produced by conventional processes (shielded metal arc, gas metal arc, and flux core arc welding) generally have a substantially poorer strength and toughness

---

*Submitted to Advances in Cryogenic Engineering—Materials, vol. 34.
†Guest scientist from Armament Development Authority (RAFAEL), Haifa, Israel
‡Guest scientist from Israel Atomic Energy Research Center, Beersheva, Israel

combination.[2] To improve the relationship between strength and toughness, the factors influencing this relationship are now being investigated.

The strength and toughness combination can be improved by modifying the composition, but this approach introduces the potential for other material problems, such as (1) a change from primarily ferritic to primarily austenitic solidification, which is more sensitive to hot cracking and (2) the introduction of strain due to the differing thermal expansion of the weld and the plate material. One way to change the strength and toughness combination without changing the material is to choose a different joining process, especially one that produces a lower inclusion content.[3]

Both the electron beam (EB) and laser welding processes are capable of producing welds with a lower inclusion content. They remelt the base metal, which initially has a lower inclusion content than more conventional welds.

Also, EB welds are produced in a vacuum and laser welds can be produced in an inert gas. These conditions nearly eliminate the inclusion-forming elements that may exist within, or may be aspirated into, the arc atmosphere of conventional welding processes.

Both the EB and laser welding processes have the advantages of high-energy-density beams. The higher travel speeds and deeper penetration of the high-energy-density beams results in higher productivity. Associated with the rapid travel is a narrower weld and heat-affected zone (HAZ), which minimizes the effect of welding on the material properties.

The energy density is also a disadvantage: the molten weld metal reaches a very high temperature at which the alloying elements with high vapor pressures will evaporate. In type 316LN stainless steel, the elements most likely to be lost are nitrogen and manganese. Since solid-solution strengthening by nitrogen has a major role in determining the strength, a significant loss in nitrogen content would result in the loss of the load-bearing capability of the joint.[4,5] A significant loss in manganese by evaporation could result in porosity or reduced strength in the weld, since the manganese raises the solubility of the nitrogen in the steel, and to a lesser degree, substitutionally strengthens the alloy.[4] Therefore, both the strength and porosity were carefully evaluated in this study.

Besides interacting with the beam to modify the mechanical properties, the nitrogen content can also affect the weldability. Brooks reported that the 0.3 wt.% nitrogen in an Fe–21Cr–6Ni–9Mn is directly responsible for undesirable weld features, such as spatter and porosity, and that the occurrence of these undesirable features is proportional to the nitrogen content.[6] Thus, the porosity may not be due only to a loss of manganese, which reduces the nitrogen solubility, but also to the effect of the high-energy beam on the dissolved nitrogen.

Electron-beam and laser welding differ in their degree of development, total beam power, and energetic particles (electrons versus photons).

Electron-beam welding was developed first and is capable of welding thicker material. It has met the stringent requirements of pressure vessel fabrication in two-pass welding of 200-mm-thick steel.[7] Also, it has been applied to the welding of stainless steels of 80-mm thickness in an application for high-temperature service.[8]

Laser welding has not been developed to the power density of some EB systems, but it is capable of joining at least 18-mm-thick steel in a single pass.[9] Unlike EB welding, laser welding does not require a vacuum chamber or even a local vacuum. Nyilas found that laser welding was the most cost-efficient process for joining 1-mm-thick stainless steel for a superconducting cable conduit.[10]

MATERIAL

The heat used in this study and other heats of AISI type 316LN base metal have been characterized previously in a study that developed predictive equations for the strength and toughness of type 316LN alloys.[5] Data for this heat agreed closely with the measured values for the other heats, confirming that this heat is representative of type 316LN base metal. Data from these tests are included in table 1 along with data on welds produced with conventional processes. Because the strength and toughness are interrelated, as shown by the trend lines in figure 1, the table also includes a quality index, QI, which normalizes the effects of varying strength and nickel content and enables easy comparison of the base metal and welds at various strength levels.

Microstructural analysis confirmed that the steel had a fully austenitic structure. Its composition is given in table 2.

PROCEDURE

Rectangular pieces machined from the plate and cleaned with acetone were oriented in the butt-joint configuration shown in figure 2. Two welds were produced by using each of the two welding processes and the parameters listed in table 3 to ensure an adequate amount of weld metal for the evaluation. Because the laser had insufficient power for full penetration of the 25-mm thickness, a two-pass procedure (one from each side) was used, with both laser passes produced in the same direction. During the EB procedure development, frequent gas eruptions occurred in the weld pool. For this reason, the welding speed was decreased so the gases could escape.

After radiography to evaluate weld quality, standard mechanical property specimens with a weld cross section were removed from the two types of weldments; specimen orientations are shown in figure 3. The specimens consisted of

- two compact (CT) specimens (CT-1 and CT-2) notched with and against the direction of welding

- four Charpy V-notch (CVN) specimens (C-1 through C-4) notched with and against the direction of welding and located near the top and bottom of the weld
- two transverse tensile specimens (T-1 and T-2) located near the top and bottom of the weld
- a metallographic specimen (M-1) for weld dimension, microstructure, and inclusion measurements.

The CT specimens had a thickness of 25 mm after removing the weld reinforcements and were produced according to ASTM specification E 399 with the notches carefully centered in the weld metal. The compact tension specimens were tested at 4 K by using the single-specimen unloading compliance technique described in ASTM E 813 to determine the $K_{Ic}(J)$ fracture toughness. The notch region was precompressed one percent of total thickness to promote a straight fatigue crack. Both sides were grooved after fatigue precracking to avoid possible propagation of the fatigue crack into the HAZ or base metal. The techniques used to measure the fracture toughness at 4 K have been described elsewhere.[12]

Charpy V-notch specimens conforming to ASTM specification E 23 were produced with their notches centered in the weld. The directional nature of welding results in a directional microstructure. The effect of this directionality on the toughness was measured by notching the CT and CVN specimens so the cracks would propagate with the direction of welding in some of the specimens and against the direction in others.

The tensile specimens conformed to ASTM specification A 370. Contrary to the usual procedure for welds, they had a transverse orientation. With conventional welding processes, an all-weld-metal specimen, 6 mm in diameter, can be removed along the length of the weld. With the EB process, 2-mm width of the welds precludes measurement of only the weld metal, and so a transverse geometry was chosen to measure the joint efficiency. The crosshead speed was 0.2 $mm \cdot min^{-1}$. The techniques used to measure the strength at 4 K have been described elsewhere.[13]

The metallographic section was examined before and after etching to enable the mechanical properties to be related to the microstructure and inclusion density. The fracture surfaces of the CT specimens were also examined for inclusion density. These weldments and undeformed specimens were measured magnetically according to the procedure of AWS A4.2 for determination of the delta-ferrite content.

RESULTS AND DISCUSSION

Tensile Tests

The transverse tensile data for the two welds are shown in table 4. The yield and tensile strengths are close to those of the base metal (listed in table 1). This similarity in strength was obvious when the specimens were examined: each broke outside the weld in the base metal, which is an

indication of a weld strength greater than the base metal strength. The EB weld specimens broke about 3 mm from the weld fusion line, and the laser weld specimens broke near the specimen shoulder. Since the weldments were limited in strength by the base metal, nitrogen and manganese loss from the molten weld puddle due to vaporization had a negligible effect on the joint strength. The measured nitrogen content of the EB weld was 0.135 wt.%, a decrease of 0.015 wt.% from the base metal analysis listed in table 2.

The fracture of the EB weld specimens so near the fusion line indicates a weak HAZ. However, examination of the fracture surface revealed the fracture initiated at a large inclusion, which could have determined the fracture location. Despite these weaknesses, the weld strength still fell within the range measured for type 316LN base metal in table 1. Its elongation was poorer than expected because this was the short transverse direction in the base metal plate.

Charpy V-notch Tests

The resistance to fracture of CVN specimens at 76 K is given in table 5. The difference between specimens with cracks running with and against the welding direction was insignificant. From the convergence of grain boundaries and possible brittle interdendritic regions in the direction of weld solidification, we would expect cracks running in the direction of welding to have slightly lower absorbed energy and thus to be the more conservative measurement of weld toughness.

The laser welds had a 19 percent lower absorbed energy than the EB welds. This difference is attributed to differences in welding parameters rather than to the type of process. However, both welds had twice the absorbed energy of conventional welds; see the representative data in table 6. The significantly higher absorbed energy indicates a substantial improvement in fracture resistance.

Compact Tension Tests

The fracture toughness values at 4 K included in table 7 are substantially larger than those for the conventional processes in table 8 and are within 10 percent of the data for the base metal in table 1. A better comparison can be made by evaluating the strength–toughness combination in the form of a Quality Index (QI), the product of strength and toughness. The QI values for the laser and EB welds are within 10 percent of that for the base material (table 1), whereas the QI values for conventional welds average 30 percent lower (table 8).

Microstructure

The radiographic and metallographic evaluation of the laser weld revealed significant porosity (up to 1 mm in diameter), which is unacceptable in a production weld. No porosity was seen in radiographic evaluation of the EB weld, but some microporosity was seen in the metallographic evaluation. The difference in porosity is attributed to differences in the welding parameters, not the type of process. If the laser weld process were

repeated using the lower travel speed of the EB weld process, porosity would not be expected. The porosity probably contributed to the lower toughness of the laser weld.

The metallographic evaluation also measured the widths of the welds. As shown in figure 4, the EB weld had a uniform width of about 2 mm, and the laser weld varied from 2 to 3 mm in width.

The solidification structures of the two welds were examined at higher magnification. Figure 5 illustrates the fine columnar nature of the EB weld. The columnar grain of the laser weld in figure 6 is similar in size, but the higher travel speed resulted in less orientation in the direction of welding and so a different appearance.

A previous study indicated that inclusion content reduces toughness.[3] Unetched micrographs of the welds (figures 7 and 8) show a higher inclusion content in the laser weld, another reason for its lower toughness. The laser weld had 1.7×10^4 inclusions per mm^2; the EB weld had 1.2×10^4 inclusions per mm^2.

The CT fracture surfaces (figures 9 and 10) reveal a fully ductile fracture mode, which is characteristic of austenitic stainless steel at 4 K. The ductile dimples initiate at inclusions, so the dimple density is another measure of the inclusion density. Fracture-surface dimple densities for these welds and more conventional welds are given in table 8. The lower dimple densities on the EB and laser welds correlate with their higher toughness.

Ferrite

Magnetic measurements were performed on the base metal and both welds. All measurements on base metal, whether on the surface or cross sections, indicated a ferrite number (FN) of zero (fully austenitic). The laser weld was measured at 2 FN on both unmachined surfaces and on a carefully polished cross section. The EB weld was measured at 2 to 3 FN on both unmachined surfaces and on a carefully polished cross section. The presence of the magnetic delta-ferrite phase in the welds is attributed to the reduction in austenitizing potential through nitrogen loss during welding and the increased solidification rate.

CONCLUSIONS

1. The electron-beam and laser welding processes produced weld strengths (near 950 MPa) that exceeded the strength of type 316LN stainless steel at 4 K.

2. The welds exhibited toughness values that averaged 30 percent larger than those of more conventional welds of comparable strength.

3. The good toughness was attributed to the lower inclusion content in these high-energy-beam welds.

ACKNOWLEDGMENTS

This work was partially supported by the Office of Fusion Energy, U.S. Department of Energy. The authors thank C. N. McCowan for assistance in the 4-K tensile testing and P. T. Purtscher for assistance in the 4-K fracture testing. The EB weld was produced by Sciaky and the laser weld was produced by Combustion Engineering.

REFERENCES

1. H. I. McHenry, Strength and toughness goals for cryogenic steels, in "Materials Studies for Magnetic Fusion Energy Applications at Low Temperatures—VIII," NBSIR 85-3025, National Bureau of Standards, Boulder Colorado (1985), pp. 121–122.

2. R. L. Tobler, T. A. Siewert, and H. I. McHenry, Strength–toughness relationship for austenitic stainless steel welds at 4 K, Cryogenics 26, July (1986), pp. 392–295.

3. T. A. Siewert and C. N. McCowan, The role of inclusions in the fracture of austenitic stainless steel welds at 4 K, in "Proceedings of International Symposium on Welding Metallurgy of Structural Steels," The Metallurgical Society, Warrendale, Pennsylvania; in press.

4. C. N. McCowan, T. A. Siewert, R. P. Reed, and F. B. Lake, Manganese and nitrogen in stainless steel SMA welds for cryogenic service, Welding Journal 66, March (1987), pp. 84-s–92-s.

5. N. J. Simon and R. P. Reed, Strength and toughness of AISI 304 and 316 at 4 K, in "Materials Studies for Magnetic Fusion Energy Applications at Low Temperatures—IX," NBSIR 86-3050, National Bureau of Standards, Boulder, Colorado (1986), pp. 27–42.

6. J. A. Brooks, Weldability of high N, high Mn austenitic stainless steel, Welding Journal 54, June (1975), pp. 189-s–195-s.

7. C. M. Weber, New developments in electron beam welding, in "Proceedings, Trends in Welding Research in the United States, S. A. David, ed., American Society for Metals, Metals Park, Ohio (1982), pp. 647–652.

8. "Technical Data of Electron Beam Welding for Austenitic Stainless Steel—Sciaky Machine EL 10," Mitsubishi Heavy Industries, Kobe Shipyard and Engine Works, Kobe, Japan (1985).

9. E. A. Metzbower, D. W. Moon, and F. W. Fraser, Mechanical behavior of laser beam weldments, in "Proceedings, Trends in Welding Research in the United States," S. A. David, ed., American Society for Metals, Metals Park, Ohio (1982), pp. 563–580.

10. A. Nyilas, Laser beam welding of advanced superconducting cable conduits, in "Proceedings of 14th SOFT," Avignon (1986); in press.

11. R. P. Reed, N. J. Simon, P. T. Purtscher, and R. L. Tobler, Alloy 316LN for low temperature structures: A summary of tensile and fracture data, in "Materials Studies for Magnetic Fusion Energy Applications at Low Temperatures—IX," NBSIR 86-3050, National Bureau of Standards, Boulder, Colorado (1986), pp. 15–26.

12. R. L. Tobler, D. T. Read, and R. P. Reed, Strength/toughness relationship for interstitially strengthened AISI 304 stainless steel at 4 K temperature, in "Fracture Mechanics: Thirteenth Conference," ASTM STP 743, R. Roberts, Ed., American Society for Testing and Materials, Philadelphia (1981), pp. 250–268.

13. D. T. Read and R. L. Tobler, Mechanical property measurements at low temperatures, in "Advances in Cryogenic Engineering—Materials," vol. 28, Plenum Press, New York (1982), pp. 17–28.

14. T. A. Siewert, Predicting the toughness of SMA austenitic stainless steel welds at 77 K, Welding Journal 65, March (1966), pp. 23–28.

Table 1. Strength, Toughness, and Quality-Index Data Developed on This and Other Heats of 316LN Base Metal at 4 K[11]

Yield Strength, σ_y (MPa)	Fracture Toughness, $K_{Ic}(J)$ (MPa•m$^{\frac{1}{2}}$)	QI, $K_{Ic}(J)\cdot\sigma_y$ (MPa^2•m$^{\frac{1}{2}}$)
855-950[a]	185	1.58-1.76 x 10^5
935	140	1.31 x 10^5
1080	220	2.38 x 10^5
830	360	2.99 x 10^5
1060	150	1.59 x 10^5
1010	210	2.12 x 10^5
710	250	1.78 x 10^5
550	400	2.20 x 10^5

[a]Heat used in this study. The range of yield strength was attributed to nitrogen segregation.

Table 2. Composition (in wt.%) of Type 316LN Stainless Steel Plate Used in This Study

Element	Heat Analysis	NBS Analysis
C	0.016	---
Mn	1.10	---
Si	0.54	---
P	0.020	---
S	0.015	---
Cr	17.97	---
Ni	10.51	---
Mo	2.12	---
N	0.14	0.15
O	---	0.009
Cu	0.17	---
Co	0.25	---

Table 3. Welding Parameters

Electron Beam	
Accelerating voltage	50 kV
Beam current	175 mA
Beam oscillation frequency	60 Hz
Beam oscillation width	2 mm
Welding speed	200 mm min^{-1}
Focal plane	38 mm in front of part
Gun-to-work distance	152 mm
Weld direction	vertical up (horizontal gun)
Laser	
Beam power	8 kW (at workpiece)
Gas shield	450 l/hr He (3-flow nozzle)
Welding speed	500 mm min^{-1}
Penetration	14 mm/side in 2-pass/2-side butt weld
Focal length	375 mm using F5 parabolic mirror
Weld position	flat

Table 4. Transverse Tensile Data at 4 K

	Specimen EB-1	Specimen EB-2	EB Average	Specimen Laser-1	Specimen Laser-2	Laser Average
Yield strength (MPa)	981	943	962	940	940	940
Tensile strength (MPa)	1220	1190	1205	1130	1080	1105
Elongation (%)[a]	9.4	8.7	9	b	b	b
Reduction in area (%)[a]	14.6	16.3	15.4	b	b	b
Fracture location	c	c	---	d	d	---

a. Lower values than typical for base metals because the specimens were oriented in the short transverse direction.
b. Not available.
c. 3 mm from fusion line near tensile specimen shoulder.
d. 12 mm from fusion line near tensile specimen shoulder.

Table 5. Charpy V-notch Data at 76 K

Weld	Electron Beam		Laser	
Notch direction (with reference to welding direction)	With	Against	With	Against
Absorbed energy (J)	81	81	63	68
	78	84	71	63
Average	80	82	67	66
Average by process	81		66	

Table 6. Charpy V-notch Data Developed Previously for Conventional Welding Processes at 77 K[14]

Weld Process	Alloy Type	CVN Absorbed Energy (J)
SMA	316	24
SMA	308	16
SMA	308L	29
SMA	308L	22
SMA	308L	26
SMA	308L	27
SMA	308L	16
SMA	308L	34
SMA	308	22
SMA	316	42
SMA	316L	45
SMA	308L	24
SMA	308L	34

Table 7. Fracture-Toughness and Quality-Index Data for EB and Laser Welds

Specimen	Notch Direction[a]	J_{Ic} ($kJ \cdot m^{-2}$)	$K_{Ic}(J)$ ($MPa \cdot m^{\frac{1}{2}}$)	QI, $K_{Ic}(J) \cdot \sigma_y$ ($MPa \cdot m^{\frac{1}{2}}$)
EB,CT-1	against	118	157	1.51×10^5
EB,CT-2	with	117	156	1.50×10^5
Laser,CT-1	against	104	147	1.38×10^5
Laser,CT-2	with	101	145	1.36×10^5

[a]With or against the direction of welding

Table 8. Fracture-Toughness and Quality-Index Data for Some Previously Tested Welds with Yield Strengths above 850 MPa[2]

Weld Process	Alloy Type	σ_y (MPa)	$K_{Ic}(J)$ ($MPa \cdot m^{\frac{1}{2}}$)	QI ($MPa \cdot m^{\frac{1}{2}}$)
SMAW	316L	879	95	8.35×10^4
SMAW	316L	886	108	9.57×10^4
SMAW	316L	881	98	8.63×10^4
SMAW	316	924	154	1.42×10^5
FCAW	308L	1117	66	7.37×10^4
GMAW	308L	918	132	1.21×10^5
SAW	316L	860	99	8.51×10^4
SMAW	316L	882	171	1.51×10^5

Table 9. Fracture-Surface Dimple Densities for Various Welds

Weld Process	Alloy Type	Dimple Density (mm^{-2})
EB[a]	316LN	1.7×10^5
Laser[a]	316LN	2.15×10^5
SMAW	308LN	3.2×10^5
SMAW	308LN	3.5×10^5

[a]This study

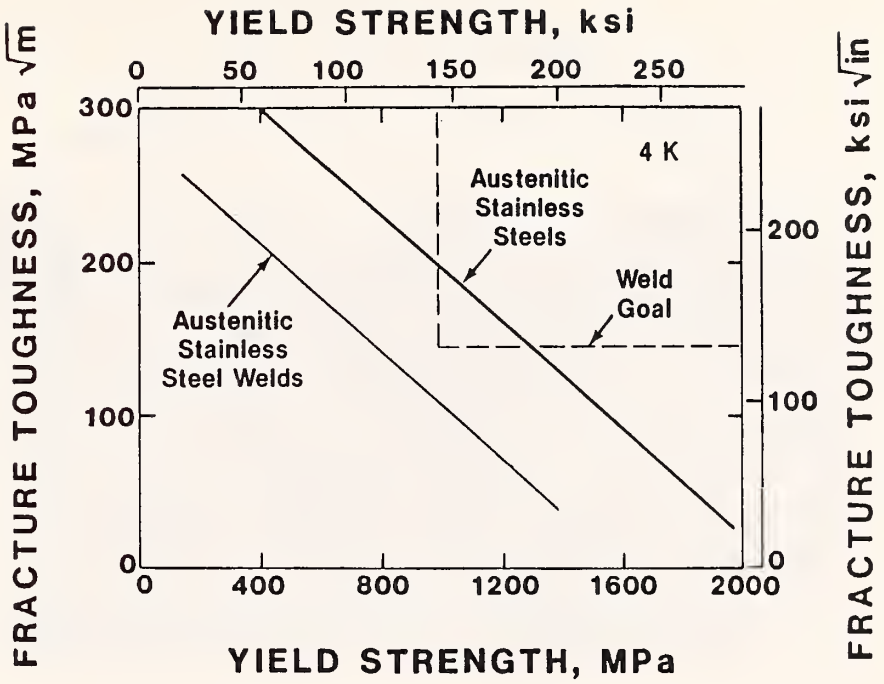

Figure 1. Strength–toughness relationships for AISI type 316LN austenitic stainless steel and matching composition welds.

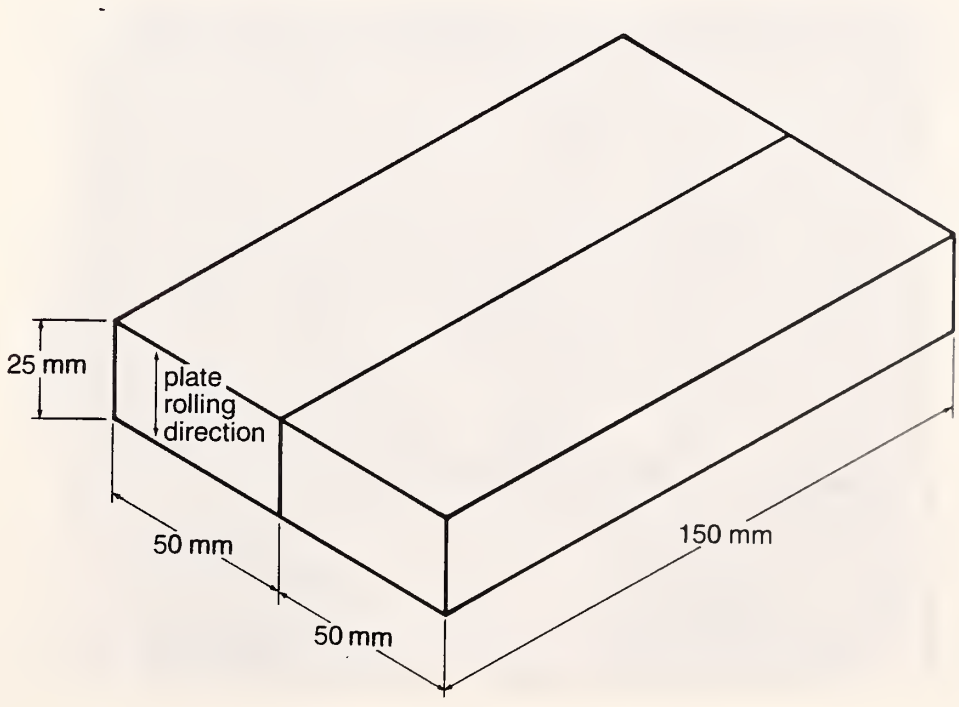

Figure 2. Butt-joint weld configuration.

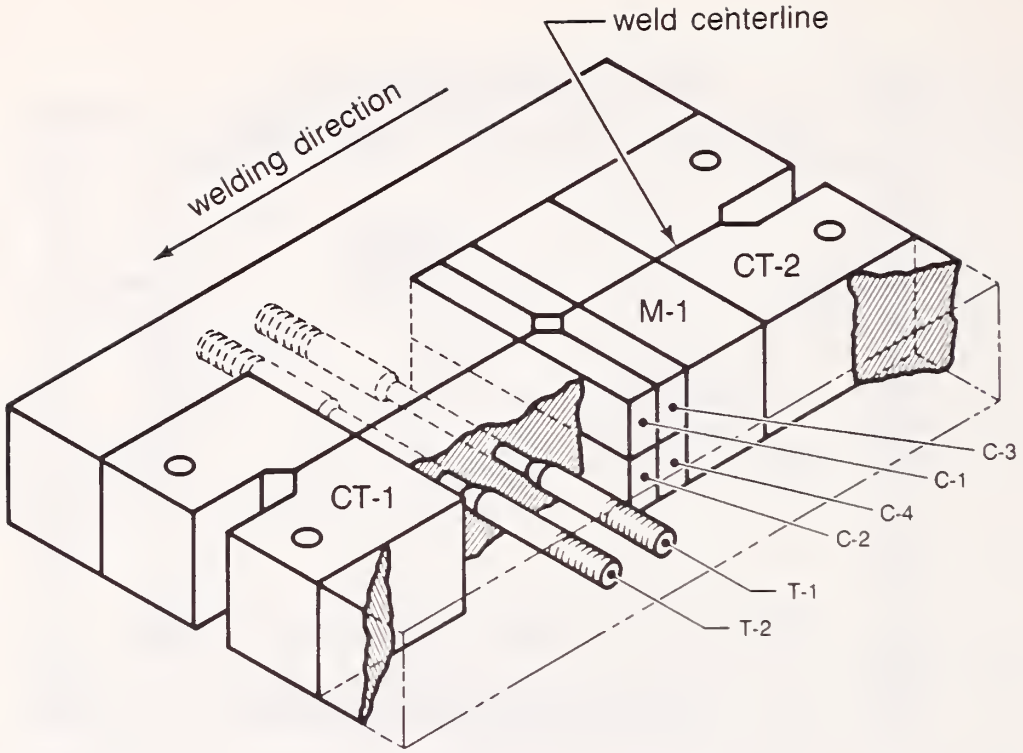

Figure 3. Orientation of mechanical test specimens removed from weld.

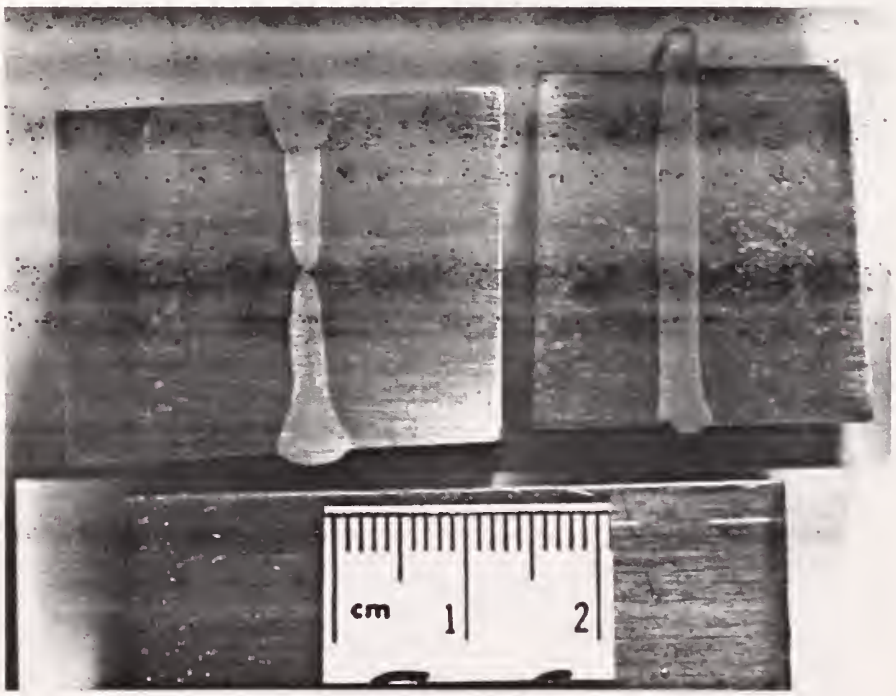

Figure 4. Polished cross sections of laser (left) and EB (right) welds.

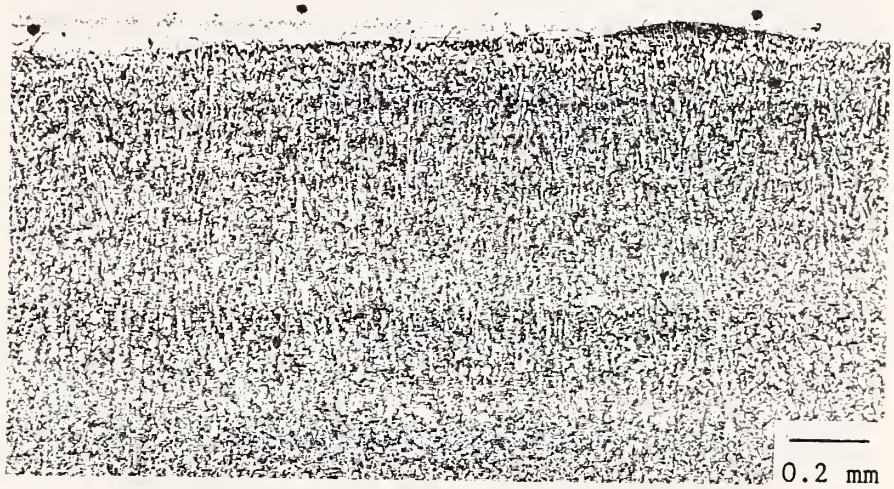

Figure 5. Micrograph of the EB fusion line showing the fine columnar dendrites in the weld (on the right). Orientation: transverse to the welding direction.

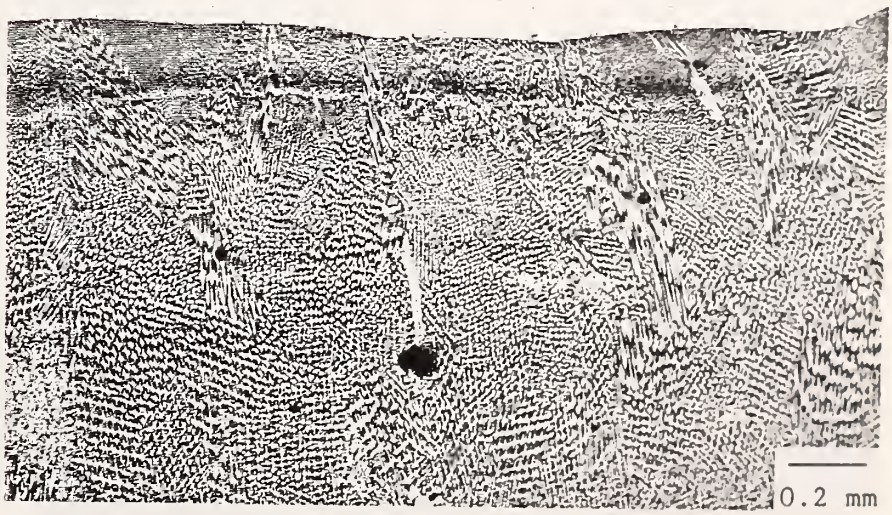

Figure 6. Micrograph of the laser fusion line showing the coarse columnar dendrites in the weld (on the right). Orientation: transverse to the welding direction.

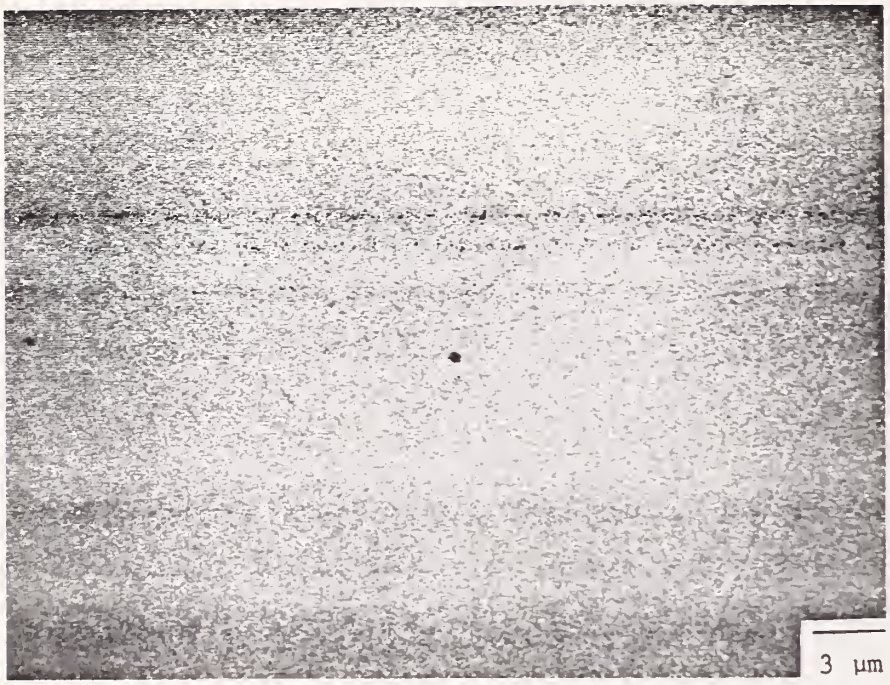

Figure 7. Higher magnification micrograph of unetched EB weld showing very few pores or inclusions.

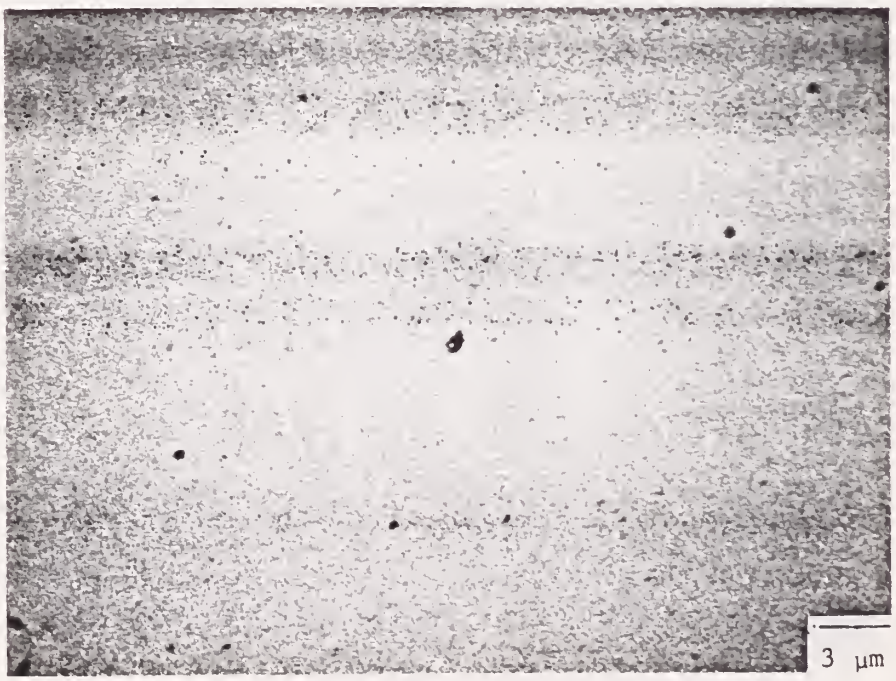

Figure 8. Higher magnification micrograph of unetched laser weld showing a large number of pores and inclusions.

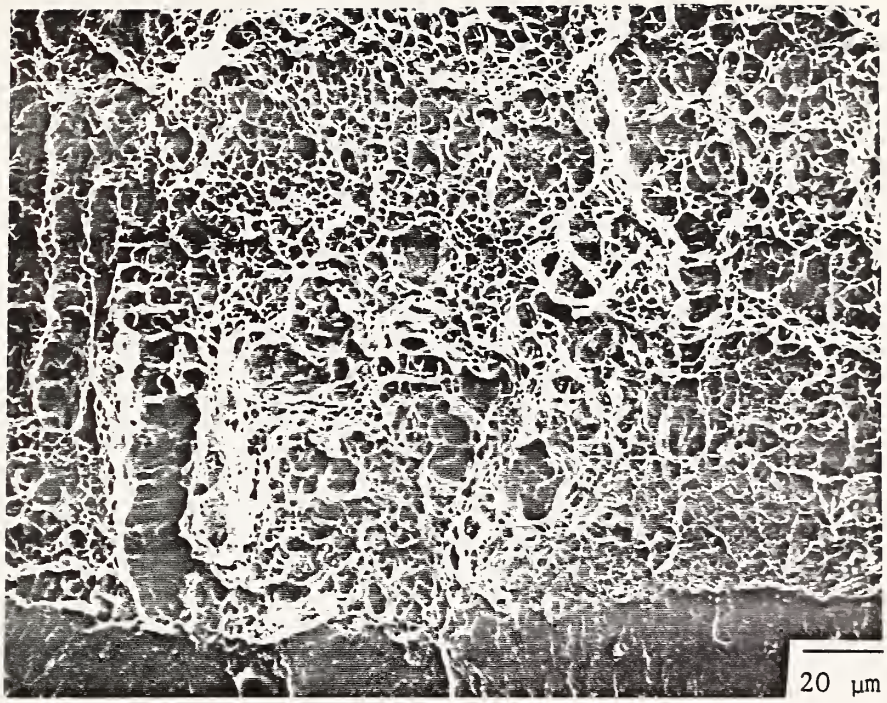

Figure 9. Micrograph of the CT fracture surface of the EB weld.

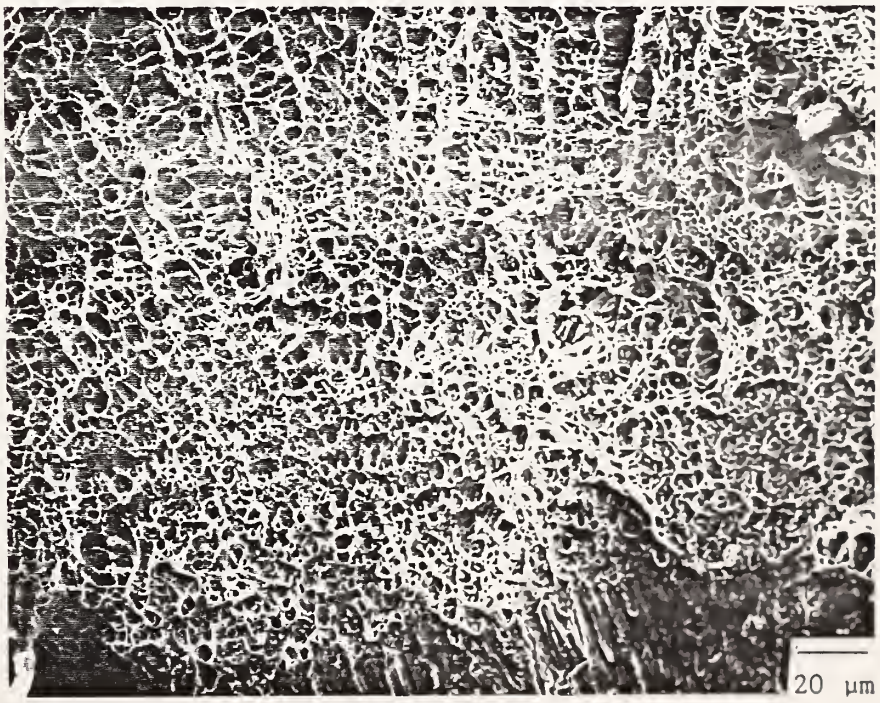

Figure 10. Micrograph of the CT fracture surface of the laser weld.

NONMETALLICS

NONMETALLICS PROGRAM

CONTRIBUTORS: R. D. Kriz and M. B. Kasen

OBJECTIVES

- Development of improved methods for screening the influence of component parameters on composite material performance
- Application of these methods to select optimal components for radiation-resistant, organic-matrix insulators to be used in superconducting magnets of magnetic fusion energy systems
- Development of analytical methods to predict the influence of component properties and internal stress state on damage development in composite materials and to predict the influence of such damage on the mechanical performance of composite materials
- Application of these techniques and methods in the development of improved electrical insulating materials for superconducting magnets subjected to neutron irradiation

RESEARCH HIGHLIGHTS

- An integrated system was developed for efficient, low-cost specimen composite production and mechanical performance screening. The 3.2-mm diameter rod specimens are produced in-house under excellent control. The rods need only be cut to length before testing. Procedures and facilities have been developed for testing the flexural, short-beam shear, and torsional moduli and the fracture strength, G_{Ic}, of the rods at temperatures from 295 K to 4 K.

- Ninety-eight unreinforced resin specimens, an equal number of specimens reinforced with 48-volume-percent type-E glass fabricated from three epoxy systems, and one bismaleimide system have been submitted to Oak Ridge National Laboratory for irradiation at 4.2 K in the National Low Temperature Neutron Irradiation Facility. The specimens will be irradiated with three increasing doses, warmed to room temperature, and returned to NBS for testing.

- Laminated plate analysis was used to demonstrate how optimal components could be fabricated from knowledge of component properties and other laminate design variables. A micromechanical model of a graphite-epoxy, fiber-reinforced laminate was used to demonstrate the relationship between thermal contraction and local residual stress due to cooling to cryogenic temperatures. Analysis also showed that replacement of the Inconel member of a copper-Inconel composite with beryllium copper would significantly lower the thermally induced residual stresses.

LAMINATED PLATE ANALYSIS FOR LOW TEMPERATURE APPLICATIONS: METALLIC AND NONMETALLIC LAMINATES

R. D. Kriz

Fracture and Deformation Division
National Bureau of Standards
Boulder, Colorado

The theory for laminated plate analysis is outlined. Simple examples illustrate mechanical load and thermal stress analysis in the temperature range 76 to 300 K for laminates reinforced with metallic and nonmetallic materials. Laminates studied were copper reinforced with Inconel, copper reinforced with a Cu–Be alloy, and a fiber-reinforced graphite–epoxy crossply laminate, $[0/90]_s$. Although layers of Inconel provided good mechanical reinforcement for layers of copper, the Cu–Be alloy provided the same reinforcement with lower residual thermal stresses in the copper. For designing laminates with a specific coefficient of thermal expansion, nonmetallic fiber-reinforced laminates are preferred. At 76 K, moisture in polymeric composite laminates eliminates thermally induced stresses.

INTRODUCTION

The design of fusion energy structures includes laminated material systems that can either be metallic or nonmetallic and isotropic or anisotropic. Nonmetallic anisotropic laminated materials are usually selected for structural applications because the individual layers of fiber-reinforced materials can be chosen to obtain specific properties for the laminate.[1] Although less common, isotropic metals can also be used to reinforce other metals in a laminate configuration. Components of metallic laminates synergistically improve performance; for example, the Japanese samurai swords derived their strength from their metallic laminate composition.[2]

The toroidal field (TF) coils recently designed for the compact ignition tokamak (CIT) include copper conductor reinforced with Inconel. In this application, the load is applied normal to the laminate midplane. Studies by Becker et al.[3] demonstrated that reinforcing copper with Inconel significantly increases its compressive yield strength.

This improved compressive property was measured at the National Bureau of Standards on full-scale laminates that were created by explosively bonding copper and Inconel plates.[4] Measurements focused on the copper–Inconel interface bond. Without a good interfacial bond between layers, reinforcement is not possible and many structural advantages are sacrificed. The interfacial bond strength is especially critical in laminates constructed of highly anisotropic layers because differences in Poisson's contractions can cause large strain gradients across the interface. For metallic laminates, variations in Poisson's ratio among the layers are not large, but differences in thermal contraction (over the temperature range 4 to 300 K) can cause large stress gradients near the interfaces. When thermal strains are superposed with strains induced by a mechanical load, these additional interfacial thermal strains can be a significant factor in the design of metal structures for low temperature applications.

This study was undertaken to provide designers of fusion energy structures with an outline to design laminates constructed with metallic and nonmetallic materials that may be suitable in the temperature range 4 to 300 K. In particular, we give examples of nonmetallic graphite–epoxy laminates and the metallic laminates similar to materials used in the TF coils of the CIT. We also illustrate how the coefficients of thermal expansion can be predicted from laminated plate theory.* Hence, structural components can be designed to operate at low temperatures with minimal problems in thermal mismatch with other structural members.

LAMINATED PLATE THEORY

Comprehensive development of laminated plate theory is found in references 1 and 5. Using the same definitions and notation of these references, this report presents an overview of the theory that is relevant to design parameters.

Laminated plate theory is based on the assumption that adjacent layers are perfectly bonded and in a state of plane stress ($\sigma_z = 0$) normal to the thin x–y plane of the laminate. The theory also adopts the Kirchhoff–Love assumptions for bending of thin plates:

1. Normals to the laminate midplane remain straight and normal to the deformed midplane. Hence, out-of-plane shear deformations ($\tau_{xz} = \tau_{yz} = 0$) are assumed to be zero.

---

*The computer program used to predict the properties for these examples is not described fully in this report. This NBS computer program is public domain and can be obtained by sending a formatted, blank, 360-kilobyte, 5-1/4-in floppy disk to R. D. Kriz, MC 430, National Bureau of Standards, Boulder, CO 80303. The program is designed to operate on any personal computer that uses DOS 3.0.

2. The length of midplane normals does not change. Hence, out-of-plane deflections, ω, are associated only with in-plane stretching: $\omega = \omega(x,y)$.

We also assume small deflections for thin, elastic plates.

Mechanical Loads

With these assumptions, stresses (σ_x, σ_y, τ_{xy}) at a point can be calculated for each layer (k) from the plate curvatures (κ_x, κ_y, κ_{xy}) and in-plane strains (ϵ_x^0, ϵ_y^0, γ_{xy}^0,) at the midplane.

$$\begin{Bmatrix} \sigma_x \\ \sigma_y \\ \tau_{xy} \end{Bmatrix}_k = \begin{bmatrix} \bar{Q}_{11} & \bar{Q}_{12} & \bar{Q}_{16} \\ \bar{Q}_{12} & \bar{Q}_{22} & \bar{Q}_{26} \\ \bar{Q}_{16} & \bar{Q}_{26} & \bar{Q}_{66} \end{bmatrix}_k \left\{ \begin{Bmatrix} \epsilon_x^0 \\ \epsilon_y^0 \\ \gamma_{xy}^0 \end{Bmatrix} - Z_k \begin{Bmatrix} \kappa_x \\ \kappa_y \\ \kappa_{xy} \end{Bmatrix} \right\} \tag{1}$$

where $\bar{Q}_{ij}$ are the elastic properties defined in reference 5, and Z_k is defined in Fig. 1. The force-moment resultants are defined in Fig. 2.

$$N_x = \int_{-t/2}^{t/2} \sigma_x dz, \quad N_y = \int_{-t/2}^{t/2} \sigma_y dz, \quad N_{xy} = \int_{-t/2}^{t/2} \tau_{xy} dz$$

$$M_x = \int_{-t/2}^{t/2} \sigma_x z dz, \quad M_y = \int_{-t/2}^{t/2} \sigma_y z dz, \quad M_{xy} = \int_{-t/2}^{t/2} \tau_{xy} z dz \tag{2}$$

For discrete layers, the integration in Eq. (2) is summed over N layers:

$$\begin{Bmatrix} N_x \\ N_y \\ N_{xy} \end{Bmatrix} = \sum_{k=1}^{N} \int_{Z_{k-1}}^{Z_k} \begin{Bmatrix} \sigma_x \\ \sigma_y \\ \tau_{xy} \end{Bmatrix} dz,$$

$$\begin{Bmatrix} M_x \\ M_y \\ M_{xy} \end{Bmatrix} = \sum_{k=1}^{n} \int_{Z_{k-1}}^{Z_k} \begin{Bmatrix} \sigma_x \\ \sigma_y \\ \tau_{xy} \end{Bmatrix} z dz \tag{3}$$

By substituting Eq. (1) into Eq. (3) and assuming that each layer is homogeneous, we obtain

$$\begin{Bmatrix} N_x \\ N_y \\ N_{xy} \end{Bmatrix} = \sum_{k=1}^{N} \left\{ \begin{bmatrix} \bar{Q}_{11} & \bar{Q}_{12} & \bar{Q}_{16} \\ \bar{Q}_{12} & \bar{Q}_{22} & \bar{Q}_{26} \\ \bar{Q}_{16} & \bar{Q}_{26} & \bar{Q}_{66} \end{bmatrix}_k \begin{Bmatrix} \epsilon_x^0 \\ \epsilon_y^0 \\ \gamma_{xy}^0 \end{Bmatrix} \int_{Z_{k-1}}^{Z_k} dz + \right.$$

$$\left. + \begin{bmatrix} \bar{Q}_{11} & \bar{Q}_{12} & \bar{Q}_{16} \\ \bar{Q}_{12} & \bar{Q}_{22} & \bar{Q}_{26} \\ \bar{Q}_{16} & \bar{Q}_{26} & \bar{Q}_{66} \end{bmatrix}_k \begin{Bmatrix} \kappa_x \\ \kappa_y \\ \kappa_{xy} \end{Bmatrix} \int_{Z_{k-1}}^{Z_k} z\,dz \right\} \tag{4}$$

$$\begin{Bmatrix} M_x \\ M_y \\ M_{xy} \end{Bmatrix} = \sum_{k=1}^{N} \left\{ \begin{bmatrix} \bar{Q}_{11} & \bar{Q}_{12} & \bar{Q}_{16} \\ \bar{Q}_{12} & \bar{Q}_{22} & \bar{Q}_{26} \\ \bar{Q}_{16} & \bar{Q}_{26} & \bar{Q}_{66} \end{bmatrix}_k \begin{Bmatrix} \epsilon_x^0 \\ \epsilon_y^0 \\ \gamma_{xy}^0 \end{Bmatrix} \int_{Z_{k-1}}^{Z_k} z\,dz + \right.$$

$$\left. + \begin{bmatrix} \bar{Q}_{11} & \bar{Q}_{12} & \bar{Q}_{16} \\ \bar{Q}_{12} & \bar{Q}_{22} & \bar{Q}_{26} \\ \bar{Q}_{16} & \bar{Q}_{26} & \bar{Q}_{66} \end{bmatrix}_k \begin{Bmatrix} \kappa_x \\ \kappa_y \\ \kappa_{xy} \end{Bmatrix} \int_{Z_{k-1}}^{Z_k} z^2\,dz \right\} \tag{5}$$

Combining like terms in Eqs. (4) and (5), integrating, and rearranging the variables yields one relationship with partitioned submatrices:

$$\left\{\begin{array}{c} N_x \\ N_y \\ N_{xy} \\ \cdots\cdots \\ M_x \\ M_y \\ M_{xy} \end{array}\right\} = \left[\begin{array}{ccc:ccc} A_{11} & A_{12} & A_{16} & B_{11} & B_{12} & B_{16} \\ A_{12} & A_{22} & A_{26} & B_{12} & B_{22} & B_{26} \\ A_{16} & A_{26} & A_{66} & B_{16} & B_{26} & B_{66} \\ \hdashline B_{11} & B_{12} & B_{16} & D_{11} & D_{12} & D_{16} \\ B_{12} & B_{22} & B_{26} & D_{12} & D_{22} & D_{26} \\ B_{16} & B_{26} & B_{66} & D_{16} & D_{26} & D_{66} \end{array}\right] \left\{\begin{array}{c} \epsilon_x^0 \\ \epsilon_y^0 \\ \epsilon_{xy}^0 \\ \cdots\cdots \\ \kappa_x \\ \kappa_y \\ \kappa_{xy} \end{array}\right\} \tag{6}$$

where $$A_{ij} = \sum_{k=1}^{N} (\bar{Q}_{ij})_k (Z_k - Z_{k-1}),$$

$$B_{ij} = \sum_{k=1}^{N} (\bar{Q}_{ij})_k (Z_k^2 - Z_{k-1}^2)/2,$$

and $$D_{ij} = \sum_{k=1}^{N} (\bar{Q}_{ij})_k \ (Z_k^3 - Z_{k-1}^3)/3.$$

Equation (6) is written in the form where the midplane strains and curvatures are prescribed and the midplane stress and moment resultants are calculated for a particular laminate. Other forms of Eq. (6) can be derived;[1] there are four possible variations. For example, in one variation, the moment resultants (M_x, M_y, M_{xy}) and stress resultants (N_x, N_y, N_{xy}) are prescribed and the corresponding strains (ϵ_x^0, ϵ_y^0, λ_{xy}^0) and curvatures (κ_x, κ_y, κ_{xy}) at the midplane are calculated. Of the four possible combinations, three are expressed in abbreviated notation in Eqs. (7) through (9).

$$\left\{ \begin{array}{c} N \\ \cdots \\ M \end{array} \right\} = \left[\begin{array}{c:c} A & B \\ \cdots & \cdots \\ B & D \end{array} \right] \left\{ \begin{array}{c} \epsilon^0 \\ \cdots \\ \kappa \end{array} \right\} \tag{7}$$

$$\left\{ \begin{array}{c} \epsilon^0 \\ \cdots \\ M \end{array} \right\} = \left[\begin{array}{c:c} A^{-1} & -A^{-1}B \\ \cdots & \cdots \\ BA^{-1} & D - BA^{-1}B \end{array} \right] \left\{ \begin{array}{c} N \\ \cdots \\ \kappa \end{array} \right\} \tag{8}$$

$$\left\{ \begin{array}{c} \epsilon^0 \\ \cdots \\ \kappa \end{array} \right\} = \left[\begin{array}{c:c} A^* - B^* D^{*-1} H^* & B^* D^{*-1} \\ \cdots & \cdots \\ -D^{*-1} H^* & D^{*-1} \end{array} \right] \left\{ \begin{array}{c} N \\ \cdots \\ M \end{array} \right\} \tag{9}$$

where $A^* = A^{-1}$, $B^* = -A^{-1}B$, $H^* = BA^{-1}$, and $D^* = D - BA^{-1}B$. Stresses in each layer can now be calculated from the following relationship.

$$\{\sigma\}_k = [\bar{Q}]_k \ (\{\epsilon^0\} - Z_k\{\kappa\}) \tag{10}$$

Thermal Loads

At low temperatures, additional strains are the result of thermal expansion and contraction, but free thermal strains alone do not cause stress in homogeneous materials. When laminates are cooled to low temperatures, the only source of stress is the thermal mismatch of different layers, which causes constraint of adjacent layers. This mismatch can be modeled by laminated plate analysis. In each layer (k), the total strain ($\{\epsilon\}_k$) is the sum of the mechanical strains ($\{\epsilon^\sigma\}_k$) and the thermal strains ($\{\epsilon^T\}_k$).

$$\{\epsilon\}_k = \{\epsilon^\sigma\}_k + \{\epsilon^T\}_k \tag{11}$$

In a comprehensive analysis, strains caused by other environmental effects are included in Eq. (11). For example, absorbed moisture or irradiation can cause swelling of polymer-base laminates. However, in this outline we consider only mechanical strains and thermal strains.

The strains in Eq. (1) are the strains that cause stresses $(\{\epsilon^{\sigma}\}_k)$. Hence, to include thermal strains in the laminate analysis, we solve for the stress-induced strains in Eq. (11) and substitute them into Eq. (2). In schematic form, Eq. (2) is rewritten in terms of total strains $(\{\epsilon\})$ and thermal strains $(\{\epsilon^T\})$:

$$\{N\} = \int_{-h/2}^{h/2} \{\sigma\}_k \, dz = \int_{-h/2}^{h/2} [\bar{Q}]_k \{\epsilon - \epsilon^T\}_k \, dz$$

$$\{M\} = \int_{-h/2}^{h/2} \{\sigma\}_k \, zdz = \int_{-h/2}^{h/2} [\bar{Q}]_k \{\epsilon - \epsilon^T\}_k \, zdz \tag{12}$$

For each layer (k), the thermal strains in Eq. (12) can be rewritten in terms of a temperature change (ΔT) and the coefficients of thermal expansion ($\{\alpha\}$):

$$\{\epsilon^T\}_k = \Delta T \{\alpha\}_k \tag{13}$$

Substituting Eq. (13) into Eq. (12) and integrating yields

$$\begin{Bmatrix} N \\ \cdots \\ M \end{Bmatrix} = \begin{bmatrix} A & \vdots & B \\ \cdots & \cdots & \cdots \\ B & \vdots & D \end{bmatrix} \begin{Bmatrix} \epsilon^0 \\ \cdots \\ \kappa \end{Bmatrix} - \begin{Bmatrix} N^T \\ \cdots \\ M^T \end{Bmatrix} \tag{14}$$

where

$$\{N^T\} = \Delta T \int_{-h/2}^{h/2} [\bar{Q}]_k \{\alpha\}_k \, dz$$

and

$$\{M^T\} = \Delta T \int_{-h/2}^{h/2} [\bar{Q}]_k \{\alpha\}_k \, zdz$$

are the midplane thermal loads (force and moment resultants).

The laminate coefficients of thermal expansion are calculated from Eq. (14) for the special case where the curvatures $(\{\kappa\})$ are zero, the mechanical loads ($\{N\}$ and $\{M\}$) are zero, and the laminate is symmetric ($[B] = 0$). Hence, Eq. (14) decouples into

$$[A] \{\epsilon^0\} = \{N^T\} \tag{15}$$

Solving Eq. (15) for midplane strain ($\{\epsilon^0\}$) yields

$$\{\epsilon^0\} = [A]^{-1}\{N^T\} = \Delta T[A]^{-1}\int_{-h/2}^{h/2}[\bar{Q}]_k\{\alpha\}_k\,dz \tag{16}$$

For the laminate, we can define this relationship:

$$\{\epsilon\bar{\alpha}^T\} = \Delta T\{\bar{\alpha}\} \tag{17}$$

where $\{\bar{\alpha}\}$ are the laminate coefficients of thermal expansion. When only thermal strains are present, $\{\epsilon^0\} = \{\epsilon^{0T}\}$, and by inspection of Eqs. (16) and (17), we arrive at an expression for $\{\bar{\alpha}\}$:

$$\{\bar{\alpha}\} = [A]^{-1}\int_{-h/2}^{h/2}[\bar{Q}]_k\{\alpha\}_k\,dz \tag{18}$$

Now the stresses in each layer can be calculated for a variety of mechanical and thermal load conditions:

$$\{\sigma\}_k = [\bar{Q}]_k\{\{\epsilon^0\} + Z_k\{\kappa\} - \{\alpha\}_k\Delta T\} \tag{19}$$

Stress Approximations for the Laminated Edge

In the previous plate analysis, plane stress is assumed through the thickness of the thin plate; therefore, the interlaminar stresses (σ_z, τ_{xz}, τ_{yz}) through the thickness are negligible. For interlaminar stresses in thick plates or for edge stresses in thin plates, the plane stress approximation is no longer valid. For thick plates, interlaminar stresses can be approximated by modifying thin laminate plate theory,[6,7] but a finite element model is a more accurate approach.[8] For thin laminated plates, these stresses exist only near the plate boundaries (edges), where stresses normal to the edge surface are zero. Originally, solutions for these edge stresses were obtained numerically;[9] more recently, complicated, exact solutions have been obtained.[10,11]

For simplicity, we use an approximation proposed by Pagano and Pipes.[12] The actual and approximate distributions for the interlaminar edge stresses (σ_z) are shown in Fig. 3. A relationship for the amplitude (σ_m) is obtained by summing the moments about the x-axis for the k layers shown in Fig. 1:

$$\sigma_{Z_k} \simeq \sigma_m = \frac{45}{14h^2}\int_{Z_k}^{h}\sigma_y\xi\,d\xi \tag{20}$$

Unfortunately, similar approximations cannot be made for the shear stresses (τ_{xz}, τ_{yz}). Thus, for each layer, we approximate only the interlaminar peeling stress $(\sigma_z)_k$ by summing stresses in the y direction (σ_y) for each layer (k). In the computer program, we integrate over four evenly spaced points for each layer.

RESULTS AND DISCUSSION

With this analysis included in a computer program, we studied three simple laminate configurations: Inconel/Cu/Inconel; Cu-Be/Cu/Cu-Be; and graphite-epoxy $[0/90]_s$. Computer program input data files with results for each of these configurations are given in Appendices A, B, and C, respectively.

Inconel/Cu/Inconel

Inconel/Cu/Inconel, an isotropic metallic laminate, was chosen as a simple example to illustrate the stresses caused by thermal mismatch among the layers. Layer thicknesses are the same as those of laminates tested in reference 3. The material properties and dimensions used by the computer program are shown in Fig. A.1 as a data file. In this data file,

- EL is Young's modulus in the textured (L) direction (defined in Fig. 1);
- ET is Young's modulus transverse to the L-direction;
- GLT and NULT are the shear modulus and Poisson's ratio in the L-T plane;
- TEXPL and TEXPT are the thermal coefficients of expansion in the L- and T-directions;
- MEXPL, MEXPT, and CV are moisture properties that apply only to swelling of polymeric materials.
- NX is the laminate load applied in the x-direction (NX and other loads are defined in Fig. 2); the angle between the textured L-direction and the x-axis is defined for each layer.

In this example, no texture exists; hence, EL = ET and TEXPL = TEXPT. (However, metal textures, even small ones, can be included in the analysis.) Also, NX = NY = NXY = MX = MY = MXY = 0 because no loads were applied in the L-T plane of the laminate. When thermal loads are studied, we assume a stress-strain-free state at room temperature (300 K) and prescribe an operating temperature of 76 K.

For this problem, only a portion of the results from the computer program are shown in Fig. A.2. Stresses are presented in a table and a graph; the graph represents only stress components only in the x, y, and z directions.

Since there is no texture in this example, all shear stresses are zero, and σ_x (SIG X) equals σ_y (SIG Y). For operating temperatures below room temperature, the opposite is true. Most significant is the large tension stress of 117 MPa (17 ksi) in the copper at 76 K, which is 42% of the yield strength of copper. Thus, for this laminate, yielding occurs at much lower mechanical loads at 76 K than at room temperature.

Cu–Be/Cu/Cu–Be

For comparison, we consider a laminate in which a Cu–Be alloy replaces the Inconel reinforcement in the first example (see Fig. 5.4.2-E1 of reference 13). The input data file is shown in Fig. B.1, and the results are shown in Fig. B.2.

The most significant result is that the residual thermal stress in the copper changes to a compressive stress of −96.5 MPa (−14.8 ksi); hence, much larger mechanical loads can be experienced before yielding occurs in the copper layer. Unfortunately, the interlaminar stress (σ_z) at the laminate edge changes from compressive to tensile (36 MPa; 5.3 ksi). If poor bonding exists between the Cu and Cu–Be layers, delaminations can occur if tensile loads are applied in the x–y plane of the laminate. If compressive loads are applied in the z-direction, these interlaminar stresses become insignificant.

From these results, we conclude that a close match of the coefficient of thermal expansion among layers results in low thermal stresses. Hence, a good reinforcement does not always result in a poor thermal mismatch and high residual thermal stresses.

The coefficient of thermal expansion for the Cu–Be/Cu/Cu–Be laminate was 16.5 10^{-6}/K and for the Inconel/Cu/Inconel laminate, 11.4 10^{-6}/K. Therefore, the designer must allow for significant residual thermal stresses when a particular coefficient of expansion is required by the designer. For metals, thermal mismatch is mainly due to differences in thermal expansion among the layers, seldom to differences in their Poisson's ratios. For laminates with fiber-reinforced composite layers, differences in Poisson's ratios are often significant.

These two examples demonstrate that metal laminates offer less control of design variables than composite-fiber-reinforced laminates, which have a much wider range of design variables (anisotropic material properties) that can be controlled by laminate theory.

Graphite–Epoxy $[0/90]_s$

This graphite–epoxy laminate, with a $[0/90]_s$ stacking sequence, was subjected to three different loads: (1) mechanical load only, (2) thermal load only, and (3) moisture load only. The data file is given in Fig. C.1 and results are shown in Figs. C.2 through C.4. For ease of comparison, all stresses are plotted on the same scale.

For this laminate with a moderate load of 4.2 kN/cm (2900 lbf/in) applied in the x-direction, the stresses that are calculated are shown in Fig. C.2. Because of elastic anisotropy, the stresses in the x- and y-directions are significantly different. The interlaminar edge stresses are very low. Shear stresses are, of course, negligible for laminates with 0° and 90° fiber orientations, but laminates with ±45° layers have much larger shear stresses.

REFERENCES

1. R. M. Jones, Mechanics of Composite Materials, McGraw-Hill, New York, 1975; pp. 147-237.
2. B. Dodd, "The Making of Old Japanese Swords," Journal of Mechanical Working Technology vol. 2, 1978; pp. 75-84.
3. H. Becker, M. Besen, E. Bobrov, J. Chen, and D. B. Montgomery, "Structural Properties of Reinforced Copper," Internal report PFC/RR-86-12, Plasma Fusion Center, Massachusetts Institute of Technology, Cambridge, Massachusetts, 1986.
4. Graham Brown, Plasma Physics Laboratory, Princeton University, Princeton, New Jersey, private communication, 1987.
5. J. E. Ashton and J. M. Whitney, Theory of Laminated Plates, Technomic Publishing Co., Stanford, Connecticut, 1970.
6. J. M. Whitney, The effect of transverse shear deformation on the bonding of laminated plates, Journal of Composite Materials, vol. 3, 1969; p. 534.
7. J. M. Whitney and N. J. Pagano, Shear deformation in heterogeneous anisotropic plates, Journal of Applied Mechanics, vol. 37, 1970; pp. 1031-1036.
8. R. D. Kriz, Influence of ply cracks on fracture strength of graphite/epoxy laminates at 76 K, Effects of Defects in Composite Materials, ASTM STP 836, American Society for Testing and Materials, Philadelphia, 1984; pp. 250-265.
9. R. B. Pipes and N. J. Pagano, Interlaminar stresses in composite laminates under uniform axial extension, Journal of Composite Materials, vol.4, 1970; pp. 538-548.
10. S. S. Wang and I. Choi, Boundary layer thermal stresses in angle-ply composite laminates, Modern Developments in Composite Materials and Structures, J. L. Vinson, ed., ASME, New York, 1979; pp. 315-341.
11. R. I. Zwiers, T. C. T. Ting, and R. L.Spilker, On the logarithmic singularity of free-edge stress in laminated composites under uniform extension, Journal of Applied Mechanics, vol. 49, 1982; pp. 561-569.
12. N. J. Pagano and B. P. Pipes, Some observations on the interlaminar strength of composite laminates, International Journal of Mechanical Science, vol. 15, 1973; pp. 679-688.
13. Handbook for Superconducting Machinery, Metals and Ceramics Information Center, Battelle Columbus Laboratories, Columbus, Ohio, 1977.

The results for thermal loads only are shown in Fig. C.3. For this laminate, stress-free states exist above room temperature (300 K, 81°F). For comparison, the same operating temperature (76 K, −323°F) was used for all three laminates. Under thermal load, the interlaminar edge stresses were three times larger than under mechanical load. With a combination of thermal and mechanical loads, delaminations are most likely to occur between 90° layers; the thermal and mechanical stresses are nearly identical. Compared with that of the metallic laminate in the second example, the thermal expansion is quite low. With a parametric study, it is possible to obtain a stacking sequence that results in zero thermal expansion, but large residual thermal stresses are unavoidable.

Residual stress states caused by absorbed moisture are shown in Fig. C.4. When moisture is absorbed by the epoxy matrix, each layer swells only in the T-direction. This swelling produces an effect which is opposite that of the thermal load; hence, all residual stresses are opposite in sign. At 1.0% moisture weight gain in the laminate, these moisture-induced stresses can cancel the thermal stresses, leaving this laminate in a stress-free state at 76 K.

CONCLUSIONS

Design methods deriving from laminate plate theory can be applied advantageously to both metallic and nonmetallic laminates. For nonmetallic laminates there are a wide variety of material properties that can be used in a laminate design. Although there is less choice among the properties of metals, the properties of a specific layer can be improved by adding reinforcement layers.

To minimize residual thermal stresses in low temperature applications, all layers within the laminate must have closely matching coefficients of thermal expansion. Metallic laminates are best suited for this purpose. In this study, both Cu–Be and Inconel provided good reinforcement, and the Cu–Be reinforcement resulted in low thermal stresses.

When a laminate is designed for a specific coefficient of thermal expansion, a large difference in the coefficients of thermal expansion among the layers is required. Nonmetallic materials are best suited for achieving a specific coefficient of thermal expansion for the laminate but large, thermally induced residual stresses are created. At 76 K, moisture in polymeric composite laminates can eliminate these thermally induced residual stresses.

Although these concepts are easily understood, the laminate plate theory outlined in this report is a tool for quantitative laminate design when a specific material response is required in a low temperature application.

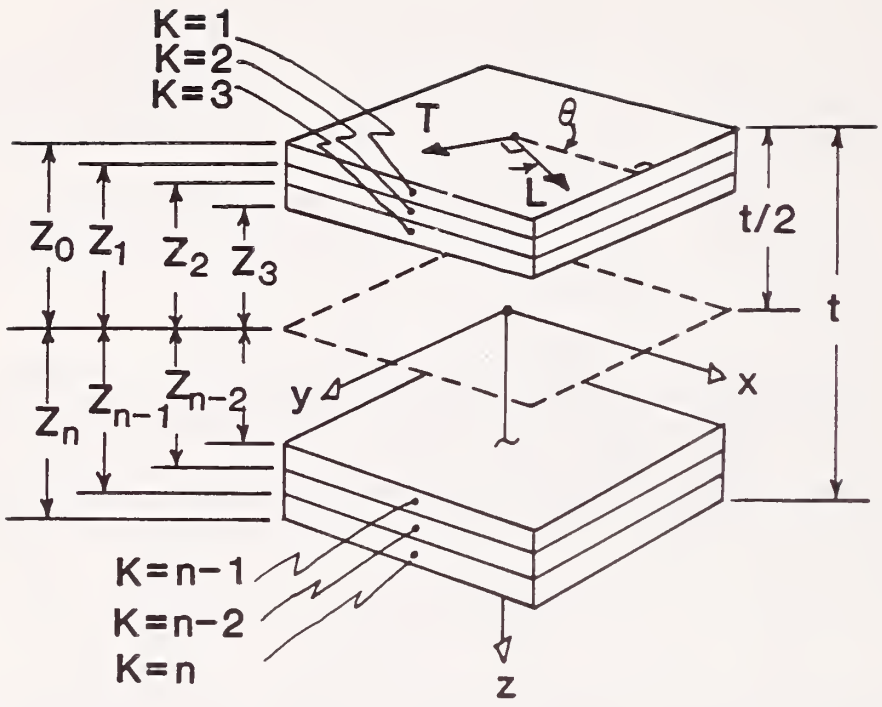

Fig. 1 Laminate configuration defined.

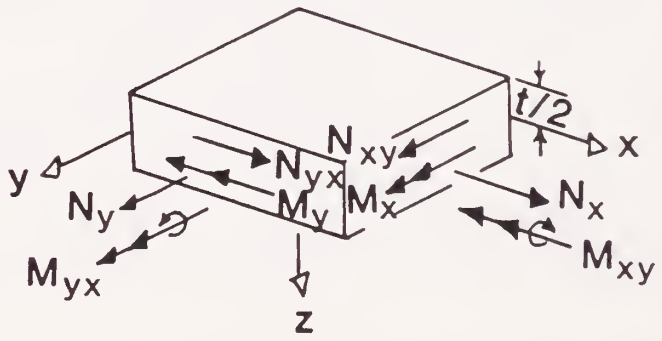

Fig. 2 Midplane loads defined.

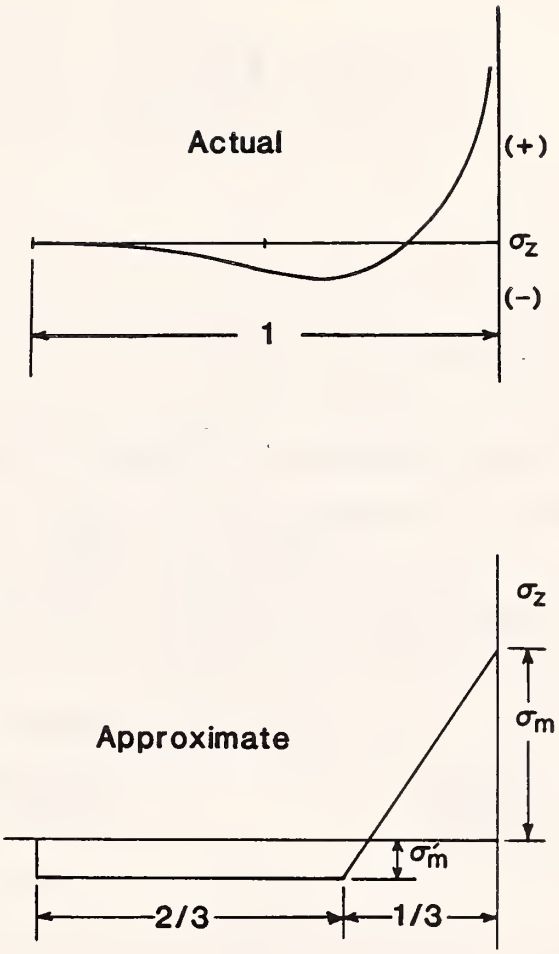

Fig. 3 Actual and approximate interlaminar stress distributions defined for the σ_z stress.

Appendix A. Computer Data File and Results for a Copper Laminate Reinforced with Inconel

```
*** COPPER/REINFORCED-INCONEL LAMINATE THERMAL LOADS, R. D. KRIZ 12/3/86 ***
NO. OF LAYERS= 3 NUMBER OF MATERIAL TYPES= 2
LAYER NO. 1 ANGLE=+00.0 THICKNESS=+0.0100 MATERIAL TYPE= 1 PLOT TYPE =INCON
LAYER NO. 2 ANGLE=+00.0 THICKNESS=+0.0100 MATERIAL TYPE= 2 PLOT TYPE =  CU
LAYER NO. 3 ANGLE=+00.0 THICKNESS=+0.0100 MATERIAL TYPE= 1 PLOT TYPE =INCON
MTL. TYPE 1  EL=+0.300E+08  ET=+0.300E+08 GLT=+0.155E+08NULT=+0.300E+00
TEXPL=+1.050E-05 TEXPT=+1.050E-05 MEXPL=+0.000E+00 MEXPT=+0.000E+00
MOISTURE THRESHOLD VOLUME, CV= 0.0
MTL. TYPE 2  EL=+1.910E+07  ET=+1.910E+07 GLT=+7.350E+06NULT=+0.300E+00
TEXPL=+1.412E-05 TEXPT=+1.412E-05 MEXPL=+0.000E+00 MEXPT=+0.000E+00
MOISTURE THRESHOLD VOLUME, CV= 0.0
NUMBER OF LOAD CASES= 1
                        LOAD CASE NUMBER= 1
+1 PLUS ONE INDICATES GIVEN LOADS AND MOMENTS CALCULATE STRAINS AND CURVATURE
NX=+0.000E+00NY=+0.000E+00NXY=+0.000E+00MX=+0.000E+00MY=+0.000E+00MXY=+0.000E+00
STRESS FREE TEMP=+300.0 OPERATING TEMP=+76.00 PERCENT MOISTURE ABSORBED= 0.000
-1 INDICATES THAT MAX MIN LIMITS ARE CHOSEN FOR PLOTTING STRESSES
```

Fig. A.1 Input data file for laminate computer program for a copper layer laminate reinforced with Inconel. Materials properties were taken from reference 13.

```
*** COPPER/REINFORCED-INCONEL LAMINATE THERMAL LOADS, R.D. KRIZ 12/3/86 ***

                              LOAD CASE NO.= 1

STRESS-FREE TEMP.= 3.00E+02  OPERATING TEMP.= 7.60E+01  MOIST. CONT.= 0.00E-01

MECHANICALIMID PLANE LAMINATE LOADS
 LOADING  I   NX= 0.00E-01   NY= 0.00E-01   NXY= 0.00E-01
  MSW= 1  I   MX= 0.00E-01   MY= 0.00E-01   MXY= 0.00E-01
          IMIDPLANE LAMINATE STRAINS AND CURVATURES
          I  EXO= 0.00E-01  EYO= 0.00E-01  EXYO= 0.00E-01
PLY       I   KX= 0.00E-01   KY= 0.00E-01   KXY= 0.00E-01
ANGLE
PLY      SIG L     SIG T     TAU LT    SIG X     SIG Y     TAU XY       SIGZ
-------------------------------------------------------------------------------
  1                                                                   0.00E-01
                                                                     -3.75E+02
  0.0  -8.39E+03 -8.39E+03  0.00E-01 -8.39E+03 -8.39E+03  0.00E-01   -1.50E+03
  1                                                                  -3.37E+03
-------------------------------------------------------------------------------
  2                                                                  -5.99E+03
                                                                     -8.24E+03
  0.0   1.68E+04  1.68E+04  0.00E-01  1.68E+04  1.68E+04  0.00E-01   -8.99E+03
  2                                                                  -8.24E+03
-------------------------------------------------------------------------------
  3                                                                  -5.99E+03
                                                                     -3.37E+03
  0.0  -8.39E+03 -8.39E+03  0.00E-01 -8.39E+03 -8.39E+03  0.00E-01   -1.50E+03
  3                                                                  -3.75E+02
-------------------------------------------------------------------------------

            SYMBOL      SYMBOL   CORRESPONDING
           PRIORITY    PLOTTED       STRESS
      LOW    5 ---------- X ---- STRESS IN X DIRECTION
             4 ---------- Y ---- STRESS IN Y DIRECTION
             3 ---------- S ---- SHEAR STRESS IN X-Y PLANE
             2 ---------- Z ---- STRESS IN Z DIRECTION
      HIGH   1 ---------- 0 ---- ZERO LINE

                        STRESS PLOT: LOAD CASE NO.= 1

MINIMUM  STRESS= -0.89908E+04                          THICKNESS     THICKNESS T(I)
MAXIMUM  STRESS=  0.16783E+05                          INCREMENT       LISTED DOWN
   STRESS  INCREMENT=  0.47000E+03                   0.25000E-02           RIGHT
                                                                          COLUMN
I         MIN= -0.92000E+04  <----------STRESS---------->  0.19000E+05=MAX    I
    PLY   V                                                             V     I
    TYPE  TTTTTTTTTTTTTTTTTTTTTTTTTTTTTTTTTTTTTTTTTTTTTTTTTTTTTTTTTTTTTTTTT    I
!---------+-Y---------+---------0---------+---------+---------+---------!0.00E-01
!         ! Y         !         0         !         !         !         !2.50E-03
!  INCON  ! Y         !       Z 0         !         !         !         !5.00E-03
!         ! Y         !  Z      0         !         !         !         !7.50E-03
!---------+-------Z---+---------0---------+---------+---------+-------Y-!1.00E-02
!         !  Z       !         0         !         !         !       Y !1.25E-02
!    CU   !Z         !         0         !         !         !       Y !1.50E-02
!         !  Z       !         0         !         !         !       Y !1.75E-02
!---------+-Y-----Z---+---------0---------+---------+---------+---------!2.00E-02
!         ! Y         !  Z      0         !         !         !         !2.25E-02
!  INCON  ! Y         !       Z 0         !         !         !         !2.50E-02
!         ! Y         !         0         !         !         !         !2.75E-02
!---------+-Y---------+---------0---------+---------+---------+---------!3.00E-02

          COEFFICIENTS OF EXPANSION FOR LAMINATE X-Y COORD.
                          THERMAL COEFF.    MOISTURE COEFF.
          X-DIRECTION       1.137E-05          0.000E-01
          Y-DIRECTION       1.137E-05          0.000E-01
        SHEAR XY-PLANE      0.000E-01          0.000E-01
```

Fig. A.2 Output data file of results calculated by the laminate computer program for data given in Fig. A.1. Stresses are given in tables and graphs.

Appendix B. Computer Data File and Results for a Copper Laminate Reinforced with a Copper–Beryllium Alloy

```
*** COPPER/REINFORCED-COPPER:BERYLLIUM, THERMAL LOADS, R.D. KRIZ 12/3/86 ***
NO. OF LAYERS= 3 NUMBER OF MATERIAL TYPES= 2
LAYER NO. 1 ANGLE=+00.0 THICKNESS=+0.0100 MATERIAL TYPE= 1 PLOT TYPE =CU:BE
LAYER NO. 2 ANGLE=+00.0 THICKNESS=+0.0100 MATERIAL TYPE= 2 PLOT TYPE =  CU
LAYER NO. 3 ANGLE=+00.0 THICKNESS=+0.0100 MATERIAL TYPE= 1 PLOT TYPE =CU:BE
MTL. TYPE 1  EL=+0.185E+08  ET=+0.185E+08 GLT=+0.712E+07NULT=+0.300E+00
TEXPL=+0.178E-04 TEXPT=+0.178E-04 MEXPL=+0.000E+00 MEXPT=+0.000E+00
MOISTURE THRESHOLD VOLUME, CV= 0.0
MTL. TYPE 2  EL=+1.910E+07  ET=+1.910E+07 GLT=+7.350E+06NULT=+0.300E+00
TEXPL=+1.412E-05 TEXPT=+1.412E-05 MEXPL=+0.000E+00 MEXPT=+0.000E+00
MOISTURE THRESHOLD VOLUME, CV= 0.0
NUMBER OF LOAD CASES= 1
                        LOAD CASE NUMBER= 1
+1 PLUS ONE INDICATES GIVEN LOADS AND MOMENTS CALCULATE STRAINS AND CURVATURE
NX=+0.000E+00NY=+0.000E+00NXY=+0.000E+00MX=+0.000E+00MY=+0.000E+00MXY=+0.000E+00
STRESS FREE TEMP=+300.0 OPERATING TEMP=+76.00 PERCENT MOISTURE ABSORBED= 0.000
-1 INDICATES THAT MAX MIN LIMITS ARE CHOSEN FOR PLOTTING STRESSES
```

Fig. B.1 Input data file for laminate computer program for a copper layer laminate reinforced with a Cu–Be alloy. Material properties were taken from reference 13.

```
*** COPPER/REINFORCED-COPPER:BERYLLIUM, THERMAL LOADS, R.D. KRIZ 12/3/86 ***

                              LOAD CASE NO.= 1

STRESS-FREE TEMP.= 3.00E+02  OPERATING TEMP.= 7.60E+01  MOIST. CONT.= 0.00E-01

MECHANICALIMID PLANE LAMINATE LOADS
 LOADING  I   NX= 0.00E-01   NY= 0.00E-01   NXY= 0.00E-01
  MSW= 1  I   MX= 0.00E-01   MY= 0.00E-01   MXY= 0.00E-01
          IMIDPLANE LAMINATE STRAINS AND CURVATURES
          I  EXO= 0.00E-01  EYO= 0.00E-01  EXYO= 0.00E-01
PLY       I   KX= 0.00E-01   KY= 0.00E-01   KXY= 0.00E-01
ANGLE
PLY      SIG L     SIG T     TAU LT    SIG X     SIG Y     TAU XY       SIGZ
-------------------------------------------------------------------- 0.00E-01
  1                                                                  3.31E+02
  0.0   7.42E+03  7.42E+03  0.00E-01  7.42E+03  7.42E+03  0.00E-01   1.32E+03
  1                                                                  2.98E+03
-------------------------------------------------------------------- 5.30E+03
  2                                                                  7.28E+03
  0.0  -1.48E+04 -1.48E+04  0.00E-01 -1.48E+04 -1.48E+04  0.00E-01   7.95E+03
  2                                                                  7.28E+03
-------------------------------------------------------------------- 5.30E+03
  3                                                                  2.98E+03
  0.0   7.42E+03  7.42E+03  0.00E-01  7.42E+03  7.42E+03  0.00E-01   1.32E+03
  3                                                                  3.31E+02
--------------------------------------------------------------------

            SYMBOL      SYMBOL    CORRESPONDING
           PRIORITY    PLOTTED       STRESS
      LOW    5 ---------- X ---- STRESS IN X DIRECTION
             4 ---------- Y ---- STRESS IN Y DIRECTION
             3 ---------- S ---- SHEAR STRESS IN X-Y PLANE
             2 ---------- Z ---- STRESS IN Z DIRECTION
      HIGH   1 ---------- 0 ---- ZERO LINE

                    STRESS PLOT: LOAD CASE NO.= 1

MINIMUM  STRESS= -0.14834E+05                          THICKNESS     THICKNESS T(I)
MAXIMUM  STRESS=  0.79470E+04                          INCREMENT       LISTED DOWN
   STRESS  INCREMENT=  0.42000E+03                   0.25000E-02          RIGHT
                                                                          COLUMN
I         MIN= -0.17000E+05  <----------STRESS---------->  0.82000E+04=MAX    I
    PLY   V                                                              V    I
    TYPE  TTTTTTTTTTTTTTTTTTTTTTTTTTTTTTTTTTTTTTTTTTTTTTTTTTTTTTTTTTTTTTTTT    I
!---------+---------+---------+---------+---------+-0---------+---------Y0.00E-01
!         !         !         !         !         ! 0         !          Y2.50E-03
!  CU:BE  !         !         !         !         ! 0  Z      !          Y5.00E-03
!         !         !         !         !         ! 0       Z!          Y7.50E-03
!---------+-------Y-+---------+---------+---------+-0---------+-------Z-!1.00E-02
!         !       Y !         !         !         ! 0         !         Z!1.25E-02
!    CU   !       Y !         !         !         ! 0         !          !1.50E-02
!         !       Y !         !         !         ! 0         !         Z!1.75E-02
!---------+---------+---------+---------+---------+-0---------+-------Z-Y2.00E-02
!         !         !         !         !         ! 0       Z!          Y2.25E-02
!  CU:BE  !         !         !         !         ! 0  Z      !          Y2.50E-02
!         !         !         !         !         ! 0         !          Y2.75E-02
!---------+---------+---------+---------+---------+-0---------+---------Y3.00E-02

          COEFFICIENTS OF EXPANSION FOR LAMINATE X-Y COORD.
                          THERMAL COEFF.    MOISTURE COEFF.
        X-DIRECTION        1.655E-05          0.000E-01
        Y-DIRECTION        1.655E-05          0.000E-01
      SHEAR XY-PLANE       0.000E-01          0.000E-01
```

Fig. B.2 Output data file of results calculated by the laminate computer program for data given in Fig. A.2. Stresses are given in tables and graphs.

Appendix C. Computer Data File and Results for a Graphite/Epoxy Fiber-Reinforced Composite Laminate with Two Layers of 90° Material Reinforced by Two Layers of 0° material, $[0/90]_s$

```
*** GRAPHITE/EPOXY LAMINATE; LOADS AND STRESSES FOR (0/90)SYM. LAMINATE ***
NO. OF LAYERS= 4 NUMBER OF MATERIAL TYPES= 1
LAYER NO. 1 ANGLE=+00.0 THICKNESS=+0.0100 MATERIAL TYPE= 1 PLOT TYPE =+00.0
LAYER NO. 2 ANGLE=+90.0 THICKNESS=+0.0100 MATERIAL TYPE= 1 PLOT TYPE =+90.0
LAYER NO. 3 ANGLE=+90.0 THICKNESS=+0.0100 MATERIAL TYPE= 1 PLOT TYPE =+90.0
LAYER NO. 4 ANGLE=+00.0 THICKNESS=+0.0100 MATERIAL TYPE= 1 PLOT TYPE =+00.0
MTL. TYPE 1  EL=+20.00E+06  ET=+2.100E+06 GLT=+0.850E+06NULT=+0.210E+00
TEXPL=-0.230E-06 TEXPT=+14.90E-06 MEXPL=+0.000E+00 MEXPT=+5.560E-03
MOISTURE THRESHOLD VOLUME, CV= 0.0
NUMBER OF LOAD CASES= 3
                        LOAD CASE NUMBER= 1
+1 PLUS ONE INDICATES GIVEN LOADS AND MOMENTS CALCULATE STRAINS AND CURVATURE
NX=+2.400E+03NY=+0.000E+00NXY=+0.000E+00MX=+0.000E+00MY=+0.000E+00MXY=+0.000E+00
STRESS FREE TEMP=+000.0 OPERATING TEMP=+00.00 PERCENT MOISTURE ABSORBED= 0.000
+1 INDICATES THAT MAX MIN LIMITS ARE ASSIGNED BELOW FOR PLOTTING STRESSES
MAX STRESS=+1.000E+04 MIN STRESS=-1.000E+04
                        LOAD CASE NUMBER= 2
+1 PLUS ONE INDICATES GIVEN LOADS AND MOMENTS CALCULATE STRAINS AND CURVATURE
NX=+0.000E+00NY=+0.000E+00NXY=+0.000E+00MX=+0.000E+00MY=+0.000E+00MXY=+0.000E+00
STRESS FREE TEMP=+100.0 OPERATING TEMP=-323.0 PERCENT MOISTURE ABSORBED= 0.000
+1 INDICATES THAT MAX MIN LIMITS ARE ASSIGNED BELOW FOR PLOTTING STRESSES
MAX STRESS=+1.000E+04 MIN STRESS=-1.000E+04
                        LOAD CASE NUMBER= 3
+1 PLUS ONE INDICATES GIVEN LOADS AND MOMENTS CALCULATE STRAINS AND CURVATURE
NX=+0.000E+00NY=+0.000E+00NXY=+0.000E+00MX=+0.000E+00MY=+0.000E+00MXY=+0.000E+00
STRESS FREE TEMP=+000.0 OPERATING TEMP=+00.00 PERCENT MOISTURE ABSORBED=+1.000
+1 INDICATES THAT MAX MIN LIMITS ARE ASSIGNED BELOW FOR PLOTTING STRESSES
MAX STRESS=+1.000E+04 MIN STRESS=-1.000E+04
```

Fig. C.1 Output data file for laminate computer program for a symmetrical crossply laminate with a stacking sequence of $[0/90]_s$. Material properties were taken from reference 8.

```
*** GRAPHITE/EPOXY LAMINATE; LOADS AND STRESSES FOR (0/90)SYM. LAMINATE ***

                              LOAD CASE NO.= 1

STRESS-FREE TEMP.= 0.00E-01  OPERATING TEMP.= 0.00E-01  MOIST. CONT.= 0.00E-01

MECHANICALIMID PLANE LAMINATE LOADS
 LOADING  I   NX= 2.40E+03   NY= 0.00E-01   NXY= 0.00E-01
  MSW= 1  I   MX= 0.00E-01   MY= 0.00E-01   MXY= 0.00E-01
          IMIDPLANE LAMINATE STRAINS AND CURVATURES
          I  EXO= 5.41E-03  EYO=-2.16E-04  EXYO=-9.51E-11
PLY       I   KX=-3.09E-09   KY=-3.97E-10   KXY= 2.30E-16
ANGLE
PLY      SIG L     SIG T     TAU LT    SIG X     SIG Y     TAU XY       SIGZ
                                                                    0.00E-01
  1                                                                 4.88E+01
  0.0   1.09E+05  1.94E+03 -8.08E-05  1.09E+05  1.94E+03 -8.08E-05   1.95E+02
  1                                                                 4.39E+02
                                                                    7.81E+02
  2                                                                 1.12E+03
 90.0  -1.94E+03  1.13E+04  4.99E-04  1.13E+04 -1.94E+03  8.08E-05   1.37E+03
  2                                                                 1.51E+03
                                                                    1.56E+03
  3                                                                 1.51E+03
 90.0  -1.94E+03  1.13E+04  4.99E-04  1.13E+04 -1.94E+03  8.08E-05   1.37E+03
  3                                                                 1.12E+03
                                                                    7.81E+02
  4                                                                 4.39E+02
  0.0   1.09E+05  1.94E+03 -8.08E-05  1.09E+05  1.94E+03 -8.08E-05   1.95E+02
  4                                                                 4.88E+01

            SYMBOL      SYMBOL    CORRESPONDING
          PRIORITY    PLOTTED        STRESS
      LOW   5 ---------- X ------ STRESS IN X DIRECTION
            4 ---------- Y ------ STRESS IN Y DIRECTION
            3 ---------- S ------ SHEAR STRESS IN X-Y PLANE
            2 ---------- Z ------ STRESS IN Z DIRECTION
      HIGH  1 ---------- 0 ------ ZERO LINE

                    STRESS PLOT: LOAD CASE NO.= 1

MINIMUM  STRESS= -0.10000E+05                          THICKNESS     THICKNESS T(I)
MAXIMUM  STRESS=  0.10000E+05                          INCREMENT       LISTED DOWN
   STRESS  INCREMENT=  0.43333E+03                   0.25000E-02          RIGHT
                                                                          COLUMN
I         MIN= -0.13000E+05  <----------STRESS---------->  0.13000E+05=MAX    I
    PLY   V                                                              V    I
    TYPE  TTTTTTTTTTTTTTTTTTTTTTTTTTTTTTTTTTTTTTTTTTTTTTTTTTTTTTTTTTTTTTTTT    I
!---------+---------+---------+---------+0----Y---+---------+---------!0.00E-01
!         !         !         !         !0    Y   !         !         !2.50E-03
!  +00.0  !         !         !         !0    Y   !         !         !5.00E-03
!         !         !         !         !0Z   Y   !         !         !7.50E-03
!---------+---------+---------+-------Y-+0-Z-------+---------+---------X-!1.00E-02
!         !         !         !       Y !0  Z     !         !         X !1.25E-02
!  +90.0  !         !         !       Y !0  Z     !         !         X !1.50E-02
!         !         !         !       Y !0   Z    !         !         X !1.75E-02
!---------+---------+---------+-------Y-+0----Z----+---------+---------X-!2.00E-02
!         !         !         !       Y !0   Z    !         !         X !2.25E-02
!  +90.0  !         !         !       Y !0  Z     !         !         X !2.50E-02
!         !         !         !       Y !0  Z     !         !         X !2.75E-02
!---------+---------+---------+---------+0-Z--Y---+---------+---------!3.00E-02
!         !         !         !         !0Z   Y   !         !         !3.25E-02
!  +00.0  !         !         !         !0    Y   !         !         !3.50E-02
!         !         !         !         !0    Y   !         !         !3.75E-02
!---------+---------+---------+---------+0----Y---+---------+---------!4.00E-02

          COEFFICIENTS OF EXPANSION FOR LAMINATE X-Y COORD.
                          THERMAL COEFF.    MOISTURE COEFF.
          X-DIRECTION       1.443E-06          6.147E-04
          Y-DIRECTION       1.443E-06          6.147E-04
        SHEAR XY-PLANE      1.422E-12          5.225E-10
```

Fig. C.2 Output data file of results calculated by the laminate computer program for load case number 1 in Fig. C.1. Stresses are given in tables and graphs.

```
*** GRAPHITE/EPOXY LAMINATE; LOADS AND STRESSES FOR (0/90)SYM. LAMINATE ***

                              LOAD CASE NO.= 2

STRESS-FREE TEMP.= 1.00E+02  OPERATING TEMP.=-3.23E+02  MOIST. CONT.= 0.00E-01

MECHANICALIMID PLANE LAMINATE LOADS
 LOADING  I   NX= 0.00E-01   NY= 0.00E-01   NXY= 0.00E-01
  MSW= 1  I   MX= 0.00E-01   MY= 0.00E-01   MXY= 0.00E-01
          IMIDPLANE LAMINATE STRAINS AND CURVATURES
          I  EXO= 0.00E-01  EYO= 0.00E-01  EXYO= 0.00E-01
PLY       I   KX= 0.00E-01   KY= 0.00E-01   KXY= 0.00E-01
ANGLE
PLY      SIG L     SIG T     TAU LT    SIG X     SIG Y     TAU XY       SIGZ
-------------------------------------------------------------------------------
                                                                      0.00E-01
  1                                                                   2.94E+02
 0.0  -1.17E+04  1.17E+04 -5.11E-04 -1.17E+04  1.17E+04 -5.11E-04     1.17E+03
  1                                                                   2.64E+03
-------------------------------------------------------------------------------
                                                                      4.70E+03
  2                                                                   6.76E+03
90.0  -1.17E+04  1.17E+04  5.11E-04  1.17E+04 -1.17E+04  5.11E-04     8.22E+03
  2                                                                   9.10E+03
-------------------------------------------------------------------------------
                                                                      9.40E+03
  3                                                                   9.10E+03
90.0  -1.17E+04  1.17E+04  5.11E-04  1.17E+04 -1.17E+04  5.11E-04     8.22E+03
  3                                                                   6.76E+03
-------------------------------------------------------------------------------
                                                                      4.70E+03
  4                                                                   2.64E+03
 0.0  -1.17E+04  1.17E+04 -5.11E-04 -1.17E+04  1.17E+04 -5.11E-04     1.17E+03
  4                                                                   2.94E+02
-------------------------------------------------------------------------------

            SYMBOL      SYMBOL   CORRESPONDING
           PRIORITY    PLOTTED       STRESS
      LOW    5 ---------- X ---- STRESS IN X DIRECTION
             4 ---------- Y ---- STRESS IN Y DIRECTION
             3 ---------- S ---- SHEAR STRESS IN X-Y PLANE
             2 ---------- Z ---- STRESS IN Z DIRECTION
     HIGH    1 ---------- 0 ---- ZERO LINE

                        STRESS PLOT: LOAD CASE NO.= 2

MINIMUM  STRESS= -0.10000E+05                          THICKNESS     THICKNESS T(I)
MAXIMUM  STRESS=  0.10000E+05                          INCREMENT       LISTED DOWN
   STRESS  INCREMENT=  0.43333E+03                   0.25000E-02          RIGHT
                                                                          COLUMN
I         MIN= -0.13000E+05  <----------STRESS----------> 0.13000E+05=MAX    I
    PLY   V                                                             V     I
    TYPE  TTTTTTTTTTTTTTTTTTTTTTTTTTTTTTTTTTTTTTTTTTTTTTTTTTTTTTTTTTTT     I
!---------+---X---+---------+---------+0---------+---------+---------Y-!0.00E-01
!         !   X   !         !         !0Z        !         !         Y !2.50E-03
!  +00.0  !   X   !         !         !0  Z      !         !         Y !5.00E-03
!         !   X   !         !         !0     Z   !         !         Y !7.50E-03
!---------+---Y---+---------+---------+0---------+-Z-------+---------X-!1.00E-02
!         !   Y   !         !         !0         !      Z  !         X !1.25E-02
!  +90.0  !   Y   !         !         !0         !         Z         X !1.50E-02
!         !   Y   !         !         !0         !         ! Z       X !1.75E-02
!---------+---Y---+---------+---------+0---------+---------+---Z-----X-!2.00E-02
!         !   Y   !         !         !0         !         ! Z       X !2.25E-02
!  +90.0  !   Y   !         !         !0         !         Z         X !2.50E-02
!         !   Y   !         !         !0         !      Z  !         X !2.75E-02
!---------+---X---+---------+---------+0---------+-Z-------+---------Y-!3.00E-02
!         !   X   !         !         !0      Z  !         !         Y !3.25E-02
!  +00.0  !   X   !         !         !0  Z      !         !         Y !3.50E-02
!         !   X   !         !         !0Z        !         !         Y !3.75E-02
!---------+---X---+---------+---------+0---------+---------+---------Y-!4.00E-02
```

Fig. C.3 Output data file of results calculated by the laminate computer program for load case number 2 in Fig. C.1. Stresses are given in tables and graphs.

```
*** GRAPHITE/EPOXY LAMINATE; LOADS AND STRESSES FOR (0/90)SYM. LAMINATE ***

                                LOAD CASE NO.= 3

STRESS-FREE TEMP.= 0.00E-01  OPERATING TEMP.= 0.00E-01  MOIST. CONT.= 1.00E+00

MECHANICALIMID PLANE LAMINATE LOADS
 LOADING  I   NX= 0.00E-01   NY= 0.00E-01   NXY= 0.00E-01
  MSW= 1  I   MX= 0.00E-01   MY= 0.00E-01   MXY= 0.00E-01
          IMIDPLANE LAMINATE STRAINS AND CURVATURES
          I  EXO= 0.00E-01  EYO= 0.00E-01  EXYO= 0.00E-01
PLY       I   KX= 0.00E-01   KY= 0.00E-01   KXY= 0.00E-01
ANGLE
PLY      SIG L     SIG T     TAU LT    SIG X     SIG Y     TAU XY       SIGZ
-------------------------------------------------------------------- 0.00E-01
  1                                                                  -2.55E+02
  0.0   1.02E+04 -1.02E+04  4.44E-04  1.02E+04 -1.02E+04  4.44E-04   -1.02E+03
  1                                                                  -2.30E+03
-------------------------------------------------------------------- -4.08E+03
  2                                                                  -5.87E+03
 90.0   1.02E+04 -1.02E+04 -4.44E-04 -1.02E+04  1.02E+04 -4.44E-04   -7.14E+03
  2                                                                  -7.91E+03
-------------------------------------------------------------------- -8.17E+03
  3                                                                  -7.91E+03
 90.0   1.02E+04 -1.02E+04 -4.44E-04 -1.02E+04  1.02E+04 -4.44E-04   -7.14E+03
  3                                                                  -5.87E+03
-------------------------------------------------------------------- -4.08E+03
  4                                                                  -2.30E+03
  0.0   1.02E+04 -1.02E+04  4.44E-04  1.02E+04 -1.02E+04  4.44E-04   -1.02E+03
  4                                                                  -2.55E+02
--------------------------------------------------------------------

              SYMBOL      SYMBOL   CORRESPONDING
            PRIORITY    PLOTTED       STRESS
        LOW   .5 ---------- X ---- STRESS IN X DIRECTION
              4 ---------- Y ---- STRESS IN Y DIRECTION
              3 ---------- S ---- SHEAR STRESS IN X-Y PLANE
              2 ---------- Z ---- STRESS IN Z DIRECTION
        HIGH  1 ---------- 0 ---- ZERO LINE

                        STRESS PLOT: LOAD CASE NO.= 3

MINIMUM  STRESS= -0.10000E+05                          THICKNESS     THICKNESS T(I)
MAXIMUM  STRESS=  0.10000E+05                          INCREMENT       LISTED DOWN
   STRESS  INCREMENT=  0.43333E+03                   0.25000E-02           RIGHT
                                                                          COLUMN
I          MIN= -0.13000E+05  <----------STRESS---------->  0.13000E+05=MAX    I
    PLY    V                                                              V    I
    TYPE   TTTTTTTTTTTTTTTTTTTTTTTTTTTTTTTTTTTTTTTTTTTTTTTTTTTTTTTTTTTTTT    I
!----------+------Y--+----------+----------+0----------+----------+------X----!0.00E-01
!          !      Y  !          !          Z0          !          !      X    !2.50E-03
!  +00.0   !      Y  !          !         Z!0          !          !      X    !5.00E-03
!          !      Y  !          !     Z    !0          !          !      X    !7.50E-03
!----------+------X--+----------+Z---------+0----------+----------+------Y----!1.00E-02
!          !      X  !       Z  !          !0          !          !      Y    !1.25E-02
!  +90.0   !      X  !    Z     !          !0          !          !      Y    !1.50E-02
!          !      X  ! Z        !          !0          !          !      Y    !1.75E-02
!----------+------X--+-Z--------+----------+0----------+----------+------Y----!2.00E-02
!          !      X  ! Z        !          !0          !          !      Y    !2.25E-02
!  +90.0   !      X  !    Z     !          !0          !          !      Y    !2.50E-02
!          !      X  !       Z  !          !0          !          !      Y    !2.75E-02
!----------+------Y--+----------+Z---------+0----------+----------+------X----!3.00E-02
!          !      Y  !          !     Z    !0          !          !      X    !3.25E-02
!  +00.0   !      Y  !          !         Z!0          !          !      X    !3.50E-02
!          !      Y  !          !          Z0          !          !      X    !3.75E-02
!----------+------Y--+----------+----------+0----------+----------+------X----!4.00E-02
```

Fig. C.4 Output data file of results calculated by the laminate computer program for load case number 3 in Fig. C.1. Stresses are given in tables and graphs.

TECHNICAL NOTE

Maurice B. Kasen[1]

High Quality Organic Matrix Composite Specimens for Research Purposes

REFERENCE: Kasen, M. B., **"High Quality Organic Matrix Composite Specimens for Research Purposes,"** *Journal of Composites Technology & Research*, Vol. 8, No. 3, Fall 1986, pp. 103-106.

ABSTRACT: An efficient method for producing and testing organic-matrix composite specimens for research purposes is described. The production method is adaptable to in-house manufacturing and provides complete control over a large variety of material and processing variables. The rod-shape, uniaxially reinforced or neat-resin specimens may be cut to length and tested without further machining. Conventional short-beam shear, flexural strength, and compression test methods may be used. Development of test methods for performing torsional shear tests and for determining the fracture energy G_{Ic} are described. Test results at room temperature and at cryogenic temperature are presented.

KEYWORDS: cryogenics, fiber-reinforced specimens, fracture energy, neat resin specimens, organic-matrix composites, research specimen production, short-beam shear, test methodology, torsional shear

Nomenclature

DGEBA	Diglycidyl ether of bisphenol A
DDS	Diamino diphenyl sulphone
AMD	Alkylated methylenedianilene
POPA	Polyoxypropylenediamine
FPA	Fatty polyamide
BF_3MEA	Boron trifluoride monoethylamime

Introduction

Experimental screening of the influence of a large number of variables on performance is sometimes necessary when developing composite materials for a specific service. These variables may include different resin systems and cure states as well as different types and contents of fiber reinforcement. One may wish to study neat resin performance as well as that of reinforced materials. Unfortunately, the cost of obtaining the large number of well-characterized specimens required for such studies can be prohibitive. We experienced this problem during an investigation of the combined influence of cryogenic temperature and neutron irradiation on the degradation of glass reinforced organic matrix electrical insulators. Such insulators are required in the superconducting magnets of magnetically confined fusion energy systems. Our solution may interest others who conduct complex composite materials screening programs.

Specimen Selection

A small specimen size was dictated by the need to simultaneously irradiate many specimens in a restricted volume and to minimize residual radioactivity. The production technique had to be simple and still provide excellent control over the variables of interest. The specimens had to be free of macroscopic defects. It was desirable to avoid machining costs and the consequent introduction of surface defects. The specimens had to be suitable for testing in a variety of modes that would provide information on degradation of the fiber-matrix interface.

The 3.2-mm (0.125-in.) diameter uniaxially reinforced and neat resin specimens illustrated on Fig. 1 best met these criteria. This specimen configuration is not new—similar specimens have been used in studies of reinforced polyester composites .[2] However, we have adapted the production method to permit its use with hot-melt epoxy and bismaleimide matrices and have refined it to produce specimens that are defect free on a macroscopic scale. Figure 2 illustrates the quality we are able to obtain.

Production Method

Resin-impregnated fiber strands are pulled into a tube mold in which they are cured. Although the method is simple in principle, obtaining specimens free of defects requires careful attention to a number of details. We find that polytetrafluoroethylene (TFE) tubes having a very smooth bore produce the best quality specimens. Glass molds introduce surface defects and require a release agent, which might contaminate the specimen surface. It is essential that the glass fiber tows be thoroughly vacuum impregnated with well-degassed resin. A head of resin must be maintained above the fiber during the pulling operation and during the cure. A

[1]Staff scientist, Fracture and Deformation Division, National Bureau of Standards, Boulder, CO 80302.

[2]Gauchel, J., Owens-Corning Fiberglas Technical Center, P.O. Box 415, Granville, OH 43023, personal communication.

0885-6804/86/0009-0103$02.50

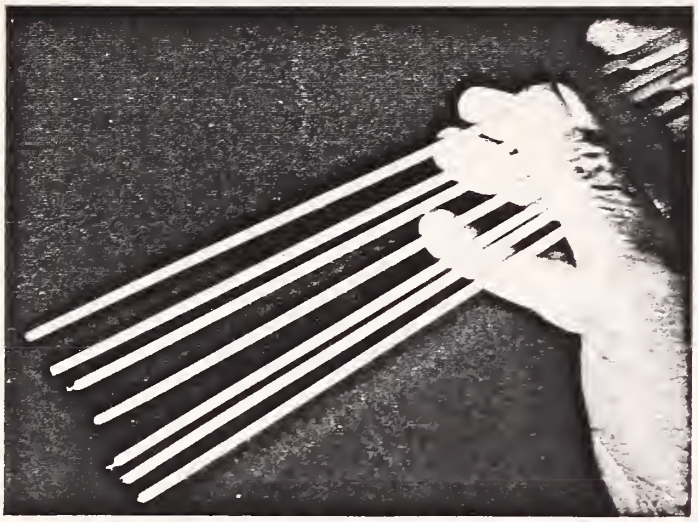

FIG. 1—*Specimen rods, 3.2 mm diameter, 40 cm long.*

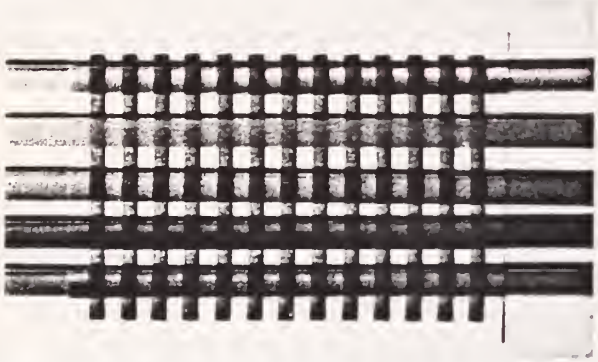

FIG. 2—*Transparency of rods illustrates the quality obtained. Top to bottom: DGBA/DDS, (neat); DGEBA/DDS, 48* V/O; *DGEBA/AMD/POPA, (neat); DGEBA/AMD/POPA, 48* V/O; *bismaleimide, (neat).*

pressure of about 420 kPa (80 psi) of nitrogen gas must be maintained during the initial stages of the cure cycle.

Proper resin working temperature is maintained by jacketing the impregnation and drawing tubes with a high temperature bath. Neat resin specimens are produced by drawing the degassed resin into the tubes with a vacuum. Reinforced specimens are pulled from the tube molds, which may be reused. Neat specimens are removed by pressing.

The fiber volume fraction is easily calculated from knowledge of the weight and density of the fiber and of the tube mold dimensions. The specimen surface is very smooth, and the coefficient of variability in diameter among rods produced with a given mold is about 0.001 to 0.003.

Evolution of solvents in the resin produces porosity in the closed mold. This apparently eliminates many systems of interest where solvents are conventionally used in the blending process to lower the melting point of solid cure agents. However, we find that ultrasonic blending frequently eliminates the need for solvents [*1*]. For example, we routinely blend the solid diamino diphenyl sulphone (DDS) cure agent into an epoxy resin by this method. Preliminary experiments indicate that it may be possible to work with solvent-containing resin systems by degassing the impregnated fibers under a vacuum just before pulling into the tube mold. Although specimens of reasonable quality have been produced in this manner, the technique requires additional development.

Test Methodology

Our current interest is to assess the radiation-induced degradation of the fiber-matrix interface. We have, therefore, concentrated on developing methods for testing in short-beam and torsional shear. We have also developed a unique method for measuring the change in longitudinal fracture energy G_{1c} of the specimens. The specimens may also be tested in longitudinal compression using a fixture described elsewhere [*2*] or in flexure. Each of these methods requires only that the specimens be cut to the desired length.

The short-beam test method is conventional except for the small specimen size and contouring of the loading nose and supports to match the specimen radius. Specimens are 16 mm (0.6 in.) long for testing at a span/depth ratio of 3.0. Table 1 summarizes apparent interlaminar shear data obtained by this method at 76 K. The coefficient of variability *CV* is relatively low among specimens from different rods of the same material. These data indicate that the short-beam shear test method is relatively insensitive to variation in fiber volume fraction *V/O* within the range tested.

Symmetry of the torsional shear test causes the combined tension, compression, and shear stresses resolved at the fiber-matrix interface to change more systematically with increasing deformation than is the case for short-beam shear. For a given rotational angle, the magnitude of the shear component is inversely proportional to the gage length and directly proportional to the distance of the fiber-matrix interface from the specimen center. As shown in Fig. 3*a*, the failure in this type of test initiates near the specimen surface and progresses inward. Figure 3*b* illustrates the interfacial nature of the failure mode. Table 2 summarizes the ultimate torsional strengths and coefficients of variation obtained during testing three epoxy matrix systems at 76 K.

The torsional specimen is 89 mm (3.5-in.) long, 35 mm (1.375 in.) of which is embedded in 9.52-mm (0.375-in.) diameter end caps, leaving a gage length of 19 mm (0.75 in.). Specimens are epoxy bonded into linen phenolic end caps for room temperature testing. For cryogenic testing, we freeze the specimens into aluminum end caps to permit recovery of the specimen ends for additional testing. Several types of aqueous slurries provided sufficient bond strength to fracture the specimen. However, progressive cracking of the bond from the gage section into the end caps increased the effective gage length, complicating calculation of the torsional modulus. This was corrected by incorporating a series of four set screws into the end caps as illustrated on Fig. 4. Contact of these

TABLE 1—*Short-beam shear data, 76 K, DGEBA/FPA, Type E Glass (10 specimens each condition).*

V/O Glass	Rod	Strength, MPa	*CV*
41	1	23.6	0.042
	2	23.0	0.087
		23.3	0.064
48	1	23.3	0.047
	2	23.6	0.013
		23.5	0.034

FIG. 3—*Cross sections of 48 V/O glass reinforced specimen after torsion testing at 76 K.* (a) *Full cross section illustrating initiation of fracture at the surface and propagation inward.* (b) *Magnified view of the fracture showing the interfacial nature of the crack propagation. Original magnification × 1000.*

TABLE 2—*Torsional shear data, 76 K, (5 specimens each condition, 48 V/O Type E glass).*

Epoxy Matrix	Strength, MPa	*CV*
DGEBA/DDS/BF_3MEA	158.4	0.086
DGEBA/DDS	160.8	0.036
DGEBA/AMD/POPA	148.6	0.078

screws with the specimen prevents rotation and confines the failure to the gage section. The torsional load is applied by a stainless steel shaft that mates with a slot in the upper end cap, while the lower end cap is pinned to a stainless steel reaction tube.

Although the above tests are useful in a materials screening program, they provide only qualitative information on the integrity of the fiber-matrix interface. We are, therefore, developing a test method that provides information on the longitudinal fracture energy G_{1c}. The principle is illustrated on Fig. 5*a*. A razor blade is pressed an arbitrary distance into the end of the fiber reinforced specimen causing a crack to propagate lengthwise down the specimen. The fracture energy is then calculated by the equation

$$G_{1c} = 0.01372\ d^3Ey^2/x^4 \qquad (1)$$

where E is the Young's modulus and where d, y and x are as defined on Fig. 5*a*. This approach is based on the original work of Obreimoff [*3*] who developed a similar expression for the splitting strength of mica and on the subsequent work of Barlow and Windle [*4*], who suggested that the basic method could be applied to uniaxially reinforced composite materials. However, Eq 1 differs from that of Obreimoff in that the moment of inertia has been calculated about the centroidal axis of a semicircular cross section to take into consideration the geometry of the rod-shape specimens. Obreimoff defined the fracture energy Q as the energy release required to create one of the two new surfaces. This was equated to G_{1c} by Barlow and Windle, and we have followed this convention rather than that in which G_{1c} is taken as the energy required to create both surfaces.

The prototype fixture illustrated in Fig. 5*b* was used to generate the G_{1c} values presented in Table 3 for several materials and temperatures. The results are in reasonable agreement with the 1.9 to

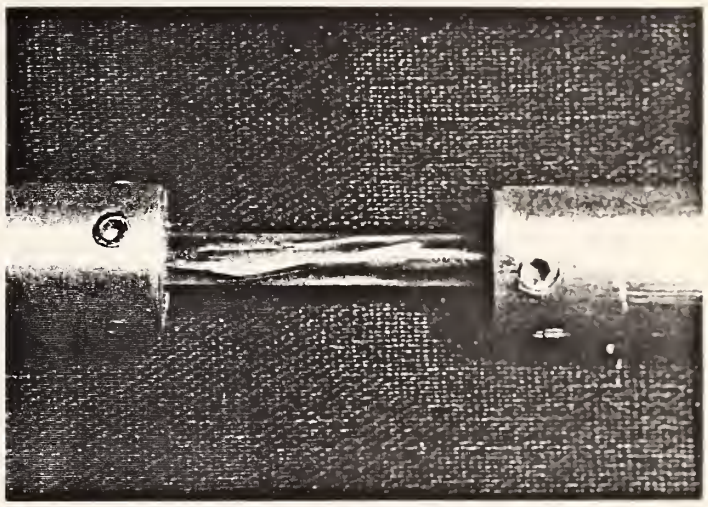

FIG. 4—*Gripping system for cryogenic torsional shear test.*

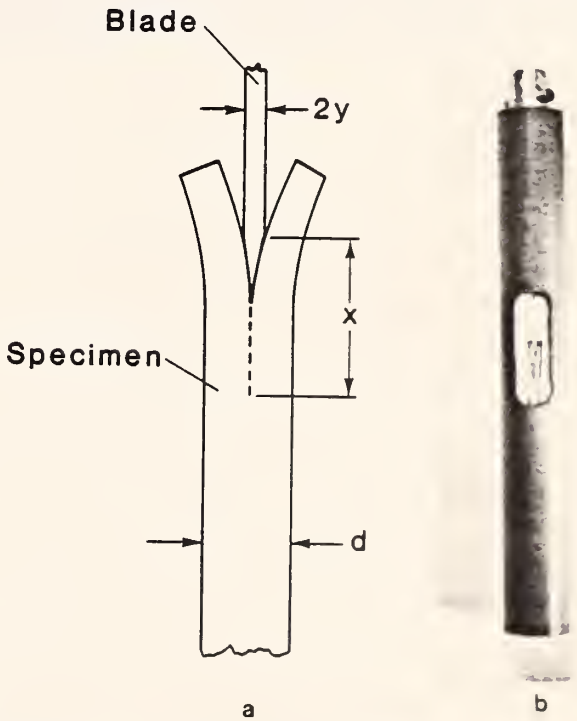

FIG. 5—*Test method for determining fracture energy G_{1c} on 3.2-mm diameter fiber-reinforced specimens.* (a) *Schematic of the geometry defining the terms in Eq 1. Blade thickness 2y was 0.635 mm (0.025 in.) in the present work.* (b) *Prototype fixture used for fracture energy tests. Pin in plunger restricts blade penetration to 4 mm.*

TABLE 3—*Fracture strength G_{1c} 48 V/O Type E glass (one specimen each).*

Resin System	*T*, K	*x*, mm	G_{1c}, kJ m^{-2}
DGEBA/FPA	76	6.0	2.09
DGEBA/DDS/BF_3MEA	76	9.0	0.41
DGEBA/AMD/POPA	76	8.5	0.52
DGEBA/AMD/POPA	295	6.5	1.52

3.2 kJ · m^{-2} values reported for the fracture energy of similar materials, as determined by the double cantilever beam method [*4*], suggesting that this may be a useful test. The direction and magnitude of the changes are also reasonable for the differing materials and test temperatures.

International Cooperation

Development of the described production method and test methodologies is currently being pursued by NBS, the Institute for Scientific and Industrial Research, Osaka University, Japan, and the Rutherford Appleton Laboratories in England. The Japanese group has successfully applied the technique to specimens reinforced with graphite, silicon carbide, and aluminum oxide fibers in addition to glass [*5, 6*]. The objective is to achieve a commonality in specimen configuration and testing procedure that will increase the effectiveness of technology transfer between laboratories having common research goals.

Acknowledgment

This work was sponsored by the Office of Fusion Energy, U.S. Department of Energy. The author acknowledges the assistance of P. T. Purtscher and R. Stoddard in specimen preparation and testing. The contribution of R. D. Kriz in deriving Eq 1 is particularly appreciated.

References

[*1*] Hodges, W. T. and St. Clair, T. L., "Ultrasonic Mixing of Epoxy Curing Agents," Technical Memorandum 85643, NASA Langley Research Center, Hampton, VA, 1983.

[*2*] Schramm, R. E. and Kasen, M. B., "Cryogenic Mechanical Properties of Boron-, Graphite-, and Glass-reinforced Composites", *Materials Science and Engineering*, Vol. 30, 1977, pp. 197-204.

[*3*] Obreimoff, J. W., "The Splitting Strength of Mica", *Proceedings of the Royal Society*, Vol. A127, 1930, pp. 290-297.

[*4*] Barlow, C. Y. and Windle, A. H., "Razor Blade Test for Composite Toughness," *Journal of Materials Science and Letters*, Vol. 4, 1985, pp. 233-234.

[*5*] Okada, T., Nishijima, S., Yamaoka, H., Miyata, K., Tsuchida, Y., Mizobuchi, K., Kuraoka, Y., and Namba, S., "Mechanical Properties of Unidirectionally Reinforced Materials," *Nonmetallic Materials and Composites at Low Temperatures—3*, G. Hartwig and D. Evans, Eds., Plenum Press, New York, in press.

[*6*] Takeno, M., Nishijima, S., Okada, T., Fujioka, K., Tsuchida, Y., and Kuraoka, Y., "Thermal and Mechanical Properties of Advanced Composite Materials," *Advances in Cryogenic Engineering (Materials)*, Vol. 32, Plenum Press, New York, 1986, pp. 217-224.

STRATEGY FOR THE DATA BASE CONSTRUCTION ON RADIATION-RESISTANT CRYOGENIC COMPOSITE INSULATORS FOR MAGNETIC FUSION ENERGY APPLICATIONS*

Maurice B. Kasen
Fracture and Deformation Division
National Bureau of Standards
Boulder, Colorado

A strategy is suggested for the development of fiber-reinforced, organic insulators to be used in superconducting magnets for magnetic fusion energy power systems. Two data bases are required. The first is a component data base providing information for basic material selection. The second is an engineering data base generated on insulators fabricated from the selected components. Successful completion of these tasks requires multidisciplinary expertise. Cooperative research is presently under way among laboratories in the United States, Japan, and England.

INTRODUCTION

The conversion of fusion energy to electrical power by magnetic confinement of the plasma will require the use of superconducting magnets. Such magnets must function without repair over the lifetime of the installation. The large magnet size will create substantial electromagnetically induced forces on the structural components. Furthermore, portions of the magnets will have to sustain an accumulated irradiation dose equivalent to 100 to 1000 MGy (MGy = 10^8 rads), if excessive shielding costs are to be avoided.[1] More than half the dose will come from neutrons.

Under these conditions, the performance of a number of magnet components, such as the superconducting elements and stabilizing materials, is uncertain. However, it appears likely that the permissible fluence will be primarily limited by radiation-induced degradation of the polymeric materials that conventionally serve as electrical and thermal insulators.[2] The use of inorganic insulators could alleviate this problem but they might be prohibitively expensive.

*Published in Proceedings, International Symposium on Fundamental Research Strategy in the Development of New Materials for Efficient Energy Conversion. Osaka, Japan: University of Osaka; 1986. pp. 112-118.

Therefore, it is necessary to define the radiation tolerance and potential insulation capabilities of organic materials and to develop the most promising materials. These organic insulators are unreinforced polymer films and sheets, potting compounds, and fiber-reinforced composite products. The fiber-reinforced insulators are particularly critical because they also serve as structural elements.

This document therefore addresses the strategy for efficient development of the fiber-reinforced insulating materials. Although the specific ideas expressed are those of the author, they reflect many discussions held with other individuals, especially with Prof. T. Okada and Dr. S. Nishijima, Institute of Industrial and Scientific Research (ISIR), Osaka University, Japan, and with Dr. David Evans, Rutherford Appleton Laboratory, England.

APPROACH TO THE PROBLEM

Successful development of fiber-reinforced composite materials for such demanding service requires knowledge of the intrinsic performance of the composite constituents under the prevailing environmental conditions. It is the basis for optimal selection of the individual components from which functional insulating materials are to be fabricated. It is also required for determining the parameters that must be controlled during fabrication to achieve minimal variability in performance. The characterization of practical insulating laminates produced with this component data base will provide the engineering data base required by magnet designers.

This effort requires the cooperation of individuals having expertise in polymer science and physics, composite material fabrication, cryogenic testing, and cryogenic radiation science. The fundamental strategy envisions close cooperation among laboratories having these areas of expertise. Laboratories in the United States (NBS, ORNL), in Japan (ISIR, Osaka University), and in England (Rutherford Appleton Laboratory) are presently cooperating in this effort.

THE COMPONENT DATA BASE

Establishing a component data base requires an extensive materials screening program, which must be carefully planned to avoid unnecessary effort and to minimize cost. A significant element in the strategy is to ensure maximum efficiency in technology transfer among laboratories cooperating in such research. The first step, a common approach to specimen design, has been completed.

Specimen Standardization

The many variables that need to be evaluated mandate that the studies be conducted with small, highly characterized, unreinforced resin and fiber-reinforced specimens that are easily produced and tested. Their fabrication process must be simple, inexpensive, and very flexible so that the parameters to be studied can be systematically altered. Machining of specimens,

which is expensive and introduces surface flaws, must be avoided. The configuration must not be susceptible to edge effects, which could invalidate test data; at the same time, the specimens must be suitable for testing in a variety of modes.

These considerations have led to international agreement that the optimum specimen configuration would be a rod approximately 3.2 mm in diameter, produced by a variation of the vacuum pultrusion process. Techniques for production of such specimens have been successfully developed in Japan,[3] England,[4] and the United States.[5] Typical specimens are shown in Fig. 1.

Mechanical Testing

Efficient test methods for use with this standard specimen design are under cooperative development. Emphasis is on mechanical property testing because it is commonly accepted that the dielectric strength of insulators is degraded only after the mechanical performance has been degraded.[6] Therefore, electrical insulating performance is not included in the component data base but it will be a part of the engineering data base.*

The specimens, cut to appropriate lengths, will be tested by a variety of methods. Flexural tests are traditional and easily performed. However, lack of symmetry introduces a complex and changing stress state throughout the test, making it difficult to quantify the results. The high failure strain of glass-reinforced specimens at cryogenic temperatures further complicates interpretation of the test data.[3,7] The short-beam shear test appears to be useful for rough screening of the integrity of the fiber-matrix interface, and this test method requires very little specimen material.[8] However, the data remain qualitative.

A cryogenic torsional shear test method developed at NBS may prove to be very useful in this program.[8,9] Figure 2(a) illustrates a typical torsional stress-strain curve obtained at 4 K on a glass-fiber-reinforced specimen. The test method generates quantitative information on the modulus, yield strength, and ultimate strength. Progressive damage accumulation is evidenced by successive load drops. Figure 2(b) illustrates the interfacial nature of the failure path. This is advantageous because available data suggest that degradation of this interface may be a dominant factor in overall mechanical property degradation during cryogenic irradiation.[10] The torsional test method has also been applied to unreinforced resin specimens at 4 K.

A test procedure for measuring the longitudinal fracture energy, G_{Ic}, of the fiber-reinforced rod specimens at cryogenic temperatures has also been developed at NBS.[5] As illustrated by Fig. 3(a), the method is very

*A three year research program on the dielectric strength of insulators at cryogenic temperatures will start at ISIR in 1986 as a program complementary to that discussed in this paper.

simple, requiring only measurement of the length of the crack that is produced by pressing a razor blade into the specimen end. The sensitivity of this method is illustrated in Fig. 3(b). With this test procedure, changes in the integrity of the fiber-matrix interface due to irradiation can be associated directly with a change in the fracture energy.

To obtain the maximum amount of information from a minimum number of specimens, NBS has developed a method for recovering the undamaged portions of the torsional test specimen after the test has been completed.[9] Each specimen end may then be subjected to a fracture strength test plus a short-beam shear test.

Failure Mode Characterization

Fractographic analysis by scanning electron microscopy contributes to an understanding of how radiation influences the failure mode. However, a full understanding of the radiation degradation process requires correlating the degradation in mechanical properties with specific damage induced on a molecular level. This will require cooperation of individuals skilled in the use of advanced analytical techniques in polymer chemistry and physics. The results will contribute much to basic polymer science and will provide a firm scientific basis for selecting polymer systems for additional study.

Component Parameters

Selection of matrix resin systems for this study should be made by individuals with a background in polymer chemistry and familiarity with the current state of knowledge about the influence of ionizing irradiation on polymer degradation. Several recent publications have addressed parameters that must be considered.[11-13]

The influence of resin chemistry must be carefully evaluated. Catalysts added to reduce processing time frequently contain boron compounds. It must be determined whether the resulting increase in neutron capture cross section contributes significantly to the level of degradation. The significance of trace metallic elements on resin performance should also be evaluated, and the influence of the resin cure state on resin degradation should be determined.

The type E glass fiber normally used in insulator construction contains 10 to 12% B_2O_3. It must be determined whether the higher neutron capture cross section of this type of fiber is sufficiently detrimental to warrant the additional expense of fabricating insulators with boron-free glass fiber. The radiation performance of specimens reinforced with new fibers, such as Al_2O_3 and SiC, should also be evaluated. This work has already begun at ISIR.[14]

Dependence of radiation resistance on fiber volume fraction must be studied to distinguish between the amount of damage sustained by the resin and by the resin-matrix interface. This information is needed to establish the optimum fiber content for maximum radiation resistance.

The high hydrogen content in the surface finishes normally applied to glass fibers to improve the fiber-matrix bond strength is expected to concentrate neutron-induced damage at the fiber interface.[1] This must be evaluated to determine whether control of the surface finish chemistry is necessary in fabricating functional insulating laminates.

Radiation Parameters

Selection of the irradiation conditions must be made by individuals having expertise in radiation science and knowledgeable about the anticipated environment in a fusion reactor. There must be access to a reactor capable of providing the required fluence and spectra at 4 K. The required radiation environment can be simulated to some extent in a fission reactor where neutron and gamma rays coexist. However, few fission reactors have facilities for irradiation at liquid helium temperature, and the available fluence is inadequate to provide the required dosage in a reasonable time.

Completion of the National Low Temperature Neutron Irradiation Facility (NLTNIF) facility at the Oak Ridge National Laboratory (ORNL) will provide the necessary irradiation environment for this work.[16] Scheduled to become operative in the summer of 1986, this facility will provide the required fluence level of about 10^{18} neutrons/cm^2 in a relatively short time as well as providing a relatively large irradiation volume.

The exact radiation spectra that will exist at the superconducting magnets in a functioning MFE system are not known. Therefore, it will be valuable to assess damage accumulation and property degradation as a function of a known change in radiation spectra. This can also be accomplished in the NLTNIF reactor.

Nevertheless, radiation research at 4 K is expensive and requires unique facilities. Therefore, the extent to which studies conducted at higher temperatures are relevant to 4-K performance should be determined.

Damage accumulated during irradiation at 4 K must be distinguished from that occurring due to the release of stored energy during warmup. This is important because the magnets will be periodically warmed up during their lifetime. In situ damage assessment will require development of techniques for testing either in the NLTNIF cryostat irradiation zone or in the test chamber located immediately above the irradiation zone. Alternatively, irradiated specimens could be transferred at 4 K from the NLTNIF facility to a remote test where they would then be transferred without warmup into the test apparatus. Neither task will be easily accomplished.

CURRENT PROGRAM STATUS

One hundred sixty-five specimens provided by NBS will be irradiated in the NLTNIF facility as soon as it becomes operative. These consist of unreinforced resin specimens and specimens reinforced with 48 volume percent of type E glass. One set of specimens duplicates the commercial G-11CR formulation to provide a baseline of performance against which the performance of the other materials can be compared. Another series of specimens

duplicates the G-11CR formulation except for the BF_3MEA accelerator. A third set was fabricated with an epoxy matrix typical of that which would be used for impregnation or potting purposes. A fourth set of specimens was fabricated with a state-of-the-art bismaleimide resin.

The specimens will be irradiated at ORNL to three increasing fluence levels at 4 K. The specimens will be warmed to room temperature and returned to NBS for 4-K testing. A duplicate set of unirradiated materials will also be tested at 4 K.

Following this initial test run, a second irradiation program will be undertaken with specimens provided by ISIR. NBS will submit these specimens to ORNL for irradiation, after which they will be returned to NBS for testing by visiting personnel from ISIR.

SUMMARY

The goal of developing functional organic insulators required by superconducting magnets in MFE reactors requires a systematic, interdisciplinary research program following a well-defined strategy. The initial objective is to develop a data base defining the optimum components for the required service. This data base can then be used in the design and fabrication of engineering laminates required for specific applications in magnet construction. The characterization of such laminates will provide an engineering data base for the designer. This document presents the elements of the strategy necessary to attain these goals.

The magnitude of the task at hand and recognition of the various disciplines required for its successful accomplishment has stimulated cooperation between laboratories in the United States, Japan, and England. Significant progress has already been made in standardizing test specimens and test methodology. Cooperation will soon extend to the irradiation programs.

ACKNOWLEDGMENT

The work at NBS is sponsored by the Division of Magnetic Fusion Energy, U.S. Department of Energy, Washington, D.C.

REFERENCES

1. G. F. Hurley and R. R. Coltman, Organic Materials for Fusion Reactor Applications, J. Nucl. Mater. 123 and 124: 1327-1337, 1984.

2. B. S. Brown, Radiation Effects in Superconducting Fusion-Magnet Materials, J. Nucl. Mater., 97: 1-14, 1981.

3. T. Okada, S. Nishijima, H. Yamaoka, K. Miyata, Y. Tsuchida, K. Mizobuchi, Y. Kuraoka, and S. Namba, Mechanical Properties of Unidirectionally Reinforced Materials, in "Nonmetallic Materials and Composites at Low Temperatures--3," G. Hartwig and D. Evans, eds, Plenum Press, New York (in press).

4. D. Evans, Rutherford Appleton Laboratories, Chilton, Didcot, Oxon, England (private communication, 1983).

5. M. B. Kasen, High Quality Organic Matrix Composite Specimens for Research Purposes, J. Compos. Technol. Res. (accepted for publication).

6. R. H. Kernohan, C. J. Long, and R. R. Coltman, Jr., Cryogenic Radiation Effects on Electrical Insulators, J. Nucl. Mater. 85 and 86: 379-383, 1979.

7. T. Okada, S. Nishijima, and H. Yamaoka, Radiation Damage of Composite Materials--Methods and Evaluation, in "Advances in Cryogenic Engineering--Materials," 32, R. P. Reed and A. F. Clark, eds., Plenum Press, New York, 1986, 145-151.

8. M. B. Kasen and R. B. Stoddard, Screening the Performance of Organic Insulators under Cryogenic Neutron Irradiation, in "Advances in Cryogenic Engineering--Materials," 32, R. P. Reed and A. F. Clark, eds., Plenum Press, New York, 1986, 153-159.

9. M. B. Kasen, Cryogenic Torsional Mechanical Test Apparatus, submitted for publication to Cryogenics.

10. H. W. Weber, Low Temperature Neutron and Gamma Irradiation of Glass Fiber Reinforced Epoxies, J. Nucl. Mater., 115: 11-15, 1983.

11. D. Evans and J. T. Morgan, A Review of the Effects of Ionizing Radiation on Plastic Materials at Low Temperatures, in "Advances in Cryogenic Engineering--Materials," 28, R. P. Reed and A. F. Clark, eds., Plenum Press, New York, 1982, 147-164.

12. H. M. Banford, Electrical Insulation and Fusion Reactors, in "Advances in Nuclear Science and Technology," 16: 1-73, J. Lewins and M. Becker, eds., Plenum Press, New York, 1984, 1-73.

13. W. Maurer, Neutron and Gamma Irradiation Effects on Organic Insulating Materials for Fusion Magnets, Report KFK 3974, Institut für Technische Physik, Kernforschungszentrum Karlsruhe, Germany, 1985.

14. M. Takeno, S. Nishijima, T. Okada, K. Fujioka, Y. Tsuchida, and Y. Kuraoka, Thermal and Mechanical Properties of Advanced Composite Materials at Low Temperature, in "Advances in Cryogenic Engineering--Materials," 32, R. P. Reed and A. F. Clark, eds., Plenum Press, New York, 1986, 217-224.

15. R. R. Coltman, Jr., C. E. Klabunde, and F. W. Young, Jr., A National Low Temperature Neutron Irradiation Facility, J. Nucl. Mater., 122 and 123: 1357-1358, 1984.

Fig. 1. Specimen rods, 3.2-mm diameter and 40-cm long, containing 48 volume percent type E glass in an epoxy matrix. Similar specimens are produced from unreinforced epoxy resin.

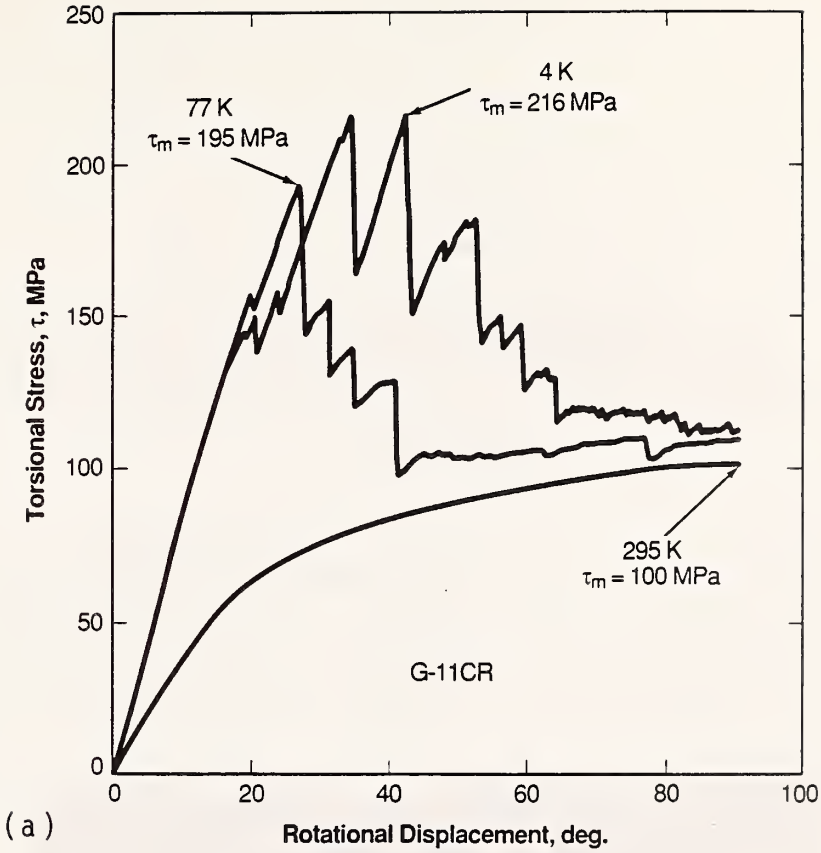

Fig. 2. (a) Typical torsional stress-strain curves for a glass-fiber-reinforced specimen obtained at 4, 77, and 295 K. (b) Cross section of the failed specimen illustrating the interfacial nature of the crack path.

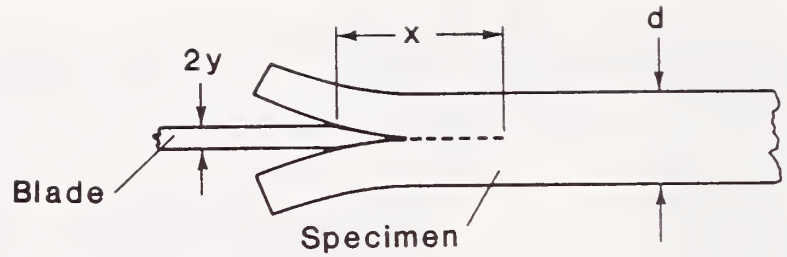

$$G_{Ic} = 0.01372 \frac{d^3 E y^2}{x^4}$$

(a)

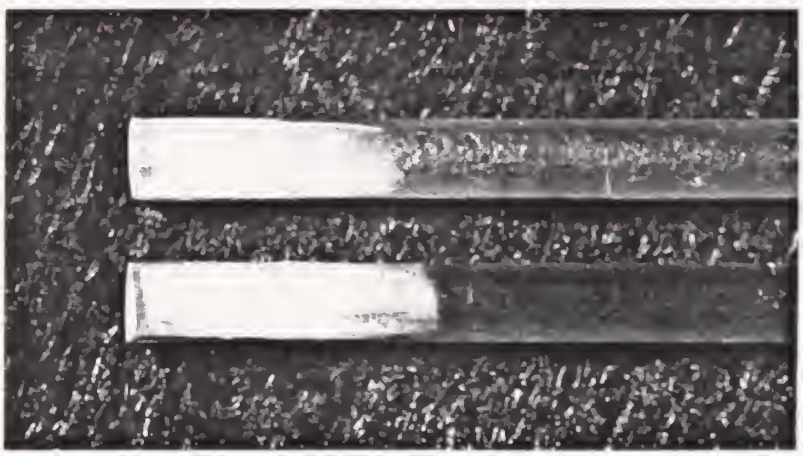

(b)

Fig. 3. (a) Method for determining the fracture energy, G_{Ic}, on 3.2-mm diameter, fiber-reinforced specimens. The equation was derived for the specific specimen configuration.[5] E = Young's modulus. (b) Difference in crack length observed at 295 K (upper specimen) and at 77 K (lower specimen). Their G_{Ic} values are 1.52 and 0.52 $kJ \cdot m^{-2}$, respectively.

TECHNOLOGY TRANSFER

TECHNOLOGY TRANSFER PROGRAM

LEADER: N. J. Simon
CONTRIBUTORS: L. Delgado, C. J. King, R. P. Reed

OBJECTIVES

- Organization of workshops to promote interaction between designers and material specialists, to discuss issues related to low-temperature material needs of the fusion energy program, and to present new low-temperature data for structural alloys, composites, and weldments
- Preparation of an annual report, as well as monthly highlight reports to the Office of Fusion Energy, U.S. Department of Energy
- Evaluation of low-temperature mechanical and physical properties of conductor and structural materials for cryogenic copper and superconducting magnets; preparation of handbook pages and supporting documentation; distribution of handbook pages to participants in the fusion energy program and to the "Materials Handbook for Fusion Energy Systems"

RESEARCH HIGHLIGHTS

- The Ninth Annual Cryogenic Structural Materials Workshop was organized; it was held October 6–8, 1986 in Reno, Nevada in conjunction with the United States–Japan Low Temperature Structural Materials and Standards Workshop on October 9–10.

- "Materials Studies for Magnetic Fusion Energy Applications-IX," (NBSIR 86-3050, 338 pages, 1986, editor R. P. Reed) was prepared, published, and distributed.

- Data were collected for handbook pages on C10100–C10700 copper and C17000–C17510 beryllium copper. Over one thousand documents (reports and journal articles) were acquired, coded for property information, and entered into a data base management system. Evaluation of documents pertaining to C10100–C10700 tensile, electromagnetic, creep, and fatigue properties has been completed.

- Handbook pages and supporting documentation covering tensile and electromagnetic properties of C10100–C10700 copper have been distributed. Cryogenic C10100–C10700 data on creep and fatigue were evaluated and reviewed together with tensile and electrical property data at the Ninth Annual Cryogenic Structural Materials Workshop.

NINTH ANNUAL

CRYOGENIC STRUCTURAL MATERIALS WORKSHOP

Airport Plaza Hotel
Reno, Nevada
October 6–8, 1986

This annual workshop provides an opportunity for discussion of problems, advances, and goals in the development of low-temperature materials for cryogenic and superconducting magnets for fusion energy systems. The 1986 workshop emphasized:

- Cryogenic properties of copper alloys and laminates pertaining to design requirements for the compact ignition tokamak (CIT)
- Identification of materials needs for future magnet systems
- New low-temperature materials developments in the United States and Japan and international research cooperation

9th annual
Cryogenic Structural Materials Workshop
Program

MONDAY, OCTOBER 6

8:30 a.m.	Introductions	R. P. Reed, NBS, and V. Der, OFE
	COMPACT IGNITION TOKAMAKS	
8:45 a.m.	Toroidal Field Coil Design	J. Citrolo, PPPL
9:30 a.m.	Design of Alcator C-Mod	H. Becker, MIT
10:00 a.m.	Copper Alloy and Composite Properties	
	Review	N. J. Simon, NBS
	Mechanical Properties of Copper	L. L. Summers, LLNL
	Mechanical and Physical Properties of Copper Alloys	R. P. Reed, NBS
	Composite Properties	H. Becker, MIT
	Laminate Data	L. L. Scull, NBS
12:15 p.m.	Lunch	
1:30 p.m.	Discussion of Structural Alloy Research Needs for Compact Ignition Tokamaks	
	NONMETALLIC STRUCTURAL COMPOSITES	
2:30 p.m.	Edge Stresses in Woven Laminates	R. D. Kriz, NBS
3:00 p.m.	Characterization of Cryogenic Composite Materials	M. K. Abdelsalam, U. Wisconsin
3:30 p.m.	Cryogenic Nonmetallic Composite Research at ISIR	S. Nishijima, Osaka U.
4:00 p.m.	Composite Test Method Development	M. B. Kasen, NBS
4:30 p.m.	Low Temperature Irradiation Facility	H. R. Kerchner, ORNL

TUESDAY, OCTOBER 7

LARGE-SCALE TOKAMAK AND MIRROR FUSION ENERGY DEVICES: DESIGN AND MATERIALS

9:00 a.m.	Advanced Magnet Designs and Materials Problems	J. R. Miller, LLNL
9:45 a.m.	NET Plans and Related Materials Research	A. Nyilas, KFK
10:30 a.m.	LCP Experiments	T. McManus, ORNL
11:00 a.m.	Material Selections for the SSC	T. H. Nicol, Fermilab
11:30 a.m.	Activation of Structural Alloys in Fusion Reactor Magnets	F. M. Mann, Westinghouse Hanford

TUESDAY, OCTOBER 7, continued

12:00 m.	Lunch	
2:00 p.m.	Modification of 316LN-Type Alloys	P. T. Purtscher, NBS
2:30 p.m.	Design of 316LN-Type Alloys	N. J. Simon, NBS
3:00 p.m.	Sources of Intergranular Embrittlement in Fe-Mn Alloys	M. Strum, LBL
3:30 p.m.	Low-Coefficient-of-Expansion Structural Materials Development for Conductor Applications	R. Ballinger, MIT
4:00 p.m.	Preliminary Test Results of Magnetic Field Effects on Fracture Toughness	H. Takahashi and T. Shoji, Tohoku U.
4:30 p.m.	Mechanical Properties of Al-Li 2090-T8	A. Sunwoo, LBL
6:00 p.m.	Reception	

WEDNESDAY, OCTOBER 8

LARGE-SCALE TOKAMAK AND MIRROR FUSION ENERGY DEVICES:
MATERIALS AND WELDING

8:30 a.m.	Effects of Strain Rate on Mechanical Properties of Austenitic Stainless Steels at 4 K	Y. Kohsaka, NKK
9:00 a.m.	The Effect of Inclusions and Nickel on Weld Toughness and Fracture Appearance	T. A. Siewert, NBS
9:30 a.m.	High Compliance Fracture Toughness Test at 4 K for 310S Stainless Steel and Its Weldments	H. Takahashi, Tohoku U.
10:00 a.m.	Welding of Austenitic Manganese Steels	J. W. Chan, LBL
10:30 a.m.	Manganese, Molybdenum, and Nitrogen in Stainless Steel SMA Welds	C. N. McCowan, NBS
11:00 a.m.	Mechanical Properties of Welded Joints of Newly Developed Stainless Steel	K. Yoshida, JAERI
11:30 a.m.	Extension of Mechanical Property Test Standards of Metals and Composites to Liquid Helium Temperature	B. M. Strauss, Teledyne Eng.
12:00 m.	Discussion of Structural Alloy Research Needs for Large Superconducting Magnets	

THURSDAY and FRIDAY, OCTOBER 9 and 10

UNITED STATES–JAPAN WORKSHOP
on
Low Temperature Structural Materials and Standards

NINTH ANNUAL CRYOGENIC STRUCTURAL MATERIALS WORKSHOP

SUMMARY OF TECHNICAL PRESENTATIONS

SESSION I. COMPACT IGNITION TOKAMAKS

Because of the planned construction of an intermediate ignition fusion reactor with copper or copper alloy coils operating at 77 K, the workshop this year opened with a session on design requirements and properties of copper and copper alloys. J. Citrolo (PPPL) reviewed the design features of the Compact Ignition Tokamak (CIT) toroidal field coils that will attain a field of 16 T. Since operating stresses in the copper are expected to be ~490 MPa (70 ksi), considerably above the yield strength of the cold-worked C10700 copper conductor, a current design places the conductor between Inconel 718 plates, to which it will be explosively bonded. Design requirements of another compact copper-coil device, the Alcator C-Mod, were discussed by H. Becker (MIT). This machine will be held together by vertical tie rods (nonwelded), between 316L and 316LN cover plates; it will experience 50,000 pulse cycles over its expected period of operation. Therefore, the device is being designed to meet fatigue criteria, and provisions for periodic inspection will be included in the design. (The CIT is designed for only 3000 pulses.) Following a discussion of design requirements for these copper machines, a review of the C10100–C10700 copper data base was presented by N.J. Simon of NBS. One important conclusion of the review is that long-term creep data at room temperature and below are not available. L. L. Summers (LLNL) reviewed results of a copper alloy testing program in which the C10400, C15500, and C17510 alloys were evaluated. A significant result is that at room temperature, the magnitude of the C15500 ultimate tensile strength approaches that of the yield strength, which results in less safety margin than is usually provided when the design allowable stresses are set as a fraction of yield strength. Results of extensive testing of C10400, C15500, and C17510 in the annealed, half-hard, and hard conditions were presented by R. P. Reed (NBS). Both yield and tensile strength were found to increase significantly below room temperature for material in the hard condition. Tensile test results, measurements of the electrical resistivity as a function of temperature, and the time-dependent properties (creep, fatigue, and fatigue–creep) at 77 K and ambient temperature were presented. The session continued with reports by H. Becker (MIT) and L. Scull (NBS) on the testing of laminated copper. Under compression loading, copper extruded from the Inconel–C10200 laminates tested at MIT. For the roll-bonded copper–stainless steel (Fe–18Cr–13Mn–3Ni) laminates tested at NBS, reasonable agreement was found between the measurements of yield strength and Young's modulus and predictions based on mixture rules and copper and stainless steel properties.

A discussion session on materials requirements for compact ignition tokamaks followed. Reasons for the selection of a laminate reinforcement to compensate for the inadequate yield strength of half-hard C10700 copper were discussed. Since other high-conductivity copper alloys approach the

required strengths, other considerations, such as thermal conductivity, entered into the selection process in which a complex computer code was utilized. Further discussion indicated some uncertainty over the amount of cold work that 19-mm (3/4-in) thick C10700 plate could be subjected to. The planned test matrix for the laminate material was outlined by G. Brown (PPPL). Since the matrix is extensive, and therefore it will be expensive, comments were solicited from representatives of the various national laboratories.

SESSION II. NONMETALLIC STRUCTURAL COMPOSITES

New results from modeling studies of woven glass–epoxy laminates such as G-10CR and G-11CR were presented by R. D. Kriz (NBS). Finite-element results demonstrated that the weave geometry reduces edge stresses at low temperatures, in accord with previous experimental results that showed that most of the damage occurs in the interior of these laminates. M. K. Abdelsalam (University of Wisconsin) presented an overview of property measurements on several different load-bearing thermal insulators to be used in compression. Thermal conductivity, fracture, and fatigue studies were discussed. The extensive facilities of the Institute of Scientific Industrial Research (ISIR) at Osaka University, Japan, were described by S. Nishijima. Their facilities are capable of conducting flexural, tensile, compressive, impact, creep, thermal, electrical, and radiation tests at cryogenic temperatures. An adhesive bonding method for producing composite cryostats of complicated shape has been developed. M. B. Kasen (NBS) described the development of well-characterized small specimens for a screening program that will include the effects of low-temperature irradiation. The National Low-Temperature Neutron Irradiation Facility (NLTNIF) in which these specimens will be irradiated was described by H. R. Kerchner (ORNL). Specimens can be neutron irradiated at 3.2 K in a 12-T field and tested without warmup.

SESSION III. LARGE-SCALE TOKAMAK AND MIRROR FUSION ENERGY DEVICES: DESIGN AND MATERIALS

An overview of the superconducting magnet development program at LLNL was presented by L. L. Summers. Expected future use of an advanced superconductor, NbN, for which J_c is much less sensitive to degradation from strain or irradiation than that of Nb_3Sn and NbTi superconductors in current use, is now driving some of the materials selection processes. The TIBER II steady-state ignition tokamak, a very compact machine with a high radiation fluence and very high stress levels, also places increased requirements on materials. However, 316LN may fulfill magnet case requirements. The effects of thermomechanical processing schedules on conduit alloys for a superconducting cable-in-conduit magnet configuration were also discussed.

Plans for the NET (Next European Torus) were presented by A. Nyilas (KFK). This machine will be intermediate between the existing JET (Joint European Torus) and the larger DEMO. NET will burn deuterium and so provide

materials testing in a reactor environment and also a test of tritium handling capabilities. Laser welding will be used for the superconducting coil conduit in NET. A program was described for scaling up tests on small specimens so that stresses in complicated geometries can be identified. Again, 316LN is the chief structural material under consideration, which reinforces the relevance of recent NBS fundamental studies of this alloy.

T. McManus (ORNL) described recent testing of the General Dynamics, General Electric, and Westinghouse superconducting magnets for the Large Coil Project (LCP), a collaborative effort between the United States, Europe, and Japan. Six separate D-coils have been provided for testing. The GD and GE coils use helium pool boiling: both showed degraded heat transfer during quench testing, which is believed to be due to vapor accumulation. The Westinghouse coil showed a significant reduction of critical current that was assumed to be due to straining of the Nb_3Sn conductor during fabrication. In spite of these imperfections, the overall results of the LCP are encouraging,since all magnets were successfully tested as single coils with peak fields near 6 T.

The focus changed with a presentation by T. H. Nicol (Fermilab) on materials selection considerations for the Superconducting Super Collider (SSC). This facility, although not a fusion device, will have about ten thousand superconducting magnets in an underground tunnel about one hundred kilometers in diameter. Design considerations are based on the successful Tevatron built by Fermilab, another large-scale device with more than one thousand superconducting magnets and similar refrigeration requirements. To keep operational costs low, the SSC will have a relatively small refrigeration load for a device of its size. A key feature of the SSC is a support post of reinforced composite designed to minimize the heat leak. Reliable information on low-temperature reinforced composite properties is, therefore, an important consideration.

F. W. Mann (HEDL) discussed the use of the existing Starfire conceptual design code to determine neutron flux and to predict transmutation activation for a series of representative alloy compositions supplied by NBS. The neutron flux spectrum at the magnet was found to be relatively soft; thus, the conclusion was that there should be no significant activation problems regarding short-term maintenance or long-term disposal requirements. However, T. Okada (Osaka University) reached the opposite conclusion with the assumption of 10% hard (14 MeV) neutrons in the spectra. Thus, the activation problems would be similar to the first-wall conditions, where Ni and Fe transmute to radioisotopes of long half-life. After the workshop, F. W. Mann and D. G. Doran reexamined some of their assumptions in this calculation; we recently learned that their final results are in closer agreement with the results of Okada.

The effect of Mo additions on 316LN-type alloys was discussed by P. T. Purtscher (NBS). Additions of Mo increase 4-K yield strength more than additions of Ni, but Mo decreases the 4-K fracture toughness. Thus the quality index (QI), the product of yield strength and fracture toughness, is not changed appreciably. In contrast, additions of Ni improve the fracture

toughness and also the QI because yield strength is not strongly affected. N. J. Simon (NBS) also discussed 316LN alloy modification by presenting predictive equations that quantify the effects of Ni, yield strength, and inclusion spacing upon the 4-K fracture toughness. The work described is an extension of the well-established inverse dependence of fracture toughness upon yield strength. Studies of low-temperature intergranular fracture in binary Fe–Mn alloys were presented by M. Strum (LBL). Although this type of fracture is usually attributed to formation of brittle grain-boundary phases of grain-boundary precipitation, the work showed that low grain-boundary cohesion and heterogeneous slip distribution were more plausible explanations.

Improvement of Incaloy 905 by chemistry modification was described by R. Ballinger (MIT). This alloy has a low coefficient of thermal expansion that enables it to be used as a conductor sheath with Nb_3Sn, a strain-sensitive superconductor. Improvements in microstructural stability enable the modified 905 alloy to withstand the high-temperature, long-duration thermal processing of the superconductor. However, as A. Nyilas (KFK) indicated, in some designs of cable in conduit magnets long sections may be laser-welded and the conductor may even be added after it has been thermally processed.

A study of micromechanical aspects of fracture at 4 K using acoustic emission techniques was presented by H. Takahashi (Tohoku University). Significant levels of acoustic emission were observed during fracture tests of three different alloys systems. Internal temperature rises of up to 53 K were reported during discontinuous yielding. The session ended with a report on a new Al–Li alloy, 2090-T8, by A. Sunwoo (LBL). This alloy is important because, unlike more common Al alloys, its fracture toughness increases with decreasing temperature. Progress in welding this alloy was described.

SESSION IV. LARGE-SCALE TOKAMAK AND MIRROR FUSION ENERGY DEVICES: MATERIALS AND WELDING

Y. Kohsaka (Nippon Kokan K.K.) presented results that showed a change in the number of serrations (per unit strain) in the stress-strain curves of 22Mn–13Cr–7.5Ni steel with an increase in the strain rate of the test. (Discontinuous plastic, or serrated, flow is observed in tensile testing at 4 K when localized adiabatic heating results from a very low specific heat.) Measured tensile and yield strengths also were affected by strain rate. Strain rates below 4×10^{-3} s^{-1} did not decrease the measured strengths.

Previous talks by P. T. Purtscher and N. J. Simon had presented the quantitative effects of Ni and inclusion spacing upon fracture toughness of 316 LN austenitic base alloys at 4 K. T. A. Siewert (NBS) extended this work to 4-K weld data, showing that equations with similar coefficients apply to the weld data and that a variation in the equation improved the overall fit. Fracture surface dimple density was also correlated with Charpy V-notch absorbed energy and inclusion spacing.

H. Takahashi (Tohoku University) reported results of fracture toughness testing on 310S and its weldment with and without a high-compliance loading system. The instability point tended to move close to the maximum load when a high-compliance spring was used to connect the specimen to the tensile machine. The 4-K serrations in the stress–strain curve were strongly dependent upon the spring constants.

J. W. Chan (LBL) presented results of gas-tungsten-arc and autogenous electron-beam welds on a high-manganese alloy, 18Mn-16Cr-5Ni-0.22N. Strength–toughness combinations at 4 K were lower than that of the base metal, owing in part to volatilization of interstitial nitrogen in the fusion zone. Alloying additions of N, Ni, and Mo improved the properties. C. McCowan (NBS) discussed tests on weld metals of varying Mn, Mo, and N compositions to determine the effects of these alloying additions on 4-K yield strength and 77-K Charpy lateral expansion. The 4-K mechanical properties of several of the new austenitic steels developed in Japan under the auspices of the Japan Atomic Energy Research Institute (JAERI) were discussed by K. Yoshida. Some thick-plate weld results matched the base-plate results well, with fracture toughness [$K_{Ic}(J)$] equal to 200 MPa$\sqrt{m}$. A status report on the Demonstration Poloidal Coil (DPC), a cable-in-conduit design, was also presented.

B. Strauss (Teledyne Engineering Services) described some of the problems with testing methodology at cryogenic temperatures that will be investigated in a project sponsored by the Material Properties Council. Problems, such as adiabatic heating, that affect allowable strain rates will be addressed for both metals and composites.

A discussion of research needs for superconducting magnets concluded this session. An scheme for optimizing both the interlaminar shear strength (or some other fracture parameter) and the allowable radiation dose for composites, analogous to the quality index (QI) for alloys and weldments, was discussed. Returning to consideration of alloys, V. Der (OFE) presented some problems involved in converting data to design allowables. For example, an allowable stress level of 1/2 σ_u does not provide the usual safety margin if σ_y and σ_u are quite close, as is the case for some new alloys and for cold-worked copper. The different approaches taken in different countries to resolve conductor sheath problems were also discussed. The United States has invested in modifying and testing alloys to determine compatibility with high-temperature superconductor processing and thermal contraction, whereas the European NET project hopes to solve this problem by design strategies. Problems of testing thin plates were also considered.

UNITED STATES - JAPAN COOPERATIVE PROGRAM

UNITED STATES-JAPAN COOPERATIVE PROGRAM

PRINCIPAL INVESTIGATOR: R. L. Tobler

CONTRIBUTING ORGANIZATIONS: National Bureau of Standards,
Tohoku University,
Japan Atomic Energy Research Institute,
Kobe Steel,
National Research Institute for Metals

OBJECTIVES

- Preparation of a draft standard for tensile testing of structural alloys at 4 K
- Preparation of a draft standard for fracture testing at 4 K
- Administration of a round-robin test program to support the standards development
- Administration of a one-year research program to evaluate critical aspects of test standardization at 4 K
- Revision of the draft standards to include results of the one-year research program

PROGRAM HIGHLIGHTS

- Cryogenic materials scientists were interviewed at government, industrial, and academic institutions in Japan. Their experience and advice was helpful in preparing the drafts of the test procedure standards.

- Three drafts of a proposed standard 4-K tensile test procedure were written and submitted for review at Japanese domestic and United States-Japan workshops. The fourth revision is now approved and has been submitted to the American Society for Testing and Materials.

- Three drafts of a proposed standard for 4-K fracture toughness testing were written and reviewed at Japanese domestic workshops. The fourth revision is ready for international review.

- Round-robin tensile and fracture tests were conducted on a Fe-13Cr-22Mn alloy. A summary of results is scheduled for presentation at the 1987 International Cryogenic Materials Conference (ICMC) and will be submitted for publication in the proceedings.

- An experimental research program was completed by participants at NBS and four Japanese laboratories. From 70 J_{Ic} fracture toughness tests, the effects of specimen size, side grooves, test speed, and fatigue cracking on the test procedure were determined. Five papers containing the results will be presented at the 1987 ICMC and submitted for publication in the proceedings.

- New methods of fracture characterization were explored, including the use of acoustic emission and key-curve analysis for fracture toughness determination. The advantages and disadvantages of these methodologies are summarized in two of the research papers that will be submitted to ICMC.

- Four workshops were an integral part of the program:

  Standardization of Fracture Toughness Testing of Low-Temperature Structural Materials at Tohoku University, Sendai, Japan in March 1986

  Low-Temperature Structural Materials and Standards at Japan Atomic Energy Research Institute in Tokai-mura, Japan in August 1986

  DOE–JAERI Low Temperature Structural Materials and Standards Workshop in Reno, Nevada in October 1986

  United States–Japan Cooperative Research Program Review at Tohoku University in January 1987

UNITED STATES–JAPAN

LOW-TEMPERATURE STRUCTURAL MATERIALS AND STANDARDS WORKSHOP

Airport Plaza Hotel
Reno, Nevada
October 9–10, 1986

The results of the United States–Japan collaboration on structural materials development and test-method standardization were presented and discussed at this meeting of program participants. Research goals to be accomplished before the next meeting, at the Japan Atomic Energy Research Institute in 1988, were formalized.

UNITED STATES–JAPAN

LOW TEMPERATURE STRUCTURAL MATERIALS AND STANDARDS WORKSHOP

Airport Plaza Hotel
Reno, Nevada
October 9–10, 1986

PROGRAM

October 9

SESSION I. OVERVIEW

9:00 – 10:30 a.m. V. K. Der (DOE) and S. Shimamoto (JAERI), cochairpersons

A. Introduction and Welcome

B. JAERI Program Overview,
S. Shimamoto and K. Yoshida

C. DOE Program Overview,
V. K. Der

D. NBS Program Overview,
R. P. Reed

SESSION II. TESTING

11:00 a.m. – 12:10 p.m. T. A. Siewert (NBS) and K. Ishikawa (NRIM), cochairpersons

A. Fracture, Adiabatic Heating, and Acoustic Emission of Austenitic Stainless Steels at Liquid Helium Temperature,
H. Takahashi and T. Shoji (Tohoku University)

B. Dynamic Yield Stress and Fracture Toughness of Some Materials at Low Temperature,
K. Kishida, T. Kataoka, and M. Nakano (Osaka University)

C. Evaluation of Tensile and Fracture Properties of Austenitic Iron Alloys in Liquid Helium,
K. Ishikawa, T. Ogata, T. Yuri, and K. Nagai (NRIM)

D. Construction of 100 Ton Cryogenic Testing Machine and Test Results of Newly Developed Stainless Steels with This Machine at 4 K,
S. Shimamoto, H. Nakajima, K. Yoshida, and M. Oshikiri (JAERI)

SESSION II. TESTING, continued

1:30 – 2:30 p.m.

E. Strategy for the Development of the Data Base for the Radiation-Resistant Superconductive Magnet Materials,
T. Okada and S. Nishijima (Osaka University)

F. Research on Development of Low Temperature Test Standards and Property Measurements,
R. P. Reed (NBS)

G. Standardizing Nonmetallic Composite Materials for Cryogenic Applications,
M. B. Kasen (NBS)

SESSION III. MATERIALS

2:30 – 5:30 p.m. L. T. Summers (LLNL) and T. Okada (Osaka University), Cochairpersons

A. Fatigue Properties of 22Mn Steel in Cryogenic Temperature,
M. Shimada, S. Tone, T. Mizoguchi, and T. Horiuchi (Kobe Steel)

B. Low Temperature Mechanical Properties of 12Cr–12Ni–10Mn–5Mo Steel and its Weld,
R. Miura and J. Ishizaka (Japan Steel Works)

C. Change in the Cryogenic Properties of the Welded Joint of V-bearing Austenitic Stainless with Nb_3Sn Precipitation Heat Treatment,
K. Nohara (Kawasaki Steel)

D. Mechanical Properties of Welded Joints in Austenitic Stainless Steels at 4 K,
C. Ouchi and K. Kohsaka (Nippon Kokan K.K.)

E. Mechanical Properties of Fully Austenitic Weld Deposits for Cryogenic Structure,
T. Matsumoto (Hitachi)

F. Research on Structural Steels for High-Field Superconducting Magnets,
J. W. Morris, Jr. (LBL)

G. SMA and FCAW Compositions for Magnetic Fusion Superconducting Magnet Cases,
D. J. Kotecki (Teledyne McKay)

H. A Fully Austenitic Stainless Steel Weldment for Cryogenic Service,
F. S. Babish (Sandvik) and T. A. Siewert (NBS)

October 10

SESSION IV. DESIGN EXPERIENCE AND STANDARDS

9:00 – 10:00 a.m. H. Becker (MIT) and K. Yoshida (JAERI), cochairpersons

A. Mechanical Design Guideline of the Superconducting Coils for the Fusion,
K. Yoshida, K. Koizumi, H. Nakajima, and S. Shimamoto (JAERI)

B. Thoughts on Structural Design Standards for Magnet Casings,
H. Becker (MIT)

C. MFTF-B: Experience with Structural Materials and Operating Stresses,
E. N. C. Dalder, J. O. Myall, R. M. Scanlon, and J. P. Zbasnik (LLNL)

SESSION V. OPEN DISCUSSION: JOINT DEVELOPMENT OF TESTING STANDARDS

10:20 a.m. – 12;40 p.m.

A. Progress Towards 4-K Tensile and Fracture Toughness Testing Standardization,
H. Takahashi, T. Shoji, and R. L. Tobler (Tohoku University and NBS)

B. Round-Robin Test Results for Tensile and Fracture Toughness Testing Standardization,
H. Takahashi, K. Ishikawa, M. Shimada, T. Matsumoto, S. Shimamoto, and H. Nakajima (Tohoku Univesity, NRIM, Kobe Steel, Hitachi, and JAERI)

C. Evaluation of Low Temperature Mechanical Properties of Fe–22Mn–13Cr–5Ni Austenitic Steel,
L. Summers (LLNL)

D. Round Robin Test Results on 316LN Stainless Steels in the United States.
P. T. Purtscher (NBS)

12:40 p.m. SESSION VI. SUMMARY

UNITED STATES–JAPAN

LOW-TEMPERATURE STRUCTURAL MATERIALS AND STANDARDS WORKSHOP

SUMMARY OF TECHNICAL PRESENTATIONS

SESSION I. OVERVIEW SESSION

S. Shimamoto presented an overview of the Japan Atomic Energy Research Institute (JAERI) program on developing new cryogenic structural steels in collaboration with Japanese steel companies. Electron-beam and gas-tungsten-arc welding of thick plate is progressing, with expectations that 90% of the base metal properties will be retained and that the K_{Ic} fracture toughness values of the weldments at 4 K will be 200 MPa$\sqrt{m}$. Nine organizations in Japan are capable of cryogenic K_{Ic} measurements, and round-robin testing has begun. R. L. Tobler (NBS) is helping to standardize cryogenic test procedures. Construction of the Fusion Experimental Reactor (FER) is expected to start in 1992. Meanwhile, experience is being acquired in the Demonstration Poloidal Coils (DPC) program, where both Nb-Ti and Nb_3Sn will be used as conductor materials.

V. Der (OFE) described current structural alloy research at NBS, LLNL, LBL, and MIT, summarizing many of the details reported on in the preceding Cryogenic Structural Materials Workshop). Test methods and standards development were described for both alloys and nonmetallics. Progress in round-robin measurements was noted, as were exchanges of personnel and information. Additional work and collaboration is needed in the development of design guidelines and standards.

The low-temperature structural materials research at NBS was reviewed by R. P. Reed. Study of 316LN-based alloys from a number of sources led to predictive equations for their 4-K yield strength and fracture toughness, indicating that the U.S. goals for these properties can be met through control of chemistry, grain size, and inclusion spacing. Weldment properties are still challenging. Progress in the development of standard nonmetallic specimens and test methods was described.

SESSION II. TESTING SESSION

H. Takahashi (Tohoku University) discussed a key-curve method of fracture toughness measurements, a simpler and cheaper method of 4-K fracture toughness evaluation. Success of this method depends upon the existence of a correlation between J_{Ic} and the slope dJ/da for the alloys of interest. Further evaluation is required. Strain rate effects on fracture toughness and yield strength measurements were presented by K. Kishida (Osaka University). In the static limit, the curve of K_{Ic} versus temperature falls above the dynamic testing results. K. Yoshida (JAERI) presented results of studies on specimen size effects on tensile properties. No effect was found for diameter variations from 24 to 7 mm. Work on K_{Ic} specimen size effects will be carried out this fall in collaboration with R. L. Tobler.

A newly constructed 1000-kN cryogenic testing machine will be used in this work.

The problem of radiation degradation and radioactivation of magnet alloys was addressed by T. Okada (Osaka University). The results given for the time for radiation to subside to acceptable levels for maintenance operations differed from those presented by F. Mann earlier in the Cryogenic Structural Materials Workshop. This difference is due to the different radiation energy spectra assumed in the two calculations. Mann used the Starfire configuration, which assumed a soft spectrum at the magnet. Okada used a spectrum that assumed 10% hard (14 MEV) neutrons so that problems with Ni and Fe activation were similar to those encountered at the first wall; his calculation used a flux of $\sim 10^{10} n/cm^2 s$. The Starfire-based calculation has since been revised (see discussion in section III of the Ninth Annual Cryogenic Structural Materials Workshop Summary.)

R. P. Reed (NBS) discussed strain-rate effects on measured tensile properties of alloys at 4 K. Effects on flow strength were minimal at 4 K. In discontinuous yielding, the measured specimen temperature rise (ΔT) of about 50 K for 304L at 4 K was consistent with results of a model in which no heat was conducted away from the deformed region (adiabatic heating). Calculations for 316LN tests at 4 K showed that the observed temperature rise with strain rate increase coincided with the transition from nucleate to film boiling heat transfer in the liquid helium, which results in an increased ΔT between the solid and liquid.

M. B. Kasen (NBS) discussed a coding scheme for identifying composite materials in a standardized manner. This would allow for nonmetallic specification in the way that the AISI specifications for stainless steel identify those materials. Such a system has not been available for nonmetallics.

SESSION III. MATERIALS SESSION

Fatigue tests on 22Mn steel at 4 K were reported by M. Shimada (Kobe Steel). Surface temperature rise was studied as a function of stress and frequency. Serrated yield was reported as a function of strain rate and compared with that of 304LN. Strain- and stress-controlled fatigue life, fatigue crack growth data, and threshold fatigue data were reported.

Mechanical properties of 12Cr-12Ni-10Mn-5Mo steel and weldments were reported by R. Miura (Japan Steel Works). Electroslag remelted base material and GTA weldments exceeded the minimum JAERI criteria for yield strength and toughness. A new 316-type austenitic stainless steel with low-C, high-N, and V additions was found to retain favorable 4-K properties after the type of heat treatment required by the Nb_3Sn superconductor. This work at the Kawasaki Steel Corporation was described by K. Nohara. Plate was prepared by vacuum induction melting and EB welding was utilized. The gas-tungsten-arc and electron-beam welding of Mn-Cr and Ni-Cr austenitic stainless steels that met the JAERI criteria was reported by Y. Kohsaka (Nippon Kokan K.K). Satisfactory 4-K test results were obtained. Fully

austenitic weld deposits were studied by T. Matsumoto of Hitachi. Effects of Mo, C, and C+N on fracture toughness were reported. No delta ferrite was found in the weld microstructure, magnetic permeability was not significantly larger than for base material, and microfissuring was not observed.

J. W. Morris (LBL) reported results of fundamental studies on fracture mechanisms that could explain the favorable trend of fracture toughness of aluminum alloy 2090 as temperature is decreased. As the temperature decreases, the fracture mode does not change, but elongation increases because $d\sigma/d\epsilon$ increases.

D. J. Kotecki (Teledyne McKay) described welding filler metal development work for the fabrication of MFTF-B at LLNL. Lateral expansion was improved for compositions to the left of the 0 ferrite number line on the DeLong diagram, and this criteria proved suitable for the selection of filler material for flat welding positions. However, a ferrite number of 3 was necessary for vertical-up position welding. Satisfactory K_{Ic} properties were obtained with this composition change.

Yield strength and $K_{Ic}(J)$ at 4 K for 18Cr-20Ni-5Mn-0.16N austenitic weld metal were reported by T. A. Siewert (NBS). The properties obtained from a GMA weld process were comparable to base metal properties, and SEM analysis showed ductile failure by microvoid coalescence.

SESSION IV. DESIGN EXPERIENCE AND STANDARDS SESSION

A document setting forth mechanical design guidelines for superconducting magnets for a tokamak fusion machine was discussed by K. Yoshida (JAERI). Tests are required for each production batch of alloys and nonmetallics because the existing data base is not sufficient. Design allowables, fabrication, and inspection are also covered. The guideline is based on the 1986 ASME Boiler and Pressure Vessel Code. Yoshida concluded that it was impractical at present to use high-performance cryogenic steels in a tokamak machine, and that use of these new steels to improve current density would be the most effective application.

H. Becker (MIT) presented a draft "Structural Design Basis." This document suggests that since it may be impossible to eliminate all cracks or the possibility of crack initiation, it may be necessary to assume crack existence as a basis for design and to provide for remotely controlled inspection during service.

J. Zbasnik (LLNL) described MFTF-B experience with structural materials and operational stresses. Cryogenic testing of the 304LN production plate was required. Tensile properties usually exceeded the specifications. Properties of the qualified welding electrodes were similar to austenitic plate properties. Allowable stresses depended on types of loading and the probability of occurrence. The magnets were instrumented with strain gages to test agreement with predicted values. In all cases, measured stresses were lower than or in good agreement with design values, which validates the design approach.

SESSION V. JOINT DEVELOPMENT OF TESTING STANDARDS

The status of cooperative 4-K tensile and fracture toughness testing standardization was described by H. Takahashi. A draft of a proposed standard was distributed earlier this year, and initial round-robin tests have been completed. Supportive research on a number of aspects of testing is also in progress. R. L. Tobler (NBS) has been participating in this program in Japan. S. Shimamoto (JAERI) set forth the results of 4-K round-robin tests on a 22Mn–2Cr–5Ni steel carried out at five laboratories. Both tensile and fracture toughness tests showed good correspondence. Some research questions for fracture toughness test standardization have been answered; others are still under investigation. Further round-robin tests on 316LN stainless steel and a new Japanese cryogenic steel are planned. L. Summers gave the results of $K_{Ic}(J)$ tests at LLNL on the 22Mn steel; more scatter was found in results from specimens of TL orientation than of LT orientation, but the results were in general agreement with the Japanese results (TL orientation). A comparison of Japanese and NBS test results on the 22Mn steel specimens was presented by P. T. Purtscher (NBS). Especially good agreement was noted for yield strength results. Fracture toughness testing procedures were detailed. The TL $K_{Ic}(J)$ results from NBS, with a mean of 156 $MA\sqrt{m}$, are lower than most of the Japanese test results; LT results were in better agreement. A change in $K_{Ic}(J)$ test procedure is that fatigue cracking is now carried out at 77 K rather than at room temperature.

SESSION VI. SUMMARY SESSION

The following action items were agreed upon and will be carried out before the next United States–Japan Workshop, which will be held at JAERI in the fall of 1988.

Test Methods and Standards

- Participants from both the United States and Japan will continue research on test methods and standards. R. L. Tobler will continue collaboration on $K_{Ic}(J)$ standards.
- Japan will send machined specimens to the United States for a second round-robin test series. The U.S. test results will be reported prior to the next workshop.
- The U.S. participants will draft a summary report on the first round-robin test results.
- The round-robin testing on 316LN specimens will be completed.
- A joint paper on test standards will be drafted: tensile tests will be addressed in one part, $K_{Ic}(J)$ in another part of this paper.
- A plan will be developed for comparing test methods on strengths of composites.

Materials

A. Alloys

- At JAERI, tests of large specimens will determine the true K_{Ic} instead of J_{Ic} and may enable future large specimen tests.

- A test matrix leading to a data base will be composed (this should determine whether observed variability arises from the microstructure, metastability, or mechanistic causes.)

- A discussion of the factors and parameters that should be considered in the formulation of a test matrix for an adequate data base will initiate with a letter from J. Morris (LBL) to S. Shimamoto (JAERI). This letter will urge the expansion of the program to include fundamental metallurgical studies of relevant alloys by participation of one or more Japanese university professors of metallurgy.

B. Weldments

- Japanese participants will provide a representative plate alloy and a welded thick plate to the U.S. participants for conducting welding tests. The test specimens used and any results obtained will be shared with Japanese participants. The U.S. participants will explore possible welding processes and electrodes.

C. Nonmetallics

- Materials samples will be exchanged.

- Jointly, Japanese and U.S. participants will develop a test matrix for characterization of model commercial materials and will proceed with the program after agreement on the test matrix.

D. Design Standards and Guidelines

- Data on past magnet design and experience leading to design changes will be acquired.

- Reports on magnet failure (structural failures) will be collected.

- Data on failure and failure prevention (fracture control) will be collected.

- U.S. and Japanese participants will draft a preliminary recommended basis for structural design. Specialists from each country will meet to discuss the specifics of the design basis.

JAPAN—U.S. COOPERATIVE PROGRAM COMMITTEE ON TEST METHODOLOGY
FOURTH DRAFT
MARCH 1987

NOTE: This is a working document of a standard being developed by the above committee for eventual submission to ASTM; it is intended for committee review purposes, but not for general distribution at this time.

Proposed Standard Method for

TENSILE TESTING OF STRUCTURAL ALLOYS AT LIQUID HELIUM TEMPERATURE

1. Scope

1.1 This standard describes the procedures to be used for the tensile testing of metals in liquid helium [4 or 4.2 K (−452°F)]. The format is similar to that of other ASTM tensile test standards, but the contents include modifications for cryogenic testing, which requires special apparatus, smaller specimen size, and concern for serrated yielding, adiabatic heating, and strain rate effects.

1.2 To conduct a tensile test by this standard, the specimen in a cryostat is fully submerged in normal liquid helium (He I) and tested using crosshead displacement control at a moderate strain rate. Tests that use load control or high strain rates are not considered in this standard.

1.3 This standard details methods for the measurement of yield strength, tensile strength, elongation, and reduction of area. The determination of the elastic modulus is treated in Method E 111.

1.4 Values stated in SI units are treated as primary; values stated in U.S. customary units are treated as secondary.

1.5 This standard does not address the issue of safety associated with cryogenic testing. It is the user's responsibility to learn and observe appropriate safety practices. Safety guidelines for handling liquid helium and other cryogens are available elsewhere (1).

NOTE 1—The boiling point of normal liquid helium (He I) at sea level is 4.2 K. This value decreases slightly with geographic elevation; it is 4.0 K at NBS in Boulder, Colorado, 1677 m (5500 ft) above sea level. In this standard, the test temperature is nominally designated 4 K.

2. Applicable Documents

2.1 ASTM Standards:

A 370 Methods and Definitions for Mechanical Testing of Steel Products (ANNUAL BOOK OF ASTM STANDARDS, Vol. 01.04)

E 4 Practices for Load Verification of Testing Machines (ANNUAL BOOK OF ASTM STANDARDS, Vols. 03.01, 04.02, 07.01, and 08.03)

E 6 Definition of Terms Relating to Methods of Mechanical Testing (ANNUAL BOOK OF ASTM STANDARDS, Vols. 03.01 and 08.03)

E 8 Methods for Tension Testing of Metallic Materials (ANNUAL BOOK OF ASTM STANDARDS, Vols. 01.02, 02.01, 02.02, 02.03, and 03.01)

E 8M Methods for Tension Testing of Metallic Materials, Metric (ANNUAL BOOK OF ASTM STANDARDS, Vol. 03.01)

E 29 Recommended Practice for Indicating Which Places of Figures Are to Be Considered Significant in Specified Limiting Values (ANNUAL BOOK OF ASTM STANDARDS, Vols. 02.03, 03.01, 03.03, 03.05, and 14.02)

E 83 Practice for Verification and Classification of Extensometers (ANNUAL BOOK OF ASTM STANDARDS, Vol. 03.01)

E 111 Method for Young's Modulus, Tangent Modulus, and Chord Modulus (ANNUAL BOOK OF ASTM STANDARDS, Vol. 03.01)

3. Definitions

3.1 The definitions of terms relating to tension testing that appear in ASTM Standard E 6 shall apply here. The following definitions also apply:

3.1.1 tensile cryostat—a test apparatus for applying loads to test specimens in cryogenic environments. A schematic illustration is shown in Fig. 1.

3.1.2 Dewar—a vacuum-insulated container for cryogenic fluids.

3.1.3 adiabatic heating—the internal heating of a specimen resulting from tensile testing under conditions such that the heat generated by plastic work cannot be quickly dissipated to the surrounding cryogen.

3.1.4 reduced section—section in the central portion of the specimen, which has a cross section smaller than the gripped ends.

3.1.5 length of the reduced section—the distance between the tangent points of the fillets that bound the reduced section.

3.1.6 adjusted length of the reduced section—the length of the reduced section plus an amount calculated to compensate for strain in the fillet region.

3.1.7 gage length—the original distance between gage marks made on the specimen for determining elongation after fracture.

3.1.8 axial strain—the average of the strain measured on opposite sides of the specimen at equal distances from the specimen axis.

3.1.9 bending strain—the difference between the strain at the surface of the specimen and the axial strain. The bending strain varies from point to point around and along the reduced section of the specimen.

3.1.10 maximum bending strain—the largest value of bending strain in the reduced section of the specimen. It is calculated from strains measured at three circumferential positions, at each of two different longitudinal positions.

4. Significance and Use

4.1 In general, tensile tests provide information on the strength and ductility of materials under uniaxial tensile stresses. This information may be useful for alloy development, comparison and selection of materials, and quality control. Under certain circumstances, the information may also be useful for design.

4.2 At 4 K, the load-time and load-deflection records for metals tested in displacement control are serrated (2). Serrations are formed by repeated bursts of unstable plastic flow, followed by arrests. The unstable plastic flow (or discontinuous yielding) is a free-running process that occurs locally with sizable heat evolution at higher than nominal rates of strain. Typical stress–strain curves for an austenitic stainless steel with serrated yielding at 4 K are shown in Fig. 2.

4.3 Constant specimen temperature cannot be maintained at all times during tests in a liquid helium environment. Owing to adiabatic heat, the specimen temperature temporarily rises above that of the cryogen at 4 K during the discontinuous yielding events (see Fig. 2). This behavior varies with specimen size and testing speed, but altering the mechanical test variables cannot eliminate the periods of internal heating (3). Therefore, tensile property measurements of alloys in liquid helium (especially ultimate strength, elongation, and reduction of area) lack the full significance of property measurements at higher temperatures where discontinuous yielding does not occur.

4.4 At 4 K, the stress–strain behavior of a material during unstable plastic deformation depends on whether load control or displacement control is used (4). Crosshead displacement control is specified because the goal

of this standard is material characterization by conventional methods. This limitation must be taken into account when data are used for structural design in applications when actual circumstances may approach load-controlled conditions.

5. Apparatus

5.1 Test Machines—Machines used for tensile testing shall meet the requirements of Practices E 4 regarding verification of load accuracy.

5.2 System Design—Alloy strengths often double or triple between room temperature and 4 K. For the same specimen geometry, higher loads must be applied to the cryostat, test specimen, load train members, and grips at cryogenic temperatures. For most conventional test machines, which have a maximum load capacity of 10 tons, it is recommended that the apparatus be designed to accommodate one of the small specimens cited in section 7.2.2 of this standard.

5.3 Construction Materials—Many construction materials, including the vast majority of ferritic steels, are brittle at 4 K. To resist embrittlement, the grips and other load-train members must be fabricated using strong, tough, cryogenic alloys. Austenitic stainless steels (AISI 304LN), maraging steels (200, 250, or 300 grades, with nickel plating to prevent rust), and extra-low-interstitial (ELI) grade titanium alloys (Ti–6Al–4V and Ti–5Al–2.5Sn) have been used, with proper design, to fabricate grips, pull rods, and cryostat frames.

5.4 Alignment:

5.4.1 Single-Specimen Apparatus—To avoid bending strains in the specimen, proper system alignment is essential. For a conventional single-specimen test apparatus, the machine and grips shall be capable of loading a precisely machined specimen so that the maximum bending strain does not exceed 10% of the axial strain. This calculation is based on the strain readings taken at zero load and at the highest load for which the machine is being qualified.

> NOTE 2—This requirement will minimize contributions from the test apparatus to the bending strain. Tests performed with a qualified apparatus may still vary in percent bending strain owing to small variations in the specimens.

5.4.2 Multiple-Specimen Apparatus—For this type of cryostat, the alignment depends on the type of fixtures used. The maximum bending strain shall be measured and reported.

5.4.3 Axiality Tests—The testing apparatus may be qualified by axiality measurements at room temperature and at 4 K. To perform axiality tests of the apparatus, the specimen form should be the same as that used during cryogenic tests,

the specimen concentricity should be as nearly perfect as possible, and no plastic strains should occur in the reduced section. In some cases, this may necessitate the use of a relatively stiff, high-strength calibration specimen.

5.4.3.1 For round bar specimens, the maximum bending strain, as defined in 3.1.10, is calculated from the strains measured at three circumferential positions, at each of two different longitudinal positions. The strains are measured with three electrical-resistance strain gages equally spaced around the reduced section of the specimen. The two longitudinal positions should be as far apart as possible, but not closer than one diameter to a fillet.

5.4.3.2 For specimens of rectangular cross section, strain may be measured at the center of each of the four sides, or in the case of thin strips, near the outer edges of each of the two broad sides.

5.4.3.3 To eliminate the effect of specimen bias, repeat the axiality measurements with the specimen rotated 180 degrees, but with the grips and pull rods retained in their original positions. The maximum bending strain and strain at the specimen axis are then calculated as the average of the two readings at the same position relative to the machine.

5.4.4 Strain Averaging Technique—Nonaxiality of loading is usually sufficient to introduce errors in tensile tests at small strains when strain is measured on only one side of the specimen. To rectify this, two extensometers or strain gages may be attached to opposite sides of the specimen. The reported strain should be the average of the strains on both sides.

5.5 Gripping Mechanisms—The choice of gripping mechanism to be used at 4 K is influenced by specimen type. Any suitable mechanism described in Methods E 8 and E 8M may be used.

5.6 Dimension-Measuring Devices—Micrometers and devices used for measuring the dimensions of specimens shall be accurate and precise to at least one-half the smallest unit to which a given dimension must be measured.

5.7 Cryostats and Support Apparatus:

5.7.1 Cryostats—A cryostat capable of retaining liquid helium is prerequisite. In general, cryostat load frames for existing test machines must be custom-built, but they may accommodate commercially available Dewars. The cryostat may employ adjustable load columns to facilitate alignment. Several practical designs, including turret-disc designs for multiple-specimen testing with a single cooling, are discussed in the literature (5–9).

5.7.2 Dewars—Stainless steel Dewars are recommended because they are safer than glass Dewars and less expensive than fiberglass Dewars. A single helium Dewar (see Fig. 1) is usually sufficient for short-term tests, but a double-Dewar arrangement in which an outer Dewar of liquid nitrogen jackets the inner Dewar of liquid helium is also possible.

5.7.3 Ancillary Equipment—Dewars and transfer lines for liquid helium must be vacuum insulated. Vacuum pumps, pressurized gas, and liquid nitrogen facilities are therefore required. After testing, the helium may be released to the atmosphere, recycled as a gas, or reliquefied. Recycling or reliquefaction requires large investments in purification and support systems.

5.8 Temperature Maintenance and Liquid Level Indicators:

5.8.1 Thermocouples—The intended temperature of 4 K is ensured by maintaining a liquid helium environment. A thermocouple to measure the specimen temperature is not required for routine tests.

5.8.2 Indicators—Although a thermocouple attached to the specimen is not necessary, an indicator or meter is required to ensure that the specimen remains fully submerged for the duration of testing. On–off indicators of the carbon-resistor type may be used to verify that the liquid level always exceeds some reference point above the specimen, or the liquid level may be continuously monitored with superconducting wire sensors of appropriate lengths positioned vertically inside the cryostat.

5.9 Strain Gages:

5.9.1 Selection—Strain-gage films bonded directly to the specimen surface may be used to measure strain at 4 K (10). A satisfactory combination of gage active element, backing material, and bonding agent should be selected on the basis of experience and manufacturer's recommendations. One common choice is a Ni–Cr-alloy gage with a temperature-compensated active element (7,11).

5.9.2 Characteristics—Strain gages are typically wired to a dummy bridge using a three-wire temperature-compensating hookup, like that shown in Fig. 3. The gage resistance is typically 120 or 350 Ω. A low excitation voltage of about 1 to 2 V is recommended at 4 K to reduce Joule heating. Typical full-scale operating ranges are 1% at room temperature and 2% at 4 K.

5.9.3 Calibration—Strain gage calibration at room temperature requires calibration of the electronics to changes in resistance. Calibration at 4 K requires consideration of the temperature dependence of the resistance in the electronic calibration. Gage factors as a function of temperature are provided by the manufacturers and in published research.

5.10 Clip-Gage Extensometers:

5.10.1 Types—Detachable clip-gage extensometers for use at 4 K may be built or purchased. An example is the beam gage, which uses four strain-gage films bonded in a Wheatstone bridge arrangement (11). Extension within the specimen gage length is sensed by the extensometer, which is clipped to retaining pins that are fixed to the specimen reduced section.

5.10.2 Characteristics—To measure the 0.2% offset yield strength, a Class B-2 extensometer, as identified in Method E 83, may be used. The extensometer shall meet the sensitivity and accuracy requirements of Method E 83 and shall be tested to ensure accuracy at 4 K. Whenever possible, the extensometer should be mounted directly to the specimen reduced section.

5.10.3 Calibration—Extensometers should be calibrated at room temperature and at 4 K with a suitable device. For calibrations at 4 K, a micrometer with vertical extension tubes can be used with the extensometer(s) mounted at the lower end and immersed in liquid helium. Once the calibration is known and proven to be accurate, linear, and reproducible, room-temperature checks may be performed prior to each test series for indirect verification of the calibration at 4 K. Direct calibration at 4 K, however, must be performed periodically, when damage is suspected or repairs have been made.

5.11 Capacitance Extensometers—Extensometers that use capacitance measurement to monitor strain may be used (10). The type with overlapping concentric cylinders has an extended strain range, an output that is linear with displacement, and an adjustable sensitivity. The type with parallel plates has high sensitivity, but the output must be compensated for the hyperbolic dependence of the capacitance on displacement.

6. Sampling

6.1 Stock Condition—Samples for tensile testing should be taken from the material in its final condition to ensure that the properties measured are representative of the end product. Allowance should be made for any superficial effects introduced by cutting operations.

6.2 Location—Specimens should be cut from locations thought to be most representative of the stock material, realizing that test results for specimens taken from selected locations of a part or material may not be representative of the whole. The conventional locations should normally be used:

6.2.1 For products 40 mm or less in thickness, diameter, or distance between flats, the location should be at the center.

6.2.2 For products over 40 mm in thickness, diameter, or distance between flats, the location should be midway from the surface to the center.

6.3 Specimen Configuration—The choice of specimen size and shape should be based on the requirements necessary to obtain representative samples of the material, and on test machine load capability (section 5.2).

6.4 Orientation—The orientation of the specimen axis relative to the principal working directions of the stock shall be specified using the notation in section 4 of Methods A 370.

7. Test Specimens

7.1 General:

7.1.1 Types and Specifications—Any specimen configuration cited in Methods E 8 or E 8M may be used. The specifications for dimensions, tolerances, and surface finish are stated in sections 6.1 through 6.17 of those standards.

7.1.2 Size—Specimens from sheet or wire products having relatively small cross-sectional areas can be tested within the load limits of conventional apparatus. Specimens from thick plate or bar products, however, may need to be machined to a reduced cross-sectional area so the load capacity of the machine is not exceeded.

7.2 Round Bar Specimens:

7.2.1 Standard Room-Temperature Specimen—A 12.5-mm (0.5-in) diameter round bar specimen is the standard configuration for room-temperature tests according to Methods E 8 and E 8M. For strong alloys, however, this specimen requires excessive loads at 4 K. For example, 210 kN is required to test typical AISI 304LN steel at 4 K, whereas 100 kN or 10 tons is the limit for most machines.

7.2.2 Standard 4-K Specimens—To meet the load limitations of conventional test machines, the round bar specimens in sections 7.2.2.1 and 7.2.2.2 are recommended as standard for 4-K tests. The required dimensions and tolerances for these specimens are given in Table 1. Threaded or shouldered ends are common for gripping these specimens, and the requirement of section 5.4.1 can be met by precise machining.

7.2.2.1 Standard, small metric specimens. These specimens have a 7-mm diameter and a gage-length-to-diameter ratio of 5:1.

7.2.2.2 Standard, small U.S. customary specimens. These specimens have a 6.25-mm (0.25-in) diameter and a gage-length-to-diameter ratio of 4:1.

7.2.3 Alternatives—If the 4-K standard specimens recommended above are not appropriate, other sizes may be selected following the guidelines of Methods E 8 and E 8M. The proportions of such specimens should be similar to those of the standard specimens (see Fig. 4 of this standard and Fig. 8 of Methods E 8 and E 8M).

7.2.4 Subsize specimens—Special care in fabrication and testing is required for specimens with diameters less than 6 mm. As the specimen size is reduced, factors such as machining, surface finish, alignment, and the number of grains per cross section are of increasing importance.

8. Procedures

8.1 Marking and Measuring the Test Specimen:

8.1.1 Gage Length—Gage length marks should be lightly punched, scribed, or inked at appropriate locations on the reduced section of the specimen, which is the conventional method. The gage length should normally be five times the diameter for metric specimens or four times the diameter for U.S. customary specimens. If another gage length is used, it must be described in the report. Measure the gage length to the nearest 0.05 mm.

> NOTE 3—For metals of low ductility, gage marks punched or scribed on the reduced section may induce failure at those locations due to stress concentrations. To avoid this, it may be possible to coat the reduced section with layout ink, and then mark the gage length by rotating the specimen in a jig with knife edges scraping off the ink at the appropriate intervals. Alternatively, gage marks may be placed on the specimen shoulders, or the overall length of the specimen may be measured.

8.1.2 Reduced Section—Measure the length of the reduced section and the adjusted length of the reduced section, if applicable, to the nearest 0.05 mm.

8.1.3 Cross Section—Measure the cross-sectional area of the reduced section as specified in section 7.1.1 of Methods E 8 and E 8M.

8.2 Specimen Installation—Install the specimen in the cryostat, leaving sufficient slack for instrumentation wires so they will not be stretched or crimped during positioning of the Dewar and subsequent testing

8.3 Seating and Alignment—If the gripping fixture involves loose-fitting components, such as spherically seated bearings, prevent friction or mismatch of the bearing surfaces at 4 K by first checking the seating and alignment at room temperature. During this process of alignment, the applied loads should be kept below one-third of the proportional limit of the test material.

8.4 Cooling Procedure—Remove any moisture from the apparatus prior to cooling by drying it thoroughly with a pressurized air jet or heat gun. Ice can block cryogenic transfer lines or cause erratic loading behavior if it forms between various parts of the specimen, clip gage, and load train. Next, position the Dewar and precool the apparatus to 77 K by transferring liquid nitrogen into the cryostat. After attaining equilibrium at 77 K, remove all the liquid nitrogen from the cryostat, and transfer liquid helium into the cryostat until the specimen and grips are fully submerged. Testing may begin after the system has reached thermal equilibrium at 4 K. The specimen must remain fully at all times during the test.

NOTE 4—The heat transfer characteristics of gaseous helium are inferior to those of liquid helium; therefore, a liquid helium environment is required to minimize specimen heating effects during discontinuous yielding.

8.5 Testing Speed:

8.5.1 Rate Control—Owing to adiabatic heating, tensile property measurements at 4 K can be significantly affected by the testing speed. Therefore, the test procedure must include a means of measuring and controlling the rate of crosshead motion. A nominal strain rate must be specified, since the actual rate cannot be precisely controlled or maintained when discontinuous yielding occurs. The nominal strain rate is calculated by dividing the crosshead rate by the length of the reduced section. Alternatively, a pacing or indicating device may be used to monitor the strain rate or an average strain rate may be determined by observing the time required to effect a known increment of strain.

8.5.2 Rate Limit—The nominal strain rate at any time during the test shall not exceed 1×10^{-3} s^{-1}. Higher rates may cause excessive specimen temperature rises and therefore are not satisfactory for determining the acceptability of materials.

8.5.3 Rate Change—The strain at which discontinuous yielding begins usually increases with decreasing strain rate. If the first serration for a given material occurs near 0.2% plastic strain, it may be desirable to reduce the speed to prevent interference in the measurement of the yield strength (see Fig. 5). Then, a relatively low strain rate may be used to determine the yield strength, followed by a higher strain rate to complete the test. Any convenient crosshead speed may be used up to a stress of one-half the yield strength; after that, the crosshead speed must be such that the nominal strain rate does not exceed the 1×10^{-3} s^{-1} limit.

8.6 Measurement of Mechanical Properties:

8.6.1 Load-Extension Curve Method—To measure the yield strength, a record of load versus extension must be obtained, up to at least 0.2% plastic strain. The use of a strain measurement device for autographic recording is recommended. Measure the yield strength via the 0.2% offset method, following Methods E 8 or E 8M, section 7.3.1. If the 0.2% offset line intersects the curve at a load drop owing to discontinuous yielding, then report the highest stress prior to that load drop as the yield strength (see Fig. 5).

8.6.2 Load-Time Curve Method—Yield strength measurements based on a 0.2% offset procedure applied to load-versus-time curves at 4 K are not recommended, except for commercial test purposes with the agreement of all parties involved. If this method is used, it should be stated clearly in the report.

NOTE 5—Load–time curves for tests at 4 K are typically nonlinear at the start and less regular than load–extension curves. Also, the effective modulus of a thermally efficient load train may be low and dependent on the liquid helium level and the degree of temperature stabilization achieved throughout the system in the temperature range 295 to 4 K. As a result, yield strength data from load–time curves may be less accurate than those of the recommended method.

8.6.3 Tensile Strength—Calculate the tensile strength by dividing the maximum load carried by the specimen during the tensile test by the original cross-sectional area of the specimen.

8.6.4 Elongation—Calculate the percentage increase of elongation according to Methods E 8 or E 8M, section 7.6.

8.6.5 Reduction of Area—Calculate the percentage of reduction of area according to Methods E 8 or E 8M, section 7.7.

8.6.6 Rounding Reported Test Data—Round-off the calculated test results according to Methods E 8 or E 8M, section 7.8.

8.6.7 Replacement Specimens—If necessary, discard data and test replacement specimens as per Methods E 8 or E 8M, section 7.9.

9. Precision and Bias

9.1 Precision—The precision of these methods is being established.

9.2 Bias—The bias of these methods includes quantitative estimates of the uncertainties of the dimension-measuring devices, the calibration of test equipment, and the skill of the operators. At present, bias statements should be limited to the documented performance or particular laboratories.

10. Report

10.1 The test report shall include the following:

10.1.1 Material Characterization—Describe the material tested, including manufacturing, processing, and metallurgical information.

10.1.2 Specimen Characterization—Describe the specimen location and orientation relative to the principal working directions of the stock. Also report the specimen dimensions, including the cross-sectional size, the fillet radius, the length of reduced section, and the adjusted length of the reduced section (if used).

10.1.3 Strain Rate—Report the crosshead speed and the nominal strain rate during yielding and after yielding, if a rate change is used.

10.1.4 Mechanical Property Measurements—Report the yield strength, ultimate strength, and method of offset yield strength determination. Include the method of extension measurement and location of extensometer attachment, if used. Also report the elongation and its method of calculation, the gage-length-to-diameter ratio for round specimens, and the reduction of area.

10.2 Optional Data—Report any optional data, such as measurements of Young's modulus at 4 K, the mechanical properties at room temperature, and the average grain size of the test material.

10.3 Replicate Tests—If replicate specimens are tested, state the number of tests, the average values of all mechanical property measurements, and a measure of scatter.

10.4 Subsize Specimens—If subsize specimens are tested, state any precautions taken with respect to specimen machining, surface condition, or alignment, and report the grain size of the test material.

10.5 Anomalies—Report any anomalies in material behavior, test records, or failure type and location.

REFERENCES

(1) Cryogenics Safety Manual—A Guide to Good Practice, 2nd Ed., Mechanical Engineering Publications, London, 1982.

(2) Basinski, Z. S., "the Instability of Plastic Flow of Metals at Very Low Temperatures," Proceedings of the Royal Society, Vol. A 240, 1957, pp. 229–242.

(3) Ogata, T., Ishikawa, K., and Nagai, K., "Effects of Strain Rate on the Tensile Behavior of Stainless Steels, Copper, and an Aluminum Alloy at Cryogenic Temperatures," Transactions of the Iron and Steel Institute of Japan, Vol. 71, No. 10, 1985, pp. 1390–1397. Tetsu-to-Hagane

(4) Ogata, T. and Ishikawa, K. "Time-dependent Deformation of Austenitic Stainless Steels at Cryogenic Temperatures," Cryogenics, Vol. 26, 1986, pp. 365–369.

(5) Schwartzberg, F. R., "Mechanical Property Testing Techniques for the Cryogenic Temperature Range," in: Advances in Cryogenic Engineering, Vol. 8, Plenum Press, New York, 1963, pp. 608–623.

(6) Evans, D., Simmonds, G. E., and Stapleton, G. B., "Improved Facility for Determining Mechanical Properties of Materials in Liquid Helium," in: Proceedings, Fourth International Cryogenic Engineering Conference, IPC Science and Technology Press, Guildford, Surrey, England, 1972, pp. 331–337.

(7) Hartwig, G. and Wuchner, F., "Low Temperature Mechanical Testing Machine," Review of Scientific Instruments, Vol. 46, 1975, pp. 481–485.

(8) Novikov, N. V. "Mechanical Property Measurement Techniques of Structural Materials at Cryogenic Temperatures," in: Advances in Cryogenic Engineering, Vol. 22, Plenum Press, New York, 1977, pp.113–118.

(9) Horiuchi, T., Shimada, M., Fukutsuka, T., and Tokuda, S., "Design and Construction of an Apparatus for Testing Materials at Cryogenic Temperatures," in: Proceedings, Fifth International Cryogenic Engineering Conference, IPC Science and Technology Press, Guildford, Surrey, England, 1977, pp. 465–468.

(10) Sparks, L. L., "Temperature, Strain, and Magnetic Field Measurements," in: Materials at Low Temperatures, R. P. Reed and A. F. Clark, eds., American Society for Metals, Metals Park, Ohio, 1983.

(11) Read, D. T. and Tobler, R. L., "Mechanical Property Measurements at Low Temperatures," in: Advances in Cryogenic Engineering—Materials, Vol. 28, Plenum Press, New York, 1982, pp. 17–28.

TABLE 1 Standard Specimens for Room Temperature Tests and Recommended Proportionally Reduced Standard Small Specimens for 4-K Tests[1]

(a) Metric Versions G/D ratio = 5 (dimensions, mm)	Standard Specimen (room-temperature)	Standard Small Specimen (4-K)
Nominal Diameter	12.5	7
G, gage length	62.5 ± 0.1	35 ± 0.1
D, diameter	12.5 ± 0.1	7 ± 0.1
R, fillet radius	10	7
A, reduced section	75	42

(b) U.S. Customary Versions G/D ratio = 4 (dimensions, in)	Standard Specimen (room-temperature)	Standard Small Specimen (4-K)
Nominal Diameter	0.5	0.25
G, gage length	2.000 ± 0.005	1.000 ± 0.005
D, diameter	0.500 ± 0.010	0.250 ± 0.005
R, fillet radius	0.375	0.1875
A, reduced section	2.25	1.25

[1]See also the notes to Fig. 8 in Methods E 8 and E 8M.

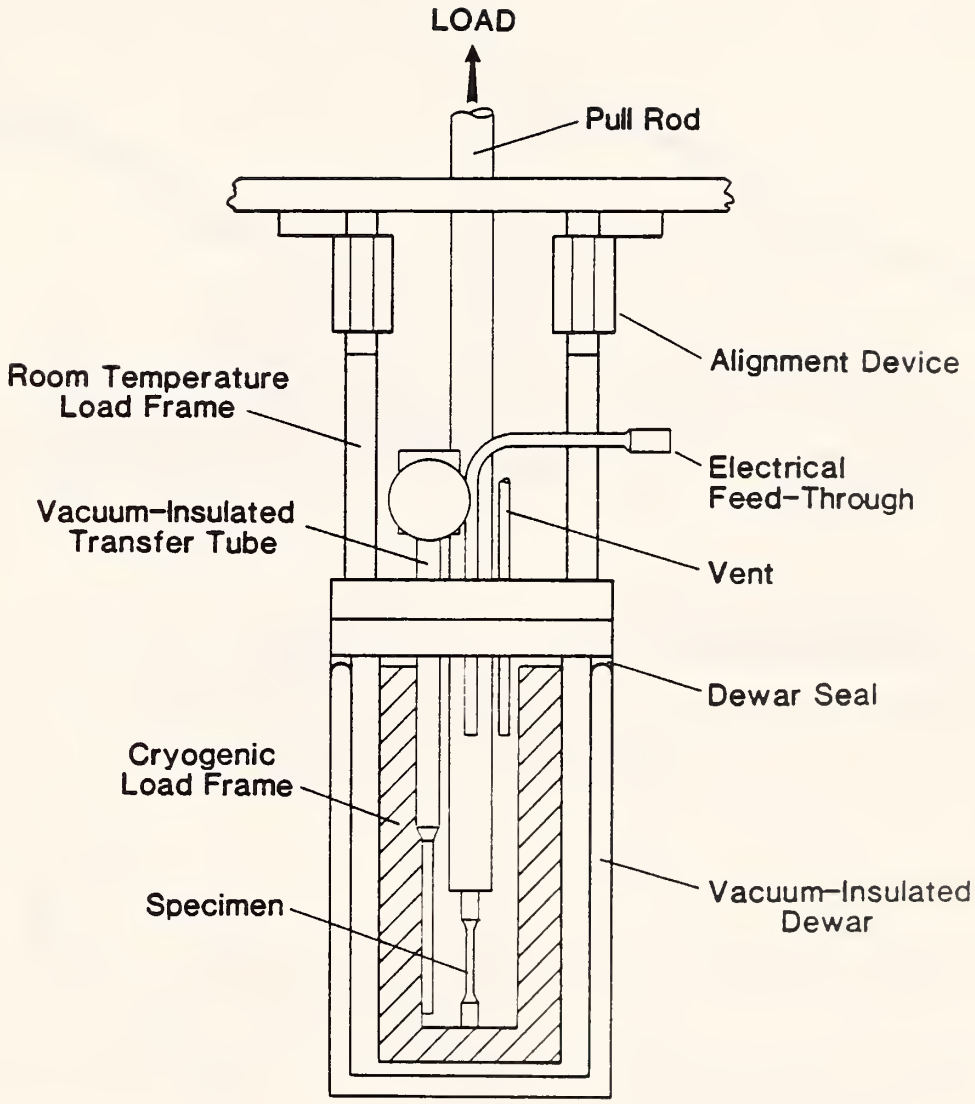

FIG 1 Example of a cryostat with Double-Dewar Arrangement for Tensile Testing at 4 K

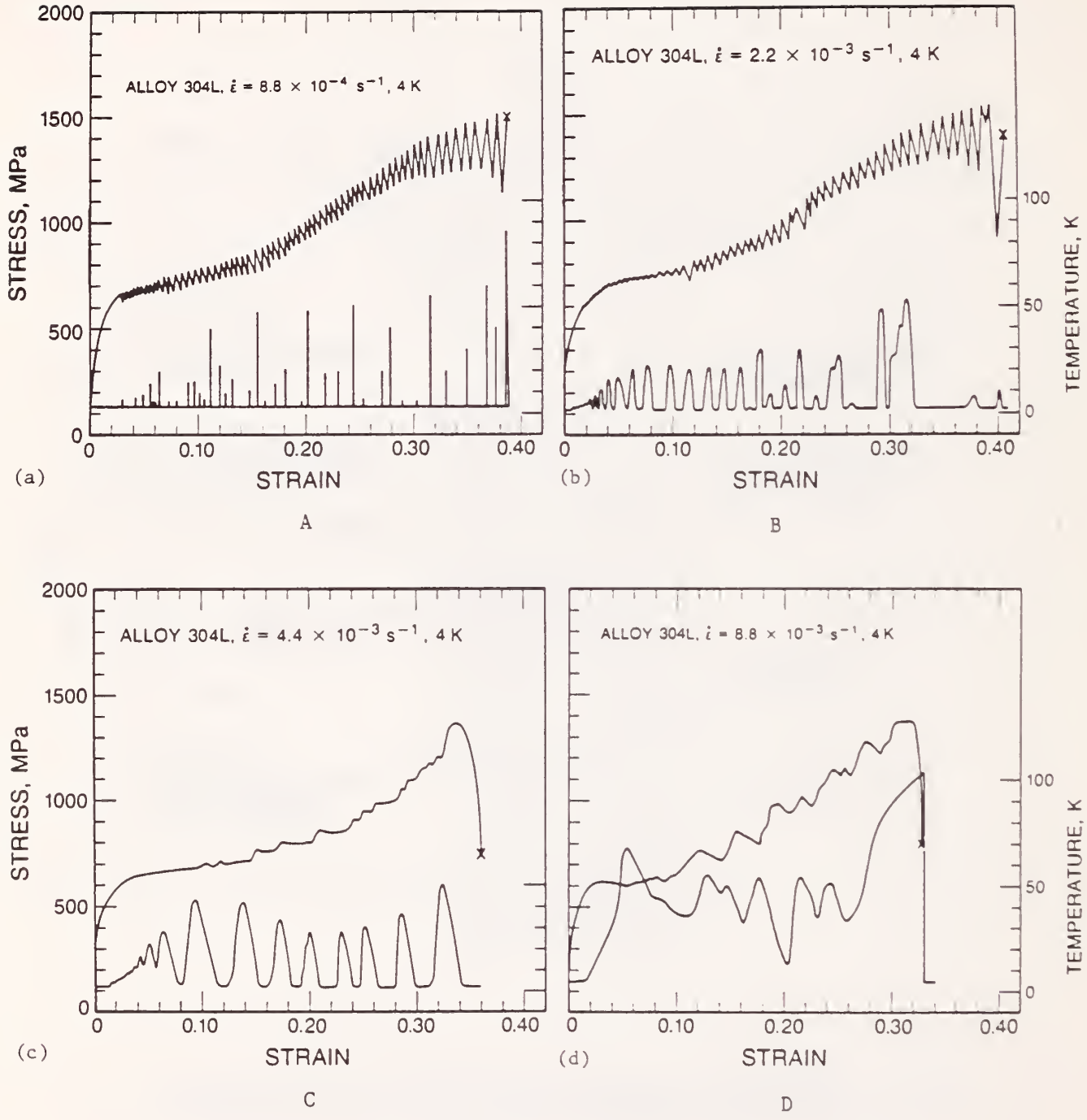

FIG 2 Engineering Stress-Strain Curves for an AISI 304L Austenitic Stainless Steel at 4 K

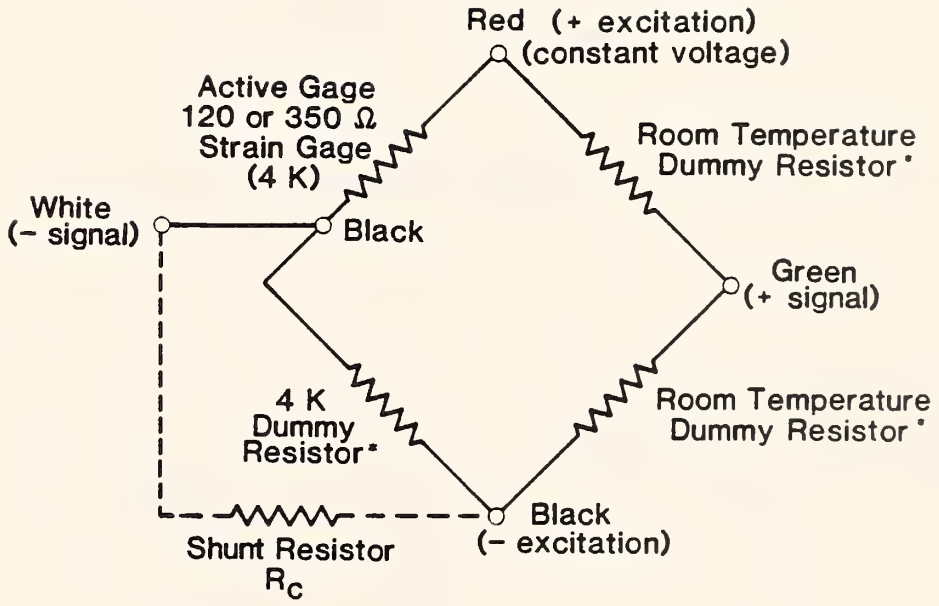

FIG 3 Method of Strain Gage Wiring for Cryogenic Tests

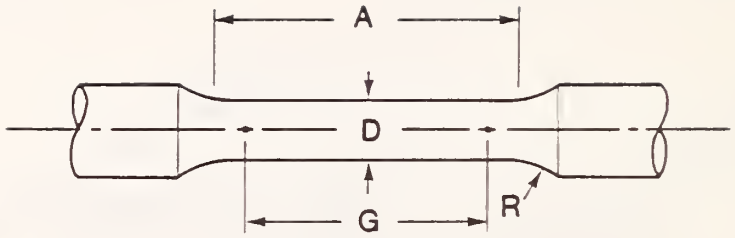

FIG 4 Round Bar Specimen Configuration (see Table 1)

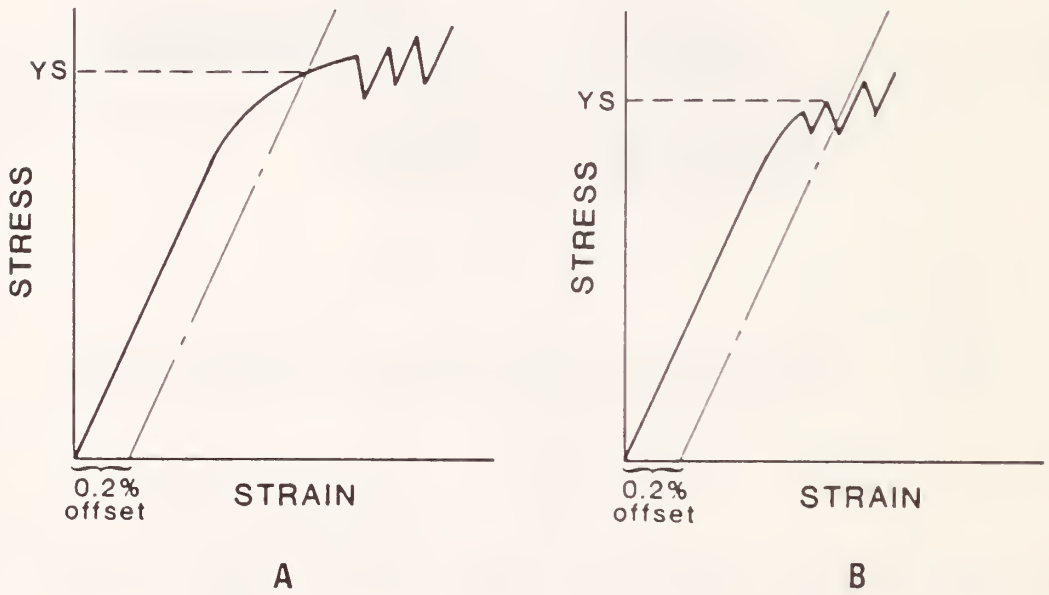

FIG 5 Stress–Strain Diagram for Determination of Yield Strength by the Offset Method: A) Serrations occurring after 0.2% strain; B) Serrations occurring before 0.2% strain.

U.S.—JAPAN COOPERATIVE PROGRAM COMMITTEE ON TEST METHODOLOGY
FOURTH DRAFT
MARCH 1987

NOTE: This is a working document of a standard being developed by the above committee. Some technical aspects are still being resolved and are subject to revision. The document in its present state is intended for committee review purposes, but not for general distribution at this time.

Proposed Standard Method for FRACTURE TOUGHNESS TESTING OF STRUCTURAL ALLOYS AT LIQUID HELIUM TEMPERATURE

1. Scope

1.1 This standard describes the equipment, procedures, and data analysis used for measuring the fracture toughness of structural alloys in liquid helium [4 or 4.2 K (−452°F)]. Procedures described in ASTM Methods E 399-83 and E 813-81 are adopted and modified to address the specific needs and concerns of cryogenic testing.

NOTE 1—The boiling point of normal liquid helium (He I) at sea level is 4.2 K. This value decreases slightly with geographic elevation; it is 4.0 K at NBS in Boulder, Colorado, 1677 m (5500 ft) above sea level. In this standard, the test temperature is nominally designated 4 K.

1.2 To measure the fracture toughness according to this standard, a fatigue-cracked specimen is cooled in a cryostat to 4 K and then loaded at a moderate speed while fully submerged in normal liquid helium (He I). The standard specimen is a pin-loaded, compact specimen, nominally 25 mm (1 in) thick and 50 mm wide.

1.3 This standard specifies the measurement of K_{Ic} or J_{Ic} whichever is appropriate for the load-displacement behavior at 4 K. For high-toughness alloys, J_{Ic} is determined by a resistance curve technique, but methods for measuring resistance curve slope, $\Delta J/\Delta a$, are not included in this standard.

1.4 Values stated in SI units are treated as primary; values stated in U.S. customary units, secondary.

1.5 This standard does not address safety issues. It is the user's responsibility to implement appropriate safety practices. Safety guidelines for handling liquid helium and other cryogens are available elsewhere (1)

2. Applicable Documents

2.1 ASTM Standards:

E 4 Practices for Load Verification of Testing Machines (ANNUAL BOOK OF ASTM STANDARDS, Vols. 03.01, 04.02, 07.01, and 08.03)

E 8 Methods of Tension Testing of Metallic Materials (ANNUAL BOOK OF ASTM STANDARDS, Vols. 01.02, 02.01, 02.02, 02.03, and 03.01)

E 8M Methods of Tension Testing of Metallic Materials, Metric (ANNUAL BOOK OF ASTM STANDARDS, Vol. 03.01)

E 399 Standard Test Method for Plane-Strain Fracture Toughness of Metallic Materials (ANNUAL BOOK OF ASTM STANDARDS, Vol. 03.01)

E 616 Terminology Relating to Fracture Testing (ANNUAL BOOK OF ASTM STANDARDS, Vol. 03.01)

E 813 Standard Test Method for J_{Ic}, A Measure of Fracture Toughness (ANNUAL BOOK OF ASTM STANDARDS, Vol. 03.01)

3. Definitions

3.1 The terms relating to tensile testing as defined in Definitions E 616 shall apply in this standard.

3.2 stress intensity factor, plane-strain fracture toughness, and crack plane orientation—the definitions in Methods E 399 apply in this standard.

3.3 J-integral, physical crack size, original crack size, crack extension, effective yield strength, blunting line, initiation of stable crack growth, regression line slope, and normalized crack size—the definitions in Methods E 813 shall apply in this standard.

3.4 fracture cryostat—an apparatus consisting of a loading frame and Dewar for testing specimens in cryogenic environments. A schematic is shown in Fig. 1.

3.5 Dewar—a vacuum-insulated container for cryogenic fluids.

3.6 adiabatic heating—the internal heating of a specimen caused by fracture testing under conditions such that the heat generated by plastic work cannot be quickly dissipated to the cryogen.

3.7 J_c—a critical value of J at the onset of fast fracture causing large, uncontrolled crack propagation.

4. Summary of Methods

4.1 This standard is based on Methods E 399-83 and E 813-81. From them procedures are adapted and modified in some respects for use at 4 K. Familiarity with them is assumed.

4.2 The object of this standard is to measure the fracture toughness of structural alloys at 4 K using a K- or J-based fracture criterion. The type of load-deflection behavior exhibited by the test material in the thickness tested determines which fracture criterion is to be used (see Fig. 2).

4.3 The compact specimen configuration is adopted as standard because it offers a larger fracture toughness measurement capacity for its size than any of the common fracture specimens. A relatively low load applied to the compact specimen produces a large stress intensity factor. This enables the mass of the cryostat, grips, and load train to be minimized, lowering the cryogen consumption and cost per test.

4.4 To determine the fracture toughness by this standard, a fatigue-cracked specimen is cooled to 4 K in a suitably designed cryostat containing liquid helium. Using displacement control, the specimen is loaded while the load versus displacement curve is autographically recorded. The material response determines the appropriate method of analysis.

4.4.1 The parameter K_{Ic} is used to characterize materials with a Type I record. The loading is linear-elastic and the crack-tip plastic zone is small compared with the crack size and specimen dimensions. Except for the provision of appropriate cryogenic apparatus, the method of K_{Ic} measurement is similar to that set forth in Methods E 399-83.

4.4.2 The parameters J_c is used in this standard to characterize Type II records where the loading is nonlinear and the crack-tip plastic zone is sizable compared with the crack size and specimen dimensions. This parameter is not a material constant, but it may be used to designate the toughness of materials that lack sufficient section thickness or toughness for valid K_{Ic} or J_{Ic} tests. The value of J_c is calculated from the area under the load-vs-displacement curve up to the point of fast fracture.

4.4.3 The parameter J_{Ic} is used to characterize materials displaying a Type III record where the loading is nonlinear (elastic-plastic, or fully plastic), the crack-tip plastic zone is large compared with the crack size and specimen dimensions, and a satisfactory resistance curve can be obtained for the material. The recommended method for J_{Ic} measurement is the single-specimen unloading-compliance test procedure.

5. Significance and Use

5.1 At 4 K, the significance and use of the parameter K_{Ic} as a material parameter is the same as that discussed in Methods E 399-83, section 4, for room-temperature tests.

5.2 The parameter J_c, as described in this standard, is not a material constant because its value depends on specimen configuration and size. The significance of J_c values with respect to material behavior or structural design is not addressed by this standard. The intent of such a measurement is determine a value of toughness for materials that do not fit either a K_{Ic} or J_{Ic} characterization in practical section thicknesses.

5.3 At room temperature, the significance and use of the parameter J_{Ic} is discussed in Methods E 813-81, section 4. At 4 K, discontinuous plastic flow may affect the significance of J_{Ic} as a material property. This subject is currently being evaluated.

5.4 The load-deflection curves of alloys fracture-tested at 4 K typically exhibit instabilities or serrations. The serrations are free-running events, that may arise from: a) subcritical crack extensions (pop-ins) owing to brittle cracking in low-toughness materials or b) ductile flow instabilities due to discontinuous plastic deformation in tough materials (2). Serrations are always accompanied by temporary temperature rise, as shown for a ductile austenitic steel in Fig. 3. Owing to this phenomenon the J-integral calculations, resistance curve slope, and tearing modulus parameters at 4 K lack the significance they have at ambient temperatures, where crack growth is exclusively a slow, stable tearing process.

5.5 The J_{Ic} values measured for high-toughness alloys may be used to estimate K_{Ic} values following Methods E 813-81, section 9.4:

$$K_{Ic}(J) = (J_{Ic} \times E)^{\frac{1}{2}}$$

Such conversions are useful to compare different materials quantitatively on the basis of a single parameter. These estimates are denoted by the symbol $K_{Ic}(J)$. Thus, K_{Ic} values are estimated from small, ductile test specimens that do not actually exhibit linear-elastic fracture or Type I records in practical section sizes.

5.6 Owing to adiabatic heating, fracture toughness measurements at 4 K may be affected by rapid loading (3). Therefore, tests at 4 K are performed at low loading rates (see section 9.4). The potential effects of heating must be considered in applications subject to high loading rates.

5.7 The fracture parameters K_{Ic} and J_{Ic} are suitable for characterizing a wide range of materials at 4 K. Nevertheless, some materials cannot be tested satisfactorily by the methods of this standard. These materials are:

a. too brittle to be properly fatigue-cracked or too thin ($B < 1.6$ mm) for K_{Ic} testing (see Methods E 399-83, section 1.1),
b. of intermediate toughness such that the loading behavior is not sufficiently linear for a K_{Ic} test, yet fast fracture prevents the full development of a resistance curve,
c. too tough for a valid J_{Ic} test (see Methods E 813-81, section 4.3).

Retesting with a change in specimen dimensions may be necessary to obtain valid data for some materials, but there is no assurance that valid results for a given material will be obtained by the procedures of this standard.

6. Apparatus

6.1 Test Machines—Tests shall be performed in displacement control with a screw-driven or servohydraulic tensile machine that meets the requirements of Practices E 4 regarding the verification of load accuracy. The equipment must include a means for autographic recording of the applied loads and specimen displacements. The machine compliance shall be measured with the cryostat to be used at 4 K; this may be accomplished by replacing the specimen with a rigid block.

6.2 Cryogenic System Design—For conventional test machines having a maximum load capacity of 10 tons, it is recommended that the cryogenic apparatus be designed to accommodate a standard, 25-mm-thick compact specimen (see section 8.1.3). A servohydraulic test machine with an inverted stage (actuator mounted above the specimen) and a cryogenic loading frame that is free at the bottom end is also recommended. Such a system is nearly optimum in regard to operating convenience and cost effectiveness for testing a wide range of materials at 4 K.

6.3 Cryogenic Construction Materials—Many materials, including most steels, are brittle at 4 K. All cryostat components must be well designed and fabricated using cryogenic alloys of suitable strength and toughness. Austenitic stainless steels are generally recommended. Maraging steels, nickel-plated to prevent rusting, are useful for specimen clevises. The alpha–titanium alloys are attractive for certain applications requiring high strength-to-thermal conductivity ratios, such as pull rods.

6.4 Dimension-Measuring Devices—Micrometers and other devices used for measuring the dimensions of specimens shall be accurate and precise to at least one-half the smallest unit to which the individual dimension is required to be measured.

6.5 Cryostats and Support Apparatus:

6.5.1. Cryostats—A cryostat is required to retain liquid helium for the duration of testing. Usually, cryostats must be custom-built, but they can be designed for use with commercially available, vacuum-insulated Dewars. Efficient design involves trade-offs between thermal and mechanical considerations (4). Some practical designs are described in the literature, including turret-disc apparatus for testing several specimens successively after a single cooling (4-7).

6.5.2 Dewars—Stainless steel Dewars are recommended for low maintenance, durability, and safety. Glass Dewars are fragile and hazardous, and fiberglass Dewars are relatively expensive. A single helium Dewar should generally be sufficient for tests of short duration. Double-Dewar

arrangements using an outer Dewar of liquid nitrogen to surround the inner Dewar containing liquid helium are also possible (4–6).

6.5.3 Ancillary Equipment—Dewars and transfer lines for handling the liquid helium must be vacuum-insulated. Pressurized gases, vacuum pumps, and liquid nitrogen apparatus are therefore required. After testing, the helium may be released as a vapor to the atmosphere, recycled, or reliquefied. Recycling or reliquefaction requires substantial investment in purification and cryogenic systems.

6.6 Clevis Grips:

6.6.1 Design—Conventional clevis grips conforming to the design in Fig. 3 of Methods E 813-81 may be used. The loading pin holes are designed with flats to allow specimen rotation during testing. To minimize friction, the flats must remain free of plastic indentations. Structural alloys with adequate 4-K strength, toughness, and fatigue resistance are required.

6.6.2 Construction—The maraging steels (i.e., 250 and 300 grades) have been used for clevis grips of the conventional design (4–7). If materials of lower strength are used, such as AISI 304LN, the thickness of the clevis arms should be enlarged.

6.7 Extensometer:

6.7.1 Requirements—An extensometer device is required to measure edge and load-line displacements for K_{Ic} or J tests, respectively. In addition to rendering accurate displacement measurements at 4 K, the device must be able to sustain repeated thermal shock, moisture condensation, and mechanical fatigue.

6.7.2 Types—Conventional clip gages, such as those described in Methods E 399 and E 813, may be purchased or built using good cryogenic materials and fabrication techniques (8). The clip gage recommended in Methods E 399 may be used if the total displacement is expected to be 2.5 mm or less. For a larger linear working range, enlarged gages are necessary (see Fig. 4 of Methods E 813).

6.7.3 Construction—A satisfactory combination of active strain gage elements, backing materials, and bonding agents must be used for constructing cryogenic extensometers. One common choice is a Ni–Cr-alloy gage with a temperature-compensated active element. Typically, 120- or 350-Ω gages are wired in a Wheatstone bridge arrangement. Electrical wires insulated with polytetrafluoroethylene and soft solders with low tin contents are recommended to reduce mechanical failures and shorts at 4 K.

6.7.4 Calibration—The clip gage or other extensometer device must be calibrated at room temperature and at 4 K. This may be done with a barrel-micrometer calibration device fitted with vertical extension tubes with the gage mounted at the lower end and immersed in liquid helium for calibration at 4 K (8). Once the calibration is known and proven linear, accurate, and reproducible, room-temperature checks may be performed to verify the 4-K

calibration indirectly. Periodically, the 4-K calibration must be directly verified, especially when damage is suspected or repair has been performed.

6.8 Temperature Maintenance and Liquid-Level Indicators—The intended cryogenic environment is ensured by the fixed boiling point of the liquid helium bath. A thermocouple on the specimen is not necessary, but a meter or indicator is required to ensure the proper liquid level. An on-off carbon-resistor meter, a continuous-level meter with superconducting wires, or a thermocouple (Chromel-versus-gold + 0.07% iron) shall be positioned in the cryostat above the specimen to ensure that it remains fully submerged at all times during the test.

7. Sampling

7.1 Material Condition—Samples for specimen preparation shall be taken from the material in its final metallurgical condition. All heat treatments shall be performed prior to sampling and specimen machining.

7.2 Sample Location—The sample location shall be chosen to be representative of the stock material. Allowance must be made for areas affected by the cutting process.

7.3 Specimen Orientation—The orientation of the specimen notch plane and the direction of load application relative to the principal stock working directions must be stated in the notation of Methods E 399.

8. Specimens

8.1 Specimen Configuration:

8.1.1 Specimen Types—In principle, any specimen configuration cited in Methods E 399-83 or 813-81 may be used if the standard's guidelines are observed. Current practice at 4 K is limited, however, to compact and bend specimens. The compact specimen predominates. Bend specimens require more mass for an equivalent ligament size. In addition, the long span of the bend specimen transverse to the loading axis requires cumbersome fixtures that are inconvenient for some cryostats.

8.1.2 Standard 4-K Test Specimen—A standard compact specimen is used for tests at 4 K. Its thickness, B, is 25.4 mm; its width, W, is 50.8 mm. The W/B ratio is 2.0, and the planar dimensions are proportional to W. This specimen is generally recommended because it is large enough to provide valid results at 4 K for most structural alloys, including the austenitic stainless steels.

8.1.3 Alternative Specimens—Selection of specimen size and shape will depend on technical purpose, the load limit of the testing machine, and the need to obtain representative samples of the material being tested. If the standard specimen is not practical, an alternative geometry or size may be selected, following Methods E 399 and E 813.

8.2 Specimen Preparation:

8.2.1 Starter Notch—The notch should be machined according to Methods E 813-81.

8.2.2 Loadline Notch Modification—For J_{Ic} measurements, a loadline notch modification (see Methods E 813-81) for clip-gage attachment between razor blades is recommended. Integrally machined knife edges may tend to increase friction effects. If the loadline displacement is not directly measured in J_{Ic} tests, then the method of determining the displacement at the loadline from measurements at the edge location must be described.

NOTE 2—If a loadline modification is used and a Type I load–displacement curve is obtained, then K_{Ic} may be calculated as usual.

8.3 Fatigue Precracking:

8.3.1 General Requirements—All specimens shall be carefully fatigue-cracked. The load range (ΔP) during fatigue shall not be less than 90% of the maximum fatigue load. Also, the maximum stress intensity factor during the fatigue crack extension shall not exceed 0.005 $mm^{\frac{1}{2}}$ times the Young's modulus, E.

8.3.1.1 Fatigue precracking at 4 K. If the specimen exhibits linear-elastic behavior, the maximum stress intensity factor during fatigue crack extension shall not exceed 60% of K_{Ic}. If the specimen exhibits plastic behavior, the maximum fatigue load must not exceed $0.4P_L$, where P_L is the limit load. For the compact specimen:

$$P_L = Bb^2\sigma_y/(2W + a)$$

8.3.1.2 Fatigue precracking at higher temperatures. Fatigue precracking can be performed at a higher temperature if the procedure does not affect the subsequent fracture toughness measurement at 4 K. At the present time, however, no clear rules have been established for fatigue precracking at higher temperatures, such as 295 K. If fatigue precracking is performed at a higher temperature, the maximum loads should be reduced by the ratio of the yield strength at the fatigue temperature to that at 4 K. If any other procedure is used, it must be demonstrated that this does not affect the toughness test result.

NOTE 3—Sizeable reductions of the maximum load during fatigue cracking should be avoided because they may retard the crack growth rate or increase the degree of crack front curvature.

8.3.3 Fatigue Crack Length—The ratio of the fatigue crack length to specimen width, a/W, shall be in the range from 0.45 to 0.70. The choice of crack length ratio is influenced by the behavior of the test material. If a Type-I test record is expected, or if K_{Ic} may be directly measured, the crack length ratio shall be 0.45 to 0.55 to maintain compatibility with

Methods E 399-83. If nonlinear loading behavior is expected and a resistance curve can be determined, the ratio should be about 0.6; for the exceptionally strong and tough steels, a ratio near 0.7 may be necessary to keep within machine load limitations. For alloys of unknown toughness, a ratio of 0.6 is recommended for initial tests; this can be adjusted for retests, if necessary.

8.4 Side Grooves:

8.4.1 Acceptable Uses—Side grooves should not be used for materials having Type I or Type II test records. For Type III records, side grooves may be used to reduce the fatigue crack front curvature, to alleviate crack front tunneling, or to improve the agreement between the optically measured and compliance-calculated end-of-test Δa values.

8.4.2 Machining—Side grooves, if used, shall be machined after precracking, following Methods E 813-81, section 7.5.1. For standard 25-mm-thick compact specimens, the total depth of side grooving shall amount to not more than 20% of the gross specimen thickness.

9. General Procedures

9.1 Specimen Measurement—Measure the specimen dimensions according to Methods E 399-83 (section 8.3) and E 813-81 (section 8.8).

9.2 Installation—Install the specimen in the apparatus, leaving enough slack for the instrumentation wires so that they will be neither stretched nor crimped during positioning of the Dewar and testing. Prior to cooling, check the seating of the specimen and grips at room temperature. A slight preloading of the specimen is permitted for this purpose.

9.3 Cooling—Prior to cooling, dry the apparatus thoroughly with pressurized air or a heating gun. Also, purge any moisture from the cryogenic transfer lines. Ice can block the transfer lines or cause erratic loading behavior if it forms on the loading pins, clevises, specimens, clip gage, or load-train members. Next, position the Dewar and precool the apparatus to 77 K by transferring liquid nitrogen into the cryostat. After attaining equilibrium at 77 K, remove all the liquid nitrogen and transfer liquid helium into the cryostat. Add sufficient liquid helium to compensate for evaporation during the time required to complete the test so that the test specimen remains fully submerged at all times.

NOTE 4—Compared with liquid helium, the heat transfer characteristics of gaseous helium are inferior; therefore, liquid helium is required to minimize specimen heating.

9.4 Loading:

9.4.1 Control Mode—The test shall be conducted using displacement control, not load control. Crosshead displacement is typical for screw-driven

machines. For servohydraulic machines, stroke control is often used, but clip-gage control may be a useful alternative for J_{Ic} tests.

9.4.2 Load Rate—Load the specimen at a rate such that the time, t_p, to reach the load at first deviation from the linear portion of the test record is between 0.5 and 10 min. For other details of test procedure, see Methods E 813-81, section 8. For standard 25-mm-thick compact specimens, the crosshead rate should be 0.5 $mm \cdot min^{-1}$ or less.

9.5 Test Record—Autographically record the outputs of load-cell versus displacement following the guidelines of Methods E 399-83, section 8.4 for K_{Ic} tests, or as appropriate for J_{Ic} tests. For J_{Ic} tests, a real-time computer-calculated J–Δa curve record is also recommended.

10. Interpretation and Calculation of Results

10.1 General—Classify the test record as one of the three basic types shown in Fig. 2. Depending on the load-versus-displacement behavior, decide which fracture criterion is to be used. More than one fracture parameter may be applied in some cases.

10.2 K_{Ic} measurement—For Type I test records showing linear-elastic behavior, K_{Ic} should be calculated according to Methods E 399. Construct the secant offset line, calculate the conditional toughness value, K_Q, and determine its validity as a K_{Ic} value according to Methods E 399-83, section 9. If the test fails to qualify as a valid K_{Ic} measurement, calculate the value of J_c according to the following section, 10.3.

NOTE 5—Notch cut-out modifications (instead of the usual edge-displacement measurements) do not violate the K_{Ic} calculations at 4 K, according to this standard.

10.3 J_c measurement—For Type II tests that produce nonlinear load-versus-deflection curves, determine a value of J_c as follows: Calculate the total value of J corresponding to the total area under the load-displacement curve up to the point of fast fracture. The area to be measured is cross-hatched in Fig. 2. The measurement shall be accurate to 2% and it may be performed using a polar planimeter or numerical integration of the load-displacement signals by computer techniques. Calculate the value of Jc for compact specimens:

$$J_c = f(a_0/W) \cdot A/Bb$$

where

a_0 = original crack size, including precrack,
W = specimen width,
$f(a_0/W)$ = a dimensionless coefficient that corrects for the tensile component of loading, as given in section 9.1.1 and Table 1

A = area under the load versus load-point displacement record in energy units,
B = specimen thickness, and
b = initial uncracked ligament, $W - a_0$.

10.4 J_{Ic} measurement—For Type III tests, J_{Ic} should be measured by a resistance curve technique, where J is plotted versus physical crack growth, Δa_p. The single-specimen unloading compliance method is recommended as the most suitable technique at 4 K because it reduces the number of specimens required and the cryogenic fluid costs. Guidelines for the method are given in the appendix of Method E 813-81.

10.4.1 Calculations of the J-integral are made from the load vs load-point displacement curves by using the expression in section 10.2. For side grooved-specimens, the net thickness is used in the J calculations and effective thickness is used for crack growth predictions from unloading compliance as per Methods E 813-81 sections 8.7.1 and 9.1.1.

10.4.2 Prepare a plot of J versus Δa_p spanning the 0.15–1.5 mm exclusion interval, as given by Methods E 813-81. Calculate the area under the load–displacement curve, including the area under serrations. For tests in clip-gage displacement control, the area under a serration is zero. Thus, tests in stroke control are expected to give higher values of J for a given crack extension, owing to the positive increase of area associated with serrations. The intent is not necessarily to measure a physically meaningful J-Δa curve, but just a regular data set enabling linear extrapolation to the initiation of crack extension at J_{Ic}.

10.4.3 Construct the blunting line and plot the regression line, and qualify the J–Δa calculations according to Methods E 813-81, section 9.2.

10.4.4 Determine J_Q as the value of J at the blunting and regression line intersection. Qualify the data and determine whether J_Q value is a valid J_{Ic} determination according to Methods E 813-81, sections 9.3 and A1.

11. Report

11.1 Material Characterization:

11.1.1 Material Description—Describe the material tested, including the product form (e.g., plate, forging, casting), processing and heat treatment, and any other relevant metallurgical information.

11.1.2 Tensile Properties—Report the yield strength, tensile strength, and elastic modulus at room temperature and at 4 K.

11.2 Specimen Characterization:

11.2.1 Describe the crack-plane orientation according to the Methods E 399-83 identification code.

11.2.2 Report the specimen dimensions, including thickness, width, and ligament and length crack lengths.

11.2.3 If side grooves are used, describe the notch geometry (included angle, notch-tip radius, and net section thickness).

11.3 Fatigue Cracking Characterization:

11.3.1 Report the maximum fatigue load, the maximum stress-intensity factor, the stress-intensity factor range, and the temperature used for the fatigue precracking.

11.3.2 Report the final fatigue crack length obtained from the three-point average for K_{Ic} tests or the nine-point average for J_{Ic} tests, as described in Methods E 399-83 or E 813-81. Also measure the surface crack lengths. Report the maximum deviation of any single measurement from the average.

11.4 Test Record—Describe the load-versus-displacement record or designate the type of test record observed according to the examples shown in Fig. 2.

11.5 Loading Rate—Report the loading rate in terms of t_p or the rate of increase of the stress-intensity factor, K, during the linear region of loading. Specify whether crosshead speed, stroke displacement, or clip-gage displacement was used.

11.6 Fracture Toughness Measurements:

11.6.1 For a Type I test record, report the fracture toughness in terms of K_Q or K_{Ic} and include an assessment of the validity according to Methods E 399-83.

11.6.2 For Type II test records, where a full resistance curve cannot be developed, report the value of J_c as defined in section 3 of this standard. If an unloading compliance technique was used for $J-\Delta a$ measurements up to the point of fast fracture, estimate the value of crack extension at the J_c measurement point.

11.6.3 For Type III test records, where a full resistance curve can be developed, report the value of J_{Ic} and calculate $K_{Ic}(J)$. Assess the validity of J_{Ic} according to the criteria of Methods E 813-81.

11.7 Fracture Surface Appearance—Describe the fracture appearance. For computerized J_{Ic} tests, report the end-of-test crack extension increment and the accuracy of the compliance-predicted versus the optically measured final average crack length.

11.8 Replicate Tests—Give the number of replicate tests performed, the average fracture toughness values, and a measure of scatter.

11.9 Anomalies—Report any anomalies observed in material behavior, the test records, or failure mechanisms.

12. Accuracy and Precision

12.1 Accuracy—There is no accepted standard fracture toughness value for any material. In the absence of such a true value, any statements about accuracy are meaningless.

12.2 Precision—Information concerning the precision of 4-K fracture tests is being obtained from interlaboratory test programs in progress.

REFERENCES

(1) Cryogenics Safety Manual—A Guide to Good Practice, 2nd Ed., Mechanical Engineering Publications, London, 1982.

(2) Tobler, R. L. and Shepic, J. A. "Design and Performance of a Ring-shaped Clip Gage for Fracture Mechanics Testing," Journal of Testing and Evaluation, Vol. 13, 1985, pp. 299–302.

(3) Tobler, R. L., Ohnishi, K., Shoji, T., and Takahashi, H., "Fracture, Acoustic Emission, and Adiabatic Heating of Austenitic Stainless Steels at Liquid Helium Temperature," in: Progress in Acoustic Emission III, Japanese Society for Non-Destructive Inspection, Tokyo, 1986, pp. 453–461.

(4) Fowlkes, C. F. and Tobler, R. L., "Fracture Testing and Results for a Ti–6Al–4V Alloy at Liquid Helium Temperature," Engineering Fracture Mechanics, Vol. 8, 1976, pp. 487–500.

(5) Read, D. T. and Tobler, R. L., "Mechanical Property Measurements at Low Temperatures," in: Advances in Cryogenic Engineering—Materials, Vol. 28, Plenum Press, New York, 1982, pp. 17–28.

(6) Juhas, M. C., Duncan, D. B., and Streit, R. D., "Development of a Facility for Fatigue and Fracture Testing of Stainless Steels at Liquid Helium Temperature," Cryogenics, Vol. 23, 1983, pp. 603-607.

(7) Shimada, M., Ogawa, R., Moriyama, T., and Horiuchi, T., "Development of a Cryogenic Fracture Toughness Test System," Cryogenic Technology, Vol. 21, No. 5, 1986, pp. 269–274.

(8) Tobler, R. L., "Ductile Fracture with Serrations in AISI 310S Stainless Steel at liquid Helium Temperature," in: Elastic-Plastic Fracture: Second Symposium, Vol. II—Fracture Resistance Curves and Engineering Applications, ASTM STP 803, C. F. Shih and J. P. Gudas, eds., American Society for Testing and Materials, Philadelphia, 1983, pp. 763–776.

(9) Shimamoto, S., Nakajima, H., Yoshida, K., and Tada, E., "Requirements for Cryogenic Structural Alloys for Superconducting Magnet Cases," in: Advances in Cryogenic Engineering—Materials, Vol. 32, Plenum Press, New York, 1986, pp. 23–32.

(10) Clarke, G. A., Andrews, W. R., Paris, P. C., and Schmidt, D. W., "Single Specimen Tests for J_{Ic} Determination," in: Mechanics of Crack Growth, ASTM STP 590, American Society for Testing and Materials, Philadelphia, 1976, pp. 27–42.

(11) Joyce, J. A. and Gudas, J. P., "Computer Intractive J_{Ic} Testing of Navy Alloys," in: Elastic-Plastic Fracture, ASTM STP 668, J. D. Landes, J. A. Begley, and G. A. Clarke, eds., American Society for Testing and Materials, Philadlephia, 1976, pp. 451–468.

(12) G. A. Clarke, "Single-Specimen Tests for J_{Ic} Determination—Revisited," in: Fracture Mechanics: Thirteenth Conference, ASTM STP 743, R. Roberts, ed., American Society for Testing and Materials, 1983, pp. 553–575.

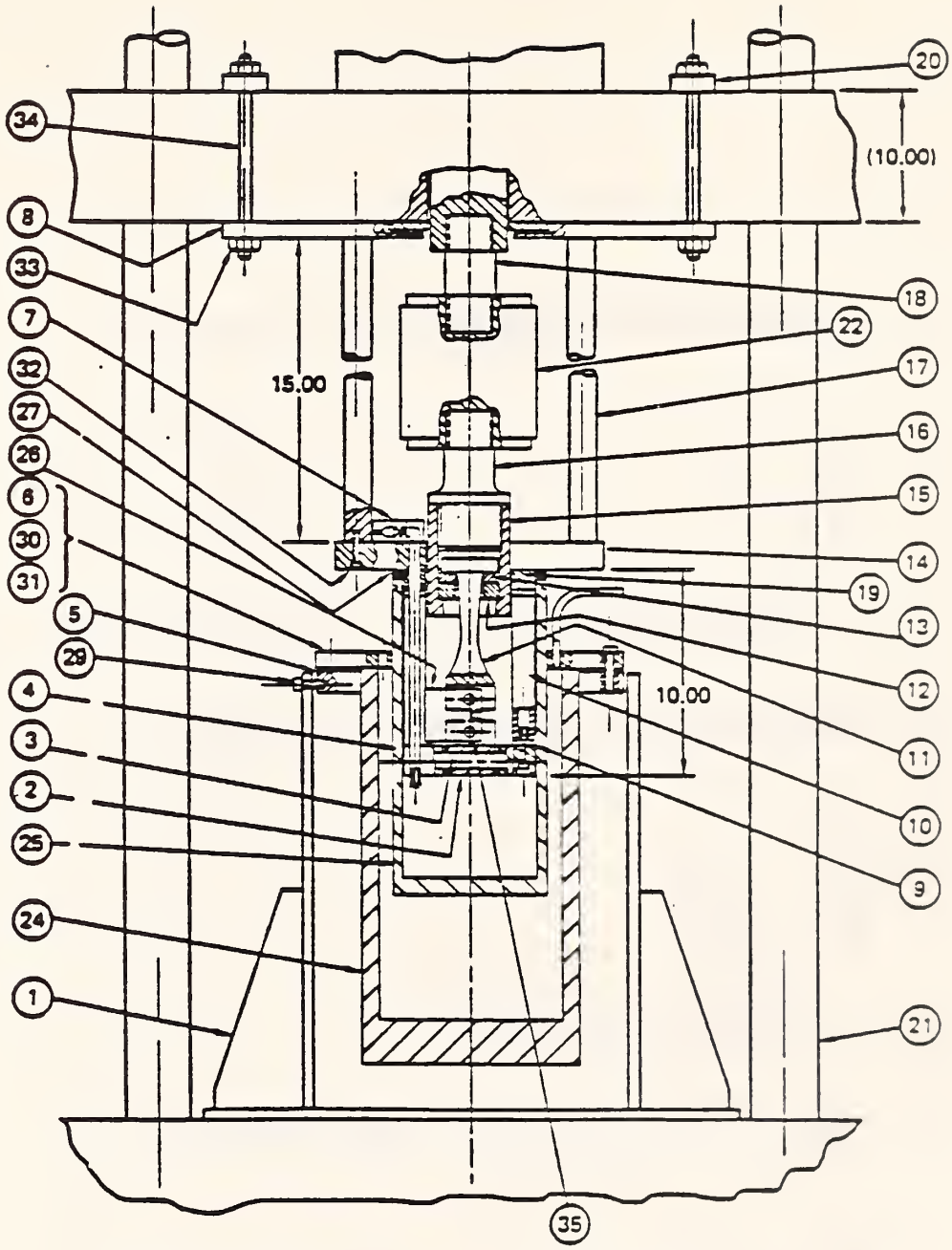

1 - Dewar pivot frame
2 - Specimen clevis
3 - Shear pin
4 - Pivot plate
5 - Outer Dewar top
6 - Inner Dewar clamp
7 - Transfer hose adapter
8 - Adapter plate
9 - Column adapter
10 - Compression column
11 - Clevis pull rod
12 - Pull rod keeper
13 - Pull rod split ring isolator
14 - Load plate
15 - Pull rod coupling
16 - Load cell adapter
17 - Load column
18 - Load cell adapter
19 - Isolator compression ring
20 - Adapter bar
21 - Test machine frame
22 - Load cell
23 - Clip gage
24 - Stainless steel Dewar
25 - Stainless steel Dewar
26 - J-integral compact tension fracture specimen
27 - Seal ring
28 - Liquid helium level meter
29 - Socket head cap screw
30 - Socket head cap screw
31 - Socket head cap screw
32 - Socket head cap screw
33 - Nut
34 - Threaded rod
35 - Shear pin

FIG 1 Example of a Cryostat with Double-Dewar Arrangement for Tensile Testing at 4 K

I. Linear-Elastic Behavior: K_{Ic} is measured

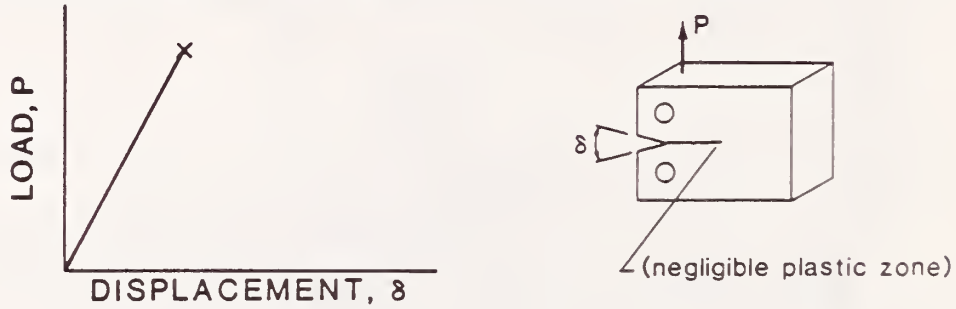

II. Elastic-Plastic Behavior: J is measured

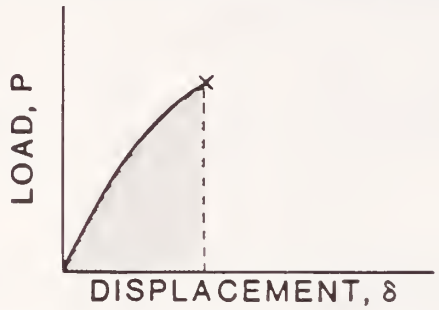

III. Fully Plastic Behavior: J_{Ic} is measured

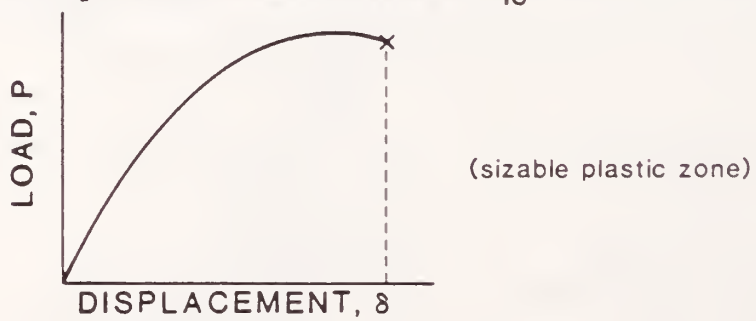

FIG 2 Load–Displacement Behavior Observed in Fracture-Toughness Tests

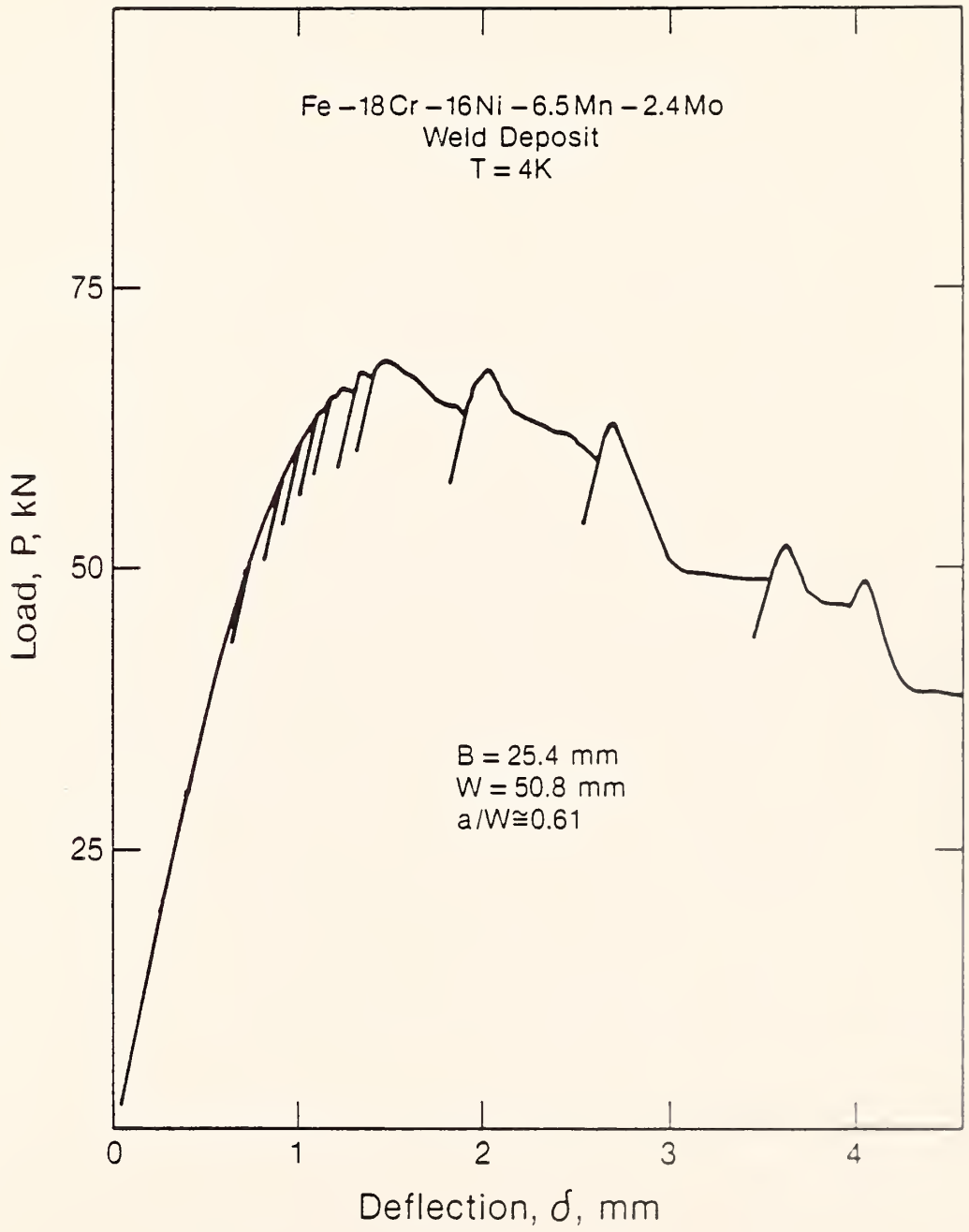

FIG 3 Typical Compact Specimen Loading Behavior at 4 K, Showing Serrations and Points of Unloading Compliance Method

FRACTURE, ACOUSTIC EMISSION, AND ADIABATIC HEATING OF AUSTENITIC STAINLESS STEELS AT LIQUID HELIUM TEMPERATURE*

R. L. Tobler,† T. Shoji, H. Takahashi, and K. Ohnishi

Research Institute for Strength and Fracture of Materials
Tohoku University
Sendai, Japan

Conventional fracture mechanics tests supplemented with acoustic emission and adiabatic heating measurements were conducted to characterize commercial austenitic stainless steels at 4 K. Three alloys, representing low, medium, and high toughness alloys, were examined, and high levels of acoustic emission are reported for each one. The high acoustic emission of these austenitic steels at 4 K is attributed to low temperature strengthening effects in general and to the peculiar failure mechanism involving discontinuous deformation and adiabatic heating that occurs in ductile materials near absolute zero.

INTRODUCTION

Detailed fracture characterization of austenitic stainless steels at extreme cryogenic temperatures is necessary for alloy development and superconducting magnet design in fusion energy research. Fracture toughness data at 4 K are usually obtained by critical stress intensity (K_{Ic}) or J-integral (J_{Ic}) measurements performed with conventional 25-mm-thick compact specimens submerged in liquid helium. Such data describe macroscopic fracture only, giving no information regarding the thermodynamic or micromechanical aspects of fracture processes at 4 K.

Acoustic emission has been previously used to monitor the operation of fully assembled superconducting magnet systems at cryogenic temperatures[1,2] and to study the microdeformation and fracture behavior of fiber-reinforced

*Published in Acoustic Emission III, The Japanese Society of Non-destructive Inspection, Tokyo, 1986; pp. 453–461.
†Visiting fellow from the Fracture and Deformation Division, National Bureau of Standards, Boulder, Colorado, USA.

plastic composites at temperatures from 295 to 4 K.[3] The purpose of this study is to explore acoustic emission and adiabatic heating monitoring as techniques to evaluate the 4-K fracture mechanisms of austenitic stainless steels in greater detail. The fact that abrupt discontinuous yielding with audible sound is common in these materials at cryogenic temperatures suggests that sensitive acoustic emission techniques may be especially appropriate for such purposes.

EXPERIMENTAL PROCEDURE

Three fully austenitic stainless steels were tested in this study, including two wrought base metals and a shielded metal arc (SMA) butt weld. This selection of materials enabled a wide variety of load–displacement (P–δ) behaviors to be evaluated. The wrought base metals were 25-mm-thick plates of Fe–18Cr–3Ni–13Mn and AISI 310S base metal (BM) tested in the annealed condition. The SMA weld, designated AISI 310S WM, was prepared commercially using a type 310S electrode with two 22-mm-thick base plates and tested in the as-welded condition. The chemical compositions and tensile properties are listed in Tables 1 and 2.

Compact specimens (nominally 1TCT size) were prepared with notches machined in the longitudinal plate or weld bead direction (TL orientation). The specimens were 50 mm wide and 22 or 25 mm thick. The Fe–18Cr–3Ni–13Mn specimens were precracked to a relative crack length (a/W) of 0.5, but they were not side-grooved in view of linear elastic test requirements. The AISI 310S weld- and base-metal specimens were precracked to $a/W = 0.6$ and were side-grooved 20% for elastic–plastic and fully plastic tests.

The specimens were fatigue-cracked at 295 K, then side-grooved or instrumented, as required. Subsequently, they were cooled in a liquid helium cryostat and fractured using a 10-ton screw-driven machine[4,5] at crosshead speeds of 1.0 or 0.1 mm/min. After testing, the fracture surfaces were examined by scanning electron microscopy (SEM) to verify the failure mechanisms and to determine the average dimple diameter and the size of the stretch zone between the fatigue crack and fracture zones. The specimen strength ratio was calculated as defined in the ASTM E 399-85 test method. The tearing modulus, T_m, and plane strain toughness values, K_{Ic} and J_{Ic}, are quoted in the text without further elaboration, since the details are published elsewhere.[5-7]

An existing acoustic emission system[8] was modified and used for tests at 4 K by employing a waveguide and reducing the gain. The waveguide was a 4-mm-diameter stainless steel rod, welded to the specimen back face as shown in Fig. 1. The guide transmitted acoustic emission signals from the specimen at 4 K to a wideband piezoelectric transducer at 295 K via a coupling outside the cryostat. A significant problem at 4 K is signal saturation owing to the high energy levels of emissions from these steels. Therefore, our tests used a 20 dB gain, reduced from the usual 60 dB gain at 295 K. The signals were fed into a distribution analyzer, which counted pulses according to their peak amplitudes and determined the individual event energies, E_{AE}.

Adiabatic heating was detected by measuring the internal temperature, T, at the crack tip at the specimen midthickness using Chromel-vs-gold-plus-0.07%-iron-alloy thermocouples embedded in the ligament along the fracture plane. Typically, four thermocouples (0.24-mm wires) were inserted through 2-mm holes drilled 3 mm apart, as shown in Fig. 1. These holes were then filled with fine Cu powder. The four thermocouple outputs were recorded on a strip chart, and as cracking propagated across the ligament, the highest T or ΔT (T − 4.2 K) provided a measure of heating.

RESULTS

The Fe–18Cr–3Ni–13Mn, AISI 310S WM, and AISI 310S BM steels of this study displayed typical linear elastic, elastic–plastic, and fully plastic fracture behaviors with K_{Ic} values of 71, 159, and 193 MPa·m$^{\frac{1}{2}}$, respectively. Scanning-electron-microscope views of the fracture surfaces after testing are shown in Fig. 2, and typical P–δ, acoustic emission, and adiabatic heating behaviors at a crosshead speed of 1.0 mm/min are shown in Fig. 3. The results, including fracture toughness properties, loading parameters, and failure mechanisms, are summarized in Table 3.

Linear Elastic Fracture

The Fe–18Cr–3Ni–13Mn steel at 4 K demonstrates brittle fracture behavior. The ratio of the net section fracture stress to the yield strength, R_{SC}, is 0.5. The failure mechanisms was transgranular cleavage on {111} planes, as shown in Fig. 2A and previously confirmed by X-ray diffraction.[7]

The P–δ curves are only slightly nonlinear prior to complete fracture at the maximum load, P_{max}. A high level of acoustic emission is observed beginning at low loads and continuing up to P_{max} (Fig. 3A). On the other hand, adiabatic heating is zero until the terminal stages of loading; then a small temperature rise, to 7 K, occurs owing to a minor pop-in, followed by a more substantial rise to 22.5 K during the final fracture (Fig. 3B).

Elastic–Plastic and Fully Plastic Fracture

Both the AISI 310S weld- and base-metal steels at 4 K display the essential aspects of ductile fracture: highly nonlinear P–δ curves, R_{SC} ratios greater than unity, and dimpled fracture surfaces corresponding to microvoid coalescence (MVC) processes (Fig. 2B,C). Compared with the weld metal, the base metal has significantly higher toughness and smaller, more numerous serrations. The fully plastic behavior (base metal) is distinguished from elastic–plastic behavior (weld metal) by its approach to limit load failure and its higher resistance to instability. The base metal also shows a higher displacement at maximum load, a higher T_m, a larger stretch zone size, and a larger average dimple diameter (Table 3).

In this paper, ductile fracture is viewed as follows: First, crack tip blunting occurs via stretch zone formation with microvoid or microcrack initiation. Ductile tearing then ensues as a macrocrack forms and advances

by linking with growing voids. At 4 K, this process is accompanied by discontinuous loading, which gives the P–δ curves a serrated appearance. Each load drop is a free-running event that occurs in milliseconds, accompanied by the evolution of heat and acoustic emission with audible sound. The load drops are faint at first but steadily increase as testing proceeds.

Continuous loading: During the initial stages of testing, the behavior featured stable deformation with smoothly rising loads. As nonlinear loading developed, the acoustic emission activity rose, owing presumably to plastic zone growth, microfracture events, or both. Adiabatic heating also developed during nonlinear loading, but only at a crosshead speed above some critical value. At the 1.0 mm/min speed, the maximum temperature during AISI 310S weld- and base-metal tests reached 4.8 and 8.0 K, respectively. On the other hand, at the lower speed of 0.1 mm/min (data not shown), the cooling from the cryogen was sufficient to prevent adiabatic heating during continuous loading.

As shown in Fig. 4A, it is possible to correlate the mutual rise of acoustic emission and temperature in terms of crosshead speed. In this graph, the change of the total acoustic emission energy per unit time ($\Delta\Sigma E_{AE}/\Delta t$) is plotted versus $\Delta T/\Delta t$, with data for both crosshead speeds. This result indicates the existence of a threshold acoustic emission rate at about 8.5×10^{-2} V^2s/s, below which adiabatic heating during continuous loading was zero for the AISI 310S steels of this study.

Discontinuous loading: As testing continued, load drops formed with increasing magnitude, coincident with high level bursts of acoustic emission and adiabatic heating. The temperature rise associated with each serration was transient and quickly fell to background levels after the discontinuous deformation was arrested. The temperature rise increases with ΔP, independent of material type for AISI 310S weld and base metal.

The acoustic emission bursts during serrations usually exceeded the signal saturation limits, even for a 20 dB gain. For the case of nonsaturated signals in an AISI 310S weld-metal test, however, a correlation between acoustic emission energy and ΔT for individual events is demonstrated in Fig. 4B.

DISCUSSION

On the basis of previous experience in general,[9,10] annealed austenitic stainless steels at 295 K must be classified as poor acoustic emission signal emitters. At 4 K, however, the situation changed favorably: all alloys were significantly strengthened, their ratios of tensile yield strength to ultimate tensile strength increased, and the process of serrated yielding with adiabatic heating was prominent in the elastic–plastic and fully plastic alloys. Reasoning inductively from the three examples of this study, we predict that most austenitic stainless steels will be acoustically active at 4 K. The acoustic emission technique is, therefore, an available tool for microfracture studies in these steels at 4 K.

The identification of acoustic emission sources by metallurgical methods was not pursued in this study, but the existence of correlations between acoustic emission and adiabatic heating implies that these parameters describe the same physical processes. In any case, the diverse failure mechanisms of these alloys provide a key to understanding the adiabatic heating results. In the high strength Fe–18Cr–3Ni–13Mn steel, cleavage fracture at 4 K was the result of an exceptionally high nitrogen content (0.37 wt.% N). In the medium strength AISI 310S weld- and base-metal materials, dimpled fracture occurred via the growth and coalescence of voids initiated at inclusion–matrix interfaces. The weld metal toughness was compromised, however, by a high inclusion content derived from welding, and thus, many more voids were initiated in the weld metal. The distance between voids was relatively small, and, compared with the base metal, less plastic work was required to cause fracture. Thus, the failure mechanisms determine the levels of toughness.

The maximum temperatures for the three alloys during their instability events were 22.5, 53, and 30.2 K (see Fig. 3). Since the corresponding crack extension increments were dissimilar, comparison is best made in terms of the normalizing parameter $T/\Delta a$. The three Δa increments are 24, 5.5, and 0.08 mm, respectively, where the first value is the ligament length for Fe–18Cr–3Ni–13Mn steel, and the other two values for AISI 310S weld- and base-metal steels were estimated from compliance changes made before and after serrations. On this basis, the adiabatic heating behavior during discontinuous loading is compared in Fig. 5. Also shown are the data for continuous loading. We suggest that adiabatic heating should correlate with the level of plastic deformation associated with fracture, as reflected by various physical and mechanical parameters. In Fig. 5, stretch zone size and J are taken to characterize crack initiation resistance; dimple size and tearing modulus function similarly for crack propagation.

Clearly, continuous loading contributes only a modest level of heating, and that can be totally eliminated by the appropriate selection of crosshead speed. But the huge temperature spikes that develop during serrations in plastic alloys are independent of crosshead speed at normal rates; they cannot be avoided, and their effects on fracture may be significant. The relevance of this finding to standard 4-K test procedures for elastic–plastic and fully plastic materials must be considered in future work.

CONCLUSIONS

High levels of acoustic emission are emitted during fracture testing of austenitic stainless steels at 4 K. Therefore, acoustic emission techniques appear to be useful for microfracture evaluations of these materials. In this study, two distinctly different correlations between acoustic emission and adiabatic heating were demonstrated for the continuous and discontinuous deformation stages of ductile fracture. Significant adiabatic heating occurred, and internal temperature rises of up to 53 K were reported. Apparently, the magnitude of heating can be explained in terms of the level of plastic deformation associated with fracture.

ACKNOWLEDGMENTS

This work was sponsored by the Ministry of Education of Japan (Monbusho), with the first author being supported by the U.S. Department of Energy, Office of Magnetic Fusion Energy. The authors are also indebted to Mr. K. Nakano (Tohoku University) for performing some of the tests.

REFERENCES

1. R. S. Kensley, K. Yoshida, H. Tsuji, and S. Shimamoto, Cryogenics, 23 (1983) 17–25.
2. J. Lore, N. Tamada, O. Tsukamoto, and Y. Iwasa, Cryogenics 24 (1984) 201–207.
3. T. Nishiura, K. Katagiri, S. Owaki, and T. Okada, Cryogenics, 24 (1984) 329–33.
4. M. Takeuchi, T. Shoji, H. Takahashi, and T. Anayama, Reports of the Research Institute for Strength and Fracture of Metals, Tohoku University, Sendai, Japan, 17 (1984) 1–12.
5. M. Takeuchi, T. Shoji, H. Takahashi, and T. Anayama, Trans. JSME (A), 51 (1985) 2256–2264 (in Japanese).
6. K. Ohnishi, T. Shoji, and H. Takahashi, Trans. JSME (A), 52 (1986) 170–173 (in Japanese).
7. R. L. Tobler and D. Meyn, in: "Materials Studies for Magnetic Fusion Energy Applications at Low Temperatures—VIII," NBSIR 85-3025, National Bureau of Standards, Boulder, Colorado (1985) 167–177.
8. H. Niitsuma, M. Kikuchi, H. Takahashi, M. Suzuki, and R. Sato, in: "Proceedings of the Fifth International Acoustic Emission Symposium," Japanese Society for Non-destructive Inspection, Tokyo (1980) 411–420.
9. T. Ingham, A. L. Stott, and A. Cowan, Int. J. Press. Ves. Piping 3 (1975) 247–293.
10. H. N. G. Wadley, C. B. Scruby, and J. H. Speake, Int. Met. Rev., Review 249, No. 2 (1980) 41–64.

Table 1. Chemical Compositions of Test Materials (wt.%)

Material	Cr	Ni	Mn	C	Si	P	S	N	Mo
Fe-18Cr-3Ni-13Mn	18.09	3.26	13.32	0.038	0.52	0.028	0.005	0.37	0.12
AISI 310S WM	24.68	20.96	2.10	0.10	0.48	0.002	0.003	—	—
AISI 310S BM	24.58	19.64	1.52	0.06	0.37	0.013	0.003	—	—

Table 2. Tensile Properties of Test Materials

Material	Temperature (K)	Yield Strength, σ_y (MPa)	Ultimate Tensile Strength, σ_u (MPa)	σ_y/σ_u	Elongation (%)
Fe-18Cr-3Ni-13Mn	295	440	796	0.55	56
	4	1540	1811	0.85	4
AISI 310S WM	293	319	577	0.55	26
	4	819	1048	0.78	12
AISI 310S BM	293	225	558	0.40	80
	4	796	1322	0.60	52

Table 3. Load Curve Characteristics, Fracture Properties, and Failure Mechanism Parameters at 4 K

Material	Curve Type	Load Drops	σ_y/σ_u	R_{SC}	J_{Ic} (kJ/m^2)	K_{Ic} (MPa·m$^{1/2}$)	T_m	Failure Mechanism	Stretch Zone Size (μm)	Dimple Size (μm)
Fe-18Cr-3Ni-13Mn	LE	one	0.85	0.5	24	71	0	cleavage	0	0
AISI 310S WM	EP	several	0.78	2.2	118	159	23	MVC	10	4
AISI 310S BM	FP	many	0.60	2.0	333	293	66	MVC	100	25

LE = linear elastic; EP = elastic-plastic; FP = fully plastic; MVC = microvoid coalescence

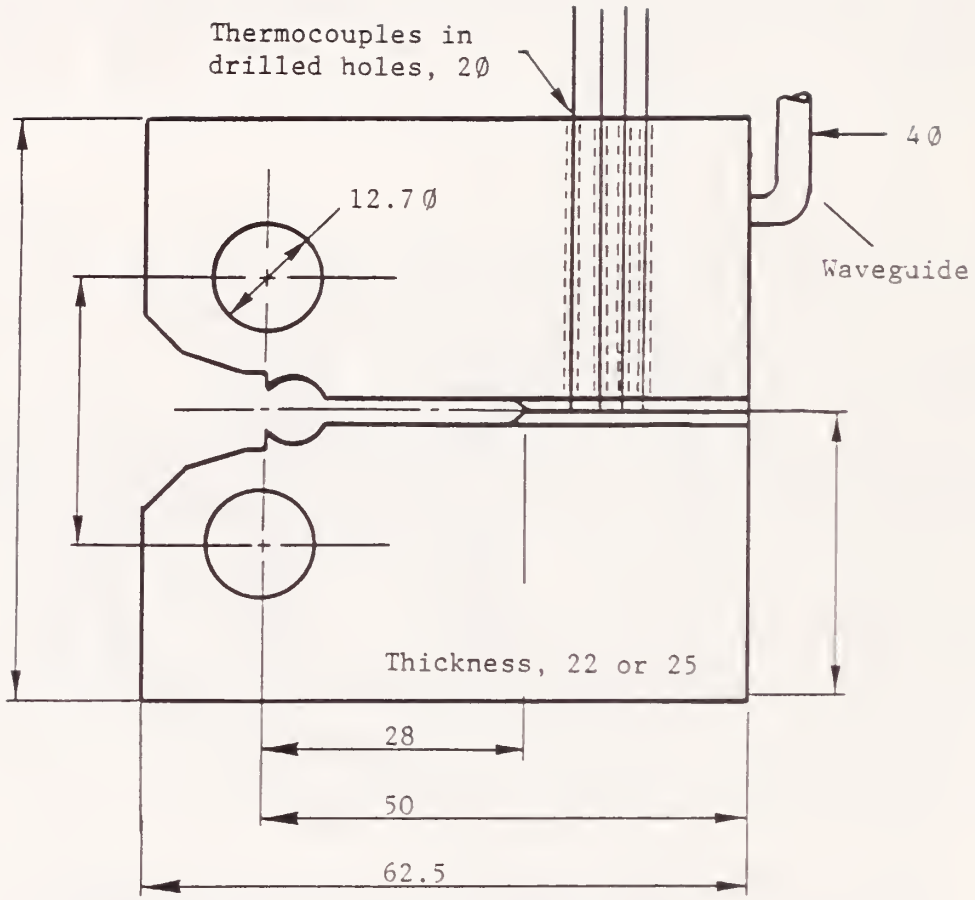

Fig. 1. Nominal 1TCT specimen with instrumentation (dimensions in millimeters).

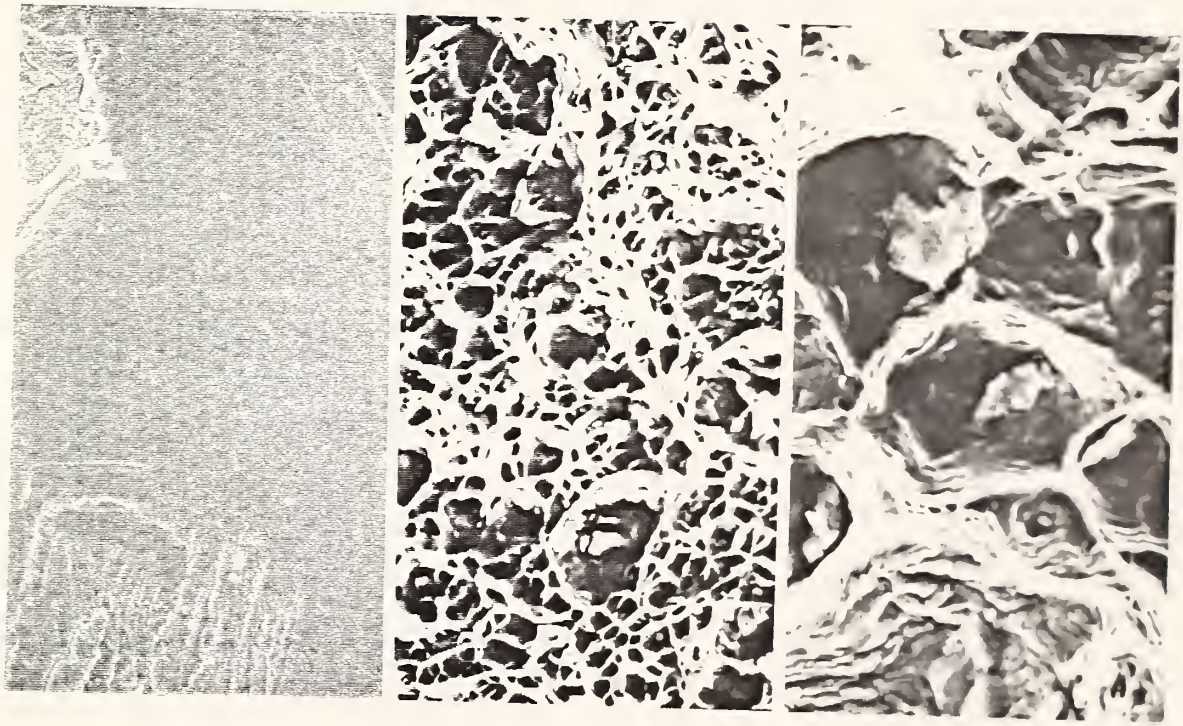

Fig. 2. SEM fractographs of the 4-K fracture surfaces: A, Fe–18Cr–3Ni–13Mn; B, AISI 310S WM; C, AISI 310S BM.

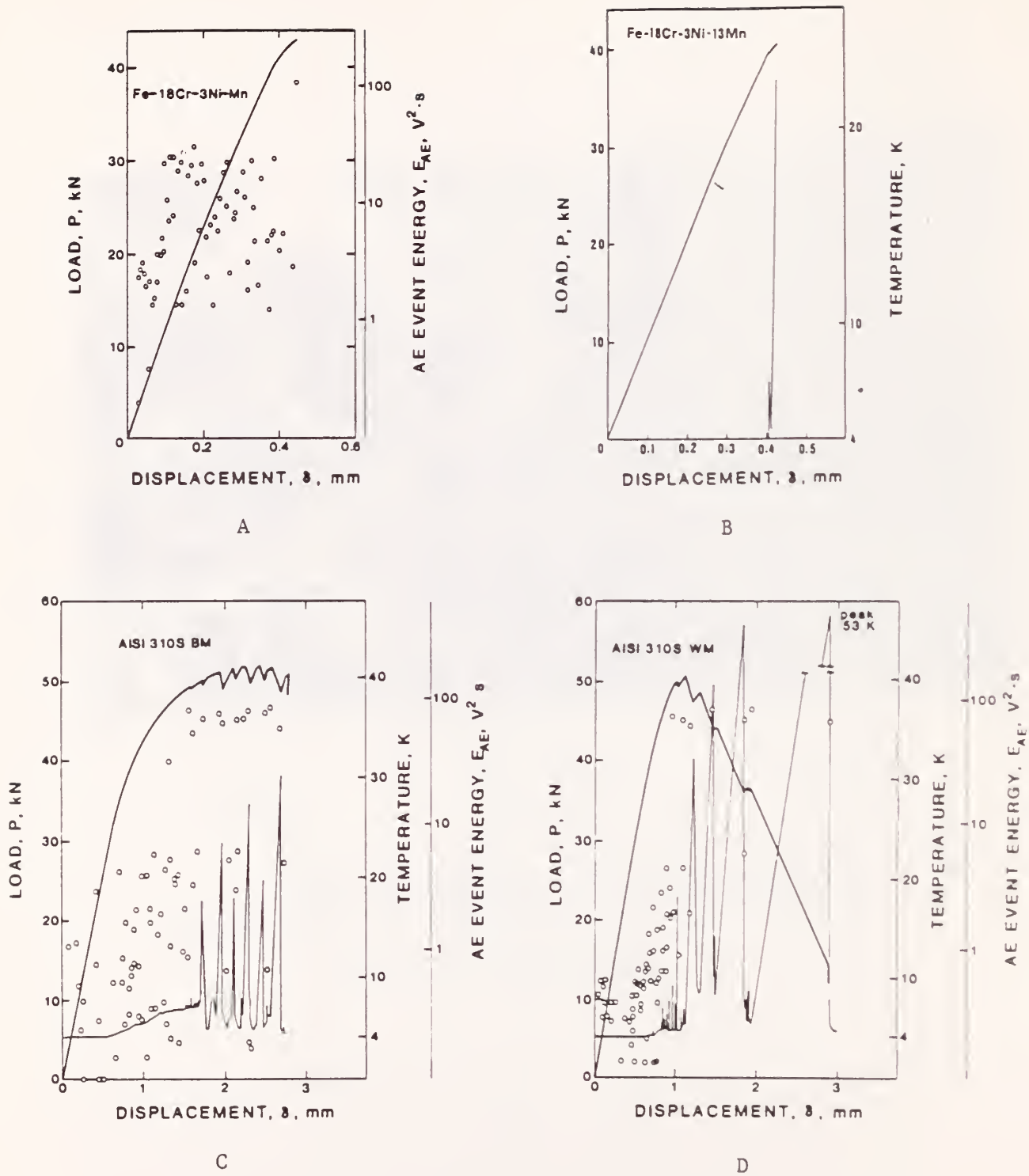

Figure 2. Load-versus-displacement records for three steels tested in liquid helium at 4 K, showing AE data and internal temperature response. (AE gain, 20 dB; crosshead speed, 1.0 mm/min).

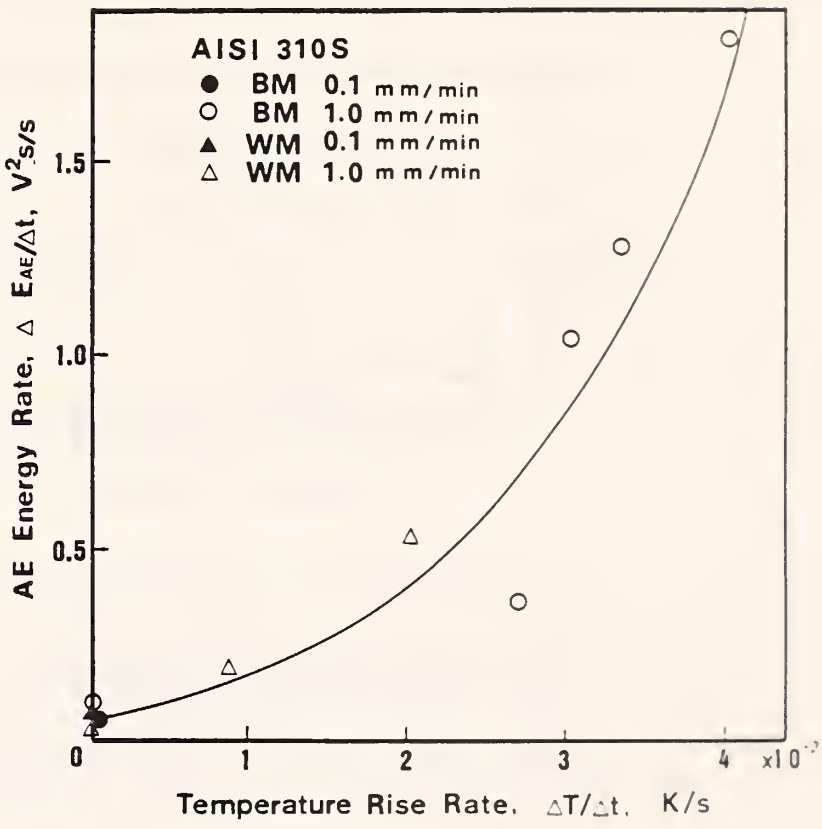

A

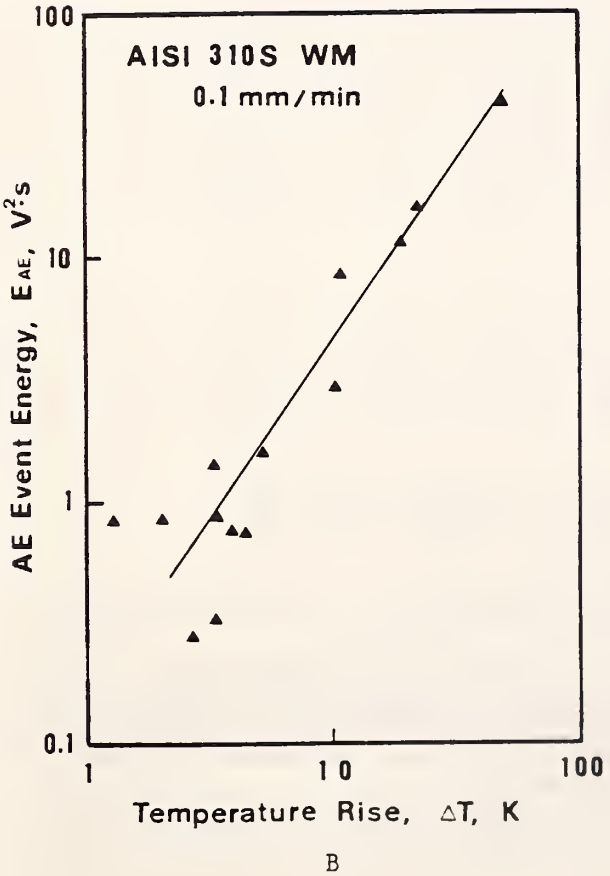

B

Fig. 4. Acoustic emission and adiabatic heating correlations
(A) for continuous loading;
(B) for serrations.

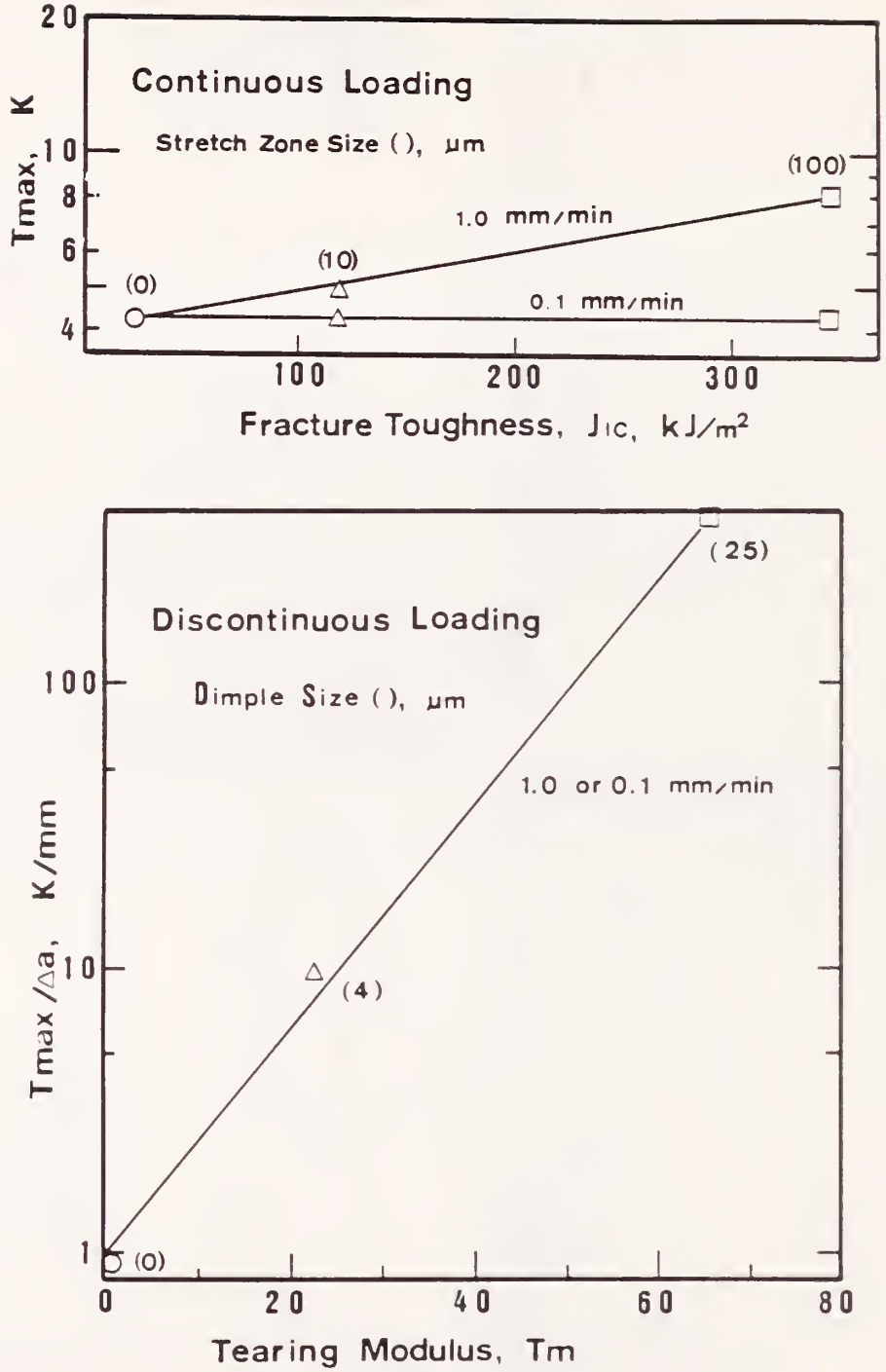

Fig. 5. Adiabatic heating dependence on toughness parameters. (A) maximum temperature observed in continuous loading; (B) maximum temperature per unit crack extension during final fracture or serration events.
O: Fe-18Cr-3Ni-13Mn; Δ: AISI 310S WM; □: AISI 310S BM

NBS-114A (REV. 2-8C)

U.S. DEPT. OF COMM. BIBLIOGRAPHIC DATA SHEET (See instructions)	1. PUBLICATION OR REPORT NO. NBSIR 87-3067	2. Performing Organ. Report No.	3. Publication Date May 1987

4. TITLE AND SUBTITLE

Materials Studies for Magnetic Fusion Energy Applications at Low Temperatures--X

5. AUTHOR(S)

R.P. Reed, Editor

6. PERFORMING ORGANIZATION (If joint or other than NBS, see instructions)

NATIONAL BUREAU OF STANDARDS
DEPARTMENT OF COMMERCE
WASHINGTON, D.C. 20234

7. Contract/Grant No.

8. Type of Report & Period Covered

9. SPONSORING ORGANIZATION NAME AND COMPLETE ADDRESS (Street, City, State, ZIP)

Department of Energy
Office of Fusion Energy
Washington, DC 20545

10. SUPPLEMENTARY NOTES

Previous reports in this series: NBSIR 86-3050, NBSIR 85-3025, NBSIR 84-3000, NBSIR 83-1690, NBSIR 82-1667, NBSIR 81-1645, NBSIR 80-1627, NBSIR 79-1609, NBSIR 78-884

☐ Document describes a computer program; SF-185, FIPS Software Summary, is attached.

11. ABSTRACT (A 200-word or less factual summary of most significant information. If document includes a significant bibliography or literature survey, mention it here)

This report contains the results of a research program to determine the properties of materials that may be used in cryogenic structures for the superconducting magnets of magnetic fusion energy power plants and prototypes. Its purpose is to facilitate their design and development. The program was developed jointly by the staffs of the National Bureau of Standards and the Office of Fusion Energy of the Department of Energy; it is managed by NBS and sponsored by DOE. Research is conducted at NBS and at other laboratories through subcontracts with NBS.

Research results for 1986 are presented in technical papers under five headings that reflect the main program areas: Structural Alloys, Welding, Nonmetallics, Technology Transfer, and United States-Japan Cooperative Program. Objectives and research highlights are summarized in the introduction to each program area.

12. KEY WORDS (Six to twelve entries; alphabetical order; capitalize only proper names; and separate key words by semicolons)

austenitic steels; composites; cryogenic properties; elastic properties; low temperatures; mechanical properties; nonmetallics; stainless steels; structural alloys; welds

13. AVAILABILITY

☒ Unlimited

☐ For Official Distribution. Do Not Release to NTIS

☐ Order From Superintendent of Documents, U.S. Government Printing Office, Washington, D.C. 20402.

☒ Order From National Technical Information Service (NTIS), Springfield, VA. 22161

14. NO. OF PRINTED PAGES 444

15. Price

USCOMM-DC [illegible]